

Introductory Raman Spectroscopy

(Second edition)

Elsevier, 2003

Author: John R. Ferraro, Kazuo Nakamoto and Chris W. Brown

ISBN: 978-0-12-254105-6

Preface to the Second Edition, Page x

Acknowledgments, Page xi

Preface to the First Edition, Page xii

Acknowledgments, Page xiii

Chapter 1 - Basic Theory, Pages 1-94

Chapter 2 - Instrumentation and Experimental Techniques, Pages 95-146

Chapter 3 - Special Techniques, Pages 147-206

Chapter 4 - Materials Applications, Pages 207-266

Chapter 5 - Analytical Chemistry, Pages 267-293

Chapter 6 - Biochemical and Medical Applications, Pages 295-324

Chapter 7 - Industrial, Environmental and Other Applications, Pages 325-361

Appendix 1 - Point Groups and Their Character Tables, Pages 364-370

Appendix 2 - General Formulas for Calculating the Number of Normal Vibrations in Each Symmetry Species, Pages 371-375

Appendix 3 - Direct Products of Irreducible Representations, Pages 376-377

Appendix 4 - Site Symmetries for the 230 Space Groups, Pages 378-383

Appendix 5 - Determination of the Proper Correlation Using Wyckoff's Tables, Pages 384-389

Appendix 6 - Correlation Tables, Pages 390-401

Appendix 7 - Principle of Laser Action, Pages 402-405

Appendix 8 - Raman Spectra of Typical Solvents, Pages 406-421

Index, Pages 423-434

Preface to the Second Edition

The second edition of *Introductory Raman Spectroscopy* treats the subject matter on an introductory level and serves as a guide for newcomers in the field.

Since the first edition of the book, the expansion of Raman spectroscopy as an analytical tool has continued. Thanks to advances in laser sources, detectors, and fiber optics, along with the capability to do imaging Raman spectroscopy, the continued versatility of FT-Raman, and dispersive based CCD Raman spectrometers, progress in Raman spectroscopy has flourished. The technique has moved out of the laboratory and into the workplace. In situ and remote measurements of chemical processes in the plant are becoming routine, even in hazardous environments.

This second edition contains seven chapters. Chapter 1 remains a discussion of basic theory. Chapter 2 expands the discussion on Instrumentation and Experimental Techniques. New discussions on FT-Raman and fiber optics are included. Sampling techniques used to monitor processes in corrosive environments are discussed. Chapter 3 concerns itself with Special Techniques; discussions on 2D correlation Raman spectroscopy and Raman imaging spectroscopy are provided. The new Chapter 4 deals with materials applications in structural chemistry and in solid state. A new section on polymorphs is presented and demonstrates the role of Raman spectroscopy in differentiating between polymorphs, an important industrial problem, particularly in the pharmaceutical field. The new Chapter 5 is based on analytical applications and methods for processing Raman spectral data, a subject that has generated considerable interest in the last ten years. The discussion commences with a general introduction to chemometric processing methods as they apply to Raman spectroscopy; it then proceeds to a discussion of some analytical applications of those methods. The new Chapter 6 presents applications in the field of biochemistry and in the medical field, a very rich and fertile area for Raman spectroscopy. Chapter 7 presents industrial applications, including some new areas such as ore refinement, the lumber/paper industry, natural gas analysis, the pharmaceutical/prescription drug industry, and polymers. The second edition, like the first, contains eight appendices.

With these inclusions, we believe that the book brings the subject of Raman spectroscopy into the new millennium.

Acknowledgments

The authors would like to express their thanks to Prof. Robert A. Condrate of Alfred University, Prof. Roman S. Czernuszewicz of the University of Houston, Dr. Victor A. Maroni of Argonne National Laboratory, and Prof. Masamichi Tsuboi of Iwaki-Meisei University of Japan who made many valuable suggestions. Special thanks are given to Roman S. Czernuszewicz for making drawings for Chapters 1 and 2. Our thanks and appreciation also go to Prof. Hiro-o Hamaguchi of Kanagawa Academy of Science and Technology of Japan and Prof. Akiko Hirakawa of the University of the Air of Japan who gave us permission to reproduce Raman spectra of typical solvents (Appendix 8). Professor Kazuo Nakamoto also extends thanks to Professor Yukihiro Ozaki of Kwansei-Gakuin University in Japan and to Professor Kasem Nithipatikom of the Medical College of Wisconsin for help in writing sections 3.7 and 6.2.4 of the second edition respectively. Professor Chris W. Brown would like to thank Su-Chin Lo of Merck Pharmaceutical Co. for aid in sections dealing with pharmaceuticals and Scott W. Huffman of the National Institute of Health for measuring Raman spectra of peptides. All three authors thank Mrs. Carla Kinney, editor for Academic Press, for her encouragement in the development of the second edition.

2002

John R. Ferraro
Kazuo Nakamoto
Chris W. Brown

Preface to the First Edition

Raman spectroscopy has made remarkable progress in recent years. The synergism that has taken place with the advent of new detectors, Fourier-transform Raman and fiber optics has stimulated renewed interest in the technique. Its use in academia and especially in industry has grown rapidly.

A well-balanced Raman text on an introductory level, which explains basic theory, instrumentation and experimental techniques (including special techniques), and a wide variety of applications (particularly the newer ones) is not available. The authors have attempted to meet this deficiency by writing this book. This book is intended to serve as a guide for beginners.

One problem we had in writing this book concerned itself in how one defines "introductory level." We have made a sincere effort to write this book on our definition of this level, and have kept mathematics at a minimum, albeit giving a logical development of basic theory.

The book consists of Chapters 1 to 4, and appendices. The first chapter deals with basic theory of spectroscopy; the second chapter discusses instrumentation and experimental techniques; the third chapter deals with special techniques; Chapter 4 presents applications of Raman spectroscopy in structural chemistry, biochemistry, biology and medicine, solid-state chemistry and industry. The appendices consist of eight sections. As much as possible, the authors have attempted to include the latest developments.

Acknowledgments

The authors would like to express their thanks to Prof. Robert A. Condrate of Alfred University, Prof. Roman S. Czernuszewicz of the University of Houston, Dr. Victor A. Maroni of Argonne National Laboratory, and Prof. Masamichi Tsuboi of Iwaki-Meisei University of Japan who made many valuable suggestions. Special thanks are given to Roman S. Czernuszewicz for making drawings for Chapters 1 and 2. Our thanks and appreciation also go to Prof. Hiro-o Hamaguchi of Kanagawa Academy of Science and Technology of Japan and Prof. Akiko Hirakawa of the University of the Air of Japan who gave us permission to reproduce Raman spectra of typical solvents (Appendix 8). We would also like to thank Ms. Jane Ellis, Acquisition Editor for Academic Press, Inc., who invited us to write this book and for her encouragement and help throughout the project. Finally, this book could not have been written without the help of many colleagues who allowed us to reproduce figures for publication.

1994

John R. Ferraro
Kazuo Nakamoto

Chapter 1

Basic Theory

1.1 Historical Background of Raman Spectroscopy

In 1928, when Sir Chandrasekhra Venkata Raman discovered the phenomenon that bears his name, only crude instrumentation was available. Sir Raman used sunlight as the source and a telescope as the collector; the detector was his eyes. That such a feeble phenomenon as the Raman scattering was detected was indeed remarkable.

Gradually, improvements in the various components of Raman instrumentation took place. Early research was concentrated on the development of better excitation sources. Various lamps of elements were developed (e.g., helium, bismuth, lead, zinc) (1–3). These proved to be unsatisfactory because of low light intensities. Mercury sources were also developed. An early mercury lamp which had been used for other purposes in 1914 by Kerschbaum (1) was developed. In the 1930s mercury lamps suitable for Raman use were designed (2). Hibben (3) developed a mercury burner in 1939, and Spedding and Stamm (4) experimented with a cooled version in 1942. Further progress was made by Rank and McCartney (5) in 1948, who studied mercury burners and their backgrounds. Hilger Co. developed a commercial mercury excitation source system for the Raman instrument, which consisted of four lamps surrounding the Raman tube. Welsh *et al.* (6) introduced a mercury source in 1952, which became known as the Toronto Arc. The lamp consisted of a four-turn helix of Pyrex tubing and was an improvement over the Hilger lamp. Improvements in lamps were made by

Ham and Walsh (7), who described the use of microwave-powered helium, mercury, sodium, rubidium and potassium lamps. Stammreich (8–12) also examined the practicality of using helium, argon, rubidium and cesium lamps for colored materials. In 1962 laser sources were developed for use with Raman spectroscopy (13). Eventually, the Ar^+ (351.1–514.5 nm) and the Kr^+ (337.4–676.4 nm) lasers became available, and more recently the Nd-YAG laser (1,064 nm) has been used for Raman spectroscopy (see Chapter 2, Section 2.2).

Progress occurred in the detection systems for Raman measurements. Whereas original measurements were made using photographic plates with the cumbersome development of photographic plates, photoelectric Raman instrumentation was developed after World War II. The first photoelectric Raman instrument was reported in 1942 by Rank and Wiegand (14), who used a cooled cascade type RCA IP21 detector. The Heigl instrument appeared in 1950 and used a cooled RCA C-7073B photomultiplier. In 1953 Stamm and Salzman (15) reported the development of photoelectric Raman instrumentation using a cooled RCA IP21 photomultiplier tube. The Hilger E612 instrument (16) was also produced at this time, which could be used as a photographic or photoelectric instrument. In the photoelectric mode a photomultiplier was used as the detector. This was followed by the introduction of the Cary Model 81 Raman spectrometer (17). The source used was the 3 kW helical Hg arc of the Toronto type. The instrument employed a twin-grating, twin-slit double monochromator.

Developments in the optical train of Raman instrumentation took place in the early 1960s. It was discovered that a double monochromator removed stray light more efficiently than a single monochromator. Later, a triple monochromator was introduced, which was even more efficient in removing stray light. Holographic gratings appeared in 1968 (17), which added to the efficiency of the collection of Raman scattering in commercial Raman instruments.

These developments in Raman instrumentation brought commercial Raman instruments to the present state of the art of Raman measurements. Now, Raman spectra can also be obtained by Fourier transform (FT) spectroscopy. FT-Raman instruments are being sold by all Fourier transform infrared (FT-IR) instrument makers, either as interfaced units to the FT-IR spectrometer or as dedicated FT-Raman instruments.

1.2 Energy Units and Molecular Spectra

Figure 1-1 illustrates a wave of polarized electromagnetic radiation traveling in the z -direction. It consists of the electric component (x -direction) and magnetic component (y -direction), which are perpendicular to each other.

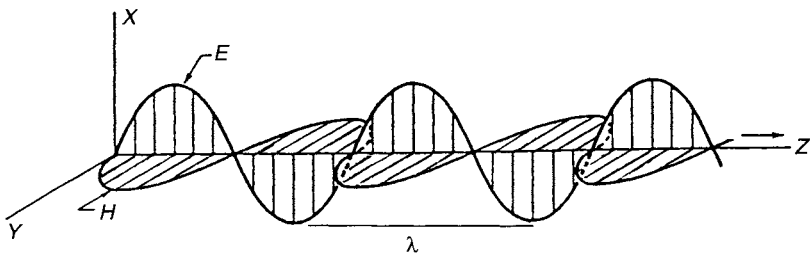


Figure 1-1 Plane-polarized electromagnetic radiation.

Hereafter, we will consider only the former since topics discussed in this book do not involve magnetic phenomena. The electric field strength (E) at a given time (t) is expressed by

$$E = E_0 \cos 2\pi v t, \quad (1-1)$$

where E_0 is the amplitude and v is the frequency of radiation as defined later.

The distance between two points of the same phase in successive waves is called the “wavelength,” λ , which is measured in units such as Å (angstrom), nm (nanometer), $m\mu$ (millimicron), and cm (centimeter). The relationships between these units are:

$$1 \text{ \AA} = 10^{-8} \text{ cm} = 10^{-1} \text{ nm} = 10^{-1} m\mu. \quad (1-2)$$

Thus, for example, $4,000 \text{ \AA} = 400 \text{ nm} = 400 m\mu$.

The frequency, v , is the number of waves in the distance light travels in one second. Thus,

$$v = \frac{c}{\lambda}, \quad (1-3)$$

where c is the velocity of light (3×10^{10} cm/s). If λ is in the unit of centimeters, its dimension is $(\text{cm}/\text{s})/(\text{cm}) = 1/\text{s}$. This “reciprocal second” unit is also called the “hertz” (Hz).

The third parameter, which is most common to vibrational spectroscopy, is the “wavenumber,” \tilde{v} , defined by

$$\tilde{v} = \frac{v}{c}. \quad (1-4)$$

The difference between v and \tilde{v} is obvious. It has the dimension of $(1/\text{s})/(\text{cm}/\text{s}) = 1/\text{cm}$. By combining (1-3) and (1-4) we have

$$\tilde{v} = \frac{v}{c} = \frac{1}{\lambda} (\text{cm}^{-1}). \quad (1-5)$$

Table 1-1 Units Used in Spectroscopy*

10^{12}	tera	T
10^9	giga	G
10^6	mega	M
10^3	kilo	k
10^2	hecto	h
10^1	deca	da
10^{-1}	deci	d
10^{-2}	centi	c
10^{-3}	milli	m
10^{-6}	micro	μ
10^{-9}	nano	n
10^{-12}	pico	p
10^{-15}	femto	f
10^{-18}	atto	a

*Notations: T, G, M, k, h, da, μ , n—Greek; d, c, m—Latin; p—Spanish; f—Swedish; a—Danish.

Thus, 4,000 Å corresponds to $25 \times 10^3 \text{ cm}^{-1}$, since

$$\tilde{\nu} = \frac{1}{\lambda(\text{cm})} = \frac{1}{4 \times 10^3 \times 10^{-8}} = 25 \times 10^3 \text{ (cm}^{-1}\text{)}.$$

Table 1-1 lists units frequently used in spectroscopy. By combining (1-3) and (1-4), we obtain

$$\nu = \frac{c}{\lambda} = c\tilde{\nu}. \quad (1-6)$$

As shown earlier, the wavenumber ($\tilde{\nu}$) and frequency (ν) are different parameters, yet these two terms are often used interchangeably. Thus, an expression such as “frequency shift of 30 cm^{-1} ” is used conventionally by IR and Raman spectroscopists and we will follow this convention through this book.

If a molecule interacts with an electromagnetic field, a transfer of energy from the field to the molecule can occur only when Bohr's frequency condition is satisfied. Namely,

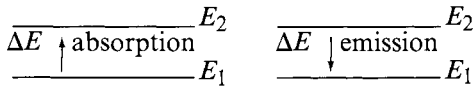
$$\Delta E = h\nu = h\frac{c}{\lambda} = hc\tilde{\nu}. \quad (1-7)$$

Here ΔE is the difference in energy between two quantized states, h is Planck's constant ($6.62 \times 10^{-27} \text{ erg s}$) and c is the velocity of light. Thus, $\tilde{\nu}$ is directly proportional to the energy of transition.

Suppose that

$$\Delta E = E_2 - E_1, \quad (1-8)$$

where E_2 and E_1 are the energies of the excited and ground states, respectively. Then, the molecule “absorbs” ΔE when it is excited from E_1 to E_2 , and “emits” ΔE when it reverts from E_2 to E_1^* .



Using the relationship given by Eq. (1-7), Eq. (1-8) is written as

$$\Delta E = E_2 - E_1 = hc\tilde{\nu}. \quad (1-9)$$

Since h and c are known constants, ΔE can be expressed in terms of various energy units. Thus, 1 cm^{-1} is equivalent to

$$\begin{aligned} \Delta E &= [6.62 \times 10^{-27} \text{ (erg s)}][3 \times 10^{10} \text{ (cm/s)}][1(1/\text{cm})] \\ &= 1.99 \times 10^{-16} \text{ (erg/molecule)} \\ &= 1.99 \times 10^{-23} \text{ (joule/molecule)} \\ &= 2.86 \text{ (cal/mole)} \\ &= 1.24 \times 10^{-4} \text{ (eV/molecule)} \end{aligned}$$

In the preceding conversions, the following factors were used:

$$\begin{aligned} 1 \text{ (erg/molecule)} &= 2.39 \times 10^{-8} \text{ (cal/molecule)} \\ &= 1 \times 10^{-7} \text{ (joule/molecule)} \\ &= 6.2422 \times 10^{11} \text{ (eV/molecule)} \end{aligned}$$

$$\text{Avogadro number, } N_o = 6.025 \times 10^{23} \text{ (1/mole)}$$

$$1 \text{ (cal)} = 4.184 \text{ (joule)}$$

Figure 1-2 compares the order of energy expressed in terms of $\tilde{\nu} (\text{cm}^{-1})$, $\lambda (\text{cm})$ and $\nu (\text{Hz})$.

As indicated in Fig. 1-2 and Table 1-2, the magnitude of ΔE is different depending upon the origin of the transition. In this book, we are mainly concerned with vibrational transitions which are observed in infrared (IR) or Raman spectra**. These transitions appear in the $10^4 \sim 10^2 \text{ cm}^{-1}$ region and

*If a molecule loses ΔE via molecular collision, it is called a “radiationless transition.”

**Pure rotational and rotational-vibrational transitions are also observed in IR and Raman spectra. Many excellent textbooks are available on these and other subjects (see general references given at the end of this chapter).

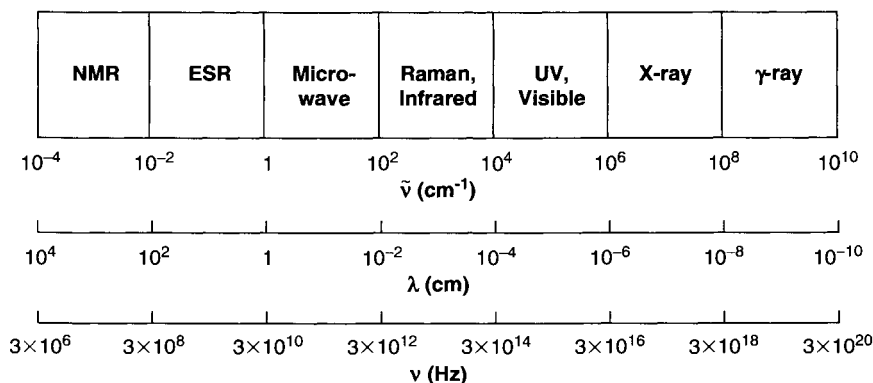


Figure 1-2 Energy units for various portions of electromagnetic spectrum.

Table 1-2 Spectral Regions and Their Origins

Spectroscopy	Range ($\tilde{\nu}$, cm^{-1})	Origin
γ-ray	$10^{10} - 10^8$	Rearrangement of elementary particles in the nucleus
X-ray (ESCA, PES)	$10^8 - 10^6$	Transitions between energy levels of inner electrons of atoms and molecules
UV-Visible	$10^6 - 10^4$	Transitions between energy levels of valence electrons of atoms and molecules
Raman and infrared	$10^4 - 10^2$	Transitions between vibrational levels (change of configuration)
Microwave	$10^2 - 1$	Transitions between rotational levels (change of orientation)
Electron spin resonance (ESR)	$1 - 10^{-2}$	Transitions between electron spin levels in magnetic field
Nuclear magnetic resonance (NMR)	$10^{-2} - 10^{-4}$	Transitions between nuclear spin levels in magnetic fields

originate from vibrations of nuclei constituting the molecule. As will be shown later, Raman spectra are intimately related to electronic transitions. Thus, it is important to know the relationship between electronic and vibrational states. On the other hand, vibrational spectra of small molecules in the gaseous state exhibit rotational fine structures.* Thus, it is also important to

*In solution, rotational fine structures are not observed because molecular collisions (10^{-13}s) occur before one rotation is completed (10^{-11}s) and the levels of individual molecules are perturbed differently. In the solid state, molecular rotation does not occur because of intermolecular interactions.

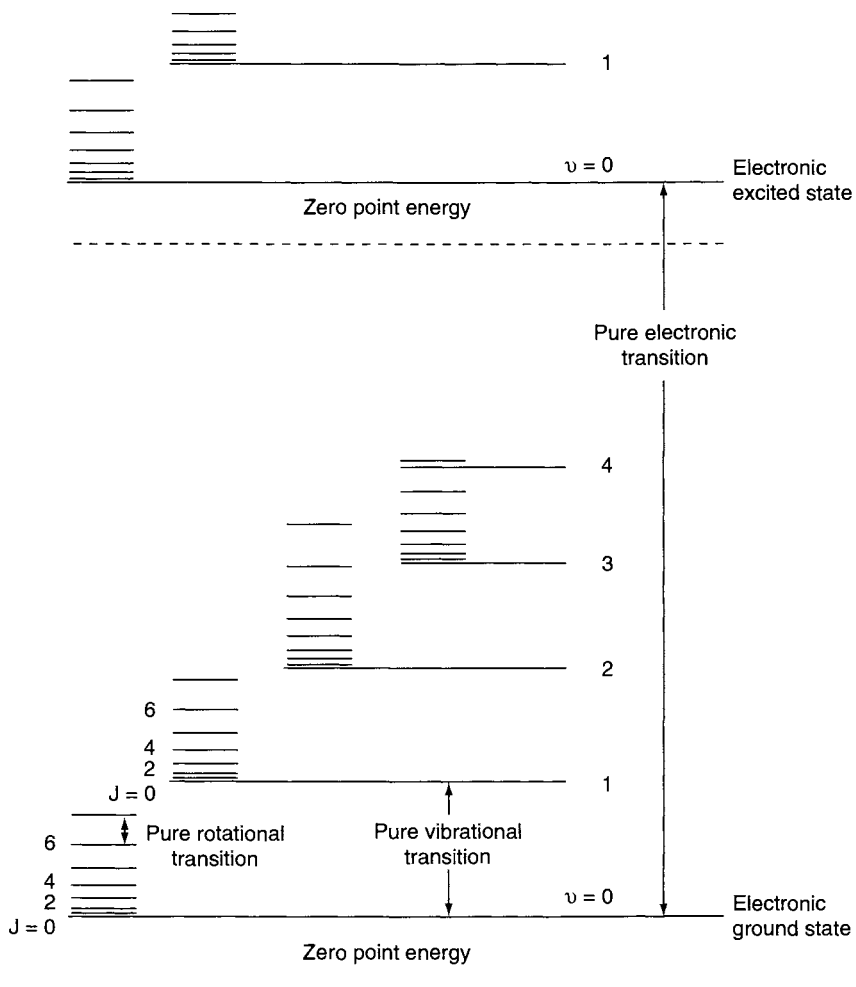
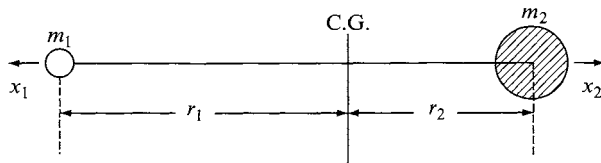


Figure 1-3 Energy levels of a diatomic molecule. (The actual spacings of electronic levels are much larger, and those of rotational levels much smaller, than those shown in the figure.)

know the relationship between vibrational and rotational states. Figure 1-3 illustrates the three types of transitions for a diatomic molecule.

1.3 Vibration of a Diatomic Molecule

Consider the vibration of a diatomic molecule in which two atoms are connected by a chemical bond.



Here, \$m_1\$ and \$m_2\$ are the masses of atom 1 and 2, respectively, and \$r_1\$ and \$r_2\$ are the distances from the center of gravity (C.G.) to the atoms designated. Thus, \$r_1 + r_2\$ is the equilibrium distance, and \$x_1\$ and \$x_2\$ are the displacements of atoms 1 and 2, respectively, from their equilibrium positions. Then, the conservation of the center of gravity requires the relationships:

$$m_1 r_1 = m_2 r_2, \quad (1-10)$$

$$m_1(r_1 + x_1) = m_2(r_2 + x_2). \quad (1-11)$$

Combining these two equations, we obtain

$$x_1 = \left(\frac{m_2}{m_1} \right) x_2 \quad \text{or} \quad x_2 = \left(\frac{m_1}{m_2} \right) x_1. \quad (1-12)$$

In the classical treatment, the chemical bond is regarded as a spring that obeys Hooke's law, where the restoring force, \$f\$, is expressed as

$$f = -K(x_1 + x_2). \quad (1-13)$$

Here \$K\$ is the force constant, and the minus sign indicates that the directions of the force and the displacement are opposite to each other. From (1-12) and (1-13), we obtain

$$f = -K \left(\frac{m_1 + m_2}{m_1} \right) x_2 = -K \left(\frac{m_1 + m_2}{m_2} \right) x_1. \quad (1-14)$$

Newton's equation of motion (\$f = ma; m = \text{mass}; a = \text{acceleration}\$) is written for each atom as

$$m_1 \frac{d^2 x_1}{dt^2} = -K \left(\frac{m_1 + m_2}{m_2} \right) x_1, \quad (1-15)$$

$$m_2 \frac{d^2 x_2}{dt^2} = -K \left(\frac{m_1 + m_2}{m_1} \right) x_2. \quad (1-16)$$

By adding

$$(1-15) \times \left(\frac{m_2}{m_1 + m_2} \right) \quad \text{and} \quad (1-16) \times \left(\frac{m_1}{m_1 + m_2} \right),$$

we obtain

$$\frac{m_1 m_2}{m_1 + m_2} \left(\frac{d^2 x_1}{dt^2} + \frac{d^2 x_2}{dt^2} \right) = -K(x_1 + x_2). \quad (1-17)$$

Introducing the reduced mass (μ) and the displacement (q), (1-17) is written as

$$\mu \frac{d^2 q}{dt^2} = -Kq. \quad (1-18)$$

The solution of this differential equation is

$$q = q_0 \sin(2\pi\nu_0 t + \varphi), \quad (1-19)$$

where q_0 is the maximum displacement and φ is the phase constant, which depends on the initial conditions. ν_0 is the classical vibrational frequency given by

$$\nu_0 = \frac{1}{2\pi} \sqrt{\frac{K}{\mu}}. \quad (1-20)$$

The potential energy (V) is defined by

$$dV = -f dq = Kq dq.$$

Thus, it is given by

$$\begin{aligned} V &= \frac{1}{2} Kq^2 \\ &= \frac{1}{2} Kq_0^2 \sin^2(2\pi\nu_0 t + \varphi) \\ &= 2\pi^2 \nu_0^2 \mu q_0^2 \sin^2(2\pi\nu_0 t + \varphi). \end{aligned} \quad (1-21)$$

The kinetic energy (T) is

$$\begin{aligned} T &= \frac{1}{2} m_1 \left(\frac{dx_1}{dt} \right)^2 + \frac{1}{2} m_2 \left(\frac{dx_2}{dt} \right)^2 \\ &= \frac{1}{2} \mu \left(\frac{dq}{dt} \right)^2 \\ &= 2\pi^2 \nu_0^2 \mu q_0^2 \cos^2(2\pi\nu_0 t + \varphi). \end{aligned} \quad (1-22)$$

Thus, the total energy (E) is

$$\begin{aligned} E &= T + V \\ &= 2\pi^2 \nu_0^2 \mu q_0^2 = \text{constant} \end{aligned} \quad (1-23)$$

Figure 1-4 shows the plot of V as a function of q . This is a parabolic potential, $V = \frac{1}{2} Kq^2$, with $E = T$ at $q = 0$ and $E = V$ at $q = \pm q_0$. Such a vibrator is called a *harmonic oscillator*.

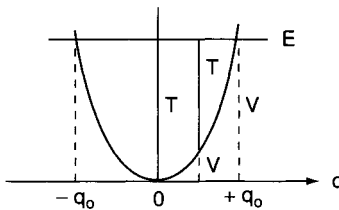


Figure 1-4 Potential energy diagram for a harmonic oscillator.

In quantum mechanics (18,19) the vibration of a diatomic molecule can be treated as a motion of a single particle having mass μ whose potential energy is expressed by (1-21). The Schrödinger equation for such a system is written as

$$\frac{d^2\psi}{dq^2} + \frac{8\pi^2\mu}{h^2} \left(E - \frac{1}{2}Kq^2 \right) \psi = 0. \quad (1-24)$$

If (1-24) is solved with the condition that ψ must be single-valued, finite and continuous, the eigenvalues are

$$E_v = \hbar v \left(v + \frac{1}{2} \right) = \hbar c \tilde{v} \left(v + \frac{1}{2} \right), \quad (1-25)$$

with the frequency of vibration

$$v = \frac{1}{2\pi} \sqrt{\frac{K}{\mu}} \quad \text{or} \quad \tilde{v} = \frac{1}{2\pi c} \sqrt{\frac{K}{\mu}}. \quad (1-26)$$

Here, v is the vibrational quantum number, and it can have the values 0, 1, 2, 3, ... The corresponding eigenfunctions are

$$\psi_v = \frac{(\alpha/\pi)^{1/4}}{\sqrt{2^v v!}} e^{-\alpha q^2/2} H_v(\sqrt{\alpha}q), \quad (1-27)$$

where

$$\alpha = 2\pi\sqrt{\mu K/h} = 4\pi^2\mu v/h \quad \text{and} \quad H_v(\sqrt{\alpha}q)$$

is a Hermite polynomial of the v th degree. Thus, the eigenvalues and the corresponding eigenfunctions are

$$\begin{aligned} v = 0, \quad E_0 &= \frac{1}{2}\hbar v, \quad \psi_0 = (\alpha/\pi)^{1/4} e^{-\alpha q^2/2} \\ v = 1, \quad E_1 &= \frac{3}{2}\hbar v, \quad \psi_1 = (\alpha/\pi)^{1/4} 2^{1/2} q e^{-\alpha q^2/2}. \\ &\vdots \quad \vdots \quad \vdots \end{aligned} \quad (1-28)$$

One should note that the quantum-mechanical frequency (1-26) is exactly the same as the classical frequency (1-20). However, several marked differences must be noted between the two treatments. First, classically, E is zero when q is zero. Quantum-mechanically, the lowest energy state ($v = 0$) has the energy of $\frac{1}{2}\hbar\nu$ (zero point energy) (see Fig. 1-3) which results from Heisenberg's uncertainty principle. Secondly, the energy of a such a vibrator can change continuously in classical mechanics. In quantum mechanics, the energy can change only in units of $\hbar\nu$. Thirdly, the vibration is confined within the parabola in classical mechanics since T becomes negative if $|q| > |q_0|$ (see Fig. 1-4). In quantum mechanics, the probability of finding q outside the parabola is not zero (tunnel effect) (Fig. 1-5).

In the case of a harmonic oscillator, the separation between the two successive vibrational levels is always the same ($\hbar\nu$). This is not the case of an actual molecule whose potential is approximated by the Morse potential function shown by the solid curve in Fig. 1-6.

$$V = D_e \left(1 - e^{-\beta q}\right)^2. \quad (1-29)$$

Here, D_e is the dissociation energy and β is a measure of the curvature at the bottom of the potential well. If the Schrödinger equation is solved with this potential, the eigenvalues are (18,19)

$$E_v = \hbar c \omega_e \left(v + \frac{1}{2}\right) - \hbar c \chi_e \omega_e \left(v + \frac{1}{2}\right)^2 + \dots, \quad (1-30)$$

where ω_e is the wavenumber corrected for anharmonicity, and $\chi_e \omega_e$ indicates the magnitude of anharmonicity. Equation (1-30) shows that the energy levels of the anharmonic oscillator are no longer equidistant, and the separation decreases with increasing v as shown in Fig. 1-6. Thus far, anharmonicity

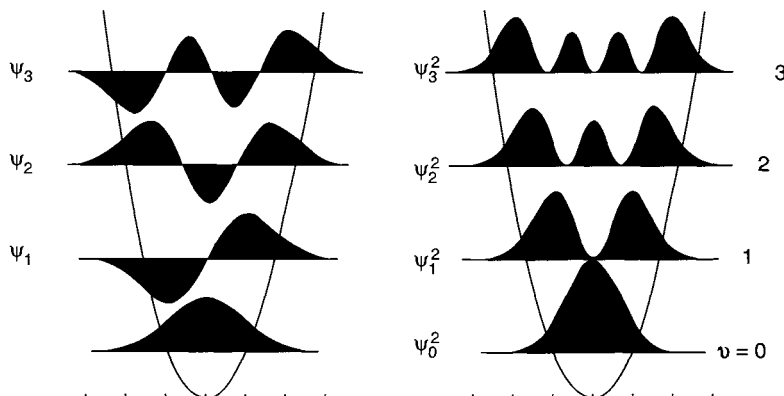


Figure 1-5 Wave functions (left) and probability distributions (right) of the harmonic oscillator.

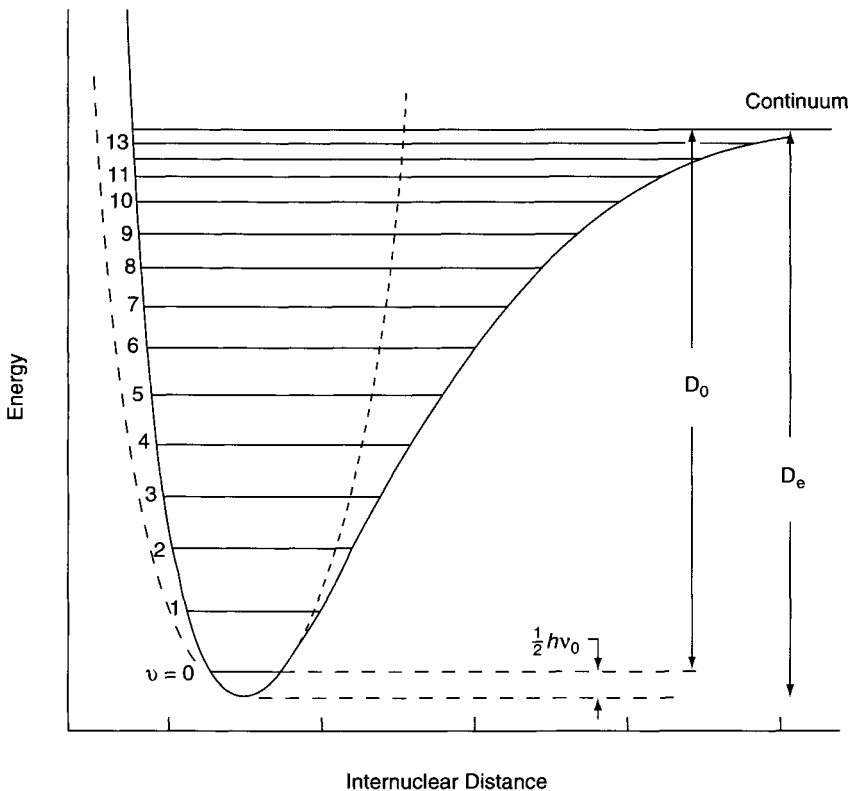


Figure 1-6 Potential energy curve for a diatomic molecule. Solid line indicates a Morse potential that approximates the actual potential. Broken line is a parabolic potential for a harmonic oscillator. D_e and D_0 are the theoretical and spectroscopic dissociation energies, respectively.

corrections have been made mostly on diatomic molecules (see Table 1-3), because of the complexity of calculations for large molecules.

According to quantum mechanics, only those transitions involving $\Delta v = \pm 1$ are allowed for a harmonic oscillator. If the vibration is anharmonic, however, transitions involving $\Delta v = \pm 2, \pm 3, \dots$ (overtones) are also weakly allowed by selection rules. Among many $\Delta v = \pm 1$ transitions, that of $v = 0 \leftrightarrow 1$ (fundamental) appears most strongly both in IR and Raman spectra. This is expected from the Maxwell-Boltzmann distribution law, which states that the population ratio of the $v = 1$ and $v = 0$ states is given by

$$\frac{P_{v=1}}{P_{v=0}} = e^{-\Delta E/kT}, \quad (1-31)$$

Table 1-3 Relationships among Vibrational Frequency, Reduced Mass and Force Constant

Molecule	Obs. $\tilde{\nu}$ (cm $^{-1}$)	ω_e (cm $^{-1}$)	μ (awu)	K (mdyn/Å)
H ₂	4,160	4,395	0.5041	5.73
HD	3,632	3,817	0.6719	5.77
D ₂	2,994	3,118	1.0074	5.77
HF	3,962	4,139	0.9573	9.65
HCl	2,886	2,989	0.9799	5.16
HBr	2,558	2,650	0.9956	4.12
HI	2,233	2,310	1.002	3.12
F ₂	892	—	9.5023	4.45
Cl ₂	546	565	17.4814	3.19
Br ₂	319	323	39.958	2.46
I ₂	213	215	63.466	1.76
N ₂	2,331	2,360	7.004	22.9
CO	2,145	2,170	6.8584	19.0
NO	1,877	1,904	7.4688	15.8
O ₂	1,555	1,580	8.000	11.8

where ΔE is the energy difference between the two states, k is Boltzmann's constant (1.3807×10^{-16} erg/degree), and T is the absolute temperature. Since $\Delta E = hc\tilde{\nu}$, the ratio becomes smaller as $\tilde{\nu}$ becomes larger. At room temperature,

$$\begin{aligned}
 kT &= 1.38 \times 10^{-6} \text{ (erg/degree)} \cdot 300 \text{ (degree)} \\
 &= 4.14 \times 10^{-14} \text{ (erg)} \\
 &= [4.14 \times 10^{-14} \text{ (erg)}] / [1.99 \times 10^{-16} \text{ (erg/cm}^{-1}\text{)}] \\
 &= 208 \text{ (cm}^{-1}\text{).}
 \end{aligned}$$

Thus, if $\tilde{\nu} = 4,160 \text{ cm}^{-1}$ (H₂ molecule), $P(v=1)/P(v=0) = 2.19 \times 10^{-9}$. Therefore, almost all of the molecules are at $v=0$. On the other hand, if $\tilde{\nu} = 213 \text{ cm}^{-1}$ (I₂ molecule), this ratio becomes 0.36. Thus, about 27% of the I₂ molecules are at $v=1$ state. In this case, the transition $v=1 \rightarrow 2$ should be observed on the low-frequency side of the fundamental with much less intensity. Such a transition is called a "hot band" since it tends to appear at higher temperatures.

1.4 Origin of Raman Spectra

As stated in Section 1.1, vibrational transitions can be observed in either IR or Raman spectra. In the former, we measure the absorption of infrared light by the sample as a function of frequency. The molecule absorbs $\Delta E = hv$ from

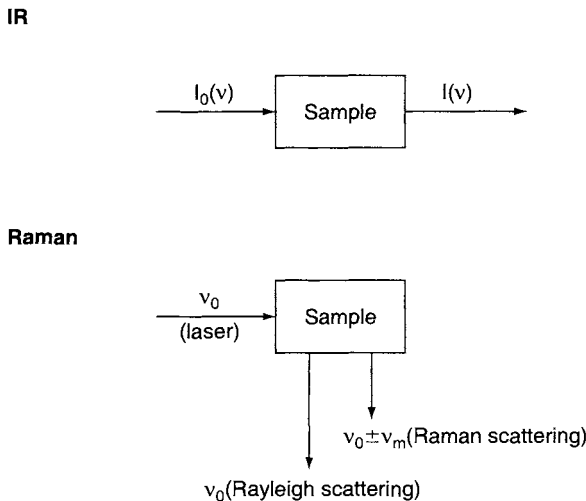


Figure 1-7 Differences in mechanism of Raman vs IR.

the IR source at each vibrational transition. The intensity of IR absorption is governed by the Beer–Lambert law:

$$I = I_0 e^{-\varepsilon c d}. \quad (1-32)$$

Here, I_0 and I denote the intensities of the incident and transmitted beams, respectively, ε is the molecular absorption coefficient,* and c and d are the concentration of the sample and the cell length, respectively (Fig. 1-7). In IR spectroscopy, it is customary to plot the percentage transmission (T) versus wave number (\bar{v}):

$$T(\%) = \frac{I}{I_0} \times 100. \quad (1-33)$$

It should be noted that T (%) is not proportional to c . For quantitative analysis, the absorbance (A) defined here should be used:

$$A = \log \frac{I_0}{I} = \varepsilon c d. \quad (1-34)$$

The origin of Raman spectra is markedly different from that of IR spectra. In Raman spectroscopy, the sample is irradiated by intense laser beams in the UV-visible region (v_0), and the scattered light is usually observed in the direction perpendicular to the incident beam (Fig. 1-7; see also Chapter 2,

* ε has the dimension of 1/moles cm when c and d are expressed in units of moles/liter and centimeters, respectively.

Section 2.3). The scattered light consists of two types: one, called *Rayleigh scattering*, is strong and has the same frequency as the incident beam (v_0), and the other, called *Raman scattering*, is very weak ($\sim 10^{-5}$ of the incident beam) and has frequencies $v_0 \pm v_m$, where v_m is a vibrational frequency of a molecule. The $v_0 - v_m$ and $v_0 + v_m$ lines are called the *Stokes* and *anti-Stokes* lines, respectively. Thus, in Raman spectroscopy, we measure the vibrational frequency (v_m) as a shift from the incident beam frequency (v_0).^{*} In contrast to IR spectra, Raman spectra are measured in the UV-visible region where the excitation as well as Raman lines appear.

According to classical theory, Raman scattering can be explained as follows: The electric field strength (E) of the electromagnetic wave (laser beam) fluctuates with time (t) as shown by Eq. (1-1):

$$E = E_0 \cos 2\pi v_0 t, \quad (1-35)$$

where E_0 is the vibrational amplitude and v_0 is the frequency of the laser. If a diatomic molecule is irradiated by this light, an electric dipole moment P is induced:

$$P = \alpha E = \alpha E_0 \cos 2\pi v_0 t. \quad (1-36)$$

Here, α is a proportionality constant and is called *polarizability*. If the molecule is vibrating with a frequency v_m , the nuclear displacement q is written

$$q = q_0 \cos 2\pi v_m t, \quad (1-37)$$

where q_0 is the vibrational amplitude. For a small amplitude of vibration, α is a linear function of q . Thus, we can write

$$\alpha = \alpha_0 + \left(\frac{\partial \alpha}{\partial q} \right)_0 q_0 + \dots \quad (1-38)$$

Here, α_0 is the polarizability at the equilibrium position, and $(\partial \alpha / \partial q)_0$ is the rate of change of α with respect to the change in q , evaluated at the equilibrium position.

Combining (1-36) with (1-37) and (1-38), we obtain

$$\begin{aligned} P &= \alpha E_0 \cos 2\pi v_0 t \\ &= \alpha_0 E_0 \cos 2\pi v_0 t + \left(\frac{\partial \alpha}{\partial q} \right)_0 q_0 E_0 \cos 2\pi v_0 t \\ &= \alpha_0 E_0 \cos 2\pi v_0 t + \left(\frac{\partial \alpha}{\partial q} \right)_0 q_0 E_0 \cos 2\pi v_0 t \cos 2\pi v_m t \end{aligned}$$

^{*}Although Raman spectra are normally observed for vibrational and rotational transitions, it is possible to observe Raman spectra of electronic transitions between ground states and low-energy excited states.

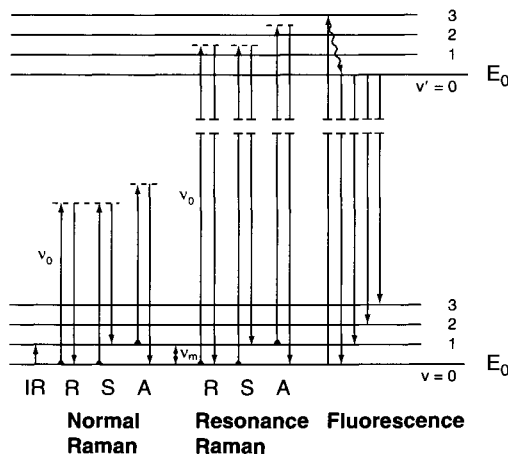


Figure 1-8 Comparison of energy levels for the normal Raman, resonance Raman, and fluorescence spectra.

$$\begin{aligned}
 &= \alpha_0 E_0 \cos 2\pi v_0 t \\
 &+ \frac{1}{2} \left(\frac{\partial \alpha}{\partial q} \right)_0 q_0 E_0 [\cos \{2\pi(v_0 + v_m)t\} + \cos \{2\pi(v_0 - v_m)t\}].
 \end{aligned} \quad (1-39)$$

According to classical theory, the first term represents an oscillating dipole that radiates light of frequency v_0 (Rayleigh scattering), while the second term corresponds to the Raman scattering of frequency $v_0 + v_m$ (anti-Stokes) and $v_0 - v_m$ (Stokes). If $(\partial\alpha/\partial q)_0$ is zero, the vibration is not Raman-active. Namely, to be Raman-active, the rate of change of polarizability (α) with the vibration must not be zero.

Figure 1-8 illustrates Raman scattering in terms of a simple diatomic energy level. In IR spectroscopy, we observe that $v = 0 \rightarrow 1$ transition at the electronic ground state. In normal Raman spectroscopy, the exciting line (v_0) is chosen so that its energy is far below the first electronic excited state. The dotted line indicates a “virtual state” to distinguish it from the real excited state. As stated in Section 1.2, the population of molecules at $v = 0$ is much larger than that at $v = 1$ (Maxwell–Boltzmann distribution law). Thus, the Stokes (S) lines are stronger than the anti-Stokes (A) lines under normal conditions. Since both give the same information, it is customary to measure only the Stokes side of the spectrum. Figure 1-9 shows the Raman spectrum of CCl_4^* .

*A Raman spectrum is expressed as a plot, intensity vs. Raman shift ($\Delta\tilde{\nu} = \tilde{\nu}_0 \pm \tilde{\nu}$). However, $\Delta\tilde{\nu}$ is often written as $\tilde{\nu}$ for brevity.

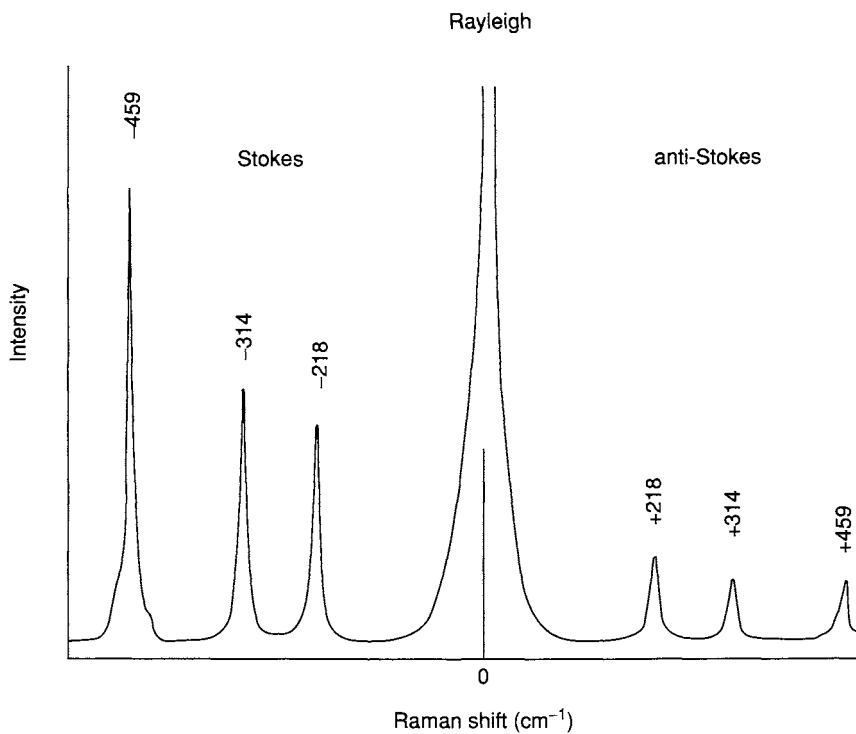


Figure 1-9 Raman spectrum of CCl_4 (488.0 nm excitation).

Resonance Raman (RR) scattering occurs when the exciting line is chosen so that its energy intercepts the manifold of an electronic excited state. In the liquid and solid states, vibrational levels are broadened to produce a continuum. In the gaseous state, a continuum exists above a series of discrete levels. Excitation of these continua produces RR spectra that show extremely strong enhancement of Raman bands originating in this particular electronic transition. Because of its importance, RR spectroscopy will be discussed in detail in Section 1.15. The term “pre-resonance” is used when the exciting line is close in energy to the electronic excited state. Resonance fluorescence (RF) occurs when the molecule is excited to a discrete level of the electronic excited state (20). This has been observed for gaseous molecules such as I_2 , Br_2 . Finally, fluorescence spectra are observed when the excited state molecule decays to the lowest vibrational level via radiationless transitions and then emits radiation, as shown in Fig. 1-8. The lifetime of the excited state in RR is very short ($\sim 10^{-14}$ s), while those in RF and fluorescence are much longer ($\sim 10^{-8}$ to 10^{-5} s).

1.5 Factors Determining Vibrational Frequencies

According to Eq. (1-26), the vibrational frequency of a diatomic molecule is given by

$$\tilde{\nu} = \frac{1}{2\pi c} \sqrt{\frac{K}{\mu}} \quad (1-40)$$

where K is the force constant and μ is the reduced mass. This equation shows that $\tilde{\nu}$ is proportional to \sqrt{K} (force constant effect), but inversely proportional to $\sqrt{\mu}$ (mass effect). To calculate the force constant, it is convenient to rewrite the preceding equations as

$$K = 4\pi^2 c^2 \omega_e^2 \mu. \quad (1-41)$$

Here, the vibrational frequency (observed) has been replaced by ω_e (Eq. (1-30)) in order to obtain a more accurate force constant. Using the unit of millidynes/Å (mdyn/Å) or 10^5 (dynes/cm) for K , and the atomic weight unit (awu) for μ , Eq. (1-41) can be written as

$$\begin{aligned} K &= 4(3.14)^2 (3 \times 10^{10})^2 \left[\frac{\mu}{6,025 \times 10^{23}} \right] \omega_e^2 \\ &= (5.8883 \times 10^{-2}) \mu \omega_e^2. \end{aligned} \quad (1-42)$$

For H^{35}Cl , $\omega_e = 2,989 \text{ cm}^{-1}$ and μ is 0.9799. Then, its K is 5.16×10^5 (dynes/cm) or 5.16 (mdyn/Å). If such a calculation is made for a number of diatomic molecules, we obtain the results shown in Table 1-3. In all four series of compounds, the frequency decreases in going downward in the table. However, the origin of this downward shift is different in each case. In the $\text{H}_2 > \text{HD} > \text{D}_2$ series, it is due to the mass effect since the force constant is not affected by isotopic substitution. In the $\text{HF} > \text{HCl} > \text{HBr} > \text{HI}$ series, it is due to the force constant effect (the bond becomes weaker in the same order) since the reduced mass is almost constant. In the $\text{F}_2 > \text{Cl}_2 > \text{Br}_2 > \text{I}_2$ series, however, both effects are operative; the molecule becomes heavier and the bond becomes weaker in the same order. Finally, in the $\text{N}_2 > \text{CO} > \text{NO} > \text{O}_2$, series, the decreasing frequency is due to the force constant effect that is expected from chemical formulas, such as $\text{N}\equiv\text{N}$, and $\text{O}=\text{O}$, with CO and NO between them.

It should be noted, however, that a large force constant does not necessarily mean a stronger bond, since the force constant is the curvature of the potential well near the equilibrium position,

$$K = \left(\frac{d^2 V}{dq^2} \right)_{q \rightarrow 0} \quad (1-43)$$

whereas the bond strength (dissociation energy) is measured by the depth of the potential well (Fig. 1-6). Thus, a large K means a sharp curvature near the bottom of the potential well, and does not directly imply a deep potential well. For example,

	HF	HCl	HBr	Hl			
K (mdyn/ \AA)	9.65	>	5.16	>	4.12	>	3.12
D_e (kcal/mole)	134.6	>	103.2	>	87.5	>	71.4

However,

	F_2	Cl_2	Br_2	I_2			
K (mdyn/ \AA)	4.45	>	3.19	>	2.46	>	1.76
D_e (kcal/mole)	37.8	<	58.0	>	46.1	>	36.1

A rough parallel relationship is observed between the force constant and the dissociation energy when we plot these quantities for a large number of compounds.

1.6 Vibrations of Polyatomic Molecules

In diatomic molecules, the vibration occurs only along the chemical bond connecting the nuclei. In polyatomic molecules, the situation is complicated because all the nuclei perform their own harmonic oscillations. However, we can show that any of these complicated vibrations of a molecule can be expressed as a superposition of a number of “normal vibrations” that are completely independent of each other.

In order to visualize normal vibrations, let us consider a mechanical model of the CO_2 molecule shown in Fig. 1-10. Here, the C and O atoms are represented by three balls, weighing in proportion to their atomic weights, that are connected by springs of a proper strength in proportion to their force constants. Suppose that the C—O bonds are stretched and released

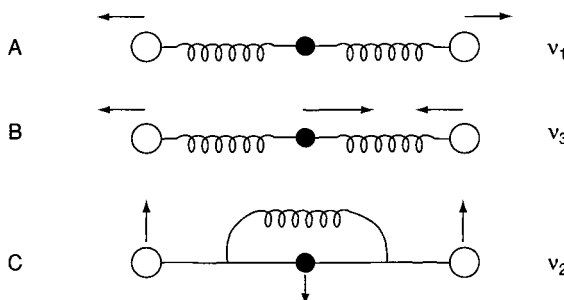


Figure 1-10 Atomic motions in normal modes of vibrations in CO_2 .

simultaneously as shown in Fig. 1-10A. Then, the balls move back and forth along the bond direction. This is one of the normal vibrations of this model and is called the symmetric (in-phase) stretching vibration. In the real CO_2 molecule, its frequency (v_1) is ca. $1,340\text{ cm}^{-1}$. Next, we stretch one C—O bond and shrink the other, and release all the balls simultaneously (Fig. 1-10B). This is another normal vibration and is called the antisymmetric (out-of-phase) stretching vibration. In the CO_2 molecule, its frequency (v_3) is ca. $2,350\text{ cm}^{-1}$. Finally, we consider the case where the three balls are moved in the perpendicular direction and released simultaneously (Fig. 1-10C). This is the third type of normal vibration called the (symmetric) bending vibration. In the CO_2 molecule, its frequency (v_2) is ca. 667 cm^{-1} .

Suppose that we strike this mechanical model with a hammer. Then, this model would perform an extremely complicated motion that has no similarity to the normal vibrations just mentioned. However, if this complicated motion is photographed with a stroboscopic camera with its frequency adjusted to that of the normal vibration, we would see that each normal vibration shown in Fig. 1-10 is performed faithfully. In real cases, the stroboscopic camera is replaced by an IR or Raman instrument that detects only the normal vibrations.

Since each atom can move in three directions (x, y, z), an N -atom molecule has $3N$ degrees of freedom of motion. However, the $3N$ includes six degrees of freedom originating from translational motions of the whole molecule in the three directions and rotational motions of the whole molecule about the three principal axes of rotation, which go through the center of gravity. Thus, the net vibrational degrees of freedom (number of normal vibrations) is $3N - 6$. In the case of linear molecules, it becomes $3N - 5$ since the rotation about the molecular axis does not exist. In the case of the CO_2 molecule, we have $3 \times 3 - 5 = 4$ normal vibrations shown in Fig. 1-11. It should be noted that v_{2a} and v_{2b} have the same frequency and are different only in the direction of vibration by 90° . Such a pair is called a set of doubly degenerate vibrations. Only two such vibrations are regarded as unique since similar vibrations in any other directions can be expressed as a linear combination of v_{2a} and v_{2b} . Figure 1-12 illustrates the three normal vibrations ($3 \times 3 - 6 = 3$) of the H_2O molecule.

Theoretical treatments of normal vibrations will be described in Section 1.20. Here, it is sufficient to say that we designate “normal coordinates” Q_1, Q_2 and Q_3 for the normal vibrations such as the v_1, v_2 and v_3 , respectively, of Fig. 1-12, and that the relationship between a set of normal coordinates and a set of Cartesian coordinates (q_1, q_2, \dots) is given by

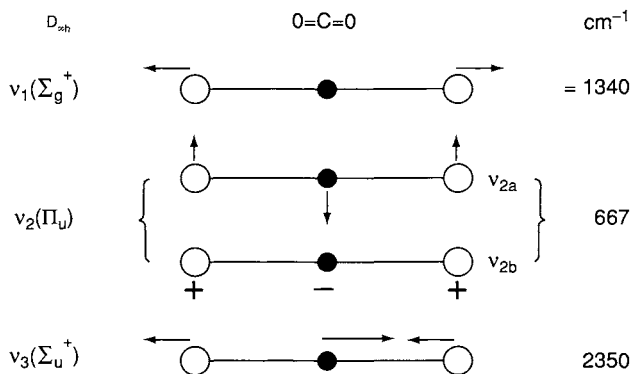


Figure 1-11 Normal modes of vibration in CO_2 (+ and – denote vibrations going upward and downward, respectively, in direction perpendicular to the paper plane).

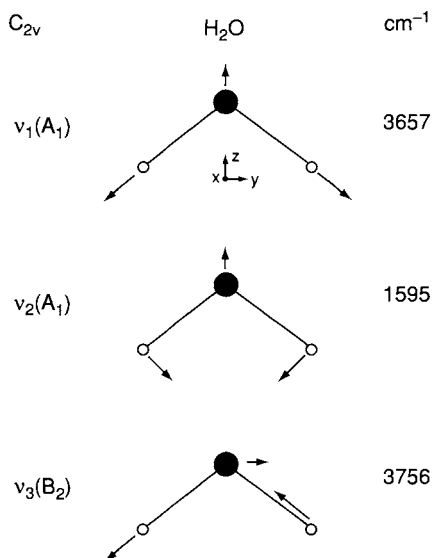


Figure 1-12 Normal modes of vibrations in H_2O .

$$q_1 = B_{11}Q_1 + B_{12}Q_2 + \dots,$$

$$q_2 = B_{21}Q_1 + B_{22}Q_2 + \dots,$$

....,

so that the modes of normal vibrations can be expressed in terms of Cartesian coordinates if the B_{ij} terms are calculated.

(1-44)

1.7 Selection Rules for Infrared and Raman Spectra

To determine whether the vibration is active in the IR and Raman spectra, the selection rules must be applied to each normal vibration. Since the origins of IR and Raman spectra are markedly different (Section 1.4), their selection rules are also distinctively different. According to quantum mechanics (18,19) a vibration is IR-active if the dipole moment is changed during the vibration and is Raman-active if the polarizability is changed during the vibration.

The IR activity of small molecules can be determined by inspection of the mode of a normal vibration (normal mode). Obviously, the vibration of a homopolar diatomic molecule is not IR-active, whereas that of a heteropolar diatomic molecule is IR-active. As shown in Fig. 1-13, the dipole moment of the H₂O molecule is changed during each normal vibration. Thus, all these vibrations are IR-active. From inspection of Fig. 1-11, one can readily see that ν_2 and ν_3 of the CO₂ molecule are IR-active, whereas ν_1 is not IR-active.

To discuss Raman activity, let us consider the nature of the polarizability (α) introduced in Section 1.4. When a molecule is placed in an electric field (laser beam), it suffers distortion since the positively charged nuclei are attracted toward the negative pole, and electrons toward the positive pole (Fig. 1-14). This charge separation produces an induced dipole moment (P) given by

$$P = \alpha E. \quad (1-45)*$$

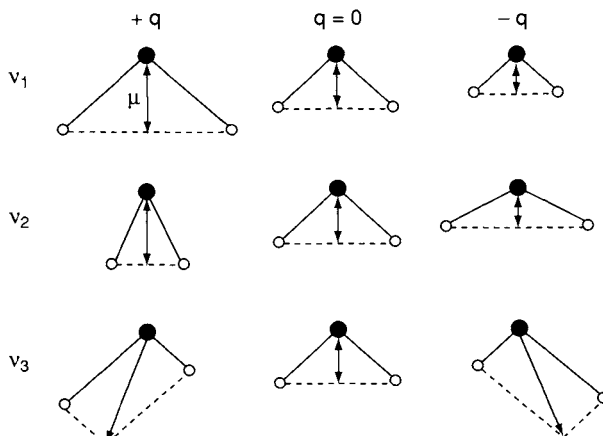


Figure 1-13 Change in dipole moment for H₂O molecule during each normal vibration.

*A more accurate expression is given by Eq. 3-1 in Chapter 3.

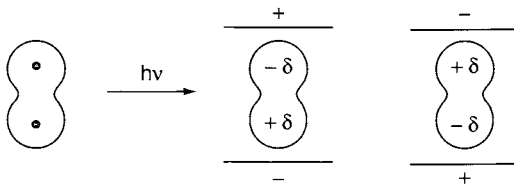


Figure 1-14 Polarization of a diatomic molecule in an electric field.

In actual molecules, such a simple relationship does not hold since both P and E are vectors consisting of three components in the x , y and z directions. Thus, Eq. (1-45) must be written as

$$\begin{aligned} P_x &= \alpha_{xx}E_x + \alpha_{xy}E_y + \alpha_{xz}E_z, \\ P_y &= \alpha_{yx}E_x + \alpha_{yy}E_y + \alpha_{yz}E_z, \\ P_z &= \alpha_{zx}E_x + \alpha_{zy}E_y + \alpha_{zz}E_z. \end{aligned} \quad (1-46)$$

In matrix form, this is written as

$$\begin{bmatrix} P_x \\ P_y \\ P_z \end{bmatrix} = \begin{bmatrix} \alpha_{xx} & \alpha_{xy} & \alpha_{xz} \\ \alpha_{yx} & \alpha_{yy} & \alpha_{yz} \\ \alpha_{zx} & \alpha_{zy} & \alpha_{zz} \end{bmatrix} \begin{bmatrix} E_x \\ E_y \\ E_z \end{bmatrix} \quad (1-47)$$

The first matrix on the right-hand side is called the *polarizability tensor*. In normal Raman scattering, this tensor is symmetric; $\alpha_{xy} = \alpha_{yz}$, $\alpha_{xz} = \alpha_{zx}$ and $\alpha_{yz} = \alpha_{zy}$. According to quantum mechanics, the vibration is Raman-active if one of these components of the polarizability tensor is changed during the vibration.

In the case of small molecules, it is easy to see whether or not the polarizability changes during the vibration. Consider diatomic molecules such as H_2 or linear molecules such as CO_2 . Their electron clouds have an elongated water melon like shape with circular cross-sections. In these molecules, the electrons are more polarizable (a larger α) along the chemical bond than in the direction perpendicular to it. If we plot α_i (α in the i -direction) from the center of gravity in all directions, we end up with a three-dimensional surface. Conventionally, we plot $1/\sqrt{\alpha_i}$ rather than α_i itself and call the resulting three-dimensional body a *polarizability ellipsoid*. Figure 1-15 shows the changes of such an ellipsoid during the vibrations of the CO_2 molecule.

In terms of the polarizability ellipsoid, the vibration is Raman-active if the *size, shape or orientation* changes during the normal vibration. In the v_1 vibration, the size of the ellipsoid is changing; the diagonal elements (α_{xx} , α_{yy} and α_{zz}) are changing simultaneously. Thus, it is Raman-active. Although the size of the ellipsoid is changing during the v_3 vibration, the ellipsoids at

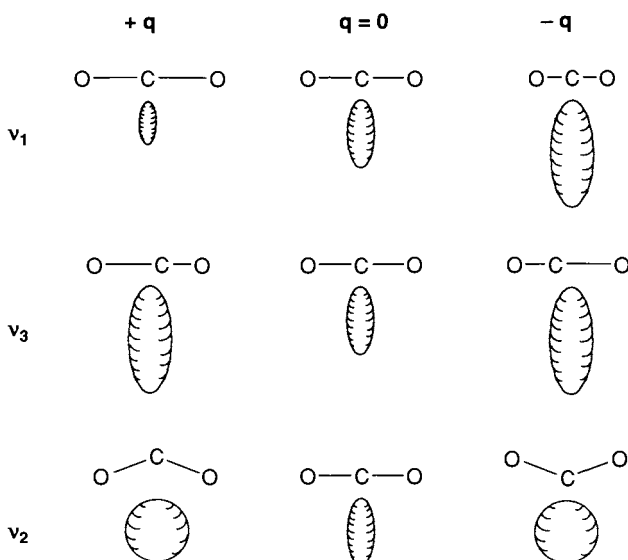


Figure 1-15 Changes in polarizability ellipsoids during vibration of CO_2 molecule.

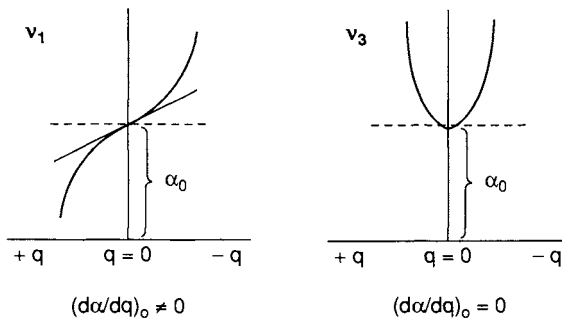


Figure 1-16 Difference between v_1 and v_3 vibrations in CO_2 molecule.

two extreme displacements ($+q$ and $-q$) are exactly the same in this case. Thus, this vibration is not Raman-active if we consider a small displacement. The difference between the v_1 and v_3 is shown in Fig. 1-16. Note that the Raman activity is determined by $(d\alpha/dq)_0$ (slope near the equilibrium position). During the v_2 vibration, the shape of the ellipsoid is sphere-like at two extreme configurations. However, the size and shape of the ellipsoid are exactly the same at $+q$ and $-q$. Thus, it is not Raman-active for the same reason as that of v_3 . As these examples show, it is not necessary to figure out the exact size, shape or orientation of the ellipsoid to determine Raman activity.

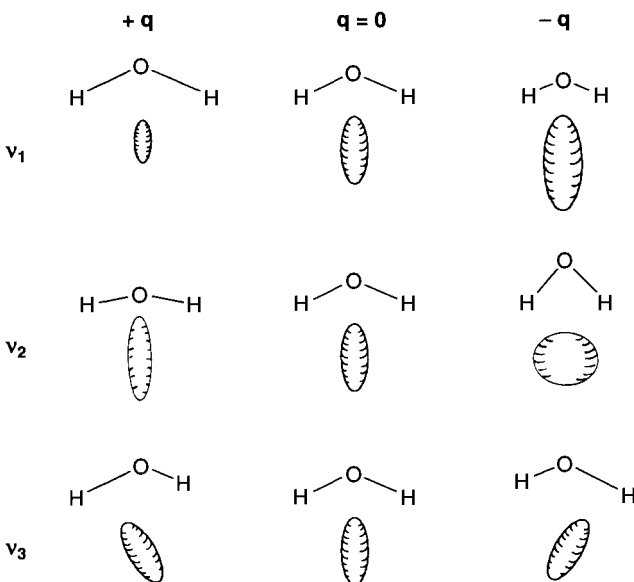


Figure 1-17 Changes in polarizability ellipsoid during normal vibrations of H_2O molecule.

Figure 1-17 illustrates the changes in the polarizability ellipsoid during the normal vibrations of the H_2O molecule. Its v_1 vibration is Raman-active, as is the v_1 vibration of CO_2 . The v_2 vibration is also Raman-active because the *shape* of the ellipsoid is different at $+q$ and $-q$. In terms of the polarizability tensor, α_{xx} , α_{yy} and α_{zz} are all changing with different rates. Finally, the v_3 vibration is Raman-active because the *orientation* of the ellipsoid is changing during the vibration. This activity occurs because an off-diagonal element (α_{yz} in this case) is changing.

One should note that, in CO_2 , the vibration that is symmetric with respect to the center of symmetry (v_1) is Raman-active but not IR-active, whereas those that are antisymmetric with respect to the center of symmetry (v_2 and v_3) are IR-active but not Raman-active. This condition is called the *mutual exclusion principle* and holds for any molecules having a center of symmetry.*

The preceding examples demonstrate that IR and Raman activities can be determined by inspection of the normal mode. Clearly, such a simple approach is not applicable to large and complex molecules. As will be shown in Section 1.14, group theory provides elegant methods to determine IR and Raman activities of normal vibrations of such molecules.

*This principle holds even if a molecule has no atom at the center of symmetry (e.g., benzene).

1.8 Raman versus Infrared Spectroscopy

Although IR and Raman spectroscopies are similar in that both techniques provide information on vibrational frequencies, there are many advantages and disadvantages unique to each spectroscopy. Some of these are listed here.

1. As stated in Section 1.7, selection rules are markedly different between IR and Raman spectroscopies. Thus, some vibrations are only Raman-active while others are only IR-active. Typical examples are found in molecules having a center of symmetry for which the mutual exclusion rule holds. In general, a vibration is IR-active, Raman-active, or active in both; however, totally symmetric vibrations are always Raman-active.
2. Some vibrations are inherently weak in IR and strong in Raman spectra. Examples are the stretching vibrations of the $\text{C}\equiv\text{C}$, $\text{C}=\text{C}$, $\text{P}=\text{S}$, $\text{S}-\text{S}$ and $\text{C}-\text{S}$ bonds. In general, vibrations are strong in Raman if the bond is covalent, and strong in IR if the bond is ionic ($\text{O}-\text{H}$, $\text{N}-\text{H}$). For covalent bonds, the ratio of relative intensities of the $\text{C}\equiv\text{C}$, $\text{C}=\text{C}$ and $\text{C}-\text{C}$ bond stretching vibrations in Raman spectra is about 3:2:1.* Bending vibrations are generally weaker than stretching vibrations in Raman spectra.
3. Measurements of depolarization ratios provide reliable information about the symmetry of a normal vibration in solution (Section 1.9). Such information can not be obtained from IR spectra of solutions where molecules are randomly orientated.
4. Using the resonance Raman effect (Section 1.15), it is possible to selectively enhance vibrations of a particular chromophoric group in the molecule. This is particularly advantageous in vibrational studies of large biological molecules containing chromophoric groups (Sections 4.1 and 6.1.)
5. Since the diameter of the laser beam is normally 1–2 mm, only a small sample area is needed to obtain Raman spectra. This is a great advantage over conventional IR spectroscopy when only a small quantity of the sample (such as isotopic chemicals) is available.
6. Since water is a weak Raman scatterer, Raman spectra of samples in aqueous solution can be obtained without major interference from water vibrations. Thus, Raman spectroscopy is ideal for the studies of biological compounds in aqueous solution. In contrast, IR spectroscopy suffers from the strong absorption of water.

*In general, the intensity of Raman scattering increases as the $(d\alpha/dq)_0$ becomes larger.

7. Raman spectra of hygroscopic and/or air-sensitive compounds can be obtained by placing the sample in sealed glass tubing. In IR spectroscopy, this is not possible since glass tubing absorbs IR radiation.
8. In Raman spectroscopy, the region from 4,000 to 50 cm^{-1} can be covered by a single recording. In contrast, gratings, beam splitters, filters and detectors must be changed to cover the same region by IR spectroscopy.

Some disadvantages of Raman spectroscopy are the following:

1. A laser source is needed to observe weak Raman scattering. This may cause local heating and/or photodecomposition, especially in resonance Raman studies (Section 1.15) where the laser frequency is deliberately tuned in the absorption band of the molecule.
2. Some compounds fluoresce when irradiated by the laser beam.
3. It is more difficult to obtain rotational and rotation-vibration spectra with high resolution in Raman than in IR spectroscopy. This is because Raman spectra are observed in the UV-visible region where high resolving power is difficult to obtain.
4. The state of the art Raman system costs much more than a conventional FT-IR spectrophotometer although less expensive versions have appeared which are smaller and portable and suitable for process applications (Section 2-10).

Finally, it should be noted that vibrational (both IR and Raman) spectroscopy is unique in that it is applicable to the solid state as well as to the gaseous state and solution. In contrast, X-ray diffraction is applicable only to the crystalline state, whereas NMR spectroscopy is applicable largely to the sample in solution.

1.9 Depolarization Ratios

As stated in the preceding section, depolarization ratios of Raman bands provide valuable information about the symmetry of a vibration that is indispensable in making band assignments. Figure 1-18 shows a coordinate system which is used for measurements of depolarization ratios. A molecule situated at the origin is irradiated from the y -direction with plane polarized light whose electric vector oscillates on the yz -plane (E_z). If one observes scattered radiation from the x -direction, and measures the intensities in the

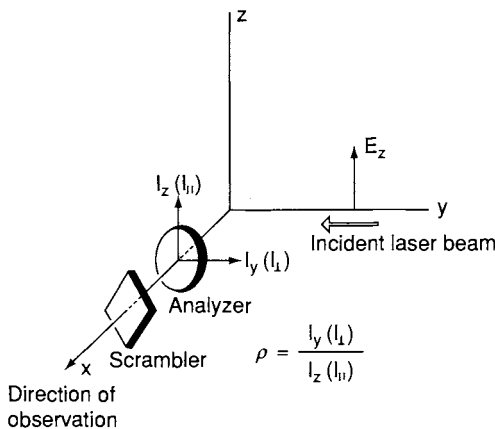


Figure 1-18 Irradiation of sample from the y -direction with plane polarized light, with the electronic vector in the z -direction.

$y(I_y)$ and $z(I_z)$ -directions using an analyzer, the depolarization ratio (ρ_p) measured by polarized light (p) is defined by

$$\rho_p = \frac{I_{\perp} (I_y)}{I_{\parallel} (I_z)}. \quad (1-48)$$

Figure 2-1 of Chapter 2 shows an experimental configuration for depolarization measurements in 90° scattering geometry. In this case, the polarizer is not used because the incident laser beam is almost completely polarized in the z direction. If a premonochromator is placed in front of the laser, a polarizer must be inserted to ensure complete polarization. The scrambler (crystal quartz wedge) must always be placed after the analyzer since the monochromator gratings show different efficiencies for \perp and \parallel polarized light. For information on precise measurements of depolarization ratios, see Refs. 21–24.

Suppose that a tetrahedral molecule such as CCl_4 is irradiated by plane polarized light (E_z). Then, the induced dipole (Section 1.7) also oscillates in the same yz -plane. If the molecule is performing the totally symmetric vibration, the polarizability ellipsoid is always sphere-like; namely, the molecule is polarized equally in every direction. Under such a circumstance, $I_{\perp} (I_y) = 0$ since the oscillating dipole emitting the radiation is confined to the xz -plane. Thus, $\rho_p = 0$. Such a vibration is called *polarized* (abbreviated as *p*). In liquids and solutions, molecules take random orientations. Yet this conclusion holds since the polarizability ellipsoid is spherical throughout the totally symmetric vibration.

If the molecule is performing a non-totally symmetric vibration, the polarizability ellipsoid changes its shape from a sphere to an ellipsoid during the

vibration. Then, the induced dipole would be largest along the direction of largest polarizability, namely along one of the minor axes of the ellipsoid. Since these axes would be randomly oriented in liquids and solutions, the induced dipole moments would also be randomly oriented. In this case, the ρ_p is nonzero, and the vibration is called *depolarized* (abbreviated as *dp*). Theoretically, we can show (25) that

$$\rho_p = \frac{3g^s + 5g^a}{10g^0 + 4g^s} \quad (1-49)$$

where

$$\begin{aligned} g^0 &= \frac{1}{3} (\alpha_{xx} + \alpha_{yy} + \alpha_{zz})^2, \\ g^s &= \frac{1}{3} [(\alpha_{xx} - \alpha_{yy})^2 + (\alpha_{yy} - \alpha_{zz})^2 + (\alpha_{zz} - \alpha_{xx})^2] \\ &\quad + \frac{1}{2} [(\alpha_{xy} + \alpha_{yx})^2 + (\alpha_{yz} + \alpha_{zy})^2 + (\alpha_{xz} + \alpha_{zx})^2], \\ g^a &= \frac{1}{2} [(\alpha_{xy} - \alpha_{yx})^2 + (\alpha_{xz} - \alpha_{zx})^2 + (\alpha_{yz} - \alpha_{zy})^2]. \end{aligned}$$

In normal Raman scattering, $g^a = 0$ since the polarizability tensor is symmetric. Then, (1-49) becomes

$$\rho_p = \frac{3g^s}{10g^0 + 4g^s} \quad (1-50)$$

For totally symmetric vibrations, $g^0 > 0$ and $g^s \geq 0$. Thus, $0 \leq \rho_p < \frac{3}{4}$ (polarized). For non-totally symmetric vibrations, $g^0 = 0$ and $g^s > 0$. Then, $\rho_p = \frac{3}{4}$ (depolarized).

In resonance Raman scattering ($g^a \neq 0$), it is possible to have $\rho_p > \frac{3}{4}$. For example, if $\alpha_{xy} = -\alpha_{yx}$ and the remaining off-diagonal elements are zero, $g^0 = g^s = 0$ and $g^a \neq 0$. Then, (1-49) gives $\rho_p \rightarrow \infty$. This is called *anomalous* (or *inverse*) *polarization* (abbreviated as *ap* or *ip*). As will be shown in Section 1.15, resonance Raman spectra of metalloporphyrins exhibit polarized (A_{1g}) and depolarized (B_{1g} and B_{2g}) vibrations as well as those of anomalous (or inverse) polarization (A_{2g}).

Figure 1-19 shows the Raman spectra of CCl_4 obtained with 90° scattering geometry. In this case, the ρ_p values obtained were 0.02 for the totally symmetric (459 cm^{-1}) and 0.75 for the non-totally symmetric modes (314 and 218 cm^{-1}). For ρ_p values in other scattering geometry, see Ref. 26.

Although polarization data are normally obtained for liquids and single crystals,* it is possible to measure depolarization ratios of Raman lines from solids by suspending them in a material with similar index of refraction (27).

*For an example of the use of polarized Raman spectra of calcite single crystal, see Section 1.19.

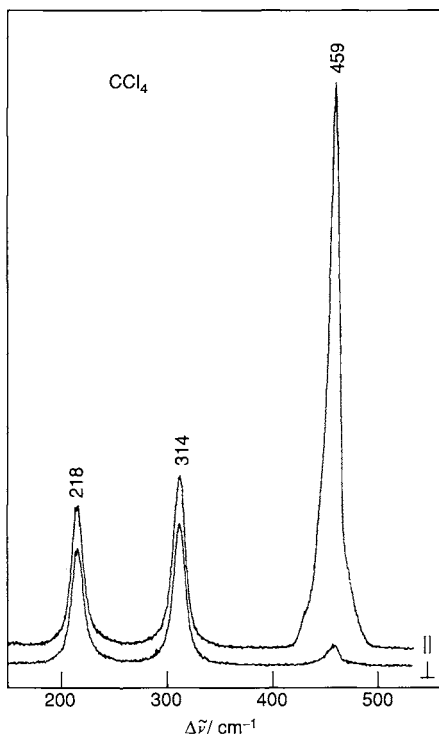


Figure 1-19 Raman spectrum of CCl₄ (500–200 cm⁻¹) in parallel and perpendicular polarization (488 nm excitation).

The use of suspensions can be circumvented by adding carbon black or CuO (28). The function of dark (black) additives appears to be related to a reduction of the penetration depth of the laser beam, causing an attenuation of reflected or refractive radiation, which is scrambled relative to polarization.

1.10 The Concept of Symmetry

The various experimental tools that are utilized today to solve structural problems in chemistry, such as Raman, infrared, NMR, magnetic measurements and the diffraction methods (electron, X-ray, and neutron), are based on symmetry considerations. Consequently, the symmetry concept as applied to molecules is thus very important.

Symmetry may be defined in a nonmathematical sense, where it is associated with beauty—with pleasing proportions or regularity in form, harmonious arrangement, or a regular repetition of certain characteristics (e.g.,

periodicity). In the mathematical or geometrical definition, symmetry refers to the correspondence of elements on opposite sides of a point, line, or plane, which we call the center, axis, or plane of symmetry (symmetry elements). It is the mathematical concept that is pursued in the following sections. The discussion in this section will define the symmetry elements in an isolated molecule (the point symmetry)—of which there are five. The number of ways by which symmetry elements can combine constitute a group, and these include the 32 crystallographic point groups when one considers a crystal. Theoretically, an infinite number of point groups can exist, since there are no restrictions on the order of rotational axes of an isolated molecule. However, in a practical sense, few molecules possess rotational axes C_n where $n > 6$. Each point group has a character table (see Appendix 1), and the features of these tables are discussed. The derivation of the selection rules for an isolated molecule is made with these considerations. If symmetry elements are combined with translations, one obtains operations or elements of symmetry that can define the symmetry of space as in a crystal. Two symmetry elements, the screw axis (rotation followed by a translation) and the glide plane (reflection followed by a translation), when added to the five point group symmetry elements, constitute the seven space symmetry elements. This final set of symmetry elements allows one to determine selection rules for the solid state.

Derivation of selection rules for a particular molecule illustrates the complementary nature of infrared and Raman spectra and the application of group theory to the determination of molecular structure.

1.11 Point Symmetry Elements

The spatial arrangement of the atoms in a molecule is called its equilibrium configuration or structure. This configuration is invariant under a certain set of geometric operations called a group. The molecule is oriented in a coordinate system (a right-hand xyz coordinate system is used throughout the discussion in this section). If by carrying out a certain geometric operation on the original configuration, the molecule is transformed into another configuration that is superimposable on the original (i.e., indistinguishable from it, although its orientation may be changed), the molecule is said to contain a symmetry element. The following symmetry elements can be cited.

1.11.1 IDENTITY (E)

The symmetry element that transforms the original equilibrium configuration into another one superimposable on the original without change in

orientation, in such a manner that each atom goes into itself, is called the identity and is denoted by E or I (E from the German *Einheit* meaning “unit” or, loosely, “identical”). In practice, this operation means to leave the molecule unchanged.

1.11.2 ROTATION AXES (C_n)

If a molecule is rotated about an axis to a new configuration that is indistinguishable from the original one, the molecule is said to possess a rotational axis of symmetry. The rotation can be clockwise or counterclockwise, depending on the molecule. For example, the same configuration is obtained for the water molecule whether one rotates the molecule clockwise or counterclockwise. However, for the ammonia molecule, different configurations are obtained, depending on the direction around which the rotation is performed. The angle of rotation may be $2\pi/n$, or $360^\circ/n$, where n can be 1, 2, 3, 4, 5, 6, ..., ∞ . The order of the rotational axis is called n (sometimes p), and the notation C_n is used, where C (cyclic) denotes rotation. In cases where several axes of rotation exist, the highest order of rotation is chosen as the principal (z) axis. Linear molecules have an infinitefold axes of symmetry (C_∞).

The selection of the axes in a coordinate system can be confusing. To avoid this, the following rules are used for the selection of the z axis of a molecule:

- (1) In molecules with only one rotational axis, this axis is taken as the z axis.
- (2) In molecules where several rotational axes exist, the highest-order axis is selected as the z axis.
- (3) If a molecule possesses several axes of the highest order, the axis passing through the greatest number of atoms is taken as the z axis.

For the selection of the x axis the following rules can be cited:

- (1) For a planar molecule where the z axis lies in this plane, the x axis can be selected to be normal to this plane.
- (2) In a planar molecule where the z axis is chosen to be perpendicular to the plane, the x axis must lie in the plane and is chosen to pass through the largest number of atoms in the molecule.
- (3) In nonplanar molecules the plane going through the largest number of atoms is located as if it were in the plane of the molecule and rule (1) or (2) is used. For complex molecules where a selection is difficult, one chooses the x and y axes arbitrarily.

1.11.3 PLANES OF SYMMETRY (σ)

If a plane divides the equilibrium configuration of a molecule into two parts that are mirror images of each other, then the plane is called a symmetry

plane. If a molecule has two such planes, which intersect in a line, this line is an axis of rotation (see the previous section); the molecule is said to have a vertical rotation axis C ; and the two planes are referred to as vertical planes of symmetry, denoted by σ_v . Another case involving two planes of symmetry and their intersection arises when a molecule has more than one axis of symmetry. For example, planes intersecting in an n -fold axis perpendicular to n twofold axes, with each of the planes bisecting the angle between two successive twofold axes, are called diagonal and are denoted by the symbol σ_d . Figure 1-20a–c illustrates the symmetry elements of

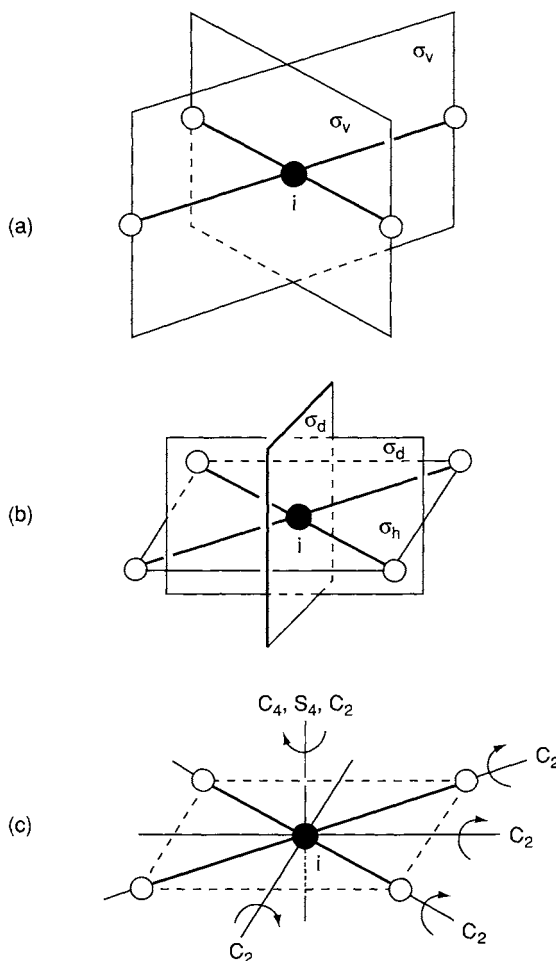


Figure 1-20 Symmetry elements for a planar AB_4 molecule (e.g., PtCl_4^{2-} ion).

the planar AB_4 molecule (e.g., PtCl_4^{2-} ion). If a plane of symmetry is perpendicular to the principal rotational axis, it is called horizontal and is denoted by σ_h .

1.11.4 CENTER OF SYMMETRY (i)

If a straight line drawn from each atom of a molecule through a certain point meets an equivalent atom equidistant from the point, we call the point the center of symmetry of the molecule. The center of symmetry may or may not coincide with the position of an atom. The designation for the center of symmetry, or center of inversion, is i . If the center of symmetry is situated on an atom, the total number of atoms in the molecule is odd. If the center of symmetry is not on an atom, the number of atoms in the molecule is even. Figure 1-20C illustrates a center of symmetry and rotational axes for the planar AB_4 molecule.

1.11.5 ROTATION REFLECTION AXES (S_n)

If a molecule is rotated $360^\circ/n$ about an axis and then reflected in a plane perpendicular to the axis, and if the operation produces a configuration indistinguishable from the original one, the molecule has the symmetry element of rotation-reflection, which is designated by S_n .

Table 1-4 lists the point symmetry elements and the corresponding symmetry operations. The notation used by spectroscopists and chemists, and used here, is the so-called Schoenflies system, which deals only with point groups. Crystallographers generally use the Hermann–Mauguin system, which applies to both point and space groups.

Table 1-4 Point Symmetry Elements and Symmetry Operations

Symmetry Element	Symmetry Operation
1. Identity (E or I)	Molecule unchanged
2. Axis of rotation (C_n)	Rotation about axis by $2\pi/n, n = 1, 2, 3, 4, 5, 6, \dots, \infty$ for an isolated molecule and $n = 1, 2, 3, 4$ and 6 for a crystal.
3. Center of symmetry or center of inversion (i)	Inversion of all atoms through center.
4. Plane of symmetry (σ)	Reflection in the plane.
5. Rotation reflection axis (S_n)	Rotation about axis by $2\pi/n$ followed by reflection in a plane perpendicular to the axis

(a) *Point Groups*

It can be shown that a group consists of mathematical elements (symmetry elements or operations), and if the operation is taken to be performing one symmetry operation after another in succession, and the result of these operations is equivalent to a single symmetry operation in the set, then the set will be a mathematical group. The postulates for a complete set of elements A, B, C, \dots are as follows:

- (1) For every pair of elements A and B , there exists a binary operation that yields the product AB belonging to the set.
- (2) This binary product is associative, which implies that $A(BC) = (AB)C$.
- (3) There exists an identity element E such that for every A , $AE = EA = A$.
- (4) There is an inverse A^{-1} for each element A such that $AA^{-1} = A^{-1}A = E$.

For molecules it would seem that the point symmetry elements can combine in an unlimited way. However, only certain combinations occur. In the mathematical sense, the sets of all its symmetry elements for a molecule that adhere to the preceding postulates constitute a point group. If one considers an isolated molecule, rotation axes having $n = 1, 2, 3, 4, 5, 6$ to ∞ are possible. In crystals n is limited to $n = 1, 2, 3, 4$, and 6 because of the *space-filling requirement*. Table 1-5 lists the symmetry elements of the 32 point groups.

(b) *Rules for Classifying Molecules into their Proper Point Group*

The method for the classification of molecules into different point groups suggested by Zeldin (29) is outlined in Table 1-6. The method can be described as follows:

- (1) Determine whether the molecule belongs to a special group such as $D_{\infty h}$, $C_{\infty v}$, T_d , O_h or I_h . If the molecule is linear, it will be either $D_{\infty h}$ or $C_{\infty v}$. If the molecule has an infinite number of twofold axes perpendicular to the C_∞ axis, it will fall into point group $D_{\infty h}$. If not, it is $C_{\infty v}$.
- (2) If the molecule is not linear, it may belong to a point group of extremely high symmetry such as T_d , O_h , or I_h .
- (3) If (1) or (2) is not found to be the case, look for a proper axis of rotation of the highest order in the molecule. If none is found, the molecule is of low symmetry, falling into point group C_3 , C_i , or C_1 . The presence in the molecule of a plane of symmetry or an inversion center will distinguish among these point groups.
- (4) If C_n axes exist, select the one of highest order. If the molecule also has an S_{2n} axis, with or without an inversion center, the point group is S_n .

Table 1-5 The 32 Crystallographic Point Groups^a

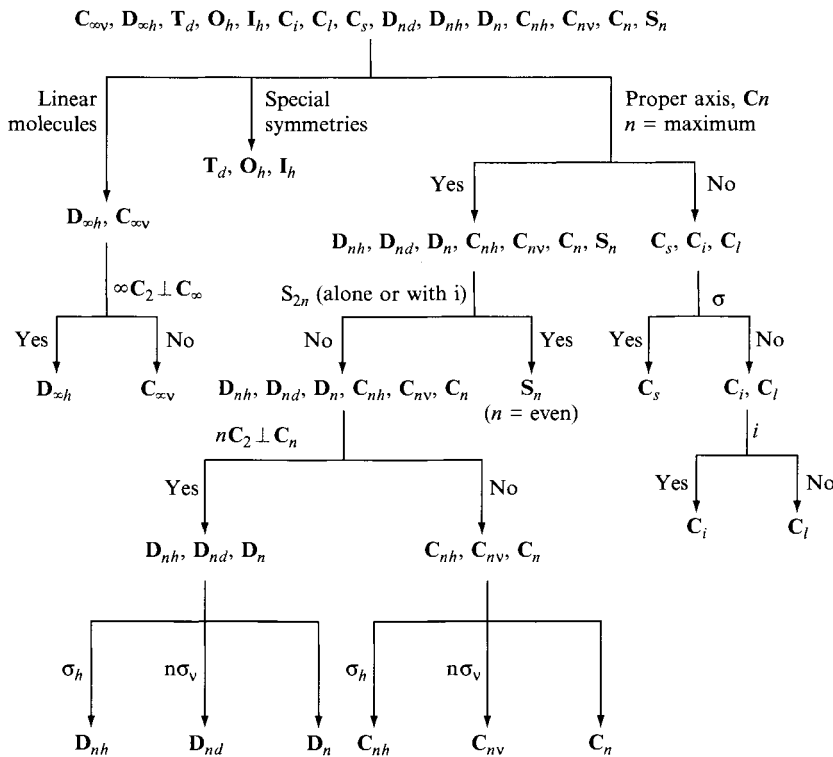
Symbol	Plane σ	Axes of Symmetry				Center i	Example
		$6(C_6)$	$4(C_4)$	$3(C_3)$	$2(C_2)$		
C_1	—	—	—	—	—	—	CH_3CHO
C_2	—	—	—	—	1	—	H_2O_2
C_3	—	—	—	1	—	—	$\text{B}(\text{OH})_3$
C_4	—	—	—	—	—	—	$\text{H}_2\text{S}(s)$
C_6	—	—	—	—	—	—	—
C_s	1	—	—	—	—	—	HCOCl
C_{2h}	1	—	—	—	1	1	$\text{trans-CHCl}=\text{CHCl}$
C_{3h}	1	—	—	—	1	—	$\text{C}^+(\text{NH}_2)_3$
C_{4h}	1	—	—	—	1	1	$\text{C}_4\text{H}_4\text{Cl}_4$
C_{6h}	1	—	—	—	1	—	—
D_2	—	—	—	—	—	—	$\text{Co}(\text{H}_2\text{NCH}_2\text{CH}_2\text{NH}_2)_3^{3+}$
D_3	—	—	—	—	—	—	cyclobutane
D_4	—	—	—	—	—	—	—
D_6	—	—	—	—	—	—	C_2H_4
D_{2h}	3	—	—	—	6	1	—
D_{3h}	4	—	—	—	3	3	BCl_3

"Special Point Groups"

—One can find an infinite number of τ — σ HCN special limit Groups.

Infinite fold axes (C_∞) infinite number of planes through C_∞ axis $\rightarrow C_\infty$

infinite-fold axes (C_∞), infinite number $C_2 \perp C_\infty$, plane $\perp C_\infty$

Table 1-6 Method of Classifying Molecules into Point Groups (29)

- (5) If no S_n exists look for a set of n twofold axes lying perpendicular to the major C_n axis. If no such set is found, the molecule belongs to C_{nh} , C_{nv} or C_a . If a σ_h plane exists, the molecule is of C_{nh} symmetry even if other planes of symmetry are present. If no σ_h plane exists and a σ_v plane is found, the molecule is of C_{nv} symmetry. If no planes exist, it is of C_n symmetry.
- (6) If in (5) nC_2 axes perpendicular to C_n axes are found, the molecule belongs to the D_{nh} , D_{nd} , or D_n point group. These can be differentiated by the presence (or absence) of symmetry planes (σ_h , σ_v , or no σ , respectively).

Several examples will be considered to illustrate the classification of molecules into point groups. Consider, for instance, the bent triatomic molecule of type AB₂(H₂O) shown in Fig. 1-21. Following the rules

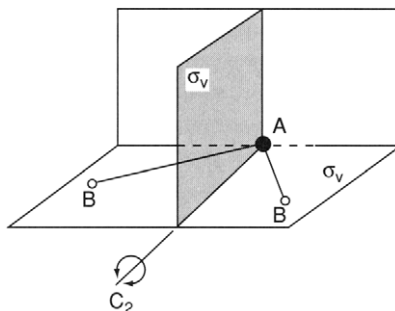


Figure 1-21 Symmetry elements for a bent AB_2 molecule. (Reproduced with permission from Ref. 30.)

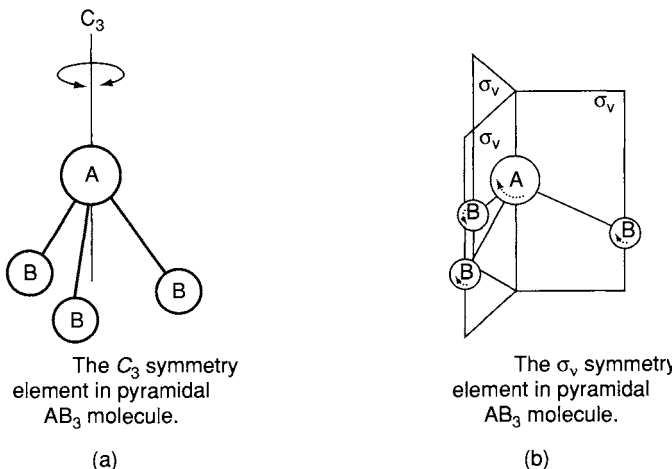


Figure 1-22 Symmetry elements for a pyramidal AB_3 molecule: (a) C_3 element; (b) σ_v elements. (Reproduced with permission from Ref. 30.)

and Table 1-6, it can be determined that the molecule is not of a special symmetry. It does have a C_2 axis of rotation but no S_4 axis. There are no $nC_2 \perp C_n$, and therefore the molecule is either C_{2h} , C_{2v} , or C_2 . The molecule possesses two vertical planes of symmetry but no σ_h plane, and therefore belongs to the C_{2v} point group.

Now consider the pyramidal molecule of type AB_3 (NH_3) shown in Fig. 1-22. This molecule also is not of a special symmetry. It has a C_3 axis of rotation but no S_6 axis. There are no nC_n axes perpendicular to the C_3 axis, and therefore the molecule belongs to the C classification. Since three vertical

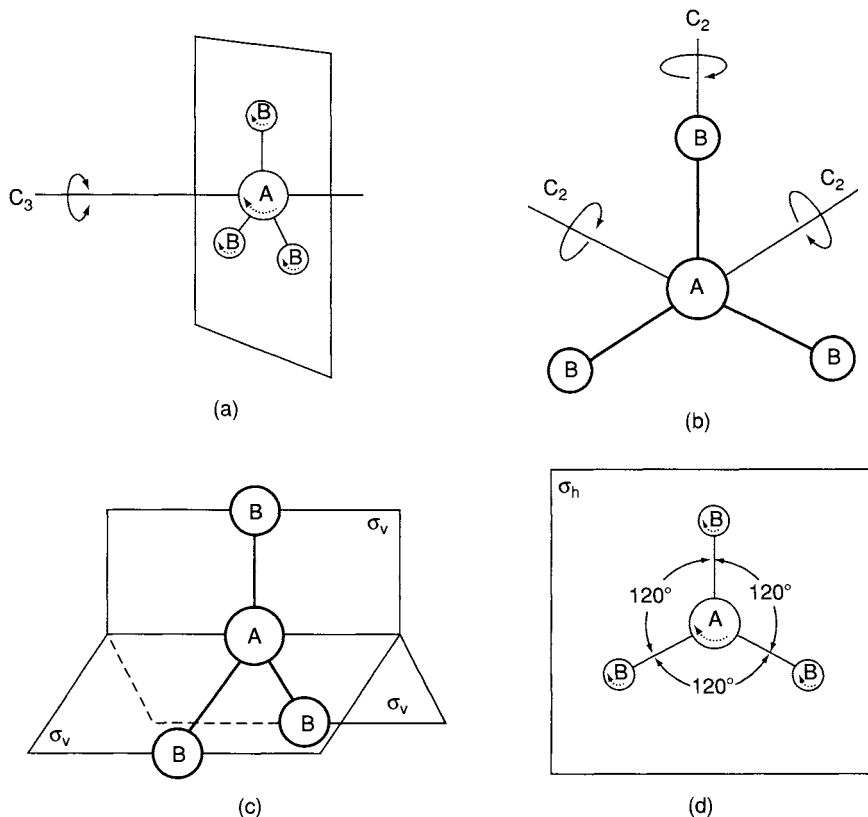


Figure 1-23 Symmetry elements for a planar AB_3 molecule (a) C_3 , (b) C_2 (c) σ_v , and (d) σ_h . (Reproduced with permission from Ref. 30.)

planes of symmetry are found but no σ_h plane, the molecule can be classified into C_{3v} .

Next, consider the planar AB_3 molecule (BF_3) shown in Fig. 1-23. This molecule has no special symmetry. It has a C_3 axis of rotation without a collinear S_6 axis. It has three C_2 axes perpendicular to the C_3 axis, and therefore falls into the D classification. It has a σ_h plane of symmetry perpendicular to the C_3 axis and three σ_v planes of symmetry. However, the σ_h plane predominates and the molecule is of D_{3h} symmetry.

The next example is the hexagonal planar molecule of type A_6 or A_6B_6 (benzene) shown in Fig. 1-24. The molecule is not of a special symmetry. It has a center of symmetry and a C_6 axis of symmetry. No S_2 axis exists. Since six C_2 axes perpendicular to the C_6 axis are found, this molecule also falls into the D classification. Since it has a horizontal plane of symmetry perpendicular to the C_6 axis, the molecule belongs to the D_{6h} point group.

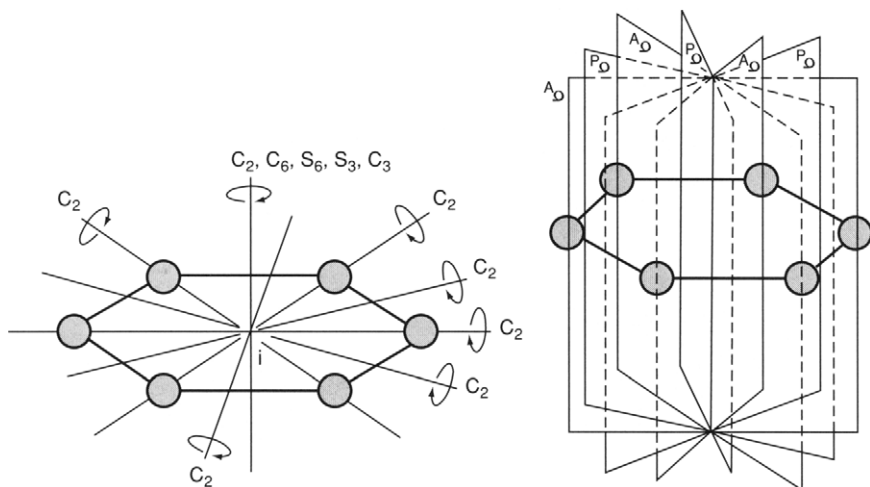


Figure 1-24 Symmetry elements for a planar hexagonal A_6B_6 molecule. (Reproduced with permission from Ref. 30.)

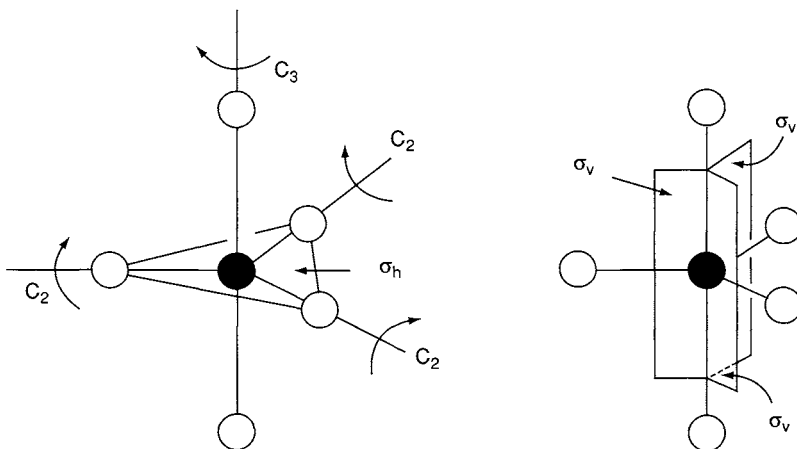
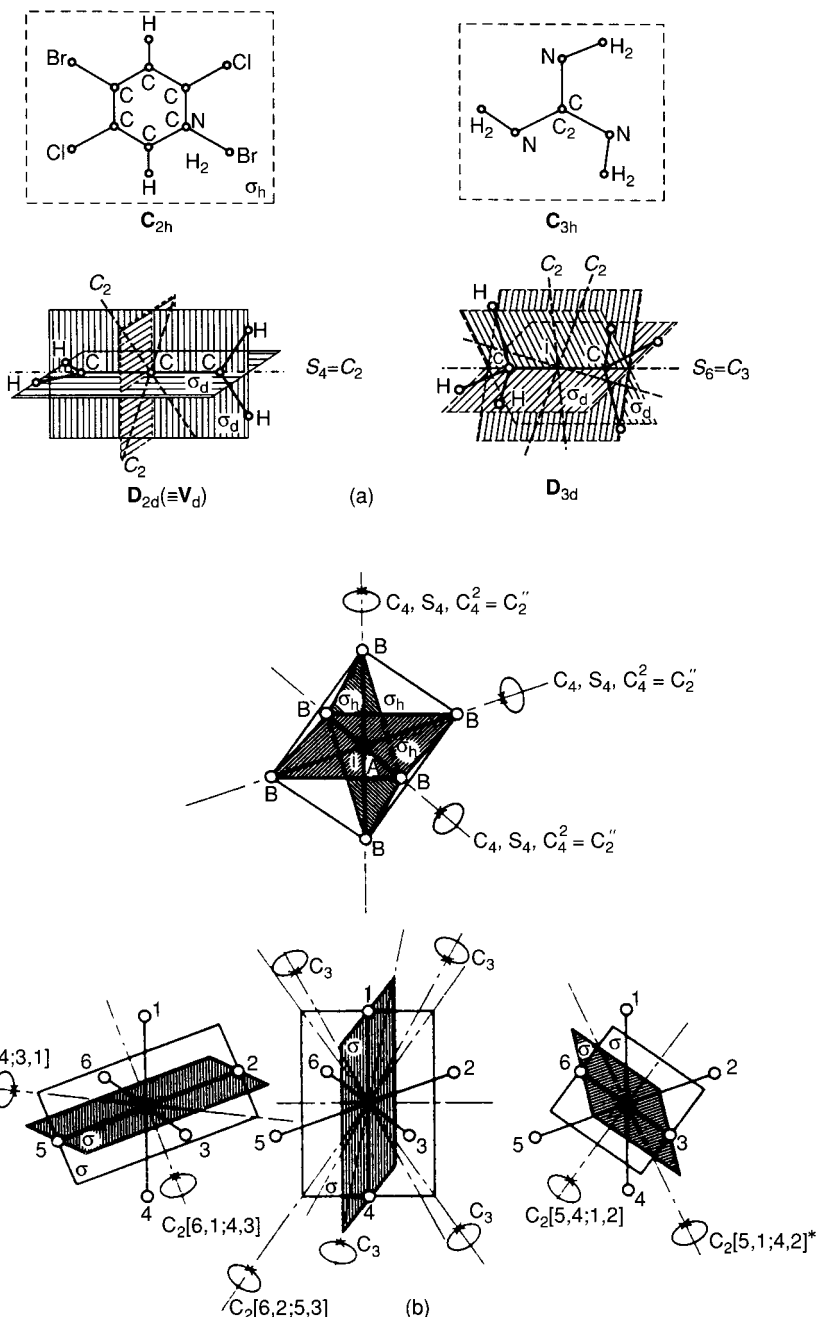


Figure 1-25 Symmetry elements for a trigonal bipyramidal AB_5 molecule.

As the last example, consider the AB_5 trigonal bipyramidal (e.g., gaseous PCl_5) shown in Fig. 1-25. This molecule does not belong to a special symmetry. The axis of highest order is C_3 . There is no S_6 collinear with C_3 . There are three C_2 axes perpendicular to the C_3 axis, and therefore the molecule belongs to one of the D groups. Since it possesses a σ_h plane perpendicular to the C_3 axis, the proper classification is D_{3h} . Figure 1-26a, b, c shows symmetry elements for several other common point groups.



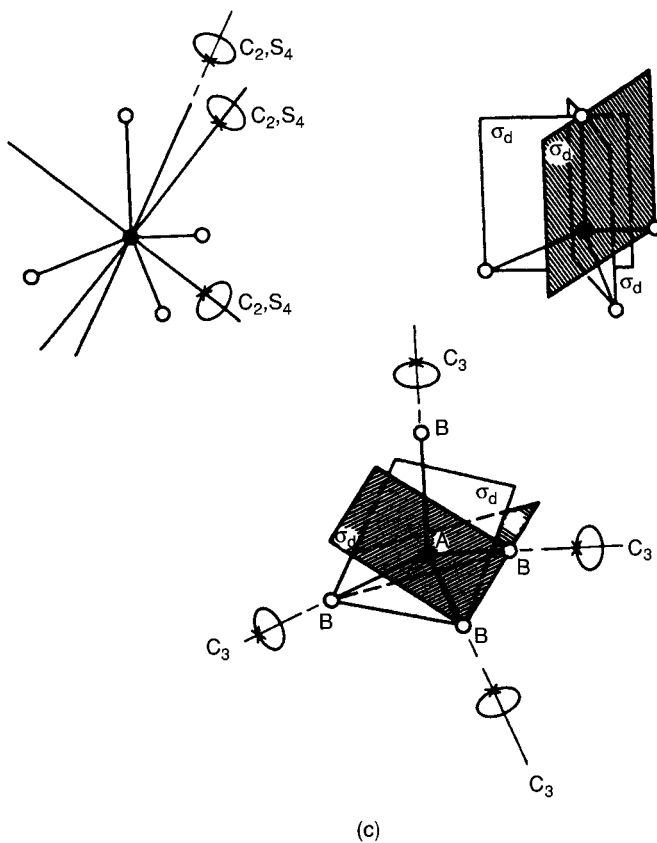


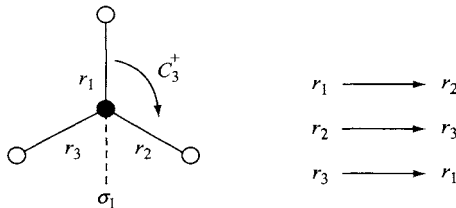
Figure 1-26 Symmetry elements for other point groups. (a) C_{2h} , C_{3h} , D_{2d} , D_{3d} ; (b) O_h and (c) T_d . (Reproduced with permission from Ref. 30.)

1.12 The Character Table

Prior to interpreting the character table, it is necessary to explain the terms *reducible* and *irreducible representations*. We can illustrate these concepts using the NH_3 molecule as an example. Ammonia belongs to the point group C_{3v} and has six elements of symmetry. These are E (identity), two C_3 axes (threefold axes of rotation) and three σ_v planes (vertical planes of symmetry) as shown in Fig. 1-22. If one performs operations corresponding to these symmetry elements on the three equivalent NH bonds, the results can be expressed mathematically by using 3×3 matrices.*

*The reader should consult introductory textbooks on matrix theory.

Consider the C_3^+ (clockwise rotation by 120°) operation, shown with its changes:



Using matrix language, this is expressed as

$$C_3^+ \begin{bmatrix} r_1 \\ r_2 \\ r_3 \end{bmatrix} = \begin{bmatrix} 0 & 1 & 0 \\ 0 & 0 & 1 \\ 1 & 0 & 0 \end{bmatrix} \begin{bmatrix} r_1 \\ r_2 \\ r_3 \end{bmatrix}. \quad (1-51)$$

The square matrix on the right-hand side is called a *representation* for the symmetry operation, C_3^+ . For the σ_1 operation, we obtain

$$\sigma_1 \begin{bmatrix} r_1 \\ r_2 \\ r_3 \end{bmatrix} = \begin{bmatrix} 1 & 0 & 0 \\ 0 & 0 & 1 \\ 0 & 1 & 0 \end{bmatrix} \begin{bmatrix} r_1 \\ r_2 \\ r_3 \end{bmatrix}. \quad (1-52)$$

Similarly, for the E operation, we obtain

$$E \begin{bmatrix} r_1 \\ r_2 \\ r_3 \end{bmatrix} = \begin{bmatrix} 1 & 0 & 0 \\ 0 & 1 & 0 \\ 0 & 0 & 1 \end{bmatrix} \begin{bmatrix} r_1 \\ r_2 \\ r_3 \end{bmatrix}. \quad (1-53)$$

These representations are called *reducible representations* since they can be block-diagonalized in the form

$$\begin{bmatrix} 1 & 0 & 0 \\ 0 & A & B \\ 0 & C & D \end{bmatrix} \quad (1-54)$$

via similarity transformation.* If such simplification is no longer possible, the resulting representations are called *irreducible representations*. In the present case, the irreducible representations thus obtained are

*In general, similarity transformation is expressed as $S^{-1}R(K)S$ where $R(K)$ is a reducible representation for the symmetry operation, $R(K)$, S is a matrix of the same dimension, and S^{-1} is its reciprocal (or inverse), defined by the relationship, $S^{-1}S = SS^{-1} = E$, where E is a unit matrix such as (1-53). In the present case, the S matrix is obtained by writing a U matrix (Section 1.20) for the pyramidal XY_3 molecule.

$$\text{for } C_3^+ : \begin{bmatrix} 0 & 1 & 0 \\ 0 & 0 & 1 \\ 1 & 0 & 0 \end{bmatrix} \rightarrow \begin{bmatrix} 1 & 0 & 0 \\ 0 & -\frac{1}{2} & \frac{\sqrt{3}}{2} \\ 0 & -\frac{\sqrt{3}}{2} & -\frac{1}{2} \end{bmatrix}, \quad (1-55)$$

$$\text{for } \sigma_1 : \begin{bmatrix} 1 & 0 & 0 \\ 0 & 0 & 1 \\ 0 & 1 & 0 \end{bmatrix} \rightarrow \begin{bmatrix} 1 & 0 & 0 \\ 0 & 1 & 1 \\ 0 & 0 & -1 \end{bmatrix}. \quad (1-56)$$

The reducible representation for E (1-53) is already diagonalized.

The sum of the diagonal elements of a matrix is called the character (χ) of the matrix. Hereafter, we use the term character rather than the representation since there is a one-to-one correspondence between them and since mathematical manipulation with χ is simpler than with the representation. The characters of the reducible representations for the E , C_3^+ and σ_1 operations are 3, 0 and 1, respectively. The characters for C_3^- (counterclockwise rotation by 120°) is the same as that of C_3^+ , and those for σ_2 and σ_3 are the same as that of σ_1 . By grouping symmetry operations of the same character ("class"), we obtain

C_{3v}	E	$2C_3$	$3\sigma_v$
	3	0	1

As seen in (1-53), (1-55) and (1-56), this set of reducible representations can be resolved into a sum of characters of the irreducible representations:

A_1	1	1	1
E	2	-1	0
$A_1 + E$	3	0	1

The characters of irreducible representations are listed in the *character table* of each point group (Appendix 1). Figure 1-27 shows the character table for the point group C_{3v} . It is seen that there are three sets of characters corresponding to the A_1 , A_2 and E species. In practical terms, the above result indicates that the three N—H bond stretching vibrations of the NH_3 molecule can be classified into one A_1 and one E (doubly degenerate) vibration. Thus, the character tables are important in classifying normal vibrations according to their symmetry properties (Section 1.13).

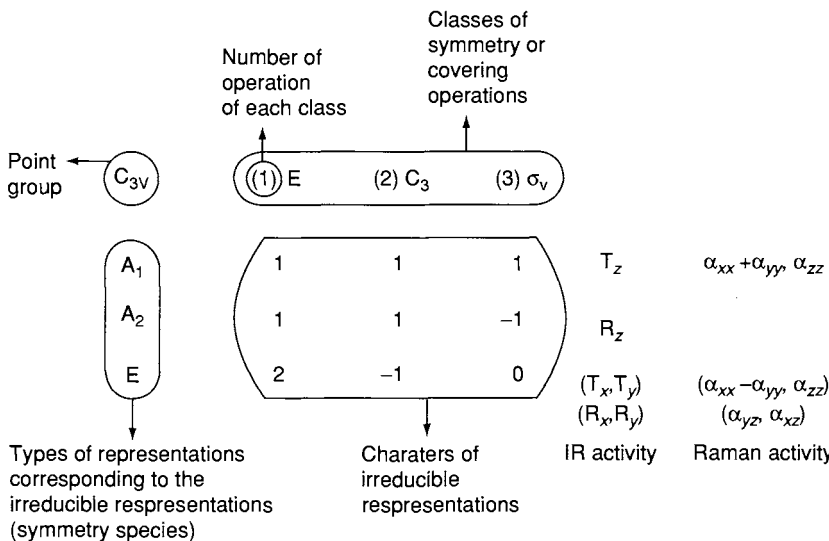


Figure 1-27 Diagrammatic interpretation of the character table for the C_{3v} point group.

The last two columns of the character table provide information about IR and Raman activities of normal vibrations. One column lists the symmetry species of translational motions along the x , y and z axes (T_x , T_y and T_z) and rotational motions around the x , y and z axes (R_x , R_y and R_z). The last column lists the symmetry species of the six components of polarizability. As will be discussed in Section 1.14, the vibration is IR-active if it belongs to a symmetry species that contains any T components and is Raman-active if it belongs to a symmetry species that contains any α components. Pairs of these components are listed in parentheses when they belong to degenerate species.

TYPES OF SPECIES OF IRREDUCIBLE REPRESENTATIONS

(a) Nonlinear Molecules

A species is designated by the letter A if the transformation of the molecule is symmetric (+1) with respect to the rotation about the principal axis of symmetry. In NH_3 , this axis is C_3 , and, as can be seen, A_1 is totally symmetric, being labeled with positive 1's for all symmetry classes. A species that is symmetric with respect to the rotation, but is antisymmetric with respect to a rotation about the C_2 axis perpendicular to the principal axis or the vertical plane of reflection, is designated by the symbol A_2 .

If a species of vibration belongs to the antisymmetric (-1) representation, it is designated by the letter B . If it is symmetric with respect to the rotation about the C_2 axis perpendicular to the principle axis of symmetry or to the vertical plane of reflection, it is a B_1 vibration, and if it is antisymmetric, it is a B_2 vibration. The letter E designates a twofold degenerate* vibration and the letter F denotes** a triply degenerate vibration. The character under the class of identity gives the degeneracy of the vibration, 1 for singly degenerate, 2 for doubly degenerate, and 3 for triply degenerate. For point groups containing a σ_h operation, primes (e.g., A') and double primes (e.g., A'') are used. The single prime indicates symmetry and the double prime antisymmetry with respect to σ_h . In molecules with a center of symmetry i , the symbols g and u are used, g standing for the German word *gerade* (which means even) and u for *ungerade* (or uneven). The symbol g goes with the species that transforms symmetrically with respect to i , and the symbol u goes with the species that transforms antisymmetrically with respect to i .

(b) Linear Molecules

Different symbols are used for linear molecules belonging to the point groups $C_{\infty v}$ and $D_{\infty h}$, namely Greek letters identical with the designations used for the electronic states of any diatomic molecules. The symbols σ or Σ are used for species symmetric with respect to the principal axis. A superscript plus sign (σ^+ or Σ^+) is used for species that are symmetric, and a superscript minus sign (σ^- or Σ^-) for species that are antisymmetric with respect to a plane of symmetry through the molecular axis. The symbols Π , Δ , and Φ are used for degenerate vibrations, with the degree of degeneracy increasing in this order. This is illustrated in Table 1-7.

Table 1-7 Character Table for the $C_{\infty v}$ Point Group

$C_{\infty v}$	E	$2C_{\infty}^{\phi}$	$2C_{\infty}^{2\phi}$	$2C_{\infty}^{3\phi}$...	$\infty\sigma_v$
Σ^+	+1	+1	+1	+1	...	+1
Σ^-	+1	+1	+1	+1	...	-1
Π	+2	$2 \cos \phi$	$2 \cos 2\phi$	$2 \cos 3\phi$...	0
Δ	+2	$2 \cos 2\phi$	$2 \cos 2 \cdot 2\phi$	$2 \cos 3 \cdot 2\phi$...	0
Φ	+2	$2 \cos 3\phi$	$2 \cos 2 \cdot 3\phi$	$2 \cos 3 \cdot 3\phi$...	0
...

*The bending vibration of CO_2 is an example of a degenerate vibration. The frequency and character of the vibrations are the same, but they occur perpendicular to one another.

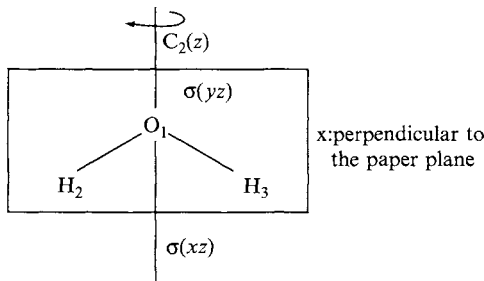
**Some texts use the symbol T for the triply degenerate vibration.

(c) *Molecules of Highest Symmetry*

Although it has been generally believed that molecules would never be found in icosahedral (I_h) symmetry (31, 32), we now know that such is not the case. There are at least three molecules possessing icosahedral symmetry. These are the borohydride anion (33) $B_{12}H_{12}^{2-}$; dodecahedrane, $C_{20}H_{20}$ (34), and the buckminsterfullerene or buckyball C_{60} cluster (35) (see Chapter 4, Section 4.2.7). The I_h symmetry contains fivefold to twofold axes of rotation as well as a center of symmetry. As a result, additional species of vibrations such as G and H appear in the I_h character table (36). These correspond to four-dimensional and five-dimensional representations. G is a four-fold and H is a five-fold degenerate vibration. The character table for the I_h point group is shown in Appendix 1.

1.13 Classification of Normal Vibrations by Symmetry

The $3N - 6(5)$ normal vibrations of an N -atom molecule can be classified into symmetry species of a point group according to their symmetry properties. As an example, consider the displacements of individual atoms of the H_2O molecule (C_{2v}) using the Cartesian coordinates shown below:

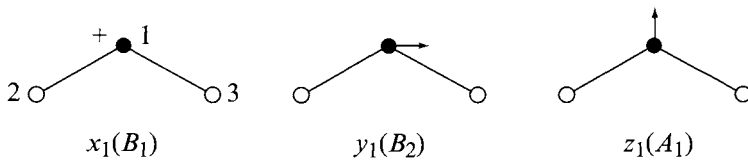


The symmetry operations to be considered are given in the table.

C_{2v}	$C_2(z)$	$\sigma(xz)$	$\sigma(yz)$
A_1	+1	+1	+1
A_2	+1	-1	-1
B_1	-1	+1	-1
B_2	-1	-1	+1

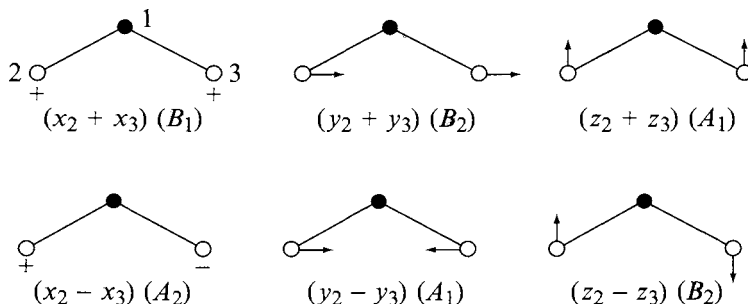
It is not necessary to consider $\sigma(yz)$ since $C_2 \times \sigma(xz) = \sigma(yz)$.

First, the symmetry species of the three displacements of the oxygen atom are readily determined as shown below:



Here the + sign denotes the out-of-plane displacement in the $+x$ direction.

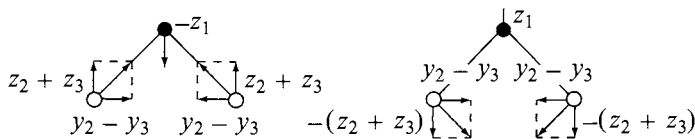
Since the two hydrogen atoms are equivalent, we consider symmetry species of six linear combinations of their displacements:



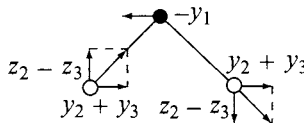
Since these nine displacements include three translational (T) and three rotational (R) motions of the whole molecule, we must subtract them from our calculations. It is readily seen that T_x , T_y and T_z belong to the B_1 , B_2 and A_1 , whereas R_x , R_y and R_z belong to the B_2 , B_1 and A_2 species, respectively. Table 1-8 summarizes these results. Thus, we find that two vibrations belong to the A_1 and one vibration belongs to the B_2 species. The approximate vibrational modes of the two A_1 type vibrations can be derived by combining z_1 , $(z_2 + z_3)$ and $(y_2 - y_3)$ as follows:

Table 1-8 Number of Normal Vibrations of H_2O Molecule

C_{2v}	Number of Coordinates			Translation and Rotation	Number of Vibrations
	O	H	Total		
A_1	1	2	3	T_z	$3 - 1 = 2$
A_2	0	1	1	R_z	$1 - 1 = 0$
B_1	1	1	2	T_x, R_y	$2 - 2 = 0$
B_2	1	2	3	T_y, R_x	$3 - 2 = 1$



The vibrational mode of the B_2 vibration is obtained by combining $-y_1$, $(y_2 + y_3)$ and $(z_2 - z_3)$ as follows:



More accurate mode descriptions can be made if we consider the masses of individual atoms, bond distances, bond angles and force constants (Section 1.20). It is clear that these three vibrations correspond to the v_1 , v_2 and v_3 , respectively, of Fig. 1-12.

More generally, the number of normal vibrations in each species can be calculated by using Herzberg's formulas (31) given in Appendix 2. In the case of the C_{2v} point group, they are expressed as:

$$A_1: 3m + 2m_{xz} + 2m_{yz} + m_0 - 1,$$

$$A_2: 3m + m_{xz} + m_{yz} - 1,$$

$$B_1: 3m + 2m_{xz} + m_{yz} + m_0 - 2,$$

$$B_2: 3m + m_{xz} + 2m_{yz} + m_0 - 2,$$

and N (total number of atoms) is given by $4m + 2m_{xz} + 2m_{yz} + m_0$. In the foregoing, the parameters are defined as follows:

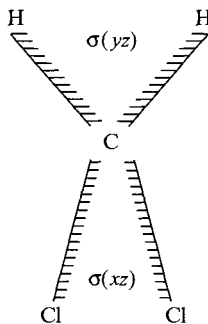
m : number of sets of nuclei not on any symmetry elements.

m_0 : number of nuclei on all symmetry elements.

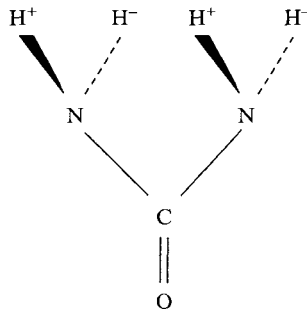
m_{xy} , m_{yz} , m_{xz} : number of sets of nuclei lying on the xy , yz and xz planes, respectively, but not on any other axis going through these planes.

For H_2O , $m = 0$, $m_0 = 1$ (oxygen atom), $m_{xy} = 0$, $m_{yz} = 1$ (hydrogen atom), $m_{xz} = 0$ and $N = 3$. Thus, the numbers of normal vibrations are 2, 0, 0 and 1 for the A_1 , A_2 , B_1 and B_2 species, respectively.

The preceding general equations can be obtained from our calculations on H_2O . As shown earlier, the displacements of the oxygen atom (m_0) are distributed into $1A_1$, $1B_1$, and $1B_2$. The displacements of the two hydrogen atoms (m_{yz}) are distributed among $2A_1$, $1A_2$, $1B_1$ and $2B_2$. Although m_{xz} is zero for H_2O , it is not zero for other C_{2v} molecules. For example, it is 1 for CH_2Cl_2 :



It is easily seen that m_{xz} is distributed into $2A_1$, $1A_2$, $2B_1$ and $1B_2$. m is zero in the case of H_2O . However, it is not zero for other molecules of C_{2v} symmetry. For example, consider an imaginary conformation of urea in which the four hydrogen atoms take the positions shown below:



Here, H^+ and H^- are mirror images of each other with respect to the molecular plane (the whole molecule is nearly planar in the real molecule). Then, $m = 1$. The displacements of $4m$ atoms are expressed by $3 \times 4m$ coordinates, which are distributed equally into the four species ($3m$ for each). The summation of these calculations leads to the general equations given earlier.

As another example, consider the NH_3 molecule of C_{3v} symmetry. Using the table given in Appendix 2, we find that $m_0 = 1$ (nitrogen atom), $m = 0$ and $m_v = 1$ (hydrogen atom). Thus, the number of normal vibrations in the A_1 , A_2 and E species are 2, 0, and 2, respectively.

Although not described earlier, classification of normal vibrations can be made by applying group theoretical treatments to individual molecules (37). The latter is useful for confirming the results obtained from Herzberg's tables.

1.14 Symmetry Selection Rules

As shown in Section 1.7, IR and Raman activities for small molecules can be determined by inspection of their normal modes. Clearly, it is difficult to apply such an approach to large and complex molecules. This problem can be solved by using the group theoretical consideration described next.

According to quantum mechanics (18, 19), the selection rule for the IR spectrum is determined by the integrals

$$\begin{aligned} [\mu_x]_{v',v''} &= \int \psi_{v'}^*(Q_a) \mu_x \psi_{v''}(Q_a) dQ_a, \\ [\mu_y]_{v',v''} &= \int \psi_{v'}^*(Q_a) \mu_y \psi_{v''}(Q_a) dQ_a \\ [\mu_z]_{v',v''} &= \int \psi_{v'}^*(Q_a) \mu_z \psi_{v''}(Q_a) dQ_a. \end{aligned} \quad (1-57)$$

Here, μ_x , μ_y and μ_z are the x , y and z components of the dipole moment at the electronic ground state, respectively. $\psi_{v'}$ and $\psi_{v''}$ are vibrational wavefunctions where v' and v'' are the vibrational quantum numbers before and after the transition, respectively. Q_a is the *normal coordinate* of the normal vibration, a . If one of these integrals is nonzero, this vibration is infrared-active. If all three integrals are zero, it is infrared-inactive.

Using (1-57) as an example, let us determine whether such an integral is zero or nonzero. For this purpose, we first expand μ_x in terms of the normal coordinate, Q_a :

$$\mu_x = (\mu_x)_0 + \left(\frac{\partial \mu_x}{\partial Q_a} \right) Q_a + \dots$$

Then, (1-57) can be rewritten as

$$\begin{aligned} [\mu_x]_{v',v''} &= (\mu_x)_0 \int \psi_{v'}^*(Q_a) \psi_{v''}(Q_a) dQ_a \\ &\quad + \left(\frac{\partial \mu_x}{\partial Q_a} \right) \int \psi_{v'}^*(Q_a) Q_a \psi_{v''}(Q_a) dQ_a + \dots \end{aligned} \quad (1-58)$$

The integral in the first term vanishes because of the orthogonality of $\psi_{v'}$ and $\psi_{v''}$ (except for $v' = v''$, no transition). In order for the second term to be nonzero,

$$\left(\frac{\partial \mu_x}{\partial Q_a} \right) \neq 0 \quad \text{and} \quad \int \psi_{v'}^*(Q_a) Q_a \psi_{v''}(Q_a) dQ_a \neq 0.$$

The latter is nonzero only when $\Delta v = \pm 1$ (harmonic oscillator, Section 1.3). In order to understand the significance of the former, we approximate the second term in (1-58) as

$$\left(\frac{\partial \mu_x}{\partial Q_a} \right) \int \psi_{v'}^*(Q_a) Q_a \psi_{v''}(Q_a) dQ_a \approx e \int \psi_v(Q_a) x \psi_{v''}(Q_a) dQ_a. \quad (1-59)$$

Here, $\mu_x = \sum_i e_i x_i$, where e_i is the charge on the i th electron or nucleus and x_i is the x component of its position.

Consider the fundamental vibration in which the transition occurs from $v' = 0$ to $v'' = 1$. From Eq. (1-28), it is obvious that ψ_0 is invariant under any symmetry operation since it contains the Q_a^2 term. On the other hand, the symmetry of ψ_1 is the same as that of Q_a since it contains a $Q_a e^{-Q_a^2/2}$ term. In general, any integral such as

$$\int f_A f_B f_C d\tau$$

does not vanish if the representation of the direct product, $f_A f_B f_C$, contains the totally symmetric representation.* In the present case, ψ_0 is totally symmetric. Then the integral such as (1-59) is nonzero if the representation of the product $x \psi_1$ is totally symmetric. This is possible only when x and ψ_1 belong to the same symmetry species.

The symmetry species of $\mu_x(x)$, $\mu_y(y)$ and $\mu_z(z)$ are listed in the character tables of the respective point groups (Appendix 1).** As shown in the preceding section, the symmetry species of normal vibrations can be found by using Herzberg's tables (Appendix 2). Thus, IR activity is readily determined by the inspection of character tables; *the vibration is IR-active if the component(s) of the dipole moment belong(s) to the same symmetry species as that of the vibration.*

As an example, consider IR activity of the six normal vibrations of the NH_3 molecule, which are classified into $2A_1$ and $2E$ species of C_{3v} point group. The character table shows that μ_z belongs to the A_1 and the pair of (μ_x, μ_y) belongs to the E species. Thus, all six normal vibrations are IR-active.

The selection rule for Raman spectrum is determined by the integrals

*The proof of this theorem is given in Ref. 36.

**The symmetry property of μ_x (x -component of the dipole moment) is the same as that of T_x (translational motion along the x -axis).

$$[\alpha_{xx}]_{v', v''} = \int \psi_{v'}^*(Q_a) \alpha_{xx} \psi_{v''}(Q_a) dQ_a, \quad (1-60)$$

$$[\alpha_{xy}]_{v', v''} = \int \psi_{v'}^*(Q_a) \alpha_{xy} \psi_{v''}(Q_a) dQ_a, \quad (1-61)$$

$$\vdots \qquad \vdots$$

Here $\alpha_{xx}, \alpha_{yy}, \alpha_{zz}, \alpha_{xy}, \alpha_{yz}$, and α_{xz} are the components of the polarizability tensor discussed in Section 1.7. If one of these six integrals is nonzero, this vibration is Raman-active. If all the integrals are zero, it is Raman-inactive.

Symmetry selection rules for Raman spectrum can be derived by using a procedure similar to that for the IR spectrum. One should note, however, that the symmetry property of α_{xy} , for example, is determined by the product, $\mu_x \mu_y(xy)$ (19). The symmetry species of six components of polarizability are readily found in character tables. In point group C_{3v} , for example, $\alpha_{xx} + \alpha_{yy}$ and α_{zz} belong to the A_1 species while two pairs, $(\alpha_{xx} - \alpha_{yy}, \alpha_{xy})$ and $(\alpha_{yz}, \alpha_{xz})$, belong to the E species.* Thus, all six normal vibrations of the NH_3 molecule ($2A_1$ and $2E$) are Raman-active. More generally, *the vibration is Raman-active if the component(s) of the polarizability belong(s) to the same symmetry species as that of the vibration.*

As another example, consider an octahedral XY_6 -type molecule of O_h symmetry. Using Herzberg's table, its 15 ($3 \times 7 - 6$) vibrations are classified into $A_{1g} + E_g + 2F_{1u} + F_{2g} + F_{2u}$. It is readily seen from the character table that only F_{1u} vibrations are IR-active, while A_{1g}, E_g and F_{2g} vibrations are Raman-active.

1.15 Resonance Raman Spectra

As stated in Section 1.4, resonance Raman (RR) scattering occurs when the sample is irradiated with an exciting line whose energy corresponds to that of the electronic transition of a particular chromophoric group in a molecule. Under these conditions, the intensities of Raman bands originating in this chromophore are selectively enhanced by a factor of 10^3 to 10^5 . This selectivity is important not only for identifying vibrations of this particular chromophore in a complex spectrum, but also for locating its electronic transitions in an absorption spectrum.

Theoretically, the intensity of a Raman band observed at $v_0 - v_{mn}$ is given by (38):

*Instead of α_{xx} and α_{yy} , their linear combinations, $\alpha_{xx} + \alpha_{yy}$ and $\alpha_{xx} - \alpha_{yy}$ are used for mathematical convenience.

$$I_{mn} = \text{constant} \cdot I_0 \cdot (v_0 - v_{mn})^4 \sum_{\rho\sigma} |(\alpha_{\rho\sigma})_{mn}|^2. \quad (1-62)$$

Here, m and n denote the initial and final states, respectively, of the electronic ground state. Although not explicit in Eq. (1-62), e represents an electronic excited state (Fig. 1-28) involved in Raman scattering. I_0 is the intensity of the incident laser beam of frequency v_0 . The $(v_0 - v_{mn})^4$ term expresses the v^4 rule to be discussed in Chapter 2, Section 2.6. Finally $(\alpha_{\rho\sigma})_{mn}$ represents the change in polarizability α caused by the $m \rightarrow e \rightarrow n$ transition, and ρ and σ are x , y and z components of the polarizability tensor (Section 1.7). This term can be rewritten as (38)

$$(\alpha_{\rho\sigma})_{mn} = \frac{1}{h} \sum_e \left(\frac{M_{me} M_{en}}{v_{em} - v_0 + i\Gamma_e} + \frac{M_{me} M_{en}}{v_{en} + v_0 + i\Gamma_e} \right), \quad (1-63)$$

where v_{em} and v_{en} are the frequencies corresponding to the energy differences between the states subscribed and h is Planck's constant. M_{me} , etc., are the electric transition moments, such as

$$M_{me} = \int \Psi_m^* \mu_\sigma \Psi_e d\tau. \quad (1-64)$$

Here, Ψ_m and Ψ_e are total wavefunctions of the m and e states, respectively, and μ_σ is the σ component of the electric dipole moment. Γ_e is the band width of the e th state, and the $i\Gamma_e$ term is called the damping constant. In normal Raman scattering, v_0 is chosen so that $v_0 \ll v_{em}$. Namely, the energy of the incident beam is much smaller than that of an electronic transition. Under these conditions, the Raman intensity is proportional to $(v_0 - v_{mn})^4$. As v_0 approaches v_{em} , the denominator of the first term in the brackets of Eq. (1-63)

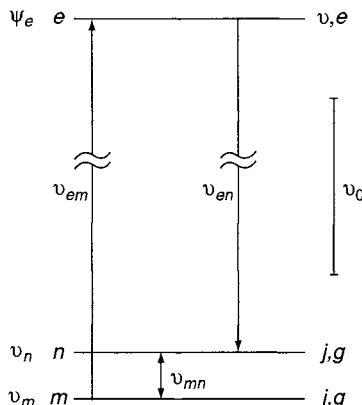


Figure 1-28 Energy level diagram for resonance Raman transition.

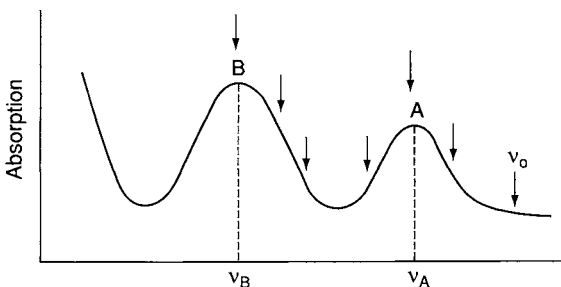


Figure 1-29 Absorption spectrum of a compound containing two chromophoric groups (A and B).

becomes very small. Hence, this term (“resonance term”) becomes so large that the intensity of the Raman band at $\nu_0 - \nu_{mn}$ increases enormously. This phenomenon is called *resonance Raman (RR) scattering*.

Suppose that a compound contains two chromophoric groups that exhibit electronic bands at ν_A and ν_B as shown in Fig. 1-29. Then, vibrations of chromophore A are resonance-enhanced when ν_0 is chosen near ν_A , and those of chromophore B are resonance-enhanced when ν_0 is chosen near ν_B . For example, heme proteins such as hemoglobin and cytochromes (Chapter 6, Section 6.1) exhibit porphyrin core $\pi-\pi^*$ transitions in the 400–600 nm region and peptide chain transitions below 250 nm. Thus, the porphyrin core and peptide chain vibrations can be selectively enhanced by choosing exciting lines, in the regions of these electronic absorptions.

More specific information can be obtained by expressing the total wavefunction as the product of the electronic and vibrational wavefunctions. (See the right-hand side labeling in Fig. 1-28). The results are (38, 39)

$$(\alpha_{p\sigma})_{mn} \cong A + B. \quad (1-65)$$

The *A*-term is written as

$$A \cong M_e^2 \frac{1}{\hbar} \sum_v \frac{\langle j|v\rangle\langle v|i\rangle}{\nu_{vi} - \nu_0 + i\Gamma_v}. \quad (1-66)^*$$

Here M_e is the pure electronic transition moment for the resonant excited state e , of which v is a vibrational level of band width Γ_v , ν_{vi} is the transition frequency from the ground state vibrational level (i) to the excited vibrational level (v). The *A*-term becomes larger as the denominator becomes smaller (resonance condition) and as M_e becomes larger (stronger electronic absorption). The numerator contains the product of two overlap integrals of vibrational wavefunctions (*Franck-Condon overlap*) involving the i , j and v states. Because of the orthogonality of vibrational wavefunctions (Section 1.2),

*Only the resonance term is shown in (1-66) as well as in (1-67).

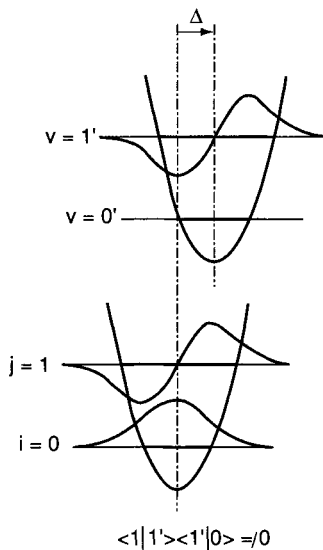


Figure 1-30 Shift of equilibrium position caused by a totally symmetric vibration.

either one of the integrals becomes zero unless the equilibrium position is shifted upon electronic excitation (Fig. 1-30). Since this occurs only for totally symmetric vibrations, the *A*-term enhancement can be seen only for totally symmetric modes.

The *A*-term resonance has been observed for a number of compounds. Figure 1-31 shows the RR spectra of TiI_4 obtained by 514.5 nm excitation (40). An overtone (nv) series up to $n = 12$ was observed in this case. (Also see Fig. 3-11 and Fig. 4-11.) The appearance of such a series can be explained if one calculates Franck-Condon overlaps under rigorous resonance conditions (41). Among the totally symmetric modes, the mode that leads to the excited state configuration is most strongly resonance-enhanced (42). For example, the NH_3 molecule is pyramidal in the ground state and planar at the excited state (216.8 nm above the ground state). Thus, the symmetric bending mode near 950 cm^{-1} is enhanced 10 times more than the symmetric stretching mode near $3,300\text{ cm}^{-1}$ when the exciting line is changed from 514.5 to 351.1 nm.

The *B*-term involves two electronic excited states (*e* and *s*) and provides a mechanism for resonance-enhancement of non-totally symmetric vibrations. The *B*-term, can be expressed as

$$B \cong M_e M'_e \frac{1}{h} \sum_v \frac{\langle j|Q|v\rangle\langle v|i\rangle + \langle j|v\rangle\langle v|Q|i\rangle}{v_{vi} - v_0 + i\Gamma_v}, \quad (1-67)$$

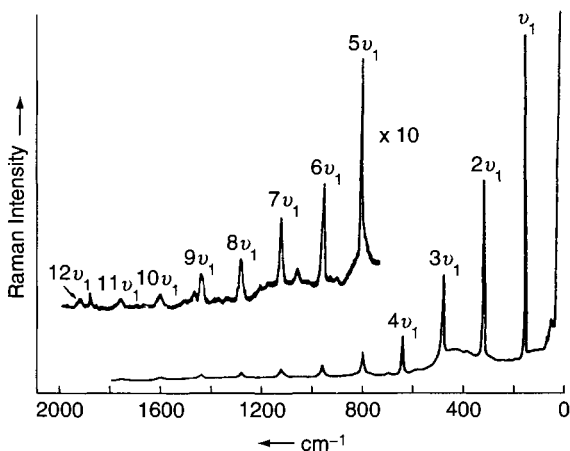


Figure 1-31 Resonance Raman spectrum of solid TiI_4 (514.5 nm excitation). $v_1 = 160.8 \text{ cm}^{-1}$. (Reproduced with permission from Ref. 40. Copyright 1973 American Chemical Society.)

$$M'_e = \mu_s \langle s | \partial H / \partial Q | e \rangle / \langle v_s - v_e \rangle, \quad (1-68)$$

where v_s and μ_s are the frequency and transition dipole moment of the second excited state(s). Although the denominator in the B -term is the same as that of the A -term, its numerator contains Q -dependent vibrational overlap integrals as well as Franck–Condon overlap integrals. Here, Q is the normal coordinate of a particular vibration. Thus, it does not vanish even when the equilibrium position is not shifted by electronic excitation (non-totally symmetric vibration). The most important term in Eq. (1-67) is the vibronic coupling operator $\langle s | \partial H / \partial Q | e \rangle$, where H is the electronic Hamiltonian. As will be shown later, this term becomes nonzero if normal coordinates of proper symmetry are chosen. Thus, it is possible to resonance-enhance these vibrations via the B -term. A typical example of B -term resonance is found in RR spectra of heme proteins and their model compounds (43). As shown in Fig. 1-32, metalloporphyrins such as Ni(OEP) exhibit two electronic transitions; Q_0 (α) and B (or Soret) bands together with a vibronic sideband, Q_1 (or β) in the 600–350 nm region. According to MO calculations on the porphyrin core of D_{4h} symmetry, the $a_{1u} \rightarrow e_g^*$ and $a_{2u} \rightarrow e_g^*$ transitions have similar energies and the same excited state symmetry, since $a_{1u} \times e_g = a_{2u} \times e_g = E_u$. This results in a strong configuration interaction to produce two separate states, Q_0 and B (see the inset in Fig. 1-32). The transition dipole moments nearly cancel each other to produce a weak Q_0 band in the visible region, but add up to produce a strong B band in the UV region.

As stated earlier, the vibronic coupling operator, $\langle s | \partial H / \partial Q | e \rangle$, determines which normal vibration is resonance-enhanced via the B -term. This term

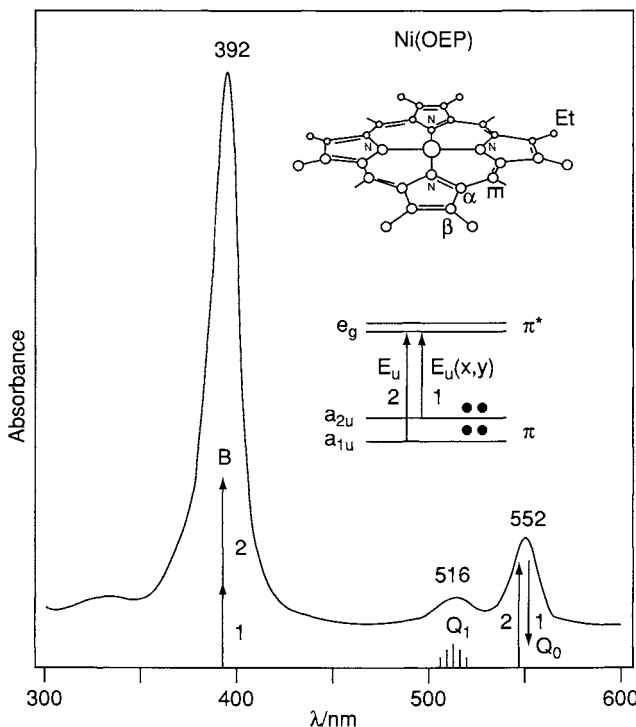


Figure 1-32 Absorption spectrum and energy level diagram of Ni (OEP). (Reproduced with permission from Ref. 43. Copyright © 1988 John Wiley & Sons, Inc.)

becomes nonzero only when the normal vibration has a proper symmetry. As discussed in Section 1.14, an integral such as

$$\int f_A f_B f_C d\tau \quad (1-69)$$

is nonzero if the direct product of the irreducible representations of f_A , f_B and f_C contains the totally symmetric component. Since both $e(Q_0)$ and $s(B)$ states are of E_u symmetry, only the A_{1g} , B_{1g} , B_{2g} and A_{2g} vibrations,

$$E_u \times E_u = A_{1g} + B_{1g} + B_{2g} + A_{2g}, \quad (1-70)$$

can be resonance-enhanced via the B -term.* Figure 1-33 shows the RR spectra of Ni(OEP) obtained by B , Q_1 and Q_0 excitation (44). The former is

*The general method for resolving direct products into symmetry species is found in textbooks of group theory^{14–18}. Appendix 3 summarizes the general rules for obtaining the symmetry species of direct products.

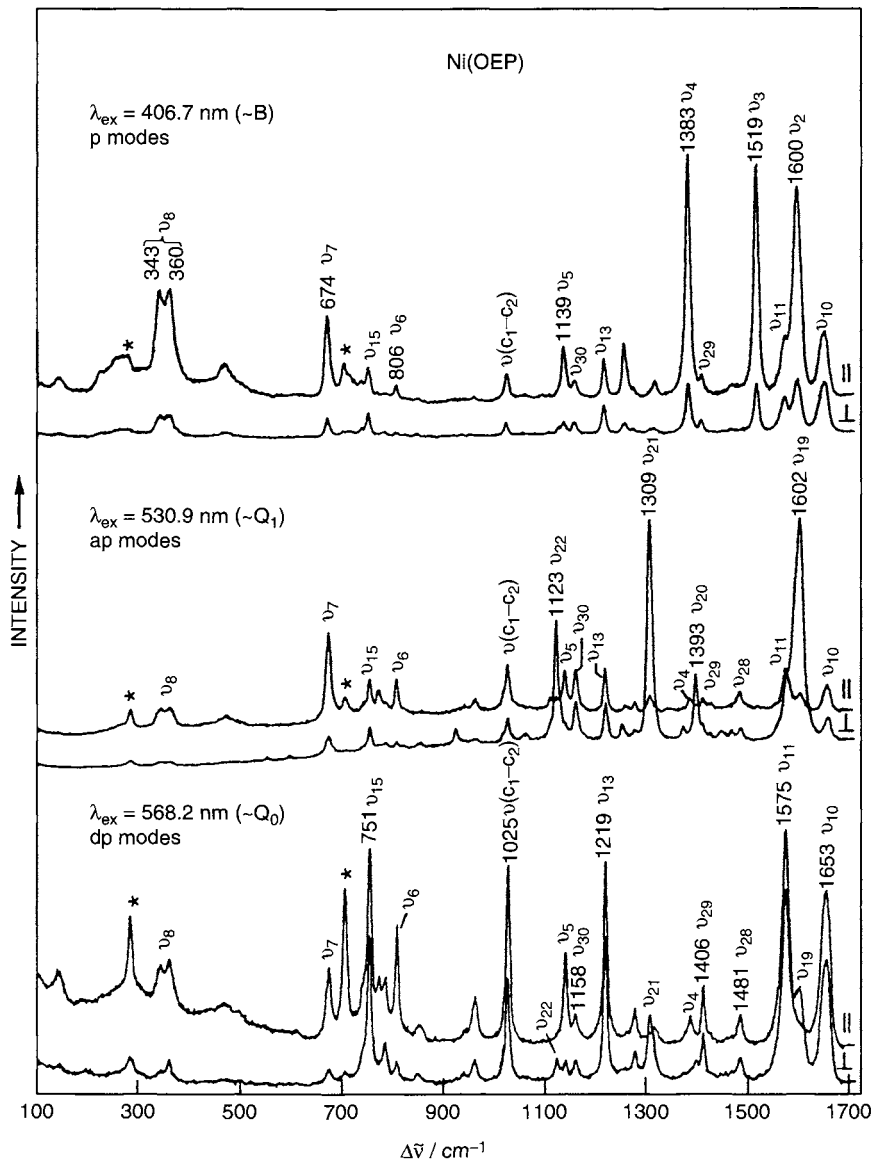


Figure 1-33 Resonance Raman spectra of Ni (OEP) obtained by three different excitations. (Reproduced with permission from Ref. 44. Copyright 1990 American Chemical Society.)

dominated by totally symmetric vibrations, whereas the latter two are dominated by B_{1g} , B_{2g} and A_{2g} vibrations since A_{1g} modes are not effective in mixing the B and Q_0 states because of the high symmetry of the porphyrin core. Distinction of these modes can be made by measuring the depolarization ratios (Section 1.9), which should be $\frac{3}{4}$ (depolarized) for B_{1g} and B_{2g} , and $\frac{3}{4} \sim \infty$ (inverse polarization) for A_{2g} vibrations. It should be noted that the RR spectrum obtained by Soret (B) excitation is dominated by A_{1g} vibrations, since resonance enhancement occurs through the A -term discussed earlier.

1.16 Space Group Symmetry

1.16.1 SYMMETRY ELEMENTS FOR A MOLECULE IN THE CONDENSED STATE

If one takes into account symmetry elements combined with translations, one obtains operations or elements that can be used to define the symmetry of space. Here, a translation is defined as the superposition of atoms or molecules from one site onto the same atoms or molecules in another site without the use of a rotation. The symmetry element called the *screw axis* involves an operation combining a translation with a rotation. The symmetry element called the glide plane involves an operation combining a reflection with a translation. These operations can be used to describe the symmetry of homogeneous spatial materials such as crystals and polymers, as well as space itself if one takes the identity element to be the set of all translations. This condition implies that these translations in a crystal are those that describe the lattice in contrast to those that are fractional translations associated with some rotation (screw motions and glides). A crystal may be considered to be made up of a large number of blocks of the same size and shape. One such block is defined as a unit cell. The unit cell must be capable of repetition in space without leaving any gap. The unit cell may be a primitive or nonprimitive unit cell. The distinction between these will be made later in this section.

The screw axis and the glide plane are further defined as follows:

Screw axis (n_p)

Rotation followed by a translation;

n = order of axis;

p/n = fraction of the unit cell over which translation occurs;

$n = 2, 3, 4$ or 6 ;

$p = 1, 2, 3, \dots, n - 1$.

For example, 2_1 = twofold screw axis, translation one-half the distance of the unit cell; and 3_1 = threefold screw axis, translation one-third the distance of the unit cell.

Figure 1-34 shows the operation of a twofold screw axis, in which the translation is $\frac{1}{2}$ of the unit cell (fractional translation).

Glide Plane

Reflection followed by a translation.

Figure 1-35 shows the operation of a glide plane.

The new symmetry elements that are added to the point symmetry elements are the screw axis and glide plane. As a result, 230 different combinations of symmetry elements become possible in what are called space groups. For a development of space groups see Burns and Glazer (45). Table 1-9 shows the distribution of the space groups among the seven crystal systems. Some of the space groups are never found in actual crystals, and about one-half of the known crystals belong to the 13 space groups of the monoclinic system. Figure 1-36 shows the lattices of the seven major crystal systems (one triclinic, four orthorhombic, two monoclinic, two tetragonal, three cubic, one hexagonal, one trigonal).

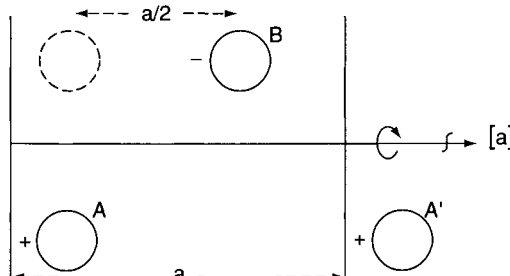


Figure 1-34 The operation of a twofold screw axis. (Reproduced with permission from Ref. 46.)

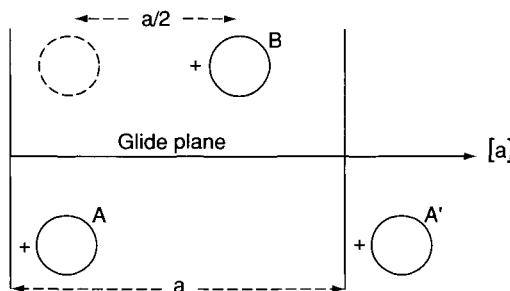
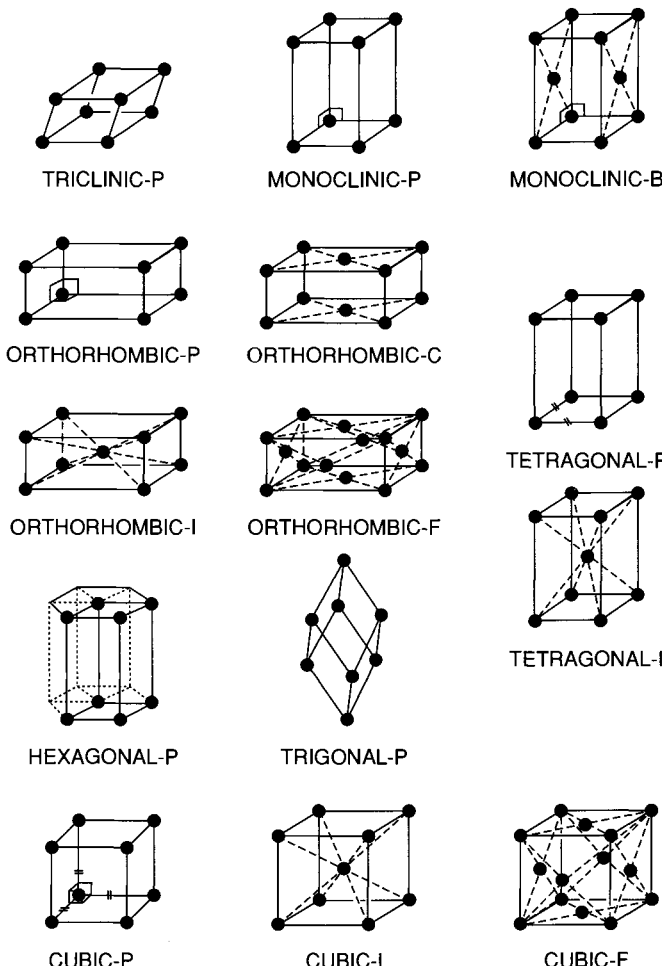


Figure 1-35 The operation of a glide plane. (Reproduced with permission from Ref. 46.)

Table 1-9 Distribution of Space Groups among the Seven Crystal Systems

Crystal System	Number of Space Groups
Triclinic	2
Monoclinic	13
Orthorhombic	59
Trigonal	25
Hexagonal	27
Tetragonal	68
Cubic	36

**Figure 1-36** The seven crystal systems corresponding to 14 Bravais lattices. (Reproduced with permission from Ref. 45.)

1.16.2 SPACE GROUP

Just as the point group collects all of the point symmetry elements, the space group is seen collecting all of the space symmetry elements in crystals involving translation. For the space group selection rules, it is necessary to work on crystals for which space groups are known from X-ray studies, or where sufficient information is available to make a choice of structure. Alternatively, the structure may be assumed, and the space group selection rules can serve as a test of this assumption. In deriving space group selection rules, one must deal with a primitive unit cell. A primitive unit cell is the smallest unit in a crystal which, by a series of translations, would build up the whole crystal.

The Hermann–Mauguin notation is generally used by crystallographers to describe the space group. Tables exist to convert this notation to the Schoenflies notation. The first symbol is a capital letter and indicates whether the lattice is primitive. The next symbol refers to the principal axis, whether it is rotation, inversion, or screw, e.g.,

$P2_1$ = primitive lattice with a two-fold axis of rotation, translation one-half the distance of the unit cell

$C2$ = nonprimitive centered lattice with a twofold axis of rotation.

A mirror plane is symbolized as m , and a glide plane by c , e.g.,

$P2_1/m$ m = mirror plane perpendicular to principal axis;

$C2/c$ c = glide plane perpendicular to principal axis.

Table 1-10 shows the space group symbolism used.

Table 1-10 Space Group Symbolism

First symbol refers to the Bravais lattice

P = primitive lattice

C = centered lattice

F = face-centered lattice

I = body-centered lattice

R = rhombohedral (unit cell can be primitive or nonprimitive; see notes to Table 1-11)

Principal axis of rotation given number n = order

e.g., 2 = twofold axis of rotation

For screw axis p/n = fraction of primitive lattice over which translation parallel to screw axis occurs.

e.g., $P2_1$ = primitive lattice with a twofold axis of rotation, translation; one-half unit cell

Mirror plane = m

Glide planes = symbols a , b , c along (a) , (b) , (c) axes

symbol $n = (b + c)/2$ or $(a + b)/2$

symbol $d = (a + b)/4$ or $(b + c)/4$ or $(a + c)/4$

e.g., $P2_1/m$; m = mirror plane perpendicular to principal axis

$C2/c$; c = glide plane axis perpendicular to principal axis

As previously mentioned, the primitive unit cell is the smallest unit of a crystal that reproduces itself by translations. Figure 1-37 illustrates the difference between a primitive and a centered or nonprimitive cell. The primitive cell can be defined by the lines a and c . Alternatively, we could have defined it by the lines a' and c' . Choosing the cell defined by the lines a'' and c'' gives us a nonprimitive cell or centered cell, which has twice the volume and two repeat units. Table 1-11 illustrates the symbolism used for the various types of lattices and records the number of repeat units in the cell for a primitive and a nonprimitive lattice. The spectroscopist is concerned with the primitive (Bravais) unit cell in dealing with lattice vibrations. For factor group selection rules, it is necessary to convert the number of molecules per crystallographic unit cell Z to Z' , discussed later, which is the number of molecules per primitive cell. For example,

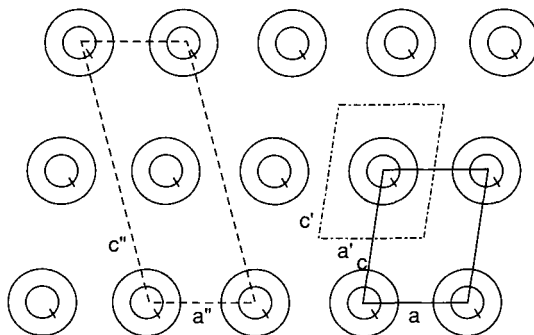


Figure 1-37 Differentiation between primitive and centered unit cells. (Reproduced with permission from Ref. 46.)

Table 1-11 Primitive and Centered Lattices

Type	Symbol	Number of Repeat Units in Cell
Primitive	P	1
Rhombohedral ^a	R	3 or 1 ^b
Body-centered	I	2
Side-centered	A, B, or C	2
Face-centered	F	4

^aAlso called trigonal.

^bThere are cases in which the number of repeat units in the crystallographic cell may be three or one. For the cases where it is three, Z will be divisible by three. For example, for TiS, $D_{3d}^5 - R\bar{3}m$ (No. 166), $Z = 9$, and therefore $Z' = 9/3 = 3$. However, for Cr_2O_3 , $D_{3d}^6 - R\bar{3}c$ (No. 167), $Z = 2$, and $Z' = 2/1 = 2$. Thus, in the latter crystal the cell can be considered to be primitive.

$$Z' = \frac{Z(\text{number of molecules in crystallographic cell})}{\text{repeat units in cell}}$$

If $Z = 4$ for an F -type lattice, then

$$Z' = 4/4 = 1.$$

In the site symmetry compilation for the 230 space groups given in Appendix 4, the data are for a primitive cell and can be used directly.

1.16.3 FACTOR GROUP

It is necessary to define a factor group and to describe how it relates to a space group. In a crystal, one primitive cell or unit cell can be carried into another primitive cell or unit cell by a translation. The number of translations of unit cells then would seem to be infinite since a crystal is composed of many such units. If, however, one considers only one translation and consequently only two unit cells, and defines the translation that takes a point in one unit cell to an equivalent point in the other unit cell as the identity, one can define a finite group, which is called a *factor group* of the space group.

The factor groups are isomorphic (one-to-one correspondence) with the 32 point groups and, consequently, the character table of the factor group can be obtained from the corresponding isomorphic point group.

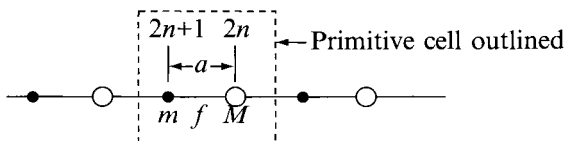
1.16.4 SITE GROUP

It also becomes necessary to define a site group. A unit cell of a crystal is composed of points (molecules or ions) located at particular positions in the cell. It turns out, however, that the points can only be located at certain positions in the lattice that are called sites, that is, they can only be located on one of the symmetry elements of the factor group and thus remain invariant under that operation independent of translation. The point has fewer symmetry elements than the parent factor group and belongs to what is called a “site group,” which is a subgroup of the factor group. [A subgroup (S) contains a set of symmetry elements that are also part of a parent group (G).] In general, factor groups can have a variety of different sites possible, that is, many subgroups can be formed from the factor group. Also, a number of distinct sites in the Bravais unit cell with the same site group are possible.

1.17 Normal Vibrations in a Crystal

In order to discuss the selection rules for crystalline lattices it is necessary to consider elementary theory of solid vibrations. The treatment essentially follows that of Mitra (47). A crystal can be regarded as a mechanical system of nN particles, where n is the number of particles (atoms) per unit cell and N is the number of primitive cells contained in the crystal. Since N is very large, a crystal has a huge number of vibrations. However, the observed spectrum is relatively simple because, as shown later, only where equivalent atoms in primitive unit cells are moving in phase as they are observed in the IR or Raman spectrum. In order to describe the vibrational spectrum of such a solid, a frequency distribution or a distribution relationship is necessary. The development that follows is for a simple one-dimensional crystalline diatomic linear lattice. See also Turrell (48).

Consider a simple one-dimensional infinite chain, consisting of alternating masses M and m separated by a distance a with a force constant f :



The two particles are located at the even- and odd-numbered lattice points $2n$ and $2n + 1$, respectively. The displacements u_{2n} and u_{2n+1} of the even and odd particles are given by the equations of motion

$$\begin{aligned} M\ddot{u}_{2n} &= f(u_{2n+1} + u_{2n-1} - 2u_{2n}), \\ m\ddot{u}_{2n+1} &= f(u_{2n+2} + u_{2n} - 2u_{2n+1}). \end{aligned} \quad (1-71)$$

Assuming the following solutions for u_{2n} and u_{2n+1} :

$$u_{2n} = y_1 \exp i(2\pi vt + 2nka), \quad (1-72)$$

$$u_{2n+1} = y_2 \exp i[2\pi vt + (2n + 1)ka], \quad (1-73)$$

and substituting the values of u_{2n} and u_{2n+1} in Eq. (1-71) one obtains two equations for the amplitudes y_1 and y_2 . Here k is the wave vector and corresponds to the phase differences for each successive cell. A solution for these equations exists, and the secular determinant is illustrated as follows:

$$\begin{vmatrix} 2f - 4\pi^2 v^2 M & -2f \cos ka \\ -2f \cos ka & 2f - 4\pi^2 v^2 m \end{vmatrix} = 0. \quad (1-74)$$

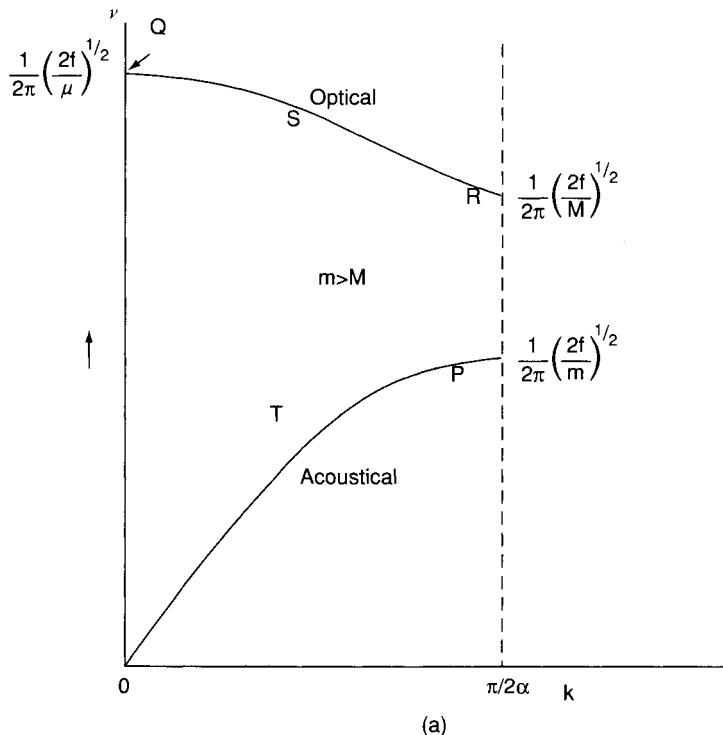
A dispersion formula results, based on frequency dependency on masses, force constant and distance between the two masses, such as

$$\nu^2 = \frac{1}{4\pi^2} \left[\frac{f}{\mu} \pm \left(\frac{f^2}{\mu^2} - \frac{4f^2 \sin^2 ka}{Mm} \right)^{\frac{1}{2}} \right], \quad (1-75)$$

where μ is the reduced mass. The finite length of the lattice restricts the values of k in the range $-\pi/2a \leq k \leq \pi/2a$. The region between these limits of k is called the first Brillouin zone. There are two solutions for ν , since in Eq. (1-75) ν depends on the positive or negative signs and these correspond to the optical and acoustical branches, respectively. The two roots are

$$\begin{aligned} \nu &= 1/2\pi(2f/\mu)^{1/2} && \text{(optical branch),} \\ \nu &= 1/2\pi[2f(M+m)]^{1/2}ka && \text{(acoustic branch).} \end{aligned} \quad (1-76)$$

The positive roots of Eq. (1-75) are plotted in the positive half of the Brillouin zone as shown in Fig. 1-38a. It may be observed that the upper curve, which is called the optical branch, represents frequencies occurring in the optical



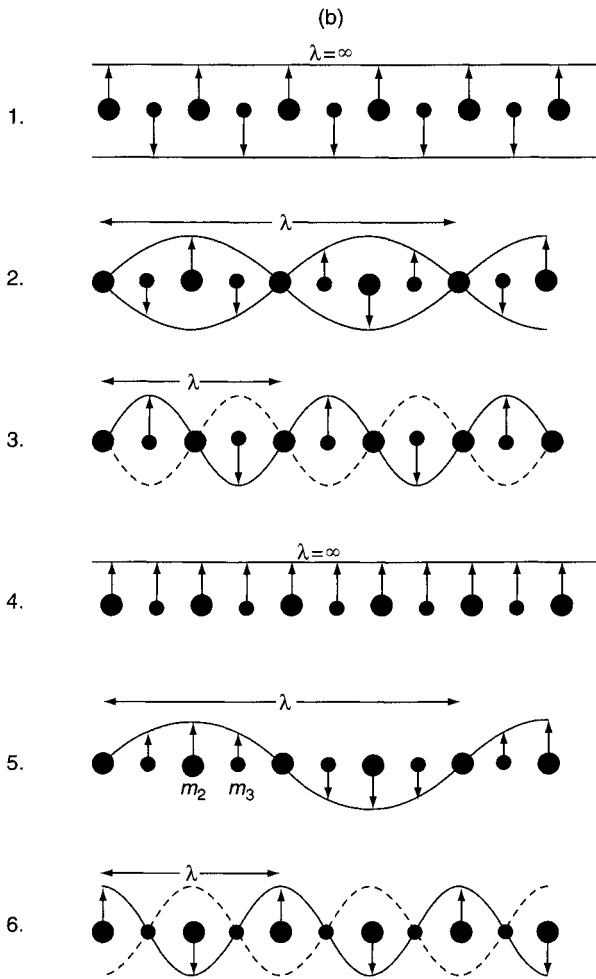


Figure 1-38 (a) Dispersion relation for the optical and acoustical branches in solids. (b) Wave motion in an infinite diatomic lattice. (Reproduced with permission from Ref. 49.)

spectral region (infrared or Raman). The low curve passes through $\nu = 0$ and is termed the acoustical branch (so-called because the frequencies occur in the sonic or ultrasonic region). Various wave motions are associated with both the optical and acoustical branches illustrated in Fig. 1-38b. Figure 1-38b-1 illustrates the wave motion of the optical branch at $k = 0$ and at point Q in Fig. 1-38a. Here the two atoms vibrate rigidly against each other. Figure 1-38b-2 shows the wave motion at point S on the optical branch. Figure 1-38b-3 demonstrates the wave motion at point R on the optical branch, where the light atoms are moving back and forth against

each other with the heavy atoms being fixed. In Fig. 1-38b-4 at point O ($k = 0$) of the acoustic branch, the wave motion involves a translation at the entire lattice. Figure 1-38b-5 shows the wave motion at point T on the acoustic branch. Figure 1-38b-6 shows the wave motion at point P of the acoustical branch, where only the heavy atoms vibrate back and forth against each other and the light atoms are stationary.

The optical spectral region consists of internal vibrations (discussed in Section 1.13) and lattice vibrations (external). The fundamental modes of vibration that show infrared and/or Raman activities are located in the center Brillouin zone where $k = 0$, and for a diatomic linear lattice, are the long-wave limit. The lattice (external) modes are weak in energy and are found at lower frequencies (far infrared region). These modes are further classified as translations and rotations (or librations), and occur in ionic or molecular crystals. Acoustical and optical modes are often termed “phonon” modes because they involve wave motions in a crystal lattice chain (as demonstrated in Fig. 1-38b) that are quantized in energy.

If the primitive cell contains σ molecules, each of which contains ρ atoms, then the number of acoustic modes is 3, and that of optical modes is $(3\sigma\rho - 3)$. The latter is classified into $(3\rho - 6)\sigma$ internal modes and $(6\sigma - 3)$ lattice modes. Analysis of these optical modes will be carried out in the following section.

Further discussion of solid vibrations of three-dimensional lattices is beyond the scope of this text. The reader may refer to Turrell (48) or other solid state texts (49).

1.18 Selection Rules for Solids (Factor Group)

By simply extending the methods used for the point group selection rules, one can obtain selection rules for molecules involving rotation–translation and reflection–translation. Two approaches are available. The older method is the Bhagavantam–Ventkatarayudu (BV) method (50), and necessitates the availability of the structure of the material being studied. The other method is that of Halford–Hornig (HH) (51–53) and considers only the local symmetry of a solid and the number of molecules in the unit cell and is simpler to work with. This method is also called the correlation method and depends on the proper selection of the site symmetry in the unit cell.

1.18.1 UNAMBIGUOUS CHOICE OF SITE SYMMETRY IN THE UNIT CELL

For cases where an unambiguous choice of site symmetry cannot be made, the use of Wyckoff’s tables of crystallographic data (54) can prove helpful. Wyckoff’s tables consist of the site correlations for some space groups. In instances where there is some doubt as to which site correlates (Appendix 5)

with an axis of rotation, e.g., $[C_2(x), C_2(y), C_2(z)]$, or with a plane of symmetry $[\sigma(xy), \sigma(yz), \sigma(zx)]$, the proper site can be chosen. For example, consider orthorhombic PuBr_3 , which has a D_{2h}^{17} ($Cmcm$) space group and a crystallographic unit cell with $Z = 4$. For a C -type lattice there are two repeat units in the cell, and therefore

$$\begin{aligned} Z' &= \text{number of molecules in the cell} \\ &= \frac{Z(\text{number of molecules in crystallographic cell})}{\text{repeat units in cell}} = \frac{4}{2} = 2. \end{aligned}$$

From Appendix 4, we can observe that for D_{2h}^{17} (space group 63) the following site symmetries are possible: $2C_{2h}(2)$; $C_{2v}(2)$; $C_i(4)$; $C_2(4)$; $2C_s(4)$; $C_1(8)$. With the number of molecules in the unit cell equal to two, we must place two Pu^{3+} ions on a set of particular sites and six Br^- on other sets of sites. We observe that two site symmetries are available for the two Pu^{3+} ions—either C_{2h} or C_{2v} , each having two equivalent sites per set to place the metal ions. An unambiguous choice cannot be made with the data available. For the six Br^- ions, no site symmetry has six equivalent sites available. Thus, we must conclude that the six Br^- ions must be nonequivalent, and some are on one site and others on another site. At this point one must consult the Wyckoff tables (see Appendix 5) on published crystallographic data, and when this is done, we find the notation tabulated here.

Ion	Site Position
2Pu^{3+}	c
2Br^-	c
4Br^-	f

We can deduce the Wyckoff nomenclature of the site positions from the site symmetries by listing the site positions in alphabetical order, as shown in the next table.

Site in Appendix 4	Alphabetical Order	Wyckoff's Alphabetical Ordering of Site Position	Ion Site
$2C_{2h}(2)$	$C_{2h}(2)$	a	
	$C_{2h}(2)$	b	
$C_{2v}(2)$	$C_{2v}(2)$	c	$2\text{Pu}^{3+}(c)$
			$2\text{Br}^-(c)$
$C_i(4)$	$C_i(4)$	d	
$C_2(4)$	$C_2(4)$	e	
$2C_s(4)$	$C_s(4)$	f	$4\text{Br}^-(f)$
	$C_s(4)$	g	
$C_1(8)$	$C_1(8)$	h	

We can place the two Pu^{3+} ions on a c site (C_{2v}), two Br^- ions on a c site (C_{2v}), and four Br^- must be on an f site (C_s). If we examine the correlation tables in Appendix 6, we observe that three correlations are possible for a D_{2h} space group with a site symmetry of C_{2v} . Similarly, three correlations are possible for the site symmetry C_s . Each correlation is based on a different rotational axis or reflection plane being involved. For example:

	$C_2(z)$	$C_2(y)$	$C_2(x)$	$\sigma(xy)$	$\sigma(zx)$	$\sigma(yz)$
D_{2h}	C_{2v}	C_{2v}	C_{2v}	C_s	C_s	C_s
Site Correlation		c	$a, b, e,$	g		f

One must decide which site group to use. Appendix 5 can be used to determine the proper site. For each space group, the correlation to go with each site is included. Knowing the site symmetry as given by the Wyckoff tables, one can determine which site correlation to use. For this example, the c -site position for a C_{2v} site is correlated with C_{2v} involving a C_2 rotation around the y axis, and the f -site position for a C_s site is correlated with C_s , involving a reflection plane in the yz plane. In this manner an unambiguous choice of the site symmetry for the Pu^{3+} and Br^- ions is made. This method of obtaining the proper site symmetry is possible whenever the Wyckoff tables contain the molecule of interest. If the information is not available in the Wyckoff tables, then one must resort to a study of the actual crystallographic structure of the crystalline material, if it is available.

Although only two equivalent sites per set are available for C_{2v} symmetry, it is possible to place the two Pu^{3+} and two Br^- ions in a C_{2v} site, since the number of such sites is infinite. When the site symmetry is C_p , C_{pv} , or C_s and $p = 1, 2, 3$, etc., the number of sites is infinite. This point should be kept in mind when using Appendix 5. Figure 1-39 demonstrates the packing diagram of PuBr_3 .

1.18.2 EXAMPLES OF THE HALFORD-HORNING SITE GROUP METHOD

In this section, we shall attempt to illustrate the HH method using several examples.

To derive factor group (space group) selection rules, it is necessary to utilize X-ray data for a molecule from a literature source or from Wyckoff's (54) *Crystal Structures*. The factor group and site symmetries of the ion, molecule, or atoms must be available, as well as the number of molecules per unit cell reduced to a primitive unit cell.

(a) LaCl_3 Solid

Let us consider the LaCl_3 crystal. The unit cell of LaCl_3 is seen in Fig. 1-40. The data available from Wyckoff indicate a space group #176, $C_{6h}^2-P\bar{6}3/m$.

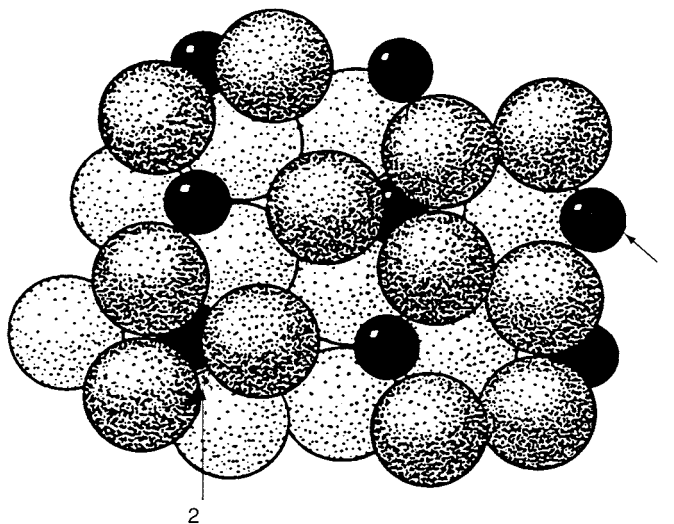


Figure 1-39 Packing diagram for PuBr_3 . 1 and 2 indicate Br atom sites. (Reproduced with permission from Ref. 55. Copyright © 1972 John Wiley & Sons, Inc.)

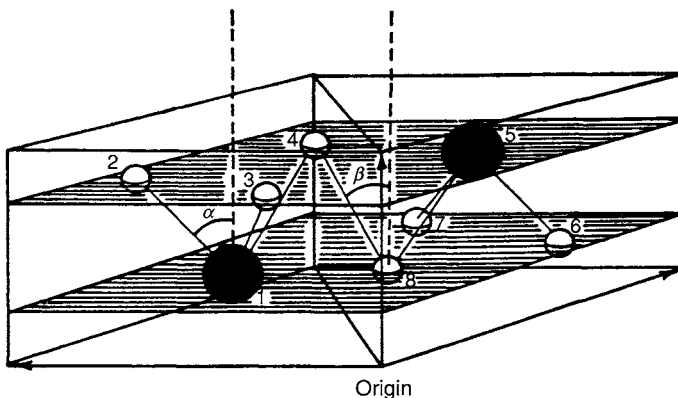


Figure 1-40 Unit cell for LaCl_3 . The large circles represent lanthanum ions while the small circles represent chlorine ions.

The unit cell is $2(Z')$. The two La atoms sit on a C_{3h} site, and the six chlorine atoms are on a C_s site (see Appendix 4). Since the Hermann–Mauguin nomenclature cites that the unit cell is primitive ($\text{Pb}6_3/m$) we need not reduce it. For the two La atoms there are six degrees of freedom $(3n, Z') = 3 \times 1 \times 2 = 6$. The six Cl atoms possess 18 degrees of freedom $(3n, Z') = 3 \times 3 \times 2 = 18$. Since all vibrational modes can be considered external modes, we need only correlate the site group to factor group. For the

Table 1-12 Correlation Table for La³⁺ in LaCl₃

Degrees of Freedom (DOF)		Site Group C_{3h}	Factor Group C_{6h}^2	Modes	
<i>T</i>	<i>R</i>			<i>T</i>	<i>R</i>
0	0		A'	$A_x (R_z)$	0 0
				B_u	0 0
4	0	$(T_x, T_y)E'$	E_{2g}	1 0	
			$E_{lu} (T_x, T_y)$	1 0	
2	0	$(T_z)A''$	$A_u (T_g)$	1 0	
			B_g	1 0	
0	0		E''	E_{2u}	0 0
				$E_{lg} (R_x, R_y)$	0 0

La atoms we can initiate a correlation chart using the correlation tables (Appendix 6) (55). See Table 1-12. For a derivation of the correlation tables, see Ref. 45.

The six degrees of freedom (DOF) for the La atoms are placed where the site group indicates translation vectors. For example, the E' species in the C_{3h} site has T_x, T_y (two vectors). Therefore, the two La atoms with four DOF are placed with E' species. Likewise, the remaining two DOF are placed with A'' species. We need not consider site rotations since there can be no site rotations for single atoms. Examining the correlation tables (see Appendix 6), we can assign the four E' species to one E_{2g} and one E_{lu} in the C_{6h}^2 factor group, since “doubly degenerate” counts for two. Likewise, we can assign the two A'' species in C_{3h} sites to A_u and B_g in the factor group C_{6h}^2 . Thus, two La atoms have E_{2g}, E_{lu}, B_g , and A_u as the active modes totaling the six DOF.

Similarly, one can calculate the correlation chart for the six Cl atoms as illustrated in Table 1-13. For the six Cl atoms, activity is demonstrated for $2A_g, 2B_u, 2E_{2g}, 2E_{lu}, A_u, B_g, E_{2u}$ and E_{lg} totaling 18 DOF. Summarizing the modes for LaCl₃ we obtain

$$\text{For 2 La: } \Gamma_{T'} = E_{2g} + E_{lu} + A_u + B_g,$$

$$\text{For 6 Cl: } \Gamma_{T'} = 2A_g + 2E_{2g} + E_{1g} + B_g + 2B_u + 2E_{lu} + E_{2u} + A_u,$$

where T' equals the total lattice or external modes of vibration. Including the three acoustic modes ($A_u + E_{1u}$), the total of 24 modes for LaCl₃ is distributed as follows:

$$\Gamma n_i = 3E_{2g} + E_{1g} + 2B_g + 2A_g + 3E_{lu} + 2B_u + E_{2u} + 2A_u.$$

Table 1-13 Correlation Table For Cl^- in LaCl_3

Degrees of Freedom (DOF)		Site Group C_s	Factor Group C_{6h}^2	Modes	
T	R			T	R
12	0	$(T_x, T_y)A'$	$A_g (R_z)$	2	0
			B_u	2	0
			E_{2g}	2	0
			$E_{1u} (T_x, T_y)$	2	0
6	0	$(T_z)A''$	$A_u (T_z)$	1	0
			B_g	1	0
			E_{2u}	1	0
			$E_{1g} (R_x, R_y)$	1	0

For a C_{6h}^2 factor group, the vibrations B_g , B_u and E_{2u} are inactive. Subtracting off the inactive modes, the three acoustic, total modes are

$$3E_{2g} + E_{1g} + 2A_g + 2E_{1u} + A_u \\ \text{R} \quad \text{R} \quad \text{R} \quad \text{IR} \quad \text{IR}$$

The $3E_{2g}$, E_{1g} and $2A_g$ modes would be Raman-active, and the $2E_{1u} + A_u$ modes would be IR-active. The summary for LaCl_3 is

$$\begin{array}{cccc} \text{R} & \text{IR} & \text{C} & \text{P} \\ 10 & 5 & 0 & 1 \end{array}$$

At $k = 0$, acoustic modes have zero frequency and are not observed in the Raman or IR experiments. They may be observed by performing slow neutron scattering experiments.

As shown in the following section, one can apply the same procedures for an organic molecule such as cyclopropane, C_3H_6 . For such molecules one correlates for the molecular point group \rightarrow site group \rightarrow factor group to obtain the internal modes, and the site group \rightarrow factor group for the external modes. This would be the procedure if one is dealing with covalent organic compounds with internal modes of vibrations as well as external modes.

(b) Solid Cyclopropane, C_3H_6

Cyclopropane belongs to the C_{2v}^7 - $Pmn2_1$ space group (No. 31) with $Z' = 2$. Figure 1-41 shows the structure of cyclopropane. The molecular point group is D_{3h} . The site group C_s is a subgroup of both the C_{2v}^7 , and D_{3h} groups. The proper choice of C_s is obtained from Appendix 5 and is found to be $C_s(\sigma_{yz})$. A total of $3n \cdot Z' = 3 \cdot 9 \cdot 2 = 54$ modes are expected, of which $(3n - 6)Z' = 42$ are internal modes. There are, therefore, $54 - 42 = 12$ external modes. For

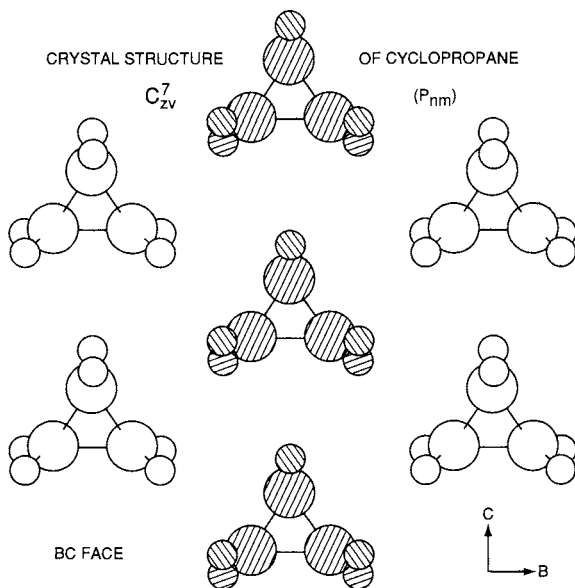


Figure 1-41 Proposed crystal structure of cyclopropane. The shaded molecules are not in the same plane as the unshaded ones and are inclined oppositely. (Reproduced with permission from Ref. 47.)

organic molecules such as cyclopropane, it is necessary to correlate the molecular point group to the site group and factor group to obtain the internal modes. For cyclopropane the correlation follows:

Point Group → Site Group → Factor Group.

$$\text{D}_{3\text{h}} \quad \text{C}_s(\sigma_{yz}) \quad \text{C}_{2v}^7$$

The external modes are determined as for the LaCl₃ case by correlating the site group → factor group.

Internal modes for C₃H₆:

$$\Gamma_n = 12A_1 + 9A_2 + 9B_1 + 12B_2$$

External modes for C₃H₆:

$\Gamma_{T+T'} = A_2 + B_1 + 2A_1 + 2B_2$	Total translations + acoustics
$\Gamma_T = A_1 + B_1 + B_2$	Translations
$\Gamma_{T'} = A_2 + A_1 + B_2$	Acoustics
$\Gamma_R = A_1 + 2B_1 + 2A_2 + B_2$	Rotations

Summary for C₃H₆:

A total of 3nZ' = 3 · 9 · 2 = 54 modes are expected:

$$\begin{aligned}
 \Gamma_{n_i} &= 12A_1 + 9A_2 + 9B_1 + 12B_2 && \text{Internal modes} \\
 \Gamma_T &= A_1 + B_1 + B_2 && \text{Translations} \\
 \Gamma'_T &= A_1 + A_2 + B_2 && \text{Acoustics} \\
 \Gamma'_R &= A_1 + 2A_2 + 2B_1 + B_2 && \text{Rotations} \\
 \Gamma_n &= 15A_1 + 12A_2 + 12B_1 + 15B_2 && \text{Total}
 \end{aligned}$$

Activity (IR,R) (R) (IR,R) (IR,R)

Of these, 39 are infrared-active and 51 are Raman-active, and A₁ + B₁ + B₂ are acoustic modes and are not observed.

Correlation tables for cyclopropane internal and external modes are tabulated in Tables 1-14 and 1-15.

We have illustrated the methods to obtain solid state selection rules. It should be mentioned that tables for factor group or point group analyses have been prepared by Adams and Newton (56, 57) where one can read the number and type of species allowed directly from the table. Although useful, the approach neglects the procedures as how to obtain results in the tables. For further examples of the correlation method, see Refs. 58–61, and the Correlation Theory Bibliography.

In general, a vibrational band in the free state splits into several bands as a result of solid intermolecular interactions in the unit cell. The number of split components can be predicted by the factor group analysis discussed earlier. Such splitting is termed factor group splitting or Davydov splitting, and the magnitude of this splitting is determined by the strength of the intermolecular interaction and the number of molecules in the unit cell interacting. In molecular crystals this splitting is in the range of 0–10 cm⁻¹.

Table 1-14 Correlation Table for Cyclopropane Internal Modes

Molecular Point Group D_{3h}*	Site Group C₃(σ_{yz})	Factor Group C_{2v}⁷

*Number of species for molecular point group determined from Appendix 2.

Table 1-15 Correlation Table for Cyclopropane External Modes

Degrees of Freedom (DOF)		Site Group $C_s(\sigma_{yz})$	Factor Group C_2^7	Modes	
T	R			T	R
4	2	$(T_x, T_y)(R_z)A'$	$A_1(T_z)$ $A_2(R_z)$	2	1
2	4	$(T_z)(R_x, R_y)A''$	$B_1(T_x)(R_y)$ $B_2(T_y)(R_x)$	1	2

1.19 Polarized Raman Spectra of Single Crystals

Porto et al. (61) illustrated the importance of polarized Raman spectra in obtaining the symmetry properties of normal vibrations, and their assignments. If one examines the character table for the D_{3d} point group (see Appendix 1), one may observe that the A_{1g} and E_g vibrations are Raman-active. The A_{1g} modes become Raman-active if any of the polarizability components $\alpha_{xx}, \alpha_{yy}, \alpha_{zz}$ change during irradiation. Let us consider a single crystal of calcite, which exists in a D_{3d}^6 space group ($Z = 2$), and having $1A_{1g}$ and $4E_g$ vibrations (a total of nine) as determined by factor group analysis. If we irradiate this crystal in the y direction (see Fig. 1-42) and observe the Raman scattering in the x direction and polarized scattering in the z direction ($y(zz)x$)

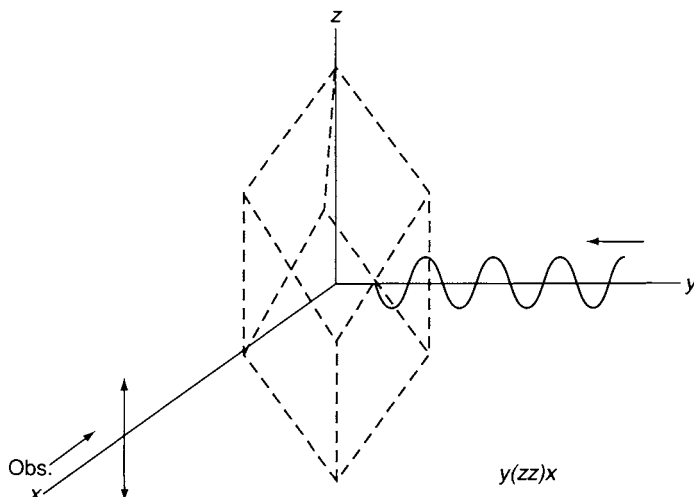


Figure 1-42 Schematic representation of experimental conditions used for the measurement of depolarization ratios of calcite crystal. (Reproduced with permission from Ref. 29. Copyright © 1986, John Wiley & Sons, Inc.)

in the Damen–Porto nomenclature); we should observe only the A_{1g} species. We can understand how this occurs by simplifying Eq. (1-46) and obtaining

$$P_z = \alpha_{zz} E_z,$$

since $E_x = E_y = 0$ and $P_x = P_y = 0$. The polarizability component α_{zz} belongs to the A_{1g} species, and only A_{1g} modes should be observed under the conditions of $y(zz)x$. Figure 1-43a illustrates the Raman spectrum obtained at $y(zz)x$ radiation (61). Only the $1,088\text{ cm}^{-1}$ vibration appears, and this belongs to the A_{1g} species. Under the radiation conditions $z(xx)y$, both A_{1g} and E_g species should appear. Figure 1-43b shows four of five vibrations appearing (the $1,434\text{ cm}^{-1}$ band is not shown). The $1,088\text{ cm}^{-1}$ band is the A_{1g} mode, while the others are the E_g modes. The assignments for calcite are therefore made using the polarized Raman technique. These assignments may be confirmed by irradiating the calcite crystal under the $y(xy)x$ and $x(zx)y$ conditions (Fig. 1-43c,d), where only the E_g modes appear.

This example illustrates the usefulness of the polarized Raman technique. For a further discussion on the analysis of calcite, see Nakamoto (37), Nakagawa and Walter (62) and Mitra (47) for data on gypsum.

1.20 Normal Coordinate Analysis

As shown in Section 1.3, force constants of diatomic molecules can be calculated by using Eq. (1-20). In the case of polyatomic molecules, force constants can be calculated via normal coordinate analysis (NCA), which is much more involved than simple application of Eq. (1-20). Its complete description requires complex and lengthy mathematical treatments that are beyond the scope of this book. Here, we give only the outline of NCA using the H_2O molecule as an example. For complete description of NCA, the reader should consult references (63–65) and general reference books cited at the end of this chapter.

1.20.1 INTERNAL COORDINATES

The kinetic and potential energies of a polyatomic molecule can be expressed in terms of Cartesian coordinates ($\Delta x, \Delta y, \Delta z$) or internal coordinates such as increments of bond length (Δr) and bond angles ($\Delta\alpha$). In the former case, $3N$ coordinates are required for an N -atom molecule. Figure 1-44 shows the nine Cartesian coordinates of the H_2O molecule. Since the number of normal vibrations is 3 ($3 \times 3 - 6$), this set of Cartesian coordinates includes six extra coordinates. On the other hand, only three coordinates ($\Delta r_1, \Delta r_2$ and $\Delta\alpha$) shown in Fig. 1-44 are necessary to express the energies in terms of internal

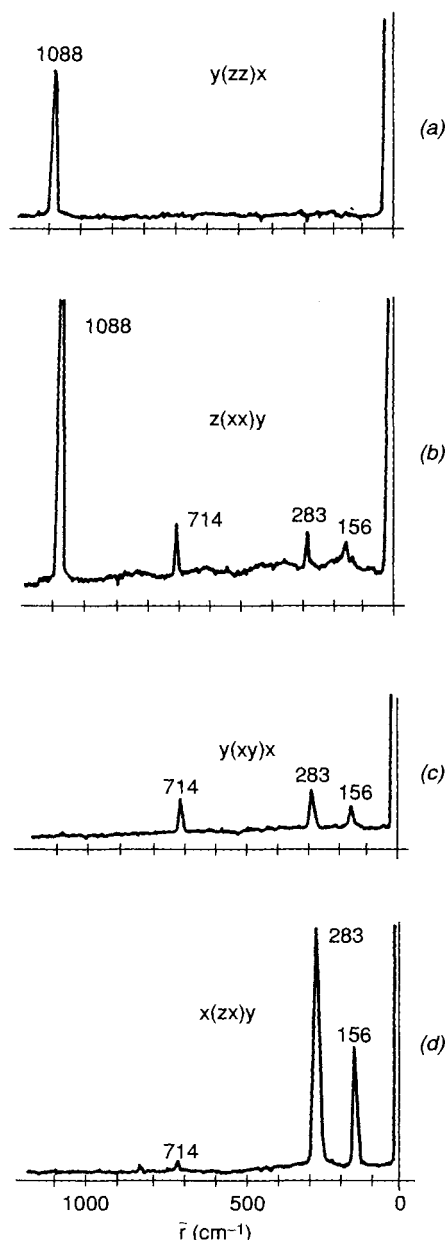


Figure 1-43 Polarized Raman spectra of calcite. (Reproduced with permission from Ref. 61.)

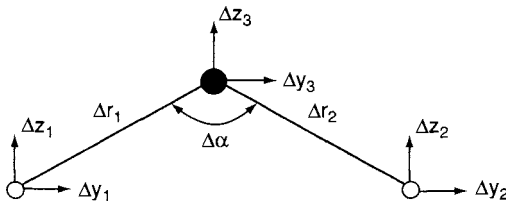


Figure 1-44 The nine Cartesian and three internal coordinates for H₂O. The three *x* coordinates are not shown since they are in the direction perpendicular to the paper plane.

coordinates. Furthermore, the latter has the advantage that the force constants obtained have clearer physical meaning than those obtained by using Cartesian coordinates since they represent force constants for particular bond stretching and angle bending. Thus, internal coordinates are commonly used for NCA. If it is necessary to use more than $3N-6(5)$ internal coordinates, such a set includes extra (redundant) coordinates that can be eliminated during the process of calculation. Using the general formulas developed by Decius (65), one can calculate the types and numbers of internal coordinates for a given molecule, as follows.

The number of bond stretching coordinates is given by

$$n_r = b, \quad (1-77)$$

where b is the number of bonds disregarding type, which for H₂O is two. The number of angle bending coordinates is given by

$$n_\alpha = 4b - 3a + a_1, \quad (1-78)$$

where a is the number of atoms in the molecule, and a_1 is the number of bonds meeting at the central atom. For H₂O, n_α is equal to one.

1.20.2 SYMMETRY COORDINATES

If a molecule contains equivalent coordinates due to its symmetry properties, it is possible to simplify the calculation (*vide infra*) by using symmetry coordinates rather than internal coordinates. In the case of H₂O, they are

$$R_1 \sim (\Delta r_1 + \Delta r_2) \quad (1-79)$$

$$R_2 \sim \Delta\alpha, \quad (1-80)$$

$$R_3 \sim (\Delta r_1 - \Delta r_2). \quad (1-81)$$

R_1 and R_2 correspond to the two A_1 , whereas R_3 corresponds to the B_2 vibration (see Fig. 1-12). Selection of symmetry coordinates can be facilitated

by use of the method of Nielsen and Berryman (66). However, the preceding symmetry coordinates must be normalized so that

$$\sum_k (U_{jk})^2 = 1, \quad (1-82)$$

where U_{jk} is the coefficient of the k th internal coordinate in the j th symmetry coordinate. For R_1 , $(U_{11})^2 + (U_{12})^2 = 1$. This gives $U_{11} = U_{12} = 1/\sqrt{2}$. Thus,

$$R_1 = (1/\sqrt{2})(\Delta r_1 + \Delta r_2).$$

Similarly

$$R_3 = (1/\sqrt{2})(\Delta r_1 - \Delta r_2), \quad (1-83)$$

$$R = \Delta\alpha.$$

Next, a set of symmetry coordinates must satisfy the orthogonality condition:

$$\sum_k (U_{jk})(U_{ik}) = 0. \quad (1-84)$$

$$\text{For } R_1 \text{ and } R_2, \quad (1/\sqrt{2})(0) + (1/\sqrt{2})(0) + (0)(1) = 0.$$

$$\text{For } R_1 \text{ and } R_3, \quad (1/\sqrt{2})(1/\sqrt{2}) + (1/\sqrt{2})(-1/\sqrt{2}) + (0)(0) = 0.$$

$$\text{For } R_2 \text{ and } R_3, \quad (0)(1/\sqrt{2}) + (0)(-1/\sqrt{2}) + (1)(0) = 0.$$

Thus, R_1 , R_2 and R_3 shown in Eqs. (1-83) are orthogonal to each other.

It is necessary to determine if the preceding symmetry coordinates transform according to the character table of the point group C_{2v} (Appendix 1). By applying each symmetry operation, we find that R_1 and R_2 transform as A_1 species, while R_3 transforms as B_2 species. For example,

$$\begin{aligned} E(R_1) &= 1, & C_2(R_1) &= 1, & \sigma_v(xz)(R_1) &= 1 & \text{and} & \sigma_v(yz)(R_1) &= 1; \\ E(R_3) &= 1, & C_2(R_3) &= -1, & \sigma_v(xz)(R_3) &= -1 & \text{and} & \sigma_v(yz)(R_3) &= 1. \end{aligned}$$

Using matrix notation, the relationship between the internal and symmetry coordinates is written as

$$\begin{bmatrix} R_1(A_1) \\ R_2(A_1) \\ R_3(B_2) \end{bmatrix} = \begin{bmatrix} \frac{1}{\sqrt{2}} & \frac{1}{\sqrt{2}} & 0 \\ 0 & 0 & 1 \\ \frac{1}{\sqrt{2}} & \frac{-1}{\sqrt{2}} & 0 \end{bmatrix} \begin{bmatrix} \Delta r_1 \\ \Delta r_2 \\ \Delta\alpha \end{bmatrix}, \quad (1-85)$$

where the first matrix on the right is called the U-matrix.

1.20.3 POTENTIAL ENERGY-*F*-MATRIX

The next step is to express the potential energy in terms of the *F*-matrix, which consists of a set of force constants. In the case of H₂O, it is written as

$$2V = f_{11}(\Delta r_1)^2 + f_{11}(\Delta r_2)^2 + f_{33}r^2(\Delta\alpha)^2 + 2f_{12}(\Delta r_1)(\Delta r_2) + 2f_{13}r(\Delta r_1)(\Delta\alpha) + 2f_{13}r(\Delta r_2)(\Delta\alpha) \quad (1-86)$$

Here, f_{11} , f_{12} , f_{13} and f_{33} are the stretching, stretching-stretching interaction, stretching-bending interaction, and bending force constants, respectively, and r (equilibrium distance) is multiplied to make f_{13} and f_{33} dimensionally similar to the others. Using matrix expression, Eq. (1-86) is written as

$$2V = [\Delta r_1 \Delta r_2 \Delta\alpha] \begin{bmatrix} f_{11} & f_{12} & rf_{13} \\ f_{12} & f_{11} & rf_{13} \\ rf_{13} & rf_{13} & r^2 f_{33} \end{bmatrix} \begin{bmatrix} \Delta r_1 \\ \Delta r_2 \\ \Delta\alpha \end{bmatrix}. \quad (1-87)$$

Using matrix notation, the general form of Eq. (1-87) is written as

$$2V = \tilde{\mathbf{R}} \mathbf{F} \mathbf{R}, \quad (1-88)^*$$

where \mathbf{F} is the force constant matrix (*F*-matrix), and \mathbf{R} and its transpose $\tilde{\mathbf{R}}$ are column and row matrices, respectively, which consist of internal coordinates. To take advantage of symmetry properties of the molecule, one must transform the *F*-matrix into \mathbf{F}_s via

$$\mathbf{F}_s = \mathbf{U} \mathbf{F} \tilde{\mathbf{U}}. \quad (1-89)$$

In the case of H₂O, \mathbf{F}_s becomes:

$$\mathbf{F}_s = \left[\begin{array}{cc|c} f_{11} + f_{12} & r\sqrt{2}f_{13} & 0 \\ r\sqrt{2}f_{13} & r^2f_{33} & 0 \\ \hline 0 & 0 & f_{11} - f_{12} \end{array} \right] \quad (1-90)$$

Thus, the original 3×3 matrix is resolved into one 2×2 matrix (A_1 species) and one 1×1 matrix (B_2 species). In large molecules, such coordinate transformation greatly simplifies the calculation.

In the preceding, the potential energy was expressed in terms of the four force constants (stretching, stretching-stretching interaction, stretching-bending interaction, and bending). This type of potential field is called the *generalized valence force* (GVF) field and is most commonly used for normal coordinate calculations. In large molecules, however, the GVF field requires too many force constants, which are difficult to determine with limited experimental data. To overcome this difficulty, several other force fields have been

*Hereafter, the bold-face letters indicate matrices.

developed, and some of these are given in reference books cited at the end of this chapter.

1.20.4 KINETIC ENERGY—G-MATRIX

The kinetic energy is not easily expressed in terms of internal (symmetry) coordinates. Wilson (63) has shown that

$$2T = \tilde{\mathbf{R}}\mathbf{G}^{-1}\tilde{\mathbf{R}}, \quad (1-91)$$

where $\dot{\mathbf{R}}$ is the time derivative of \mathbf{R} , $\tilde{\mathbf{R}}$ is its transpose, and \mathbf{G}^{-1} is the reciprocal of the G-matrix. G-matrix elements can be calculated by using Decius table (65). In the case of H₂O, it becomes

$$\mathbf{G} = \begin{bmatrix} \mu_3 + \mu_1 & \mu_3 \cos \alpha & -\frac{\mu_3}{r} \sin \alpha \\ \mu_3 \cos \alpha & \mu_3 + \mu_1 & -\frac{\mu_3}{r} \sin \alpha \\ -\frac{\mu_3}{r} \sin \alpha & -\frac{\mu_3}{r} \sin \alpha & \frac{2\mu_1}{r^2} + \frac{2\mu_3}{r^2}(1 - \cos \alpha) \end{bmatrix}. \quad (1-92)$$

Here, μ_1 and μ_3 are the reciprocal masses of the H and O atoms, respectively, and α is the bond angle. Again, it is possible to diagonalize the G-matrix via coordinate transformation:

$$\mathbf{G}_s = \mathbf{U}\mathbf{G}\tilde{\mathbf{U}}$$

where \mathbf{G}_s is the G-matrix that is expressed in terms of symmetry coordinates. In the case of H₂O, it becomes

$$\mathbf{G}_s = \begin{bmatrix} \mu_3(1 + \cos \alpha) + \mu_1 & -\frac{\sqrt{2}}{r} \mu_3 \sin \alpha & 0 \\ -\frac{\sqrt{2}}{r} \mu_3 \sin \alpha & \frac{2\mu_1}{r^2} + \frac{2\mu_3}{r^2}(1 - \cos \alpha) & 0 \\ 0 & 0 & \mu_3(1 - \cos \alpha) + \mu_1 \end{bmatrix}. \quad (1-93)$$

1.20.5 SOLUTION OF SECULAR EQUATION

As stated in Section 1.6, normal vibrations are completely independent of each other. This means that the potential and kinetic energies in terms of normal coordinates (\mathbf{Q}) must be written without cross terms. Namely,

$$2T = \tilde{\mathbf{Q}}\mathbf{Q},$$

$$2V = \tilde{\mathbf{Q}}\Lambda\mathbf{Q},$$

where Λ is a diagonal matrix containing $\lambda (= 4\pi^2 c^2 \tilde{v}^2)$ terms as diagonal elements (19). On the other hand, the energy expressions in terms of internal (symmetry) coordinates contain cross terms such as $(\Delta r)(\Delta \alpha)$:

$$2T = \tilde{\mathbf{R}}\mathbf{G}^{-1}\dot{\mathbf{R}}, \quad (1-91)$$

$$2V = \hat{\mathbf{R}}\mathbf{F}\mathbf{R}. \quad (1-88)$$

To eliminate these cross terms, it is necessary to solve the secular equation of the form $|\mathbf{GF} - \mathbf{E}\lambda| = 0$ (63) where \mathbf{E} is a unit matrix containing ones as the diagonal elements.* In the case of H_2O , this equation for the A_1 block becomes

$$|\mathbf{GF} - \mathbf{E}\lambda| = \begin{vmatrix} G_{11}F_{11} + G_{12}F_{21} - \lambda & G_{11}F_{12} + G_{12}F_{22} \\ G_{21}F_{11} + G_{22}F_{21} & G_{21}F_{12} + G_{22}F_{22} - \lambda \end{vmatrix} = 0, \quad (1-94)$$

or

$$\lambda^2 - (G_{11}F_{11} + G_{22}F_{22} + 2G_{12}F_{12})\lambda + (G_{11}G_{22} - G_{12}^2)(F_{11}F_{22} - F_{12}^2) = 0. \quad (1-95)$$

For the B_2 vibration,

$$\lambda = F_{33}G_{33}.$$

1.20.6 CALCULATION OF FORCE CONSTANTS

In general, normal coordinate analysis is carried out on a molecule for which the atomic masses, bond distances and overall structures are known. Thus, the G -matrix can be readily calculated using known molecular parameters. Since the force constants are not known *a priori*, it is customary to assume a set of force constants that have been obtained for similar molecules, and to calculate vibrational frequencies by solving the secular equation $|\mathbf{GF} - \mathbf{E}\lambda| = 0$. Then, these force constants are refined until a set of calculated frequencies gives reasonably good agreement with those observed.

For the A_1 vibrations of H_2O , the G -matrix elements are calculated by using the following parameters:

$$\begin{aligned} \mu_1 &= \mu_H = \frac{1}{1.008} = 0.99206, \\ \mu_3 &= \mu_o = \frac{1}{15.995} = 0.06252, \\ r &= 0.96(\text{\AA}), \alpha = 105^\circ, \end{aligned}$$

*All the off-diagonal elements are zero in a diagonal as well as in a unit matrix.

$$\begin{aligned}\sin \alpha &= \sin 105^\circ = 0.96593, \\ \cos \alpha &= \cos 105^\circ = -0.25882.\end{aligned}$$

If we assume a set of force constants,

$$\begin{aligned}f_{11} &= 8.4280, & f_{12} &= -0.1050, \\ f_{13} &= 0.2625, & f_{33} &= 0.7680,\end{aligned}$$

we obtain a secular equation,

$$\lambda^2 - 10.22389\lambda + 13.86234 = 0.$$

The solution of this equation gives

$$\lambda_1 = 8.61475, \quad \lambda_2 = 1.60914.$$

These values are converted into $\tilde{\nu}$ through the $\lambda = 4\pi^2 c^2 \tilde{\nu}^2$ relationship. The results are

$$\tilde{\nu}_1 = 3,824 \text{ cm}^{-1}, \quad \tilde{\nu}_2 = 1,653 \text{ cm}^{-1}.$$

For the B_2 vibration, we obtain

$$\begin{aligned}\lambda_3 &= G_{33}F_{33} = [\mu_1 + \mu_3(1 - \cos \alpha)](f_{11} - f_{12}) \\ &= 9.13681, \\ \tilde{\nu}_3 &= 3,938 \text{ cm}^{-1}.\end{aligned}$$

The calculated frequencies just obtained are in good agreement with the observed values, $\tilde{\nu}_1 = 3,825 \text{ cm}^{-1}$, $\nu_2 = 1,654 \text{ cm}^{-1}$ and $\tilde{\nu}_3 = 3,936 \text{ cm}^{-1}$, all corrected for anharmonicity (66). Thus, the set of force constants assumed initially is a good representation of the potential energy of the H₂O molecule. For large molecules, use of computer programs such as those developed by Schachtschneider (67) greatly facilitate the calculation.

1.21 Band Assignments and Isotope Shifts

Inspection of IR and Raman spectra of a large number of compounds shows that a common group exhibits its group vibrations in the same region regardless of the rest of the molecule. These “group frequencies” are known for a number of inorganic (37) and organic compounds (68,69). Figures 1-45 and 1-46 show group frequencies and corresponding normal modes for the CH₃ and CH₂ groups, respectively. Notations such as ν (stretching) and δ (bending) will be used throughout this book. Band assignments of other small molecules are tabulated by Shimanouchi (70). Using group frequency tables, it is possible to assign the observed spectra and to identify the atomic groups responsible for each group vibrations.

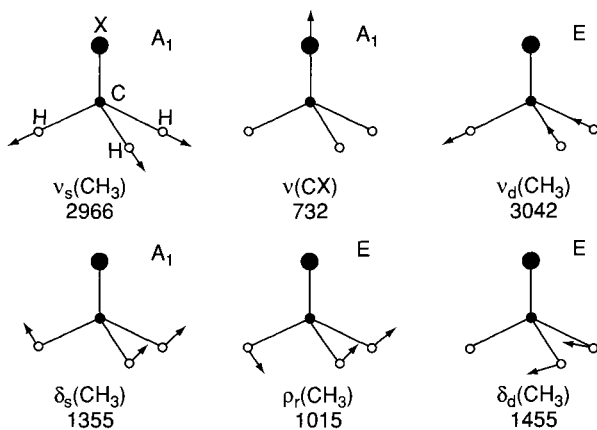


Figure 1-45 Normal vibrations of CH_3X -type molecule (frequencies are given for $\text{X} = \text{Cl}$): v_s , symmetric stretching; v_d , degenerate stretching; δ_s , symmetric bending; δ_d , degenerate bending; ρ_r , rocking.

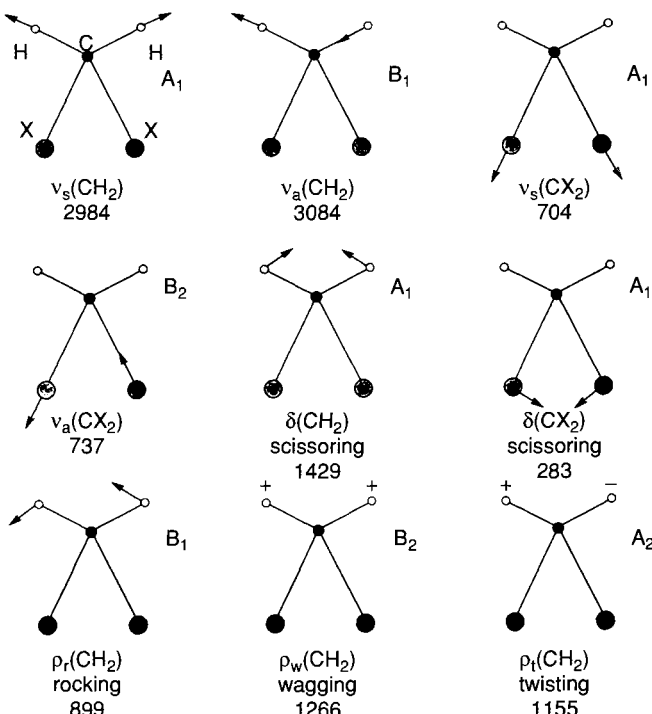
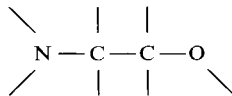


Figure 1-46 Normal vibrations of CH_2X_2 -type molecule (frequencies are given for $\text{X} = \text{Cl}$): v_s , symmetric stretching; v_a , antisymmetric stretching; δ , symmetric bending (scissoring); ρ_r , rocking; ρ_w , wagging; ρ_t , twisting.

However, the concept of group frequencies is applicable only when the vibrations of a particular group are isolated from those of the rest of the molecule. If atoms of similar masses are connected by bonds of similar strength, the amplitudes of oscillation are similar for all atoms. For example, this situation occurs in a system like



In such a case, it is not possible to describe normal modes in terms of one local mode such as $\nu(\text{C—C})$, $\nu(\text{C—N})$ or $\nu(\text{C—O})$. Instead, they are described as a mixing of these local modes (“vibrational coupling”). As will be shown in Chapter 4, Section 4.1.2, examples of such vibrational couplings are seen in metalloporphyrins and peptides.

In Section 1.6, we have shown the relationship between Cartesian and normal coordinates (Eq. (1-44)). Similar relationships exist between internal (symmetry) and normal coordinates:

$$\begin{aligned} R_1 &= l_{11}Q_1 + l_{12}Q_2 + \dots + l_{1N}Q_N, \\ R_2 &= l_{21}Q_1 + l_{22}Q_2 + \dots + l_{2N}Q_N, \\ &\vdots \qquad \qquad \vdots \\ R_i &= l_{i1}Q_1 + l_{i2}Q_2 + \dots + l_{iN}Q_N. \end{aligned}$$

Thus, the mixing ratio of individual coordinates in a given normal vibration (e.g., Q_1) is determined by the ratio

$$l_{11}:l_{21}:\dots:l_{i1}.$$

If one of these values (e.g., l_{11}) is large relative to others, this normal vibration is assigned to the local mode, R_1 . If both l_{11} and l_{21} are large relative to others, it is assigned to a coupled vibration between R_1 and R_2 . The l_{iN} values are obtained once vibrational frequencies are calculated by the procedures described in the preceding section (37). Such calculations show that the $\nu_1(Q_1)$ at $3,825\text{ cm}^{-1}$ and $\nu_2(Q_2)$ at $1,653\text{ cm}^{-1}$ are almost pure $\nu(\text{O—H})$ and $\delta(\text{HOH})$, respectively.

Experimentally, band assignments are facilitated by the observation of isotope shifts. As shown in Table 1-3, the vibrational frequency of H_2 ($4,160\text{ cm}^{-1}$) is markedly downshifted ($2,994\text{ cm}^{-1}$) when H is replaced by D. The magnitude of this isotope shift is predicted by Eq. (1-40):

$$\frac{\tilde{\nu}_{\text{H}_2}}{\tilde{\nu}_{\text{D}_2}} = \sqrt{\frac{\mu_{\text{D}_2}}{\mu_{\text{H}_2}}} \cong \sqrt{2} = 1.414.$$

Obviously, this large shift originates in the mass effect; the mass of D is twice that of H. Such isotope shifts are seen in many isotopic pairs such as $^6\text{Li}/^7\text{Li}$, $^{10}\text{B}/^{11}\text{B}$, $^{12}\text{C}/^{13}\text{C}$, $^{14}\text{N}/^{15}\text{N}$, $^{16}\text{O}/^{18}\text{O}$, $^{32}\text{S}/^{34}\text{S}$ and $^{35}\text{Cl}/^{37}\text{Cl}$. As will be shown in Section 4.1.3, heavy metal isotopes ($^{58}\text{Ni}/^{62}\text{Ni}$ and $^{54}\text{Fe}/^{56}\text{Fe}$, etc.) are indispensable in assigning metal-ligand vibrations of coordination compounds (71).

References

1. F. P. Kerschbaum, *Z. Instrumentenk* **34**, 43 (1914).
2. B. Veskatesachar and L. Sibaiya, *Indian J. Phys.* **5**, 747 (1930).
3. J. H. Hibben, "The Raman Effect and Its Chemical Application" Reinhold Publishing Corp., New York, 1939.
4. F. H. Spedding and R. F. Stamm, *J. Chem. Phys.* **10**, 176 (1942).
5. D. H. Rank and J. S. McCartney, *J. Opt. Soc. Am.* **38**, 279 (1948).
6. H. L. Welsh, M. F. Crawford, T. R. Thomas, and G. R. Love, *Can. J. Phys.* **30**, 577 (1952).
7. N. S. Ham and A. Walsh, *Spectrochim. Acta* **12**, 88 (1958).
8. H. Stammreich, *Spectrochim. Acta* **8**, 41 (1956).
9. H. Stammreich, *Phys. Rev.* **78**, 79 (1950).
10. H. Stammreich, R. Forneris, and K. Sone, *J. Chem. Phys.* **23**, 1972 (1955).
11. H. Stammreich, R. Forneris, and Y. Tavares, *J. Chem. Phys.* **25**, 580, 1277 and 1278 (1956).
12. H. Stammreich, *Experientia* **6**, 224 (1950).
13. T. R. Gilson and P. J. Hendra, "Laser Raman Spectroscopy," pp. 1-266. Wiley-Interscience, London, 1970.
14. D. H. Rank and R. V. Wiegand, *J. Opt. Soc. Am.* **32**, 190 (1942).
15. R. F. Stamm and C. F. Salzman, *J. Opt. Soc. Am.* **43**, 126 (1953).
16. J. R. Ferraro, in "Raman Spectroscopy, Theory and Practice" (H. A. Szymanski, ed.), pp. 44-81. Plenum Press, New York, 1967.
17. J. R. Ferraro, R. Jarnutowski, and D. C. Lankin, *Spectroscopy* **7**, 30 (1992).
18. G. W. King, "Spectroscopy and Molecular Structure." Holt, Rinehart and Winston, New York, 1964.
19. H. Eyring, J. Walter, and G. E. Kimball, "Quantum Chemistry." John Wiley, 1944.
20. C. F. Shaw, III, *J. Chem. Educ.* **58**, 343 (1981).
21. C. D. Allemand, *Appl. Spectrosc.* **24**, 348 (1970).
22. F. G. Dijkman and J. H. Van der Maas, *Appl. Spectrosc.* **30**, 545 (1976).
23. G. Fini and P. Mirone, *Appl. Spectrosc.* **29**, 230 (1975).
24. J. R. Scherer and G. F. Bailey, *Appl. Spectrosc.* **24**, 259 (1970).
25. T. G. Spiro and T. C. Strekas, *Proc. Nat. Acad. Sci.* **69**, 2622 (1972).
26. D. A. Long, "Raman Spectroscopy." McGraw-Hill, New York, 1977.
27. P. J. Hendra, "Raman instrumentation and sampling," in "Laboratory Methods in Infrared Spectroscopy" (R. G. Miller, ed.), p. 249. Heyden, London, 1971.
28. D. P. Strommen and K. Nakamoto, *Appl. Spectrosc.* **37**, 436 (1983).
29. M. Zeldin, *J. Chem. Educ.* **43**, 17 (1966).
30. J. R. Ferraro and J. S. Ziomek, "Introductory Group Theory and Its Application to Molecular Structure" (2nd Ed.). Plenum Press, New York, 1975.
31. G. Herzberg, "Molecular Spectra and Molecular Structure. II. Infrared and Raman Spectra of Polyatomic Molecules." D. Van Nostrand, New York, 1945.

32. M. Hammermesh, "Group Theory and Its Applications to Physical Problems," p. 51. Addison Wesley, Reading, Massachusetts, 1972.
33. E. L. Muettterties, R. E. Merrifield, H. C. Miller, W. H. Knoth, and J. R. Downing, *J. Am. Chem. Soc.* **84**, 2506 (1962).
34. L. A. Paquette, R. L. Taransky, D. W. Balough, and G. Kentgen, *J. Am. Chem. Soc.* **105**, 5446 (1983).
35. H. W. Kroto, A. W. Allaf, and S. P. Balm, *Chem. Rev.* **91**, 1213 (1991).
36. F. A. Cotton, "Chemical Applications of Group Theory." John Wiley, New York, 1971.
37. K. Nakamoto, "Infrared and Raman Spectra of Inorganic and Coordination Compounds" (5th ed.). Parts A and B John Wiley, New York, 1997.
38. J. Tang and A. C. Albrecht, "Developments in the theories of vibrational Raman intensities," in "Raman Spectroscopy" (H. A. Szymanski, Ed.), Vol. 2. Plenum Press, New York, 1970.
39. A. C. Albrecht, *J. Chem. Phys.* **34**, 1476 (1961).
40. R. J. H. Clark and P. D. Mitchell, *J. Am. Chem. Soc.* **95**, 8300 (1973).
41. L. A. Nafie, P. Stein, and W. L. Petcolas, *Chem. Phys. Lett.* **12**, 131 (1971).
42. Y. Hirakawa and M. Tsuboi, *Science* **188**, 359 (1975).
43. T. G. Spiro and X.-Y. Li, "Resonance Raman spectroscopy of metalloporphyrins," in "Biological Applications of Raman Spectroscopy" (T. G. Spiro, Ed.), Vol. 3. John Wiley, New York, 1988.
44. X.-Y. Li, R. S. Czernuszewicz, J. R. Kincaid, P. Stein, and T. G. Spiro, *J. Phys. Chem.* **94**, 47 (1990).
45. G. Burns and A. M. Glazer, "Space Groups for Solid State Scientists," p. 81. Academic Press, 1978.
46. P. S. Wheatley, "The Determination of Molecular Structure" (2nd Ed.). Clarendon Press, Oxford, 1968.
47. S. S. Mitra, "Optical Properties of Solids" (S. Nadelman and S. S. Mitra, Eds.), p. 333. Plenum Press, New York, 1969.
48. G. Turrell, "Infrared and Raman Spectra of Crystals." Academic Press, New York, 1972.
49. P. M. A. Sherwood, "Vibrational Spectroscopy of Solids," p. 15. Cambridge University Press, 1972.
50. S. Bhagavantam and T. Venkatarayudu, *Proc. Ind. Acad. Sci.* **A9**, 224(1939); **A13**, 543 (1941).
51. R. S. Halford, *J. Chem. Phys.* **14**, 8 (1946).
52. D. F. Hornig, *J. Chem. Phys.* **16**, 1063 (1948).
53. H. Winston and R. S. Halford, *J. Chem. Phys.* **17**, 607 (1949).
54. R. L. C. Wyckoff, "Crystal Structures," Vol. 2. John Wiley-Interscience, New York, 1964.
55. W. G. Fateley, F. R. Dollish, N. T. McDevitt, and F. F. Bentley, "Infrared and Raman Selection Rules for Molecular and Lattice Vibrations: The Correlation Method." John Wiley-Interscience, New York, 1972.
56. D. M. Adams and D. C. Newton, "Tables for factor group and point group analysis," Beckman-RHC Ltd., Surley House, U.K.; *J. Chem. Soc.*, 2822 (1970).
57. D. M. Adams, *Coord. Chem. Rev.* **10**, 183 (1973).
58. W. G. Fateley, N. T. McDevitt, and F. F. Bentley, *Applied Spectrosc.* **25**, 155 (1971).
59. R. Kopelman, *J. Chem. Phys.* **47**, 2631 (1967).
60. J. E. Bertie and J. W. Bell, *J. Chem. Phys.* **54**, 160 (1971).
61. S. P. Porto, J. A. Giordmaine, and T. C. Damen, *Phys. Rev.* **147**, 608 (1966).
62. I. Nakagawa and J. L. Walter, *J. Chem. Phys.* **51**, 1389 (1969).
63. E. B. Wilson, *J. Chem. Phys.* **7**, 1047 (1939); **9**, 76 (1941).
64. E. B. Wilson, J. C. Decius, and P. C. Cross, "Molecular Vibrations." McGraw-Hill, New York, 1955.
65. J. C. Decius, *J. Chem. Phys.* **16**, 1025 (1948).

66. J. R. Nielsen and L. H. Berryman, *J. Chem. Phys.* **17**, 659 (1949).
67. J. H. Schachtschneider, "Vibrational analysis of polyatomic molecules," Parts V and VI. Technical Reports 231-64 and 53-65. Shell Development Co., Emeryville, California, 1964 and 1965.
68. F. R. Dollish, W. G. Fateley, and F. F. Bentley, "Characteristic Raman Frequencies of Organic Compounds." John Wiley, New York, 1974.
69. D. Lin-Vien, N. B. Colthup, W. G. Fateley, and J. G. Grasselli, "The Handbook of Infrared and Raman Characteristic Frequencies of Organic Molecules." Academic Press, Boston, 1991.
70. T. Shimanouchi, "Tables of Molecular Vibrational Frequencies, Consolidated Volume," Nat. Stand. Ref. Data Ser., Nat. Bur. Stand., Vol. 39, June (1972). Also see *J. Phys. Chem. Ref. Data* **1**, 189 (1972); **2**, 121 and 225 (1973); and **3**, 269 (1974).
71. K. Nakamoto, *Angew. Chem. Int. Ed.* **11**, 666 (1972).

General References on Vibrational Spectroscopy

BASIC THEORY

1. G. Herzberg, "Molecular Spectra and Molecular Structure. Vol. I. Spectra of Diatomic Molecules." Van Nostrand, New York, 1951.
2. G. Herzberg, "Molecular Spectra and Molecular Structure. Vol. II. Infrared and Raman Spectra of Polyatomic Molecules." Van Nostrand, New York, 1945.
3. "Raman Spectroscopy: Theory and Practice" (H. A. Szymanski, Ed.), Vol. 1 (1967) and Vol. 2 (1970). Plenum Press, New York.
4. T. R. Gilson and P. J. Hendra, "Laser Raman Spectroscopy." John Wiley, New York, 1970.
5. D. Steele, "Theory of Vibrational Spectroscopy." Saunders, London, 1971.
6. J. A. Koningstein, "Introduction to the Theory of the Raman Effect." D. Reidel, Dordrecht, The Netherlands, 1973.
7. D. A. Long, "Raman Spectroscopy." McGraw-Hill, New York, 1977.
8. A. J. Sonnessa, "Introduction to Molecular Spectroscopy." Reinhold, New York, 1966.
9. C. N. Banwell, "Fundamentals of Molecular Spectroscopy" (2nd Ed.), McGraw-Hill, London, 1972.
10. J. M. Hollas, "Modern Spectroscopy" (2nd Ed.), John Wiley, New York, 1992.
11. M. Diem, "Introduction to Modern Vibrational Spectroscopy", John Wiley, New York, 1993.

NORMAL COORDINATE ANALYSIS

12. E. B. Wilson, J. C. Decius, and P. C. Cross, "Molecular Vibrations." McGraw-Hill, New York, 1955.
13. L. A. Woodward, "Introduction to the Theory of Molecular Vibrations and Vibrational Spectroscopy." Oxford University Press, London, 1972.

SYMMETRY AND GROUP THEORY

14. F. A. Cotton, "Chemical Applications of Group Theory" (3rd Ed.), John Wiley, New York, 1990.

15. J. R. Ferraro and J. S. Ziomek, "Introductory Group Theory and Its Application to Molecular Structure" (2nd Ed.). Plenum Press, New York, 1975.
16. J. M. Hollis, "Symmetry in Molecules." Chapman and Hall, London, 1972.
17. D. C. Harris and M. D. Bertolucci, "Symmetry and Spectroscopy." Oxford University Press, New York, 1978.
18. R. L. Carter, "Molecular Symmetry and Group Theory", John Wiley, New York, 1998.

CORRELATION THEORY

19. W. G. Fateley, F. R. Dollish, N. T. McDevitt and F. F. Bentley, "Infrared and Raman Selection Rules for Molecular and Lattice Vibrations: The Correlation Method." John Wiley-Interscience, New York, 1972.

GENERAL APPLICATION

20. N. B. Colthup, L. H. Daly, and S. E. Wiberley, "Introduction to Infrared and Raman Spectroscopy" (3rd Ed.). Academic Press, Boston, 1990.
21. J. G. Grasselli, M. K. Snavely, and B. J. Bulkin, "Chemical Applications of Raman Spectroscopy." John Wiley, 1981.
22. "Infrared and Raman Spectroscopy" (E. G. Brame, Jr., and J. G. Grasselli, eds.), Vol. 1, Pts. A and B. Marcel Dekker, New York, 1976-77.
23. "Infrared and Raman Spectroscopy. Methods and Applications" (B. Schrader, ed.) VCH, Weinheim, Germany, 1995.
24. R. A. Nyquist, "Interpreting Infrared, Raman and Nuclear Magnetic Resonance Spectra", Academic Press, San Diego, 2001.

RAMAN INSTRUMENTATION

25. D. P. Strommen and K. Nakamoto, "Laboratory Raman Spectroscopy" John Wiley, New York, 1984.
26. D. P. Strommen, "Raman Spectroscopy" in "Handbook of Instrumental Techniques for Analytical Chemistry" (F. A. Settle, ed.), Prentice-Hall, New Jersey, 1997, Chapter 16. p. 285.

ANALYTICAL CHEMISTRY

27. "Analytical Raman Spectroscopy" (J. G. Grasselli and B. J. Bulkin, eds.) John Wiley, New York, 1991.
28. "Analytical Applications of Raman Spectroscopy" (M. J. Pelletier, ed.) Blackwell Science, Oxford, England, 1999.

INORGANIC, ORGANIC, AND ORGANOMETALLIC COMPOUNDS

29. K. Nakamoto, "Infrared and Raman Spectra of Inorganic and Coordination Compounds" (5th Ed.), Parts A and B John Wiley, New York, 1997.
30. J. R. Ferraro, "Low-frequency Vibrations of Inorganic and Coordination Compounds." Plenum Press, New York, 1971.
31. L. H. Jones, "Inorganic Vibrational Spectroscopy." Marcel Dekker, New York, 1971.

32. E. Maslowsky, Jr., "Vibrational Spectra of Organometallic Compounds." John Wiley, New York, 1976.
33. F. R. Dollish, W. G. Fateley, and F. F. Bentley, "Characteristic Raman Frequencies of Organic Compounds." John Wiley, New York, 1974.
34. D. Lin-Vien, N. B. Colthup, W. G. Fateley, and J. G. Grasselli, "The Handbook of Infrared and Raman Characteristic Frequencies of Organic Molecules." Academic Press, Boston, 1991.

BIOLOGICAL COMPOUNDS

35. F. S. Parker, "Application of Infrared, Raman and Resonance Raman Spectroscopy in Biochemistry." Plenum Press, New York, 1983.
36. P. R. Carey, "Biochemical Application of Raman and Resonance Raman Spectroscopies." Academic Press, New York, 1982.
37. A. T. Tu, "Raman Spectroscopy in Biology." John Wiley, New York, 1982.
38. "Biological Applications of Raman Spectroscopy" (T. G. Spiro, ed.), Vols. 1, 2 and 3. John Wiley, New York, 1987-88.
39. "Infrared and Raman Spectroscopy of Biological Materials" (H. U. Gremlich and B. Yan, eds.), Marcel Dekker, New York 2001.

ADVANCES SERIES

40. R. J. H. Clark and R. E. Hester, eds., "Advances in Infrared and Raman Spectroscopy," Vols. 1 to present. John Wiley, New York.
41. J. R. Durig, ed., "Vibrational Spectra and Structure," Vols. 1 to present. Elsevier, Amsterdam.
42. C. B. Moore, ed., "Chemical and Biochemical Applications of Lasers," Vols. 1 to present. Academic Press, New York.
43. "Spectroscopic Properties of Inorganic and Organometallic Compounds," Vols. 1 to present. The Chemical Society, London.
44. "Molecular Spectroscopy," Vols. 1 to present. The Chemical Society, London.

SPECIAL APPLICATIONS

45. A. Weber, ed., "Raman Spectroscopy of Gases and Liquids." Springer-Verlag, New York, 1979.
46. G. Turrell, "Infrared and Raman Spectra of Crystals." Academic Press, New York, 1972.
47. G. H. Atkinson, "Time-Resolved Vibrational Spectroscopy." Academic Press, New York, 1983.
48. D. B. Chase and J. F. Rabolt, eds; "Fourier Transform Spectroscopy from Concept to Experiment," Academic Press, Cambridge, MA. 1994.
49. J. R. Ferraro, "Vibrational Spectroscopy at High External Pressures. The Diamond Anvil Cell." Academic Press, New York, 1984.
50. C. Karr, ed., "Infrared and Raman Spectroscopy of Lunar and Terrestrial Minerals." Academic Press, New York, 1975.
51. W. B. Person and G. Zerbi, eds., "Vibrational Intensities in Infrared and Raman Spectroscopy." Elsevier, Amsterdam, 1982.
52. J. L. Koenig, "Spectroscopy of Polymers." American Chemical Society, Washington, D. C., 1992.

53. M. W. Urban. "Vibrational Spectroscopy of Molecules and Macromolecules on Surfaces," John Wiley, New York, 1993.
54. J. L. Koenig, "Spectroscopy of Polymers" (2nd Ed.), Elsevier, New York, 1999.
55. J. Workman, Jr., "Handbook of Organic Compounds, NIR, IR, Raman and UV-Vis Spectra Featuring Polymers and Surfactants", Vol. 1 to 3, Academic Press, Orlando, Florida, 2000.
56. "Ultrafast Infrared and Raman Spectroscopy" (M. D. Fayer, ed.) Marcel Dekker, New York, 2001.

INDEX AND COLLECTIONS OF SPECTRAL DATA

57. N. N. Greenwood, E. J. F. Ross and B. P. Straughan, "Index of Vibrational Spectra of Inorganic and Organometallic Compounds." Vols. 1 to 3, Butterworth, London, 1972-1977.
58. B. Schrader, "Raman/IR Atlas of Organic Compounds", VCH, Germany, 1989.
59. "The Sadler Standard Raman Spectra Collection", Bio-Rad Laboratory, Inc., Sadler Division, Philadelphia, Pennsylvania, 1999.
60. R. A. Nyquist, R. O. Kagel, C. L. Putzig and M. A. Leugers, "The Handbook of Infrared and Raman Spectra of Inorganic Compounds and Organic Salts", Academic Press, San Diego, California, 1997.

HANDBOOKS

61. "Handbook of Raman Spectroscopy" (I. R. Lewis and H. G. M. Edwards, eds.), Marcel Dekker, New York, 2001.
62. "Handbook of Vibrational Spectroscopy" (J. Chalmers and P. G. Griffiths, eds), five volumes, John Wiley, West Sussex, England, 2001.

Chapter 2

Instrumentation and Experimental Techniques

The instrumentation for conventional Raman spectroscopy will be discussed in this chapter. Special techniques of Raman spectroscopy will be described in Chapter 3. Most Raman spectroscopic investigations have been performed on dispersive instruments. However, Fourier transform (FT) techniques have become increasing important as a means of reducing interference from fluorescence. Both dispersive and FT-Raman spectroscopy will be discussed in this chapter.

2.1 Major Components

Four major components make up the commercially available Raman spectrometer. These consist of the following:

- (1) Excitation source, which is generally a continuous-wave (CW) laser
- (2) Sample illumination and collection system
- (3) Wavelength selector
- (4) Detection and computer control/processing systems

A schematic of the typical arrangement of these components is shown in Fig. 2-1 (1). At present, a wide variety of the systems with this general format has been marketed. The major categories for different instruments are defined by the wavelength region for the excitation sources, the type of wavelength

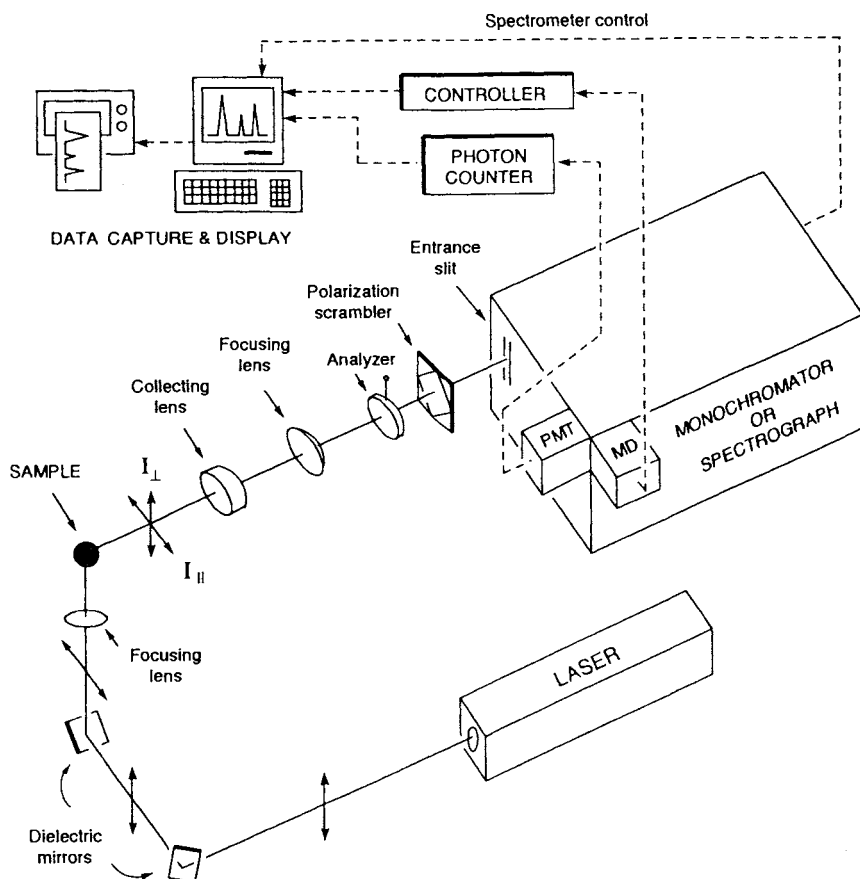


Figure 2-1 Schematic diagram of the major components in a Raman Spectrometer. (Reproduced with permission from Ref. 1.)

selector, and the detection system. Most of the instrumentation will have similar sample illumination and collection systems.

2.2 Excitation Sources

Prior to the development of lasers in the 1960s, the excitation source for Raman spectroscopy was typically a mercury lamp, which was fitted with a filter to transmit a single or limited wavelength range of light. Elaborate systems were developed to supply a single wavelength with enough power to produce Raman scattering. The Toronto (mercury) arc eventually became the standard source for Raman spectroscopy; this strange-looking

lamp consisted of a 2-in. helical tube having a total length of ~ 4 ft coiled about a 6-in. radius connecting two large pools of mercury covering high-voltage electrodes. Considering that a great deal of time was required to warm and ignite the lamp, only to have it shut down intermittently, the advent of lasers was greatly welcomed by the spectroscopic community.

Most of the early gas lasers emitted in the visible region. Continuous-wave (CW) lasers such as Ar^+ (351.1–514.5 nm), Kr^+ (337.4–676.4 nm), and He–Ne (632.8 nm) are now commonly used for Raman spectroscopy. More recently, pulsed lasers such as Nd:YAG, diode, and excimer lasers have been used for time-resolved and ultraviolet (UV) resonance Raman spectroscopy.

Lasers are ideal excitation sources for Raman spectroscopy due to the following characteristics of the laser beam: (1) Single lines from large CW lasers can easily provide 1–2 W of power, and pulsed lasers produce huge peak powers on the order of 10–100 MW (see Tables 2-1 and 2-5). (2) Laser beams are highly monochromatic (band width $\sim 0.1 \text{ cm}^{-1}$ for Ar^+ laser), and extraneous lines are much weaker. The extraneous lines can be eliminated easily by using notch filters or pre-monochromators. (3) Most laser beams have small diameters (1–2 mm), which can be reduced to 0.1 mm by using simple lens systems. Thus all the radiant flux can be focused on a small sample, enabling fruitful studies of microliquids ($\sim 1 \mu\text{L}$) and crystals ($\sim 1 \text{ mm}^3$). In the case of Raman microscopy (Section 3.2), sample areas as small as $\sim 2 \mu\text{m}$ in diameter can be studied. (4) Laser beams are almost completely linearly polarized and are ideal for measurements of depolarization ratios. (5) It is possible to produce laser beams in a wide wavelength range by using dye lasers and other devices. For the principles of laser action, see Appendix 7.

2.2.1 CW GAS LASERS

Gas lasers operate mainly in the visible region of the electromagnetic spectrum. The basic components of a noble gas ion laser are illustrated in Fig. 2-2. A very high current discharge passes through Ar or Kr gas contained in the plasma tube. The outside of the tube is water jacketed to cool the tube. The discharge ionizes the gas and populates the excited state involved in the lasing. The ends of the tube are enclosed with Brewster windows that have an angle defined by $\tan \Theta = \eta$, where η is the index of refraction of the window material. For fused silica (quartz) in the visible region, Θ is 55.6° . At the Brewster's angle, the output beam is almost completely polarized in a fixed direction (in the same plane that contains the angle Θ). The resonant cavity, which is defined by the semitransparent output mirror and the high-reflectance mirror, provides a mechanism for amplification of

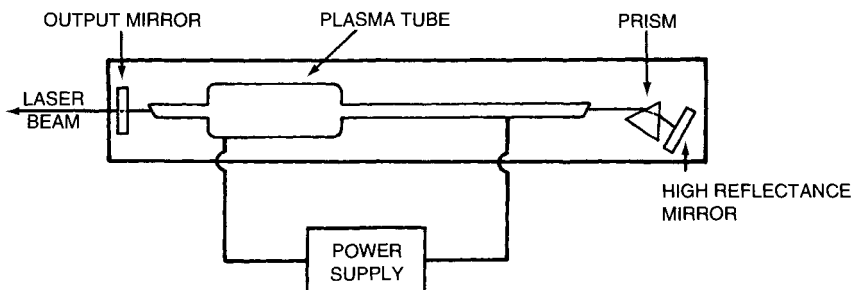


Figure 2-2 Schematic of a typical gas CW laser.

photons that are emitted parallel to the cavity axis; they are reflected by the two mirrors and interact with other excited ions. Stimulated emission (Appendix 7) produces photons of equal energy, phase, and direction, and this process continues until an equilibrium between excitation and emission is reached. Both mirrors are coated to reflect the light of wavelength(s) of interest. The output mirror transmits a fraction of the energy that is stored in the cavity, and the transmitted radiation becomes the output beam of the laser. A prism is inserted between the two mirrors to force the laser to output a specific wavelength (single-line operation). The prism can be removed from the cavity, and the mirrors alone allow the laser to resonate simultaneously on a number of laser transitions (multiline operation). This provides the highest output power and is used for exciting dye lasers.

The major wavelengths at which each of the CW gas lasers can be operated are listed in Table 2-1. Since the intensity of scattered light is governed by the ν^4 rule (Section 1.15), the 488.0-nm line of an Ar⁺ laser produces 2.8 times stronger scattering than the 632.8-nm line of He-Ne laser if other conditions are equal. Tables 2-2 to 2-4 list the plasma lines of gas lasers, which can be used for frequency calibration (Section 2.6). Plasma lines may cause problems unless proper optical filtering is employed. Interference filters are used commonly to remove unwanted laser lines. However, they are inconvenient in that each exciting line requires its own filter, and the filtering is usually not complete with an interference filter. Recently, improved interference filters made by a holographic process have become available. These filters, referred to as *notch filters*, are characterized by high optical densities, very narrow spectral bandwidths, and steep cuton/cutoff regions. Pre-monochromators (prism or grating types) are also applicable for filtering over a wide frequency range and can isolate the desired laser line from the rest with high efficiency. Plasma lines can be identified readily because they are quite sharp in contrast to Raman bands and disappear or shift on changing the frequency of the exciting line.

Table 2-1 Some Lasing Lines of Typical Gas Lasers in the Visible Region

Laser	Wavelength in Air (nm)	Wavenumber in Air (cm^{-1})	Typical Power (mW)
Ar-ion ^a	351.1–363.8 (UV)	28,481.9–27,487.6	100–400
	454.4 (blue-violet)	22,002.1	120
	457.9 (blue-violet)	21,838.8	350
	465.8 (blue)	21,468.4	200
	472.7 (blue)	21,155.1	300
	476.5 (blue)	20,986.4	750
	488.0 (blue)	20,491.8	1,500
	496.5 (blue-green)	20,141.0	700
	501.7 (green)	19,932.2	400
	514.5 (green)	19,436.3	2,000
	337.4 (UV)	29,638.4	200
	350.7 (UV)	28,514.4	1,200
	356.4 (UV)	28,058.4	600
	406.7 (violet)	24,588.1	900
Kr-ion ^b	413.1 (violet)	24,207.2	1,800
	415.4 (violet)	24,073.2	275
	468.0 (blue)	21,367.5	500
	476.2 (blue)	20,999.6	400
	482.5 (blue)	20,725.4	400
	520.8 (green-yellow)	19,201.2	700
	530.9 (green-yellow)	18,835.9	1,500
	568.2 (yellow)	17,599.4	1,100
	647.1 (red)	15,453.6	3,500
	676.4 (red)	14,784.2	900
	752.5 (near-IR)	13,289.0	1,200
	799.3 (near-IR)	12,510.9	300
	632.8 (red)	15,802.8	50
	441.6 (blue-violet)	22,644.9	40
He-Ne ^c	325.0 (UV)	30,769.2	10

^aPower value for Spectra-Physics Model 2025.^bPower value for Coherent Innova 100-K3.^cPower value for Spectra-Physics Model 125A.^dPower value for Liconix Model 4240NB.

Note: The values in Tables 2-1 and 2-2 are expressed as wavelengths and wavenumbers in air. The difference between $\Delta\nu$ (air) and $\Delta\nu$ (vacuum) is usually less than 1cm^{-1} and can be ignored in Raman spectroscopy. When molecular constants are calculated from absolute Raman frequencies, $\Delta\nu$ (air) must be converted to $\Delta\nu$ (vacuum).

2.2.2 NEODYMIUM-YAG LASERS

Neodymium-YAG (Nd: YAG) are solid-state lasers. The YAG, or yttrium-aluminum-garnet ($\text{Y}_3\text{Al}_5\text{O}_{12}$), in rod shape is host to Nd^{3+} ions, which actually do the lasing. The lasers are made in both CW and pulsed formats.

Table 2-2 Some Plasma Lines from a Detuned Argon-Ion Laser

Line	Wavelength in Air (Å)	Wavenumber in Air (cm ⁻¹)	Reference
1	4,545.05	22,001.96	a
2	4,579.35	21,837.16	a
3	4,589.93	21,786.82	b
4	4,609.56	21,694.04	a
5	?	?	—
6	4,657.89	21,468.95	a
7	4,726.86	21,155.69	a
8	4,735.93	21,115.18	b
9	4,764.89	20,986.84	b
10	4,806.07	20,807.02	b
11	4,847.90	20,627.49	b
12	4,879.86	20,492.39	c
13	4,889.03	20,453.96	c
14	4,904.75	20,388.40	c
15	4,933.21	20,270.78	c
16	4,965.07	20,140.70	c
17	4,972.16	20,111.98	c
18	5,009.33	19,962.75	c
19	5,017.16	19,931.59	c
20	5,062.04	19,754.88	c
21	5,141.79	19,448.48	c
22	5,145.32	19,435.14	c

^aR. Beck, W. Englisch, and K. Gurs, "Tables of Laser Lines in Gases and Vapors," 2nd Ed., pp. 4–5. Springer-Verlag, New York, 1978.

^bA. N. Zeidel, V. K. Prokofev, and S. M. Raiskii, "Tables of Spectrum Lines," pp. 299–301. Pergamon Press, New York, 1961.

^cN. C. Craig and L. W. Levin, *Appl. Spectrosc.* 33, 475 (1979).

Early versions of the laser were pumped with flashlamps, whereas newer versions use an array of diode lasers operating in the range of 800–900 nm. The primary lasing wavelength for the Nd:YAG laser is 1,064 nm, which is ideal for FT-Raman systems operating in the near-infrared (near-IR) regions. The outputs from these lasers can exceed 10 W. The Nd:YAG laser can be frequency doubled (half the wavelength) with an intracavity crystal to lase at 532 nm with outputs from 50 to 200 mW. The output power and wavelength in the visible range make them strong rivals to water-cooled gas-ion lasers. Outputs also can be obtained at one-third the wavelength (355 nm) and at one-fourth the wavelength (266 nm).

2.2.3 DIODE LASERS

Diode lasers can be obtained at specific wavelengths from the blue to the IR region, and currently, there is considerable effort to develop UV-emitting

Table 2-3 Some Plasma Lines from a Krypton-Ion Laser^a

Wavelength in Air (nm)	Relative Intensity	Wavelength in Air (nm)	Relative Intensity
522.95	600	587.09	750
530.87	2,300	599.22	1,000
533.24	2,000	624.02	700
544.63	900	657.01	1,000
546.82	1,100	721.31	600
552.29	1,050	728.98	900
556.86	1,000	740.70	800
557.03	550	752.45	600
563.50	1,400	758.74	550
567.28	570	760.15	600
568.19	3,500	784.07	520
569.03	2,000	785.48	500
575.30	1,000	799.32	700
577.14	1,700	805.95	600

^aThese lines (relative intensity > 500) were chosen from the table of C. Julien and C. Hirlmann, *J. Raman Spectrosc.* **9**, 62 (1980).

Table 2-4 Principal Plasma Lines from a He-Ne Laser^a

Wavelength in Air (nm)	Relative Intensity	Wavelength in Air (nm)	Relative Intensity
638.299	53	706.519	31
640.108	>100	717.394	4
640.975	31	724.517	5
644.472	30	728.135	11
650.653	50	748.887	0.5
659.895	41	753.577	0.4
667.815 667.828 }	91	754.405 777.730	0.3 5
671.704	36	794.318	0.1
692.947	19	813.641	0.2

^aReproduced with permission of Spex Industries.

diode lasers. These lasers produce optical emission at semiconductor *p-n* junctions. Their use in consumer products such as CD readers/writers and in fiber optic communication networks has greatly influenced their development and lowered the costs of these lasers. The major advantages of these lasers is their high efficiency with minimum power and cooling and their small size. For Raman excitation sources, it is necessary to reduce their tendency to drift in wavelength and to stabilize the mode structure. Improvements have been made by carefully controlling the temperatures to within $\pm 0.01^\circ\text{C}$ and by incorporating a grating into the laser cavity to

maximize one particular laser mode and, consequently, one particular wavelength.

2.2.4 TUNABLE LASERS

Dye lasers are used to provide a range of wavelengths for Raman excitation. Basically, three types of dye lasers exist: those pumped by a CW gas laser, those pumped by a pulsed laser, and those pumped by a flashlamp. Relatively large volumes of organic dye solutions are required. The wavelength ranges obtained by a dye laser, pumped by argon-ion and krypton-ion lasers, are shown in Fig. 2-3. Similar ranges may be obtainable from pulsed lasers and flashlamp-pumped instruments. Bandwidths are typically 1 cm^{-1} but can be reduced to 0.1 cm^{-1} by the use of fine-tuning etalons. A recently developed solid-state laser uses a titanium-sapphire crystal; it is tunable in the 700- to 1,030-nm range and can provide 3 W of output power when pumped by a 20-W Ar^+ laser.

2.2.5 OTHER LASERS

There are a number of other lasers, including excimer and nitrogen lasers, that have been used as Raman excitation sources. Third (355 nm) and fourth (266 nm) harmonics of the Nd:YAG laser have been used along with dye

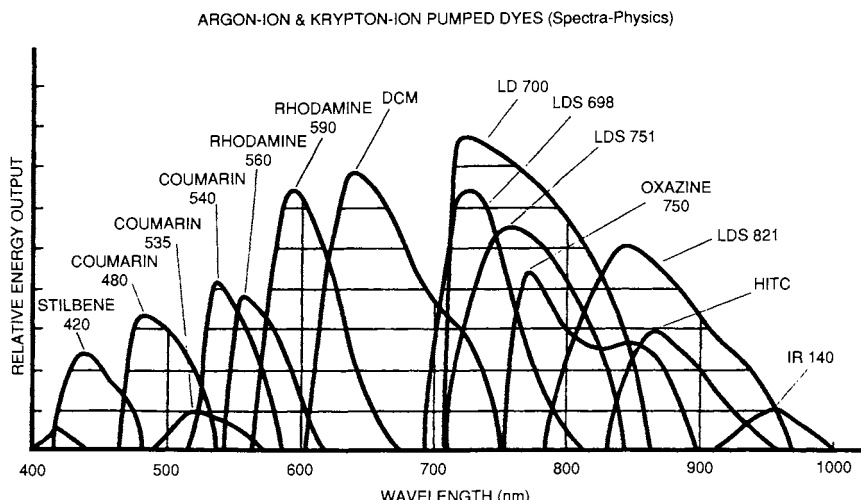


Figure 2-3 Output powers and wavelengths obtainable from a Spectra Physics Model 375 dye laser pumped with Ar-ion and Kr-ion lasers. (Reproduced with permission.)

Table 2-5 Other Laser Lines

Laser	Wavelength	Type and Typical Power
Solid State Laser		
Ruby	694.3 nm	Pulsed, up to 100 MW
Nd:YAG ^a	1,064 nm (near IR)	CW/pulsed, up to 100 MW
Diode	3,500–380 cm ⁻¹ (IR)	CW/pulsed, up to 25 W
Gas Laser		
Nitrogen	337.1 nm (UV)	Pulsed, 100–1,000 kW
Carbon dioxide	9–11 μm (IR)	CW/pulsed, up to 10 MW
Excimer (XeCl) ^a	308 nm (UV)	Pulsed, up to 40 MW

^aFor more information, see Table 3-1.

lasers and hydrogen Raman shifters* to provide excitation in the UV range starting at 185 nm (2, 3). The characteristics of a number of possible laser configurations are summarized in Table 2-5.

2.3 Sample Illumination

Since the Raman scattering is inherently weak, the laser beam must be focused properly onto the sample and the scattered radiation collected efficiently. The focusing of the laser onto the sample can be readily achieved because of the small diameter of the laser beam (~1 mm). Excitation and collection from the sample can be accomplished by using several optical configurations, such as the 90° and 180° scattering geometries illustrated in Figs. 2-4a and 2-4b, respectively. Collection optics consist of an achromatic lens system with a collecting lens and a focusing lens, as shown in Fig. 2-4. An oblique illumination angle is also a common configuration for illuminating the front surface of a sample with the incident laser beam at ~85° to normal. A configuration that avoids the use of a collecting lens and uses mirrors is shown in Fig. 2-5; an off-axis ellipsoid is used to collect the scattered light and focus it on the entrance slits. It has advantages when the measurement is made in the UV region.

The light-gathering power of a lens is expressed in terms of *F* number, defined by

$$F = \frac{f}{D} \quad (2-1)$$

where *f* is the focal length of the lens and *D* is the lens diameter. The smaller the *F* number, the larger is the light-gathering power (i.e., either a larger *D* or

*A long-path gas cell containing high-pressure H₂ gas (e.g., 0.75-m path length with 6.8 atm of pressure).

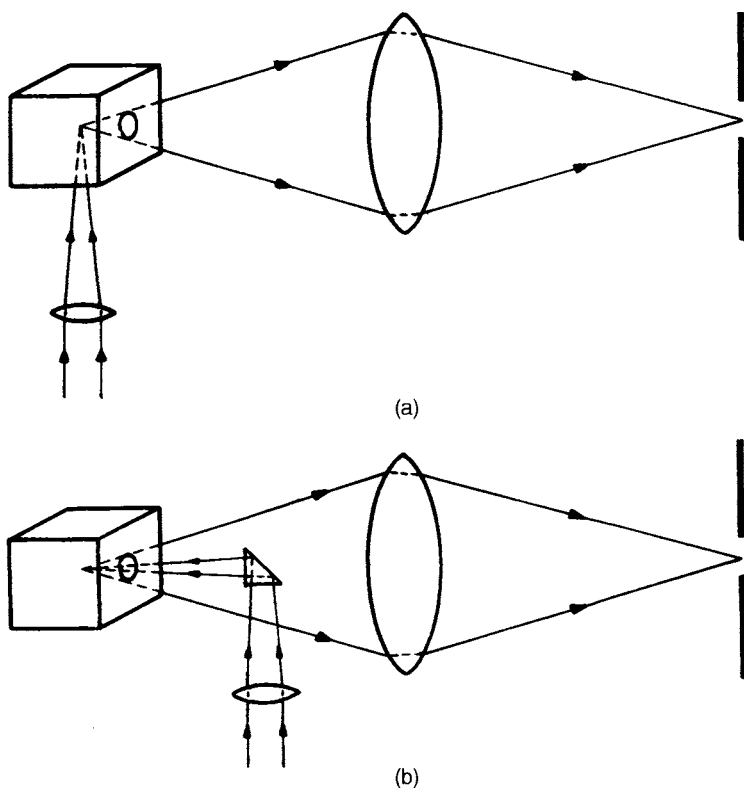


Figure 2-4 Configurations for (a) 90° and (b) 180° scattering geometries.

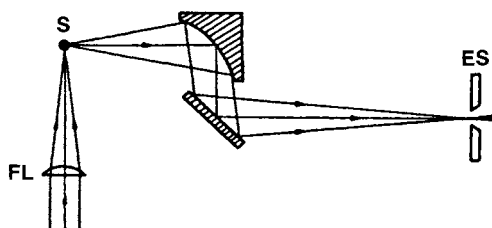


Figure 2-5 Collection optics with an off-axis ellipsoidal mirror for the UV region. FL, focusing lens; S, sample; and ES, entrance slits.

a smaller focal length f). It is important to match the F number with the wavelength selector or else the total light throughput will not be at a maximum.

Preliminary focusing of the incoming laser beam may be achieved by removing the sample holder and observing the focus position by interposing

a piece of lens paper in the beam. The focal point may be observed readily by moving the paper along the beam direction. The position of the focus is adjusted by changing the position of the lens. The final adjustment of the lens can be made by observing the effect of its position on a Raman signal. Considerable time can be saved if the laser-focusing lens is achromatic because the foregoing procedure does not need to be repeated when changing the laser wavelength. During this procedure, the laser power should always be kept at a minimum, and *care should be taken to protect the eyes during the procedure*. An excellent review article concerning the radiation hazards of lasers is available (4).

In the case of a dispersive wavelength selector, image positioning of the irradiated sample on the entrance slits of the monochromator is most important. This image can be seen by holding a small section of a 3×5 in. file card near the slit. Again, caution should be exercised because *reflections at this point may seriously damage your eyes*. For 90° or an oblique-configuration scattering, a bright image sometimes may be observed at the entrance to the wavelength selector. However, this is not due to Raman scattering but to fluorescence or reflections of the laser beam from glass, quartz, or the surface of the sample. Since the Raman image is rather weak, the room must be kept as dark as possible during this procedure.

2.4 Wavelength Selectors

Wavelength selectors can be classified into several categories. The simplest device is an interference filter, which depends on its two optically flat surfaces to generate a constructive interference and transmit an integer number of wavelengths corresponding to twice the thickness of the filter. Interference filters are constructed for single wavelengths (wavelengths corresponding to this wavelength divided by integers also will have constructive interferences and be observed). Variable, wedge-shaped interference filters are available for selecting desired wavelengths; however, the spectral resolution of these devices is generally too large for Raman spectra. Recently, acoustic and liquid-crystal tunable filters have been used successfully for measuring Raman spectra and Raman spectral images; these are discussed in Section 3.8 of Chapter 3 under "Special Techniques."

Both prism and grating monochromators and spectrographs have been used extensively for measuring Raman spectra. While monochromators are still the mainstay of Raman instrumentation, FT-Raman has made considerable advancement in recent years and is now considered to be competitive with monochromators. Both monochromators and FT-Raman will be discussed in detail.

2.4.1 MONOCHROMATORS WITH A SINGLE DETECTOR

In a single monochromator, extraneous or stray light that bounces around the spectrometer overlaps the weak Raman scattered light. This stray light is caused mainly by undiffracted light being scattered from the face of the grating. Such stray light can be reduced considerably by arranging two spectrometers in tandem so that the Raman output of one is filtered (or purified) by the second. Thus the construction of double monochromators began. A schematic of a double monochromator is shown in Fig. 2-6. A triple monochromator has even greater stray light rejection than a double monochromator and allows observation of Raman bands located very close to the Rayleigh line. A triple monochromator has been developed by coupling a spectrograph to the output of a double monochromator. Spectrographs using array detectors will be discussed in the next section.

The *F number* of a grating monochromator is also determined by Eq. (2-1). In this case, f is the focal length of the collimator mirror, and D is usually calculated by

$$\frac{1}{4}\pi D^2 = L^2, \quad (2-2)$$

where L is the side length of a square grating. To make F smaller, f should be smaller and D should be larger. However, the resolution decreases as f

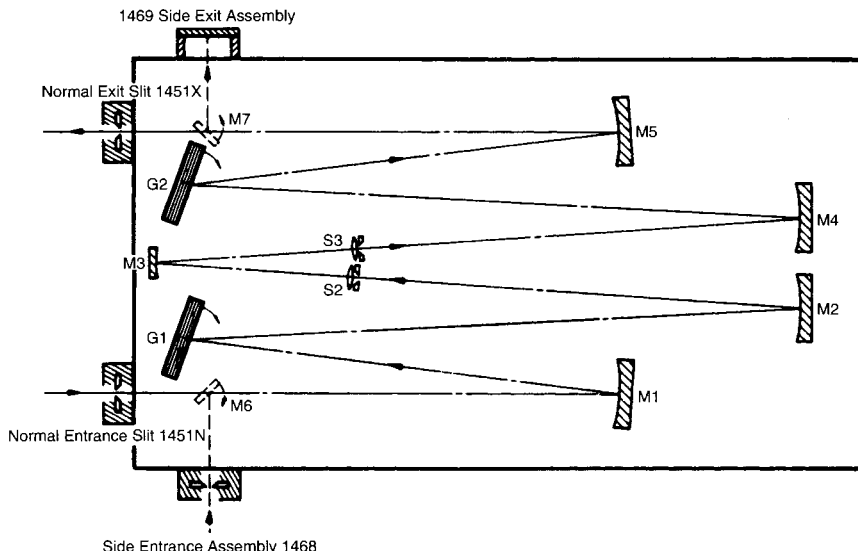


Figure 2-6 Schematic of a Spex Model 1403/4 double monochromator. (Reproduced with permission.)

becomes small. To maintain good resolution, then, D must be large, and this requires a large and expensive grating. For these reasons, most Raman monochromators have F numbers between 5 and 10. For example, a double monochromator with $f = 0.85\text{ m}$ has an F number of 7.8 with gratings $110 \times 110\text{ mm}$ in size. Gratings determine the resolution of a spectrometer to a large extent. The more grooves per millimeter, the better is the dispersion, and the greater is the resolution. The signal loss caused by improved resolution can be compensated by widening the slit width. Using an 1,800 grooves/mm grating, the double monochromator being discussed can cover the range from $31,000$ to $11,000\text{ cm}^{-1}$ with a cosecant drive system. However, this range would decrease with gratings of higher-density grooves (2,400 and 3,600 grooves/mm).

The slit width and monochromator advancing speed (increments between data points) are important in obtaining maximum resolution. The effect of changing the slit width (SW) is seen clearly in Fig. 2-7a, where the 459-cm^{-1} band of CCl_4 has been scanned at bandpasses (BP)* of 1, 2, 3, and 4 cm^{-1} . The signals were made comparable by lowering the laser power along the series, since the signal is proportional to $P_0 \times \text{SW}^2$, where P_0 is the incident power. Rapid scanning can also cause distortion of the true spectral pattern, as is shown in Fig. 2-7b. A simple method to detect this problem is to remeasure the spectrum at a slower scan speed with smaller increments and look for significant changes in the band patterns.

Mechanical backlash of the wavenumber reading is another problem that may be encountered when measuring a spectrum on some instruments. Finally, the temperature of the monochromator should be kept constant because band position may vary by as much as 3 cm^{-1} with temperature fluctuations. Although the monochromator normally is thermostated above room temperature, it is recommended that a laboratory temperature be reasonably controlled.

2.4.2 FT-RAMAN

When the conventional Raman effect was discovered by Sir C. N. Raman, the expectations were very high. It was believed that the technique would be a major tool for chemical analyses. Those expectations were not realized primarily because of fluorescence problems, where fluorescence completely masks the Raman spectrum (see discussion on fluorescence in Chap. 1). The advent of FT-Raman makes Raman spectroscopy more useful in chemical

* $\text{BP} = D_L^{-1} \times \text{SW}$, where D_L^{-1} is the inverse linear dispersion of the grating and SW is the mechanical slit width.

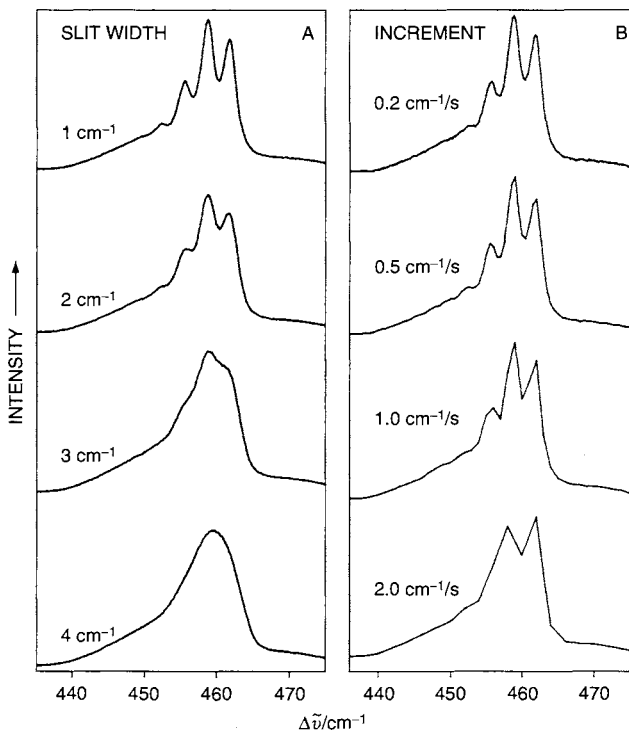


Figure 2-7 Raman spectra of CCl_4 (488.0-nm excitation) obtained under different conditions using a Spex Model 1403 double monochromator equipped with 1,800 grooves/mm gratings and a Hamamatsu R928 photomultiplier. (a) The effect of spectral bandpass (0.2-cm^{-1} increments per data point). (b) The effect of size of increments between the data points (1-cm^{-1} slit width; accumulation time for all spectra was 1 second per data point.)

analyses because the fluorescence is reduced (or eliminated) by measuring spectra in the near-IR region.

A number of methods have surfaced to reduce or eliminate fluorescence. The FT technique involves measuring the Raman effect using an Nd:YAG laser emitting at 1,064 nm ($9,395\text{ cm}^{-1}$) and interfacing the Raman sampling module with an FT-IR instrument (5). The technique was first suggested in 1964 by Chantry and Gebbie (6). Because of a lack of technological development at that time, it took more than 20 years for the technique to become viable. At present, most FT-IR instruments can be coupled with a Raman accessory to obtain Raman spectra and use the FT-IR capabilities with computer manipulations and software programs developed for IR spectroscopy.

Besides aiding in the fluorescence problems in Raman scattering by performing the measurements in the near-IR region, FT-Raman can be of aid in

other problems of conventional Raman spectroscopy. Raman spectroscopy suffers from a lack of frequency precision, and therefore, good spectral subtractions are not always possible. In addition, high-resolution experiments are difficult to achieve with conventional Raman spectroscopy. For all three problems, FT-Raman has been shown to be an improvement over conventional Raman spectroscopy.

In the conventional Raman spectroscopy, the noise level of the photomultiplier detector is proportional to the square root of the light intensity striking it. Although the signal-to-noise (S/N) ratio increases as the square root of the bandwidth of the resolution elements, the use of a multiplex spectrometer (interferometer) allows all the scattered energy to bear on the detector simultaneously. The noise increases at the detector by the same amount as the S/N increase for multiplexing, thus canceling out the two effects (7). For this reason, it was originally believed that FT-Raman spectroscopy would not be too helpful (8). However, the feasibility of FT-Raman has now been clearly demonstrated.

Conventional Raman spectroscopy measures intensity versus frequency or wavenumber. FT instruments, on the other hand, measure the intensity of light of many frequencies simultaneously. The latter is often referred to as a *time-domain spectroscopy*. This spectrum is then converted into a conventional spectrum by means of Fourier transformation using a computer algorithm. The waveform or interferogram in an FT-Raman experiment is illustrated in Fig. 2-8a. The Fourier transform (FT) of this interferogram produces a signal peak at frequency ω_0 , as shown in Fig. 2-8b. The sum of the two waveforms of different frequencies in an FT experiment is represented in Fig. 2-8c. The result of the FT (Fig. 2-8d) is the frequency spectrum with two peaks at ω_0 and $10\omega_0$, where the low-frequency ω_0 is the same as Fig. 2-8b and $10\omega_0$ is 10 times larger in frequency. The distinctive feature of the FT technique, like FT-IR, is that information for all the wavelengths falls on the detector at all times. This provides improved resolution, spectral acquisition times, and S/N ratios over conventional dispersive Raman spectroscopy.

As stated earlier, FT-Raman instruments employ a CW Nd:YAG laser with an excitation at 1,064 nm ($9,395 \text{ cm}^{-1}$). The use of such a near IR laser suffers from a 16-fold reduction in signal as compared with a visible laser lasing at 514.5 nm because the cross section of Raman scattering follows the v^4 relationship. The maximum power of the laser is as high as 10 W, although less power ($\sim 1 \text{ W}$) generally is used.

An important aspect of FT-Raman instrumentation is the necessity for optical filtering. The first task is to eliminate the stray light caused by the laser excitation because it will saturate the detector and electronics. The filtering must be capable of reducing the Rayleigh line, which is 10^6 stronger than the Stokes-shifted lines in the Raman spectrum. In order to be sufficiently

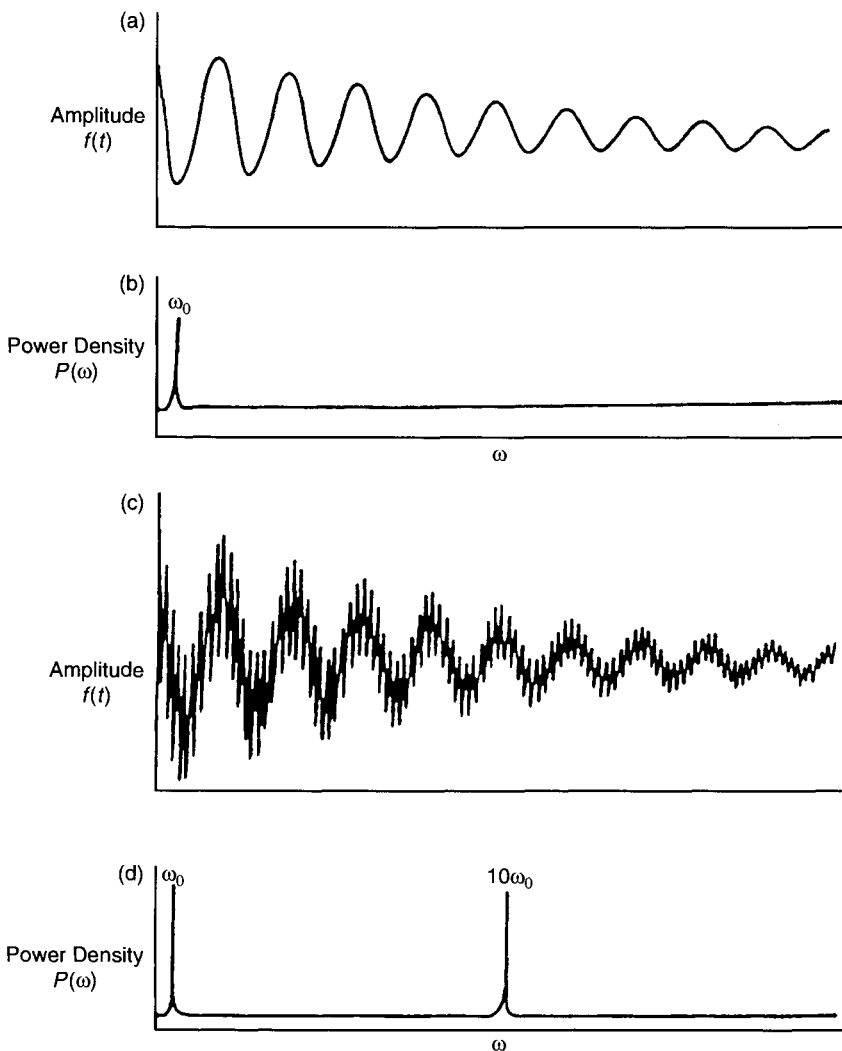


Figure 2-8 FT-Raman is a time-domain spectroscopy that is connected mathematically to a Fourier transform. A single feature in the frequency domain as shown in (b) would produce the interferogram shown in (a), whereas the two features in the frequency domain in (d) would produce the interferogram shown in (c). Each individual feature in the frequency domain would give rise to a sinusoidal wave in the time domain.

efficient and to obtain maximum information in the Raman measurement, the reduction of the Rayleigh line should be comparable with the strongest Raman line.

Holographic notch filters have been most successful in eliminating light at the laser frequency from the scattered signal. These filters are fabricated by recording interference patterns formed between two mutually coherent laser beams on multiple film layers. Since all layers are recorded simultaneously within a thick stack, the optical density of the notch filter is high, and its spectral bandwidth can be extremely narrow. In addition, the layering profile is sinusoidal instead of squarewave; thus holographic notch filters are free from extraneous reflection bands and provide significantly higher laser damage thresholds.

Several other types of filters are discussed by Chase (5, 7). Filters are also necessary to remove the optical output of the He-Ne laser (used for referencing) because the laser has optical axes colinear with the main laser source. Since the detectors used in FT-Raman are sensitive to the He-Ne wavelength, the laser is a source of interference. Here, plasma emission filters can be used. The white light of the instrument is filtered with a near-IR cutoff filter. A final filter may be used in front of the detector.

An optical diagram of a typical FT-Raman spectrometer is shown in Fig. 2-9. It may be observed that the laser radiation is directed to the sample by means of a lens and a parabolic mirror, and the scattered light from the sample is collected and passed to a beam splitter and to the moving and fixed mirrors in the interferometer head. It is then passed through a series of dielectric filters and focused onto a liquid-nitrogen-cooled detector (Ge). The advantages and disadvantages of the FT-Raman system are given in Table 2-6.

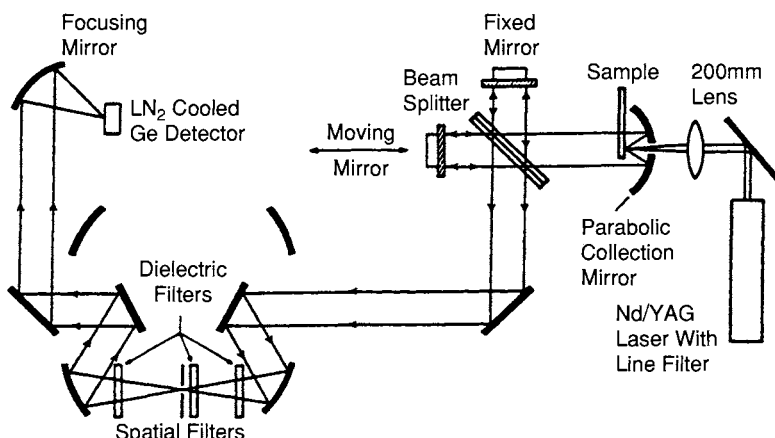


Figure 2-9 Optical diagram of an FT-Raman spectrometer. The heart of the instrument is the interferometer head, consisting of the beam splitter and fixed and moving mirrors.

Table 2-6 Advantages and Disadvantages of FT-Raman

Advantages	Disadvantages
Reduction or elimination of fluorescence	Absorptions in the NIR
High resolution	Black-body emissions in IR
High throughput	Lower scattering intensity due to ν^4 effect
Good frequency accuracy	Difficult to detect low concentrations
Collect Stokes and anti-Stokes	of impurities
Raman simultaneously	
Both IR and Raman capabilities on same instrument.	

The interest in FT-Raman has increased significantly. The capabilities of FT-Raman have been demonstrated in many applications. High-resolution gas-phase FT-Raman spectroscopy has also been demonstrated; this is not possible with conventional Raman scattering. However, Chase (9, 10) has discussed certain limits of the capability of FT-Raman; some of these conclusions are

- (1) FT-Raman will not completely eliminate fluorescence background. Materials that absorb strongly in near-NIR region will present problems (e.g., transition metal complexes, transition metal complex doped polymers, charge-transfer conductors, polycyclic aromatic compounds). Other methods of combatting fluorescence will be discussed in Section 2.7.
- (2) It will not displace dispersive-visible laser Raman spectroscopy.
- (3) It will not detect parts per million (ppm) impurities through spectral subtraction.
- (4) A serious problem of using an Nd:YAG laser to excite FT-Raman is the difficulty of attempting to study samples at temperatures $>150^\circ\text{C}$. The thermal blackbody emission from the sample becomes more intense (broad background) than the Raman signal. The S/N ratio is lowered, and the detector becomes saturated.

2.5 Detection

Since Raman signals are inherently weak, the problems involved with detection and amplification are severe. Most of the very early work was performed with photographic detection using long exposure times. Furthermore, the time to develop photographic plates and examine them with a microphotometer rendered Raman spectroscopy unfit as a routine technique. This

situation has changed considerably since the development of strong laser sources and sensitive detection techniques. Several detection techniques that are commonly used are described next.

2.5.1 PHOTON COUNTING

For spectrometers equipped with monochromators and single detectors, the Raman scattered light in the focal plane and exiting through the slits of the monochromator is collected and focused on a photomultiplier (PM) tube, which converts photons into an electrical signal. The PM tube consists of a photocathode that emits electrons when photons strike it; a series of dynodes, each of which emits a number of secondary electrons when struck by an electron; and an anode that collects these electrons as an output signal. A schematic of a head-on PM tube is shown in Fig. 2-10. The photons strike the cathode, which is at the largest negative voltage. Each of the successive dynodes represented by a curved surface is at a less negative voltage. For example, the cathode might be at $-1,100$ V dc, the first dynode at $-1,000$ V dc, the second dynode at -900 V dc, etc. A photon striking the cathode releases an electron, which is attracted to the less negative first dynode and causes the release of several electrons. These electrons are attracted to the second dynode, where they each release several electrons. This multiplication process is repeated at each dynode. Thus the electrons released by the single photon is multiplied many-fold by passing from one dynode to the next until they all reach the anode. The quantum efficiency of a primary electron being emitted from the photocathode is wavelength-dependent. The quantum efficiency and photocathode sensitivity of typical PM tubes as a function of wavelength are shown in Fig. 2-11.

For good sensitivity, proper care of the PM tube, its optics, and its housing is essential. The background noise is the primary limiting factor in PM tube

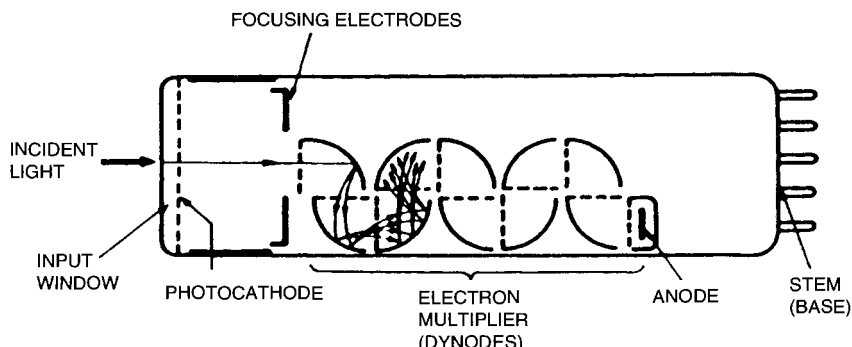


Figure 2-10 Schematic of a head-on type PM type. (Reproduced with permission from Hamamatsu.)

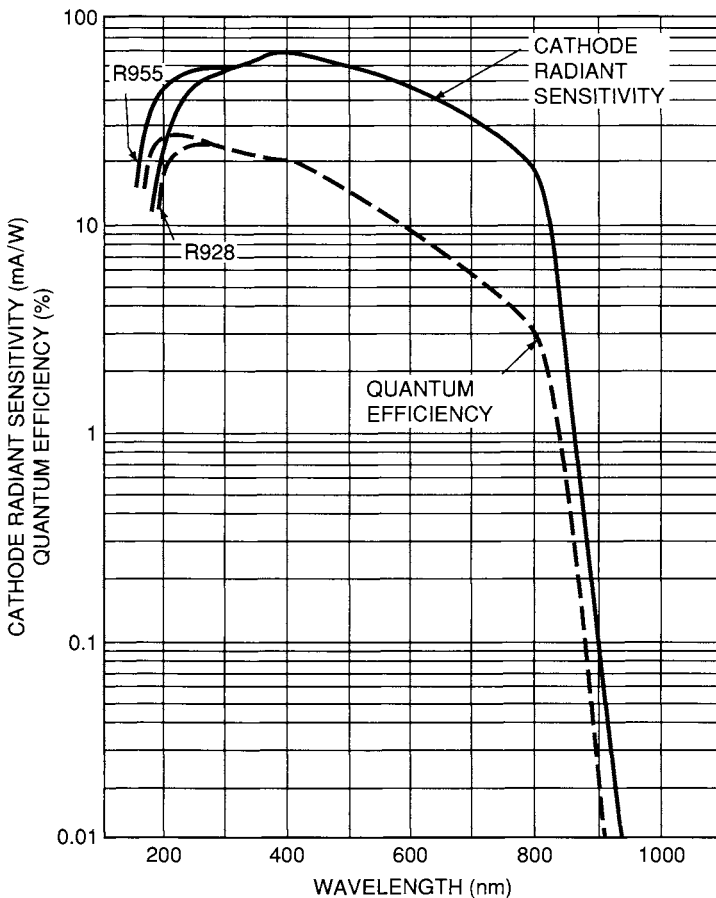


Figure 2-11 Response curve for a Hamamatsu R928 photomultiplier. (Reproduced with permission from Hamamatsu.)

performance. This is called the *dark current* and is caused primarily by the spurious emission of electrons from the photocathode and dynodes and by dielectric leakage across the PM tube base pins and resistor chain. These spurious emissions can be reduced (a large portion is of thermionic origin) if the tube is thermoelectrically cooled via the Peltier effect so that the weak Raman signal may be measured easily. Because of cooling, however, condensation of water in the lens system just in front of the tube and in the base may become a problem. The detector system should be disassembled periodically and dried by warming under reduced pressure.

The electron pulses (Raman signal) from the PM tube may be processed by the direct-current (dc) amplification or a photon-counting method. In the former, the electron pulses from the PM tube are averaged over time, and the resulting dc current is amplified directly and measured by a picoammeter or electrometer. However, this method is no longer used because the photon-counting method gives much better sensitivity.

In the photon-counting method, the electron pulses caused by individual photons reaching the photocathode are measured. Photon counting has advantages in that a substantial portion of the dark signal is electronically discriminated from photon pulses, allowing the ultimate sensitivity of the detector to be increased, typically by a factor of 10 over a dc system. These systems have a disadvantage in that the maximum signal is limited to a photon count rate at which phonon events do not overlap. In practice, this “pulse pileup” limit is around 150×10^6 photons s⁻¹, which corresponds to about 800 nanoamps. Thus this system is applicable to all but the strongest of Raman signals.

For the photon-counting mode, an optimal resolution can be maintained by coordinating integration time with monochromator scan rate or interval. For each Raman apparatus, careful optimization of the PM tube’s high voltage and pulse discriminator levels based on S/N ratios must be performed.

2.5.2 PHOTODIODE ARRAY

In normal Raman measurements, the detection of Raman signals is made for each frequency, and the Raman spectrum is obtained through scanning the entire frequency range. This single-channel technique is time-consuming, and it is not suitable when the compound is unstable or short-lived. Simultaneous detection of Raman signals in the entire frequency range can be done by using multichannel detection. (See Refs. 11–12.) Multichannel photon detectors consist of an array of small photosensitive devices that can convert an optical image into a charge pattern that can be read as a Raman spectrum. Typically, these array-type detectors are not sensitive enough for detecting Raman signals.

2.5.3 CHARGE-COUPLED DEVICE

In recent years, charge-coupled devices (CCDs) have been used increasingly in Raman spectroscopy (13, 14). A CCD is a silicon-based semiconductor arranged as an array of photosensitive elements, each one of which generates photoelectrons and stores them as a small charge. An example format of a 512×512 array is shown in Fig. 2-12. Charges are stored on each individual

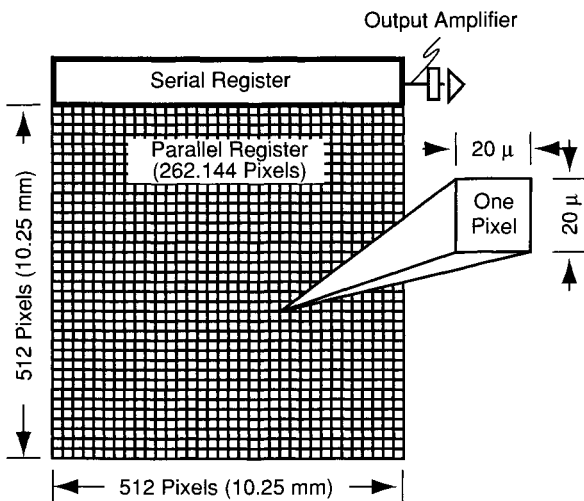


Figure 2-12 Schematic of a CCD detector. (Reproduced with permission from Ref. 14.)

pixel as a function of the number of photons striking that pixel. On command, the charges from each row are shifted to the next higher row. Charges on pixels in the top row are shifted from left to right on request and read by a single analogue-to-digital converter. The charge-transfer process is essentially noise-free, and almost all the noise contributed to the signal by the CCD is from the output stage, where the charge content of each bucket is measured. This is called the *readout noise*. To read the entire array, the top row is read one element at a time by moving the elements from left to right, and afterwards, all the rows are shifted up one to start the reading of the next row. Thus 262,144 pixels are converted to digital values before the next frame can be measured and read. Current CCDs have formats of more than $1,024 \times 1,024$ pixels, with a total size of about 25 mm^2 .

The major advantages of the CCD relative to other multichannel detectors are the low readout noise, which makes optical intensification unnecessary, and high quantum efficiency and sensitivity in a wide wavelength range (120–1,000 nm). Thus the CCD coupled with near-IR laser excitation (dye laser, diode laser) can be used to measure Raman spectra of fluorescent compounds (see FT-Raman). Complete utilization of a large number of detector elements in the CCD for spectroscopic work is under way. For example, time-resolved spectra can be obtained by using a horizontal strip of the CCD and shifting its position up vertically as a function of time (15). However, disadvantages of using a CCD for Raman spectroscopy should also be noted (14).

2.5.4 OTHER DETECTION DEVICES

In FT-Raman spectroscopy, IR laser lines such as the 1,064-nm line of the Nd:YAG laser are used for excitation. To detect such IR radiation, several detectors with the required sensitivity are available. Most of the FT-Raman instruments use indium-gallium-arsenide (InGaAs) detectors (16). For a detector 1 mm in size, a noise equivalent power (NEP) of 10^{-14} or less is usually attained when the detector is cooled. However, this detector suffers from a reduced long-wavelength cutoff at 77 K. Thus one can obtain spectra only up to $3,000\text{ cm}^{-1}$. It does have an advantage in that the dark current is negligible. This allows direct coupling of dc to the first-stage amplifier and allows for both dc and alternating-current (ac) components of the interferogram to be monitored.

Several other detectors are available for use in the near-IR. Cooled PbS, Ge, InGaAs, InSb, and platinum silicide have been investigated as detectors for use in FT-Raman. Present commercial instrumentation uses an InGaAs detector. For a discussion on detectors for use in FT-Raman, see Refs. 5 and 9.

Very high purity germanium detectors can be used in the Raman spectral range. The NEP of this type of detector approaches 10^{-15} . This detector system can operate to $3,500\text{ cm}^{-1}$. Unfortunately, it is susceptible to cosmic radiation, and care must be taken to filter such radiation (17). An InSb detector also has been tested (18). The InSb detector element responds to a wavelength of $5\text{ }\mu\text{m}$ with an NEP of 10^{-12} if used unfiltered. The major use of this detector is with lasers that operate further into the IR region (16). Other detectors have been proposed, such as the silicon-InGaAs with 256 elements and platinum silicide with 1,024 elements (16). The quantum efficiency of these detectors drops off to 10%, but the spectral range extends to $5\text{ }\mu\text{m}$. It is obvious that the search for improved and more efficient detectors continues. For further discussion on detectors for Raman use, see Ref. 18.

2.6 Instrument Calibration

2.6.1 FREQUENCY CALIBRATION

FT-Raman instruments are calibrated with an internal laser, which is used to provide the exact location of the movable mirror in the interferometer. Thus the intensity of the interferogram is known as a function of the mirror location (distance in cm), and this is converted through a fast Fourier transform to reciprocal distance or wavenumber (cm^{-1}) in the spectral domain.

For dispersive instruments, the wavenumber or wavelength readings on the instrument are not to be taken at face value. It is recommended that the instrument be calibrated periodically. The time involved in calibration

depends on the accuracy desired for a particular experiment. Dispersive spectrometers typically are calibrated for frequency by one of the following methods. For calibration of multichannel Raman spectrometers, see Ref. 19.

(a) Internal Standards

When accuracy of $\sim 1\text{ cm}^{-1}$ is required, internal standards may be employed. These can be frequencies of solvent bands or the bands of added noninteracting solutes. Bands due to the compounds being measured are compared with the frequencies of the internal standard. However, care must be taken so that significant band shifts do not occur because of chemical interaction between the substance under study and the reference itself. In addition to its simplicity, this method has a distinct advantage over the other methods in that the frequencies determined from the position of a band relative to the internal standard are essentially temperature-independent. It should be noted that the absolute readings from the monochromator may change from day to day as much as $2\text{--}3\text{ cm}^{-1}$ if the temperature control inside the monochromator is malfunctioning.

(b) Indene

If additional accuracy is desired (on the order of 0.5 cm^{-1}), then indene may be used (20). Indene also has been used as a frequency calibrant for IR spectrophotometers. Before use, it should be purified by vacuum distillation and stored in sealed capillary or an NMR tube. Figure 2-13 shows the Raman spectrum of indene, and Table 2-7 lists the frequencies that are recommended for use in calibration.

(c) Laser Plasma Lines

Table 2-2 lists the principal plasma lines of the argon-ion laser, some of which may be used for calibration (20–22). To observe these lines, the laser beam

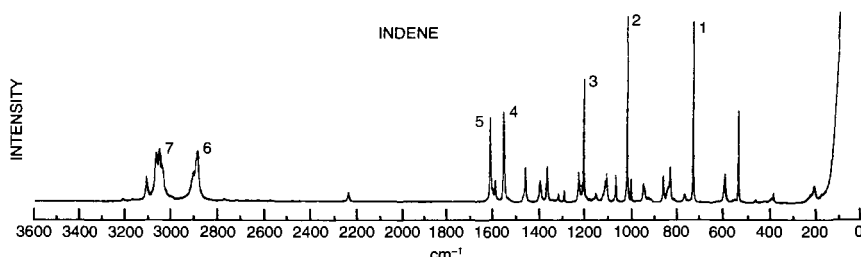


Figure 2-13 Raman spectrum of indene. The wavenumbers of the numbered bands are listed in Table 2-7.

Table 2-7 Recommended Frequencies for Calibration from the Spectrum of Indene

Band ^a	Wavenumber (cm^{-1})
1	730.4 ± 0.5
2	$1,018.3 \pm 0.5$
3	$1,205.6 \pm 0.5$
4	$1,552.7 \pm 0.5$
5	$1,610.2 \pm 0.5$
6	$2,892.2 \pm 1$
7	$3,054.7 \pm 1$

^aThe numbers refer to Fig. 2-13.

should be detuned, and the scattered radiation should be collected from a Kimax melting-point tube (23). This method gives a calibration of better than 1 cm^{-1} accuracy. Table 2-3 lists plasma lines of the krypton-ion laser (24).

(d) Neon Emission Lines

If a neon lamp is available, the Ne emission lines may be used to obtain high-frequency calibration in a wide frequency range. Figure 2-14 shows the

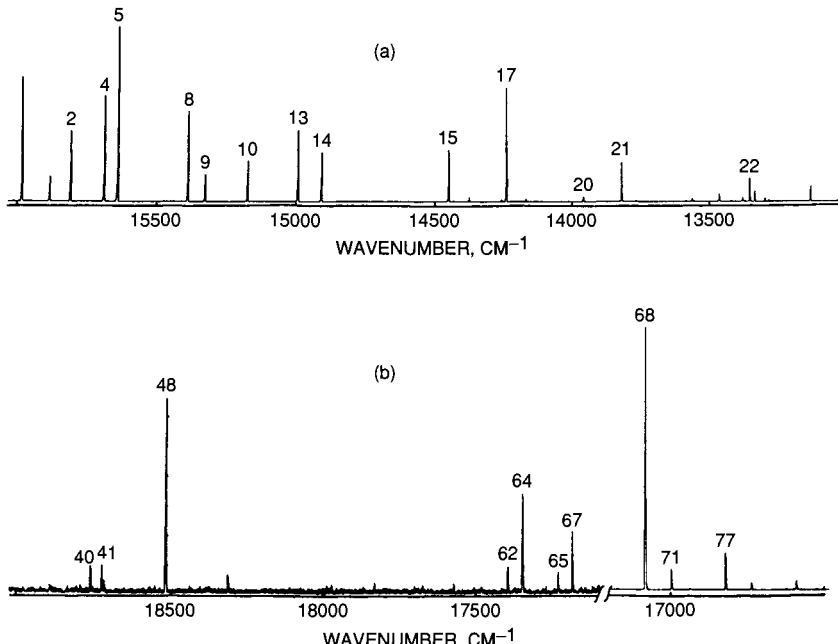


Figure 2-14 Neon lamp emission spectrum. Band numbers refer to Table 2-8 in (a) and Table 2-9 in (b).

spectra taken with a Ne lamp. Tables 2-8 and 2-9 list the Ne frequencies that are useful for calibrating the Raman spectra obtained by excitation with an He-Ne and a Kr-ion laser, respectively. For complete listing of neon emission lines, see Strommen and Nakamoto (General References).

2.6.2 INTENSITY CALIBRATION

The intensity of a Raman signal is governed by a number of factors, including incident laser power, frequency of the scattered radiation, efficiency of the grating (in the case of dispersive instruments) and detector, absorptivity of the materials involved in the scattering, molar scattering power of the normal mode, and the concentration of the sample. This situation is further complicated by the fact that many of these parameters are frequency-dependent, as indicated in the following equation:

Table 2-8 Calibration Lines of a Ne Lamp^{a,c}

Line ^b	Wavelength in Air (Å)	Wavenumber in Air (cm ⁻¹)
1	6,328.1646	15,802.3702
2	6,334.4279	15,786.7453
3	6,351.8618	15,743.4156
4	6,382.9914	15,666.6356
5	6,402.2460	15,619.5185
6	6,421.7108	15,572.1743
7	6,444.7118	15,516.5977
8	6,506.5279	15,369.1802
9	6,532.8824	15,307.179
10	6,598.9529	15,153.9193
11	6,652.0925	15,032.8637
12	6,666.8967	14,999.4824
13	6,678.2764	14,973.9235
14	6,717.0428	14,887.5038
15	6,929.4672	14,431.1239
16	7,024.0500	14,236.8007
17	7,032.4128	14,219.8706
18	7,051.2937	14,181.7948
19	7,059.1079	14,166.096
20	7,173.9380	13,939.3455
21	7,245.1665	13,802.3053
22	7,438.8981	13,442.8512

^aUseful for Raman shift spectra (0–2,400 cm⁻¹ region) obtained by 632.8-nm excitation of a He-Ne laser.

^bRefer to Fig. 2-14a.

^cSource: K. Burns, K. B. Adams, and J. Longwell, *J. Opt. Soc. Am.* **40**, 339 (1950).

Table 2-9 Calibration Lines of a Ne Lamp^{a,c}

Line ^b	Wavelength in Air (Å)	Wavenumber in Air (cm ⁻¹)
40	5,330.7775	18,758.9897
41	5,341.0938	18,722.7567
42	5,343.2834	18,715.0844
43	5,349.2038	18,694.3709
44	5,360.0121	18,656.6743
45	5,372.3110	18,613.9633
46	5,374.9774	18,604.7294
47	5,383.2503	18,576.1379
48	5,400.5616	18,516.5928
49	5,412.6490	18,475.2420
50	5,418.5584	18,455.0931
51	5,433.6513	18,403.831
52	5,448.5091	18,353.6447
53	5,494.4158	18,200.2971
54	5,533.6788	18,071.1609
55	5,538.6510	18,054.9379
56	5,562.7662	17,976.6678
57	5,652.5664	17,691.0792
58	5,656.6588	17,678.2803
59	5,662.5489	17,659.8916
60	5,689.8163	17,575.2599
61	5,719.2248	17,484.8871
62	5,748.2985	17,396.4522
63	5,760.5885	17,359.3375
64	5,764.4188	17,347.8027
65	5,804.4496	17,228.1623
66	5,811.4066	17,207.538
67	5,820.1558	17,181.6706
68	5,852.4878	17,086.7507
69	5,868.4183	17,040.3667
70	5,872.8275	17,027.5732
71	5,881.8950	17,001.3235
72	5,902.9623	16,942.082
73	5,902.7835	16,941.16
74	5,906.4294	16,930.7027
75	5,913.6327	16,910.0797
76	5,918.9068	16,895.0118
77	5,944.8342	16,821.327

^aUseful for Raman shift spectra (0–2,000 cm⁻¹ region) obtained by 530.9-nm excitation of a Kr-ion laser.

^bRefer to Fig. 2-14b.

^cSource: K. Burns, K. B. Adams, and J. Longwell, *J. Opt. Soc. Am.* **40**, 339 (1950).

$$I = K(v) \times A(v) \times v^4 \times I_0 \times J(v) \times C, \quad (2-3)$$

where I is the intensity of a Raman line, $K(v)$ describes the overall spectrometer response, $A(v)$ is the self-absorption of the medium, v is the frequency of the scattered radiation, I_0 is the intensity of the incident radiation, $J(v)$ is a molar scattering parameter, and C is the concentration of the sample. The v^4 term dominates the intensity if the remaining terms do not differ appreciably. Thus a laser beam of a higher frequency is preferred to obtain a stronger Raman signal. Since most of these factors are not known, it is extremely difficult to determine the absolute intensity defined by Eq. (2-3). However, the relative amount of a sample in solution can be determined easily by measuring the relative intensity of a Raman band.

First, a working curve is prepared from the spectra of a series of solutions that contain varying amounts of the sample under consideration and a constant amount of a noninteracting standard. For aqueous solutions, ClO_4^- is ideal because it is chemically inert and has a strong Raman band at 928 cm^{-1} . Then a relative intensity is calculated for each solution by dividing the intensity of the strongest band of the sample by that of the internal standard. Then the sample relative intensity is given by

$$I_{\text{rel}} = \frac{K(v) \times A(v) \times v^4 \times J(v) \times C}{K(v') \times A(v') \times (v')^4 \times J(v') \times C'} \quad (2-4)$$

where all the terms involving v' indicate those of the internal standard, and C and C' denote the concentrations of the sample and the internal standard, respectively. Since the lead terms remain constant, the resulting equation is

$$I_{\text{rel}} = \text{constant} \times C. \quad (2-5)$$

Thus a standard working curve can be obtained as in any other quantitative technique.

The Raman intensity plotted against the exciting laser wavelength is called an *excitation profile*. Excitation profiles such as that shown in Fig. 3-21 of Chap. 3 provide important information about electronic excited states as well as symmetry of molecular vibrations. The intensity of a Raman line is maximized if strict resonance conditions are met (Section 1.15). When constructing excitation profiles, the frequency dependence of $J(v)$ is of interest. It is difficult, however, to determine the J dependence on v from intensity changes because K and A also vary with v .

The self-absorption term in Eq. (2-4) is expressed as (25)

$$\frac{A(v)}{A(v')} = \frac{\varepsilon(v')}{\varepsilon(v)} \cdot \frac{1 - \exp[-\varepsilon(v)C \times l]}{1 - \exp[-\varepsilon(v')C \times l]}, \quad (2-6)$$

where $\varepsilon(v)$ is the molar absorptivity at v , C is the concentration of the absorber, and l is the path length. However, the correction of the spectrometer response is more involved. For detailed procedure, see Strommen and Nakamoto (General References).

2.7 Sampling Techniques

Marked differences are seen between IR and Raman spectroscopy in sampling techniques. In IR spectroscopy, sampling techniques for routine measurements are relatively simple. In contrast, Raman sampling techniques are intricate and versatile, and individual workers employ a variety of sampling techniques developed for their needs. Some of these techniques are described below.

2.7.1 FIBER OPTICS

Fiber optics are ideal light pipes for transferring optical signals to and from a sample. The instrumentation can be located in a laboratory or in another clean location using the fiber optics to connect to the sample at some remote location. Fiber optics can bend the light beam in virtually any direction and can carry the optical signals to unpleasant or dangerous environments such as high-temperature process lines and nuclear facilities.

Fiber optics consist of a core material having a relatively high refracting index surrounded by a cladding having a lower refractive index. The radiation is totally reflected at the core-cladding interface. The total diameter of the fiber can range from a few micrometers to millimeters. Typically, the core radius is much larger than that of the cladding. For Raman spectroscopy, a single fiber can be used for carrying the laser beam to excite a sample, and either single or multiple fibers can be used for carrying the Raman scattered light back to a spectrometer.

A schematic of an FT-Raman system adapted for a fiber optic interface is shown in Fig. 2-15 (26). Excitation radiation from an Nd:YAG laser is focused onto a single, center fiber of a bifurcated fiber bundle by lens L1. The Raman scattered radiation is transferred to the FT-IR through the 18 fibers surrounding the central fiber. Low-hydroxy quartz fibers with a core diameter of 200 μm are used for the probe. A bifurcated fiber bundle of this type is ideal for exciting and collecting Raman scattering because the high intensity of the

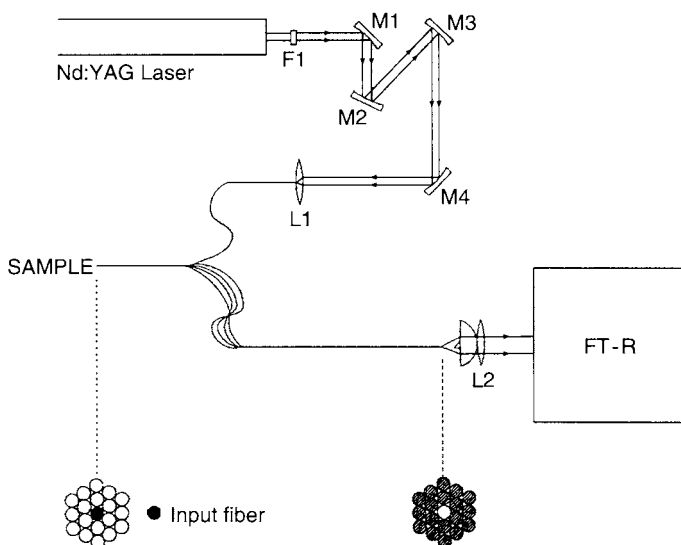


Figure 2-15 Schematic of FT-Raman instrumentation fitted with a bifurcated fiber optic interface. (Reproduced with permission from Ref. 26.)

laser is transmitted through a single fiber, whereas the weak Raman signal is carried through 18 input fibers (27–29).

The exciting radiation from a laser source can be focused into an optical fiber and carried over considerable length (on the order of a kilometer) to a sample. Some of the radiation will be lost due to Raman scattering by the fiber material; however, the amount lost will be small compared with the total power. At the sample end of the fiber, the radiation will exit in a cone shape determined by the numerical aperture (NA) of the fiber. Microlenses or gradient refractive index (GRIN) lenses can be used to focus the light onto a sample. Fiber optic Raman probes have been constructed with notched filters placed between the sample and the returning optical signals to eliminate the laser frequency and reduce the Raman scattering from the fiber material. The reduction or elimination of Raman scattering from the fiber material is not important in the excitation fiber because it merely causes a slight reduction in the excitation power. However, the Raman signal from the fiber material definitely will interfere with the spectrum of the analyte in the returning fibers, and it is necessary to reduce or eliminate the laser frequency from the signal.

(a) Monitoring Processes and Corrosive Environments

Fiber optic interfaces are ideal for monitoring chemical processes. The fiber-optic FT-Raman system shown in Fig. 2-15 was used to demonstrate the

potential of monitoring components of gasoline such as octane number, density, benzene content, and volatility (26). Spectra of gasoline and reformate obtained through this optical system are shown in Fig. 2-16. These spectra demonstrate the potential of Raman for monitoring fuels both at refineries and at points of delivery.

A good example of using a fiber optic interface for obtaining Raman spectra from a hostile environment is to monitor high-temperature molten salts. Raman spectra of molten NaCl-KCl-CaCl₂ containing varying mole percents of MgCl₂ from 4.3 to 30.8% are shown in Fig. 2-17 (30). The molten salt was held at 720°C for these measurements. An all-quartz probe consisted of four 600-μm fibers, one for excitation and three for transmitting the Raman radiation to the spectrometer. The Raman spectra obtained through the probe had a higher noise level than spectra of a sample measured conventionally without the probe; however, the results clearly demonstrate the potential of using fibers for difficult samples.

Another practical example of using Raman in a process environment is to monitor the curing of polymers. Raman spectra as a function of time for the

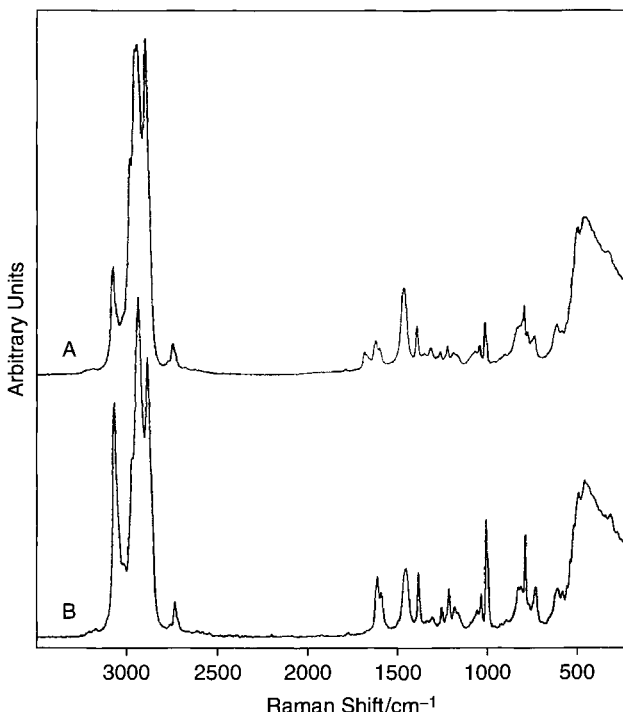


Figure 2-16 Raman spectra of gasoline (A) and reformate (B) measured with the fiberoptic probe shown in Fig. 2-15. (Reproduced with permission from Ref. 26.)

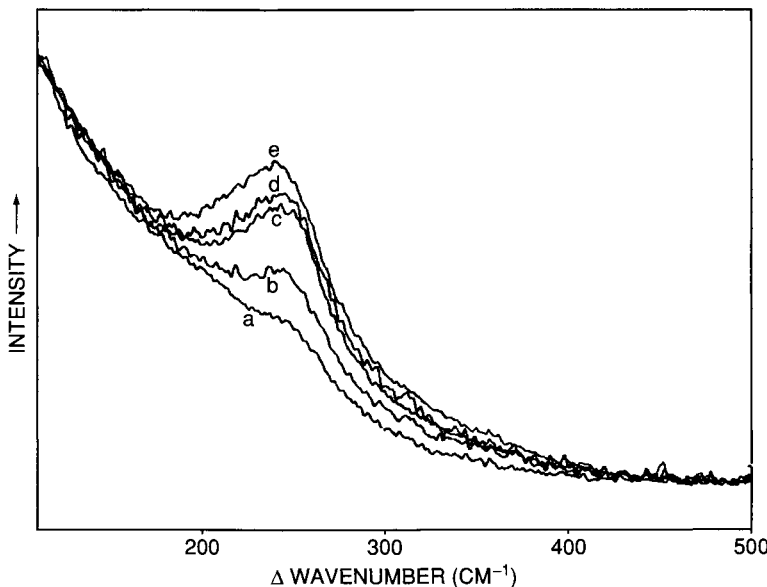


Figure 2-17 Raman spectra of molten NaCl-KCl-CaCl₂ containing (a) 4.3%, (b) 8.8%, (c) 17.8%, (d) 21.0%, and (e) 30.8% MgCl₂. (Reproduced with permission from Ref. 30.)

high-temperature curing of 4-phenoxy-4'-phenylethynylbenzophenone polymer are shown in Fig. 2-18 (31). The spectra were measured with an FT-Raman instrument and an Nd:YAG laser. In the near-IR region, black-body radiation can cause severe interference at high temperatures. To reduce this problem, the CW laser was modulated, and a dual-phase digital signal processor lock-in amplifier was placed between the detector and the spectrometer's collection electronics to demodulate and filter the signals. The resulting spectra were free from black-body emissions, as shown in the figure.

(b) Medical Applications

Potentially, the greatest use of fiber optic interfaces for obtaining Raman spectra will be in medical diagnostic procedures. One such example is the preliminary application of a fiberoptic interface to obtain Raman spectra of normal and cancerous tissue in rat palate tissue (32). Raman spectra of normal, low-grade, and high-grade dysplasia are shown in Fig. 2-19. The gray areas represent the variance within 1 standard deviation from the mean spectrum. The major changes in the spectra are the relative intensity increases at ~ 900 and 1000 cm^{-1} and at $\sim 1300\text{ cm}^{-1}$. Methods of this type eventually will lead to probes for remotely exploring many of the body parts without

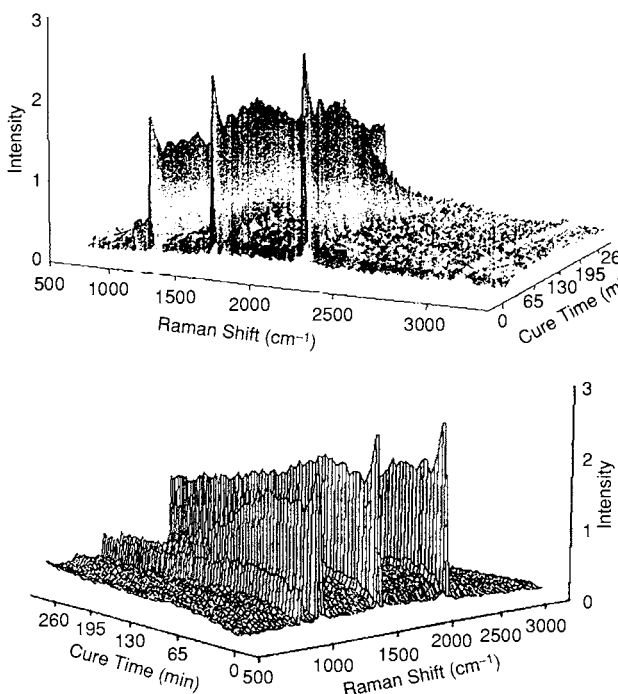


Figure 2-18 Raman spectra of 4-phenoxy-4'-phenylethynylbenzophenone polymer as a function of curing at two different orientations of the spectra-time coordinates. (Reproduced with permission from Ref. 31.)

surgery. For more applications of fiberoptic probes to medical diagnostics, see Section 6.2.4 of Chap. 6.

2.7.2 COLORLESS COMPOUNDS

If the sample is colorless, the Raman spectrum can be obtained easily by sample irradiation with a laser beam whose wavelength is in the visible region (normal Raman scattering). The major advantages of Raman over IR spectroscopy are twofold: (1) The sample is contained or sealed in a glass (Pyrex) tube because Raman-scattered light in the visible region is not absorbed by glass. Thus the Raman spectra of hygroscopic, corrosive, or oxygen-sensitive compounds can be measured easily by sealing them in glass tubes. However, some glass tubing gives rise to fluorescence or spikes if it is contaminated with rare earth salts. Use of a container or pelletization can be avoided by using a fiber optic probe if the sample is a stable solid. (2) Raman spectra of aqueous

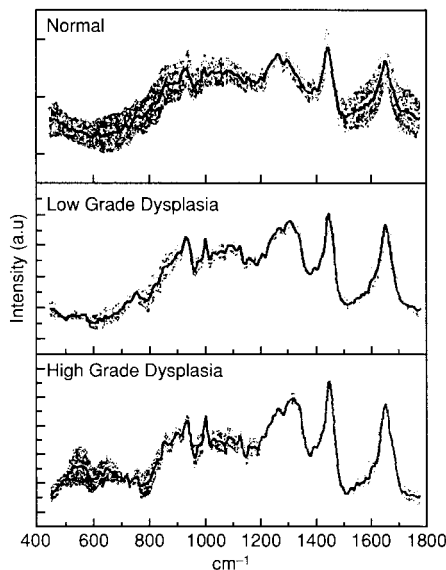


Figure 2-19 Raman spectra of normal, low-grade, and high-grade dysplasia in rat palate. (Reproduced with permission from Ref. 32.)

solutions can be measured easily because water is a very weak Raman scatterer, as contrasted to IR spectroscopy, where water is very strongly absorbing.

(a) Gases

The sample gas normally is contained in glass tubing of diameter 1–2 cm and thickness 1 mm. The gas can be sealed in a small capillary tube whose diameter is slightly larger than that of the laser beam (~ 1 mm). For weak Raman scatterers, an external resonating setup is used to increase their Raman intensity by multiple passing of the laser beam through the sample (Fig. 2-20A).

(b) Liquids

Liquid samples may be sealed in ampules, tubing, or capillaries depending on the amount of the sample available (Fig. 2-20B). For microquantities ($\sim 10^{-9}$ liter), capillaries as small as 0.5–0.1 mm bore and ~ 1 mm in length have been used. Use of a large cylindrical cell, such as that shown in Fig. 2-20C, reduces local heating and allows more accurate determination of depolarization ratios. Strong spike noise may appear if the solution contains solid particles.

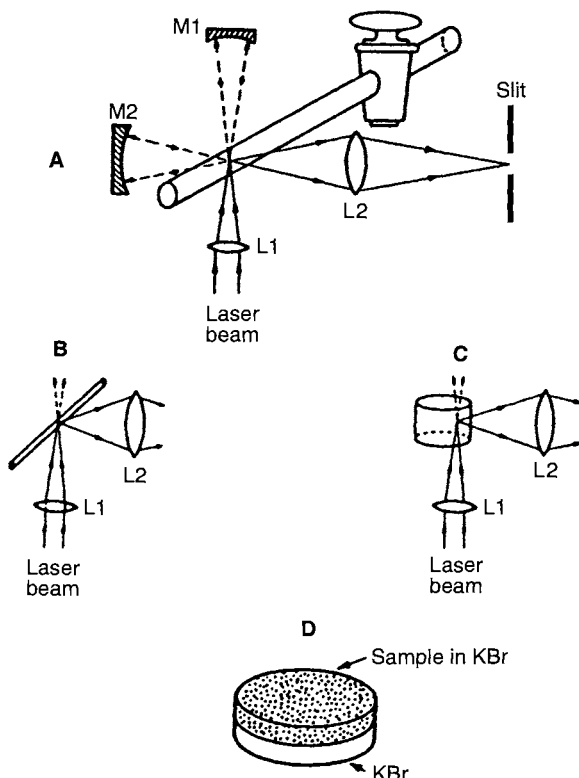


Figure 2-20 (A) Gas cell with external resonating mirrors. (B) Capillary cell for liquids. (C) Cylindrical cell for liquids. (D) KBr pellet for solid samples.

(c) Solids

Depending on the amount of the sample, powdered samples may be packed in ampules or capillaries and their Raman spectra measured in the same manner as has been described for liquid samples. The KBr pellet technique similar to that used in IR spectroscopy is also useful. First, 200 mg of KBr powder is compressed to provide a support. Then the ground sample diluted with KBr is spread evenly over the support and the die is pressed to obtain a double-layer KBr pellet (Fig. 2-20D). If necessary, an internal standard may be mixed with the sample at this stage. This technique requires a small amount of the sample, and it reduces the decomposition of the sample by local heating. If large single crystals are available, it is possible to carry out detailed analysis of polarizability tensors via measurements of polarized spectra along the three principal axes of the crystal fixed on a goniometer head (Section 1-19). The exciting radiation can be polarized in two directions, and an analyzer can be

used to view the Raman at the two extremes of polarization. In addition, the crystal can be oriented using the goniometer to view all three crystallographic axes.

2.7.3 COLORED COMPOUNDS

For colored samples that absorb the energy of the laser beam, decomposition by local heating may occur. In this case, several procedures are available in addition to simple reduction of laser power. These include the following: (1) changing the laser wavelength, (2) defocusing the laser beam on the sample, (3) diluting the sample concentration in a pellet or in solution to avoid absorption by the sample, (4) cooling the sample, (5) rotating the sample, and (6) rotating or oscillating the laser beam on a fixed sample. These techniques are extremely important in recording resonance Raman spectra that are obtained by deliberately tuning the laser excitation into strong absorption bands of samples (Section 1.15). One also may insert a cylindrical lens between the laser and the sample (Fig. 2-21a). The beam is then focused on the sample over a length of 10–25 mm instead of a few microns. This line-focus method can reduce power density per unit area by a factor of as much as 1/1,000 (33).

(a) Rotating Sample Techniques (34)

Liquids. A rotating cylindrical cell used for colored solution is illustrated in Fig. 2-21b (35). It is symmetrically glued onto a circular piece of brass, which has a central rod that fits into a chuck connected to a motor rotating at 0–3,000 rpm. Although the cell has a volume of 65 mL, only 15 mL of liquid is necessary because the centrifugal force during rotation drives the liquid to the outer part of the cell. It is necessary that the laser beam be focused to this area (near the wall) to minimize the absorption of Raman-scattered light by the liquid itself (self-absorption). The laser beam must not fall on the glass wall because that will cause spurious lines originating within the glass to be observed. Since the laser beam must be aimed at the bottom of the cell, it is necessary to use a cell with minimum distortion at the corners. The following equation has been proposed to estimate the optimal concentration required to minimize self-absorption (36):

$$A_{\text{opt}} = 1/(2kr). \quad (2-7)$$

Here, A_{opt} is the optimal absorbance of the solution, k is $\log(e) = 2.303$, and r is the path length (cm) of the scattered radiation inside the cell. The equation was derived on the assumption that r is equal to the path length from the point of scattering within the cell. If $r = 0.5$ cm, $A_{\text{opt}} = 0.434$.

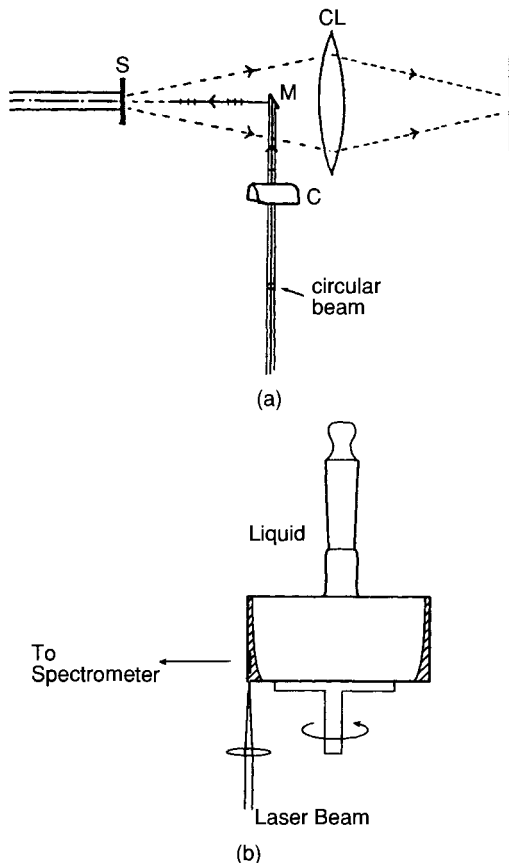


Figure 2-21 (a) Use of a cylindrical lens for line focusing. C, cylindrical lens; M, mirror; S, sample; CL collecting lens. (b) Rotating cylindrical cell.

In another technique, the solution is circulated through a capillary cell by a peristaltic pump (37). If part of the circulating loop is immersed in a constant-temperature bath, it is possible to measure the spectrum over a wide temperature range. A more sophisticated technique (38) allows the measurements of redox potentials and electronic spectra as well as Raman spectra using a circulating cell.

Solids. Resonance Raman spectra of solid samples can be measured using pellets such as those described previously and rotating them using the technique depicted in Fig. 2-22a. This rotating device is available commercially from Raman instrument manufacturers. A special die with

a ring-shaped, grooved disk connected directly to the rotating shaft is illustrated in Fig. 2-22b. The sample is packed in the groove and thus requires much smaller amounts (39). If the width of the groove is reduced to 1 mm and the sample is placed on top of a powdered KBr layer, it is possible to obtain the Raman spectra of samples as small as 1 mg (40).

Gases. Although there has not been much work done in the area of strongly absorbing vapors, the description of a rotating cell for absorbing vapors at high temperatures appeared in the literature (41).

(b) Surface Scanning Techniques

In some cases it is desirable to rotate the sample and keep it cool at the *same time*. A cell that allows the measurement of Raman spectra of rotating samples at liquid-nitrogen temperatures has been designed (42). A rotating

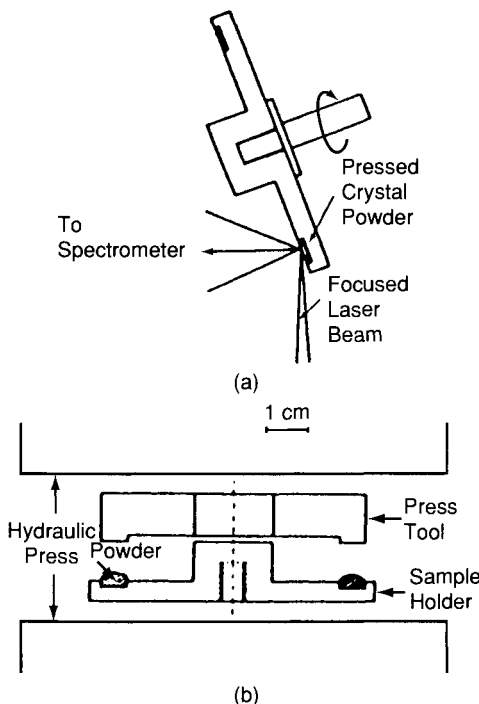


Figure 2-22 (a) Rotating device for solid samples. (b) Apparatus for making ring-shaped powder pellets. (Reproduced with permission from Ref. 39.)

surface-scanning cell that can be used for obtaining Raman spectra of anaerobic solid samples cooled by a stream of cold nitrogen is available (43). A rotating vacuum cell for spectroscopic studies of surface phenomena has been designed (44). A universal rotating system for recording Raman spectra of rotating liquid or solid samples and difference spectra as well as for automatic scanning of the depolarization ratio has been constructed (45). Sometimes it is more convenient to oscillate the laser beam along one direction (46) or rotate it on the sample rather than to rotate the sample. Thus Raman spectra have been measured by flicking the laser beam rapidly on the sample at liquid-nitrogen temperature (47). Using a setup such as that shown in Fig. 2-23, Raman spectra of samples cooled by a cryostat have been measured by using the rotating surface scanning technique (48).

2.7.4 SPECIAL CELLS

In addition to the cells already described, there are many other cells that are suited to special applications.

(a) *Thermostated Cells*

Biological molecules such as proteins and nucleic acids undergo conformational changes if the temperature is changed during the measurement. Several cells have been designed to maintain the desired temperature: 5–95°C (49) and room temperature to 100°C (50, 51).

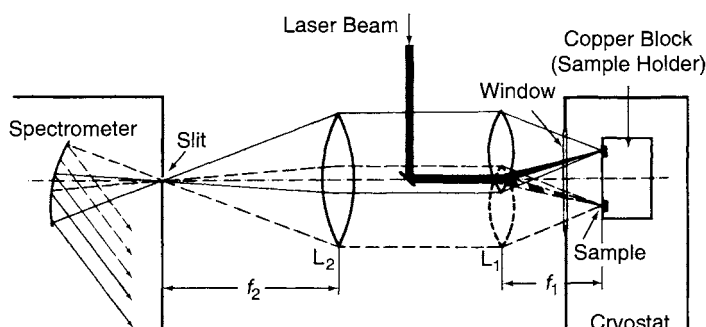


Figure 2-23 Schematic diagram of a rotating surface scanning device: L_1 , rotating lens that focuses the laser beam on the surface of the sample and simultaneously collects the backscattered Raman light; L_2 , focusing lens that focuses the Raman light on the spectrometer slit; f , focal length of the lens. (Reproduced with permission from Ref. 48.)

(b) High-Temperature Cells

Raman spectroscopy has been used to study the structures of glasses, ceramic materials, and molten salts at high temperatures. A high-temperature cell that was employed for Raman studies in the 295–483 K range is illustrated in Fig. 2-24 (52). Two types of cells were designed for metal salts that melt at higher temperatures (up to 1,000°C); one is a windowless cell (53, 54), and the other is a graphite cell with diamond windows (55). A rotating cell for gaseous compounds (~300°C) is also available (41).

(c) Low-Temperature Cells

A very simple device has been designed to obtain Raman spectra in a wide range of temperature (−150 to ~200°C) (56). A Dewar cell for low-temperature liquids (77–300 K) is available (57). A simple Dewar cell for condensing liquids or gases is shown in Fig. 2-25a. Liquid nitrogen and organic slushes are used as coolants. In some cases, Raman scattering from

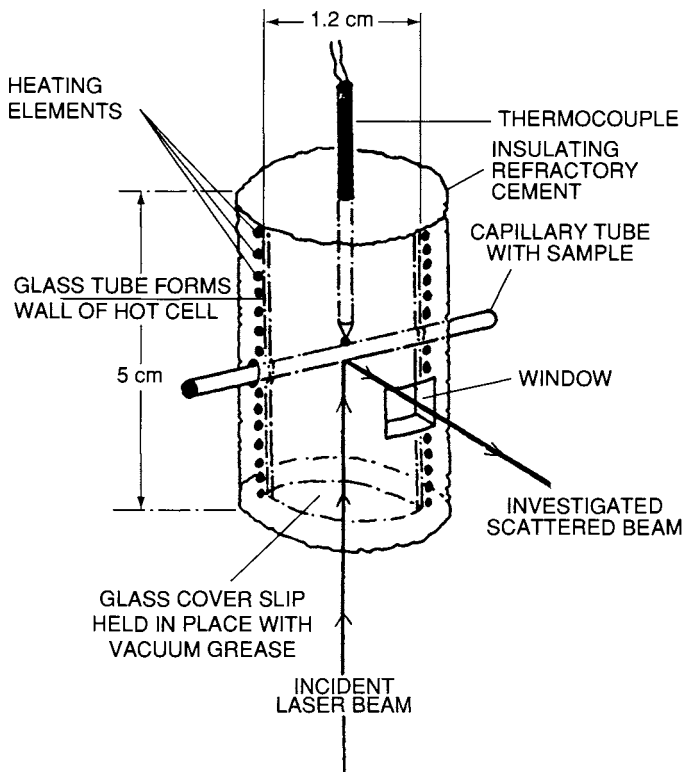


Figure 2-24 High-temperature Raman cell. (Reproduced with permission from Ref. 52.)

the glass or quartz appears between 500 and 200 cm⁻¹. This problem can be circumvented by using a cell that allows the observation of Raman scattering directly from the surface of a frozen solution kept at 77 K (58). A configuration used for obtaining Raman spectra of liquids cooled by a cryocooler is shown in Fig. 2-25b (59). The sample solution is contained in a minibulb (~0.4 mL), and any temperature between -80°C and room temperature can be obtained by controlling the temperature of a cold tip.

(d) UV Resonance Cells

In UV-resonance Raman (UVRR) studies, UV lines such as the fourth harmonic (266 nm) of the Nd:YAG laser are used for excitation. Under prolonged illumination by focused UV radiation, quartz and other UV-transparent materials tend to become fluorescent. To avoid the use of window materials and to minimize sample damage by strong UV light, several sampling techniques, such as the fluid jet stream technique (60) and the thin-film technique (61), have been developed.

2.7.5 BACKSCATTERING GEOMETRY

The backscattering geometry (135° or 180°) has several advantages over the commonly used 90° scattering geometry. A simple and versatile design that allows rotation and cooling of the sample simultaneously is shown in Fig. 2-26 (62). Further, sample replacement and laser beam focusing on the sample

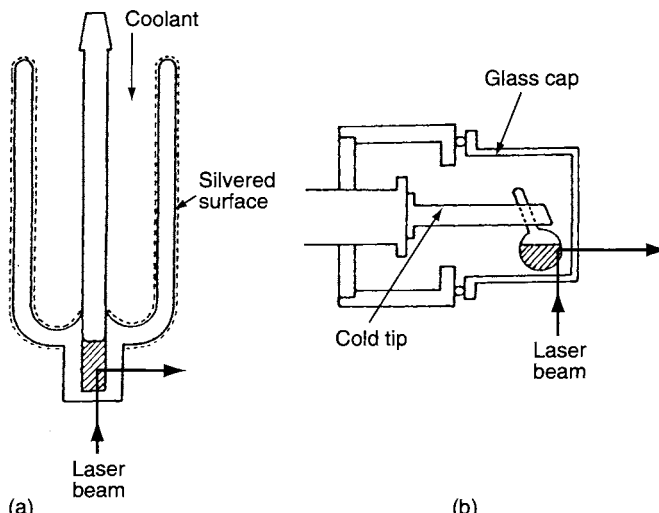


Figure 2-25 (a) Simple low-temperature Dewar cell. (b) Minibulb configuration.

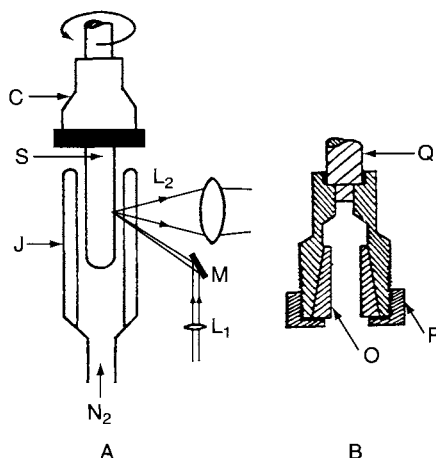


Figure 2-26 Sample spinner for 180° (or oblique) illumination. (A) Complete system with evacuated Pyrex jacket (J) surrounding the sample tube. S, cold (or warm) gas such as N₂ is passed through J to control the sample temperature. L₁, L₂, and M are lenses, and a mirror, C, is the sample chuck. (B) Details of the sample chuck. O, split nylon cone; P, knurled aluminium nut attached to aluminum body of chuck; Q, spinner shaft. (Reproduced with permission from Ref. 62.)

can be done easily and quickly. Certain advantages of backscattering include (1) ease of correction for self-absorption in highly colored solutions, (2) the ability to measure Raman scattering and UV-visible absorption simultaneously (63), (3) the ability to obtain single-crystal Raman spectra on small crystals with only one good face for each orientation, whereas two are required for 90° scattering, and (4) the ability to obtain low-temperature spectra of very small samples (58, 64). There are some disadvantages, such as the appearance of the Raman scattering background caused by various glasses and the danger of specular (mirror-like) reflection from the glass container into the monochromator (180° backscattering). The intensity of the former may be minimized by using lenses with short focal depths, whereas both can be circumvented by scattering directly from the surface of a sample (solids, frozen solutions) (43).

2.7.6 TEMPERATURE MEASUREMENTS

Either high or low temperatures (65) can be determined by measuring both the Stokes and anti-Stokes Raman spectra. The temperature of the sample is estimated from the intensity ratios of the Stokes and anti-Stokes Raman lines via the equation

$$\frac{I(\text{Stokes})}{I(\text{anti-Stokes})} = \frac{(v_0 - v_m)^4}{(v_0 + v_m)^4} \exp\{hc v_m / kT\}, \quad (2-8)$$

where v_0 is the wavenumber of the laser line, v_m is the wavenumber of a band of the solvent or sample, h is Planck's constant, c is the velocity of light, k is Boltzmann's constant, and T is absolute temperature. A more convenient equation may be written as

$$T = \frac{-v_m \times 1.43879}{\ln \frac{I(\text{anti-Stokes})}{I(\text{Stokes})} + 4 \ln \frac{(v_0 - v_m)}{(v_0 + v_m)}}. \quad (2-9)$$

However, this equation is not applicable when anti-Stokes lines are very weak. It should be noted that these equations are applicable only for the spectra obtained under off-resonance conditions. For the spectra obtained under resonance conditions, see Ref. 66.

2.8 Fluorescence Problems

Either the sample or impurities may absorb the laser radiation and reemit it as fluorescence. If this occurs, Raman spectra can be obscured by a broad, strong fluorescence band. The intensity of the latter could be as much as 10^4 greater than the Raman signal. There are several ways to minimize this problem. If impurities in the sample are causing fluorescence, the sample should be purified or irradiated by high-power laser beams for a prolonged time so that fluorescent impurities are bleached out.

If the sample itself is fluorescent, the first thing to do is to change the exciting wavelength. By shifting to a longer wavelength, fluorescence may be reduced significantly. FT-Raman spectroscopy is ideal because it employs an exciting line in the IR region (1,064 nm for an Nd:YAG laser), where electronic transitions are rare and fluorescence is not a problem. Addition of quenching agents such as potassium iodide (67) or mercury halides (68) can also be effective in some cases. Repetitive scanning coupled with background subtraction is also found to be effective (69). It is possible to discriminate fluorescence by using pulsed lasers because the lifetime of Raman scattering (10^{-12} – 10^{-13} s) is much shorter than that of fluorescence (10^{-7} – 10^{-9} s). Thus an electronic gate may be employed to preferentially measure the former (70).

A CCD Raman spectrometer coupled with a 10-mW He–Ne laser has been used to eliminate fluorescence because the long-wavelength excitation by the He–Ne laser is not as likely to cause fluorescent transitions (71). Because of its directional property, coherent anti-Stokes Raman scattering (CARS) is also effective in avoiding fluorescence interference (see CARS in Section 3.9).

2.9 Raman Difference Spectroscopy

Raman difference spectroscopy (72, 73) is a valuable technique for subtracting solvent bands from solution spectra and for determining small shifts of solute bands due to isotopic substitution or interaction with other molecules. Figure 2-27 illustrates a cylindrical rotating cell that is divided into two equal parts, one containing the solution and the other containing only the solvent (74, 75). By rotation of the cell, the laser beam irradiates the solution and the solvent alternately. To record the difference spectrum, an electronic system containing a gated differential amplifier is used.

If the frequency shift has occurred only via the solute–solvent interaction, the frequency shift is calculated by using the equation (76)

$$\Delta\nu = 0.385 \Gamma (I_d/I_0). \quad (2-10)$$

Here, Γ is the observed line width ($\Delta\nu \ll \Gamma$), I_d is the peak-to-valley intensity in the difference spectrum, and I_0 is the peak height of the Raman line. Although this equation is for Lorentzian-shaped bands, the results are approximately the same for Gaussian-shaped bands (the constant 0.385 becomes 0.350). In the case of carbon disulfide–benzene mixtures, the smallest shift observed was -0.06 cm^{-1} , and the associated error was $\pm 0.02\text{ cm}^{-1}$ (77). A convenient rotating system that can be used for (1) difference spectroscopy, (2) normal rotating sample techniques (solid and solution), and (3) automatic scanning of the depolarization ratios as a function of the wave number has been designed (45).

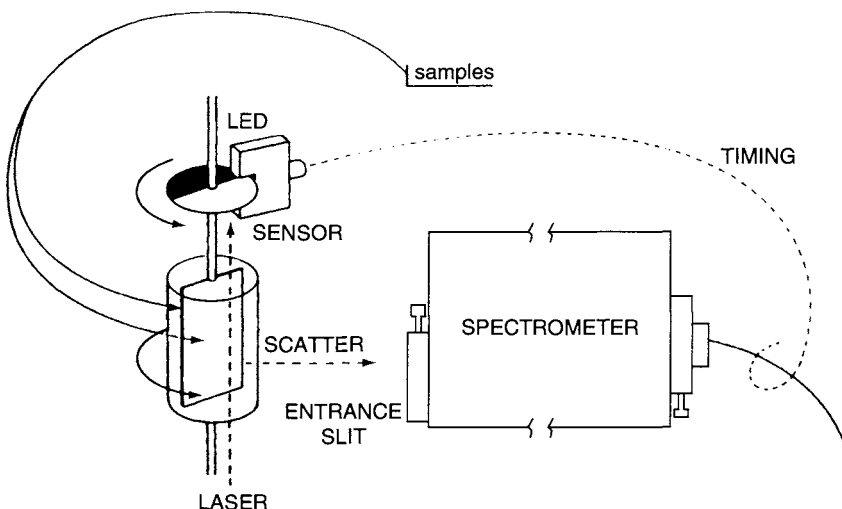


Figure 2-27 Divided rotating cell. (Reproduced with permission from Ref. 74.)

Two elaborate devices for difference spectroscopy have been constructed (78); in one, an NMR tube is divided into two equal sections (each containing solutions of 0.5 mL or less) and rotated by an NMR spinner. Then difference spectra are measured using backscattering geometry. In the other, a tuning fork equipped with a pair of sample cups is attached to a cold finger of a cryostat, and the difference spectrum is obtained by oscillating two small frozen samples horizontally via magnetic devices. The Raman spectra of SO_4^{2-} ion in K_2SO_4 and Na_2SO_4 frozen solutions obtained by the former method are shown in Fig. 2-28. Using Eq. (2-11), $\Delta\nu$ is calculated to be -0.4 cm^{-1} . This shift is clearly due to the difference in interionic interactions between the two solutions.

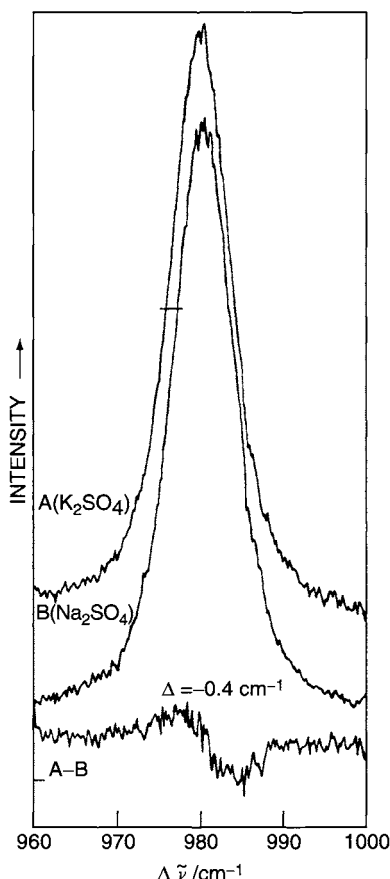


Figure 2-28 The v_1 (A_1 symmetry) band of SO_4^{2-} in K_2SO_4 and Na_2SO_4 frozen solutions. Both spectra were measured with 488-nm excitation from an Ar-ion laser at a resolution of 5 cm^{-1} . A-B is the Raman difference spectrum of K_2SO_4 minus Na_2SO_4 . (Reproduced with permission from Ref. 78.)

2.10 Miniature Raman Spectrometers

Two major innovations during the last decade of the 20th century led to the development of small, portable Raman spectrometers. Such a system requires both a miniature spectrometer and a miniature laser source. The commercialization of CCD detectors for video and still cameras provided a source of inexpensive CCD detectors for spectroscopy. These detectors were combined with miniature grating spectrometers to produce handheld devices for the UV-visible spectral region. These spectrometers were designed around fiber optic interfaces. Thus, for absorption spectroscopy, the light source and sample could be located remotely from the spectrometer. The spectrometers are small enough that they can be piggy-backed on a PC board and located inside a computer. However, in most cases, the spectrometers are located in a separate miniature box ($5 \times 5 \times 1.5$ in.) and connected to a computer (e.g., laptop) via a cable. The spectrometer, interface PC card, software drives, and display/processing software come as a single package. Gratings and detection systems can be selected for particular spectral regions.

The other required piece of hardware for small, portable Raman spectrometers was a miniature laser. Diode lasers have become the mainstay for CD players and for fiber optic communication systems; thus they are readily available as Raman sources. The instrument shown in Fig. 2-29 integrates a

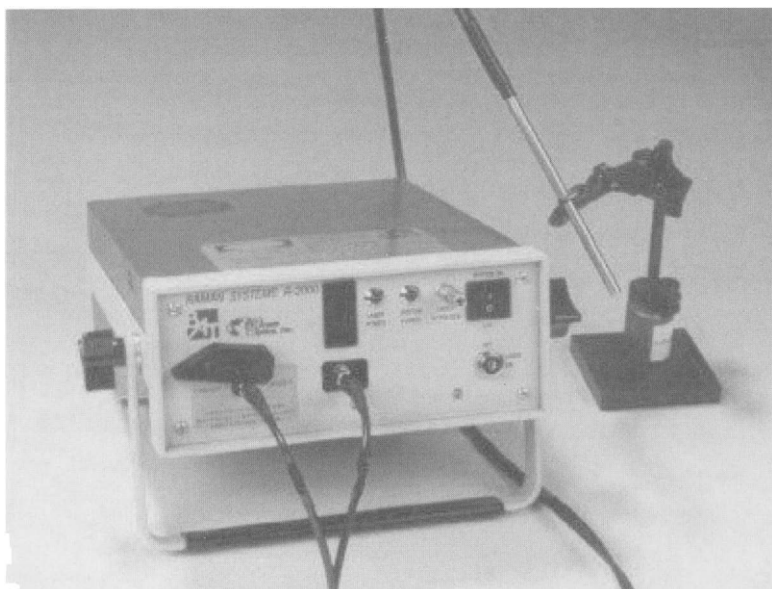


Figure 2-29 Raman Systems Model R2001 from Ocean Optics. Both the laser and the spectrometer are contained in the single unit. (Reproduced with permission from Ocean Optics.)

500-mW, 785-nm multimode diode laser as the excitation source in the same box containing the spectrometer and the analog-to-digital (A/D) converter. A spectrum of a 1:1:1 mixture of ethanol, 2-propanol, and 2-methyl-2-propanol is shown in Fig. 2-30 (79). The *S/N* ratio is excellent, and there is enough spectral information to identify the components and to perform quantitative analysis on the mixture.

A somewhat more sophisticated portable Raman system is shown in Fig. 2-31 (80). Samples can be analyzed either within the instrument or through a fiber optic probe. Samples contained in small test tubes can be placed inside the instrument for the measurements or the probe can be used. An optical diagram of the fiberoptic probe head is shown in Fig. 2-32. Typical spectra measured with this system are shown in Figs. 2-33 and 2-34. The large differences between the Raman spectra of skim and whole milk show that this low-resolution system can be used online in the food industry. Another practical use of this portable system is in forensic investigations. Spectra of three different explosives are shown in Fig. 2-34. This instrument could be used equally well in detecting and identifying illicit drugs.

Miniature, portable Raman spectrometers are just becoming available (81). There are numerous possible application areas where an inexpensive detection system is ideal for monitoring and for diagnostic measurements.

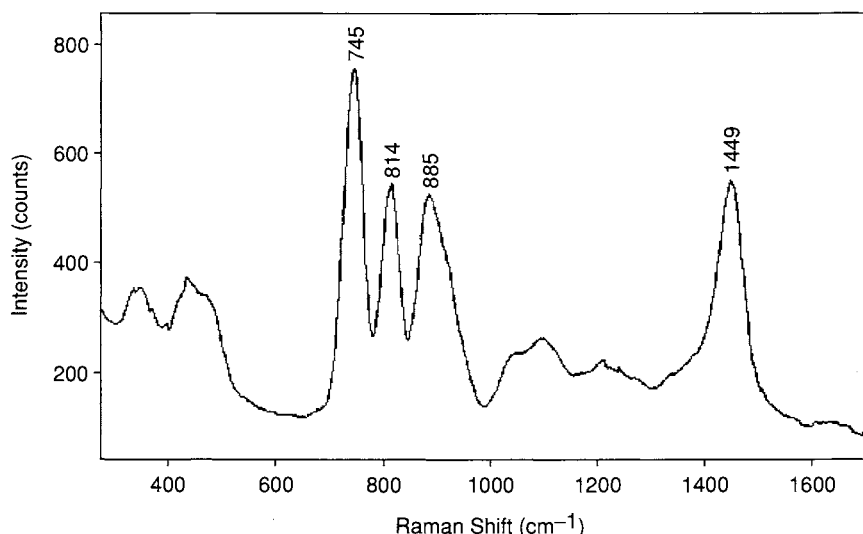


Figure 2-30 Low-resolution Raman spectra of a 1:1:1 mixture of ethanol, 2-propanol, and 2-methyl-2-propanol. (Reproduced with permission from Ref. 79.)

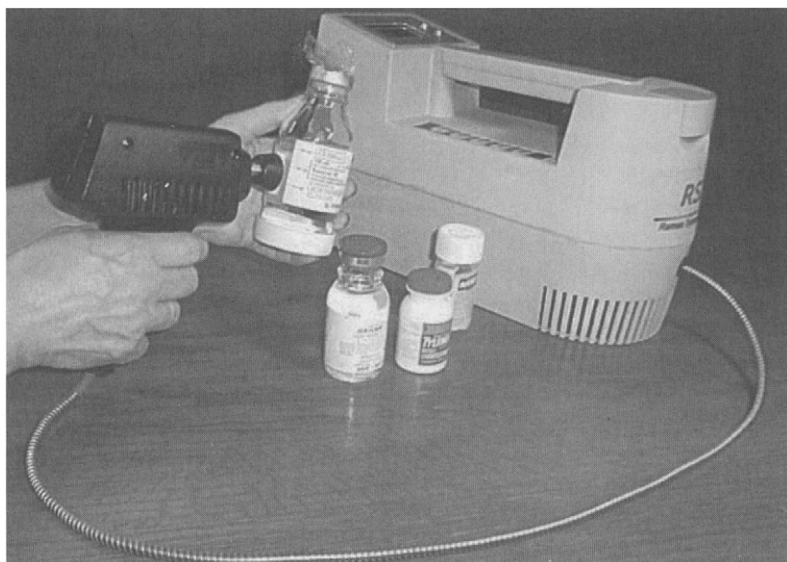


Figure 2-31 Raman Systems, Inc., self-contained spectrometer showing a fiber optic probe. (Reproduced with permission from Raman Systems, Inc.)

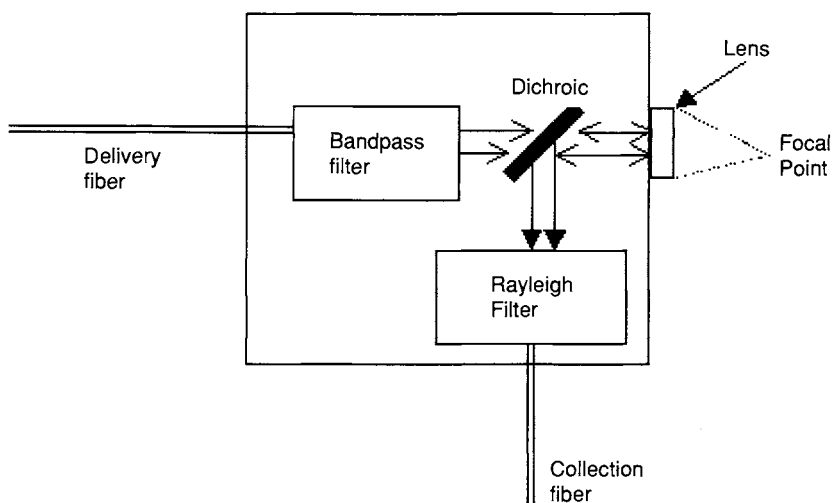


Figure 2-32 Optical diagram for fiber optic probe used with the spectrometer in Fig. 2-31. (Reproduced with permission from Raman Systems, Inc.)

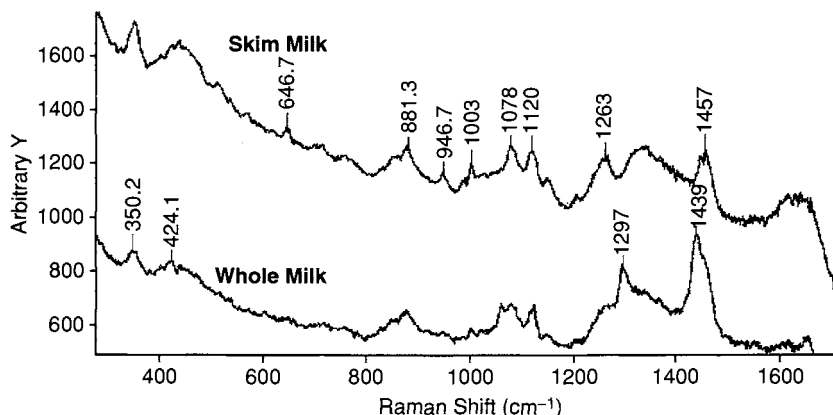


Figure 2-33 Raman spectra of skim and whole milk measured with a miniature spectrometer. (Reproduced with permission from Raman Systems, Inc.)

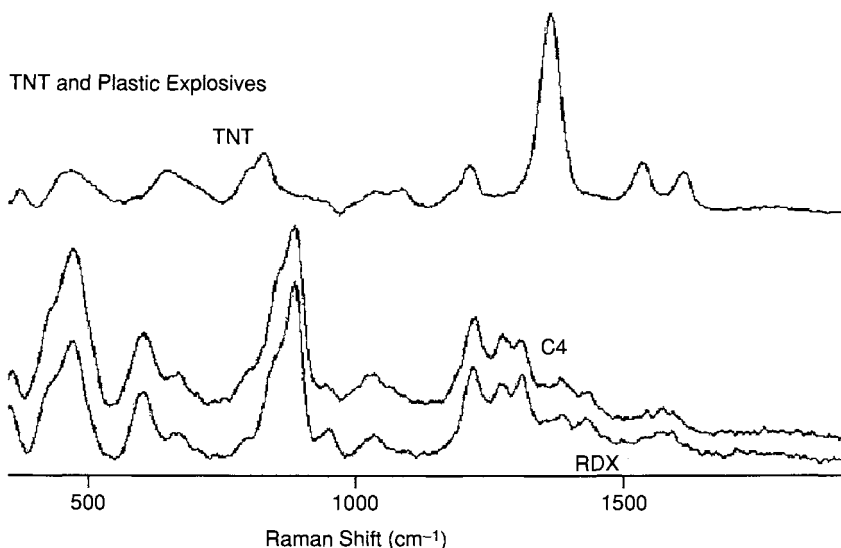


Figure 2-34 Raman spectra of TNT and plastic explosives C4 and RDX measured with the Raman System shown in Fig. 2-31. (Reproduced with permission from Raman Systems, Inc.)

References

1. R. S. Czernuszewicz, "Resonance Raman spectroscopy of metalloproteins with CW laser excitation," in "Methods in Molecular Biology: Physical Methods of Analysis" (C. Jones, B. Mulloy, and A. H. Thomas, eds.), Vol. 17. Humana Press, New Jersey, 1993.
2. J. Hecht, "The Laser Guidebook," McGraw-Hill, New York, 1986.

3. V. Wilke and W. Schmidt, *Appl. Phys.* **16**, 151 (1978); *Appl. Phys.* **18**, 177 (1979).
4. J. Marshall, "The radiation hazards of lasers and a guide to their control in the laboratory," in "Advances in Infrared and Raman Spectroscopy" (R. J. H. Clark and R. E. Hester, eds.), Vol. 10, p. 145. John Wiley, New York, 1983.
5. T. Hirschfeld and D. B. Chase, *Appl. Spectrosc.* **40**, 133 (1986).
6. G. W. Chantry, H. A. Gebbie, and C. Helsum, *Nature* **203**, 1052 (1964).
7. D. B. Chase, *Anal. Chem.* **59**, 881A (1987).
8. T. Hirschfeld and E. R. Schildkraut, in "Laser Raman Gas Diagnostics" (M. Lapp, ed.), pp. 379–388. Plenum Press, New York, 1974.
9. D. B. Chase, *Mikrochim. Acta* **111**, 81 (1987).
10. D. B. Chase, *J. Am. Chem. Soc.* **108**, 7485 (1986).
11. Y. Talmi, *Appl. Spectrosc.* **36**, 1 (1982); *Am. Lab.*, March, 1978.
12. D. G. Jones, *Anal. Chem.* **57**, 1057A (1985); 1207A (1985).
13. P. M. Epperson, I. V. Sweedler, R. B. Bilhorn, G. R. Sims, and M. B. Denton, *Anal. Chem.* **60**, 327A (1988).
14. J. E. Pemberton, R. L. Sobocinski, M. A. Bryant, and D. A. Carter, *Spectroscopy* **5**, 26 (1990).
15. R. B. Bilhorn, P. M. Epperson, I. V. Sweedler, and M. B. Denton, *Appl. Spectrosc.* **41**, 1125 (1987).
16. D. B. Chase, "Raman spectroscopy: From the visible to the infrared," in "Proceedings of XII International Conference on Raman Spectroscopy" (J. R. Durig and I. F. Sullivan, eds.), pp. 11. John Wiley, New York, 1990.
17. B. Schrader, in "Practical Fourier Transform Infrared Spectroscopy: Industrial and Laboratory Chemical Analysis" (J. R. Ferraro and K. Krishnan, eds.), pp. 168. Academic Press, San Diego, 1990.
18. R. K. Chang, in "Spectroscopic and Diffraction Techniques in Interfacial Electrochemistry" (C. Gutierrez and C. A. Melendres, eds.). Kluwer Academic Publishers, Dordrecht, The Netherlands, 1990.
19. H. Hamaguchi, *Appl. Spectrosc. Rev.* **24**, 137 (1988).
20. P. J. Hendra and E. I. Loader, *Chem. Ind.* 718 (1968).
21. R. Beck, W. Englisch, and K. Gurs, "Tables of Laser Lines in Gases and Vapors," 2nd ed., pp. 4–5. Springer-Verlag, New York, 1978.
22. A. N. Zaidel, V. K. Prokofev, and S. M. Raiskii, "Tables of Spectrum Lines," pp. 299. Pergamon Press, New York, 1961.
23. M. C. Craig and I. W. Levin, *Appl. Spectrosc.* **33**, 475 (1979).
24. C. Julien and C. Hirlmann, *J. Raman Spectrosc.* **9**, 62 (1980).
25. F. Inagaki, M. Tasumi, and T. Miyazawa, *J. Mol. Spectrosc.* **50**, 286 (1974).
26. C. J. de Bakker and P. M. Fredericks, *Appl. Spectrosc.* **49**, 1766 (1995).
27. R. L. McCreery, P. J. Hendra, and M. Fleischmann, *Anal. Chem.* **55**, 146 (1983).
28. S. D. Schwab and R. L. McCreery, *Anal. Chem.* **56**, 2199 (1984).
29. S. D. Schwab and R. L. McCreery, *Appl. Spectrosc.* **41**, 126 (1987).
30. S. Dao, G. Mamantov, J. E. Coffield, G. M. Begun, and J. P. Young, *Appl. Spectrosc.* **47**, 1286 (1993).
31. J. F. Aust, J. B. Cooper, K. L. Wise, and B. J. Jensen, *Appl. Spectrosc.* **53**, 682 (1999).
32. T. C. Bakker Schut, M. J. H. Witjes, H. J. C. M. Sterenborg, O. C. Speelman, J. L. N. Roodenburg, E. T. Marple, H. A. Bruining, and G. J. Puppels, *Anal. Chem.* **72**, 6010 (2000).
33. H. H. Eysel and S. Sunder, *Appl. Spectrosc.* **34**, 89 (1980).
34. W. Kiefer, "Recent techniques in Raman spectroscopy," in "Advances in Infrared and Raman Spectroscopy" (R. J. H. Clark and R. E. Hester, eds.), Vol. 3. John Wiley, New York, 1977.
35. W. Kiefer and H. I. Bernstein, *Appl. Spectrosc.* **25**, 500 (1971).

36. T. C. Strekas, D. H. Adams, A. Packer, and T. G. Spiro, *Appl. Spectrosc.* **28**, 324 (1974).
37. W. H. Woodruff and T. G. Spiro, *Appl. Spectrosc.* **28**, 74 (1974).
38. J. L. Anderson and J. R. Kincaid, *Appl. Spectrosc.* **32**, 356 (1978).
39. W. Kiefer and H. I. Bernstein, *Appl. Spectrosc.* **25**, 609 (1971).
40. G. J. Long, L. J. Basile, and J. R. Ferraro, *Appl. Spectrosc.* **28**, 73 (1974).
41. R. J. H. Clark, O. H. Ellestad, and P. D. Mitchell, *Appl. Spectrosc.* **28**, 575 (1974).
42. H. Homborg and W. Preetz, *Spectrochim. Acta* **32A**, 709 (1976).
43. R. S. Czernuszewicz, *Appl. Spectrosc.* **40**, 571 (1986).
44. F. R. Brown, L. E. Makovsky, and K. H. Rhee, *Appl. Spectrosc.* **31**, 563 (1977).
45. W. Kiefer, W. J. Schmid, and J. A. Topp, *Appl. Spectrosc.* **29**, 434 (1975).
46. J. A. Koningstein and B. F. Gachter, *J. Opt. Soc. Am.* **63**, 892 (1973).
47. R. J. H. Clark and P. C. Turtle, *Inorg. Chem.* **17**, 2526 (1978).
48. N. Zimmerer and W. Kiefer, *Appl. Spectrosc.* **28**, 279 (1974).
49. G. J. Thomas, Jr., and J. R. Barylski, *Appl. Spectrosc.* **24**, 463 (1970).
50. D. E. Irish, T. Jary, and O. Puzic, *Appl. Spectrosc.* **31**, 47 (1977).
51. J. W. Fox and A. T. Tu, *Appl. Spectrosc.* **33**, 647 (1979).
52. D. Duval and R. A. Condrate, *Appl. Spectrosc.* **42**, 701 (1988).
53. A. S. Quist, *Appl. Spectrosc.* **25**, 80 (1971).
54. B. Gilbert, G. Momantov, and G. M. Begun, *Appl. Spectrosc.* **29**, 276 (1975).
55. S. K. Ratkje and E. Rytter, *J. Phys. Chem.* **78**, 1449 (1974).
56. F. A. Miller and B. M. Harney, *Appl. Spectrosc.* **24**, 291 (1970).
57. C. W. Brown, A. E. Hopkins, and F. P. Daly, *Appl. Spectrosc.* **28**, 194 (1974).
58. R. S. Czernuszewicz and M. K. Johnson, *Appl. Spectrosc.* **37**, 297 (1983).
59. K. Nakamoto, Y. Nonaka, T. Ishiguro, M. W. Urban, M. Suzuki, M. Kozuka, Y. Nishida, and S. Kida, *J. Am. Chem. Soc.* **104**, 3386 (1982).
60. G. A. Reider, K. P. Traar, and A. J. Schmidt, *Appl. Optics* **23**, 2856 (1984).
61. L. D. Ziegler and B. Hudson, *J. Chem. Phys.* **74**, 982 (1981).
62. D. F. Shriver and J. B. R. Dunn, *Appl. Spectrosc.* **28**, 319 (1974).
63. E. G. Rodgers and D. P. Strommen, *Appl. Spectrosc.* **35**, 215 (1981).
64. B. M. Sjoberg, T. M. Loehr, and J. Sanders-Loehr, *Biochemistry* **21**, 96 (1982).
65. E. D. Isaacs and D. Heiman, *Rev. Sci. Instruments* **58**, 1672 (1987).
66. K. T. Schomaker, O. Bangcharoenpaurpong, and P. M. Champion, *J. Chem. Phys.* **30**, 4701 (1984).
67. J. M. Friedman and R. M. Hochstrasser, *Chem. Phys. Lett.* **33**, 225 (1975).
68. V. A. Maroni and P. T. Cunningham, *Appl. Spectrosc.* **27**, 428 (1973).
69. T. M. Loehr, W. E. Keyes, and P. A. Pincus, *Anal. Biochem.* **96**, 456 (1979).
70. R. P. Van Duyne, D. L. Jeanmaire, and D. F. Shriner, *Anal. Chem.* **46**, 213 (1974).
71. J. E. Pemberton and R. L. Sobocinski, *J. Am. Chem. Soc.* **111**, 432 (1989).
72. J. Laane, "Raman difference spectroscopy," in "Vibrational Spectra and Structure" (J. R. Durig, ed.), Vol. 12. Elsevier, Amsterdam, 1983.
73. B. P. Asthana and W. Kiefer, "Vibrational line profiles and frequency shift studies by Raman spectroscopy," in "Vibrational Spectra and Structure" (J. R. Durig, ed.), Vol. 20. Elsevier, Amsterdam, 1992.
74. W. Kiefer, *Appl. Spectrosc.* **27**, 253 (1973).
75. W. Kiefer, "Recent techniques in Raman spectroscopy," in "Advances in Infrared and Raman Spectroscopy" (R. J. H. Clark and R. E. Hester, eds.), Vol. 3, p. 1. Heyden, London, 1977.
76. J. Laane, *J. Chem. Phys.* **75**, 2539 (1981); *Appl. Spectrosc.* **37**, 474 (1983).
77. J. Laane and W. Kiefer, *Appl. Spectrosc.* **35**, 267 (1981).
78. J. F. Eng, R. S. Czernuszewicz, and T. G. Spiro, *J. Raman Spectrosc.* **16**, 432 (1985).
79. R. H. Clarke, S. Londhe, and M. E. Womble, *Spectroscopy* **13**(10), 28 (1998).

80. R. H. Clarke, S. Londhe, W. R. Premasiri, and M. E. Womble, "Low-resolution Raman spectroscopy: Instrumentation and applications in chemical analysis," *J. Raman Spectrosc.* **30**, 827 (1999).
81. C. K. Mann and T. J. Vickers, *Appl. Spectrosc.* **54**, 742 (2000).

General References

- D. P. Strommen and K. Nakamoto, "Laboratory Raman Spectroscopy," John Wiley, New York, 1984.
- D. J. Gardiner and P. R. Graves (eds.), "Practical Raman Spectroscopy," Springer-Verlag, Berlin, 1989.

Chapter 3

Special Techniques

Thus far, we have reviewed basic theories and experimental techniques of Raman spectroscopy. In this chapter we shall discuss the principles, experimental design and typical applications of Raman spectroscopy that require special treatments. These include high pressure Raman spectroscopy, Raman microscopy, surface-enhanced Raman spectroscopy, Raman spectroelectrochemistry, time-resolved Raman spectroscopy, matrix-isolation Raman spectroscopy, two-dimensional correlation Raman spectroscopy, Raman imaging spectrometry and non-linear Raman spectroscopy. The applications of Raman spectroscopy discussed in this chapter are brief in nature and are shown to illustrate the various techniques. Later chapters are devoted to a more extensive discussion of Raman applications to indicate the breadth and usefulness of the Raman technique.

3.1 High-Pressure Raman Spectroscopy

Subjecting various types of matter to high external pressure, and utilizing a spectroscopic technique as the diagnostic tool to determine the changes that have occurred, has proven very successful. Infrared and Raman spectroscopies have been the most useful of the diagnostic tools utilized. Valuable information about intermolecular interactions, phase transitions, structural changes, vibrational assignments and conversions of insulators (semiconductors) to metals is obtainable when matter is subjected to pressure. Pressure-induced

frequency shifts are often accompanied by intensity changes and can be used to identify the nature of vibrations and provide correct vibrational assignments (1). A diamond anvil cell (DAC) capable of reaching 5.7 megabar pressures and $\sim 4,000^{\circ}\text{K}$ temperature, has been developed, which allows studies to be made concerning the behavior of various minerals occurring in the depths of the earth (2). Since the core-mantle interface has a pressure of $\sim 1.6\text{ Mbar}^*$ and 3,000–4,000 K, simulation of core-mantle reactions is possible.

3.1.1 PRINCIPLES

The pressure technique involves a pressure device (DAC) that can transmit the pressure to the sample under study. If spectroscopic methods are chosen for diagnostic purposes, it is a requirement to use windows on the pressure device that are hard and transmit the irradiating light in the particular wavelength of the electromagnetic spectrum being studied. The window of choice for IR and Raman studies is Type IIa diamond.** It is the hardest material known and is transmissive for laser Raman studies. Additionally, it is an excellent thermal conductor as well. The pressure device must be compact and fit into the sample compartment of the spectrometer. The DAC fulfills all of these criteria and has been extensively used since its discovery by Weir and Van Valkenburg in 1959 (3). The interface to the Raman spectrometer is readily accomplished (unlike the IR experiment where beam condensers are required in the dispersive instrument, although presently this requirement is unnecessary in the Raman/DAC experiment), and normal commercial Raman instrumentation can be used.

Pressure calibration is necessary in pressure work, and this is accomplished by incorporating a small ruby crystal with the sample under study. The Ruby scale (4) was developed by the National Bureau of Standards (now the NIST) in 1972, and the sharp Ruby R_1 fluorescent line has been calibrated vs. pressure by NIST, and is suitable even up to megabar pressures (5).

Further details on the Ruby scale are provided in the following section on instrumentation.

3.1.2 INSTRUMENTATION

A conventional Raman instrument is suitable for high-pressure Raman measurements. The pressure device can be a piston-cylinder cell or a DAC. The first Raman studies with a piston-cylinder cell were made in 1957 (6).

*1 bar = 0.9869 atm = $10^5\text{ N/m}^2 = 10^5\text{ Pa} = 10^6\text{ dyn/cm}^2$

$10^3\text{ bar} = 1\text{ kbar} = 10^8\text{ N/m}^2 = 10^8\text{ Pa} = 100\text{ MPa}$

$10^3\text{ kbar} = 1\text{ Mbar} = 10^{11}\text{ N/m}^2 = 10^{11}\text{ Pa} = 100\text{ GPa} = 10^6\text{ atm}$

**Type IIa diamonds are better suited for optical studies because fewer impurities are present. They show absorptions at ~ 3 and $4\text{--}5.5\text{ }\mu\text{m}$ and are transparent into the FIR to $\sim 10\text{ cm}^{-1}$.

The DAC was first used in Raman studies in 1968 (7,8). Since that time, the DAC has undergone several modifications. Figure 3-1 shows the details of the first DAC. In the DAC (Fig. 3-1), pressure is applied by turning the knobs to compress the springs. The pressure is transmitted along the lever arms, and this compresses the bottom plate pushing the two pistons holding the diamonds together and affecting the pressure. Figure 3-2 shows the present ultrahigh-pressure cell capable of reaching megabar pressures. Similar transmission of pressure applies to the ultrahigh-pressure cell. Figure 3-3 shows a typical forward scattering geometry in a laser DAC experiment.

Calibration of the pressure is best accomplished using the Ruby scale. Generally this is done using a metal gasket between the two diamond windows surrounding the sample in which a liquid (such as Nujol or Teflon oil) is added to produce hydrostatic pressure. The technique measures the pressure dependence of the sharp Ruby R_1 fluorescence transition at 692.8 nm, although the R_2 band at 694.2 nm can also be used. The Ruby fluorescence is induced by the blue excitation of the Ar^+ (488.0 nm) or the He-Cd (441.6 nm) lasers.

Several other calibration methods have been suggested. Russell and Piermarini (9) used gem-cut single crystal cubic zirconia anvil as a calibrant. The crystals were examined to 132 kbar. The use of the Raman-active F_{2g} lattice mode of diamond at 1332.5 cm^{-1} as an internal standard has also been suggested (Section 3.2.5, also Refs. 10,11). It has been shown to have a linear response to pressure over the range of 50~200 kbar.

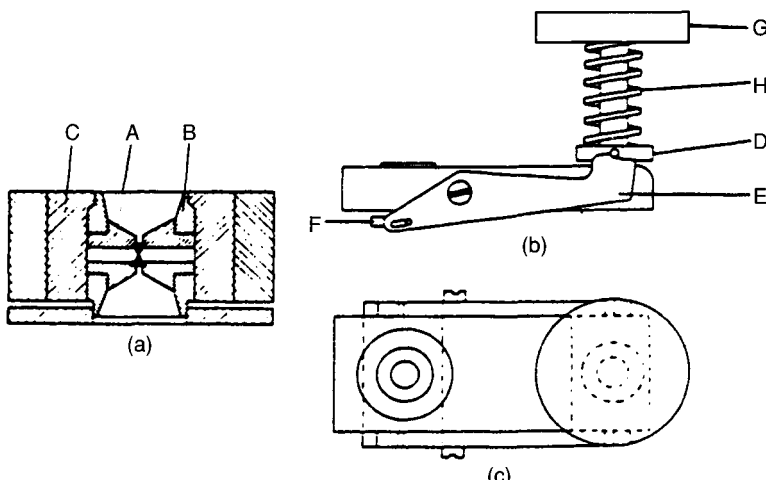


Figure 3-1 Diamond anvil high-pressure cell. (a) Detail of diamond cell. (b) Side view. (c) Front view. A and B, parts of piston; C, hardened steel insert; D, presser plate; E, lever; G, screw; H, calibrated spring. (Reproduced with permission from Ref. 1.)

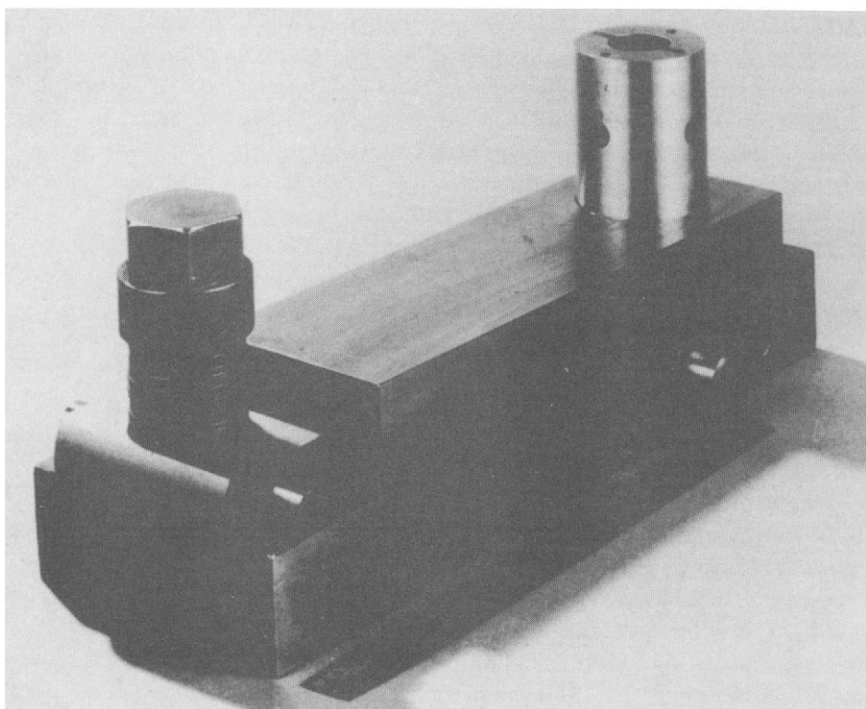


Figure 3-2 Superhigh-pressure cell for megabar use.

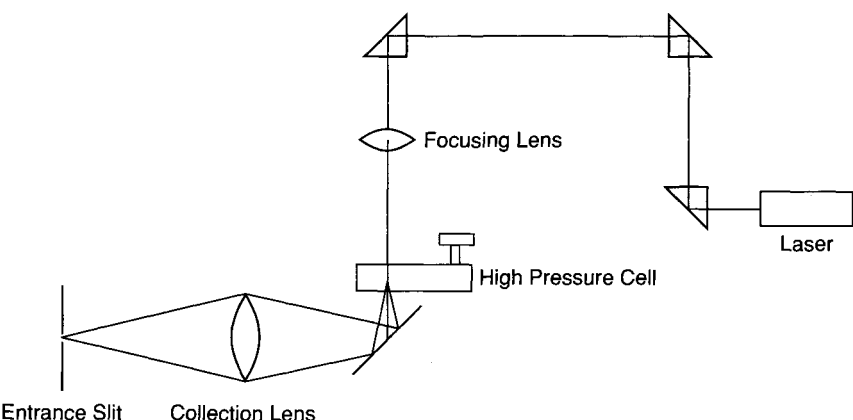


Figure 3-3 Detail of the scattering geometry in laser Raman DAC experiment. Figure not drawn to scale. (Reproduced with permission from Ref. 7.)

3.1.3 APPLICATIONS

A few applications illustrating the pressure effects on materials using Raman spectroscopy as the diagnostic tool are presented.

(a) Solid State Phase Transitions with Pressure

Phase Transitions in Solids. Solid state phase transitions with pressure are quite common (1). Solid H₂S was subjected to pressure up to 20 GPa at 300 K, and measured by Raman spectroscopy (12). Figure 3-4a shows the Raman spectra in the stretching vibration region under pressure. The symmetric stretching mode ν_1 shows a red-shift and broadens with an increase in pressure. At ~11 GPa, the broad band narrows and ν_3 (antisymmetric stretch) appears on the high-frequency side of ν_1 , indicative of a phase transition occurring. The ν_2 bending vibration at ~1,160 cm⁻¹ is only slightly affected by an increase in pressure. At the second phase transition, another ν_2 vibration appears at ~1,250 cm⁻¹ that shifts toward higher frequency with pressure. All five lattice modes blue-shift with pressure, typical of a molecular solid. Figure 3-4b records the pressure dependence of the intramolecular and lattice vibrations.

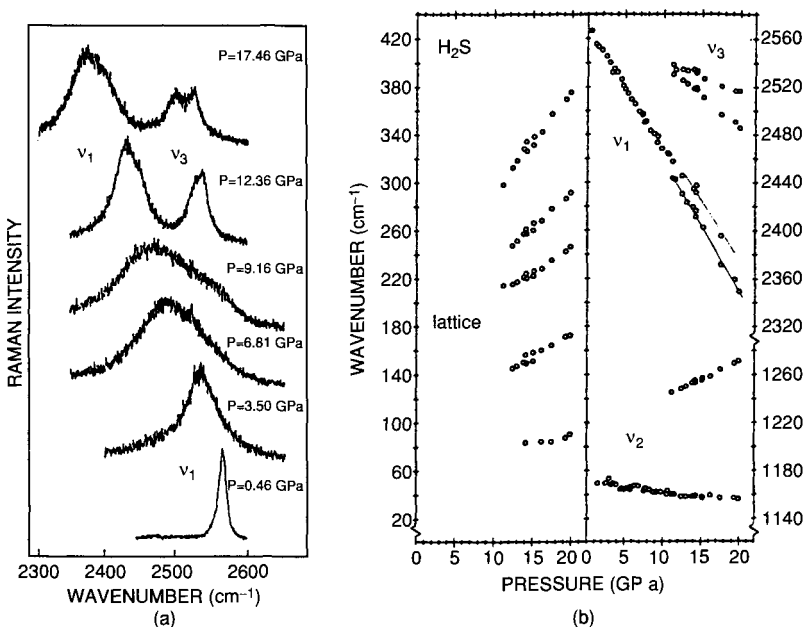


Figure 3-4 (a) Raman spectra of the symmetric (ν_1) and the anti-symmetric (ν_3) stretching modes in solid H₂S at various pressures. The phase transition occurs at about 11 GPa. (b) Pressure dependence of the intramolecular and the lattice vibrational frequencies in solid H₂S at 300 K. (Reproduced with permission from Ref. 12.)

Pressure Changes in Solid Coordination Compounds. Adams *et al.* (13) examined decacarbonyl dimanganese, $Mn_2(CO)_{10}$, and decacarbonyl dirhenium, $Re_2(CO)_{10}$, with pressure in a DAC, and followed the change in the carbonyl and low-frequency region with Raman spectroscopy. In the pressure conversion from the D_{4d} to the D_{4h} isomer, a carbonyl vibration (E_2 doublet) centered at $2,020\text{ cm}^{-1}$ becomes a single band. Three other bands in this region in the high-pressure phase appear below $2,000\text{ cm}^{-1}$. The high-pressure phase can be ascribed to a phase transition to the staggered isomer in $Mn_2(CO)_{10}$ and $Re(CO)_{10}$ (13). Figure 3-5 shows the spectral data obtained with pressure. Transformation occurs for the $Mn_2(CO)_{10}$ at 8 kbar and for

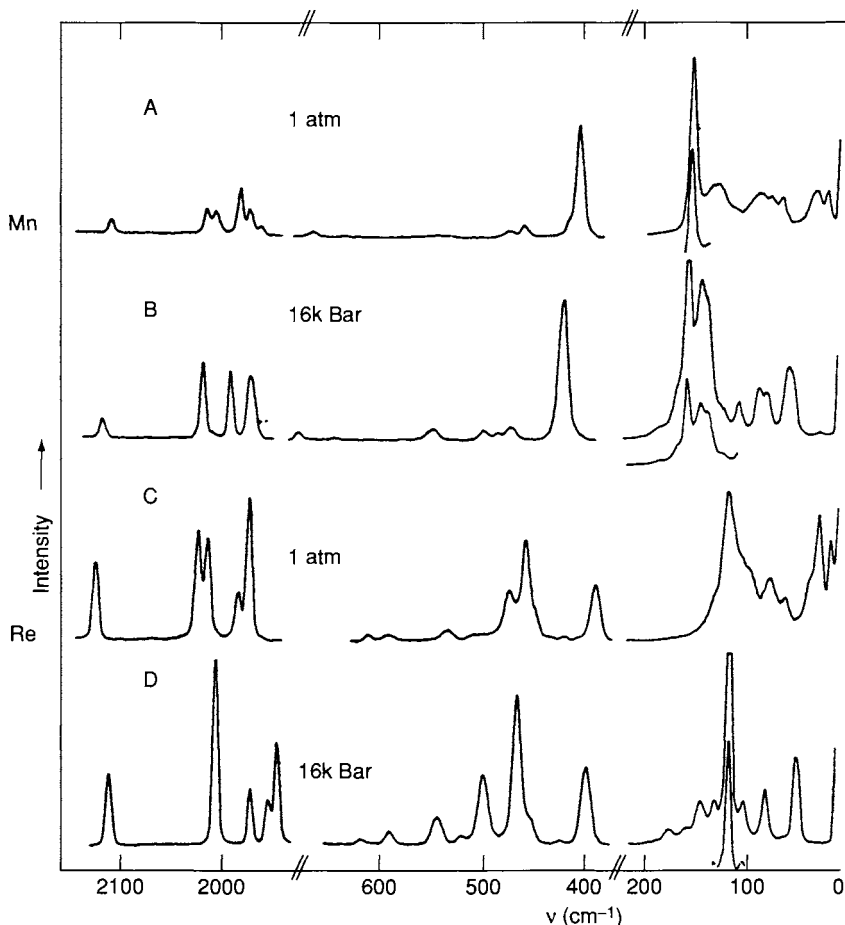


Figure 3-5 Raman spectra of $Mn_2(CO)_{10}$ at (A) ambient pressure and (B) 16 kbar, and of $Re_2(CO)_{10}$ at (C) ambient pressure and (D) 16 kbar in diamond anvil cell. (Reproduced with permission from Ref. 13.)

$\text{Re}_2(\text{CO})_{10}$ at 5 kbar. Two further phase transformations occur below 140 kbar for both carbonyls.

Evidence for Metallization of hydrogen at Megabar Pressures. The behavior of condensed hydrogen has been a subject of considerable interest since Wigner and Huntington (14) in 1935 discussed the possibility of a high-pressure metallic phase of hydrogen existing. Theoreticians have derived equations of state for both molecular and metallic phases to predict transition pressures. In recent years the effort to research for metallic hydrogen has been stimulated from attempts to understand the planetary surfaces and interiors of Jupiter, Saturn, and other outer planets.

Metallic hydrogen was first reported by the Russians in 1972 (15). However, this was not verified. Recently, optical and Raman observations by Mao and Hemley (16) of solid hydrogen, at pressures of 2.5 megabar at 77 K, have provided evidence that the metallic phase of hydrogen had been achieved. Electronic excitations in the visible region are observed at 2 megabar. Raman scattering data illustrated that the hydrogen solid was stable to ~ 2 kbar at 77 K, as evidenced by the presence of the H—H stretching mode (16). The upper trace of Fig. 3-6 shows the Raman spectrum of the H—H stretching vibration in solid hydrogen at 158 GPa and 295 K. The insulator-to-metal transition occurs at 77 K and is readily observed as two bands appear, arising from two phases (the metallic and the insulator phase). At 158 GPa, the H_2 vibron* in solid hydrogen is observed at $\sim 4,020 \text{ cm}^{-1}$. Supporting evidence has come from optical transmission and reflectance measurements. Some controversy has developed as Silvera *et al.* (17), repeating the work of Mao and Hemley, find the results suggestive, but do not establish the metallization of solid hydrogen. Ruoff and co-workers (18) also have raised objections and believe that Mao and Hemley have observed evidence for aluminum metal instead of metallic hydrogen—the aluminum coming from a chemical reaction of ruby powder (for pressure calibration) under the conditions of the experiment.

The debate on whether metallic hydrogen has been synthesized with pressure continues into the millenia. Ruoff and co-workers (19) in continuing studies on hydrogen at pressures of 342 GPa (3.42 kbar) found no evidence for metallic hydrogen. On the other hand, Nellis (20, 21) reported the preparation of metallic hydrogen at a pressure of 140 GPa (1.40 kbar). The instrumentation used was a two-stage gun capable of firing projectiles at $\sim 7 \text{ km/sec}$. The resistance was measured and observed to drop to $\sim 5 \times 10^{-4} \text{ ohm/cm}$, indicative of a metallic state being created. Deuterium behaved similarly. Further examples of useful applications to the high-pressure technique on matter, followed by Raman spectroscopy, may be found in Refs. 22–30. For recent reviews on high-pressure studies, see Refs. 31–33.

*Interaction of electrons with the H—H stretching vibration.

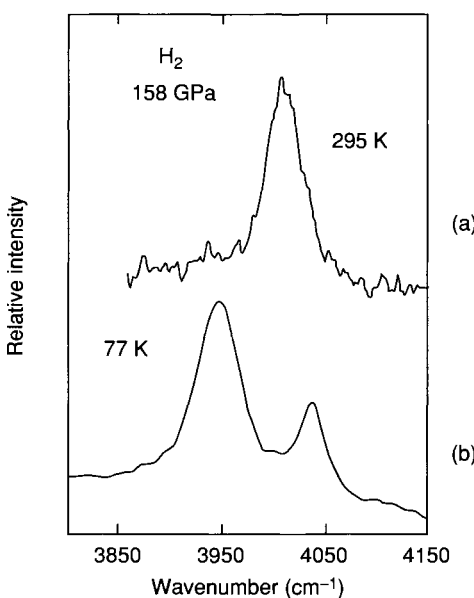


Figure 3-6 Raman spectra of the intramolecular H—H stretching vibration (vibron) in solid hydrogen at 158 GPa and 77 (B) and 295 K (A). A sloping background signal has been subtracted from the high-temperature spectrum. The estimated random errors in pressure and temperature are ± 1 GPa and ± 2 K (low temperature). (Reproduced with permission from Ref. 16.)

3.2 Raman Microscopy

Raman microscopy was developed in the 1970s. Delhaye (34) in 1975 made the first micro Raman measurement. Simultaneously, Rosasco (35, 36) designed a Raman microprobe instrument at the National Bureau of Standards (now the NIST). This early work established the utility of Raman spectroscopy for microanalysis. The technique provides the capability of obtaining analytical-quality Raman spectra with $1 \mu\text{m}$ spatial resolution using samples in the picogram range. Commercial instruments are available.

3.2.1 PRINCIPLES

The major limitations in the design of a Raman microprobe are related to the feeble Raman effect and the minute sample size. It is necessary to optimize the Raman signal, and this is accomplished by taking care in the development of the fore optical configuration to provide a high numerical operative and detector system.

The fore optical configuration is extremely important in optimization of the Raman microprobe. A high numerical aperture (NA) is necessary to collect the light scattered over a large solid angle to assure that more Raman scattered light from the sample is detected. A large-aperture collector is used, which minimizes elastic and inelastic scattering from the substrate. The substrate (37) must have a weak Raman or fluorescence spectrum in the region of interest. Periclase (MgO) can be used as the substrate, although glass slides are routinely used. It has no Raman spectrum and has good thermal properties. A microscope glass slide can be used in some cases. The substrate must be optically polished to provide visible observation of the micro-sized crystal. Additionally, it is important to align the excitation beam onto the substrate to prevent specular reflectance* from entering the Raman scattering path. A spatial filter is used to minimize other sources of spectral interferences. The design of the microprobe is made to provide totally independent optical paths for the excitation radiation and the scattered radiation, and the two paths are then coupled by the scattering properties of the particle being studied.

For monochannel instruments an efficient micro analyzer is necessary to provide enough stability to allow the measurement to be made, especially for long periods of time.

3.2.2 EXPERIMENTAL

Figure 3-7 illustrates the optical schematic of the Spex Micramate Raman microprobe. The sample being studied is placed on the stage of the microscope and is illuminated by light from the transmission illuminator. The focus on the sample is adjusted by viewing from the optical viewpoint and adjusting the objective. The illuminator lamp is switched off and the laser beam is directed to the beam splitter. The optical viewpoint is turned off and the TV camera is switched on by rotating the prism. The scattered light from the sample is collected by the objective and sent into the spectrometer. The microscope is a modified Zeiss 20 three-turret with detached stage/base. A cooled photomultiplier detector and photon-counting processing is used to provide the necessary sensitivity and low noise.

3.2.3 APPLICATIONS

Only a few applications of the Raman microprobe will be presented. The interested reader can refer to the references cited at the end of this section for further applications.

*Specular reflectance is the reflectance spectrum obtained from a flat, clean surface (e.g., a mirror).

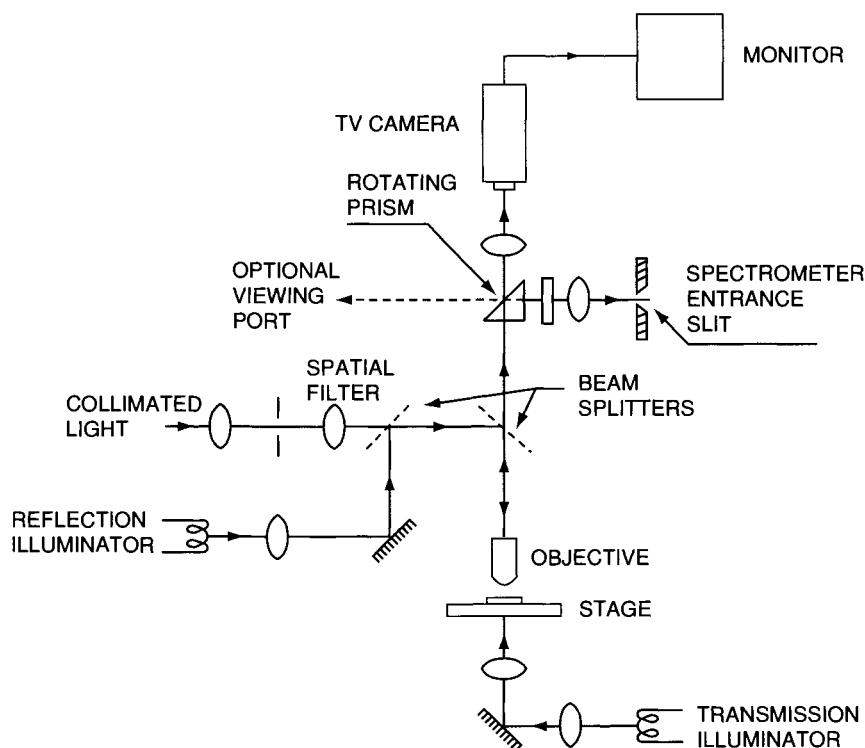


Figure 3-7 Optical path for laser input optics and transfer of the Raman signal to the monochromator for microprobe sampling (e.g., the Spex Micramate). (Reproduced with permission from Spex Industries.)

The Raman microprobe has provided applications in a number of diverse areas of science. Generally, the areas of applications fall into two major categories:

- (1) finger-print identification of microscopic contaminants, and
- (2) characterization of new materials.

(a) Surface Contaminant Identification

The presence of organic contaminants as small as $1 \mu\text{m}$ or films as thin as $1 \mu\text{m}$ on silicon wafers during the manufacturing process of integrated circuits can be readily identified (38). These contaminants can affect the performance of the device and must be identified. Figure 3-8 shows the identification of possible Teflon contaminants. Other techniques, such as IR, X-ray diffraction, Auger and electron microprobe, are insensitive in identifying the nature of the contaminant.

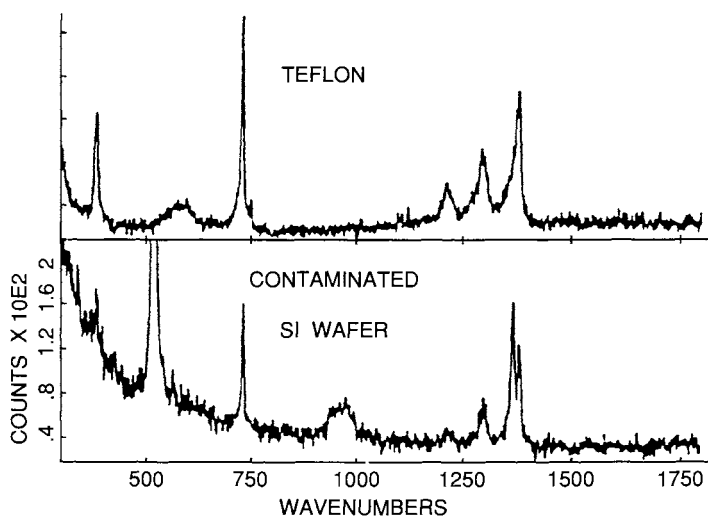


Figure 3-8 Raman microprobe spectrum of fluorinated hydrocarbon contaminant on silicon wafer that had been polished and plasma-etched (lower) and Raman spectrum of polytetrafluoroethylene (upper). Laser, 135 mW at 514.5 nm. Slits, 300 μm . Time, 0.5 s per data point. (Reproduced with permission from Adar, F., in "Microelectronics Processing: Inorganic Materials Characterization" (L. A. Casper, ed.), ACS Symposium Series Vol. 295, pp. 230–239. American Chemical Society, Washington, D.C., 1986. Copyright 1986 American Chemical Society.)

(b) Biological Compounds

The Raman microprobe has been used to detect foreign bodies in various tissues (38). Figure 3-9 shows spectra of lymph node tissue of 5 μm size, which was obtained by biopsy from a patient. The foreign body was identified as a particle of silicon rubber (dimethyl siloxane). For more biological and medical applications, see Section 6.2.4.

(c) Inclusions in Solid Inorganic Materials

The nature of solid, liquid or gaseous inclusions that may be found within transparent inorganic glass or crystalline materials can be determined by Raman microprobe techniques without breaking up the sample (39). Other analytical techniques, such as mass spectroscopy or electron microscopy, that may be used to obtain such information require destruction of the original sample. This capability of the microprobe is useful if one wants to analyze inclusions in a material before and after a sample treatment. The only limitation is that the position of the inclusion in the material must be located within the working distance of the objective lens in the microscope (39).

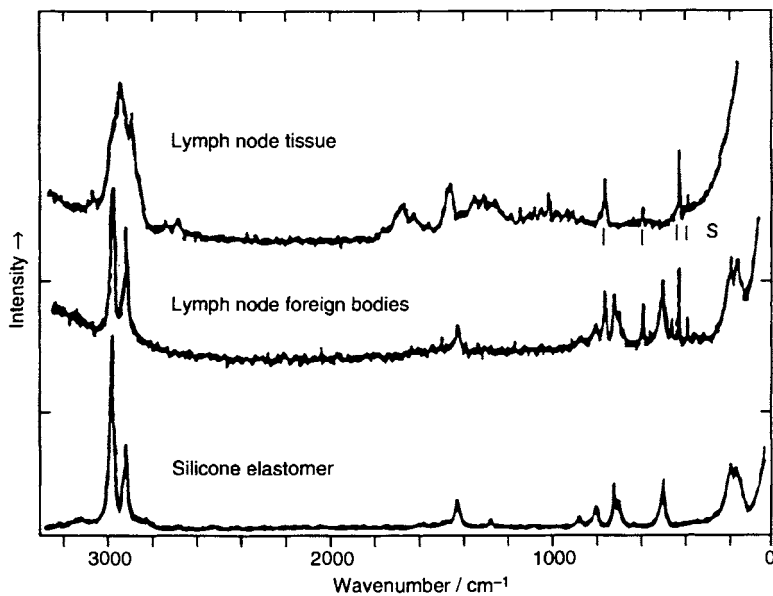


Figure 3-9 RMP spectra obtained in a study of foreign bodies in biopsy section lymph node tissue; S, features of sapphire substrate. (Reproduced with permission from Ref. 38.)

Figure 3-10 illustrates the Raman microprobe spectra that were measured for a bubble inclusion that was formed as a defect in a NaPO_3 glass during nitriding of the glass with ammonia (40). The glass had been nitrided to increase its mechanical strength. The resulting rotational Raman spectra clearly indicate that the ammonia remaining in the bubble had decomposed into molecular nitrogen and hydrogen during this treatment. If a new solid phase had been formed on the surface of the bubble during the treatment, its nature could also have been identified without destroying the sample by focusing the laser beam of the microprobe on it during spectral measurement.

3.2.4 FT-RAMAN MICROSCOPY

Messerschmidt and Chase (41) recently demonstrated that it was feasible to use a microscope to obtain the FT-Raman effect. Transfer of laser energy occurs through collection optics in their instrument. Figure 3-11 illustrates the spectrum of a single strand ($12\ \mu\text{m}$ in diameter) of Kevlar polymer as accomplished by FT-Raman microscopy. Kevlar is difficult to measure by conventional Raman spectroscopy because of fluorescence effects.

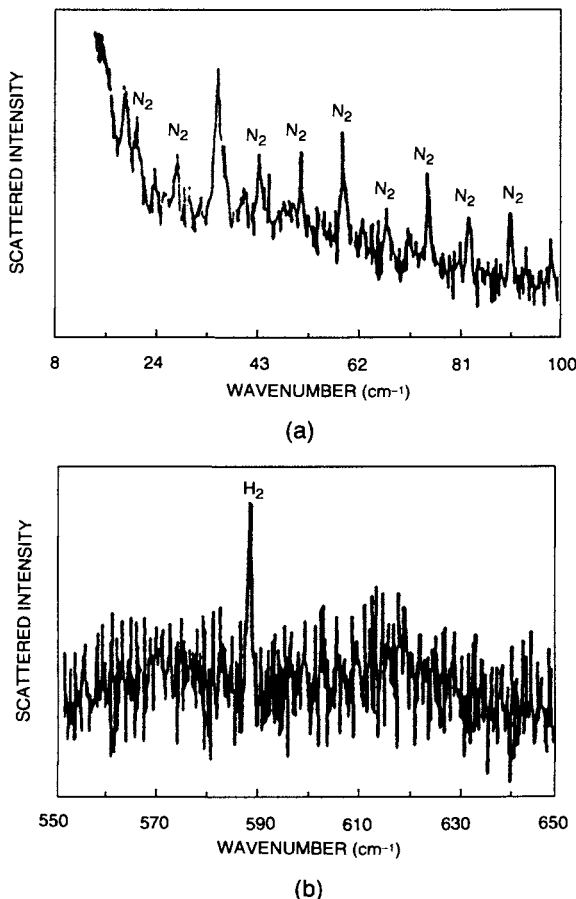


Figure 3-10 (a) Rotational Raman spectrum of a bubble in NaPO₃ glass in the 5–100 cm^{−1} region indicating N₂. (b) Rotational Raman spectrum of a bubble in NaPO₃ glass in the 550–650 cm^{−1} region indicating H₂. (Reproduced with permission from Ref. 40.)

Bruker has introduced an FT-Raman microscope which is an accessory to an FT-IR spectrometer (42). The coupling between the microscope and the Raman module is made by NIR-fiber optics. In the wavelength range of the Raman experiment excited by a Nd:YAG laser, the fiber optics transmission is at a maximum, thus allowing the experiment to be successful (43). Spatial resolution down to 5 μm can be achieved. The technique appears to be a capable adjunct to FT-IR microscopy.

For a general discussion on the Raman microprobe, see Refs. 44 and 45.

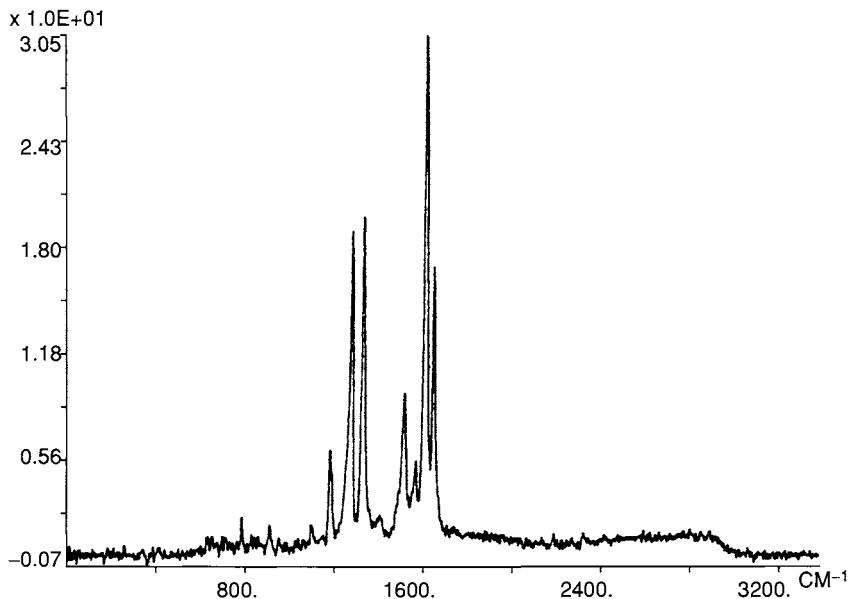


Figure 3-11 Micro FT-Raman spectrum of a single strand of Kevlar fiber with a diameter of $12 \mu\text{m}$. (Reprinted with permission from R. G. Messerschmidt and D. C. Chase, *Appl. Spectrosc.* 43, 11 (1989).)

3.2.5 RAMAN MAPPING

Two modes of illumination are available for Raman illumination. One is “point illumination”, and the other is “area (or global) illumination”. In the former, the laser beam is focused on one chosen point under the microscope image, and the Raman spectrum of this particular point is measured. If the sample is not homogeneous, another point of interest is chosen and the Raman spectrum is measured by moving the laser focus to that point. In the latter, the Raman spectrum of the entire illuminated area is measured with a two-dimensional CCD camera. By deconvoluting one particular vibration from the whole spectrum, it is possible to obtain a microscopic image of the distribution of the component associated with this vibration. This Raman mapping technique is utilized extensively to study the distribution of various components in biological samples and on the surfaces of solids such as minerals.

Use of a confocal microscope (46) greatly improves Raman microspectroscopy. As shown in Fig. 3-12, confocal microscope has a pinhole (25 to 100 μm in diameter) which rejects out-of-focus signals. The smaller the pinhole size, the better the rejection. As a result, the background (substrate) signals can be

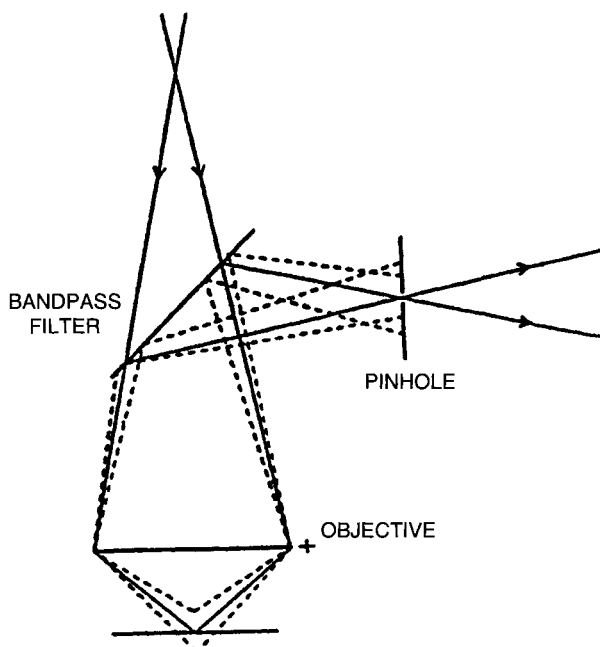


Figure 3-12 Suppression of out-of-focus signal contributions by means of confocal signal detection. (Reproduced with permission from Ref. 46.)

reduced significantly. Furthermore, it is possible to measure Raman spectra of the sample at different depth by moving the focal plane in the axial direction. For example, a pressure gradient in the interior of the diamond anvil cell (Section 3.1.2) produced under high pressure can be measured by confocal Raman microspectroscopy (47). It exhibits a Raman band at 1332 cm^{-1} when measured on the surface. As shown in the upper part of Fig. 3-13, this band is shifted to lower frequencies when the focus is moved deeper inside the diamond anvil. A quantitative relationship between the band shift and the pressure is difficult to establish by using a non-confocal microscope since the bands are much broader and the focuses are much wider as seen in the lower part of Fig. 3-13.

3.3 Surface-Enhanced Raman Spectroscopy (SERS)

Considerable interest has developed in recent years concerning the nature of adsorbed molecules on metal surfaces (e.g., electrode surfaces). Determinations of the nature of the adsorbate molecule on the surface and the frequencies of bands associated with adsorbed molecules are

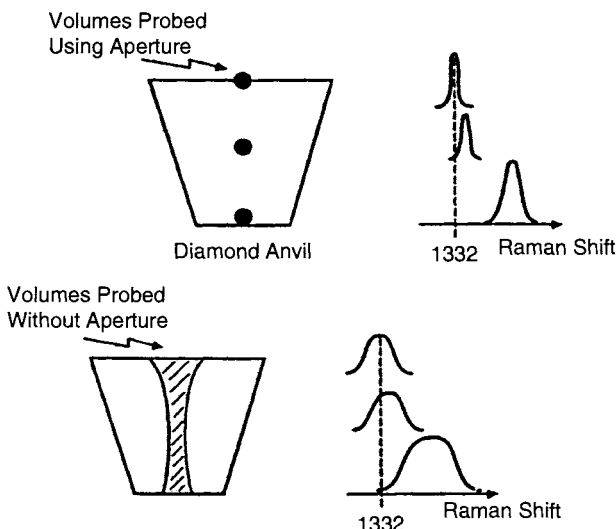


Figure 3-13 The effects of the pressure gradient on the Raman band of diamond provided by the confocal aperture (upper part) and with no aperture (lower part). (Reproduced with permission from Ref. 47.)

important data. Information concerning the strength of the adsorbate–surface interactions and the conformation of the adsorbed molecule becomes obtainable. Previously, much of this surface information has been provided by surface-sensitive infrared techniques, such as ATR and reflectance methods. In 1974, Fleischman *et al.* (48) reported the Raman spectrum of a monolayer of pyridine adsorbed on a silver electrode surface. In 1977, Jeanmaire and Van Duyne (49) and Albrecht and Creighton (50) noted that the scattering intensity from the adsorbed species is 10^5 – 10^6 times stronger than that of nonadsorbed species. Thus, SERS research had begun.

It has now been demonstrated that many molecules adsorbed on appropriately prepared metal surfaces display Raman cross-sections several orders of magnitude greater than the corresponding quantity for an isolated molecule or from a solution. Together with other surface-sensitive techniques, SERS has catalyzed the study of condensed phases on surfaces. It has demonstrated promise as a vibrational probe of *in situ* gas–solid, liquid–solid, and solid–solid environments, as well as a high-resolution probe of vacuum–solid interfaces.

The surface enhancement (51) of an adsorbate molecule obtained by the SERS technique has been the reason for the increased interest. Because of the large enhancement, small sample volumes can be used, and current detection limits are in the picomole-to-femtomole range. The large amount of data

obtainable and its surface selectivity and sensitivity make the SERS technique a welcome addition to the battery of tools available for surface studies.

3.3.1 PRINCIPLES

Normal Raman laser excitation in the visible and NIR region (52) can be used to obtain the SERS effect. The substrate surface is extremely important in providing the necessary enhancement to make the technique as valuable as it has become. A number of substrates have been used (53). These include evaporated silver films deposited on a cold surface at elevated temperature (~ 390 K) on a glass substrate, photochemically roughened surfaces (e.g., silver single crystals subjected to iodine vapor, which roughens the surface), grating surfaces, and mechanically abraded and ion-bombarded silver surfaces.

The mechanisms involved whereby surface enhancement spectra are obtainable are still the subject of considerable controversy (53). At least two mechanisms have been proposed (53, 54). If one examines the relationship $P = \alpha E$ (more thoroughly discussed in Chapter 1), it is clear that any enhancement must come from an enhancement of α (molecular polarizability) or from E (the electric field), since the intensity of Raman scattering is proportional to the square of the induced electric dipole moment P . The enhancement associated with E is termed the electromagnetic effect. This enhancement occurs because the local electromagnetic field at the surface of a metal is significantly changed from that in the incident field, because of the metal influence, and is pronounced when fine metal particles or rough metal surfaces are involved. In this case, the light excitation at the surface of the metal excites conduction electrons and generates a surface plasma resonance (sometimes called a plasmon resonance). This causes the roughness feature of the metal to be polarized and the electromagnetic field in the interior of the particle at the surface to increase significantly from the applied field.

The other enhancement is termed the chemical enhancement and can result from a charge-transfer (C-T) or bond formation of the metal and adsorbate, which can increase α , the molecular polarizability (55). For the pyridine/Ag system, the C-T band appeared on adsorption of pyridine on Ag and disappeared reversibly on desorption of pyridine (56). It was observed that the stronger the C-T band, the stronger the SERS spectrum.

3.3.2 INSTRUMENTATION

For SERS measurements on condensed-phase interfaces, a conventional Raman spectrophotometer can be used. The laser beam in the visible or

NIR region may be directed to the surface via 90°, 180° or backscattering geometry. A double monochromator with a diode array detector can be used, or alternatively, a triple monochromator with the aforementioned detector may be utilized, to give better stray light performance. To maximize the enhancement effect, the incident wavelength appropriate for a particular substrate is necessary. Krypton-ion or dye lasers operating in the red region are used for copper and gold substrate surfaces. The argon-ion laser line at 514.5 nm is suited for a silver substrate surface. The maximum enhancement is said to be at ~ 750 nm (51). Thus, the v^4 relationship (Chapter 1) is not applicable in SERS.

As was mentioned in the previous section, the nature of the substrate is extremely critical in obtaining the maximum enhancement. For visible Raman excitation, the noble metals, such as Ag and Au, and the alkali metals are the substrates of choice. For other regions, other substrates are more suitable (e.g., Ge or Pt in the IR region). Probably the most common substrates used for SERS are the colloidal suspensions of silver or gold particles ($\sim 5\text{--}20$ nm in diameter), and electrochemically roughened silver electrodes.

Since stationary electrodes are employed in most SERS experiments, a relatively small number of adsorbed molecules are continuously irradiated by laser beams. When exciting lines are within strong absorption bands of the adsorbed species, surface-enhancement resonance Raman spectra (SERRS) are obtained. However, this may lead to decomposition of such species due to local heating. Use of a cylindrical rotating electrode can circumvent this problem (57).

3.3.3 APPLICATIONS

Only a few examples of applications of SERS technique will be presented.

(a) *Trace Analyses*

SERS has been found to be useful for trace analytical applications. Organophosphorus compounds used in insecticides have been detected at the nanogram level (58). The Raman spectra of these compounds are relatively specific, and they can be readily identified. Figure 3-14 shows SERS spectra of several organophosphorus compounds. The spectra were obtained using SERS-active substrates of silver-covered microspheres on cellulose and glass surfaces. The technique has also proven fruitful in identifying ground water contaminants of an organic nature (59). Figure 3-15 shows the SERS spectra of a mixture of ground water contaminants. The spectra were obtained using a SERS substrate in the form of a silver electrode.

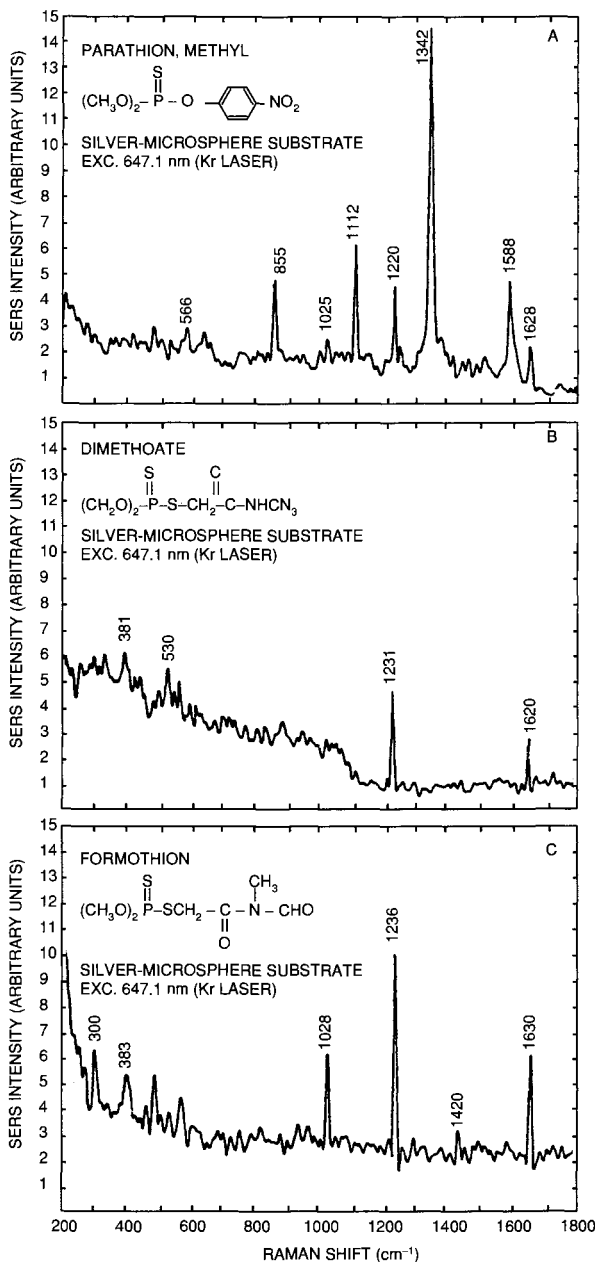


Figure 3-14 SERS spectrum of (a) methylparathion (26 ng), (b) dimethoate (23 ng), and (c) Formothion (26 ng). (Reproduced with permission from Ref. 58. Copyright 1987 American Chemical Society.)

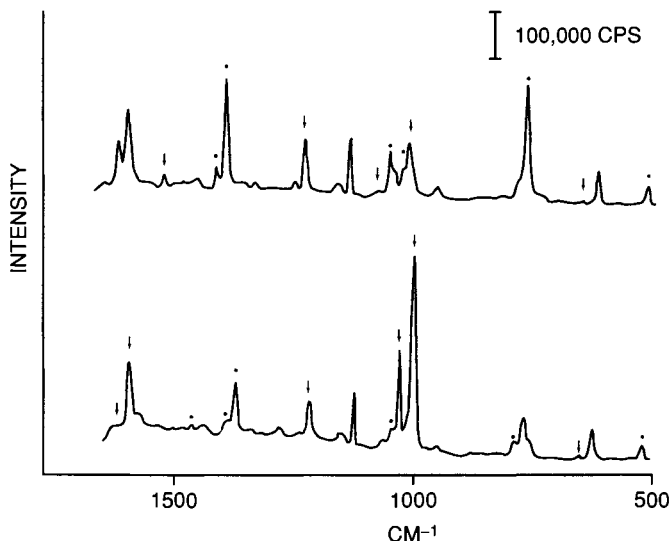


Figure 3-15 The SERS spectra of a mixture of contaminants at electrode potentials of -1.0 (top) and -0.6 (bottom) V and an excitation wavelength of 514.4 nm . The arrows and the dots indicate the major peaks due to pyridine and quinoline, respectively. (Reproduced with permission from Ref. 59. Copyright 1987 American Chemical Society.)

(b) Biological Molecules

SERS spectra of several dipeptides adsorbed on silver colloidal particles have been obtained (60). Figure 3-16 illustrates the SERS spectra of $\sim 10^{-5}\text{ M}$ dipeptides adsorbed on colloidal silver. Applications of SERS to other biological molecules are found in Section 4.1.2.

(c) Catalysis

SERS has been used in monitoring catalytic reactions (53). Figure 3-17 illustrates the measurement of catalytic formation of SO_3^{2-} and SO_4^{2-} on silver powder surfaces by exposure to SO_2 gas. It was concluded that part of the SO_3^{2-} was oxidized to SO_4^{2-} , giving a new absorption band at 962 cm^{-1} (attributed to SO_4^{2-}), and the SO_3^{2-} was thermally desorbed.

(d) Characterization of Modified Electrodes and Electrochemical Processes

SERS has also been found to be valuable in characterizing modified electrodes and electrochemical processes (61). SERS was used to observe the sequential electrochemical formation of adsorbed O^{2-} , OH^- and H_2O on a silver electrode in $0.1\text{--}0.001\text{ M}$ alkali chloride solution containing

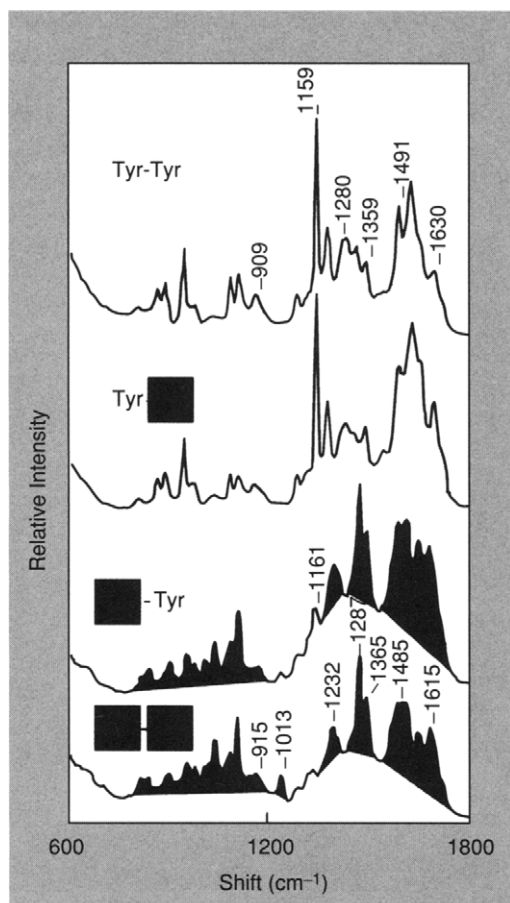


Figure 3-16 SERS spectra of $\sim 10^{-5}$ M dipeptides adsorbed on colloidal silver. (Reproduced with permission from Ref. 60. Copyright 1989 American Chemical Society.)

micromolar concentrations of KMnO_4 (62). A peak at 615 cm^{-1} has been assigned to a mixed oxide designated by $(\text{Ag}, \text{Mn})-\text{O}$. The $(\text{Ag}, \text{Mn})-\text{O}$ species are successfully protonated to produce $(\text{Ag}, \text{Mn})-\text{OH}_2$. A peak at $\sim 590\text{ cm}^{-1}$ disappears, and the hydrate $(\text{Ag}, \text{Mn})\text{OH}_2$ with a peak at about 475 cm^{-1} forms, as the V_{SCE}^* is swept cathodically. Oxidation of the silver surface by MnO_4^- produces $(\text{Ag}, \text{Mn})\text{O}$, and the surface roughness that is needed for the SERS effect. Figure 3-18 illustrates the SERS spectra of this system.

For additional reading on the SERS technique, see Refs 63–70.

* V_{SCE} : voltage of the saturated calomel electrode.

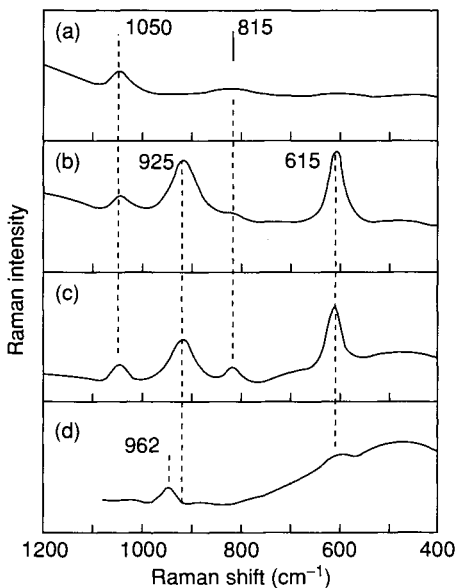


Figure 3-17 SER spectra from finely divided Ag powder. (a) Fresh powder in He atmosphere, $T = 295\text{ K}$; (b) like (a), but exposed to SO_2 gas for 1–2 min; (c) like (b), but kept in a SO_2/O_2 (ratio 1 to 5) containing atmosphere after initial exposure; (d) like (c), but slowly heated to 380 K . Spectra have been taken with 514.5 or 488 nm radiation and 4 cm^{-1} bandpass. (Reproduced with permission from Ref. 53.)

3.4 Raman Spectroelectrochemistry

Raman spectroelectrochemistry (71, 72) is a field in which one studies electrogenerated species on electrode surfaces, in electrode diffusion layers and bulk solution by Raman spectroscopy. Thus, the surface-enhanced Raman scattering (SERS) discussed in the preceding section is part of Raman spectroelectrochemistry. Here, we discuss Raman spectroscopic studies on electrogenerated species in bulk solution and in electrode diffusion layers. Since no enhancement from SERS is expected and since the concentrations of these electrogenerated species are rather low, it is imperative to take advantages of resonance Raman (RR) scattering (Section 1.15).

3.4.1 INSTRUMENTATION

Figure 3-19A illustrates a typical cell for obtaining RR spectra of electro-generated species in bulk solution (73). The laser beam is focused on a

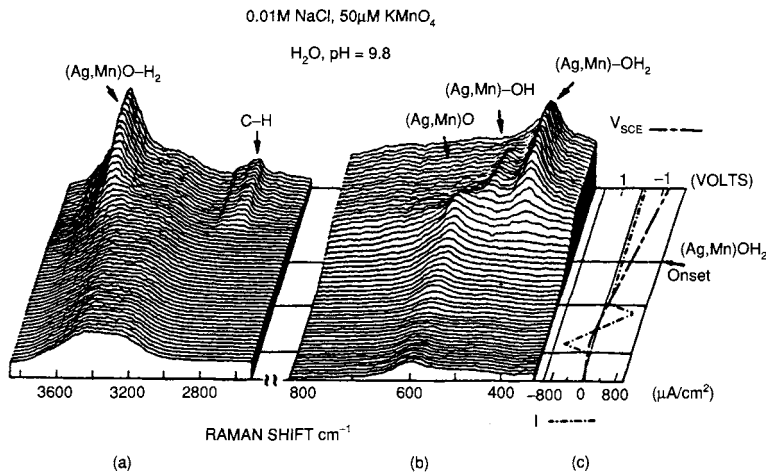


Figure 3-18 SERS spectra of $(\text{Ag}, \text{Mn})-\text{O}$, $(\text{Ag}, \text{Mn})-\text{OH}$, and $(\text{Ag}, \text{Mn})-\text{OH}_2$ adsorbed on a Ag electrode as a function of V_{SCE} . The solution is 0.01 M NaCl for the third ORC and the voltage interval is 35 mV. (a) The O—H₂ stretching mode region. The enhanced spectrum due to adsorbed $(\text{Ag}, \text{Mn})\text{O}-\text{H}_2$ is superimposed on the unenhanced Raman spectrum of bulk H₂O. (b) The $(\text{Ag}, \text{Mn})-\text{O}$ stretching mode region. (c) The “unfolded” voltammogram showing the voltage current characteristics of the cell corresponding to the evolution of the SERS spectra. The laser power at $\lambda = 514.5$ nm is 100 mW. (Reproduced with permission from Ref. 62. Copyright 1986 American Chemical Society.)

position that is well removed from the working electrode surface. Sufficient concentration of the species under investigation is accumulated via controlled potential coulometric electrogeneration. The species generated must be stable over the time required to record a spectrum so that no interference from decomposition products can occur. If electrogenerated species are stable only at low temperatures, their RR spectra must be measured using a low-temperature bulk electrolysis cell (74).

Figure 3-19B shows a “sandwich” cell for recording RR spectra of electro-generated species in the diffusion layer (73). The laser beam is reflected from a Pt working electrode and the scattered light is measured via back-scattering geometry. Spectral interference from the bulk solution can be avoided by choosing a proper system for RR excitation (*vide infra*). To create a steady-state concentration profile in the diffusion layer, a square-wave voltage is applied to the working electrode immersed in an unstirred solution containing electroactive species, solvent and supporting electrolyte.

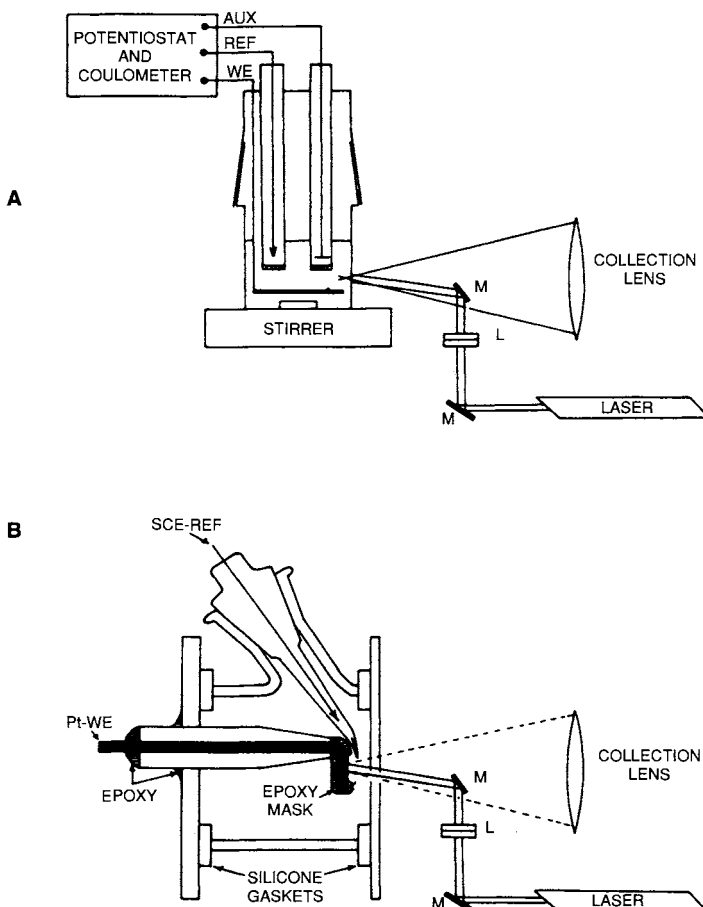
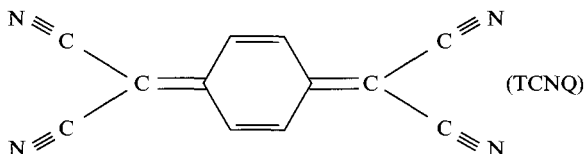


Figure 3-19 Resonance Raman spectroelectrochemistry cells and back scattering geometry. (A) Controlled potential electrolysis cell; (B) "sandwich" cell for semi-infinite diffusion conditions. (Reproduced with permission from Ref. 73. Copyright 1975 American Chemical Society.)

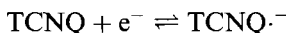
3.4.2 APPLICATIONS

(a) Bulk solution

Using the cell shown in Fig. 3-19A, Jeanmaire and Van Duyne (75) measured the RR spectrum of the tetracyanodimethane anion radical ($\text{TCNQ}^{\cdot-}$).



The radical was electrogenerated by the reaction



The $\text{TCNQ}^\cdot -$ radical thus obtained is completely stable for at least 3 hr, and its electronic spectrum shows strong absorption bands between 950 and 550 nm. Thus, the RR spectrum of $\text{TCNQ}^\cdot -$ was obtained by using the 647.1 nm line of a Kr^+ laser (Fig. 3-20a). On the other hand, TCNQ has a strong absorption band near 400 nm. Therefore, its preresonance spectrum, shown in Fig. 3-20b, was obtained by the 457.9 nm line of an Ar^+ laser. In both spectra, all strong and medium intensity bands were found to be polarized (totally symmetric). The vibrational frequency shifts in going from

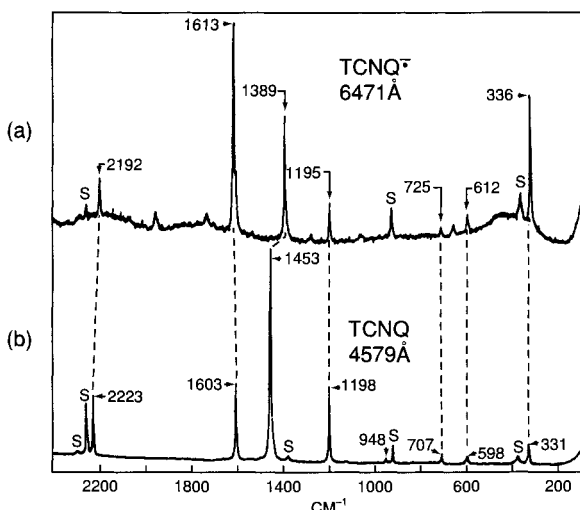


Figure 3-20 Resonance Raman spectra of TCNQ and electrogenerated $\text{TCNQ}^\cdot -$. [TCNQ] = 1.09 mM, laser power = 20 mW, bandpass = 1.2cm^{-1} ; $[\text{TCNQ}^\cdot -] = 2.24 \text{mM}$, laser power = 74 mW, bandpass = 2.2cm^{-1} . $\text{TCNQ}^\cdot -$ was electrogenerated by controlled potential coulometry at -0.10 V vs. SCE in 0.1 M TBAP/ CH_3CN . All spectra were scanned at $50\text{cm}^{-1} \text{ min}^{-1}$ using a 1.00 s counting interval. Plasma lines were removed at 4579 Å with an interference filter and at 6471 Å with a Claassen filter. S denotes a normal Raman band of the solvent (acetonitrile). No normal Raman bands are observed for the supporting electrolyte (TBAP, tetrabutylammonium perchlorate). (Reproduced with permission from Ref. 75. Copyright 1976 American Chemical Society.)

TCNQ to its anion radical can be explained in terms of π bond order changes, which can be calculated by MO methods. These workers (76) also carried out detailed excitation profile studies on several bands of TCNQ^- . Each profile contains 90 intensity points per 100 cm^{-1} , which is the most complete profile obtained for any compounds studied thus far. As shown in Fig. 3-21, the

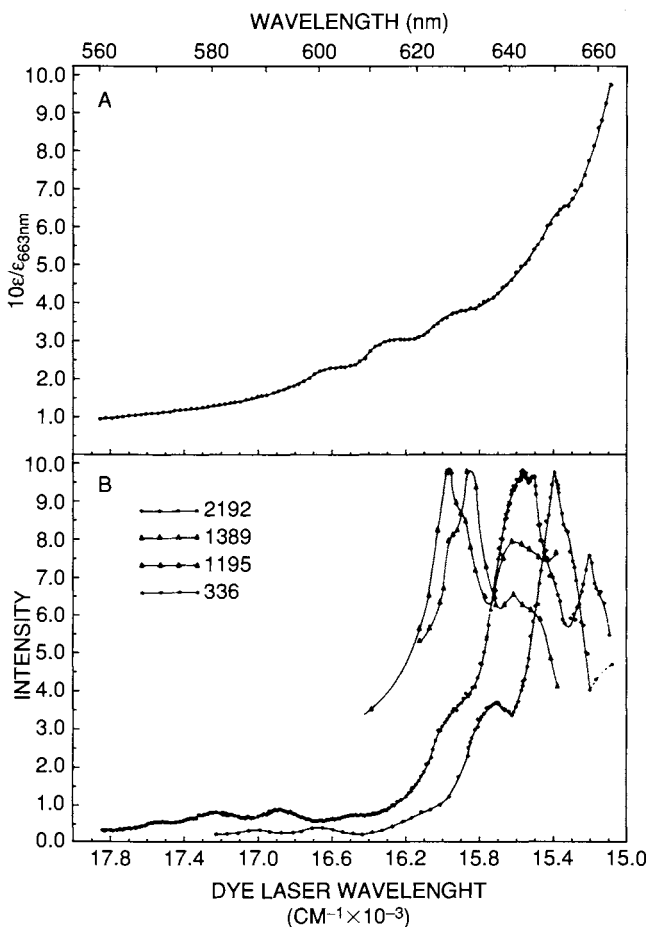


Figure 3-21 Comparison of TCNQ^- electronic absorption spectrum and resonance Raman excitation profiles. (a) Electronic absorption spectrum from $15,000$ to $17,850\text{ cm}^{-1}$. The extinction coefficient, ϵ , scale is normalized with respect to ϵ at 663.0 nm ($15,083\text{ cm}^{-1}$) = $3.0 \times 10^3 \text{ M}^{-1}\text{cm}^{-1}$. (b) Superposition of the v_2 ($2,192\text{ cm}^{-1}$), v_4 ($1,389\text{ cm}^{-1}$), v_5 ($1,195\text{ cm}^{-1}$) and v_9 (336 cm^{-1}) excitation profiles. The relative intensity scale has been scaled to 0.00 to 10.0 for all four spectra. (Reproduced with permission from Ref. 76. Copyright 1976 American Chemical Society.)

electronic absorption spectrum of TCNQ^- has almost no structure, while its RR excitation profiles show many details in the same region.

Using the low-temperature cell mentioned earlier, Czernuszewicz and Macor (74) generated $\text{O}=\text{Fe(IV)(TMP)}$ (TMP: tetramesitylporphyrinato anion) and its ^{18}O analog at -40°C via electrooxidation of Fe(III)(TMP)(OH) in CH_2Cl_2 , and measured their RR spectra shown in Fig. 3-22.

The band at 841 cm^{-1} is due to the $\nu(\text{Fe}=\text{O})$ of $\text{O}=\text{Fe(TMP)}$ since it is absent in the original solution and since it is shifted to 805 cm^{-1} by $^{16}\text{O}/^{18}\text{O}$ substitution (theoretical isotope shift, 38 cm^{-1}). Cooling was necessary because $\text{O}=\text{Fe(TMP)}$ is unstable and reacts readily with CH_2Cl_2 to form Fe(III)(TMP)Cl at higher temperatures.

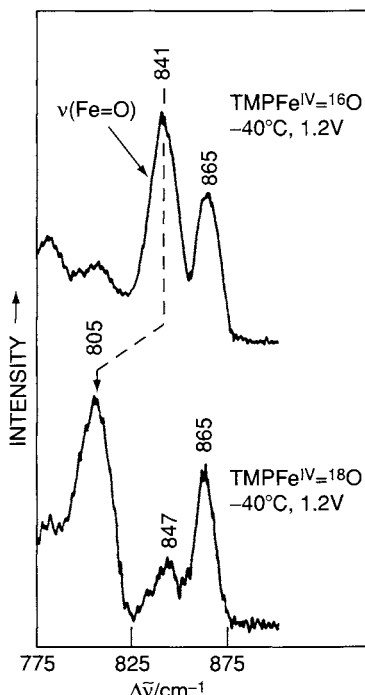
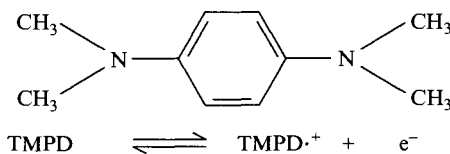


Figure 3-22 Resonance Raman spectra of $\text{O}=\text{Fe(IV)(TMP)}$ (top trace) and its ^{18}O isotope analogue (bottom trace), generated at -40°C by electrooxidation of Fe(III)(TMP)(OH) at 1.2 V in CH_2Cl_2 containing OH^- and $^{18}\text{OH}^-$, respectively. Both spectra were obtained *in situ* via backscattering from the low-temperature Raman spectroelectrochemical cell using 406.7 nm excitation ($\sim 50\text{ mW}$) and 8 cm^{-1} slit widths. (Reproduced with permission from Ref. 74. Copyright 1988 John Wiley & Sons, Ltd.)

(b) *Diffusion Layer*

Using the experimental setup and conditions mentioned earlier, Jeanmaire and Van Duyne (77) studied one-electron oxidation of *N,N,N',N'*-tetramethyl-*p*-phenylenediamine (TMPD) to its radical cation ($\text{TMPD}^{\cdot+}$, Würster's Blue).



The RR spectrum of $\text{TMPD}^{\cdot+}$, confined to the diffusion layer, was obtained by applying a square-wave voltage (repetition rate, 10 Hz). The excitation was made at 612 nm (CW dye laser) since $\text{TMPD}^{\cdot+}$ has its absorption maximum at this wavelength. TMPD in bulk solution does not interfere with the spectrum because it absorbs only in the UV region. Quantitative analysis of the time dependence of the forward and reverse portions of $\text{TMPD}^{\cdot+}$ shows excellent agreement with the expected linear relationship between the RR intensity of the strongest band at $1,628 \text{ cm}^{-1}$ (C=C stretch of benzene ring) and the calculated time factor.

3.5 Time-Resolved Raman (TR^2) Spectroscopy

Recent technical developments in laser Raman spectroscopy have made it possible to measure the Raman spectra of short-lived transient species, such as electronically excited molecules, radicals and exciplexes, which have lifetimes on the order of nano- (10^{-9}) and pico- (10^{-12}) seconds. These short-lived species may be generated by electron pulse radiolysis, photo-excitation and rapid mixing. However, the application of electron pulse radiolysis is limited in its adaptability and selectivity, while rapid mixing is limited by mixing rates, normally to a resolution on the order of milliseconds. Thus, photoexcitation is most widely used.

3.5.1 PRINCIPLES

Figure 3-23 illustrates the basic scheme involved in a typical pump-probe experiment. First, molecules are excited from S_0 (singlet ground state) to S_1 (singlet excited state) by a pump laser of frequency v_0 . Molecules excited to S_1 undergo nonradiative decay (intersystem crossing) to T_1 (triplet state). Since the pump pulse width is much narrower than the lifetime of the T_1 state (milli ~ microseconds), excitation to the S_1 state by a pump laser

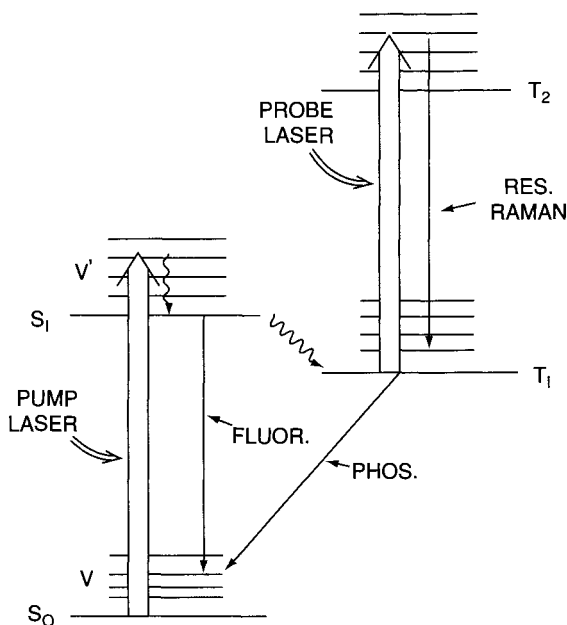


Figure 3-23 Energy level diagram in pump-probe experiment.

increases the population of molecules on T_1 , which may become sufficient to observe the Raman spectrum of the T_1 state molecule with a probe laser (v_1). If v_1 is chosen to meet the resonance condition as shown in Fig. 3-23, we can take advantage of the resonance Raman scattering discussed in Section 1.15 (extraordinary strong enhancement, selectivity and low sample concentration). Thus, time-resolved resonance Raman (TR^3) spectroscopy is ideal for obtaining Raman spectra of excited state molecules. Some compounds may have v_1 that is close to v_0 . In such a case, it is possible to obtain TR^3 spectra using a single laser. (See Refs. 78–81.)

Pulsed lasers such as Nd:YAG and excimer lasers are commonly used for the pump–probe experiment just mentioned. Some characteristics of these lasers are listed in Table 3-1. Although the fundamental of the Nd:YAG laser is at 1,064 nm, this frequency can be multiplied by using nonlinear crystals, such as KDP (potassium dideuterium phosphate), to obtain the second (532 nm), third (355 nm) and fourth (266 nm) harmonics. Furthermore, a wide range of UV-visible pulsed radiation can be generated from these harmonics by pumping a dye laser or using a Raman shifter (Section 2.2.5).

Table 3-1 Some Characteristics^a of Nd:YAG and Excimer Lasers

Nd:YAG: Rep. rate 2–40 Hz, linewidth < 1 cm⁻¹ (< 0.2 cm⁻¹ with intra-cavity etalon). Beam divergence < 0.5 mrad.

Wavelength, nm	1,064	532	355	266
Energy/pulse, mJ	280	110	50	20
Pulse width, ns	9	7	6	5
Peak power, MW	30	15	8	4
Average power, W (at 10 Hz)	2.8	1.1	0.5	0.2

Excimer: Rep. rate 0.1–100 Hz, beam divergence 5–10 mrad, beam size 10 × 25 mm, linewidth 10–30 cm⁻¹.

Laser medium	XeF	N ₂	XeCl	KrF	KrCl	ArF	F ₂
Wavelength, nm	351	337	308	249	222	193	157
Energy/pulse, mJ	400	16	500	1,000	100	500	15
Pulse width, ns	14	6	10	16	9	14	6
Peak power, MW	28	3	50	60	11	35	2.5
Average power, W (at 10 Hz)	4	0.1	5	10	1	5	0.1

^aRepresentative figures for good commercially available lasers.

3.5.2 INSTRUMENTATION

Figure 3-24 shows the arrangement for obtaining TR³ spectra of carotenoid excited states used by Dallinger *et al.* (82). In one of their experiments, Laser II (355 nm) was used to produce T₁ state molecules via excitation of a sensitizer (anthracene) and subsequent energy transfer to carotenoids. Laser I (532 nm or 555–610 nm dye laser) was used to obtain RR spectra of carotenoid triplet states. The proper time delay between the pump and probe pulses was determined by the time required to accumulate enough population in the T₁ state. In this experiment, a long delay (~ microseconds) was necessary so that two separate lasers were employed for excitation and probing. Such a delay can be accomplished electronically by triggering two lasers in sequence (timing circuitry, Fig. 3-24). If a relatively short time delay is required, an optical delay line, such as that shown in Fig. 3-24, may be employed (for example, a three-meter difference in path length causes a time delay of 10 ns). In some cases, such a delay is not necessary since the excited state of interest can be created within a single pulse width (~10 ns). Then, the leading edge of the pulse is used for pumping and the rest for probing.

Although the peak power of the pump laser must be high, the power of the probe laser should be kept low to avoid nonlinear effects (multiphoton absorption, stimulated Raman scattering; see Section 3.9.2) and dielectric breakdown (ionization of molecules) that damage the sample. Thus, signal averaging of many pulses (high repetition rate) is made to obtain acceptable S/N ratios. Multichannel detectors such as an intensified silicon photodiode

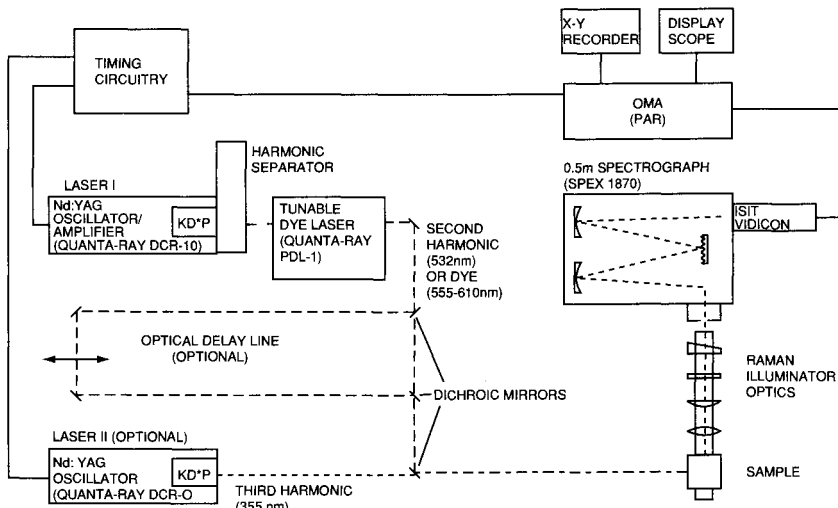


Figure 3-24 Simplified diagram of the experimental apparatus for the optically sensitized triplet generation/TR³ studies. Requisite time delays were obtained either by optical delay or by the two-laser experimental configuration. The optical delay line is not to scale; its actual length was approximately 120 ft. (Reproduced with permission from Ref. 82. Copyright 1981 American Chemical Society.)

array (ISPD) and an intensified silicon intensified target (ISIT) were used because of their efficiency in data acquisition and handling. In conjunction with such a multichannel detector, a polychromator such as a Spex Model 1870 spectrograph is used. A triple polychromator (Spex Model 1877, Section 2.4) gives a better stray light rejection.

3.5.3 APPLICATIONS

Figure 3-25 shows the RR spectra of canthaxanthin in the S_0 and T_1 state obtained by Dallinger *et al.* (82). The ground state spectrum (trace "a") exhibits two intense bands at 1,519 and 1,155 cm^{-1} , which are assigned to the in-phase $\nu(\text{C}-\text{C})$ and $\nu(\text{C}-\text{C})$, respectively, of the conjugated chain. The excited state (TR³) spectrum (trace "c"), shows that these bands are shifted by $\sim 27 \text{ cm}^{-1}$ to lower frequencies (1,491 and 1,129 cm^{-1} , respectively) relative to the ground-state spectrum. M.O. calculations predict that, in the T_1 state, the C—C bonds are shortened while the C=C bonds are lengthened. Then, the 1,519 cm^{-1} band should be downshifted, whereas the 1,155 cm^{-1} band should be upshifted, in going from the S_0 to the T_1 state. However, both bands were found to be downshifted. This apparent contradiction has led Dallinger *et al.* (82) to conclude that the interaction force constant between

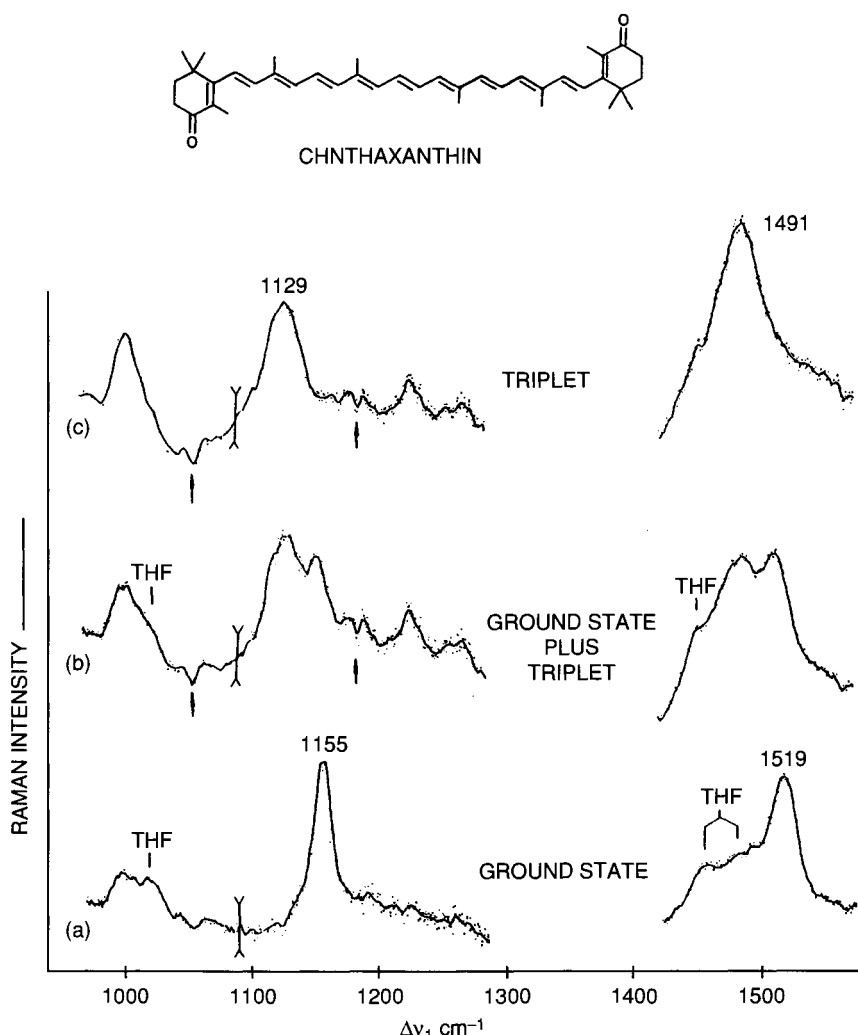


Figure 3-25 Resonance Raman spectra of canthaxanthin in the S_0 and T_1 states. Spectra were obtained with the vidicon spectrograph by using 555 nm probe wavelength and optical excitation of anthracene (at 355 nm) for triplet production. Trace "a", groundstate spectrum, no 355 nm excitation pulse; trace "b", superposition of S_0 and T_1 spectra; trace "c", T_1 spectrum, obtained by approximately normalized subtraction of trace "a" from trace "b". Three different vidicon frames (along the frequency axis) are shown; intensities are not to scale. The solid line is obtained by an 11-point quartic running smooth of the observed points. The negative base line excursions denoted by the vertical arrows are OMA artifacts. (Reproduced with permission from Ref. 82. Copyright 1981 American Chemical Society.)

the ($\text{C}=\text{C}$) and $\nu(\text{C}-\text{C})$ vibration (Section 1.20) changes sign in going from the S_0 to the T_1 state.

The $[\text{Ru}(\text{bpy})_3]^{2+}$ ion (bpy: 2, 2'-bipyridine) and related complexes have attracted much attention because of their excited-state redox properties, which may be utilized as solar-energy conversion devices. The TR³ spectrum of this ion can be obtained by using a single laser line (Nd:YAG third harmonic at 355 nm) since the S_0-S_1 transition absorbs this line considerably and since the absorption maximum of the $T_1 \rightarrow T_n$ transition is near 360 nm. The T_1 state population can be built up via efficient and rapid intersystem crossing from the S_1 to the T_1 state because of the short lifetime of the S_1 state (~ 10 ps) and the long lifetime of the T_1 state (~ 600 ns). The TR³ spectrum of the $[\text{Ru}(\text{bpy})_3]^{2+}$ ion was originally obtained by Bradley *et al.* (83). These workers found that the TR³ spectrum consists of two series of bpy vibrations; one series of bands is the same as that observed in the S_0 state and the other is close to those of $\text{Li}^+(\text{bpy}^-)$. These experiments were repeated by Mallick *et al.* (84) and are shown in Fig. 3-26. Thus, the T_1 state may be formulated as $[\text{Ru(III)}(\text{bpy})_2(\text{bpy}^-)]^{2+}$. Namely, the electron is localized on one bpy ligand rather than delocalized over all three bpy ligands. TR³ spectroscopy has also been applied to biological compounds (Section 6.1.1).

3.6 Matrix-Isolation Raman Spectroscopy

3.6.1 PRINCIPLES

The matrix-isolation (MI) technique was largely developed by Pimentel and coworkers (85) to study the IR spectra of unstable (free radicals and reaction intermediates) as well as stable species isolated in inert gas matrices. In this method, gaseous samples and an inert matrix gas, such as Ar or Kr, are mixed and deposited on an IR transparent window (e.g., alkali halide crystal) cooled to 10–20 K by a cryostat. Since the mixing ratio (sample/gas) is 1:500 or higher, the sample (solute) molecules are completely isolated from each other in the frozen gas matrix. Thus, MI spectra are similar to those of the gaseous phase; no intermolecular interaction is present, and no lattice modes are observed (although weak interaction between the solute and the inert gas is noted). Furthermore, MI spectra are simpler than gas-phase spectra because only a few or no rotational transitions are observed owing to steric restriction of molecular rotation in the matrix. The resulting sharpness of observed bands tends to resolve closely located bands. The MI technique is also applicable to solid samples as long as they can be vaporized without decomposition. Extensive research has been carried out in the field of matrix isolation IR spectroscopy, and the results are thoroughly reviewed in several monographs (86–89).

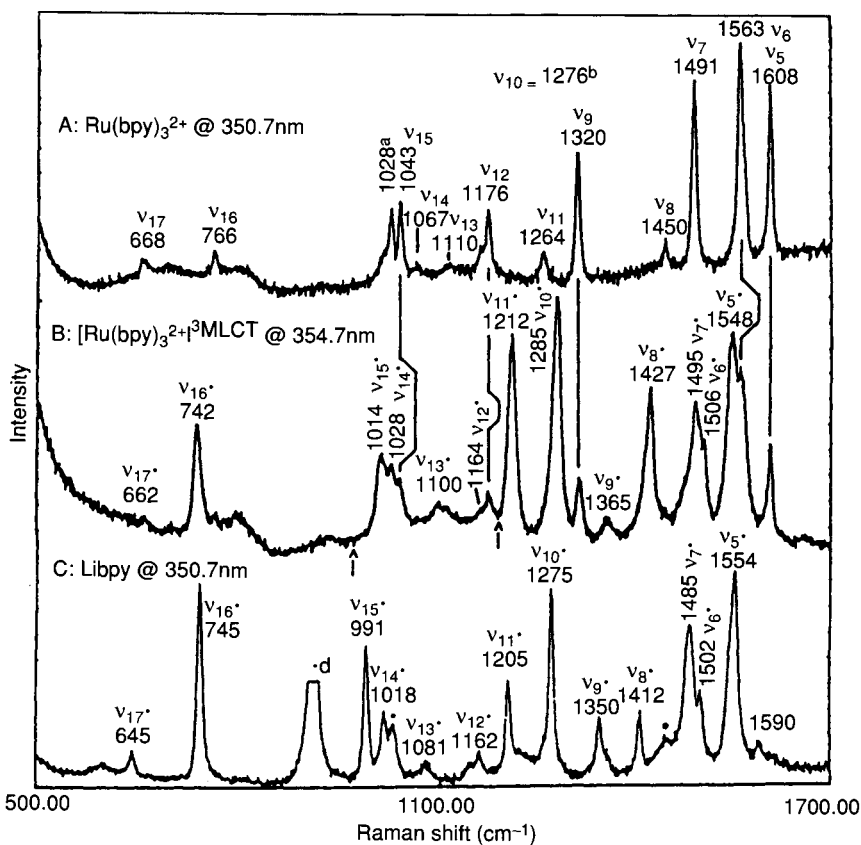


Figure 3-26 Resonance Raman (RR) and time-resolved resonance Raman (TR^3) spectra of $[\text{Ru}(\text{bpy})_3]^{2+}$. (a) RR spectrum using 350.7 nm excitation (Ar^+ laser); (b) TR^3 spectrum using 354.7 nm excitation; (c) RR spectrum of Li(bpy) using 350.7 nm excitation (Ar^+ laser). (Reproduced with permission from Ref. 84. Copyright 1990 American Chemical Society.)

Technically, Raman spectroscopy is more difficult to apply to low-temperature matrices than IR spectroscopy for the following reasons (90, 91): (1) Since Raman signals are inherently weak, relatively high concentrations of the sample or relatively wide slit widths are required. The former may cause the formation of dimeric and polymeric species, while the latter leads to the loss of resolving power of the monochromator. (2) If one increases the laser power to obtain stronger Raman signals, the matrix temperature will rise because of local heating by the laser beam, and this will accelerate the diffusion of solute molecules in the matrix. (1) and (2) can be circumvented if Raman spectra are obtained under resonance conditions (Section 1.15 and the following examples). (3) The quality of the Raman spectra obtained depends on the quality of the matrix prepared; “clear matrices” give better results than “frosty matri-

ces.” However, preparation of the former is time-consuming. (4) The matrix itself or oil contamination from the diffusion pump may cause fluorescence. In spite of these problems, matrix isolation Raman spectroscopy has advantage over its IR counterpart, as listed in Section 1.8. The first matrix isolation laser-Raman experiment was carried out by Shirk and Claassen (92) in 1971.

3.6.2 INSTRUMENTATION

The experimental setup for matrix Raman spectroscopy is essentially the same as that for matrix IR spectroscopy. The major difference lies in optical geometry. Namely, backscattering geometry must be employed in Raman spectroscopy since the matrix gas and sample vapor are deposited on a cold metal (Cu, Al) surface. Figure 3-27 shows the optical arrangement

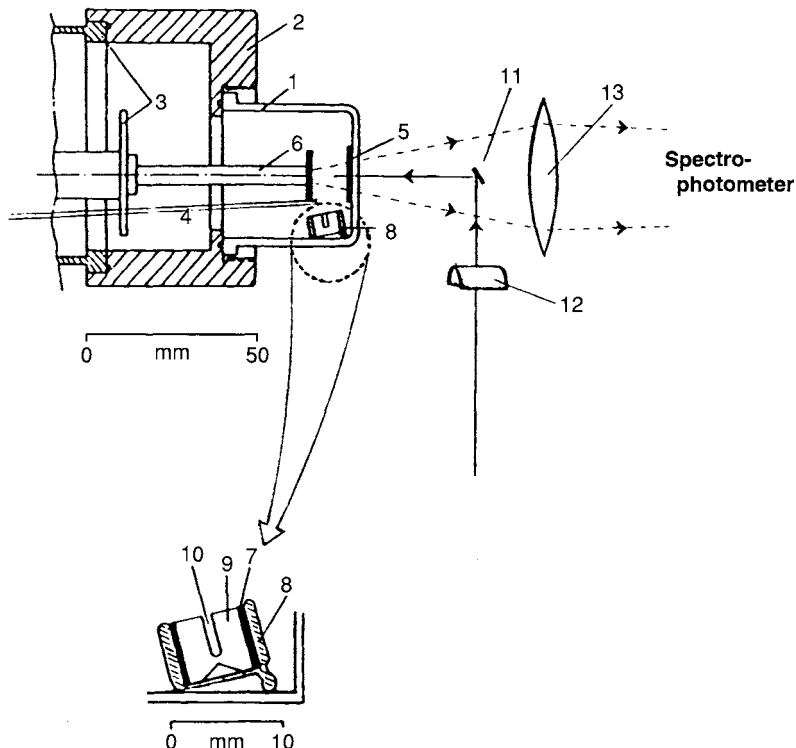


Figure 3-27 Schematic drawing of matrix-isolation apparatus for resonance Raman measurements. 1, glass envelope; 2, aluminum sleeve; 3, refrigerator; 4, gas line; 5, steel screen; 6, cold tip; 7, aluminum radiation shield; 8, Pyrex cup; 9, spectroscopic-grade spark graphite rod; 10, Pyrex capillary tube with sample; 11, small mirror; 12, cylindrical lens; 13, collecting lens. 5 is placed to prevent sample deposition in the optical path. It must be removed from the path by using an external magnet once sample deposition on 6 is completed.

used by Proniewicz *et al.* (93). Here, the miniature oven technique (94) was employed to vaporize the solid samples, and a cylindrical lens was used to produce a line-focused image on the matrix so that the local heating effect due to the laser beam is minimized (Section 2.7). As stated in Section 1.9, depolarization ratios are highly important in making band assignments in Raman spectra. These values can be obtained in inert gas matrices, although their values are somewhat higher than true values. For example, the ρ value for the totally symmetric mode of CCl_4 at 459 cm^{-1} in an Ar matrix is ~ 0.14 , although it should be close to zero (95). This is largely caused by scrambling of the polarized scattered light by the matrix and the lack of complete randomization of molecular orientation in a frozen matrix.

3.6.3 APPLICATIONS

Since the results obtained by matrix isolation Raman spectroscopy have been reviewed extensively (88–90), only two typical examples are discussed here to show the utility of this technique. It should be noted that both works took advantage of resonance Raman spectroscopy to detect Raman signals using low laser power.

Andrews and co-workers (96) studied IR and resonance Raman spectra of alkali metal atom–halogen reaction products in inert gas matrices. For example, these workers (96) reacted Cs atom vapor with Cl_2/Ar (1/100) to produce $\text{Cs}^+(\text{Cl}_2)^-$. This $(\text{Cl}_2)^-$ ion has an absorption maximum near 365 nm that tails out to 500 nm. Thus, the 457.9 nm line of an Ar-ion laser (75 mW) was used to resonance-enhance the $(\text{Cl}_2)^-$ vibration. As seen in Fig. 3-28, this anion, $[\text{Cl}_2]^-$, exhibits its fundamental at 259.0 cm^{-1} followed by a long series of overtones up to the eighth ($1,984.5\text{ cm}^{-1}$). Each band is accompanied by a side band due to its isotopic counterpart, $(^{35}\text{Cl}^{37}\text{Cl})^-$ on the low-frequency side, and the intensities of both overtone series decrease progressively in going to the higher overtone. As discussed in Section 1.15, this behavior is typical of the *A*-term resonance. The frequencies corrected for anharmonicity, anharmonicity constant and dissociation energy have been calculated based on the observed frequencies of the overtone series.

In some cases, matrix-isolation laser-Raman spectroscopy can be utilized to produce unstable species via laser photolysis and to measure their resonance Raman spectra simultaneously in the same matrix using the same laser. For example, Proniewicz *et al.* (93) measured the resonance Raman spectra of $\text{Fe}(\text{TPP}-d_8)$ ($\text{TPP}-d_8$: d_8 analogue of tetraphenylporphyrinato anion) in O_2 matrices at $\sim 30\text{ K}$ using the 406.7 nm line of a Kr-ion laser. As the first step, two types of O_2 adducts are formed via co-condensation of $\text{Fe}(\text{TPP}-d_8)$ vapor with O_2 .

The end-on type exhibits the $\nu(\text{O}_2)$, $\nu(\text{Fe}-\text{O}_2)$ and $\delta(\text{Fe}-\text{O}-\text{O})$ at 1,195, 508 and 345 cm^{-1} , respectively, whereas the side-on type exhibits the $\nu(\text{O}_2)$ and

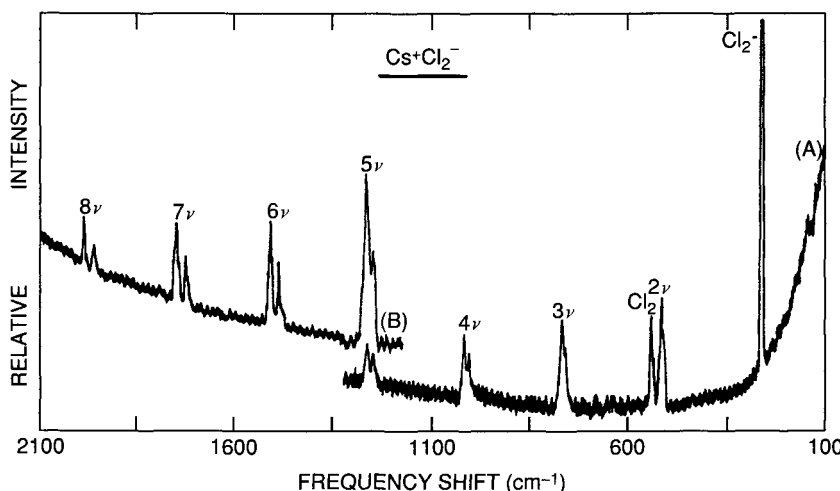
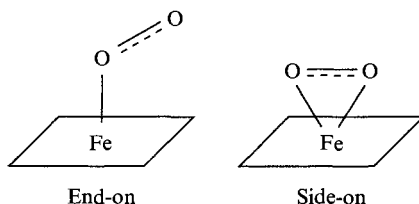


Figure 3-28 Resonance Raman spectrum of matrix-trapped $\text{Cs}^+ \text{Cl}_2^-$ (75 mW, 457.9 nm excitation). (A) 0.3×10^{-9} A range, 3-s rise time; (B) 0.1×10^{-9} A range, 10-s rise time (reproduction with permission from Ref. 96. Copyright 1975 American Chemical Society.)



$\nu_a(\text{Fe}-\text{O})$ at $1,105$ and 407 cm^{-1} , respectively. These bands are seen in Fig. 3-29A, which was obtained by using only 0.2 mW laser power.

As the laser power is increased, however, all these bands become weaker and disappear almost completely at 8 mW . In contrast, the bands at 853 and 815 cm^{-1} , which were originally weak, become stronger with increasing laser power. The latter two bands can be assigned to the $\nu(\text{Fe}=\text{O})$ of oxyferrylporphyrin and its π -cation radical, respectively, which are produced by the $\text{O}-\text{O}$ bond cleavage of the dioxygen adducts mentioned earlier. The 815 cm^{-1} band becomes weaker in going from trace C to D because the π -cation radical is converted to the non- π -cation radical at higher laser power. All of the preceding band assignments have been confirmed by $^{16}\text{O}_2/^{18}\text{O}_2$ and $^{54}\text{Fe}/^{56}\text{Fe}$ substitutions, and oxygen isotope scrambling techniques.* As will be shown

*In oxygen isotope scrambling experiments, a mixture of $^{16}\text{O}_2/^{16}\text{O}^{18}\text{O}/^{18}\text{O}_2$ ($\sim 1/2/1$ ratio) is reacted with iron porphyrin. Such a mixture can be obtained by electrical discharge of an equimolar mixture of $^{16}\text{O}_2$ and $^{18}\text{O}_2$.

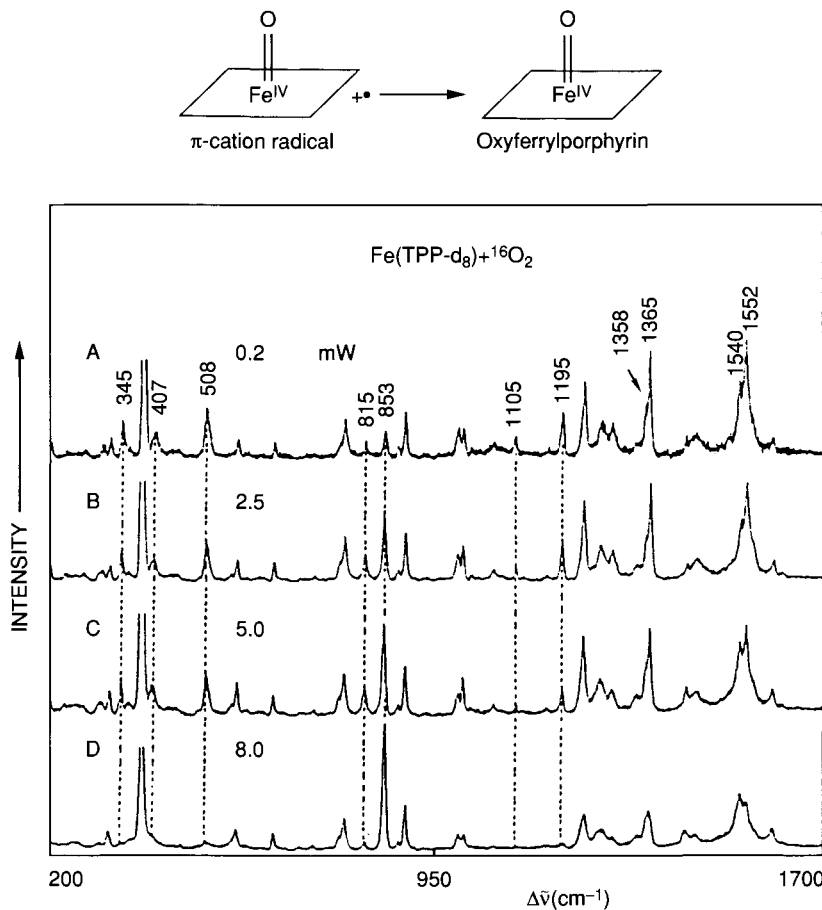


Figure 3-29 Resonance Raman spectra of $\text{Fe}(\text{TPP}-d_8)$ co-condensed with $^{16}\text{O}_2$ at 30K (406.7 nm excitation). (a) 0.2; (b) 2.5; (c) 5.0; (d) 8.0 mW. These spectra are composites of four sections measured separately. (Reproduced with permission from Ref. 93. Copyright 1991 American Chemical Society.)

in Section 6.1.2, oxyferrylporphyrin and its π -cation radical serve as model compounds of horseradish peroxidase Compounds II and I, respectively.

3.7 2D Correlation Raman Spectroscopy

3.7.1 PRINCIPLES

The concept of two-dimensional (2D) correlation spectroscopy was originally developed by Noda (97) and has been applied to a number of systems to

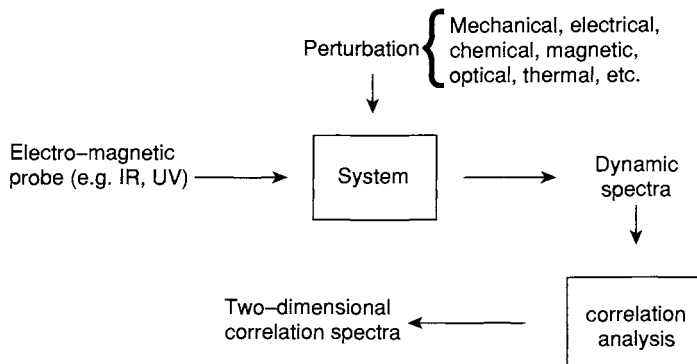


Figure 3-30 General scheme for obtaining 2D correlation spectra. (Reproduced with permission from Ref. 98)

separate overlapped bands, to make band assignments, and to study intensity variations of individual bands due to external perturbations (98). Figure 3-30 illustrates a general scheme of 2D correlation spectroscopy. The first step is to measure a series of spectra (IR, Raman, UV etc.) of a system by changing the external perturbation (temperature, pressure, concentration etc.). Then, a series of dynamic spectra are calculated by subtracting a reference spectrum from each perturbed spectrum. An average of observed spectra is generally used as the reference spectrum. In other words, a set of dynamic spectra shows intensity deviations from the standard spectrum as the magnitude of the applied perturbation is varied. Through mathematical manipulations (97, 98), the function, $X(v_1, v_2)$, which correlates the intensities of the bands at v_1 and v_2 , can be derived from the dynamic spectra. The results are expressed as:

$$X(v_1, v_2) = \phi(v_1, v_2) + i\psi(v_1, v_2)$$

The functions, ϕ and ψ , are called the synchronous and asynchronous 2D intensity correlation functions, respectively. These functions represent the overall similarity and dissimilarity, respectively, between two intensity variations at v_1 and v_2 caused by changing the magnitude of the perturbation. The results are plotted on two orthogonal axes (v_1 and v_2) with the spectral intensity plotted on the third axis normal to the 2D spectral plane. Figures 3-31A and 3-31B illustrate schematic contour maps of a synchronous and an asynchronous 2D correlation spectrum, respectively, where + and - signs indicate the directions of the contour peaks relative to the 2D spectral plane.

The synchronous spectrum (Fig. 3-31A) is symmetric with respect to the diagonal line corresponding to coordinates $v_1 = v_2$. Several peaks (A, B, C and D) on this line are called "autopeaks" which are always positive. The stronger the peak, the larger the variation of its band intensity due to external

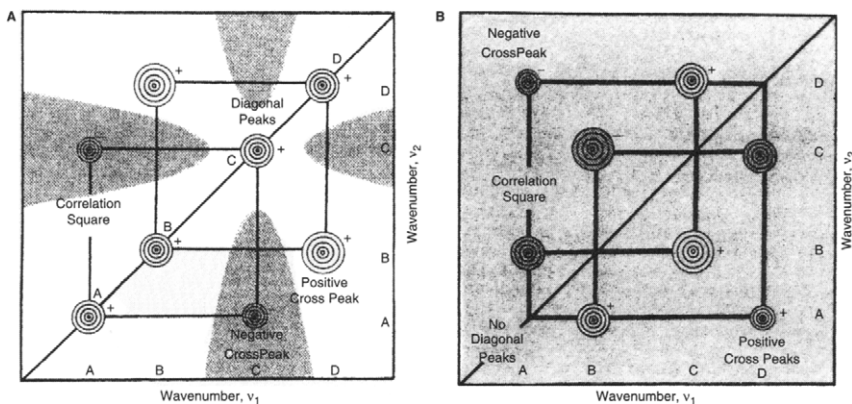


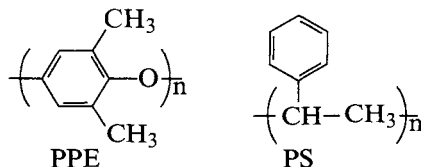
Figure 3-31 Schematic contour maps of a synchronous (A) and an asynchronous (B) 2D correlation spectra. (Reproduced with permission from Ref. 98.)

perturbation. Off-diagonal peaks are called “cross peaks” and represent simultaneous or coincidental changes of band intensities at v_1 and v_2 . In Fig. 3-31A, two bands at A and C as well as those at B and D are synchronously correlated. The positive cross peak indicates that the intensities of the two bands (B and D) increase or decrease simultaneously, whereas the negative cross peak indicates the opposite trend; the intensity of one band (A or C) is increasing while the other is decreasing.

An asynchronous spectrum shown in Fig. 3-31B is antisymmetric with respect to the diagonal line, and has “cross peaks” for a pair of bands such as (A, B), (A, D), (B, C) and (C, D) but no “autopeaks”. These “cross peaks” appear when the intensities of the two bands change out of phase (i.e. delayed or accelerated) with each other. The sign of the “cross peaks” is positive or negative when the intensity change at v_1 occurs predominantly before or after that at v_2 , respectively. In Fig. 3-31B, the intensity changes (increase or decrease) at bands A and C occur after changes at B and D.

3.7.2 APPLICATIONS

Ozaki and co-workers (99) applied 2D-FT Raman correlation spectroscopy to examine conformational changes and specific interactions in blends of atactic polystyrene (PS) and poly(2,6-dimethyl-1,4-phenylene ether) (PPE).



In this case, the varying PS/PPE ratio is regarded as the external perturbation. Figure 3-32A shows the synchronous correlation spectrum obtained by using a set of blends containing PS and PPE polymers at the ratios of 100/0, 90/10 and 70/30. (The average spectrum is drawn along both axes). The band at 1583 cm^{-1} is known to be a phenyl ring stretching mode of PS. According to the general rules given above, the positive cross peaks at (1602 , 1583 cm^{-1}) imply that the band at 1602 cm^{-1} is also due to PS, and the negative cross peaks at (1378 , 1583 cm^{-1}) and (1305 , 1583 cm^{-1}) indicate that the bands at 1378 and 1305 cm^{-1} originate in PPE. Similarly, positive cross peaks at (1378 , 1590 cm^{-1}) and (1305 , 1614 cm^{-1}) bands imply that the bands at 1590 and 1614 cm^{-1} are due to PPE. The bands at 1475 and 1428 cm^{-1} are also assigned to PPE based on the same reasoning. The ring stretching vibrations of PS and PPE are seriously overlapped in the $1620 \sim 1580\text{ cm}^{-1}$ region of the blend spectra. Thus, 2D correlation spectroscopy is highly effective in separating overlapped bands which cannot be resolved by conventional one-dimensional spectroscopy. Pure PS polymer exhibits bands of moderate-weak intensities at 1448 and 1329 cm^{-1} which are due to the CH_2 bending and CH_2 wagging modes, respectively. However, neither "auto" nor "cross" peaks of these vibrations are seen in Fig. 3-32A. This may suggest that the main chain CH_2 skeletal conformation undergoes some changes with the decrease in the PS content in the blends.

Figure 3-32B shows the corresponding asynchronous correlation spectrum. The positive cross peaks at $(1614, 1602 \text{ cm}^{-1})$, $(1590, 1602 \text{ cm}^{-1})$, $(1305, 1602 \text{ cm}^{-1})$ and $(1305, 1583 \text{ cm}^{-1})$ imply that intensity changes of the bands at 1614 , 1590 and 1305 cm^{-1} (ring stretch of PPE) occur predominantly

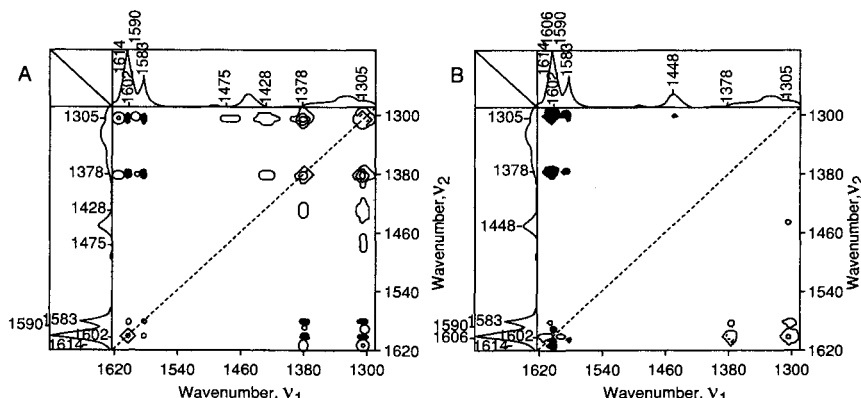


Figure 3-32 Synchronous (A) and asynchronous (B) 2D FT-Raman spectra in the range 1620~1290 cm⁻¹ constructed from the spectra of a set of blends containing PS and PPE polymers at the ratios of 100/0, 90/10 and 70/30. Black peaks indicate negative contours. (Reproduced with permission from Ref. 99.)

at higher PPE contents relative to the 1602 and 1583 cm^{-1} bands (ring stretch of PS). Since these ring vibrations are influenced only by strong interactions, specific interaction of the phenyl rings between PS and PPE must be considered. The positive cross peaks at (1378, 1602 cm^{-1}) and (1378, 1583 cm^{-1}) imply that the intensity variation of the 1378 cm^{-1} band (CH_3 symmetric deformation of PPE) occurs after those at 1602 and 1583 cm^{-1} bands (ring stretch of PS). Thus, the CH_3 group of PPE also interacts with the phenyl group of PS in the blends. The 1606 cm^{-1} band in Fig. 3-32B does not appear in Fig. 3-32A. This band cannot be attributed to either PS or PPE. It must be a “new” band resulting from blending.

3.8 Raman Imaging Spectrometry

3.8.1 PRINCIPLES

Spectra images consist of spectra measured at each spatial location on a sample. They are often referred to as hyperspectral images or a spectral data cube. In the case of Raman images, Raman spectra are measured at the various spatial locations. After all of the data are collected, it is possible to display individual Raman spectra for each spatial location or to display a false color image based on the intensities at a selected Raman frequency. In the latter representation, the intensities at a selected Raman frequency for each of the spatial locations are assigned to a color correlating to the magnitude of the scattering intensity. For example, low intensities might be assigned to dark blue and high intensities to red with the in-between spectral colors correlating to the medium intensities. A false color image at a selected frequency is often referred to as an *image slice* of the data cube.

The ability to obtain Raman images of chemical and biological samples is of great importance to the scientific community. The improvements and increased use of charge couple devices (CCD) for detection of Raman spectra has made such measurements practical. To obtain an image at a certain Raman frequency, a filter corresponding to the Raman shift could be placed in front of the CCD camera. The observed intensities of the light transmitted by the filter are then converted to a false color image and displayed. However, to obtain a full Raman spectrum at each of the pixels it is necessary to scan each of the spectra at each spatial location. Ideally, one should scan all of the spectra (i.e., at each of the pixels) at the same time, otherwise the measurements would require excessive observation times.

3.8.2 INSTRUMENTATION

Several devices have been proposed for measuring the full Raman data cube in a reasonable period of time. Currently, the two promising methods are

liquid crystal tunable filters (LCTF) (100) and acoustic optical tunable filters (AOTF) (101, 102). We will describe the two methods and show typical examples of their application.

LCTFs are notch filters, which can be controlled electronically to transmit selected wavelengths. These filters are made using a stack of linear polarizers, each separated by tunable retardation liquid crystal films on a quartz retardation plate. Anisotropic, birefringent materials such as quartz and certain liquid crystals have distinct crystal axes each possessing a different refractive index. When light enters a birefringent crystal normal to the non-equivalent axes, it is refracted into two rays each polarized with the directions oriented at right angles to one another. When linearly polarized light enters a quartz crystal with the optic axes of the crystal at 45° relative to the linear polarization direction, the incident light is divided into two equal amplitude rays, the ordinary rays and the extraordinary rays, which travel at different velocities through the birefringent crystal. The two rays recombine as they exit the crystal. However, because they have traveled through the crystal with different velocities, an interference pattern is formed, which depends upon the birefringence of the crystal, the thickness of the crystal and the wavelength of the light.

A diagram of a four stage LCTF is shown in Fig. 3-33 with white light entering from the top and a single wavelength exiting from the bottom. Each stage consists of a linear polarizer, an electronically controllable liquid crystal, and a birefringent quartz crystal. Simulated transmittance through each stage is shown in Fig. 3-34. The first stage has the longest path quartz crystal and produces an interference pattern with the largest peak-to-peak separation as shown in Fig. 3-34. Each stage contains a quartz crystal with a shorter pathlength, which causes a decrease in the peak-to-peak separation in the interference pattern. Ideally, enough stages would be used so that the output is a single peak with a very small half-band width. In the present example, the most intense output is at 500 nm, but there are weaker intensities to either side of this band. Additional stages could produce a perfectly flat output on both sides of the single peak at 500 nm.

The birefringence of the liquid crystals is controlled electronically. Either ferroelectric or nematic liquid crystals are used for the tunable retarders. By varying the input voltage to the liquid crystals the birefringence of that material can be changed to vary the retardation and change the interference pattern in such a way as to scan the spectral region of interest.

AOTFs (101, 102) work on a different principal. This type of filter functions by the interaction of light with a traveling acoustic wave in an anisotropic medium. Both crystals and polymers have been used for the anisotropic medium. An acoustic transducer is bonded to one end of the material and an

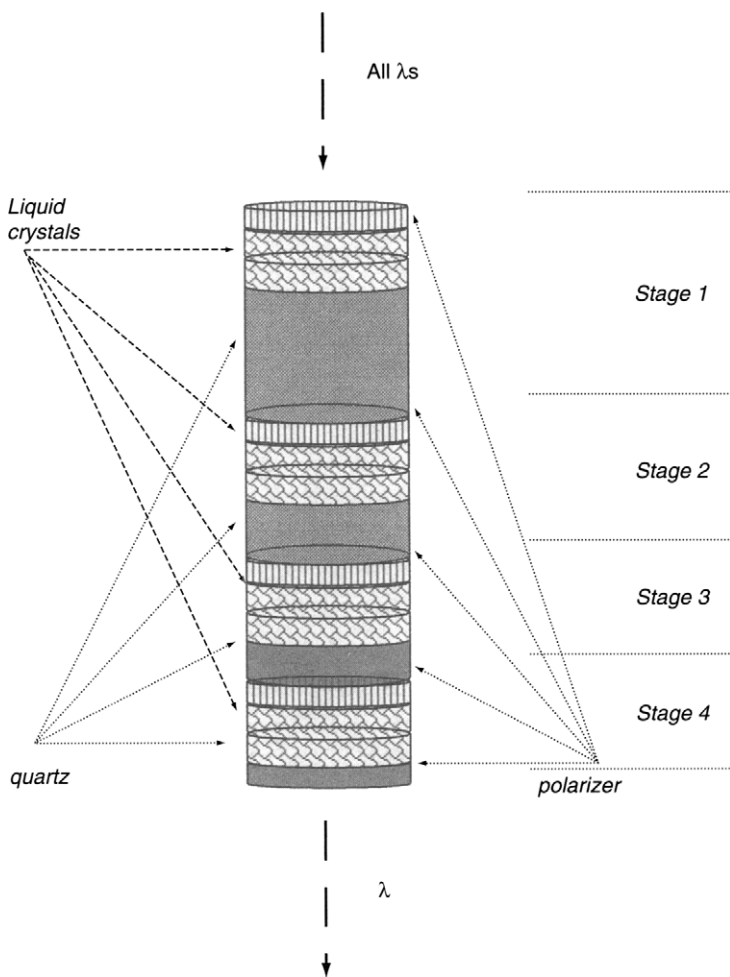


Figure 3-33 Four Stage Liquid Crystal Tunable Filter.

acoustic absorber to the other end as shown in Fig. 3-35 (103). The acoustic signals are generated from a RF source attached to the transducer. The acoustic wave moves through the crystal by forming a compressing wave, which increases the density of the material index as it moves. The effect of alternately increasing and decreasing the density of the material causes an alternating change in the refractive index across the crystal. Thus, the material resembles a transmission grating with the facets of the grating moving through the material. The waves are shown in Fig. 3-35 as moving from bottom to top.

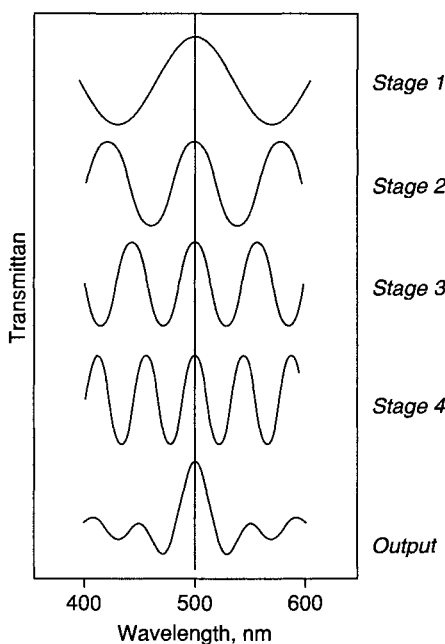


Figure 3-34 Transmission through each of 4 stages in an LCTF and the total output of the 4 stages.

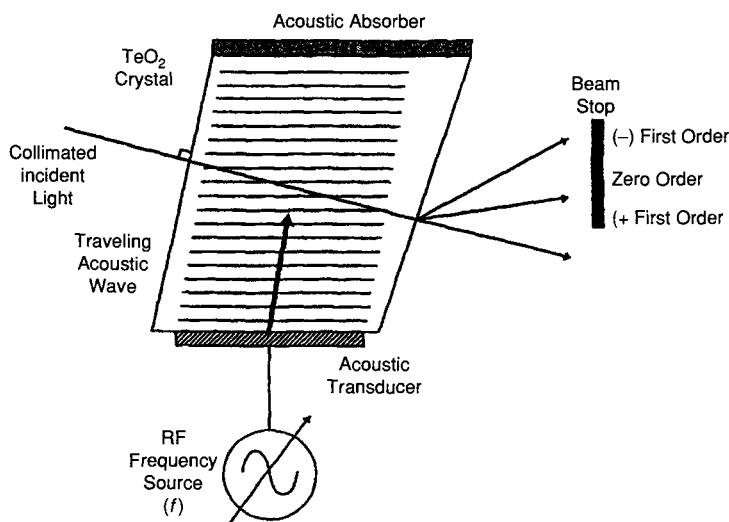


Figure 3-35 AOTF Crystal showing the RF source, the acoustic transducer, the Acoustic absorber, the Zero order ray and the two 1st order rays. (Reproduced with permission from Ref. 103.)

White light entering the crystal from the left interacts with the acoustic wave to form two diffracted waves polarized 90° to each other and exiting at different angles. The AOTF only diffracts one specific wavelength of light, so that it acts more like a filter than a diffraction grating. The intensity of the diffracted light is concentrated in the two first order rays. The zero order wave and one of the diffracted waves are blocked by a beam stop; only the second diffracted wave is transmitted and this corresponds to a single wavelength.

AOTFs are scanned by varying the frequency of the RF source. It can be switched between any randomly selected wavelengths in microseconds with bandwidths as small as 0.1 nm. Transmission efficiencies are up to 98% with the intensity divided between the (+) and (-) beams. Multiple wavelengths can be observed simultaneously by superimposing two or more RF signals onto the transducer. Most common types of AOTFs are made from TeO_2 . The TeO_2 crystals can operate from 400 to 1900 nm.

3.8.3 APPLICATIONS

An optical schematic of a Raman spectrometer built around a AOTF wavelength selector is shown in Fig. 3-36 (101). The sample is illuminated with a laser source. Raman scattering is collected at 90° from the laser and collimated by lens L2, pass through aperture A1 and into the AOTF. One of the diffracted beams and the zero order beam are blocked by a beam stop and the other diffracted beam is passed through a second aperture, A2, through a holographic filter, F2 and focus onto the CCD detector array by lens L3. This imaging spectrometer was used to measure Raman images of a model biological system consisting of a mixture of dipalmitoylphosphatidylcholine (DPPC) and L-asparagine. The AOTF spectrum of DPPC in the CH stretching region is compared to a spectrum measured with a scanning grating monochromator in Fig. 3-37. The resolution of the AOTF spectrum was

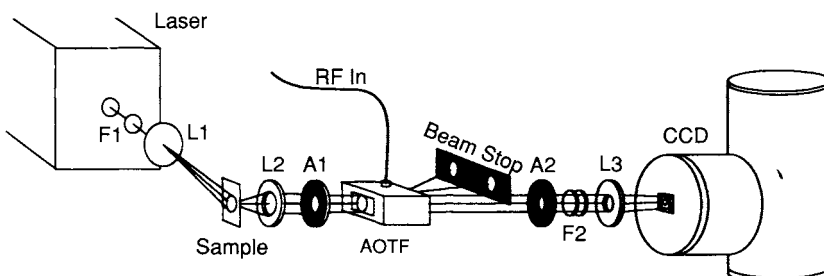


Figure 3-36 Raman spectrometer built around an AOTF. The sample is mounted on a microscope slide positioned 45° degrees relative to the incident laser. Raman scattering is collected and spectrally filtered with the AOTF. Holographic Raman filters are placed after the AOTF to eliminate intense Rayleigh scatter before the image is focused onto a liquid-nitrogen-cooled CCD. (Reproduced with permission of Ref. 101.)

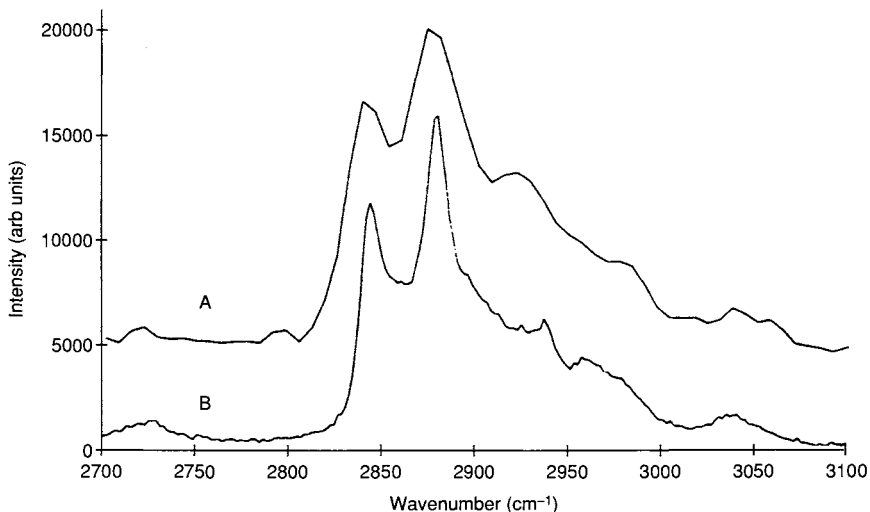


Figure 3-37 Raman spectra of DPPC in the CH stretching region: (a) measured with an AOTF followed by Fourier self-deconvolution; (b) measured with a dispersive scanning monochromator at 5 cm^{-1} resolution. The spectra show the features due to methyl and methylene vibrations arising from both the hydrocarbon chain and headgroup portions of the lipid. (Reproduced with permission from Ref. 101.)

enhanced with the use of Fourier self-deconvolution. The spectra exhibit similar contours. The original AOTF spectra of DCCP and L-asparagine in the CH and NH stretching regions obtained during the image measurement are shown in Fig. 3-38. Two Raman images were generated using the CH band at 2880 cm^{-1} and the NH at 3390 cm^{-1} , respectively. From the Raman images it was possible to identify regions of high lipid concentrations and the regions of high protein concentrations.

An example of LCTF Raman images is shown in Fig. 3-39 (100). Mixed oxides (MOX) of PuO_2 and UO_2 are used as commercial nuclear fuels. Surrogate MOX materials are prepared from CeO_2 in place of PuO_2 . Part of the difficulty with PuO_2 is the need to remove a Ga phase. Thus surrogate MOX materials have been used to attempt to find suitable means for removing the Ga phase. Raman images of surrogates have been measured following reductive heating to remove the Ga phase. Raman spectra and images of a typical surrogate pellet are shown in Fig. 3-39. Most of the pellet is CeO_2 ; however, a Ga compound is shown by the white area in the A image. This image was a slice of the data cube at 292 cm^{-1} , which is assigned to a Ga species. The B image is a slice of the data cube at 464 cm^{-1} and the white regions correspond to CeO_2 with the dark (or black) corresponding to the Ga species. In this example, the usefulness of Raman images is clearly demonstrated.

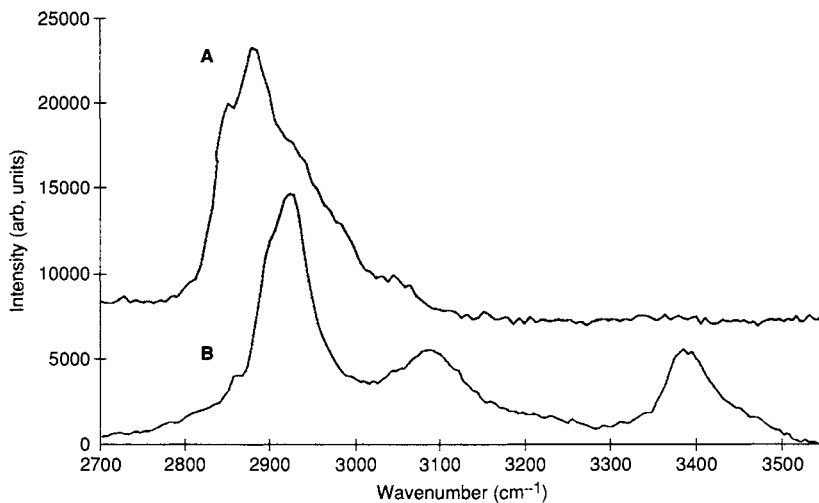


Figure 3-38 AOTF Raman spectra of (A) DPPC and (B) L-asparagine in the CH and NH stretching Region. These spectra were obtain from the AOTF Raman image data at pixels corresponding to DPPC and L-asparagine, respectively. (Reproduced with permission from Ref. 101.)

3.9 Nonlinear Raman Spectroscopy

As stated in Chapter 1, the more accurate expression of the induced dipole moment (P) is

$$P = \alpha E + \frac{1}{2} \beta E^2 + \frac{1}{6} \gamma E^3 + \dots \quad (3-1)$$

Here, E is the strength of the applied electric field (laser beam), α the polarizability and β and γ the first and second hyper-polarizabilities, respectively. In the case of conventional Raman spectroscopy with CW lasers ($E, 10^4 \text{ V cm}^{-1}$), the contributions of the β and γ terms to P are insignificant since $\alpha \gg \beta \gg \gamma$. Their contributions become significant, however, when the sample is irradiated with extremely strong laser pulses ($\sim 10^9 \text{ V cm}^{-1}$) created by Q-switched ruby or Nd-YAG lasers (10–100 MW peak power). These giant pulses lead to novel spectroscopic phenomena such as the hyper-Raman effect, stimulated Raman effect, inverse Raman effect, coherent anti-Stokes Raman scattering (CARS), and photoacoustic Raman spectroscopy (PARS). Figure 3-40 shows transition schemes involved in each type of nonlinear Raman spectroscopy. (See Refs. 104–110.)

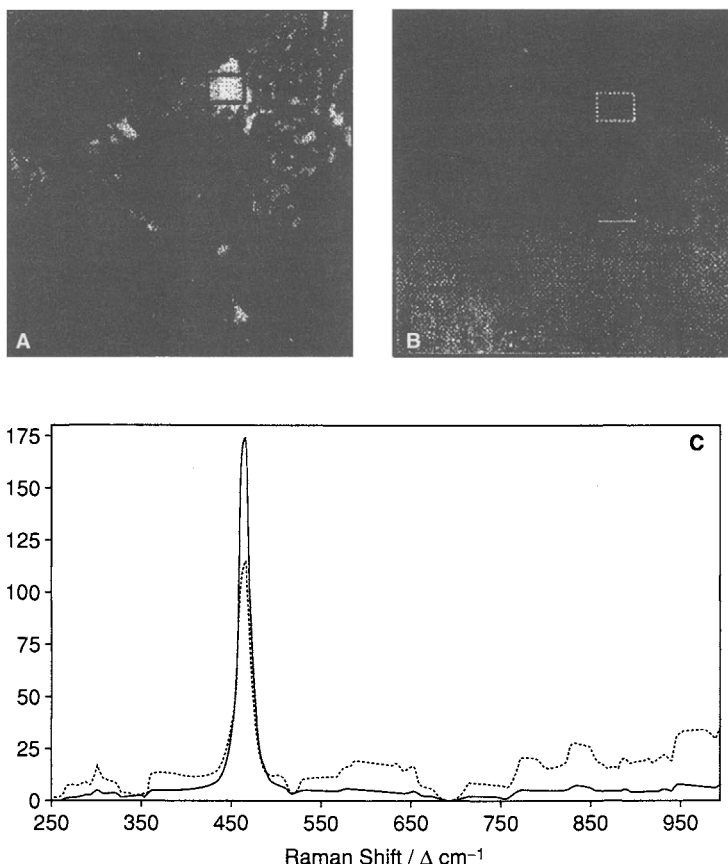


Figure 3-39 Raman spectra and Raman images of a sintered metal oxide pellet containing Ga_2O_3 in a CeO_2 matrix. The dashed spectrum in C corresponds to the dashed boxes in the A and B images. Image A is a Raman image slice for a band at 292 cm^{-1} , which is associated with Ga component in A. Image B is a Raman image slice for the band at 464 cm^{-1} , which is due to CeO_2 . Spatial resolution of the images were improved using the multivariate technique of cosine correlation analysis. (Reproduced with permission from Ref. 100.)

3.9.1 HYPER-RAMAN EFFECT

When the sample is illuminated by a giant pulse of frequency v , the scattered radiation contains frequencies of $2v$ (hyper-Rayleigh scattering) and $2v \pm v_M$ (Stokes and anti-Stokes hyper-Raman scattering), where v_M is a frequency of a normal vibration of the molecule. Clearly, this is Raman scattering caused by two incident photons ($2v$) of the laser. Experimentally, this

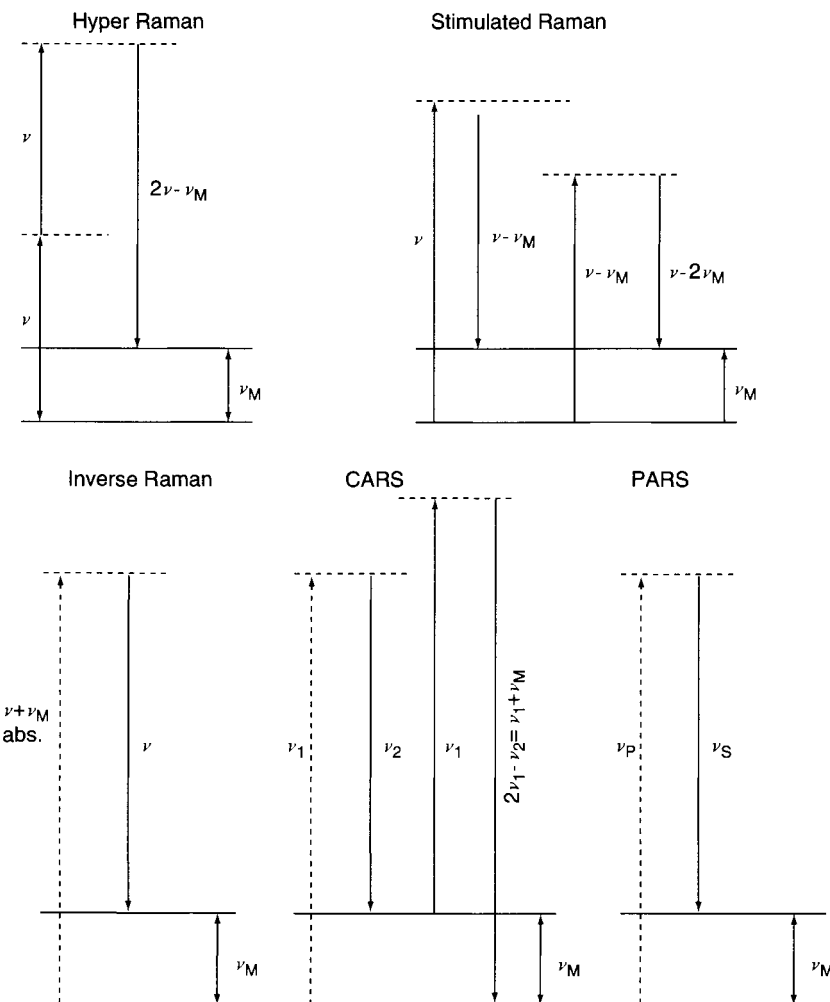


Figure 3-40 Transition schemes involved in nonlinear Raman spectroscopy.

phenomenon is rather difficult to observe since only $\sim 10^{-12}$ of the radiation (ν) is converted to $2\nu \pm \nu_M$ and since the intensity of the incident radiation can be increased only to a certain limit beyond which the stimulated Raman scattering (see below) becomes dominant. Hyper-Raman spectroscopy has several advantages over normal Raman spectroscopy because of a difference in selection rules. As already discussed in Section 1.7, a vibration is Raman-

Table 3-2 Selection Rules for IR, Raman and Hyper-Raman Spectra of Benzene (D_{6h})

Symmetry Species	μ	α	β	Number of Normal Modes
A_{1g}		$\alpha_{xx} + \alpha_{yy}, \alpha_{zz}$		2
A_{2g}				1
B_{1g}				0
B_{2g}				2
E_{1g}		$(\alpha_{yz}, \alpha_{zx})$		1
E_{2g}		$(\alpha_{xx} - \alpha_{yy}, \alpha_{xy})$		4
A_{1u}				0
A_{2u}	z		$\beta_{yyz} + \beta_{zxx}, \beta_{zzz}$	1
B_{1u}			$\beta_{xxx} - 3\beta_{xyy}$	2
B_{2u}			$\beta_{yyy} - 3\beta_{xxy}$	2
E_{1u}	(x, y)		$(\beta_{xxx} + \beta_{xyy},$ $\beta_{yyy} + \beta_{xxy})$ $(\beta_{zzx}, \beta_{yzz})$	3
E_{2u}			$(\beta_{yyz} - \beta_{zxx}, \beta_{xyz})$	2

active if at least one of the components of the polarizability tensor changes during the vibration. Similarly, a vibration is hyper-Raman active if one of the components of the hyper-polarizability tensor changes during the vibration. Table 3-2 compares symmetry properties of these two components for the point group D_{6h} (benzene). It is seen that some vibrations that are not IR or Raman-active become hyper-Raman-active (B_{1u} , B_{2u} , and E_{2u}). It is also seen that some Raman-active vibrations are not hyper-Raman-active (E_{1g} , E_{2g}), while all IR-active vibrations are hyper-Raman-active (A_{2u} , E_{1u}). Similar effects are noted for other point groups. Thus, the hyper-Raman spectrum contains all the frequency information obtained from an IR spectrum.

3.9.2 STIMULATED RAMAN EFFECT

In normal Raman scattering, laser (ν) irradiation on the sample results in “spontaneous” Raman scattering ($\nu - \nu_M$), which is very weak. If the electric field of the laser exceeds $\sim 10^9$ V cm⁻¹, the hyper-Raman scattering mentioned earlier is superseded by “stimulated” Raman scattering, which generates a strong coherent beam at Stokes frequency, ($\nu - \nu_M$) (105). Figure 3-41 shows a typical arrangement used for the observation of the stimulated Raman effect. Here, the giant laser radiation (ν) is focused on the sample (benzene), and the scattered light is observed along the direction of the

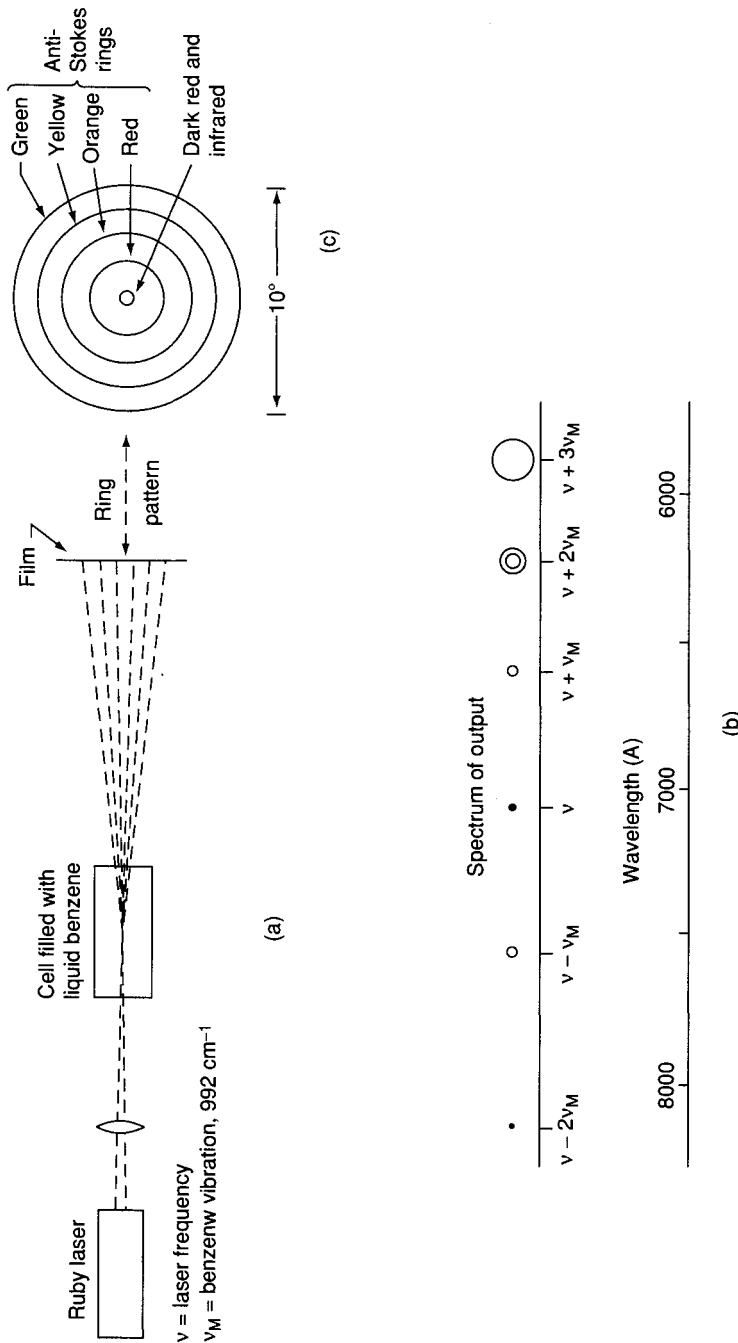


Figure 3-41 (a) Experimental setup for stimulated Raman spectroscopy, (b) a diagram showing the stimulated Raman spectrum of benzene, and (c) anti-Stokes rings of stimulated Raman spectrum of benzene. (Reproduced with permission from Ref. 104.)

incident beam. If a color-sensitive film is placed in the direction perpendicular to the incident beam, one observes the concentric colored rings shown in Fig. 3-41. Interestingly, only one normal mode (ν_M), which is the strongest in a normal Raman spectrum, is extremely strongly enhanced in the stimulated Raman effect. In benzene, it is the 992 cm^{-1} band (E_g). In fact, $\sim 50\%$ of the incident beam is converted into the first Stokes line, $\nu - \nu_M$ of this mode. Since this line is so intense, it acts as a source to excite the second Stokes line, $(\nu - \nu_M) - \nu_M = \nu - 2\nu_M$, and this line again acts as the source for the third Stokes line, and so forth. Thus, the concentric colored rings observed correspond to frequencies ν , $\nu - \nu_M$, $\nu - 2\nu_M$, $\nu - 3\nu_M$, and so forth. It should be noted that the $2\nu_M$ thus observed is exactly two times ν_M and not the first overtone of ν_M (no anharmonicity correction). The high conversion efficiency of the stimulated Raman effect can be used to generate many laser lines of a variety of frequencies (for example, the H_2 Raman shifter; see Section 2.2.5).

3.9.3 INVERSE RAMAN EFFECT

Suppose that a compound has a Raman-active vibration at ν_M . If it is illuminated by a probe laser (ν) simultaneously with a pump continuum covering the frequency range from ν to $\nu + 3,500\text{ cm}^{-1}$, one observes an absorption at $\nu + \nu_M$ in the continuum together with emission at ν . Clearly, the absorbed energy, $h(\nu + \nu_M)$, has been used for excitation ($h\nu_M$) and emission of the extra energy ($h\nu$). This upward transition is called the *inverse Raman effect* since the normal anti-Stokes transition occurs downward. Because the inverse Raman spectrum can be obtained in the lifetime of the pulse, it may be used for studies of shortlived species (Section 3.5). It should be noted, however, that the continuum pulse must also have the same lifetime as the giant pulse itself. Thus far, the inverse Raman effect has been observed only in a few compounds, because it is difficult to produce a continuum pulse at the desired frequency range.

3.9.4 COHERENT ANTI-STOKES RAMAN SPECTROSCOPY (CARS)

When the sample is irradiated by two high-energy laser beams with frequencies ν_1 and ν_2 ($\nu_1 > \nu_2$) in a collinear direction (Fig. 3-42), these two beams interact coherently to produce the strong scattered light of frequency $2\nu_1 - \nu_2$. If ν_2 is tuned to a resonance condition such that $\nu_2 = \nu_1 - \nu_M$ where ν_M is a frequency of a Raman-active mode of the sample, then a strong

light of frequency $2v_1 - v_2 = 2v_1 - (v_1 - v_M) = v_1 + v_M$ is emitted (Fig. 3-40). This multi-photon process is called *coherent anti-Stokes Raman spectroscopy (CARS)* (106).

The advantages of CARS include the following: (1) Since the CARS light ($v_1 + v_M$) is coherent and emitted in one direction with a small solid angle, it can be detected easily and efficiently without a monochromator. Furthermore, fluorescence interference can be avoided because of this directional property. (2) The CARS frequency ($v_1 + v_M$) is higher than v_1 or v_2 . Thus, it is on the anti-Stokes side of the pump frequency (v_1), whereas the fluorescence is on the Stokes side; hence, this condition also discriminates fluorescence. (3) Since CARS signals are very strong, gaseous compounds in very low concentrations can be detected. (4) Selection rules different from those of normal Raman spectroscopy are applicable to CARS. All Raman-active modes are CARS-active. In addition, many vibrations that are Raman-inactive and, in some cases, IR-inactive, become active in CARS. The main disadvantage of CARS is its high cost.

3.9.5 PHOTOACOUSTIC RAMAN SPECTROSCOPY (PARS)

The principle of photoacoustic Raman spectroscopy (107) is similar to that of CARS. When two laser beams, v_p (pump beam) and v_s (Stokes beam), impinge on a gaseous sample contained in a cell (Fig. 3-43), these two beams interact when the resonance condition, $v_p - v_s = v_M$, is met, where v_M is a frequency of a Raman-active mode. This results in the amplification of the Stokes beam and the attenuation of the pump beam. Each Stokes photon thus

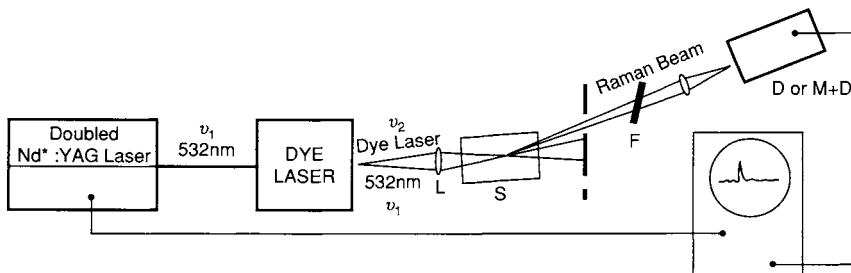


Figure 3-42 Initial apparatus for measuring anti-Stokes emission using a frequency-doubled Nd:YAG pumped dye laser. L is a short focal lens (3–4 cm); S is the sample; I is an iris for spatially filtering the two exciting beams; F is a wideband interference filter; D is the detector (usually a PIN diode); M is a monochromator (not usually necessary). Not shown are the PAR-160 box car integrator, chart recorder, and dye laser scan drive used to record spectra. (Reproduced with permission from Ref. 104.)

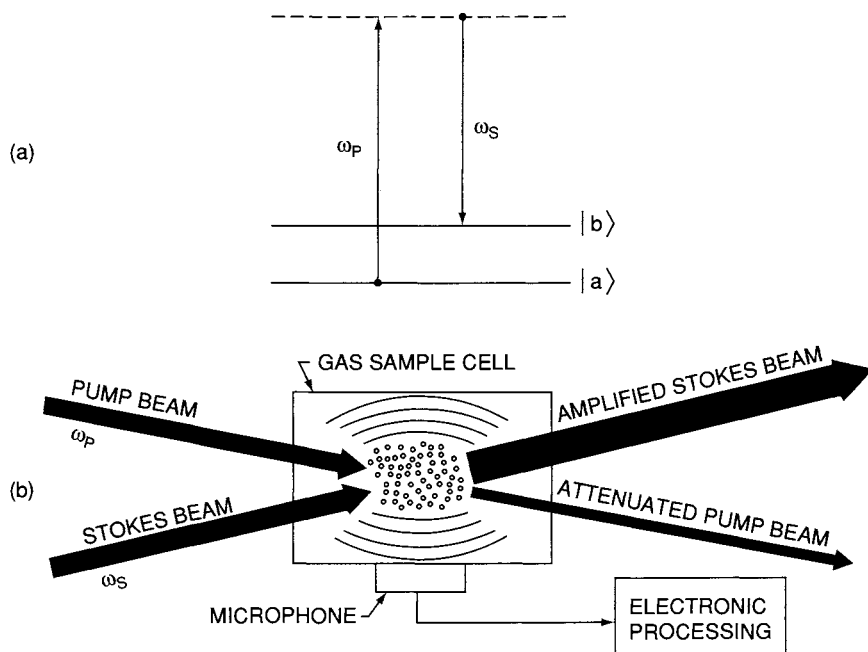


Figure 3-43 Schematic representation of the photoacoustic Raman scattering (PARS) process. (a) A simple energy level diagram illustrating the Raman interaction that occurs in the PARS process. (b) Basic elements of the PARS experimental arrangement. The pump beam is attenuated and the Stokes beam is amplified by the stimulated Raman process that takes place where the beams overlap in the gas sample cell. For each Stokes photon created by the Raman process, one molecule is transferred from the lower state to the upper state of the transition. Collisional relaxation of these excited molecules produces a pressure change that is detected by a microphone. (Reproduced with permission from Ref. 107.)

generated brings the molecule up to the excited state, and collisional deactivation of these excited state molecules increases their translational energy. This change in the translational energy results in a change in the pressure of the sample in the cell that can be detected by a microphone. Use of such an acoustic detective device is unique among spectroscopic techniques. By scanning v_s (using a dye laser), the pressure change is measured and converted into a spectrum. As an example, Fig 3-44 shows the rotational Raman spectrum of CO₂ obtained by the PARS. The absence of the strong Rayleigh band makes

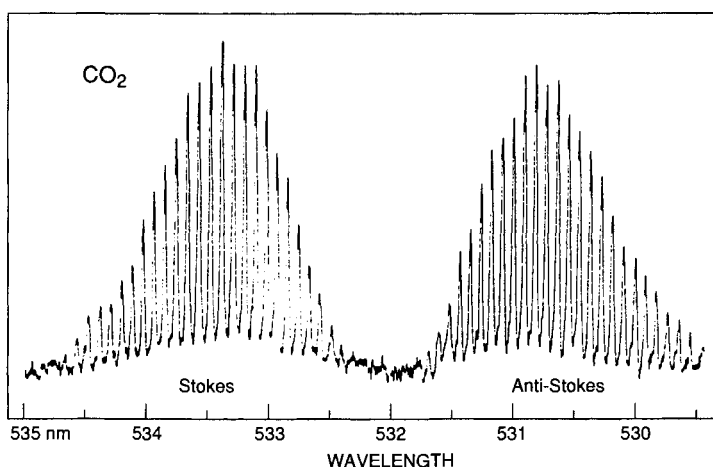


Figure 3-44 Photoacoustic rotational Raman spectrum of CO_2 at a pressure of 80 kPa (600 torr). The rotational line spacing is about 3.1 cm^{-1} . Laser powers of the pump and Stokes beams were 3.3 MW and 120 kW, respectively. (Reproduced with permission from Ref. 107.)

it particularly useful for the study of low-energy rotational transitions of gaseous compounds.

References

1. J. R. Ferraro, "Vibrational Spectroscopy at High Pressures—The Diamond Anvil Cell" pp. 1–264. Academic Press, New York, 1984.
2. J. A. Xu, H. K. Mao, and P. M. Bell, *Science* **232**, 1404 (1986); R. J. Hemley, P. M. Bell, and H. K. Mao, *Science* **237**, 605 (1987).
3. C. E. Weir, E. R. Lippincott, A. Van Valkenburg, and E. N. Bunting, *J. Res. Natl. Bur. Stand. Sec. A* **63**, 55 (1959).
4. R. A. Forman, G. J. Piermarini, J. D. Barnett, and S. Block, *Science* **176**, 284 (1972).
5. A. Jayaraman, *Science* **250**, 54 (1984).
6. M. G. Gonikberg, K. H. E. Stein, S. A. Unkholtm, A. A. Opekerinov, and V. T. Aleksanias, *Opt. Spectrosc. (Engl. Transl.)* **6**, 166 (1959).
7. C. Postmus, V. A. Maroni, and J. R. Ferraro, *Inorg. Nucl. Chem. Lett.* **4**, 269 (1968).
8. J. W. Brasch and E. R. Lippincott, *Chem. Phys. Lett.* **2**, 99 (1968).
9. T. P. Russell and G. P. Piermarini, *Rev. Sci. Instrum.*, **68**, 1835 (1997).
10. R. D. Markwell and I. S. Butler, *Can. J. Chem.*, **73**, 1019 (1995).
11. S. K. Sharma, H. K. Mao, P. M. Bell and J. A. Xu, *J. Raman Spectrosc.*, **16**, 350 (1985).
12. R. Pucci and G. Piccitto, "Molecular systems under high pressure," in "Proceedings of the II Archimedes Workshop on Molecular Solids under Pressure" (R. Pucci and G. Piccitto, eds.), Vol. 61, pp. 1–388. Elsevier, Amsterdam, 1991.
13. D. M. Adams, P. D. Hatton, A. C. Shaw, and T. K. Tan, *J. Chem. Soc. Chem. Commun.* 226 (1981).

14. E. Wigner and H. B. Huntington, *J. Chem. Phys.* **3**, 764 (1935).
15. F. V. Gigor'yev, S. B. Kormer, D. L. Mikhaylova, A. P. Tolochko, and V. D. Urlin, *Zh. Eksp. Teor. Fiz. Pisma Red.* **5**, 286 (1972).
16. H. K. Mao and R. J. Hemley, *Science* **244**, 1462 (1989); R. J. Hemley and H. K. Mao, *Science* **249**, 391 (1990).
17. J. H. Eggert, F. Moshary, W. J. Evans, H. E. Lorenzana, K. A. Goettel, J. F. Silvera, and W. C. Moss, *Phys. Rev. Lett.* **66**, 193 (1991).
18. A. L. Ruoff and C. A. Vanderborgh, *Chem. & Eng. News*, March 11, 1991, pp. 5–6.
19. C. Narayama, H. Lou, J. Orloff and A. L. Ruoff, *Nature*, **393**, 46 (1998).
20. W. J. Nellis, *Scientific American*, May, 2000, p. 84.
21. S. T. Weir, A. C. Mitchell and W. J. Nellis, *Phys. Rev. Lett.*, **76**, 1860 (1996).
22. J. R. Ferraro, *Coord. Chem. Rev.* **29**, 1 (1979).
23. J. R. Ferraro, *Coord. Chem. Rev.* **43**, 205 (1982).
24. J. R. Ferraro and L. J. Basile, *Appl. Spectrosc.* **28**, 505 (1974).
25. A. Jayaraman, *Rev. Mod. Phys.* **55**, 65 (1983).
26. A. Jayaraman, *Science* **250**, 54 (1984).
27. W. F. Sherman, *Bull. Soc. Chim. Fr.* **9–10**, 347 (1982).
28. W. F. Sherman, "Raman and infrared spectroscopy of crystals at various pressures and temperatures," in "Advances in Infrared and Raman Spectroscopy" (R. J. H. Clark and R. J. Hester, eds.), Vol. 6, Chapter 4, p. 158. Heyden, London, 1980.
29. H. G. Drickamer and C. W. Frank, "Electronic Transitions and the High Pressure Chemistry and Physics of Solids," p. 1. Chapman and Hall, London, 1973.
30. A. J. Melvegar, J. W. Brasch and E. R. Lippincott, "High pressure vibrational spectroscopy," in "Vibrational Spectra and Structure" (J. R. Durig, ed.), p. 51. Marcel Dekker, New York, 1972.
31. C. M. Edwards and I. S. Butler, *Coord. Chem. Rev.*, **199**, 1 (2000).
32. J. R. Ferraro, "Vibrational Spectroscopy at High External Pressures" in "The Handbook of Vibrational Spectroscopy" (P. R. Griffiths and co-eds.), Vol. 2, John Wiley, New York, 2002.
33. J. R. Ferraro and E. Van Valkenburg, *Spectroscopy*, **14**, 19 (1999).
34. M. Delhayé and P. Dhamelincourt, *J. Raman Spectrosc.*, **3**, 33 (1975).
35. G. J. Rosasco, E. S. Etz, and W. A. Cassatt, *Appl. Spectrosc.* **29**, 396 (1975).
36. G. J. Rosasco, in "Advances in Infrared and Raman Spectroscopy" (R. J. H. Clark and R. J. Hester, eds.), Vol. 7, Chapter 4, p. 223, and references therein. Heyden, London, 1980.
37. F. Adar, *Microchemical Journal* **38**, 50 (1988).
38. J. M. Lerner and F. Adar, *Laser Focus World*, Pennwell Publishing Co., Feb. 1989.
39. S. W. Lee, R. A. Condrate, Sr., N. Malani, D. Tammaro, and F. E. Woolley, "Considerations concerning the application of the Raman microprobe technique to the systematic analysis of bubbles in glass," *Spectrosc. Lett.* **23**(7), 945 (1990).
40. S. W. Lee and R. A. Condrate, Sr., "Raman microprobe investigation of bubbles formed in NaPO₃ glass from nitriding with ammonia," *J. Solid State Chem.* **98**, 423 (1992).
41. R. G. Messerschmidt and D. B. Chase, *Appl. Spectrosc.* **43**, 11 (1989).
42. Bruker, personal communication.
43. B. Schrader, in "Practical Fourier Transform Infrared Spectroscopy, Industrial and Laboratory Chemical Analysis" (J. R. Ferraro and K. Krishnan, eds.), p. 167. Academic Press, San Diego, 1990.
44. J. J. Blaha, "Raman microprobe spectroscopic analysis," in "Vibrational Spectra and Structure" (J. R. Durig, ed.), Vol. 10, p. 227. Elsevier, New York, 1981.
45. G. Turrell and J. Corset, "Raman Microscopy Developments and Applications", Academic Press, London, 1996.

46. G. J. Puppels, "Confocal Raman Microspectroscopy" in "Fluorescent and Luminecent Probes for Biological Activity" (W. T. Mason, ed.), Life Sci. Resources Ltd. Cambridge, UK (1999).
47. "Confocal Aperture in the Raman Microprobe", Technical Notes R12, Jobin Yvon (1990).
48. M. Fleischman, P. J. Hendra, and J. McQuillan, *Chem. Phys. Lett.* **26**, 163 (1974).
49. D. L. Jeanmaire and R. P. Van Duyne, *J. Electroanal. Chem.* **84**, 1 (1977).
50. M. G. Albrecht and J. A. Creighton, *J. Am. Chem. Soc.* **99**, 5215 (1977).
51. R. L. Garrell, *Anal. Chem.* **61**, 401A (1989), and references therein.
52. B. Chase and B. A. Parkinson, *Appl. Spectrosc.* **42**, 1186 (1988).
53. I. Pochrand, "Surface enhanced Raman vibrational studies at solid/gas interfaces," in "Springer Tracts in Modern Physics," Vol. 104, pp. 1–164, and references therein. Springer-Verlag, Berlin, 1984.
54. M. Moskovits, *Rev. of Mod. Phys.* **57**, 783 (1985).
55. D. A. Weitz, M. Moskovits, and J. A. Creighton, in "Chemical Structure at Interfaces" (R. B. Hall and A. B. Ellis, eds.), Chapter 5, p. 197. VCH, Deerfield Beach, Florida, 1986.
56. X. Jiang and A. Campion, *Chem. Phys. Lett.* **140**, 95 (1987).
57. P. Hildebrandt, K. A. Macor, and R. S. Czernuszewicz, *J. Raman Spectrosc.* **19**, 65 (1988).
58. A. M. Alak and T. Vo. Dinh, *Anal. Chem.* **59**, 2149 (1987).
59. M. M. Carabba, R. B. Edmonds, and R. D. Rauk, *Anal. Chem.* **59**, 2559 (1987).
60. R. L. Garrell, *Anal. Chem.* **61**, 401A (1989).
61. R. K. Chang and B. L. Laube, *CRC Critical Review in Solid State and Materials Sciences* **12**, 1 (1984).
62. P. B. Dorain, *Phys. Chem.* **90**, 5808 (1986).
63. D. L. Jeanmaire and R. P. Van Duyne, *J. Electroanal. Chem.* **84**, 1 (1977).
64. H. Yamada, *Appl. Spectrosc. Rev.* **17**, 227 (1986).
65. E. Koglin and J. M. Séquaris, "Surface enhanced Raman scattering of biomolecules," *Topics in Current Chemistry* **134**, 1 (1986).
66. T. M. Cotton, "The applications of surface-enhanced Raman scattering to biochemical systems," in "Spectroscopy of Surfaces" (R. J. H. Clark and R. E. Hester, eds.), Vol. 16, Chapter 3, p. 91, and references therein. John Wiley, New York, 1988.
67. J. Creighton, "The selection rules for surface-enhanced Raman spectroscopy," in "Spectroscopy of Surfaces" (R. J. H. Clark and R. E. Hester, eds.), Vol. 16, Chapter 2, p. 37, and references therein. John Wiley, New York, 1988.
68. R. Aroca and G. J. Kouracs, "Surface enhanced Raman spectroscopy," in "Vibrational Spectra and Structure" (J. R. Durig, ed.), Vol. **19**, p. 55. Elsevier, New York, 1991.
69. T. Takenaka and J. Uemura, "Application of infrared and Raman spectroscopy to the study of surface chemistry," in "Vibrational Spectra and Structure" (J. R. Durig, ed.), Vol. 19, p. 215. Elsevier, New York, 1991.
70. R. J. H. Clark and R. E. Hester, eds., "Advances in Spectroscopy," Vol. 16. John Wiley, New York, 1988. This volume contains several other Reviews related to SERS.
71. P. P. Van Duyne, *J. Phys. (Paris)* **38**, C5-239 (1977).
72. R. P. Cooney, M. R. Mahoney, and A. J. McQuillan, "Raman spectroelectrochemistry," in "Advances in Infrared and Raman Spectroscopy" (R. J. H. Clark and R. E. Hester, eds.), Vol. 9, p. 188. Heyden, London, 1982.
73. D. L. Jeanmaire and R. P. Van Duyne, *J. Am. Chem. Soc.* **97**, 1699 (1975).
74. R. S. Czernuszewicz and K. A. Macor, *J. Raman Spectrosc.* **19**, 553 (1988).
75. D. L. Jeanmaire and R. P. Van Duyne, *J. Am. Chem. Soc.* **98**, 4029 (1976).
76. D. L. Jeanmaire and R. P. Van Duyne, *J. Am. Chem. Soc.* **98**, 4034 (1976).
77. D. L. Jeanmaire and R. P. Van Duyne, *J. Electroanal. Chem.* **66**, 235 (1975).

78. H. Hamaguchi, "Transient and time-resolved Raman spectroscopy of short-lived intermediate species," in "Vibrational Spectra and Structure" (J. Durig, ed.), Vol. 16, p. 227. Elsevier, Amsterdam, 1987.
79. D. E. Morris and W. H. Woodruff, "Vibrational spectra and the structure of electronically excited molecules in solution," in "Advances in Spectroscopy" (R. J. H. Clark and R. E. Hester, eds.), Vol. 14, p. 285. John Wiley, New York, 1987.
80. "Time resolved spectroscopy," in "Advances in Spectroscopy" (R. J. H. Clark and R. E. Hester, eds.), Vol. 18, p. 1. John Wiley, New York, 1989.
81. G. H. Atkinson, "Time-resolved Raman spectroscopy," in "Advances in Infrared and Raman Spectroscopy" (R. J. H. Clark and R. E. Hester, eds.), Vol. 9. John Wiley, New York, 1982.
82. R. F. Dallinger, S. Farquharson, W. H. Woodruff, and M. A. J. Rodgers, *J. Am. Chem. Soc.* **103**, 7433 (1981).
83. P. G. Bradley, N. Kress, B. A. Hornberger, R. F. Dallinger, and W. H. Woodruff, *J. Am. Chem. Soc.* **103**, 7441 (1981).
84. P. K. Mallick, D. P. Strommen, and J. R. Kincaid, *J. Am. Chem. Soc.* **112**, 1686 (1990).
85. E. Whittle, D. A. Dows, and G. C. Pimentel, *J. Chem. Phys.* **22**, 1943 (1954).
86. H. E. Hallam, ed., "Vibrational Spectroscopy of Trapped Species." John Wiley, New York, 1973.
87. M. Moskovits and G. A. Ozin, eds., "Cryochemistry." John Wiley, New York, 1976.
88. A. J. Downs and M. Hawkins, "Raman studies of molecules in matrices," in "Advances in Infrared and Raman Spectroscopy" (R. J. H. Clark and R. E. Hester, eds.), Vol. 10, pp. 1-109. John Wiley, New York, 1983.
89. M. J. Almond and A. J. Downs, "Spectroscopy of matrix isolated species," in "Advances in Spectroscopy" (R. J. H. Clark and R. E. Hester, eds.), Vol. 17, p. 1. John Wiley, New York, 1989.
90. H. J. Jodl, "Raman spectroscopy on matrix isolated species," in "Vibrational Spectra and Structure" (J. R. Durig, ed.), Vol. 13, p. 285. Elsevier, Amsterdam, 1984.
91. A. J. Barnes, J. C. Bignall, and C. J. Purnell, *J. Raman Spectrosc.* **4**, 159 (1975).
92. J. S. Shirk and H. H. Claassen, *J. Chem. Phys.* **54**, 3237 (1971).
93. L. M. Proniewicz, I. R. Paeng, and K. Nakamoto, *J. Am. Chem. Soc.* **113**, 3294 (1991).
94. W. Scheuermann and K. Nakamoto, *Appl. Spectrosc.* **32**, 251 and 302 (1978).
95. J. W. Nibler and D. A. Coe, *J. Chem. Phys.* **55**, 5133 (1971).
96. W. F. Howard, Jr., and L. Andrews, *Inorg. Chem.* **14**, 767 (1975); L. Andrews, "Spectroscopy of molecular ions in noble gas matrices," in "Advances in Infrared and Raman Spectroscopy" (R. J. H. Clark and R. E. Hester, eds.), Vol. 7. John Wiley, New York, 1980.
97. I. Noda, *Appl. Spectrosc.*, **47**, 1329 (1993).
98. I. Noda, A. E. Dowrey, C. Marcott, G. M. Story and Y. Ozaki, *Appl. Spectrosc.*, **54**, 236A (2000).
99. Y. Ren, T. Murakami, T. Nishioka, K. Nakashima, I. Noda and Y. Ozaki, *Macromolecules*, **32**, 6307 (1999).
100. J. R. Schoonover, A. Saab, J. S. Bridgewater, G. J. Havrilla, C. T. Zugates and P. J. Treado, *Appl. Spectrosc.*, **54**, 1362 (2000).
101. P. J. Treado, I. W. Levin and E. N. Lewis, *Appl. Spectrosc.*, **46**, 1211 (1992).
102. C. D. Tran, *Anal. Chem.*, **64**, 971A (1992).
103. P. J. Treado, I. W. Levin and E. N. Lewis, *Appl. Spectrosc.*, **46**, 553 (1992).
104. D. A. Long, "Raman Spectroscopy," p. 219, McGraw-Hill, New York, 1977.
105. P. Esherick and A. Owyong, "High resolution stimulated Raman spectroscopy," in "Advances in Infrared and Raman Spectroscopy" (R. J. H. Clark and R. E. Hester, eds.), Vol. 9, p. 130. John Wiley, New York, 1982.

106. J. W. Nibler, W. M. Schaub, J. R. McDonald, and A. B. Harvey, "Coherent anti-Stokes Raman Spectroscopy," in "Vibrational Spectra and Structure" (J. Durig, ed.), Vol. 6, p. 173, Elsevier, Amsterdam 1977.
107. J. J. Barrett, *Appl. Spectrosc. Rev.* **21**, 419 (1985).
108. "Advances in Spectroscopy" (R. J. H. Clark and R. E. Hester, eds.), Vol. 15, John Wiley, New York, 1988. Contains several review articles on CARS.
109. M. D. Levenson and S. S. Kano, "Introduction to non-linear laser spectroscopy" (Revised edition). Academic Press, New York, 1988.
110. A. B. Harvey, ed., "Chemical Applications of Nonlinear Raman Spectroscopy," p. 1. Academic Press, New York, 1981.

Chapter 4

Materials Applications

Raman spectroscopy failed to live up to its original expectation when the technique was discovered. This was due to instrumental problems, high cost of the instrument, and the fluorescence problem. However, with improvement in instrumentation, the use of a near infrared laser with FT-Raman, the introduction of fiber optics, the number of applications (some of which were discussed in Chapter 3) has escalated. The applications are expanded in this chapter, which deals with materials applications involving structural chemistry, solid state, and surfaces. Additional applications are presented in Chapter 5 (analytical applications), Chapter 6 (biochemical and medical applications) and Chapter 7 (industrial applications).

4.1 Applications to Structural Chemistry

Among a variety of spectroscopic methods, vibrational spectroscopy is most commonly used in structural chemistry. IR/Raman spectroscopy provides information about molecular symmetry of relatively small molecules and functional groups in large and complex molecules. Furthermore, Raman spectroscopy enables us to study the structures of electronically excited molecules and unstable species produced by laser photolysis at low temperatures. Several other applications that are important in structural chemistry are also discussed in this section.

4.1.1 STRUCTURE DETERMINATION BY SYMMETRY SELECTION RULE

When a molecule is relatively small and/or belongs to a point group of relatively high symmetry, it is possible to elucidate the molecular structure by using the symmetry selection rules discussed in Section 1.14. Molecules of XY_2 (linear $\text{D}_{\infty\text{h}}$ or bent $\text{C}_{2\text{v}}$), XY_3 (planar $\text{D}_{3\text{h}}$ or pyramidal $\text{C}_{3\text{v}}$), XY_4 (square-planar $\text{D}_{4\text{h}}$ or tetrahedral T_d) and XY_5 (trigonal-bipyramidal $\text{D}_{3\text{h}}$ or tetragonal-pyramidal $\text{C}_{4\text{v}}$) types may take one of the structures indicated in parentheses. Since the number of IR/Raman-active vibrations is different for each structure, the most probable structure can be chosen by comparing the number of observed IR/Raman bands with that predicted for each structure by symmetry selection rules.

Vibrational spectroscopy played the major role in structure determination when XeF_4 was first prepared by Claassen *et al.* (1) in 1962. Tables 4-1 and 4-2 show the number and IR/Raman-activity of fundamental vibrations predicted for tetrahedral and square-planar XeF_4 molecules. (These results can be obtained via Appendices 1 and 2). Group theory predicts that the tetrahedral structure should exhibit two $\nu(\text{XeF})$ and two $\delta(\text{FXeF})$, while the square-planar structure should exhibit two $\nu(\text{XeF})$ and only one $\delta(\text{FXeF})$ in the Raman spectrum.* The observed Raman spectrum (2) shows two $\nu(\text{XeF})$ at 554 and 524 cm^{-1} and one $\delta(\text{FXeF})$ at 218 cm^{-1} in agreement with the square-planar structure. In the IR spectrum, one $\nu(\text{XeF})$ and one $\delta(\text{FXeF})$ are expected for the tetrahedral structure, while one $\nu(\text{XeF})$ and two $\delta(\text{FXeF})$ are predicted for the square-planar structure. The observed IR spectrum exhibits one $\nu(\text{XeF})$ at 586 cm^{-1} and two $\delta(\text{FXeF})$ at 291 and 161 cm^{-1} , again confirming the square-planar structure. The same conclusion can be

Table 4-1 Number of Fundamentals for Tetrahedral XeF_4

T_d	Activity	Number of Fundamentals	$\nu(\text{XeF})$ Stretching	$\delta(\text{FXeF})$ Bending
A_1	R	1	1	0
A_2	ia ^a	0	0	0
E	R	1	0	1
F_1	ia	0	0	0
F_2	IR, R	2	1	1
Total	IR	2	1	1
	R	4	2	2

^aia = inactive.

*In general, nine ($3 \times 5 - 6$) normal vibrations are expected for XY_4 -type molecules. As seen in Tables 4-1 and 4-2, this rule holds if we consider that vibrations belonging to E and F species are doubly and triply degenerate, respectively.

Table 4-2 Number of Fundamentals for Square-Planar XeF_4

\mathbf{D}_{4h}	Activity	Number of Fundamentals	$\nu(\text{XeF})$ Stretching	$\delta(\text{FXeF})$ Bending
A_{1g}	R	1	1	0
A_{1u}	ia ^a	0	0	0
A_{2g}	ia	0	0	0
A_{2u}	IR	1	0	1
B_{1g}	R	1	1	0
B_{1u}	ia	0	0	0
B_{2g}	R	1	0	1
B_{2u}	ia	1	0	1
E_g	R	0	0	0
E_u	IR	2	1	1
Total	IR	3	1	2
	R	3	2	1

^aia = inactive.

obtained by simple application of the IR/Raman mutual exclusion principle (Section 1.7), since the point group \mathbf{D}_{4h} has a center of symmetry that is lacking in the point group $\mathbf{T_d}$.

Christe and co-workers (3) obtained the XeF_5^- ion as the tetramethylammonium salt at -86°C , and determined its structure by x-ray diffraction as well as vibrational spectroscopy. This anion takes a highly unusual \mathbf{D}_{5h} structure, shown in Fig. 4-1, which can be derived from that of a pentagonal bipyramidal IF_7^- in which the two axial fluorine ligands are replaced by two sterically active free valence electron pairs. The XeF_5^- anion has 12 ($3 \times 6 - 6$) normal vibrations that are classified into $1A'_1(\text{R}) + 1A''_2(\text{IR}) + 2E'_1(\text{IR}) + 2E'_2(\text{R}) + E''_2$ (inactive) under \mathbf{D}_{5h} symmetry. Thus, only three vibrations (A'_1 and $2E'_2$) are Raman-active while three vibrations (A''_2 and $2E'_1$) are IR-active. The observed Raman spectrum shown in Fig. 4-2 clearly indicates the presence of three bands at 502, 422 and 377 cm^{-1} , in agreement with the \mathbf{D}_{5h} structure.

Buckminsterfullerene (C_{60}) has attracted considerable attention in recent years. As expected from its extremely high symmetry ($\mathbf{I_h}$ point group), this molecule exhibits very small numbers of vibrations in IR and Raman spectra (see Section 4.2.7).

Another example is provided by a series of octahedral $\text{MX}_n\text{Y}_{6-n}$ type ions ($n = 0-6$), where M is Pt(IV), Os(IV), and Ir(IV), and X and Y are halogens. Preetz and co-workers (4) prepared these mixed-halogeno ions and assigned their IR/Raman bands based on point group symmetry. Table 4-3 shows the point group and classification of IR/Raman-active fundamental vibrations. Figure 4-3 shows the IR/Raman spectra and band assignments of the $[\text{PtCl}_n\text{Br}_{6-n}]^{2-}$ series. It should be noted that these ions exhibit $\nu(\text{PtCl})$,

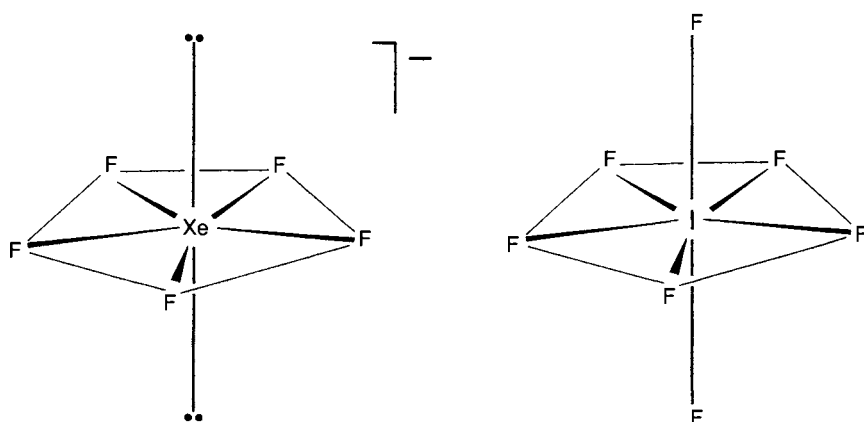


Figure 4-1 Structures of XeF_5^- and IF_7 . (Reproduced with permission from Ref. 3. Copyright 1991 American Chemical Society.)

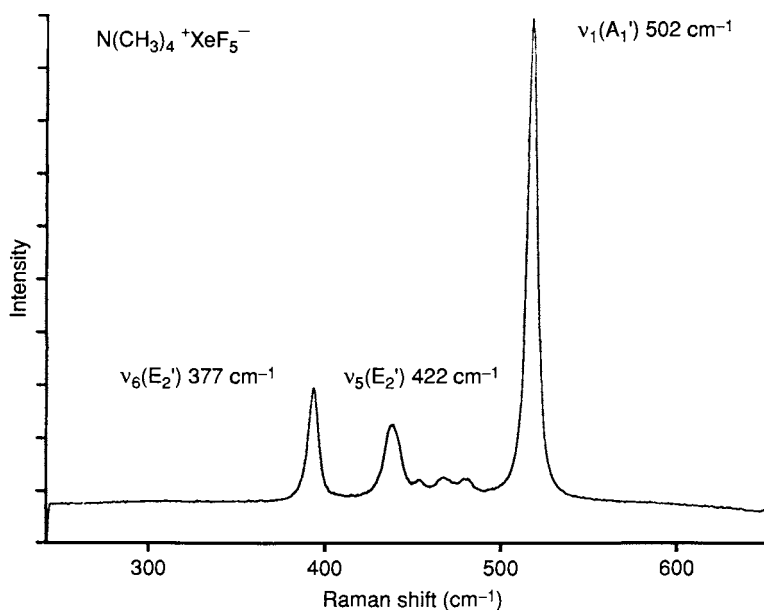


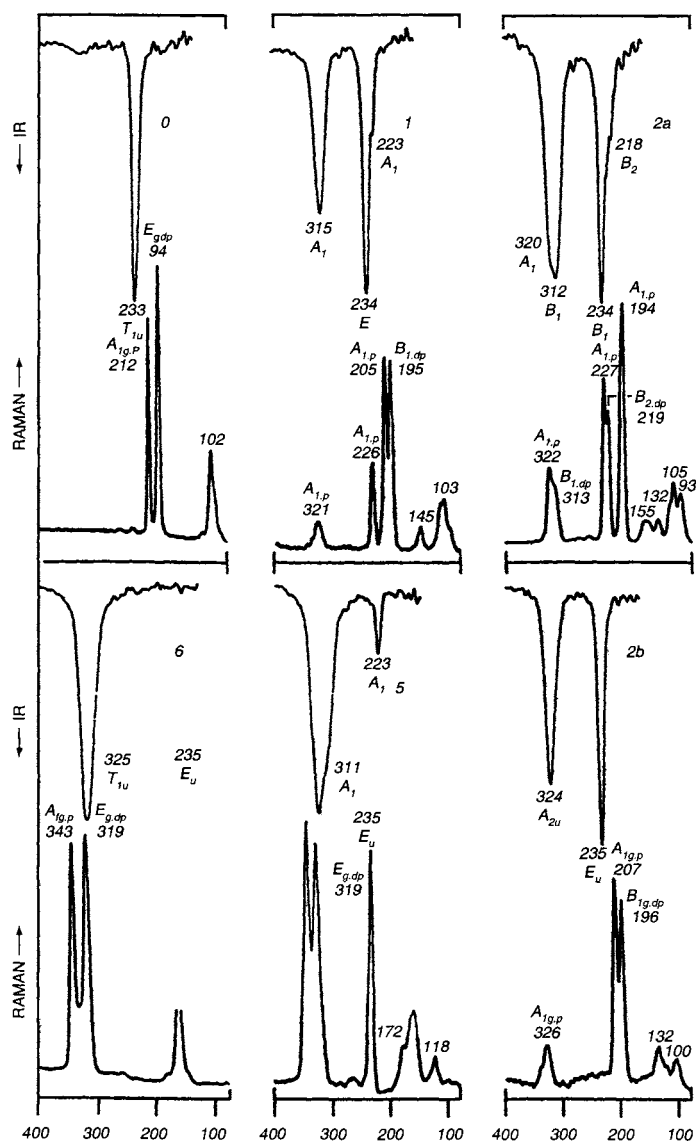
Figure 4-2 Single-crystal Raman spectrum of $\text{N}(\text{CH}_3)_4^+\text{XeF}_5^-$ obtained by 514.5 nm excitation. (Reproduced with permission from Ref. 3. Copyright 1991 American Chemical Society.)

Table 4-3 Number of IR/Raman-Active Vibrations of Octahedral MX_nY_{6-n} Type Molecules (Ref. 4)

Spectrum ^a <i>n</i>	Ion	Point Group	v(MY) ^b	v(MX) ^b	Bending ^b
0	MY ₆	O _h	$A_{1g} + E_g + F_{1u}$	—	$F_{1u} + F_{2g} + F_{2u}$
1	MXY ₅	C _{4v}	$2A_1 + B_1 + E$	$A_1 + B_1 + B_2 + \frac{3E}{2}$	$A_1 + B_1 + B_2 + \frac{3E}{2}$
2a	c ₅ -MX ₂ Y ₄	C _{2v}	$2A_1 + B_1 + B_2$	$\frac{A_1 + B_1}{2}$	$3A_1 + 2A_2 + 2B_1 + 2B_2$
2b	trans-MX ₂ Y ₄	D _{4h}	$A_{1g} + B_{1g} + E_u$	$\frac{A_{1g} + B_{1g}}{2}$	$B_{2g} + E_g + \frac{A_{2u} + B_{2u} + 2E_u}{2}$
3a	fac-MX ₃ Y ₃	C _{3v}	$A_1 + E$	$A_1 + E$	$2A_1 + A_2 + 3E$
3b	mer-MX ₃ Y ₃	C _{2v}	$2A_1 + B_1$	$2A_1 + B_2$	$2A_1 + A_2 + 3B_1 + 3B_2$
4a	c ₅ -MX ₄ Y ₂	C _{2v}	$A_1 + B_1$	$2A_1 + B_1$	$3A_1 + 2A_2 + 2B_1 + 2B_2$
4b	trans-MX ₄ Y ₂	D _{4h}	$A_{1g} + A_{2u}$	$A_{1g} + B_{1g} + E_u$	$B_{2g} + E_g + \frac{A_{2u} + B_{2u} + 2E_u}{2}$
5	MX ₅ Y	C _{4v}	A_1	$2A_1 + B_1 + E$	$A_1 + B_1 + B_2 + 3E$
6	MX ₆	O _h	—	$A_{1g} + E_g + \frac{F_{1u}}{2}$	$F_{1u} + F_{2g} + F_{2u}$

a See Fig. 4-3.

b ... Raman-active, -IR-active.



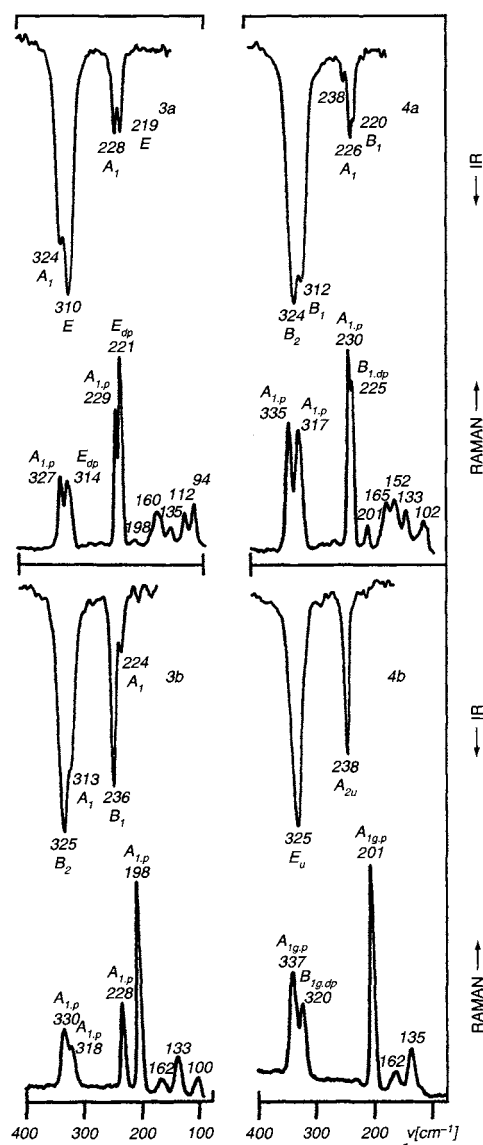
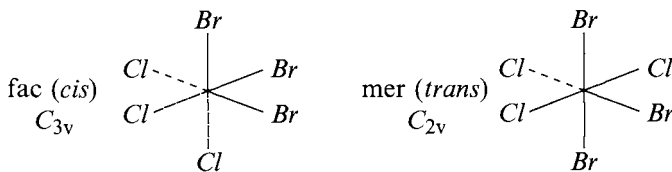


Figure 4-3 IR and Raman spectra of $(TBA)_2 [PtCl_n Br_{6-n}]$, $n = 0-6$. Excitation wavelengths: 647.1 nm for $n = 0, 2a, 3a$, and $4a$; 568.2 nm for $n = 1, 2b$, and $3b$; and 514.5 nm for $n = 4b, 5$, and 6 . (Reproduced with permission from Ref. 4.)

$\nu(\text{PtBr})$ and bending vibrations at 350–320, 220–190 and below 190 cm⁻¹, respectively. It is of particular interest to see whether symmetry selection rules are obeyed in pairs of stereoisomers. For $n = 3$, there are two isomers, fac (*cis*) and mer (*trans*).



According to Table 4-3, the former should exhibit two $\nu(\text{PtCl})$ ($A_1(p)$ and $E(dp)$) and two $\nu(\text{PtBr})$ ($A_1(p)$ and $E(dp)$) both in IR and in Raman spectra. Here, p and dp denote polarized and depolarized vibrations, respectively. This was found to be the case (trace 3a of Fig. 4-3). In contrast, the latter should exhibit three $\nu(\text{PtCl})$ ($2A_1(p)$ and $B_1(dp)$) and three $\nu(\text{PtBr})$ ($2A_1(p)$ and $B_2(dp)$) both in IR and in Raman spectra. Trace 3b of Fig. 4-3 shows that two polarized bands of A_1 -type are observed for each vibration because B -type vibrations are weaker than A -type vibrations. Thus, comparison of Raman spectra of the two isomers should be made using A -type (polarized) vibrations.

As seen earlier, some fundamental vibrations are relatively weak. Furthermore, some overtone and combination bands become unusually strong when Fermi resonance (accidental degeneracy) occurs. A typical example is given by CO₂, where the frequency of the first overtone of the ν_2 (667 cm⁻¹) is very close to that of the ν_1 fundamental(1,337 cm⁻¹). Since ν_1 and $2\nu_2$ belong to the same symmetry species (Σ_g^+), they interact with each other to give rise to two strong Raman bands at 1,388 and 1,286 cm⁻¹. Finally, it should be noted that the point group symmetry in the crystalline state is not necessarily the same as that in the isolated state. Thus, this method must be applied with caution.

4.1.2 STRUCTURE-SENSITIVE VIBRATIONS

Although molecules and ions exhibit a number of normal vibrations, some vibrations are inherently sensitive to changes in electronic structure, molecular conformation and intermolecular interaction, while others are not. These structure-sensitive vibrations are known for a number of compounds. Here, we discuss three classes of compounds of biological interest.

(a) *Iron porphyrin*

Iron porphyrins shown in Fig. 4-4 ($M = Fe$) are highly important as active sites of biological functions of heme proteins (Section 6.1.2). This is largely

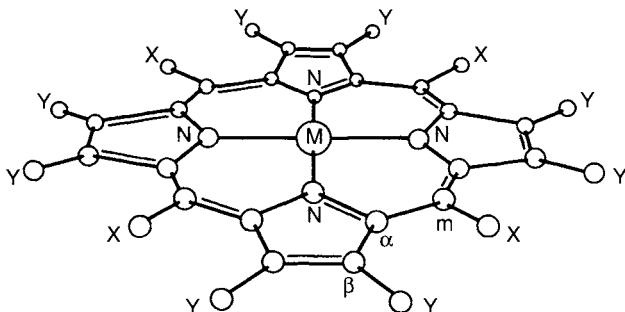


Figure 4-4 Structure of metalloporphyrin: octaethylporphyrin (OEP), $X = H$ and $Y = C_2H_5$; tetraphenylporphyrin (TPP), $X = C_6H_5$ and $Y = H$.

Table 4-4 Classification of Normal Vibrations in Metalloporphyrin of D_{4h} Symmetry

In-Plane	Vibrations	Out-of-Plane	Vibrations
$A_{1g}(R)$	9	$A_{1u}(ia)$	3
$A_{2g}(ia)^a$	8	$A_{2u}(IR)$	6
$B_{1g}(R)$	9	$B_{1u}(ia)$	5
$B_{2g}(R)$	9	$B_{2u}(ia)$	4
$E_u(IR)$	18	$E_g(R)$	8
Total	71		34

^a A_{2g} species become Raman-active under resonance conditions. ia: inactive.

due to the versatility of the Fe center, which can take a variety of oxidation states (II, III, IV, and V), spin states (high, low, and intermediate), and coordination numbers (four, five, and six). It is, therefore, important to find key bands that are sensitive to these parameters.

As shown in Fig. 1-33, metalloporphyrins exhibit a number of porphyrin core vibrations in which local modes such as $\nu(C=C)$ and $\nu(C=N)$ are strongly coupled (Section 1.21) due to its planar π -conjugated structure. Several groups of workers (5–8) have carried out normal coordinate analysis on metalloporphyrins. If we consider the simplest metalloporphyrin in which all the peripheral groups are the hydrogen atoms, it should have 105 ($3 \times 37 - 6$) normal vibrations, which can be classified under D_{4h} symmetry as shown in Table 4-4. Table 4-5 shows major local coordinates that describe general characters of 35 Raman-active in-plane vibrations (8) together with observed frequencies for Ni(OEP) (Fig. 1-32). These normal mode descriptions are applicable to other metalloporphyrins with minor modifications.

Extensive RR studies on iron porphyrins and heme proteins (9) have shown that all porphyrin core frequencies give negative linear correlations with the core size of the Fe center, and the slopes of these correlations are roughly

Table 4-5 Allocation of Ni(OEP) Skeletal Mode Frequencies (cm^{-1}) to Local Coordinates^a

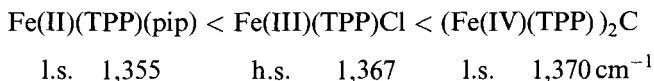
Local Mode ^b		A_{1g}	B_{1g}	A_{2g}	B_{2g}	E_u
$\nu(C_m-H)$	ν_1	[3,041] ^c				
$\nu(C_{\alpha}-C_m)_{\text{asym}}$	ν_2	1,602	ν_{10} 1,655	ν_{19} 1,603	ν_{27} [3,041]	ν_{36} [3,040]
$\nu(C_{\beta}-C_{\beta})$	ν_3	1,520	ν_{11} 1,577			ν_{37} [1,637]
$\nu(C_{\alpha}-C_m)_{\text{sym}}$						1,604
$\nu(\text{Pyr. quarter-ring})$						1,501
$\nu(\text{Pyr. half-ring})_{\text{sym}}$	ν_4	1,383	ν_{12} 1,343 ^d	ν_{20} 1,393	ν_{28} 1,483	ν_{39} 1,396
$\delta(C_m-\text{H})$						1,346
$\nu(C_{\beta}-C_1)_{\text{sym}}$	ν_5	1,138	ν_{13} 1,220	ν_{21} 1,307	ν_{29} 1,407	ν_{40} 1,231
$\nu(\text{Pyr. half-ring})_{\text{asym}}$						1,231
$\nu(C_{\beta}-C_1)_{\text{asym}}$						1,231
$\delta(\text{Pyr. def.})_{\text{asym}}$						1,153
$\nu(\text{Pyr. breathing})$	ν_6	804	ν_{14} 1,131	ν_{22} 1,121	ν_{30} 1,159	ν_{44} 1,133
$\delta(\text{Pyr. def.})_{\text{sym}}$	ν_7	674	ν_{15} 746 ^e	ν_{23} 1,058	ν_{31} 1,015	ν_{43} 996
$\delta(\text{Pyr. rot.})$						996
$\nu(\text{NIN})$	ν_8	360/343 ^f	ν_{16} 168	ν_{24} 597	ν_{32} 938	ν_{45} 927
$\delta(C_{\beta}-C_1)_{\text{asym}}$						927
$\delta(C_{\beta}-C_1)_{\text{sym}}$	ν_9	263/274 ^f	ν_{17} 305	ν_{26} [243]	ν_{34} 197	ν_{50} [358]
$\delta(\text{Pyr. transl.})$						328 ^e
				ν_{35} 144	ν_{52} 144	263 ^e
					ν_{53} 212 ^e	212 ^e

^aRef. 8 Observed values from CS₂ solution RR (A_g and B_g modes) and matrix-isolated IR (E_u modes) spectra.^bSee Fig. 4-4 for illustration of the local coordinates.^c[] calculated frequencies; not observed.^dObserved only in the meso-d₄ isotopomer and its ¹⁵N double isotopomer; not observed in the natural abundance species. Adding the calculated d₄ shift, 12 cm^{-1} to the 1,331 cm^{-1} meso-d₄ frequency gives 1,343 cm^{-1} as the assigned value for ν_{12} .^eThese frequencies from 12 K RR spectra of trigonal crystals.^fPairs of frequencies attributed to ethyl orientational isomers.

proportional to the degree of contribution of the methine stretch, $\nu(C_\alpha—C_m)$ to the normal mode. It is seen from Table 4-5 that ν_3 , ν_{10} , ν_{19} and ν_{28} are core-size sensitive. High-spin Fe(III) has a larger core size than low-spin Fe(II) because in the former, the d_{z^2} and $d_{x^2-y^2}$ orbitals contain electrons. As a result, their $C_\alpha—C_m$ bonds are weaker and the frequencies of core-size marker bands are lower. The ν_3 near $1,500\text{ cm}^{-1}$ is used as a spin state marker band because it is strong under A -term resonance. The ν_3 for Fe(II) complexes are $1,488\text{--}1,476\text{ cm}^{-1}$ (high spin) $< 1,511\text{--}1,493\text{ cm}^{-1}$ (low spin). Similarly, for Fe(III) complexes, the ν_3 are $1,495\text{--}1,493\text{ cm}^{-1}$ (high spin) $< 1,513\text{--}1,504\text{ cm}^{-1}$ (low spin) for Fe(OEP)LL' type compounds.

Frequencies of intermediate spin complexes are close to those of low spin complexes because the d_{z^2} orbital is occupied but the $d_{x^2-y^2}$ orbital is empty. The core size is also influenced by the coordination number and the degree of Fe ($d\pi$)-porphyrin (π^*) back donation in Fe(II) complexes. Thus, ν_3 must be compared with caution.

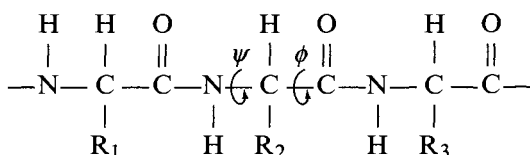
The ν_4 is the strongest when RR spectra are obtained with Soret band excitation. As shown in Table 4-5, it is mainly due to $\nu(C_\alpha—N)$, a totally symmetric pyrrole ring breathing mode. This band is well known as an oxidation state marker. It is at $\sim 1,355\text{ cm}^{-1}$ for Fe(II) and at $\sim 1,370\text{ cm}^{-1}$ for Fe(III) with relatively small dependence on spin state. For example, the order of the ν_4 are



When π -acids such as CO and O₂ are bound to Fe(II), this frequency is upshifted to the Fe(III) region because the Fe($d\pi$)-porphyrin (π^*) back donation is reduced by the Fe($d\pi$)-axial ligand (π^*) back donation. Since ν_4 is sensitive to the occupancy of the porphyrin(π^*) orbital, it is more generally called a π -electron density marker. For more detailed discussion of these structure-sensitive bands, the reader should consult Ref. 9.

(b) Peptides and Proteins

The peptide (—CO—NH—) groups in proteins are nearly planar because of resonance stabilization involving the C=O and C—N bonds.



However, the torsional angles (ψ and ϕ) between two $-\text{CO}-\text{NH}-$ groups can vary depending upon the amino acid residues involved. This, together with hydrogen bonding between the CO of one peptide and the NH of the other, produces several secondary structures of proteins such as α -helix, β -sheet and random coil (10).

Raman spectroscopy provides structure-sensitive bands for distinguishing these secondary structures. Assignments of the $-\text{CO}-\text{NH}-$ group vibrations were first made via normal coordinate analysis on *N*-methylacetamide by Miyazawa *et al.* (11).

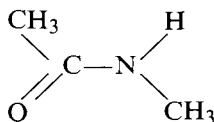


Table 4-6 lists observed frequencies and band assignments of structure-sensitive amide vibrations. Here, we discuss only amide I and III bands for which abundant data are available. The general trends shown in the table below were found by correlating x-ray structural data with Raman frequencies.

	Amide I	Amide III
α -Helix	1,645–1,600	1,300–1,260
β -Sheet	1,680–1,658	1,243–1,230
Random coil	1,665–1,660	1,243

In general, α -helix exhibits lower amide I and higher amide III frequencies than β -sheet and random coil. However, distinction of the latter two is not clear-cut. Amide III is more structure-sensitive than amide I. For example, cobramine B, a small basic protein from cobra venom, contains α -helix, β -sheet and random coil structures. As a result, three amide III bands are observed at 1,270 (α -helix), 1,254 (hydrogen-bonded random coil) and

Table 4-6 Band Assignments of Amide Vibrations in *N*-Methylacetamide (cm⁻¹)

Raman	IR	Assignment
1,657	1,653	Amide I (80% C=O str.)
—	1,507	Amide II (60% NH in-pl. bend, 40% C—N str.) ^a
1,298	1,299	Amide III (40% C—N, str., 30% NH in-pl. bend, 20% CH ₃ —C str.)
—	725	Amide V (NH out-of-pl. bend) ^b
628	627	Amide IV (40% O=C—N bend, 30% CH ₃ —C str.)
600	600	Amide VI (C=O out-of-pl. bend)

^ain-pl. bend.—bending vibration in the molecular plane.

^bout-of-pl. bend.—bending vibration in the plane perpendicular to the molecular plane.

Table 4-7 Key Raman Bands of Amino Acid Residues

Amino Acid Residue	Raman Band (cm^{-1})
Phenylalanine (Phe)	1,203 (w), 1,032 (w), 1,004 (s), 624 (w)
Tryptophan (Trp)	1,623 (w), ^a 1,555 (s), 1,436 (s), 1,016 (s), 882 (w), 762 (s)
Tyrosine (Tyr)	Doublet at 850 and 830
Histidine (His)	1,408
Disulfide (S—S) bond	540–510

^aStrong by 251 nm excitation (see Section 6.1.5)

1,235 cm^{-1} (β -sheet). However, it exhibits a single strong band at 1,672 cm^{-1} , suggesting a large fraction of β -sheet structure (12). Table 4-7 lists Raman bands of amino acid residues containing the phenyl (Phe, Tyr), imidazole (His) and indole (Trp) rings, together with those of disulfide bonds. These vibrations are sensitive to the environment in which respective amino acid residues are buried in proteins. In some cases, it is possible to enhance vibrations of individual amino acid residues selectively by using UV resonance Raman (UVRR) techniques. Figure 4-5 shows the UVRR spectra of Tyr, Trp-Tyr and Trp obtained by Rava and Spiro (13). It is seen that Tyr and Trp vibrations of tryptophyltyrosine (Trp-Tyr) are selectively enhanced by using 200 and 218 nm excitation, respectively. Asher (14) reviewed the applications of UVRR spectroscopy to analytical, physical and biophysical chemistry.

More discussions on vibrational spectra of peptides and proteins are found in Refs. 15–18.

(c) Nucleic Acids

According to X-ray analysis, double-stranded DNA can take the A, B and Z forms shown in Fig. 4-6. The A and B forms are found in low salt fiber sodium DNA at 75% and 98% relative humidity, respectively. DNA in aqueous solution contains largely the B form. The Z form is produced when the solution contains high concentrations of MgCl_2 and NaCl , etc. Table 4-8 lists the parameters that characterize these three forms. The phosphodiester stretching vibration observed in Raman spectra is useful in distinguishing these forms. The A and B forms exhibit this vibration at 810 and 835 cm^{-1} , respectively, while the Z form does not show it in this region. Figure 4-7 compares the Raman spectra of DNA (B form) and transfer-RNA (A form) obtained by Petricolas *et al.* (19). In contrast, the phosphoionic stretch near 1,100 cm^{-1} is not structure-sensitive. These forms can also be distinguished by the guanine vibrations: 665(A), 682(B) and 625(Z) cm^{-1} .

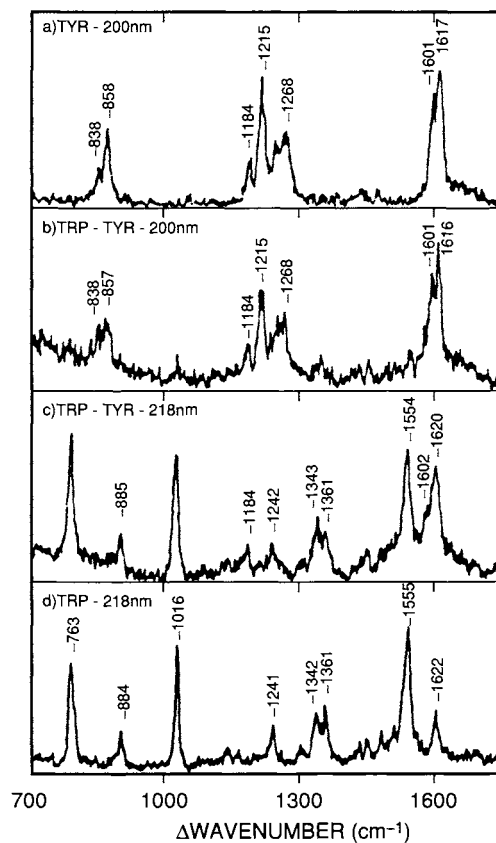
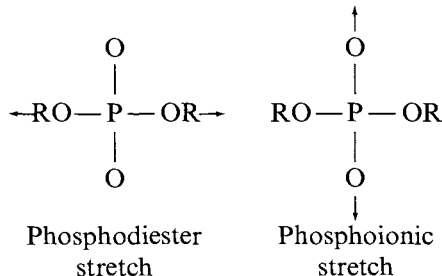


Figure 4-5 Raman spectra in the ring-mode region for aqueous solutions of (a) tyrosine, (b) and (c) tryptophyltyrosine, and (d) tryptophan (all in 10^{-3} M). (Reproduced with permission from Ref. 13. Copyright 1985 American Chemical Society.)

For more detailed conformational analysis, the reader should consult a review article by Nishimura and Tsuboi (20).



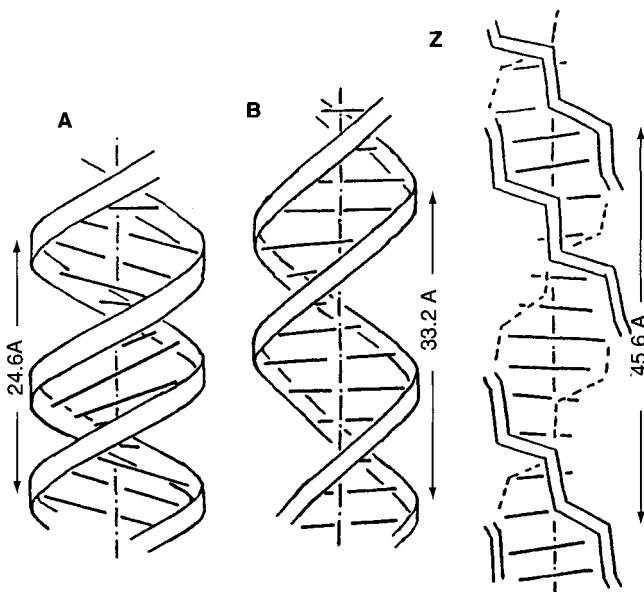


Figure 4-6 A, B and Z forms of DNA. (Provided by M. Tsuboi.)

Table 4-9 lists some prominent bands that are useful in identifying nucleic acid bases: guanine (G), cytosine (C), adenine (A), thymine (T) and uracil (U). Some of these bands are assigned in Fig. 4-7. It should be noted that most of these vibrations originate in the purine or pyrimidine rings of these bases. UVRR studies (excitation wavelength ranging from 200 to 300 nm) by Kubasek *et al.* (21) show that deoxyribonucleotides such as GMP (guanine monophosphate), CMP, AMP and UMP can be distinguished based on their excitation profiles in the UV region.

4.1.3 CHARACTERIZATION OF UNSTABLE SPECIES PRODUCED BY LASER PHOTOLYSIS

In Section 3.6, we have described the method to produce unstable species in inert gas matrices by laser-photolysis and simultaneously determine their structures by RR spectroscopy. The example given was oxyferryl(IV) porphyrins produced by laser photolysis of the corresponding oxyiron(III) porphyrins:

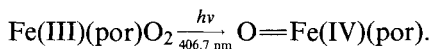


Table 4-8 Structural Parameters of A, B and Z forms of DNA.

	Helical Sense	Pitch (Å) per Turn	Base Pairs per Turn	Base Pair Distances (Å)	Base Inclination (Degrees) ^a
A form	Right	24.6	10.7	2.3	19
B form	Right	33.2	10	3.3	-1
Z form	Left	45.6	12	3.8	-9

^aFrom the normal to the helical axis.

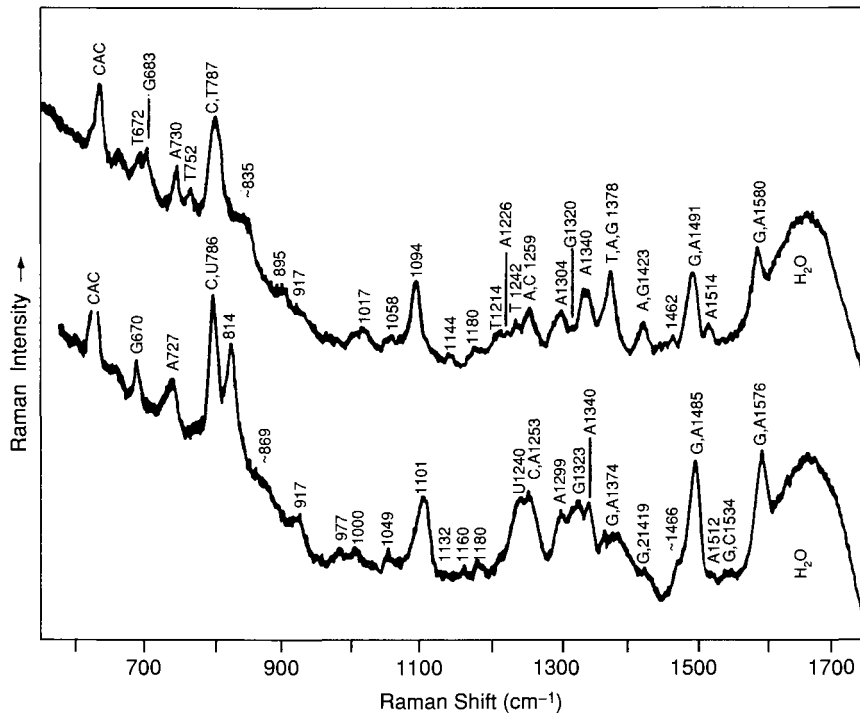
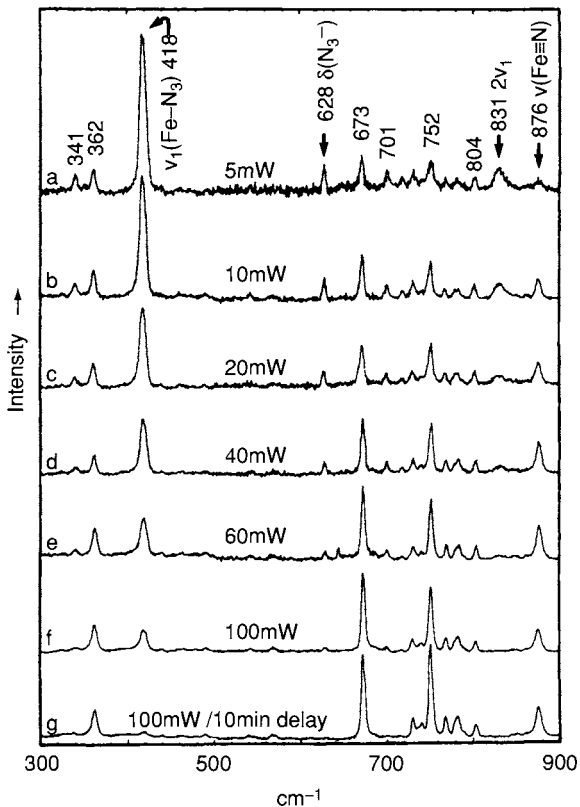
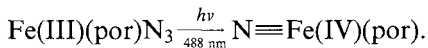


Figure 4-7 Comparison of the Raman spectra typical of DNA and RNA. The upper spectrum of a 2.5% aqueous solution of calf thymus DNA is representative of the B-form of DNA in aqueous solution. The lower spectrum of yeast RNA in a 2.5% aqueous solution at pH 7 is illustrative of the A-form structure adopted by RNA. (Reproduced with permission from Ref. 19. Copyright © 1987 John Wiley & Sons, Inc.)

Using similar procedures, Wagner and Nakamoto (23) prepared nitridoiron (V) porphyrins from laser photolysis of the corresponding azidoiron (III) porphyrins:

Table 4-9 Prominent Raman Bands of Nucleic Acid Bases (cm^{-1})^a

Adenine (A)—	1,580 (s), 1,510 (m), 1,484 (m), 1,379 (m), 1,340 (s), 1,310 (s), 1,255 (w), 729 (s)
Guanine (G)—	1,582 (s), 1,487 (s), 1,375 (m), 1,328 (m), 670 (s)
Cytosine (C)—	1,657 (m), 1,607 (m), 1,528 (m), 1,292 (s), 1,240 (s), 782(s)
Uracil (U)—	1,680 (s), 1,634 (m), 1,400 (m), 1,235 (s), 785 (s)

^aRef. 22.**Figure 4-8** RR spectra of a thin film of $\text{N}_3\text{Fe}(\text{OEP})$ at $\sim 30\text{K}$, 488 nm excitation with different excitation power as indicated. (g) was obtained after 10-min pre-irradiation with 488 nm, 100 mW.

These nitrodoiron porphyrins provided rare examples of Fe(V) compounds.

Figure 4-8 shows RR spectra of thin films of $\text{N}\equiv\text{Fe}(\text{OEP})$ obtained by gradually increasing laser power from 5 mW (trace a) to 100 mW (trace f). In

trace a, three bands characteristic of the Fe–N₃ group are readily assigned as shown in the figure. These three bands together with porphyrin bands at 710 and 341 cm⁻¹ become weaker, whereas the bands at 876, 752 and 673 cm⁻¹ become stronger as the laser power is increased and/or as irradiation time is lengthened. Figure 4-9 shows the RR spectra of photolysis products of ⁵⁴Fe(OEP)N₃ and its ^{NA}Fe, ¹⁵NN₂ and ¹⁵N₃ derivatives, respectively. (^{NA}Fe (Fe in natural abundance) contains 91.7% ⁵⁶Fe.) The upshift of the 876 cm⁻¹ band in going from trace B to trace A indicates that this vibration involves the motion of the Fe atom. Furthermore, this band is shifted to 854 cm⁻¹ by ¹⁴N/¹⁵N substitution (trace D), and the photolysis product of the ¹⁵NN₂ derivative exhibits two bands of equal intensity at 854 and 876 cm⁻¹ (trace C). It should be noted that the reaction of the ¹⁵NN₂ ion with Fe (OEP)Cl produces an equimolar mixture of

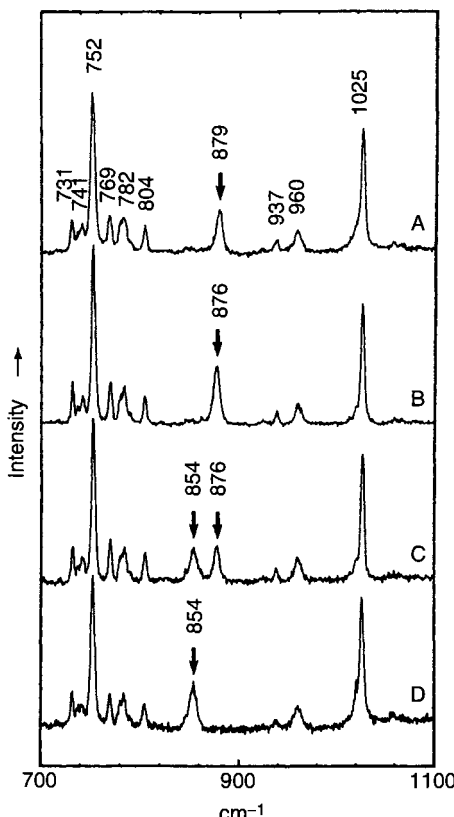
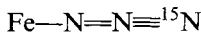


Figure 4-9 RR spectra of the photolysis products of (a) N₃⁵⁴Fe(OEP), (b) N₃Fe(OEP), (c) ¹⁵NN₂Fe(OEP) + ¹⁵N₂Fe(OEP) in a 1:1 ratio, and (d) ¹⁵N₃Fe(OEP), thin film at ~ 30 K, 488 nm excitation, 60 mW.



so that laser photolysis yields an equimolar mixture of the $\text{Fe}={}^{15}\text{N}$ and $\text{Fe}={}^{14}\text{N}$ bonds. The observed shifts ($+3 \text{ cm}^{-1}$ by ${}^{56}\text{Fe}/{}^{54}\text{Fe}$ substitution and -23 cm^{-1} by ${}^{14}\text{N}/{}^{15}\text{N}$ substitution) are in perfect agreement with theoretical values expected for a $\text{Fe}=\text{N}$ diatomic harmonic oscillator. The bands at 752 and 673 cm^{-1} are porphyrin modes of $\text{N}=\text{Fe(OEP)}$.

As stated in the preceding section, the v_4 vibration of the porphyrin core is the best oxidation state marker. In $\text{N}=\text{Fe(OEP)}$, this band appears at $1,384 \text{ cm}^{-1}$ which is higher than that of the Fe(IV) state ($1,379 \text{ cm}^{-1}$ for $\text{O}=\text{Fe(OEP)}$). Thus, the Fe(V) state is suggested. However, the spin state of $\text{N}=\text{Fe(OEP)}$ could not be determined by core size sensitive bands since core sizes are similar for the low spin ($d_{xy}^2 d_{xz}$) and the high spin ($d_{xy} d_{xz} d_{yz}$) configurations. As seen in Fig. 4-10, $\text{N}=\text{Fe(V)(OEP)}$ is isoelectronic with $\text{O}=\text{Mn(IV)}(\text{OEP})$, which is known to be high spin. Therefore, the nitrido complex is probably high spin. It should be noted that, in the Cr, Mn and Fe series, abrupt drops in the $v(\text{M}=\text{O})$ and $v(\text{M}=\text{N})$ frequencies occur when the electrons occupy anti-bonding orbitals (23).

Finally, the $v(\text{Fe}=\text{N})$ at 876 cm^{-1} disappears completely and a new set of bands appear at $798, 438$ and 341 cm^{-1} when $\text{N}=\text{Fe(OEP)}$ is irradiated by the 413.1 nm line of a Kr-ion laser. Based on ${}^{54}\text{Fe}/{}^{56}\text{Fe}$ and ${}^{14}\text{N}/{}^{15}\text{N}$ isotope shift data, the 438 cm^{-1} band is assigned to the symmetric stretching mode of a linear $\text{Fe}—\text{N}—\text{Fe}$ bridge of the $[\text{Fe(OEP)}]_2\text{N}$ dimer. The remaining bands are attributed to porphyrin core vibrations of the dimer. These results suggest that the $[\text{Fe(OEP)}]_2\text{N}$ dimer is formed via $\text{N}=\text{Fe(OEP)}$ as an intermediate species.

4.1.4 METAL–METAL BONDS AT ELECTRONIC GROUND AND EXCITED STATES

A number of compounds containing centrosymmetric metal–metal ($\text{M}—\text{M}$) bonds are known, and their totally symmetric $v(\text{M}—\text{M})$ vibrations appear strongly in Raman/RR spectra because of large changes in polarizability (24). As stated in Section 1.15, these vibrations are expected to show a series of overtones under resonance conditions (A-term resonance). As an example, Fig. 4-11 shows the RR spectrum (530.9 nm excitation) of the $[\text{Re}_2\text{F}_8]^{2-}$ ion obtained by Peters and Preetz (25). The strongest band observed at 320 cm^{-1} (v_1) is the totally symmetric $v(\text{Re}—\text{Re})$. The next strongest band at 625 cm^{-1} (v_2) is the totally symmetric $v(\text{Re}—\text{F})$. The remaining weak bands are assigned to overtones of v_1 and their combination bands as indicated in the figure.

Using Eq. (1-30) of Chapter 1, we can express the frequency of the n th overtone of a totally symmetric vibration as

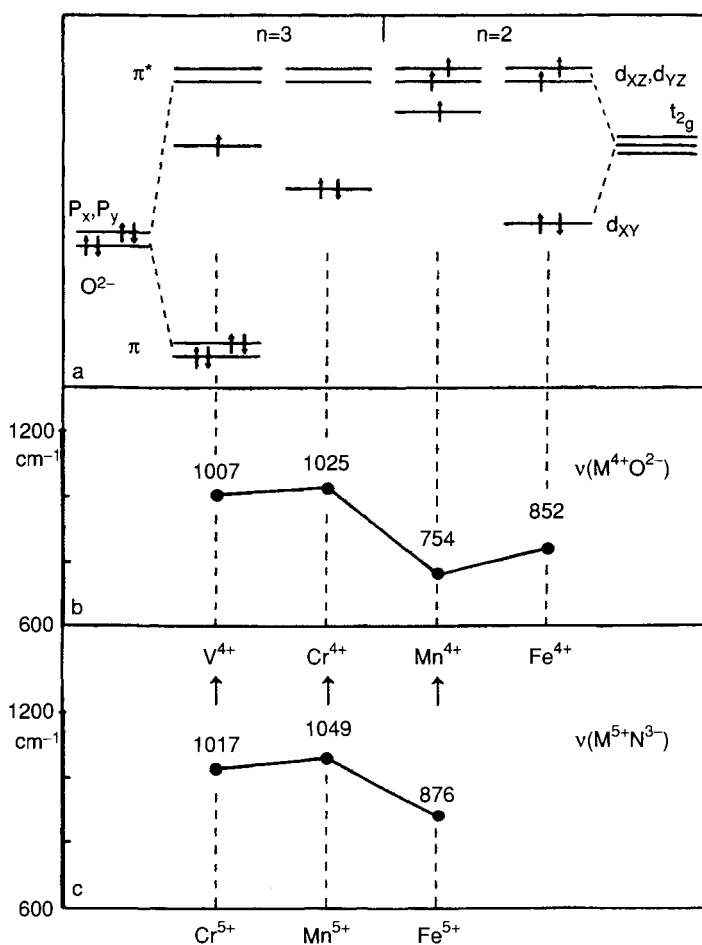


Figure 4-10 Electronic structures and vibrational frequencies of porphyrins containing $M=O$ and $M\equiv N$ groups. For the sources of vibrational frequencies, see Ref. 23.

$$v(n) = n\omega_1 - X_{11}(n^2 + n) + \text{higher terms.}$$

Here, ω_1 is the wavenumber corrected for anharmonicity, and X_{11} indicates the magnitude of anharmonicity. If we plot $v(n)/n$ against n , we obtain a straight line, and the slope and the intercept of such a plot give X_{11} and ω_1 , respectively. In the case of $Re_2Fe_8^{2-}$, these values were found to be $-0.45 \pm 0.05 \text{ cm}^{-1}$ and $319.6 \pm 0.6 \text{ cm}^{-1}$, respectively.

The Re—Re bond contains one σ -bond, two π -bonds and one δ -bond (26). The lowest electronic transition occurs from the $(\sigma)^2(\pi)^4(\delta)^2(^1A_{1g})$ to the $(\sigma)^2(\pi)^4(\delta)(\delta^*)(^1A_{2u})$, producing a strong electronic band near $19,000 \text{ cm}^{-1}$.

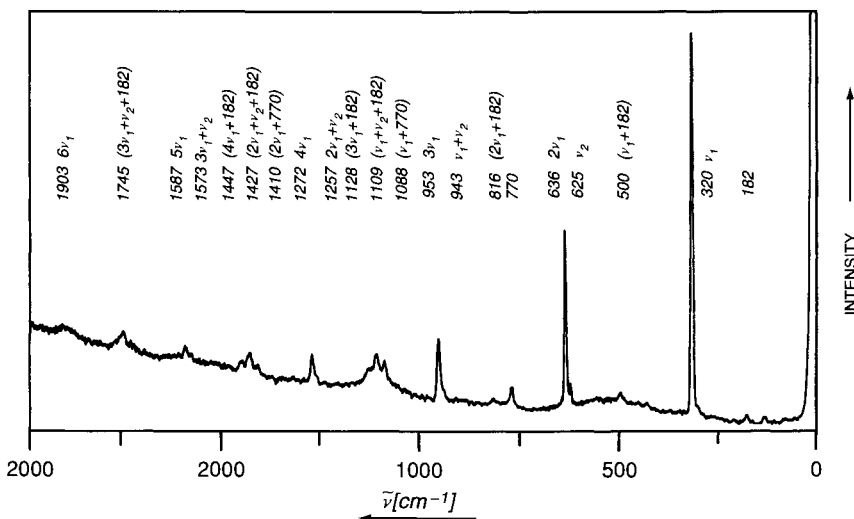


Figure 4-11 RR spectrum of $(\text{TBA})_2(\text{Re}_2\text{F}_8) \cdot 4\text{H}_2\text{O}$ (530.9 nm excitation). TBA:tetrabutylammonium cation. (Reproduced with permission from Ref. 25.)

The RR spectrum of $\text{Re}_2\text{Cl}_8^{2-}$ obtained by 647.1 nm excitation exhibits the $\nu(\text{Re—Re})$ at 272 cm^{-1} . Dallinger (27) first observed the RR spectrum at the $\delta\delta^*$ excited state by using two-color pump (640 nm)/probe (355 nm) techniques described in Section 3.5 (TR³ spectroscopy). The $\delta\delta^*$ state exhibited three bands at 138, 204 and 366 cm^{-1} . The last band was assigned to the $\nu(\text{Re—Cl})$ (ground state, 359 cm^{-1}), while the first band was attributed to the $\delta(\text{ClReRe})$ (not observed in the ground state). The remaining band at 204 cm^{-1} was assigned to the $\nu(\text{Re—Re})$ of the $\delta\delta^*$ state. The large frequency decrease in going from the ground state (272 cm^{-1}) to the excited state (204 cm^{-1}) was attributed to the decrease in bond order from 4 to 3.

For other systems, the $\nu(\text{M—M})$ becomes higher in going from the ground to the excited state. For example, Fig. 4-12 shows the RR spectra of the $[\text{Rh}_2\text{b}_4]^{2+}$ ($\text{b} = 1,3$ -diisocyanopropane) ion obtained by Dallinger *et al.* (28). The ground state spectrum shown by the lower trace exhibits the strong $\nu(\text{Rh—Rh})$ band at 79 cm^{-1} together with its overtones and the $\nu(\text{Rh—C})$ band at 467 cm^{-1} . The upper trace shows the excited state spectrum obtained by pulsed laser excitation. It is seen that the $\nu(\text{Rh—Rh})$ is now upshifted to 144 cm^{-1} . This upshift is attributed to the change in electronic structure from the $(d\sigma)^2(d\sigma^*)^2(^1A_{1g})$ ground state to the $(d\sigma^*)^2(d\sigma^*p\sigma)(^3A_{2u})$ excited state. The Rh—Rh bond order is much higher in the latter because one electron is promoted from the $d\sigma^*$ to the $p\sigma$ orbital. A review by Morris and Woodruff (29) provides more information on this and other subjects on TR² spectroscopy.

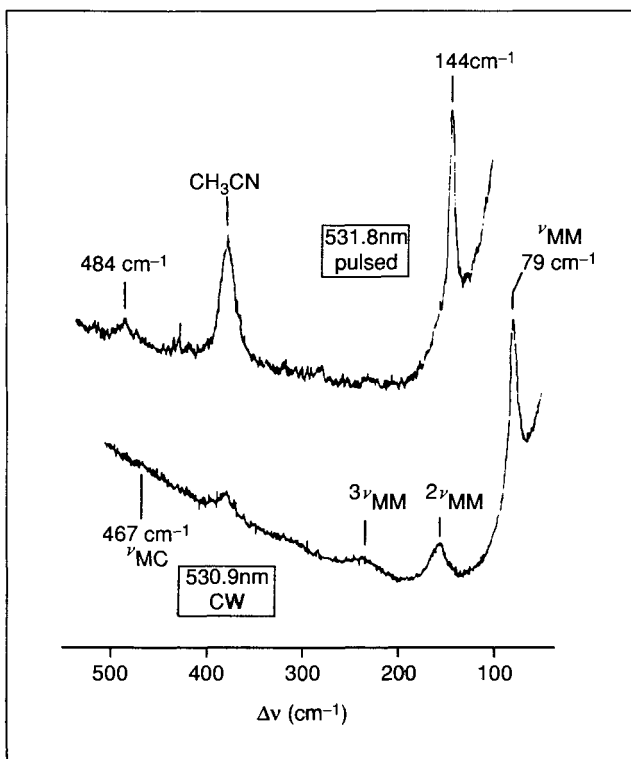


Figure 4-12 Lower trace: ground-state RR spectrum of $\text{Rh}_2\text{b}_4^{2+}$ obtained by CW excitation at 530.9 nm. Upper trace: excited-state RR spectra of $\text{Rh}_2\text{b}_4^{2+}$ obtained by pulsed laser excitation with the second harmonic of the Q-switched Nd:YAG laser (531.8 nm). (Reproduced with permission from Ref. 28. Copyright 1981 American Chemical Society.)

4.1.5 POTENTIAL ENERGIES OF VIBRATIONS OF LARGE AMPLITUDES

Ring molecules exhibit ring puckering vibrations that are anharmonic and have large amplitudes of vibration. These vibrations are observed in far-IR and low-frequency Raman spectra. As the first approximation, the potential energy of a ring puckering vibration of a four-membered ring is expressed by an anharmonic potential such as (30)

$$V(a) = ax^4 + bx^2,$$

where a and b are constants, and x is the ring puckering coordinate shown in Fig. 4-13. Planar ring compounds have a single potential minimum at $x = 0$, whereas non-planar ring compounds have two minima at positive and negative values of x .

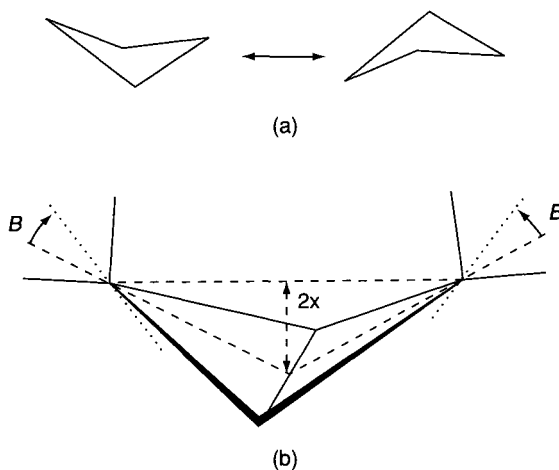
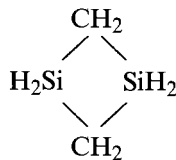


Figure 4-13 (a) Ring-puckering vibration of cyclopentene. (b) Definition of the ring-puckering coordinates for a four-membered ring molecule. (Reproduced with permission from Ref. 30.)

If the Schrödinger equation (Section 1.3) is solved using this potential, the resulting eigenvalues are expressed as a function of a quantum number, n . Selection rules for transitions are: $\Delta n = 1$ for IR and $\Delta n = 2$ for Raman. The values of a and b must be chosen so that calculated IR and Raman frequencies agree with those observed. As an example, consider 1,3-disilacyclobutane:



Figures 4-14 and 4-15 show the gas-phase IR and Raman spectra, respectively, of this compound obtained by Irwin *et al.* (31). Using the foregoing procedures, these workers obtained the potential energy curve shown in Fig. 4-16. The values of a , b and the barrier were found to be $2.3 \times 10^5 \text{ cm}^{-1}/\text{\AA}^4$, $-9.0 \times 10^3 \text{ cm}^{-1}/\text{\AA}^2$ and 87 cm^{-1} , respectively. For more details on ring puckering vibrations, see a review by Laane (32).

Another example of large amplitude of vibration is a torsional mode around the C—C single bond. The potential energy of an internal-rotation of a CH_3 group (local symmetry, C_{3v}) relative to a reference framework can be expressed by a cosine function:

$$V(\phi) = V_3(1 - \cos 3\phi),$$

where ϕ is the angle of internal rotation, and V_3 is the height of the barrier of internal rotation. $V(\phi)$ becomes zero at staggered configurations

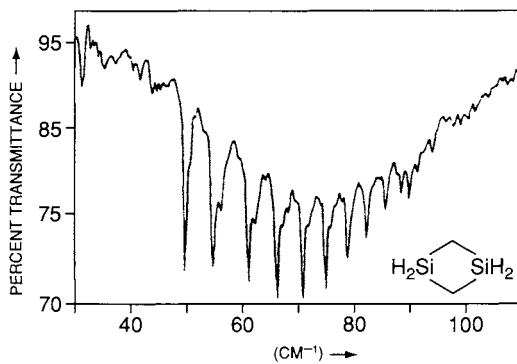


Figure 4-14 Far-IR spectrum of 1,3-disilacyclobutane. (Reproduced with permission from Ref. 31. Copyright 1977 American Chemical Society.)

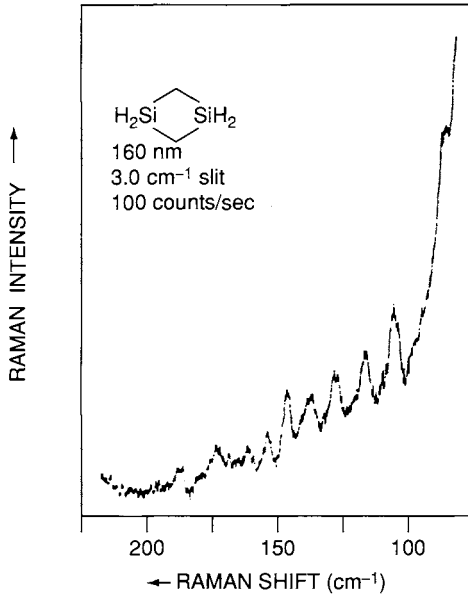


Figure 4-15 Raman spectrum of 1,3-disilacyclobutane. (Reproduced with permission from Ref. 31. Copyright 1977 American Chemical Society.)

($\phi = 0^\circ$, -60° and $+60^\circ$). Through quantum mechanical treatments (33), one can calculate eigenvalues of such a rotator as a function of v . Figure 4-17 shows a potential function of such a rotator obtained by Fateley and Miller (34). Although the energy levels are triply degenerate, they are split into the A_1 (or A_2) and E levels by the quantum mechanical tunnel effect, and the

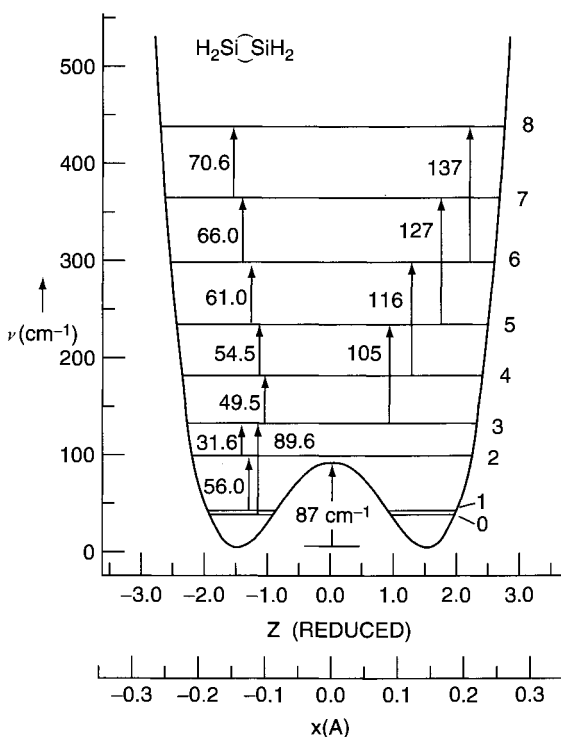


Figure 4-16 Ring-puckering potential energy function for 1,3-disilacyclobutane. (Reproduced with permission from Ref. 31. Copyright 1977 American Chemical Society.)

magnitude of splitting becomes larger as the levels approach the top of the barrier. At low energies, the CH_3 group performs torsional oscillation relative to its framework. At high energies, however, its amplitude becomes large enough to cross over the barrier (free rotation). In the former case, transitions between the levels of different ν values are observed either in IR and Raman spectra. In Raman, $\Delta\nu = 1$ transitions may be weak even if symmetry-allowed. However, $\Delta\nu = 2$ transitions are relatively strong since they are totally symmetric. As an example, Fig. 4-18 shows the gas-phase Raman spectrum of ethyl chloride ($\text{CH}_3\text{—CH}_2\text{Cl}$) obtained by Durig *et al.* (35). The three bands at 488 , 455 and 418 cm^{-1} were assigned to $2\text{—}0$, $3\text{—}1$ and $4\text{—}2$ transitions, respectively. Using these assignments, the parameters involved in theoretical expressions of torsional frequencies were determined. This led to the V_3 value of 3.72 kcal/mole (or $1,302\text{ cm}^{-1}$)* for ethylchloride.

* $1\text{ cm}^{-1} = 2.858\text{ cal/mole}$.

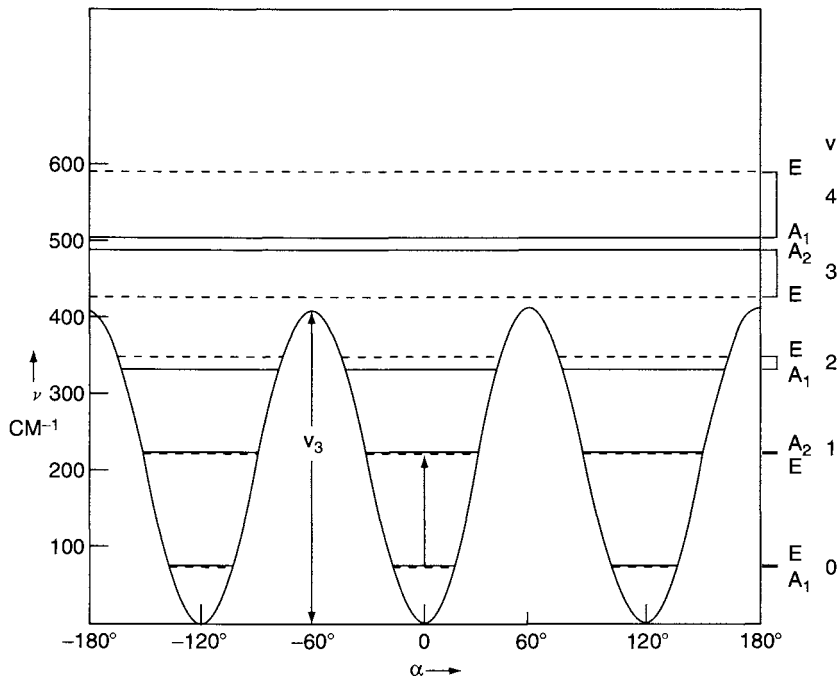


Figure 4-17 Threecold rotor potential function. (Reproduced with permission from Ref. 34.)

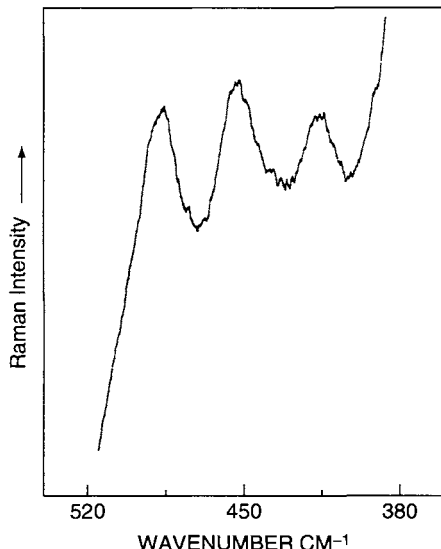


Figure 4-18 Raman torsional overtones of ethyl chloride, recorded at room temperature. (Reproduced with permission from Ref. 35. Copyright 1977 American Chemical Society.)

4.1.6 INTERMOLECULAR INTERACTIONS

(a) Donor–acceptor interaction

Molecular complexes are formed when donor and acceptor molecules are mixed in solution. Small shifts resulting from donor–acceptor interactions can be measured with high accuracy by using the difference Raman techniques described in Section 2.9. Shelnutt (36) studied the RR spectra of Cu(II) uroporphyrin I (CuURO , $M = \text{Cu(II)}$, $X = \text{H}$ and $Y = \text{CH}_2\text{COO}^-$ in Fig. 4-4) mixed with a variety of 1,10-phenanthroline derivatives. As an example, Fig. 4-19 shows the RR spectra of CuURO and CuURO of the same concentration saturated with 5-methylphenanthroline. It should be noted that phenanthroline vibrations do not appear in the latter since only the vibrations of CuURO are in resonance at 514.5 nm excitation. Although both spectra appear to be similar, the difference spectrum shown in the upper trace clearly indicates small shifts that can be determined with high accuracy ($\pm 0.1 \text{ cm}^{-1}$ in this case). It was found that $v_3(\sim 1,500 \text{ cm}^{-1})$, $v_{19}(\sim 1,582 \text{ cm}^{-1})$ and $v_{10}(\sim 1,637 \text{ cm}^{-1})$ give relatively large upshifts ($2.7 - 0.1 \text{ cm}^{-1}$), and $v_4(\sim 1,379 \text{ cm}^{-1})$ gives much smaller shifts ($0.8 - 0.1 \text{ cm}^{-1}$) when CuURO forms molecular complexes with phenanthroline derivatives. (For normal

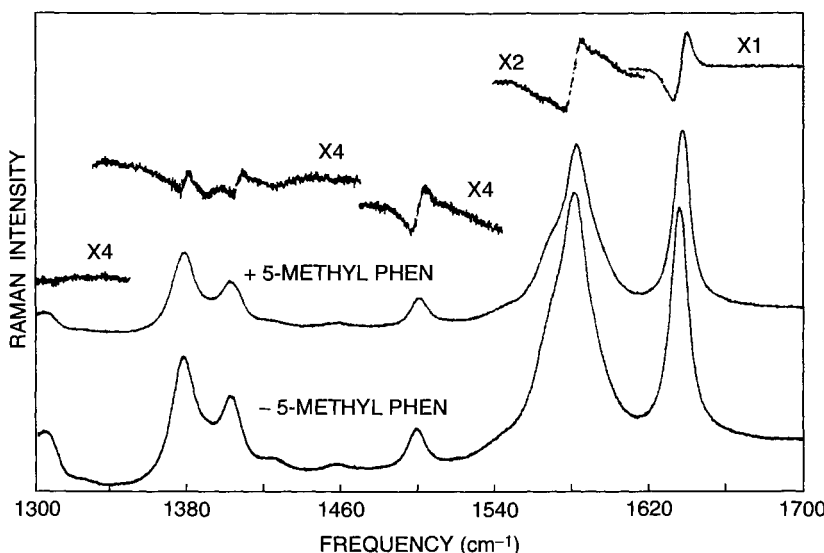
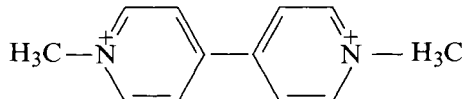


Figure 4-19 RR spectra of the 5-methylphenanthroline–CuURO complex (upper curve), CuURO (lower curve), and the Raman difference spectra. For the latter, the CuURO spectrum has been multiplied by a constant (shown) in order to balance the intensity of the Raman line in each spectrum. 514.5 nm excitation, 300 mW. (Reproduced with permission from Ref. 36. Copyright 1983 American Chemical Society.)

modes of these vibrations, see Table 4-5.) These upshifts have been attributed to the decrease of the π -electron density of CuURO as a result of electron donation to phenanthroline derivatives. In fact, these shifts are linearly related to the acceptor ability of phenanthroline derivatives and the known free energy of association. Steric properties of some phenanthroline derivatives suggest that the plane of phenanthroline is parallel to that of CuURO in these molecular complexes. Finally, all the electron-density-sensitive bands mentioned earlier are downshifted when CuURO is mixed with the viologen dication:



Thus, CuURO acts as an acceptor in this case.

(b) Solute–Solvent Interaction

As shown in Section 1.15, porphyrin core vibrations are resonance-enhanced when the exciting line is chosen within the $\pi-\pi^*$ transitions of the porphyrin (α , β , and Soret bands). The middle trace of Fig. 4-20 shows the RR spectrum (406.7 nm excitation) of $[\text{Co}(\text{TPP}-d_8)(\text{pyridine})^{18}\text{O}_2]$, which was produced by dissolving $\text{Co}(\text{TPP}-d_8)$ in toluene containing 3% pyridine (-85°C , $\sim 4\text{atm}^{18}\text{O}_2$ pressure) (37). Here, $\text{Co}(\text{TPP}-d_8)$ is the d_8 analogue of $\text{Co}(\text{TPP})$ ($X = \text{C}_6\text{H}_5$ and $Y = D$ in Fig. 4-4). The strong band at $1,094\text{ cm}^{-1}$ is assigned to the $\nu(^{18}\text{O}_2)$ of $[\text{Co}(\text{TPP}-d_8)(\text{pyridine})^{18}\text{O}_2]$, and the remaining strong bands are attributed to porphyrin core vibrations. The d_8 analogue was used in this case because $\text{Co}(\text{TPP})$ exhibits an internal mode at $1,080\text{ cm}^{-1}$ that partly overlaps on the $\nu(^{18}\text{O}_2)$ band. The $\nu(^{18}\text{O}_2)$ as well as porphyrin vibrations are resonance-enhanced since the $\text{Co}-\text{O}_2$ CT transition is located near the Soret band.

The upper trace of Fig. 4-20 shows the RR spectrum obtained by using $^{16}\text{O}_2$ instead of $^{18}\text{O}_2$. If the bound O_2 is regarded as a diatomic harmonic oscillator, the $^{16}\text{O}_2 - ^{18}\text{O}_2$ isotope shift is calculated to be $\sim 64\text{ cm}^{-1}$. Thus, the $\nu(^{16}\text{O}_2)$ band is expected to appear as a single band near $1,158\text{ cm}^{-1}$. Instead, two strong, unresolved bands are observed at $1,160$ and $1,151\text{ cm}^{-1}$. The latter at $1,151\text{ cm}^{-1}$ must originate in toluene because (1) toluene alone exhibits a weak band at $1,155\text{ cm}^{-1}$ and (2) only a single peak is observed at $1,159\text{ cm}^{-1}$ when toluene- d_8 is used (bottom trace). Strong enhancement of the solvent vibration is attributed to vibrational coupling between the $\nu(^{16}\text{O}_2)$ and the internal mode of toluene at $1,155\text{ cm}^{-1}$. Namely, resonant vibrational energy has been transferred from the $^{16}\text{O}_2$ moiety of $[\text{Co}(\text{TPP}-d_8)(\text{pyridine})^{16}\text{O}_2]$ to toluene. This is possible because these two frequencies are close to each other (energy matching) and these two moieties are closely

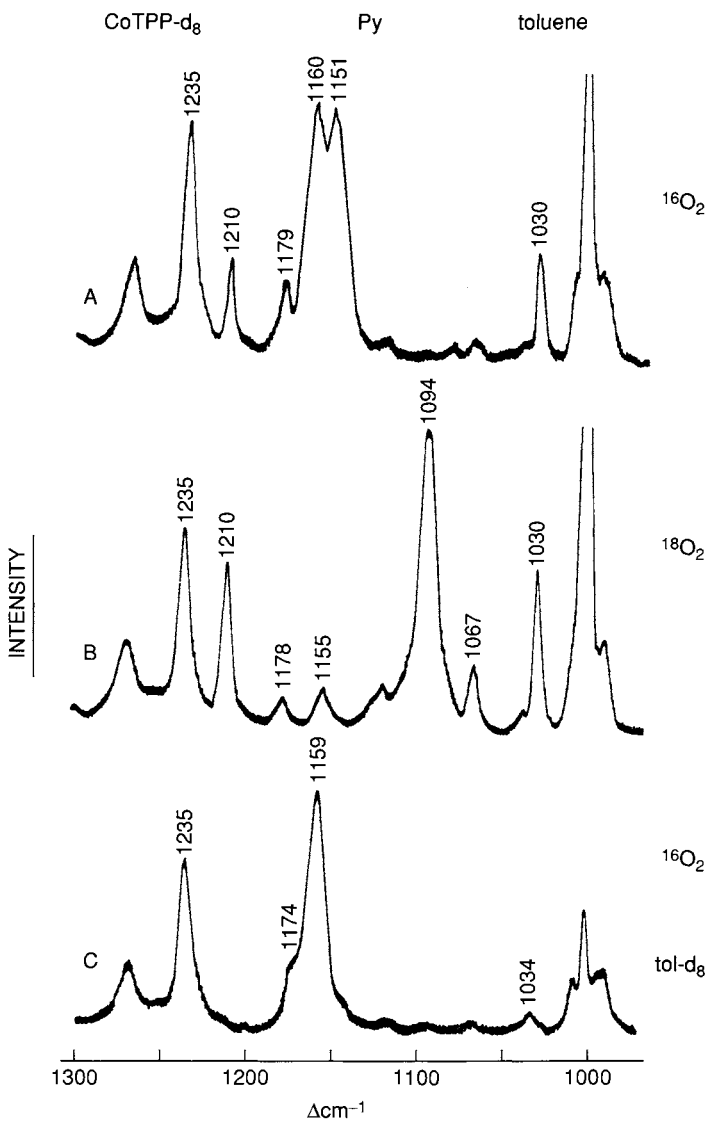


Figure 4-20 RR spectra of $\text{Co}(\text{TPP-}d_8)$ in toluene containing 3% pyridine at -85°C saturated with ${}^{16}\text{O}_2$ (trace A), ${}^{18}\text{O}_2$ (trace B) and ${}^{16}\text{O}_2$ in toluene- d_8 (406.7 nm excitation).

associated in time scale of vibrational transitions. In fact, such a coupling disappears if a picket-fence porphyrin is used instead of an open porphyrin such as $\text{Co}(\text{TPP})$. It is well known that the former prevents the access of a large molecule such as toluene to the bound O_2 inside the fence. The

preceding phenomenon was first observed by Kincaid *et al.* (37). These workers have also shown that internal modes of chlorobenzene (solvent) and pyridine (axial ligand) are also resonance-enhanced via similar mechanisms. In fact, the $1,067\text{ cm}^{-1}$ band in the middle trace of Fig. 4-20 is due to an internal mode of pyridine.

4.1.7 MOLECULAR ORIENTATION ON ELECTRODE SURFACE

As discussed in Section 3.3, surface-enhanced Raman spectroscopy (SERS) has been widely used to study the structures of a variety of compounds at surfaces. Since biological applications of SERS/SERRS have been reviewed extensively (38–41), we focus our attention of SERS dependence on the chromophore–surface distance. In 1980, Cotton *et al.* (42) first obtained the SERRS of cytochrome c and myoglobin on a silver electrode. Although the heme chromophores of these proteins are buried in the protein matrix (see Section 6.1.2), they exhibit a number of strong porphyrin ring vibrations. Later, Cotton *et al.* (43) studied the relationship between SERRS intensity and the chromophore–surface distance and showed that enhancement caused by the electromagnetic effect due to the surface can occur at distances greater than a few angstroms.

Figure 4-21 shows the SERS of cytidine-3'-monophosphate as a function of the applied electrode potential obtained by Koglin *et al.* (44). When the electrode potential was -0.1 V (vs. Ag/AgCl reference electrode), only a single band was observed at 236 cm^{-1} . This result indicates that the phosphate group is directly attached on the Ag surface, resulting in the Ag– OPO_3 vibration at 236 cm^{-1} . No enhancement of the cytosine base is observed because it is too far from the surface. When the electrode potential was changed to -0.6 V , the 236 cm^{-1} band became markedly weaker, and a series of cytosine vibrations appeared in the $1,700$ – 750 cm^{-1} region. The latter indicates that the pyrimidine ring is in direct contact with the electrode, as shown in Fig. 4-21.

Watanabe *et al.* (45) studied the SERS of adenine, adenosine, cytidine, etc., on silver electrode surfaces. They made an interesting observation that the degree of roughening of the electrode surface influences the spectra. The upper trace of Fig. 4-22 shows the normal Raman spectrum of adenosine in aqueous solution. The bottom trace shows a SERS of adenine (at -6 V vs. SCE) obtained by using a mildly roughened surface. It shows two prominent adenine vibrations at ~ 730 (ring breathing) and $1,320$ – $1,330\text{ cm}^{-1}$ ($\nu(\text{N}_7\text{—C}_5)$, not shown). This result suggests that adenosine is adsorbed preferentially via the N_7 atom with the rest of the molecule directed outward as shown. The middle trace shows a SERS obtained after heavy roughening. It exhibits a series of weak bands in the $1,100$ – 750 cm^{-1} region together with the adenine bands. Since most of the weak bands

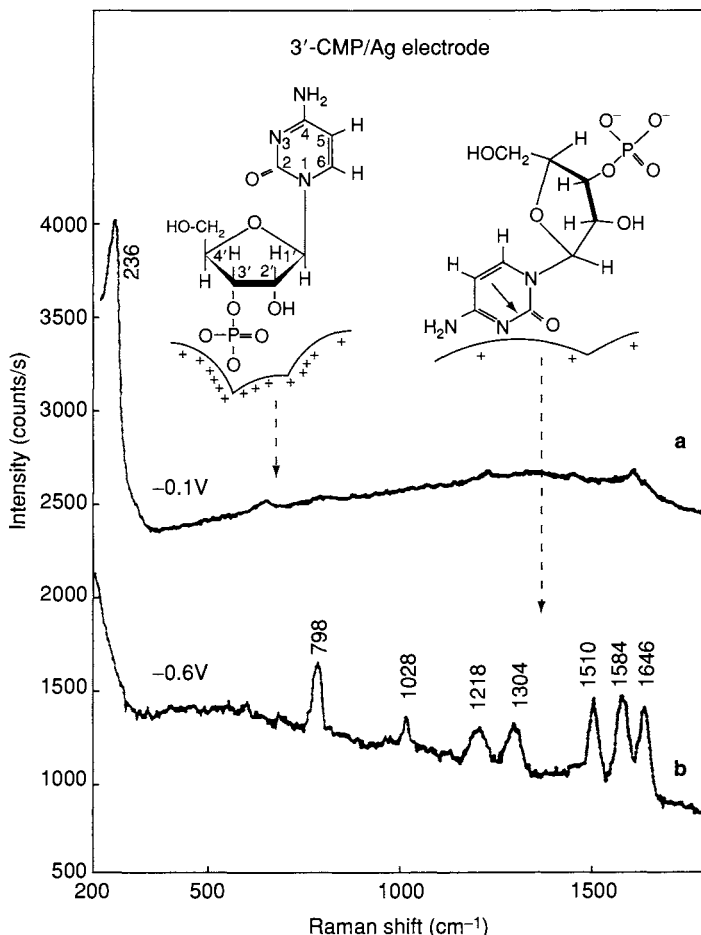


Figure 4-21 SERS in cytidine-3'-monophosphate ($3'$ -CMP). $3'$ -CMP concentration $2 \times 10^{-3} \text{ M}$, 0.15 M KCl , $2 \times 10^{-3} \text{ M Tris buffer}$ (pH 7.2). 514.5 nm excitation, laser power at the electrode 10 mW , prior activation of the Ag electrode: $1 \times 5 \text{ mC}_\text{b}$ between -0.1 V and $+0.2 \text{ V}$. (a) Adsorption potential E , -0.1 V vs. Ag/AgCl reference electrode. (b) Adsorption potential E , -0.6 V vs. Ag/AgCl reference electrode. (Reproduced with permission from Ref. 44.)

originate in the ribose moiety, both the base and sugar moieties are in close contact with the silver electrode surface as indicated.

4.2 Solid State Applications

Numerous applications in the area of the solid state have utilized Raman spectroscopy as the diagnostic tool. In some cases, infrared spectroscopy has

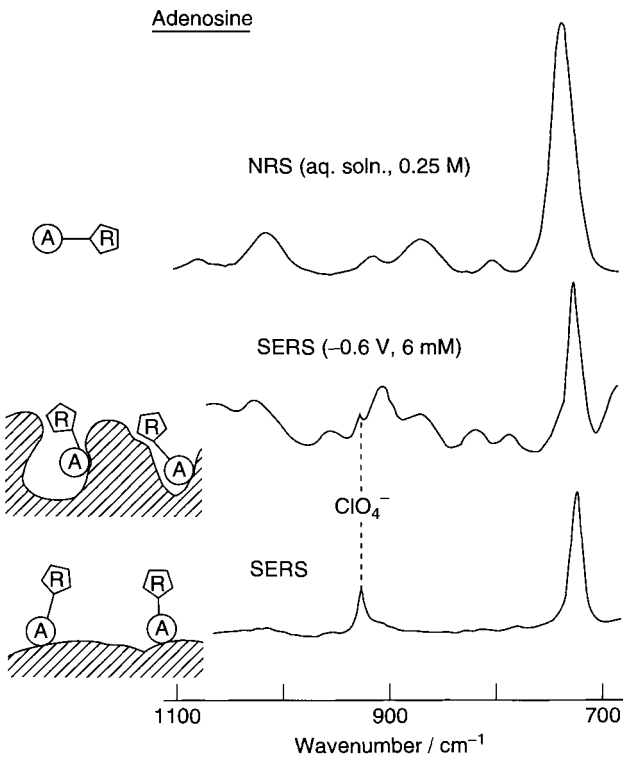


Figure 4-22 Effect of surface roughening on the SERS of adenosine; top, normal Raman spectrum; middle, SERS obtained by heavy roughening; bottom, SERS obtained by mild roughening. (Reproduced with permission from Ref. 45.)

complemented the Raman technique. Examples will be presented to demonstrate typical types of problems in which Raman spectroscopy has played a significant role for their solution. Some of these examples illustrate the usefulness in identifying different polymorphs, and phase transitions for a solid that occur at non-ambient conditions of temperature and/or pressure as determined by Raman spectroscopy. One example measures the non-stoichiometry and the point defect chemistry of the solid state, as followed by the changes in the Raman spectrum. This method has become the method of choice to determine stoichiometric information of solid materials. Another application involves the use of Raman spectroscopy to determine ZrO_2 concentrations in $\text{HfO}_2\text{-ZrO}_2$ solid solutions, which cannot be made easily by other techniques. Compressibilities of solids have been determined using Raman data. The latter three applications are also rather unusual and are included to illustrate the usefulness and versatility of Raman spectroscopy as a probe for changes in the solid state.

4.2.1 POLYMORPHS

Many organic chemicals exist in two or more crystalline forms, which are referred to as *polymorphs*. The preferred crystalline form depends on temperature and pressure; however, multiple polymorphic forms can exist under identical temperature and pressure conditions. Generally, there is one stable form at any particular temperature and pressure, but one or more metastable forms may be produced under different experimental conditions. Typically, the conditions leading to different polymorphs include solvents, seeding, and external influences during precipitation. Often a desired polymorph can be produced from solution by initiating the nucleation with seeds of the desired polymorph. A metastable polymorph may convert to the stable form, but external influences may be required to increase the rate of the conversion.

The polymorphs of a substance can possess considerable different chemical and physical properties. Their melting points and heat capacities will be different. Their x-ray diffraction patterns will depend on the arrangement of molecules in the crystal lattice. In addition, vibrational spectra of the different polymorphic forms of a material will be different. These differences may be minor, but many times there are extensive differences, which can be used to identify the form and to understand its crystalline structure.

There are two main reasons for differences in vibrational structures of polymorphs due to symmetry. As we know, selection rules for vibrational spectra are related to the molecular symmetry. In the gas phase, a molecule can possess a molecular symmetry that is independent of other molecules. It is free to rotate, vibrate, and translate with little influence from other molecules except for occasional collisions. In the liquid phase, neighboring molecules of the same or different species can influence the shape of a molecule, change its symmetry, and consequently, change its spectrum. Molecules are continually colliding with other molecules in the liquid, which leads to random influences on their rotational, vibrational, and translational energies. In the crystalline phase, the molecules are organized into unit cells, which are the repeating units in a crystal. The unit cell changes with each polymorphic form. Each individual molecule is influenced by the surrounding molecules, and each molecule possesses symmetry due to its (site) location in the crystal; this is called the *site symmetry*. The site symmetry may be the same or different from the symmetry of the free molecule; this depends on the order of the molecular symmetry and the influences from neighboring molecules. The second type of symmetry effect in crystals is referred to as *factor-group symmetry*. This effect is due to the fact that vibrations in molecules in close proximity of each other can be coupled. For example, consider two adjacent molecules with carbonyl groups coupled through a dipole–dipole interaction. The vibrations of the two carbonyls could be coupled in phase and out of phase to produce two bands in the carbonyl region. Theoretical details on the effects of site and

factor-group symmetries on vibrational selection rules are given in Sections 1.16–1.18. In this section, the practical effects of crystal structures on the spectra are considered. Site and factor-group symmetries can have several effects on a spectrum of a polymorph. Inactive bands can become active due to symmetry changes. Singlet bands can be split into two or more components by coupling of the vibrations in adjacent molecules. Finally, bands can be shifted in frequency due to interaction with neighboring molecules. The change in the activity and the extent of the splitting can be used to predict the site and factor groups for polymorphic forms.

A hypothetical example of the effects of polymorphic forms is demonstrated in Fig. 4-23. The molecule used in this example is CO₂, which has D_{∞h} molecular symmetry. The simulated infrared (IR) spectrum has a band due to the asymmetric stretch at $\sim 2,350\text{ cm}^{-1}$ and the degenerate bending vibration at 667 cm^{-1} . The Raman spectrum has a single band due to the symmetric stretching vibration at $\sim 1,350\text{ cm}^{-1}$. (Remember that these are hypothetical spectra; the actual Raman spectrum of CO₂ has a doublet in the $1,300\text{ cm}^{-1}$ region due to Fermi resonance between the symmetric stretching frequency with the overtone of the bending vibration.) For demonstration, it is assumed that the molecule is bent at its site in the crystal and that the site symmetry is C_{2v}. In this symmetry configuration, all three vibrations are both IR and Raman active; however, the symmetric stretching vibration produces the strongest Raman band, and the other two fundamental vibrations absorb more strongly in the IR spectrum. The stimulated IR and Raman spectra for two possible factor groups, C_{2v} and C_{2h}, are shown in the bottom half of Fig. 4-23. Two molecules are used for both factor groups. In the C_{2v} factor symmetry, all three fundamental vibrations appear as doublets in both the IR and Raman spectra due to the interaction between the two molecules in the factor group. The splitting of the bending mode at 667 cm^{-1} is small and not apparent in the figure, but there is a shoulder on both the IR and Raman bands in this region. The relative intensities of the other doublets were simulated to approximate real effects. For the C_{2h} factor group, each of the bands is also split; however, the center of symmetry of the factor group precludes any of the band components appearing in both the IR and the Raman spectra. For example, the symmetric stretching vibration is coupled between the two molecules to produce an IR component due to the out-of-phase coupling of the vibrations and a Raman component due to the in-phase coupling. Each of the other two vibrations are coupled in a similar manner to produce an IR active and a Raman active band. For such a simple example, it would be possible to predict both the site and factor-group symmetries by analysis of the IR and Raman spectra.

A real example of the effects of polymorphism on the Raman spectra is demonstrated by the polymorphs of *N*-cyano-*N'*-1 {1-[5-methyl-1*H*-imidazol-4-yl)methylthio]ethyl}-guanidine, which is referred to as *Cimetidine*.

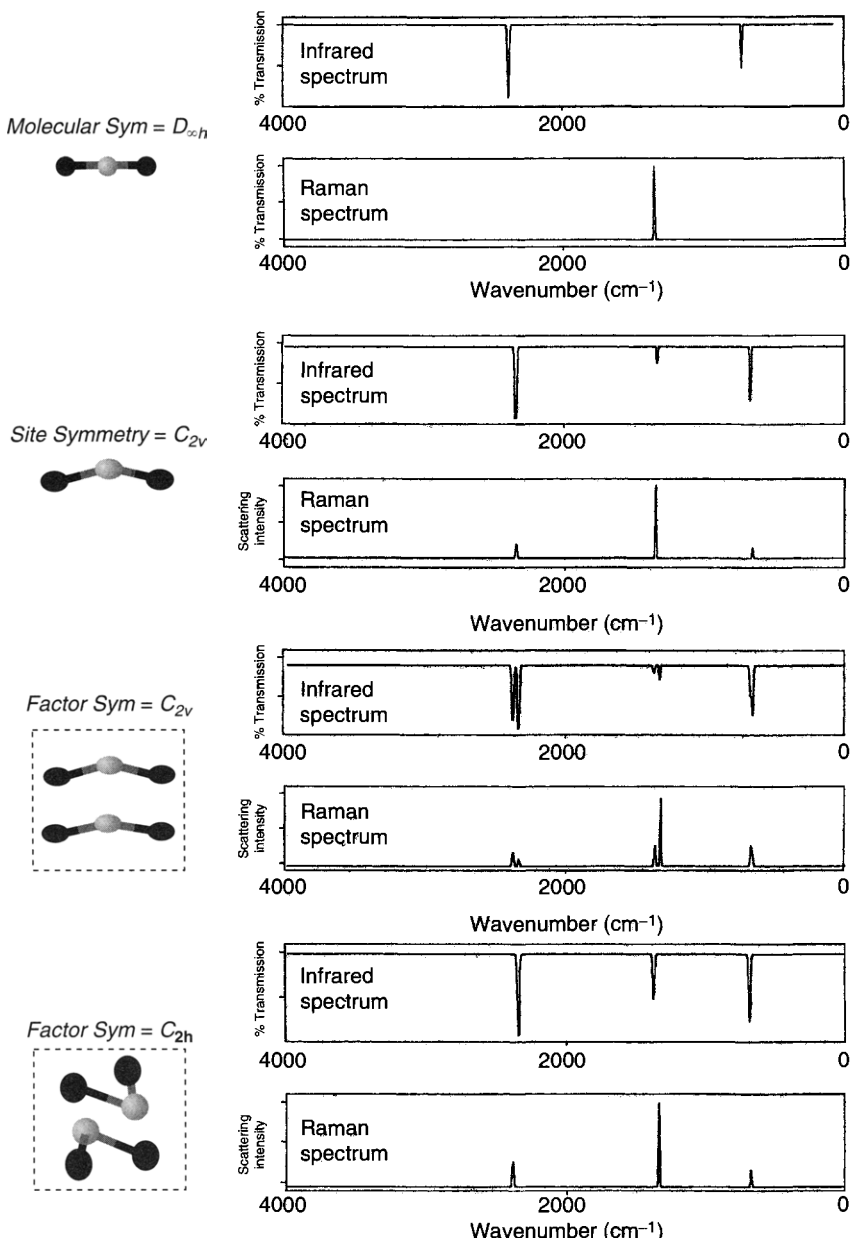


Figure 4-23 From Top to Bottom: simulated infrared and Raman spectra of molecule CO_2 ; Infrared and Raman spectra of CO_2 having a site symmetry of C_{2v} ; infrared and Raman Spectra with a factor group symmetry of C_{2v} ; and factor group symmetry of C_{2h} .

This molecule exists in six polymorphic forms. The full Raman spectra of Cimetidine polymorphs A and B are shown in Fig. 4-24 (46). Several differences are noted in the N—H and C—H stretching regions between 3,400 and 2,800 cm^{-1} . Other significant differences are noted at $\sim 1,300 \text{ cm}^{-1}$ and around 800 cm^{-1} . Raman spectra for all six polymorphs of Cimetidine in the 850- to 450- cm^{-1} region are shown in Fig. 4-25 (47). In this region, each of the six polymorphic forms has a distinctive pattern. The appearance of new bands, splitting of bands, and wavenumber shifts are observed in these spectra. Clearly, Raman spectra can be used for the positive identification of the individual polymorphs of Cimetidine.

A Raman spectrometer was interfaced to a differential scanning calorimeter (DSC) via a fiberoptic probe to monitor the four phases of ammonium nitrate, which are accessible between ambient temperature and its melting point (48). The DSC thermogram characterizing the four phases and the isothermally scanned Raman spectra of the four phases are shown in Fig. 4-26. The Raman bands below 200 cm^{-1} are due to lattice modes, i.e., the stretching and bending vibrations due to the intermolecular bonds or associations between molecules. In phase IV, the lattice vibrations appear as a triplet, which changes into an asymmetric shaped band in the other three phases. Phase III was predicted to have twice the number of molecules in its unit cell as in phase IV; thus the intensity of the lattice modes should be twice as high, and this appears to be the case. The totally symmetric nitrate band at $\sim 1,050 \text{ cm}^{-1}$ has very similar intensities in phases III and IV but decreases in

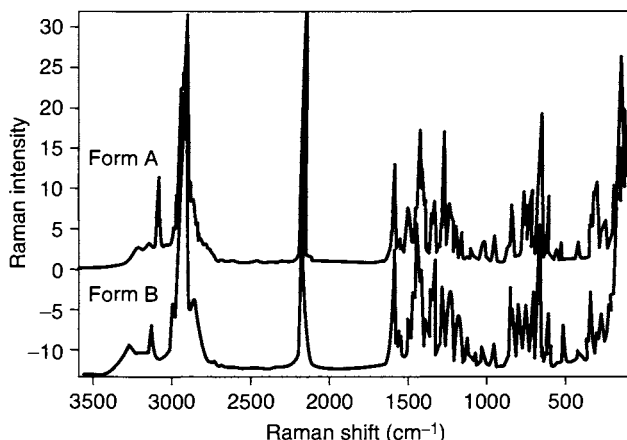


Figure 4-24 Raman spectra of two Cimetidine Polymorphs, A and B, in the 3600–100 cm^{-1} region (with permission of Ref. 46).

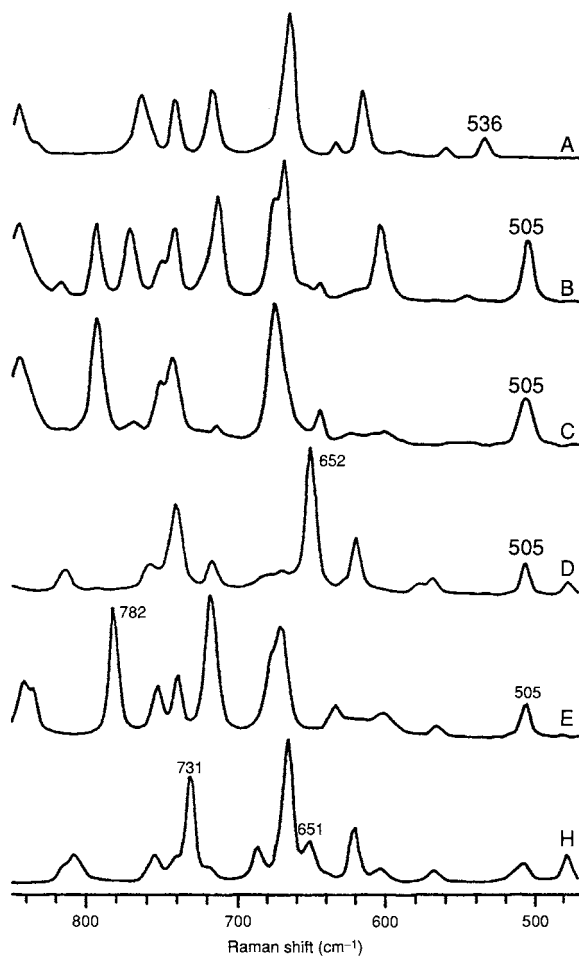


Figure 4-25 Raman spectra of six Cimetidine polymorphs in the $850\text{--}470\text{ cm}^{-1}$ region (with permission of Ref. 47).

both phases II and I. The unit cell for phase IV has two molecules with the nitrates parallel to each other. On the other hand, the unit cell for phase II has two molecules with the nitrates perpendicular to each other, and this perpendicular orientation reduces the intensity of the band; therefore, the symmetric nitrate band in phase II is about half that of phase IV. The unit cell for phase III also has the nitrates perpendicular to each other, but there are twice the number of molecules per unit cell as in phase II, and the intensity of III is approximately two times that of phase II. Phase I consists of only one

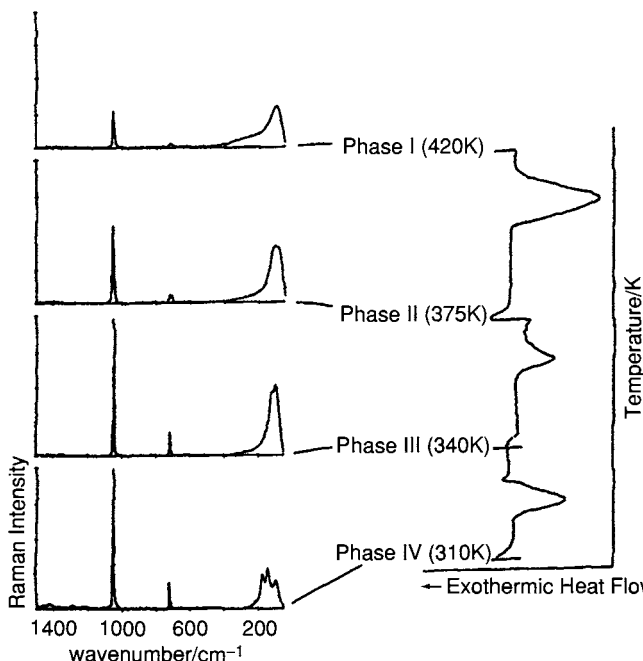


Figure 4-26 Isothermally scanned Raman spectra of phases I, II, III and IV of ammonium nitrate together with the DSC thermogram Characterizing the phases (with permission of Ref 48).

molecule per unit cell, and this explains the weaker intensity of the symmetric nitrate band for this phase compared with the other phases.

Measuring Raman spectra of polymorphs requires little or no sample preparation. Spectra can be measured from single crystals and from powders. Moreover, samples can be contained in glass capillaries or mounted on a goniometer. As mentioned earlier, fiber optics can be used to interface the instrument with the samples. Thus the measurements are straightforward and easy to perform, whereas the analyses produce information on structures and spectral fingerprints for straightforward identifications.

4.2.2 PHASE TRANSITIONS WITH TEMPERATURE VARIATIONS IN $\text{UO}_2(\text{NO}_3)_2 \cdot 6\text{H}_2\text{O}$

The Raman spectrum of uranyl nitrate hexahydrate was followed from 15 to 290 K (49). The changes taking place as a function of temperature were obtained by following the Raman spectra in the OH stretching region.

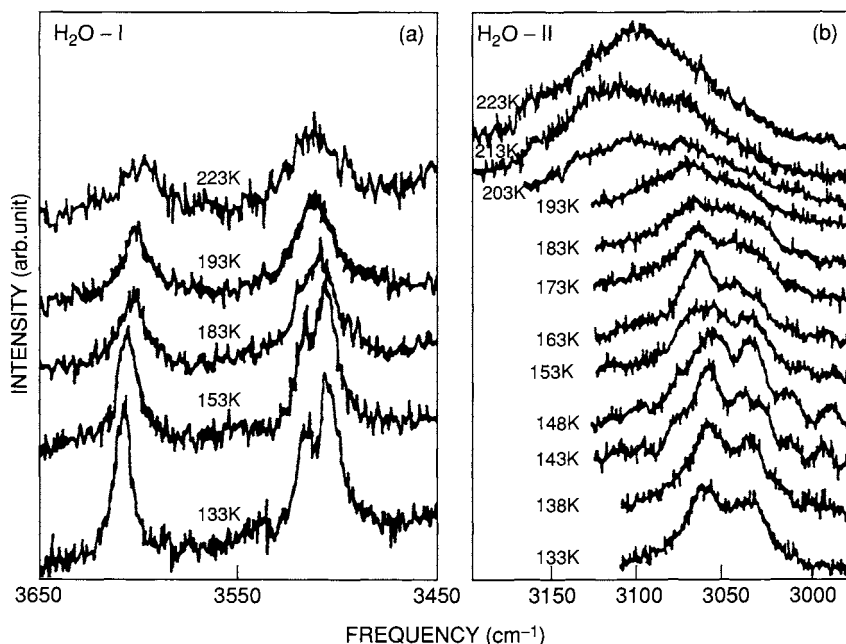


Figure 4-27 Temperature-dependent Raman spectra of uranyl nitrate hexahydrate for the O—H stretching mode of (a) H₂O-I and (b) H₂O-II (514.5 nm excitation). (Reproduced with permission from Ref. 49. Copyright © 1989 John Wiley & Sons, Ltd.)

The temperature-dependent Raman spectra are depicted in Fig. 4-27a, b. Figure 4-27a shows the spectra of H₂O-I (the water molecules in the inner coordination sphere) from 133–223 K. Figure 4-27b shows the spectra of H₂O-II (the water molecules in the outer sphere). The spectra above 223 K are not shown because of the overlap with fluorescence that is observed with the 514.5 nm excitation. Plots of the variations of band frequency with temperature are illustrated in Fig. 4-28a, b for H₂O-I and H₂O-II. Two discontinuities are observed at 195 ± 5 K and 140 ± 5 K, indicative of three distinct phases occurring in the temperature range studied, as indicated in Fig. 4-28a. The higher-frequency OH stretch region, as shown in Fig. 4-28b does not show any discontinuities for H₂O-I. A plot of full width at half maximum intensity (FWHM) vs. T for H₂O-I shows a discontinuity at ~ 140 K (Fig. 4-28c, d). Additional support for these phase transitions was found from the temperature dependences of the UO₂²⁺ vibrational mode, lattice vibrations and the NO₃⁻ ion vibrations (translations and rotations).

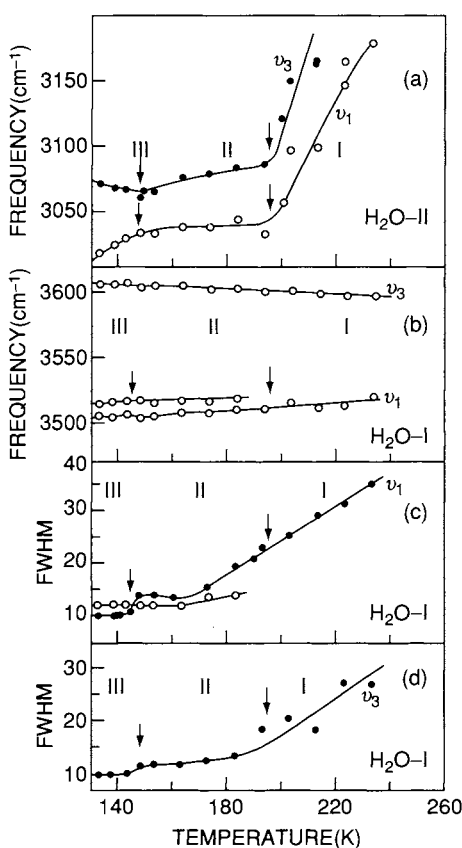


Figure 4-28 Variation with (a) temperature and (b) the frequencies of ν_1 and ν_3 modes for $\text{H}_2\text{O-II}$ and $\text{H}_2\text{O-I}$ and (c) and (d) the FWHM of the ν_2 and ν_3 modes of $\text{H}_2\text{O-I}$. (Reproduced with permission from Ref. 49. Copyright © 1989 John Wiley & Sons, Ltd.)

4.2.3 PHASE TRANSITIONS IN CsVO_3 OCCURRING WITH AN ELEVATION OF PRESSURE

Elevated pressure effects on solid CsVO_3 were followed by Raman spectroscopy (50). The study was made by using a gasketed diamond anvil cell with argon as the pressure medium to insure hydrostatic pressures. The pressure was determined using the ruby fluorescent method (see Section 3.1). At room temperature, CsVO_3 has an orthorhombic structure, and based on the changes occurring in the Raman spectra as pressure is increased, new phases are also found at 10, 11.5 and 13 GPa. Plotting the Raman frequencies as a function of pressure shows discontinuities at the aforementioned pressures, indicative of phase transitions occurring. Figure 4-29a shows the pressure dependence in

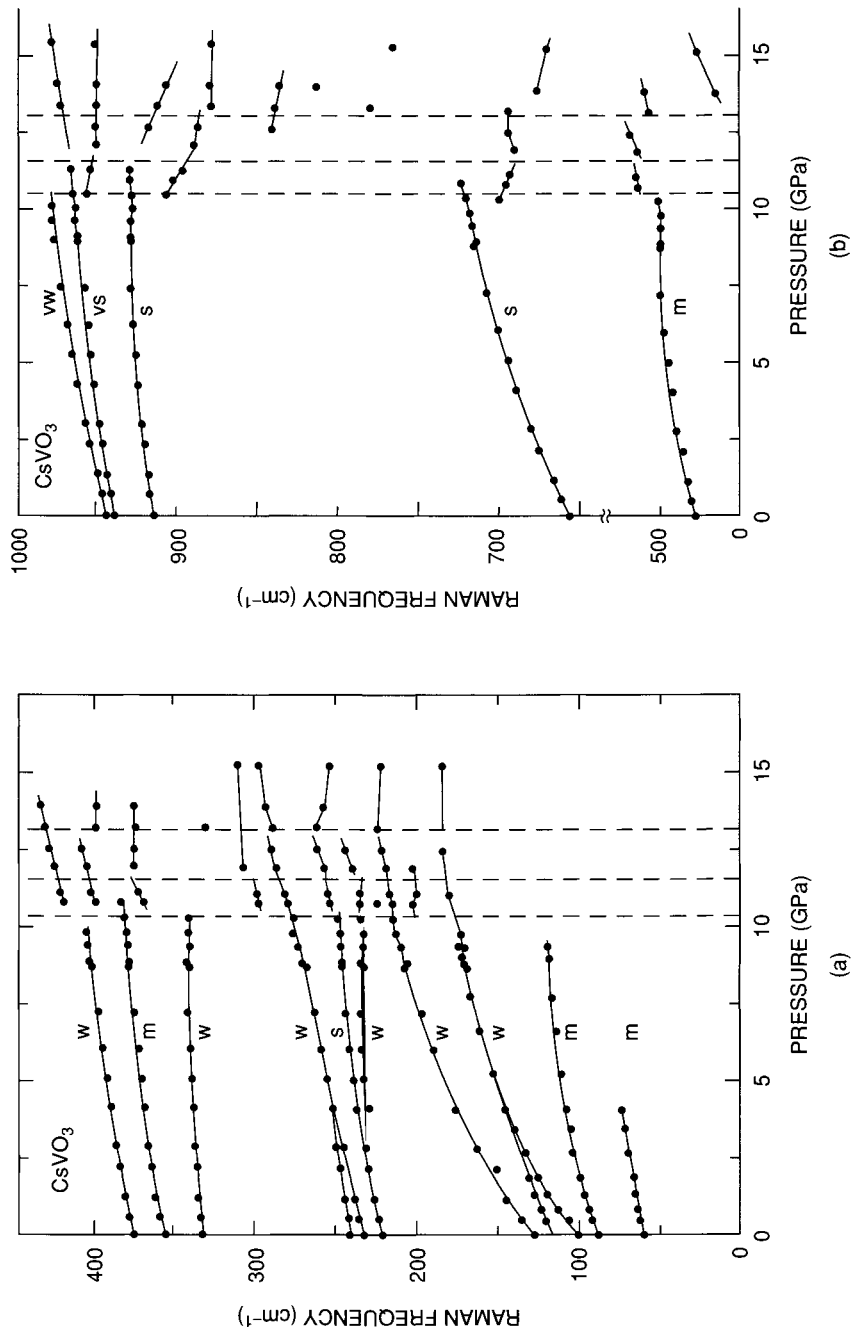


Figure 4-29 Pressure dependence of (a) the low-frequency region and (b) high-frequency region Raman peaks of CsVO_3 . The vertical dashed lines mark the pressure-induced phase transitions. The symbols (w = weak, m = medium, s = strong) signify the relative intensity of the Raman peaks. (Reproduced with permission from Ref. 50. Copyright © 1991 John Wiley & Sons, Ltd.)

the region 400 cm^{-1} and between 500 and $1,000\text{ cm}^{-1}$. Figure 4-29b shows the Raman spectra of phase I and of phases II, III and IV. The phase changes are attributed to a subtle structural change affecting the VO bond angle. The second and third transitions involve the twisting and rearrangement of the corner-sharing geometry of the polyhedral units in the chains of CsVO_3 .

4.2.4 MEASUREMENT OF NON-STOICHIOMETRY IN SOLIDS

The changes in non-stoichiometry and point defects of solid perovskite (BaTiO_3) at 900°C can be observed with Raman spectroscopy (51). The method is believed to be more sensitive than the neutron scattering technique and has become the standard in determining stoichiometric information for solid materials. The interest in perovskite-type materials stems from their use in solid-state capacitors.

Pressed pellets of BaTiO_3 were sintered in a platinum dish for six hours at 900°C in a controlled partial pressure of oxygen. The samples were quenched to room temperature, and the spectra recorded on a four-slit double-monochromator Raman spectrophotometer. An Ar^+ laser with excitation at 514.5 nm was the source. The spectra were recorded at room temperature. Figure 4-30 shows the spectrum of BaTiO_3 whose Ba/Ti ratio is equal to 0.9999. The Raman spectrum is sensitive to the Ba/Ti ratio and the oxygen non-stoichiometry. The half-band width is variable as well as the intensity ratio of the 525 and 713 cm^{-1} bands. The ratio (I_{525}/I_{713}) is at a minimum at the composition of 0.9999, and this can be observed in Fig. 4-31, which shows a plot of the intensity ratio (I_{525}/I_{713}) vs. the Ba/Ti composition.

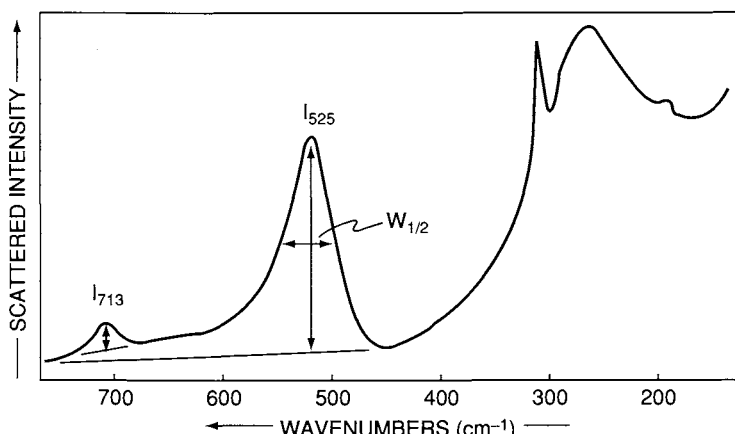


Figure 4-30 A Raman spectrum of BaTiO_3 for $\text{Ba}/\text{Ti} = 0.9999$ with spectral parameters (intensities and half-band width) defined. This sample was quenched after 3 hours in 1 atm oxygen. (Reproduced with permission from Ref. 51.)

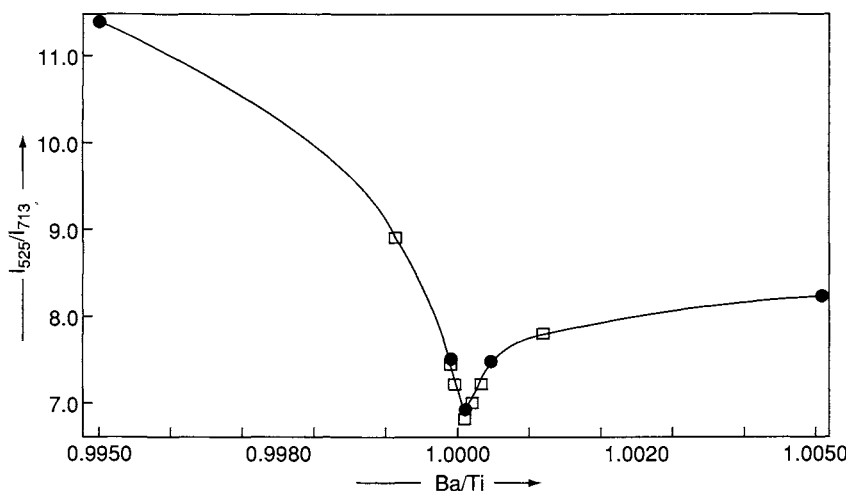


Figure 4-31 Dependence of the I_{525}/I_{713} ratio upon the Ba/Ti ratio for OGC samples (□) and MTU samples (●). The samples were quenched from 900°C in 1 atm. (Reproduced with permission from Ref. 51.)

OGC = Oregon Graduate Center Samples

MTU = Michigan Technological University Samples.

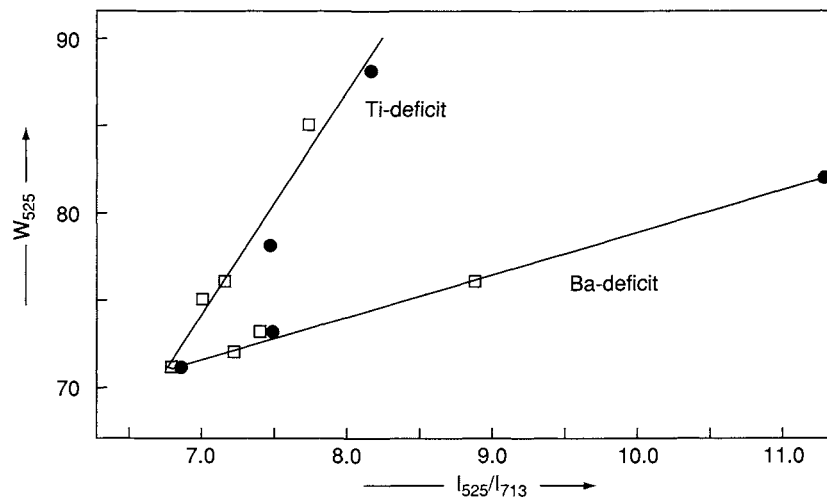


Figure 4-32 Correlation of the intensity ratio and half-band width for Ba-deficit and Ti-deficit samples (900°C, 1 atm O_2). (Reproduced with permission from Ref. 51.)

As the Ba/Ti ratio increases beyond 1.0, the intensity ratio I_{525}/I_{713} increases slightly and then levels off. When the Ba/Ti ratio decreases there is a significant rise in the I_{525}/I_{713} ratio. Figure 4-32 shows a plot of the 525 cm^{-1} band

vs. the intensity ratio I_{525}/I_{713} . The two independent lines, Ba-rich and Ti-rich, have a common origin at $\text{Ba}/\text{Ti} = 0.9999$. This allows one to determine quantitative information about stoichiometry at room temperature from Raman data. These results would be difficult to obtain by any other technique.

It has been possible to obtain intrinsic oxygen vacancies in solids of this type from Raman data. The dependence of the intensity ratio I_{713}/I_{525} upon the partial pressure of oxygen is non-linear, and the sign of the slope changes. The ratio first decreases and then increases as the partial pressure of oxygen decreases. This trend suggests that this ratio is sensitive to changes in the predominant type of defects occurring in the solid. This is illustrated in Fig. 4-33, where $\log[\Delta(I_{713}/I_{525})]$ is plotted vs. the oxygen partial pressure ($\log P_{\text{O}_2}$).

4.2.5 $\text{HfO}_2\text{-ZrO}_2$ SOLID SOLUTIONS

Hafnia and zirconia are known to form a continuous series of solid binary solutions. The use of Raman spectroscopy to provide information about the $\text{HfO}_2/\text{ZrO}_2$ ratios for the specific phases (52) (e.g., the $\text{HfO}_2/\text{ZrO}_2$ solid solutions), rather than for the total material, has proven to be more advantageous than the use of other traditional techniques such as X-ray diffraction

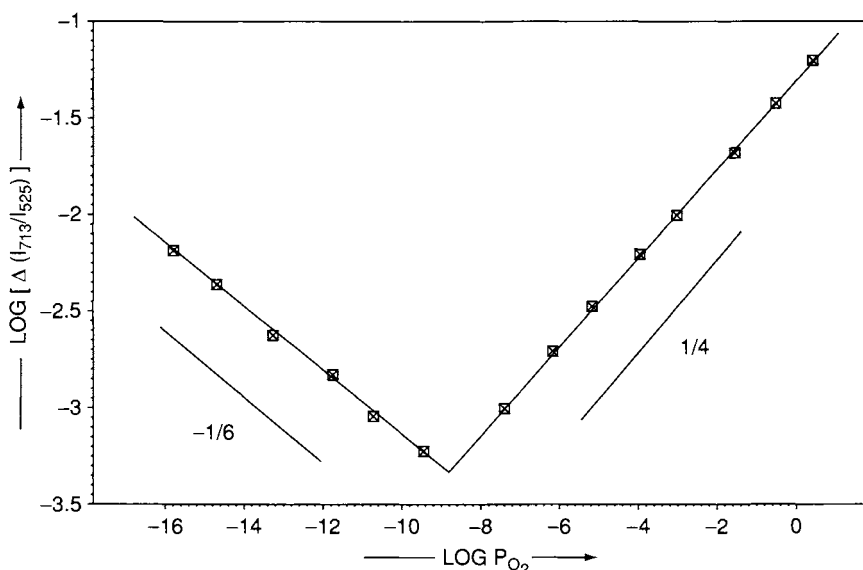


Figure 4-33 Oxygen partial pressure dependence of the change in Raman band intensity ratio for samples with $\text{Ba}/\text{Ti} = 0.9999$ ($R = I_{713}/I_{525}$, $\Delta R = R - R_0$). (Reproduced with permission from Ref. 51.)

whose peak locations do not show measurable shifts with changes in solid solution composition. Also, techniques such as fluorescence spectroscopy show relative Hf/Zr concentrations for total materials, but will not indicate whether or not these cations are occurring in solid solution phases.

Raman spectra of powdered samples in capillary tubes were obtained using a double monochromator spectrometer (Model 1401—Spex Industries, Inc.) with the blue laser line excitation (488 nm). The scattered radiation from the sample was taken at 90° to the incident beam.

Figure 4-34 shows the Raman spectra observed for the powders obtained for the various investigated $\text{HfO}_2\text{--ZrO}_2$ solid solutions. The observed

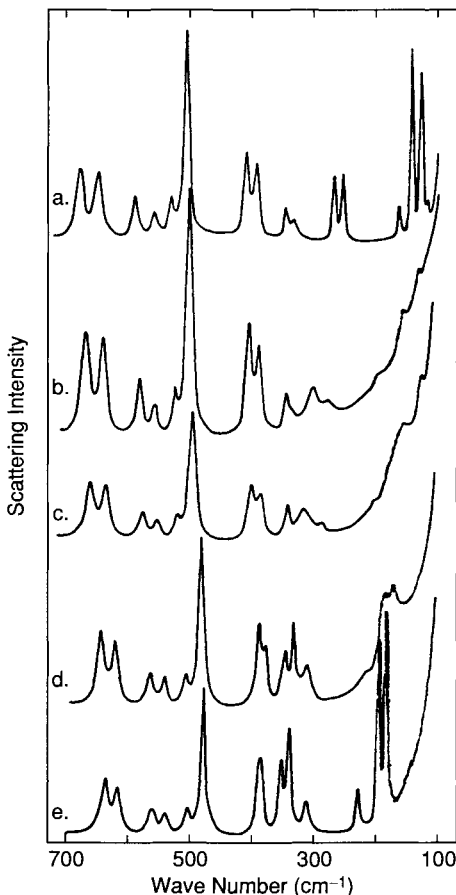


Figure 4-34 Raman spectra for precipitated and fired $\text{HfO}_2\text{--ZrO}_2$ solid solutions containing (a) 100% HfO_2 , (b) 75% HfO_2 , (c) 50% HfO_2 , (d) 25% HfO_2 , and (e) 100% ZrO_2 . (Reproduced with permission of the American Ceramic Society from Ref. 52. Copyright 1982.)

bands do not split, but gradually shift between those found for the pure end members. This is illustrated in Fig. 4-35, which shows nearly linear changes in frequency with ZrO_2 content for the six Raman bands with the highest frequencies, except for the 189 cm^{-1} band, which shows a discontinuous non-linear change with the HfO_2 content (not shown in Fig. 4-35). Figure 4-34a is 100% HfO_2 , b is 75% HfO_2 , c is 50% HfO_2 , d is 25% HfO_2 , and e is 100% ZrO_2 in mixtures of the solid solutions. The half-widths of the Raman

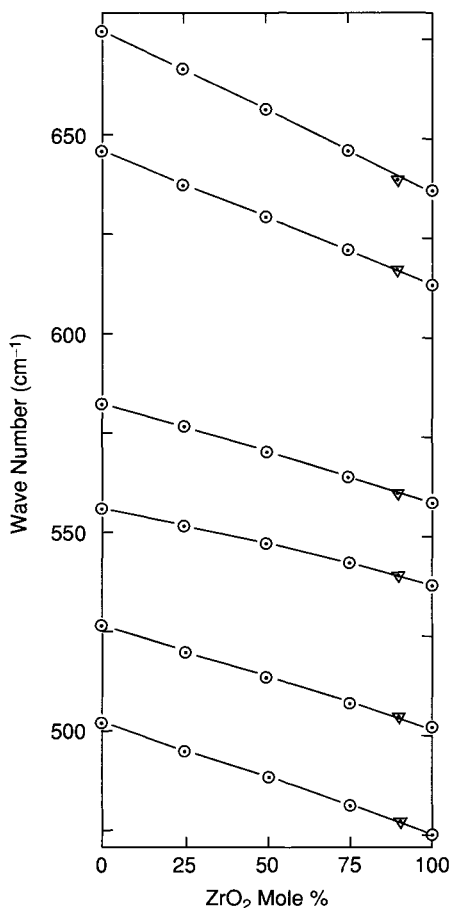


Figure 4-35 Relation between wavenumber and HfO_2 content for Raman bands of $\text{HfO}_2\text{-ZrO}_2$ solid solutions: (○) results for normally fired samples and (∇) results for plasma-fired samples. (Reproduced with permission of the American Ceramic Society from Ref. 52. Copyright 1982.)

Table 4-10 Correlation of Raman Bands of $\text{HfO}_2\text{-ZrO}_2$ Compositions

Wavenumber (cm^{-1})				
100% HfO_2	75% HfO_2	50% HfO_2	25% HfO_2	100% ZrO_2
676	667	657	647	637
646	638	630	622	614
582	577	571	565	559
556	552	548	543	538
526 (sh) ^a	520 (sh)	514 (sh)	508 (sh)	502 (sh)
502	495	489	482	475
403	398	394	387	
387	382	379	375 (sh)	382 (b) ^a
340	340	339	345	348
327	329 (sh)		330	334
262	296 (b)	311 (b)	309	310
246	274 (sh)	282 (b)		
162	185 (sh)	200 (sh)	212 (sh)	221 (sh)
141	155	155 (sh)	183	189
126	130	130 (sh)	172	177

^ash = shoulder and b = broad.

bands of the pure end members and the solid solutions are smaller than the wavenumber separations between related Raman band shifts. For example, the half-width of the Raman band for HfO_2 at 502 cm^{-1} , which correlates to the band at 475 cm^{-1} for ZrO_2 , is 8 cm^{-1} . Clear correlations can be made between the Raman bands of pure ZrO_2 and HfO_2 using those of the solid solutions since the Raman bands shift continuously with respect to the chemical compositions, and the relative Raman band intensities of the solid solutions correspond to those of the pure end members. Table 4-10 lists the wavenumbers of the correlated Raman bands from HfO_2 , ZrO_2 and $\text{HfO}_2\text{-ZrO}_2$ solid solutions.

4.2.6 COMPRESSIBILITIES OF SOLIDS USING RAMAN DATA

A study was conducted to determine an indirect method for obtaining compressibilities of solids from Raman data (53). In this study, the solids used were TbVO_4 and DyVO_4 . The method is based on determining the VO bond distance from Raman data involving the Vanadium-Oxygen (VO) stretching frequency ($v_1(A_g)$). The bonds lengths are then correlated to the size of the unit cell of the crystal. This procedure allows one to determine the change in volume of the crystals from the changes in the corresponding stretching VO frequency. For the lanthanide vanadates, a relationship between the volume

of the unit cell ($V(P)$) and the VO bond distance R in Å, density (d) at pressure P , where C is a constant is

$$V(P) = C[d(\text{VO})_P]^3. \quad (4-1)$$

The relative value $V(P)/V(0)$ is given by

$$V(P)/(V(0)) = [d(\text{VO})_P]^3 / [d(\text{VO})_0]^3. \quad (4-2)$$

If the VO bond distances can be determined as a function of pressure from Raman spectroscopy, then the compressibility of the vanadates can be estimated. Bond distances can be determined from Raman data (54).

$$\nu_1(A_g) = 21,349 \exp(-1.9176R). \quad (4-3)$$

Utilizing Eqs. (4-2) and (4-3), $V(P)/V(0)$ can be calculated at different pressures as seen in Table 4-11, and in Fig. 4-36. The compressibilities are obtained from the solid lines in Fig. 4-36 by using a simple polynomial fit of the lines. Values of $6.42 \times 10^{-3}\text{GPa}^{-1}$ for TbVO_4 and $6.07 \times 10^{-3}\text{GPa}^{-1}$ for DyVO_4 were calculated. This study demonstrates a unique application of the Raman effect.

4.2.7 ELECTRICAL CONDUCTOR APPLICATIONS

Raman spectroscopy has played a significant role in the characterization of electrical conductors, some of which have become superconductors. There are three general classes of compounds that have been investigated using Raman spectroscopy. These are the high- T_c superconducting ceramics; the low- T_c

Table 4-11 Relative Volumes of TbVO_4 and DyVO_4 at Different Pressures

Pressure (GPa)	TbVO_4		DyVO_4	
	$V(P)/V(0)$	$V(P)/V(O)$	$V(P)/V(0)$	$V(P)/V(O)$
0	1		1	
0.5	0.9968		0.9976	
1.0	0.9936		0.9941	
1.5	0.9905		0.9911	
2.0	0.9873		0.9882	
2.5	0.9842		0.9853	
3.0	0.9811		0.9824	
3.5	0.9780		0.9795	
4.0	0.9750		0.9766	
4.5	0.9719		0.9738	
5.0	0.9689		0.9709	

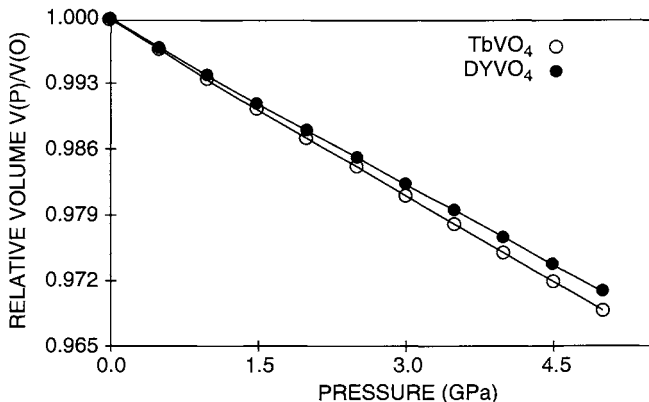


Figure 4-36 Volume compression of TbVO₄ and DyVO₄ calculated as a function of pressure. Solid lines are fits to a simple polynomial expression. (Reproduced with permission from Ref. 53.)

superconducting charge-transfer (C-T) organics, and the fullerenes (e.g., C₆₀), which form some superconducting salts with the alkali metals. Typical applications of Raman spectroscopy for each of these classes will be presented.

(a) *The Raman Spectra of C₆₀ and Several of its Superconducting Salts*

Since the discovery of the soccer-ball-like, 60-carbon buckminsterfullerene, scientists have been fascinated by this molecule. The molecule possesses a truncated icosahedral structure, of I_h symmetry, and is depicted in Fig. 4-37.

Raman spectroscopy has been an excellent diagnostic tool in the study of the C₆₀ molecule and its salts, because of the high symmetry these substances possess. In the case of C₆₀, which has a center of symmetry, the gerade modes are observed only in the Raman spectrum. Furthermore, the materials are excellent Raman scatterers.

The early spectral work on C₆₀ was suspect because of its impurities. To prevent overheating of the sample, very low values of laser power were used (~20 mW), at a resolution of 1 cm⁻¹. Figure 4-38 shows the Raman spectrum of pure C₆₀. Hendra and co-workers (55) observed 14 bands, although one was very weak, and two others were shoulders on strong bands and may be due to resonance effects. For a truncated icosahedral structure, 10 (2A_g + 8H_g) Raman-active modes are predicted. As shown in Fig. 4-38 the lowest-frequency band at 273 cm⁻¹ is the H_g “squashing” mode. The two A_g modes at 1,467 and 495 cm⁻¹ are assigned to the pentagonal pinching and cage breathing modes, respectively. For reference to the species of vibrations in an icosahedral (I_h) symmetry, see the tables given for the I_h point group in Appendices 1 and 2. The use of the correlation method has been applied to

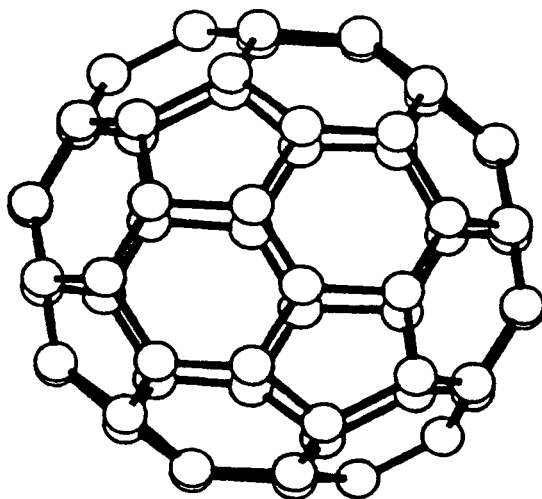


Figure 4-37 Structure of the C₆₀ molecule.

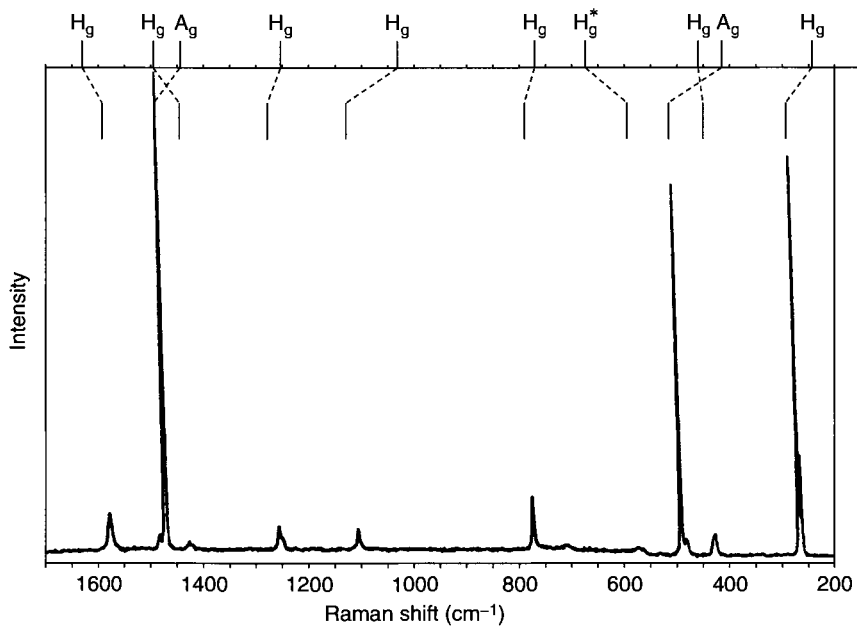


Figure 4-38 Raman spectrum of C₆₀. (Reprinted from T. J. Dennis *et al.*, *Spectrochim. Acta* 47A, 1289, Copyright 1991, with permission from Pergamon Press Ltd., Headington Hill Hall, Oxford OX3 0BW, UK.)

*The original assignment made was in error. This vibration occurs at 710 cm⁻¹ (see Ref. 56).

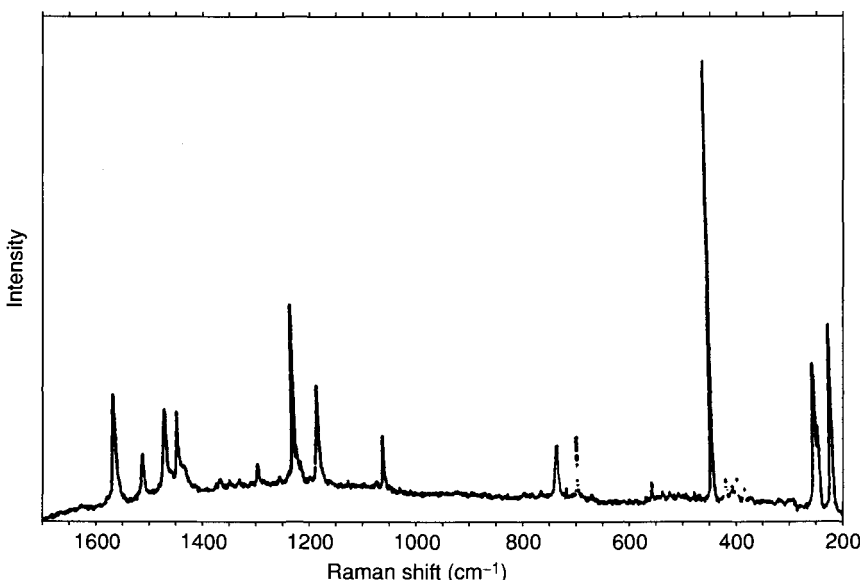


Figure 4-39 Raman spectrum of C₇₀. (Reprinted from T. J. Dennis *et al.*, *Spectrochim. Acta* 47A, 1289, Copyright 1991, with permission from Pergamon Press Ltd., Headington Hill Hall, Oxford OX3 OBW, UK.)

determine the number of IR-and Raman-active vibrations for C₂₈, C₃₂, C₅₀, C₆₀ and C₇₀ molecules (56).

It is possible to distinguish between C₆₀ and C₇₀ and higher carbon entities from their Raman spectra. Figure 4-39 shows the Raman spectrum of C₇₀. Comparison of the Raman spectrum of C₆₀ with that of C₇₀ (Figs. 4-38 and 4-39) illustrates the differences between the two molecules. In the C₇₀ molecule the symmetry has decreased to D_{5h}, and thus more bands are expected to appear in the Raman spectrum, as is observed.

Upon electron doping with alkali and alkaline earth materials, C₆₀ forms superconducting materials. C₆₀ can become superconducting as well, by hole doping and by expanding the C₆₀ lattice by inclusions of CHCl₃ and CHBr₃. The critical temperature for superconducting reaches 117K for the CHBr₃ compound. Table 4-12 lists some metal doped fullerides and fullerenes that become superconducting, along with their critical temperatures (Tc's).

In the salts of C₆₀ with K⁺ and Rb⁺, the A_g breathing mode at ~1,467 cm⁻¹ has been investigated by Raman spectroscopy. This mode shifts from 1,467 cm⁻¹ in neat C₆₀ to lower frequencies as one follows the doping process (salt formation). For the K₃C₆₀ salt (57), the shift is from 1,467 cm⁻¹ to 1,445 cm⁻¹. For the Rb₃C₆₀ salt (58), the shift is from 1,467 cm⁻¹ to 1,447 cm⁻¹. If the doping is allowed to continue, the shift is lowered

Table 4-12 Superconducting Metal Fullerides and Fullerenes (59–61)

Salt	T_c (K)	Salt	T_c (K)
$\text{Li}_2\text{KC}_{60}$	50×10^{-3}	$\text{Rb}_2\text{KC}_{60}$	22
$\text{Li}_2\text{CsC}_{60}$	50×10^{-3}	$\text{Rb}_{1.5}\text{K}_{1.5}\text{C}_{60}$	25
Na_3C_{60}	< 2	Rb_3C_{60}	29
$\text{Na}_2\text{KC}_{60}$	2.5	$\text{Rb}_2\text{CsC}_{60}$	31
$\text{Na}_2\text{RbC}_{60}$	3.5	$\text{Cs}_2\text{RbC}_{60}$	33
$\text{Na}_2\text{CsC}_{60}$	12	$\text{Cs}_x\text{C}_{60}^c$	29.5
$\text{Na}_2\text{Cs}(\text{NH}_3)_4\text{C}_{60}$	20	Cs_5C_{60}	8.5
K_3C_{60}	19	Sr_6C_{60}	4
$\text{K}_2\text{RbC}_{60}$	23	Ba_6C_{60}	6
$\text{K}_2\text{CsC}_{60}$	24	$\text{Sm}_{2.75}\text{C}_{60}$	8
$\text{KRb}_2\text{C}_{60}$	7	$\text{Yb}_{2.75}\text{C}_{60}$	6
C_{60} (holedoped) ^{a, b}	52	C_{60} (intercalated with CHCl_3) ^d	80
C_{60} (intercalated with CHBr_3) ^c	117		

^aJ. H. Schon, Ch. Kloc, and B. Battlog, *Nature* **408**, 549 (2000).

^bO. Gunnarson, *Nature*, **408**, 528 (2000).

^cNot characterized.

^dJ. H. Scon, Ch Kloc, and B. Battlog, *Science* **293**, 1570 (2001).

to $1,429\text{ cm}^{-1}$. Figure 4-40 illustrates the Raman spectra of a C_{60} film during the rubidium doping process.

Raman spectroscopy has been used to determine various features and characterization of carbon nanotubes, and has been instrumental in determining 1D electronic structure and mechanical strength and compliance of these materials (69, 61).

(b) Charge-Transfer Organic Superconductors

Charge-transfer (C-T) reactions between an organic donor and an acceptor molecule and anion have, in some instances, produced superconductors. As in the case of the C_{60} molecule, Raman spectroscopy has played an important role in the characterization of the neat organic donor, as well as the C-T salts (62). Several examples of applications follow.

A successful donor has been bis(ethylenedithio)tetrathiafulvalene (BEDT-TTF or ET). The structure of ET is depicted in Fig. 4-41. The infrared and Raman frequencies of BEDT-TTF and BEDF-TTF- d_8 have been reported and assignments made (63). Figure 4-42 shows the Raman spectra of several salts in the region of $800\text{--}50\text{ cm}^{-1}$. Here, the research was done to determine the nature of the polyiodides in the molecule (64).

The Raman-active $\text{C}=\text{C}$ stretching vibration in neat ET has been followed by Raman spectroscopy. Upon salt formation, the frequency lowers. Table 4-13 shows this result, comparing neat donors with their salts. The vibration

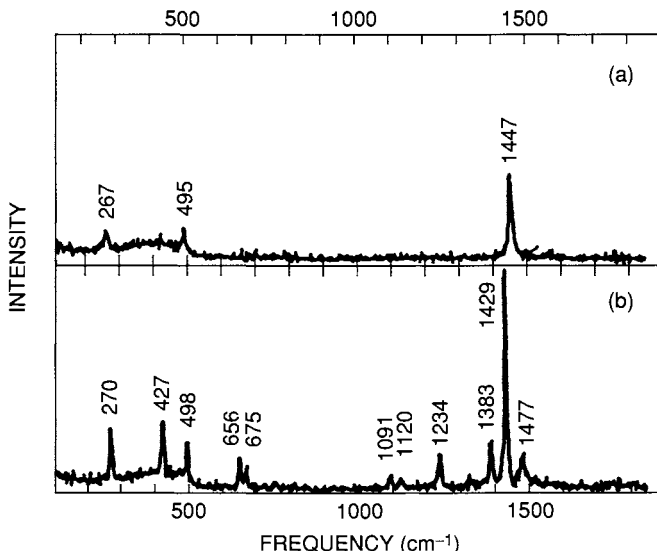


Figure 4-40 *In situ* Raman spectra of a C₆₀ film taken during rubidium doping: (a) superconducting and (b) insulating. (Reproduced with permission from Ref. 58. Copyright 1992 American Chemical Society.)

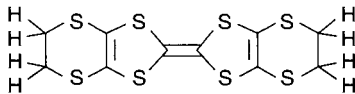


Figure 4-41 Structure of ET.

becomes IR-active and combines with the conducting electrons in the salts (electron-molecular vibration, EMV) (65) and shifts to lower frequency. The extent of this shift is a measure of the electron-molecular vibration coupling in a given superconducting salt (65).

Limited Raman studies have been made on the ET salts because they are black and absorb the laser energy, causing them to decompose. This decomposition has occurred even at low laser power levels and with a near infrared laser.

These C-T salts are metallic at room temperature and are also two-dimensional. Upon lowering the temperature some of these salts become superconducting, provided that they can avoid the electronic instability toward a metal-insulator transition. The actual mechanism of superconductivity is not known at present.

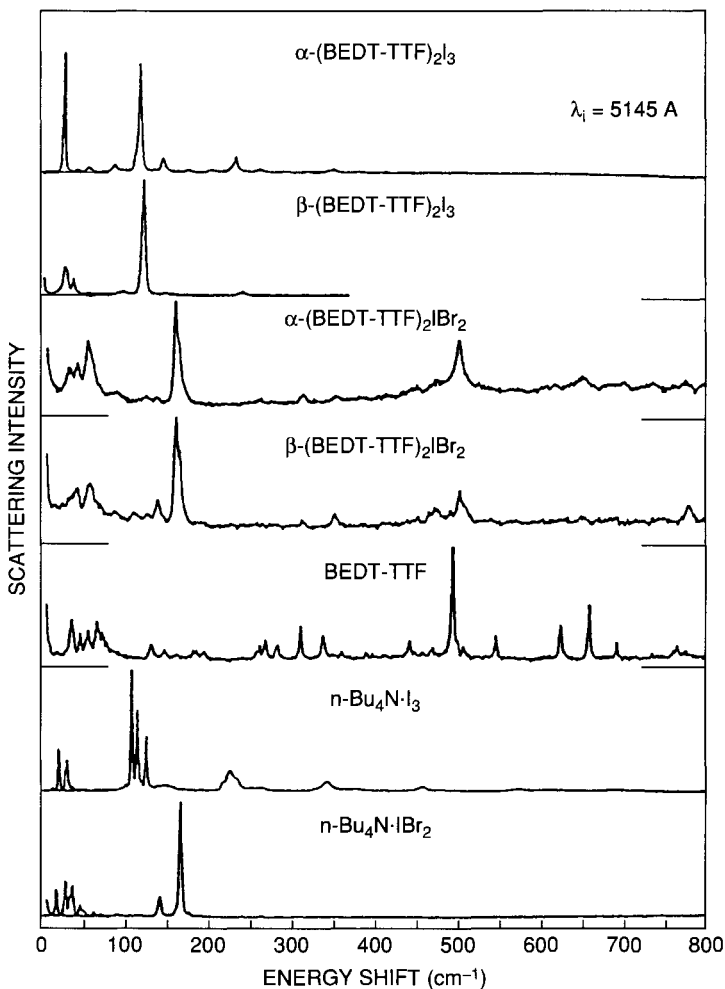


Figure 4-42 Spectra of several (ET) X salts. (Reproduced from S. Suga and G. Saito, *Solid State Commun.*, **58**, 759, Copyright 1986, with permission from Pergamon Press Ltd., Headington Hill Hall, Oxford OX3 0BW, UK.)

(c) High- T_c Ceramic Superconductor Applications

In 1986, the synthesis of copper-oxide based ceramics with a superconducting temperature (T_c) exceeding the boiling point of liquid nitrogen (77 K) was a major contribution in the scientific field. To date, a number of superconductors of this type have been prepared, and the highest T_c reached is 134 K at

Table 4-13 Comparison of the $V_{c=c}$ Frequencies of Neutral Donor Molecules with the Vibronic Frequencies of Their Salts (cm^{-1})

Donor	$V_{c=c}$	Salt	Vibronic Frequency
ET	1,511	$\kappa\text{-}(ET)_2\text{Cu}(\text{NCS})_2$	1,290
TTF	1,518	(TTF) Br	1,368
TMTTF ^a	1,538	(TMTTF)Br	1,340
TMTSF ^a	1,539	(TMTSF) ₂ ReO ₄	1,415

^aTMTTF refers to tetramethyltetrathiafulvalene, and TMTSF to tetramethyltetraselenafulvalene.

ambient pressure and 154K at high pressure for superconductor, $\text{HgBa}_2\text{Ca}_2\text{Cu}_3\text{O}_8$ (66).

Considerable vibrational studies have been made, with Raman spectroscopy being a major contributor. Most of the materials have a center of symmetry and thus the gerade, low-lying phonon modes are only observed in the Raman experiment (see Section 1.17). A typical application is presented herewith.

The original studies with the ceramic superconductors were conducted on powdered, impure phases, and therefore the early work reported bands belonging mainly to the impurities. Most of the definitive information that has contributed to the identification and assignments of the Raman bands for these compounds has come from investigations made with single crystals.

This application will concentrate on the $\text{MBa}_2\text{Cu}_3\text{O}_{7-\delta}$ (123) system, where $M = Y$. Another designation for this system is YBCO. For this system, the optimum superconductivity is obtained for $\text{YBa}_2\text{Cu}_3\text{O}_{7-\delta}$, when $\delta = 0.3$. This formulation has an orthorhombic (O) structure. Upon loss of oxygen a phase transition takes place to an insulator with a tetragonal (T) structure. Figure 4-43 shows the structures for the O and T-phases.

Figure 4-44 shows the correlation diagram (see Appendix 6) for $y = 6$ to $y = 7$ for $\text{YBa}_2\text{Cu}_3\text{O}_y$. For the orthorhombic form, $5A_g$ Raman-active modes are predicted. In going from the O form to the T form, the vibrations change to $4A_{1g} + B_{1g}$ modes. Figure 4-45 shows the Raman spectrum of the O-form. There is general agreement that $5A_g$ modes are observed for the O form of YBCO, as detected by polarization studies. With zz polarization of a single crystal, the bands are located at 502, 436, 335, 146, and 115 cm^{-1} , are attributed to the following vibrations:

- 502 cm^{-1} : axial motion of the O(4) atoms,
- 436 cm^{-1} : Cu(2)-O(2) and-O(3) bond bending with the O(2) and O(3) atoms moving in phase,
- 335 cm^{-1} : Cu(2)-O(2) and-O(3) bond bending with the O(2) and O(3) atoms moving out of phase,
- 146 cm^{-1} : axial stretching of the Cu(2) atoms, and
- 115 cm^{-1} : axial stretching of the Ba atoms.

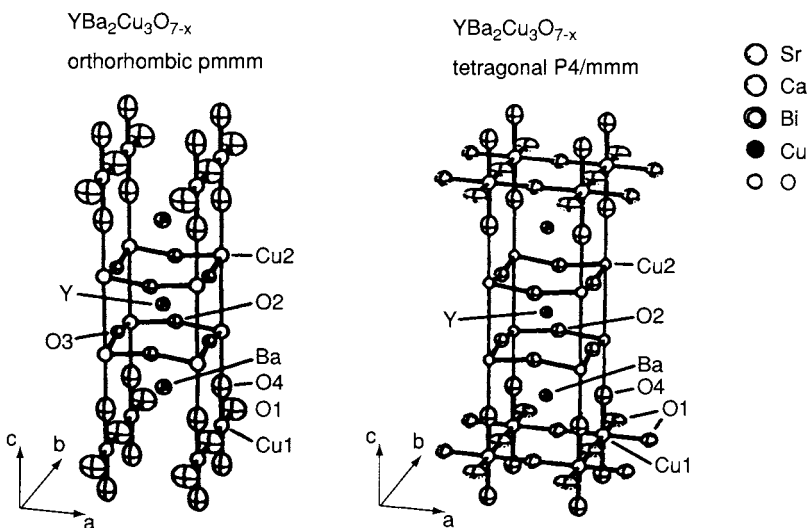


Figure 4-43 Structures of the orthorhombic and tetragonal forms of $\text{MBa}_2\text{Cu}_3\text{O}_7$. (Reproduced with permission from Ref. 67.)

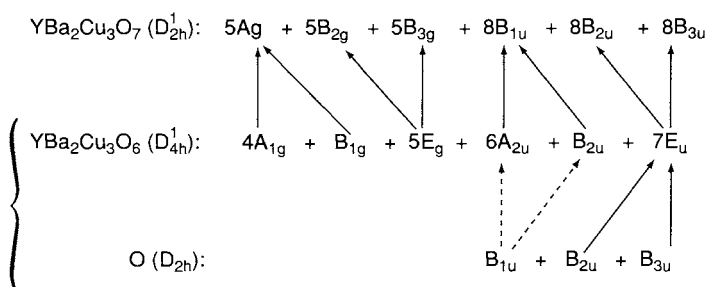


Figure 4-44 Correlation diagram for $\text{YBa}_2\text{Cu}_3\text{O}_y$, $y = 6$ to $y = 7$. (Reproduced with permission from Ref. 67.)

A major impurity found in these formulations has been BaCuO_2 . This compound has an intense absorption at 639 cm^{-1} . A second ubiquitous impurity was Y_2BaCuO_5 . This phase shows Raman scattering at 380 and 595 cm^{-1} . In a highly purified YBCO these bands are not present. Bands for the T-form of YBCO have been reported at 639, 480, 452, and 123 cm^{-1} . Distinguishing between the O-form and the T-form and the impurities is possible by Raman spectroscopy.

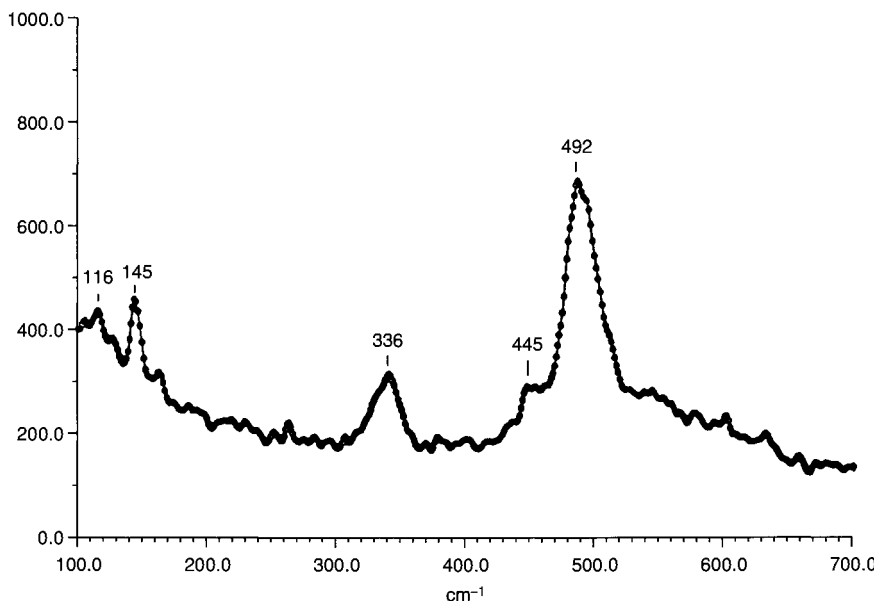


Figure 4-45 Raman spectrum of orthorhombic YBCO with no polarization. (Reproduced with permission from Ref. 68.)

Raman spectroscopy has also contributed to the characterization of other ceramic superconductors (68). A normal coordinate analysis for Y_2BaCuO_5 has been made (69).

References

1. H. H. Claassen, H. Selig, and J. G. Malm, *J. Am. Chem. Soc.* **84**, 3593 (1962).
2. P. Tsao, C. C. Cobb, and H. H. Claassen, *J. Chem. Phys.*, **54**, 5247 (1971).
3. K. O. Christe, E. C. Curtis, D. A. Doon, H. P. Mercier, J. C. P. Sanders, and G. A. Schrobilgen, *J. Am. Chem. Soc.* **113**, 3351 (1991)
4. W. Preetz and G. Rimkus, *Z. Naturforsch.*, **37b**, 579 (1982); W. Preetz, G. Peters and D. Bublitz, *Chem. Rev.*, **96**, 977 (1996).
5. H. Ogoshi, Y. Saito, and K. Nakamoto, *J. Chem. Phys.*, **57**, 4194 (1972).
6. M. Abe, T. Kitagawa, and Y. Kyogoku, *J. Chem. Phys.* **69**, 4526 (1978).
7. X.-Y. Li, R. S. Czernuszewicz, J. R. Kincaid, Y. O. Su, and T. G. Spiro, *J. Phys. Chem.* **91**, 31 (1990)
8. X.-Y. Li, R. S. Czernuszewicz, J. R. Kincaid, P. Stein, and T. G. Spiro, *J. Phys. Chem.* **94**, 47 (1990).
9. T. G. Spiro and X.-Y. Li, "Resonance Raman spectroscopy of metalloporphyrins," in "Biological Applications of Raman Spectroscopy" (T. G. Spiro, ed.), Vol. 3. John Wiley, New York, 1988.

10. For example, see L. Stryer, "Biochemistry." W. H. Freeman, New York, 1975.
11. T. Miyazawa, T. Shimanouchi, and S. Mizushima, *J. Chem. Phys.* **29**, 611 (1958).
12. N.-T. Yu, B. H. Jo, and D. C. O'Shea, *Arch. Biochem. Biophys.* **156**, 71 (1973).
13. R. P. Rava and T. G. Spiro, *J. Am. Chem. Soc.* **106**, 4062 (1984), *Biochemistry* **24**, 1861 (1985).
14. S. A. Asher, *Anal. Chem.* **65**, 59A and 201A (1992).
15. S. Krimm, "Peptides and proteins," in "Biological Applications of Raman Spectroscopy" (T. G. Spiro, ed.), Vol. 1. John Wiley, New York, 1987.
16. B. S. Hudson and L. C. Mayne, "Pepsides and protein side chains," in "Biological Applications of Raman Spectroscopy" (T. G. Spiro ed.), Vol. 2. John Wiley, New York, 1987.
17. A. T. Tu, "Peptide backbone conformation and microenvironment of protein side chains," in "Advances in Spectroscopy" (R. J. H. Clark and R. H. Hester, eds.), Vol. 13. John Wiley, New York, 1986.
18. I. Harada and H. Takeuchi, "Raman and ultraviolet resonance Raman spectra of proteins and related compounds," in "Advances in Spectroscopy" (R. A. H. Clark and R. E. Hester, eds.), Vol. 13, John Wiley, New York, 1986.
19. W. L. Peticolas, W. L. Kubasek, G. A. Thomas, and M. Tsuboi, "Nucleic acids," in "Biological Applications of Raman Spectroscopy" (T. G. Spiro, ed.), Vol. 1, p. 83. John Wiley, New York, 1987.
20. Y. Nishimura and M. Tsuboi, "Local conformations and polymorphism of DNA duplexes as revealed by their Raman spectra," in "Advances in Spectroscopy" (R. J. H. Clark and R. E. Hester, eds.), Vol. 13, 1986; Y. Nishimura, M. Tsuboi, T. Sato, and K. Aoki, *J. Mol. Structure* **146**, 123 (1986).
21. W. L. Kubasek, B. Hudson, and W. L. Peticolas, *Proc. Natl. Acad. Sci.* **82**, 2369 (1985); M. Tsuboi, Y. Nishimura, A. Hirakawa, and W. L. Peticolas, "Resonance Raman spectroscopy and normal modes of nucleic acid bases," in "Biological Applications of Raman Spectroscopy" (T. G. Spiro, ed.), Vol. 2, John Wiley, New York, 1987.
22. W. L. Peticolas and M. Tsuboi, "The Raman Spectroscopy of nucleic acids," in "Infrared and Raman Spectroscopy of Biological Molecules" (T. M. Theophanides, ed.), p. 153. Reidel Pub., Dordrecht, The Netherlands, 1979.
23. W.-D. Wagner and K. Nakamoto, *J. Am. Chem. Soc.* **111**, 1590 (1989); *ibid.* **110**, 4044 (1988).
24. For example, see D. F. Shriner and C. B. Cooper, "Vibrational spectra of metal–metal bonded transition metal compounds," in "Advances in Infrared and Raman Spectroscopy" (R. J. H. Clark and R. E. Hester, eds.), Vol. 6. John Wiley, New York, 1979.
25. G. Peters and W. Preetz, *Z. Naturforsch.* **34b**, 1767 (1979).
26. F. A. Cotton and G. Wilkinson, "Advanced Inorganic Chemistry," Third Ed., p. 552. John Wiley, New York, 1972.
27. R. F. Dallinger, *J. Am. Chem. Soc.* **107**, 7202 (1985).
28. R. F. Dallinger, V. M. Miskowski, H. B. Gray, and W. H. Woodruff, *J. Am. Chem. Soc.* **103**, 1595 (1981).
29. D. E. Morris and W. H. Woodruff, "Vibrational spectra and the structure of electronically excited molecules in solution" in "Advances in Spectroscopy" (R. J. H. Clark and R. E. Hester, eds.), Vol. 14, p. 185. John Wiley, New York, 1987.
30. J. Laane, *Pure and Appl. Chem.* **59**, 1307 (1987).
31. I. M. Irwin, J. M. Cooke, and J. Laane, *J. Am. Chem. Soc.* **99**, 3273 (1977).
32. J. Laane, "Application of Raman spectroscopy to structural and conformational problems," in "Advances in Multi-photon Processes and Spectroscopy" (S. H. Lin, ed.), Vol. 1. World Scientific Press, Singapore, 1984.
33. C. J. Wurrey, J. R. Durig, and L. A. Carreira, "Gas-phase Raman spectroscopy of anharmonic vibrations," in "Vibrational Spectra and Structure" (J. R. Durig, ed.), Vol. 5, p. 121. Elsevier, Amsterdam, 1976.
34. W. G. Fateley and F. A. Miller, *Spectrochim. Acta.* **17**, 857 (1961).

35. J. R. Durig, W. E. Bucy, L. A. Carreira, and C. J. Wurrey, *J. Chem. Phys.* **60**, 1754 (1974).
36. J. A. Shelnutt, *J. Phys. Chem.* **87**, 605 (1983).
37. J. R. Kincaid, L. M. Proniewicz, K. Bajdor, A. Bruha, and K. Nakamoto, *J. Am. Chem. Soc.* **107**, 6775 (1985).
38. T. M. Cotton, J.-H. Kim, and R. E. Holt, "Surface-enhanced resonance Raman scattering (SERRS) spectroscopy," in "Advances in Biophysical Chemistry," Vol. 2, p. 115. JAI Press, 1992.
39. T. M. Cotton, J.-H. Kim, and G. S. Chumanov, *J. Raman Spectrosc.* **22**, 729 (1991).
40. E. Koglin and J. M. Sequarts, "Surface enhanced Raman scattering of biomolecules," in "Topics in Current Chemistry," Vol. 134, Springer-Verlag, Berlin, 1986.
41. R. F. Paisley and M. D. Morris, "Surface enhanced Raman spectroscopy of small molecules," *Progr. Analys. Spectrosc.* **11**, 111 (1988).
42. T. M. Cotton, S. G. Schultz, and R. P. Van Duyne, *J. Am. Chem. Soc.* **102**, 7960 (1980).
43. T. M. Cotton, R. A. Uphaus, and D. Mobius, *J. Phys. Chem.* **90**, 6071 (1986).
44. E. Koglin, H. H. Lewinsky, and J. M. Sequarts, *Sur. Sci.* **158**, 370 (1985).
45. T. Watanabe, O. Kawanami, H. Katoh, K. Honda, Y. Nishimura, and M. Tsuboi, *Sur. Sci.* **158**, 341 (1985).
46. F. Weesner and M. Longmire, *Spectroscopy*, **16**, 68 (2001).
47. G. Jalosovszky, O. Egyed, S. Holly and B. Hegedus, *Appl. Spectrosc.*, **49**, 1142 (1995).
48. J. C. Sprunt and U. A. Jayasooriya, *Appl. Spectrosc.*, **51**, 1410 (1997).
49. P. K. Khulbe, A. Agarwal, G. S. Raghuvanski, H. D. Bist, H. Hashimoto, T. Kitagawa, T. S. Little, and J. R. Durig, *J. Raman Spectrosc.* **20**, 283 (1989).
50. G. A. Kouyouklis, A. Jayaraman, G. P. Espinosa, and A. S. Cooper, *J. Raman Spectrosc.* **22**, 57 (1991).
51. M. W. Urban and B. C. Cornilsen, "Measurement of non-stoichiometry in BaTiO₃ using Raman spectroscopy," in "Advances in Material Characterization II" (R. L. Snyder, R. A. Condrate and P. F. Johnson, eds.), pp. 89–96. Plenum Press, New York, 1985.
52. M. A. Krebs and R. A. Condrate, *J. Am. Ceramic Soc.* **65**, C144 (1982).
53. G. Chen, R. G. Haire, and J. R. Peterson, *Appl. Spectrosc.* **46**, 1495 (1992).
54. F. D. Hardcastle and I. E. Wachs, *J. Phys. Chem.* **95**, 5031 (1991).
55. T. J. Dennis, J. P. Hare, H. W. Kroto, R. Taylor, D. R. M. Walton, and P. J. Hendra, *Spec. Acta* **47A**, 1289 (1991).
56. K. Nakamoto and M. A. McKinney, *J. Chem. Educ.*, **77**, 735 (2000).
57. R. C. Haddon, A. F. Hebard, M. J. Rosseinsky, D. W. Murphy, S. J. Duclos, K. B. Lyons, B. Miller, J. M. Rosamilia, R. M. Fleming, A. R. Kortan, S. H. Glarum, A. V. Makhija, A. J. Muller, R. H. Eick, Z. M. Zahurak, R. Tycko, G. Dabbagh, and F. A. Thiel, *Nature* **350**, 320 (1991).
58. R. C. Haddon, A. F. Hebard, M. J. Rosseinsky, D. W. Murphy, S. H. Glarum, T. T. M. Palstra, A. P. Ramirez, S. J. Duclos, R. M. Fleming, T. Siegrist, and R. Tycko, in "Fullerenes: Synthesis, Properties, and Chemistry of Large Carbon Clusters" (G. S. Hammond and V. J. Kuck, eds.). ACS Symposium Series, Vol. 481, p. 78, ACS, Washington, D. C., 1992.
59. Y. A. Dubitsky and A. Zaopo, *La Chimica e l'Industria*, **82**, 299 (2000).
60. A. M. Rao, E. Richter, S. Bandow, B. Chase, P. C. Eklund, K. W. Williams, M. Menon, K. R. Subbaswamy, A. Thess, R. E. Smalley, G. Dresselhaus and M. J. Dresselhaus, *Science*, **275**, 187 (1997).
61. T. Ebbesen, "World Carbon Series" (P. M. Ajayan and P. Delhaes, eds.), Gordon and Breach, Vol. 2, Paris, France (1999).
62. J. R. Ferraro and J. M. Williams, *Appl. Spectrosc.* **44**, 200 (1990).
63. M. E. Kozlov, K. I. Pokhadnia, and A. A. Yurchenko, *Spec. Acta* **43A**, 323 (1987).
64. S. Sugai and G. Saito, *Solid State Commun.* **58**, 759 (1986).
65. J. R. Ferraro, H. H. Wang, M. -W. Whangbo, and P. Stout, *Appl. Spectrosc.* **46**, 1520 (1992).

66. P. J. Cava, *J. Am. Ceramic Society*, **81**, 5 (2000).
67. J. R. Ferraro and V. A. Maroni, *Appl. Spectrosc.* **44**, 351, 1990.
68. V. A. Maroni and J. R. Ferraro, “The use of vibrational spectroscopy in the characterization of high-critical temperature ceramic superconductors,” in “Practical Fourier Transform Infrared Spectroscopy—Industrial Laboratory Chemical Analysis” (J. R. Ferraro and K. Krishnan, eds.). Academic Press, San Diego (1990), and references therein.
69. Y. M. Guo and R. A. Condrate, *Spectrosc. Letters* **24**, 1185 (1991).

Chapter 5

Analytical Chemistry

Problems with interferences from fluorescence limited the use of Raman spectroscopy in the analytical laboratory for many years. The advent of Fourier transform (FT)-Raman in the near-infrared (near-IR) region and the implementation of Surface-Enhanced Raman Spectroscopy (SERS) and ultraviolet (UV) excitation sources for resonance Raman have increased the practical applications of the method. In addition to the instrumental improvements, methods for processing spectral data reached a high level of maturity during the latter part of the 20th century. Various statistical algorithms were applied to all types of analytical data, and eventually, this led to a whole new area of chemistry referred to as *chemometrics*. Presently, sophisticated methods for processing spectra are readily available and are accepted by many practitioners of spectroscopic techniques. This chapter will start with a general introduction to chemometric processing methods as they are applied to Raman spectra and then will proceed to discuss some practical analytical applications of the methods.

5.1 Preprocessing Spectra

Many times a certain amount of preprocessing is performed on spectral data to make the data more amenable to general processing methods. We will first cover preprocessing and then show how preprocessing is applicable to the more general processing methods. Preprocessing of spectra consists of minor

manipulations such as smoothing, averaging, mean centering, baseline removal, zeroing baseline, and derivatives to name a few. Herein we will go through the preprocessing methods applied most often to Raman spectra.

5.1.1 SMOOTHING

The signal-to-noise (S/N) ratio in Raman spectra can be low due to low scattering intensities from a sample or to low signals in specific spectral regions caused by detector falloff or, in the case of a dispersive instrument, decreases in the grating efficiency. Information can be lost by over smoothing the spectra, so it must be applied with great care. It is wiser to improve the S/N ratio by signal averaging spectra. However, in some cases, smoothing can be used to remove enough noise so that the presence of a band can be visualized. Further, taking derivatives greatly emphasizes the noise features, and smoothing is almost certainly needed.

Most commercial packages supply two smoothing routines: the Fast Fourier transform or FFT (1) and the Savitsky–Golay (2) method. In the former method, the spectral data are Fourier transformed, the transform is truncated, and the reverse transform is taken. The idea is that spectral noise is at a higher frequency than the spectral bands in the FT domain. By truncating the transform, the high frequencies are removed while retaining the low-frequency information. After taking the reverse transform, the noise has been reduced, and the spectral bands are the same or somewhat broader due to removal of the higher frequencies.

The Savitsky–Golay smoothing method is probably the most versatile method. The best way to understand this method is to consider that each point in the smoothed spectrum is a weighted average of adjacent points in the original spectrum. An equal number of data points on each side of a target data point are included in the average so that there is an odd number of total points, e.g., three, five, etc. total points, in the average. For a very simple demonstration of the weighted average, consider a seven-point triangular weighting function. The center point would be weighted by 1.0, the first pair of points on either side by 0.75, the second set of points on either side by 0.50, and the third set by 0.25. The data would be multiplied by these weights, added, and divided by the total weight of 4.0 to produce the final averaged point. This triangular weighting function (or window of weights) would then be moved and applied to each target point in the spectrum. It should be noted that it cannot be applied to the first three or last three points in the spectrum; thus for a seven-point smooth, six data points are lost.

Instead of using a triangular weight function, the Savitsky–Golay (2) method uses a selectable nonlinear function on each side of the central point. The use of an odd number of points remains the same, but each side of the center weight is fitted with a polynomial curve, which can be a quad-

ratic, cubic, or quartic. The user generally can select the degree of the polynomial and the (odd) number of data points to be included in the smoothing routine. The key feature of the Savitsky–Golay method is that the weights for the number of points and the degree of the polynomial are provided in a look-up table; i.e., they are generally calculated and stored in computer memory. Thus the process is very rapid.

An example of applying Savitsky–Golay smoothing is shown in Fig. 5-1. Both second-and third-degree polynomials were applied to the original spectrum shown at the bottom of the figure. The original spectrum was smoothed with 5, 15, and 25 points. Close examination reveals that a 5-point smooth does very little to improve the noise. A 15-point smooth starts to show some improvement in the baseline noise, and the 25-point smooth shows an even greater improvement. However, both the 15- and 25-point smoothing routines start to show significant changes in the spectral features. For example, with the second-degree polynomial, the relative intensity of the higher-frequency peak in the weak doublet at $\sim 3,300\text{ cm}^{-1}$ decreases in the 15-point smooth, and the two peaks are about the same intensity in the 25-point smooth. The changes are not as severe in the third-degree polynomial fit; however, the decrease in the noise is also less. Another noticeable change is in the relative intensities of the four stronger peaks appearing between 1,000 and

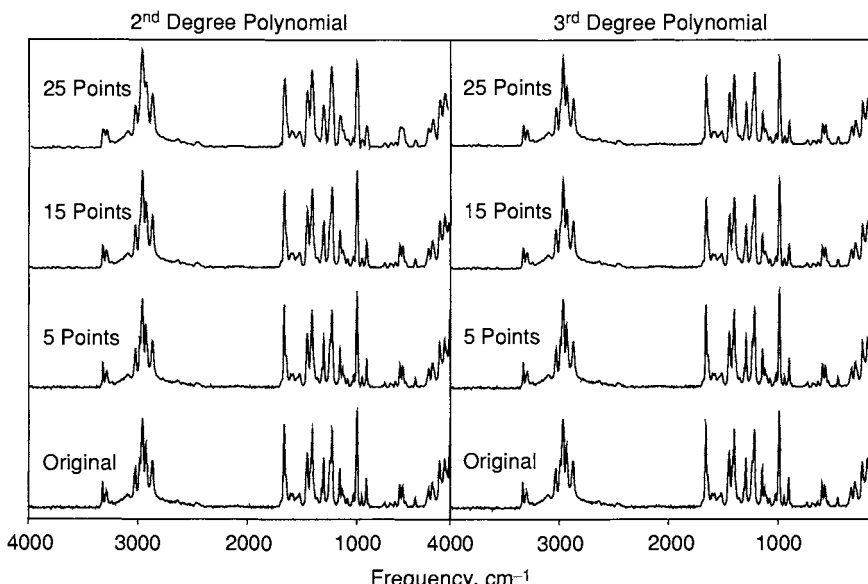


Figure 5-1 Examples of Savitsky–Golay smoothing. A second-degree polynomial was used for the left column and a third-degree polynomial was used for the right column with a 5-, 15-, and 25-point smooth.

$2,000\text{ cm}^{-1}$. The band on the left is the second strongest of the four peaks in the original and 5-point smooth, but it becomes the weakest of the four in the 15- and 25-point smooths with both the second- and third-degree polynomials. It is fairly obvious that the smoothing routine affects the sharper peaks more than the broader peaks. Basically, the effect of smoothing is very much like lowering the spectral resolution, since by lowering the instrumental resolution, the noise is decreased and the bands become broader.

5.1.2 DERIVATIVES

Raman spectra often appear with sloping or curved backgrounds. Backgrounds can be due to fluorescence, Rayleigh wings, or other anomalous causes. In any event, it is often necessary to reduce the background interferences for comparison of spectra. One way to do this conveniently is to take derivatives of the spectra (3, 4). The second derivative is often convenient because the center of a symmetric positive peak in the original spectrum will appear as the center of a negative peak in the second derivative spectrum. Sloping or curved backgrounds are removed, and the (negative) peak is much sharper than that in the original spectrum.

The first derivative spectrum can be calculated simply by plotting the difference between intensities of adjacent data points or between any selected spectral gap. This method reduces broad background contributions, but it also greatly emphasizes the spectral noise, since noise differences between adjacent data points will be amplified by taking derivatives; the higher the order of the derivative, the greater is the noise. Here again, the Savitsky–Golay (2) method can be very useful because it formalizes the derivative while providing the same type of smoothing function discussed earlier. In this case, the order of the derivative, the degree of the polynomial for smoothing the data, and the number of data points in the smoothing routine have to be provided by the user.

Two second derivatives of an original spectrum are shown in Fig. 5-2. The top derivative was calculated using the difference between adjacent points without any smoothing. A 15-point smooth was used for the bottom derivative. There are some intensity variations due to smoothing, especially for the four stronger bands between $1,000$ and $2,000\text{ cm}^{-1}$. However, the smooth derivative is much easier to follow, and it is much easier to compare with other spectra.

The same original spectrum with a sloping background added is shown in Fig. 5-3. The second derivative with a 15-point smooth was calculated and is shown in the figure, where it is compared with the second derivative with a 15-point smooth of the original spectrum. The two derivatives are identical. This demonstrates the importance of derivatives in matching an unknown with a library spectrum. Frequently, real unknown samples can be plagued with

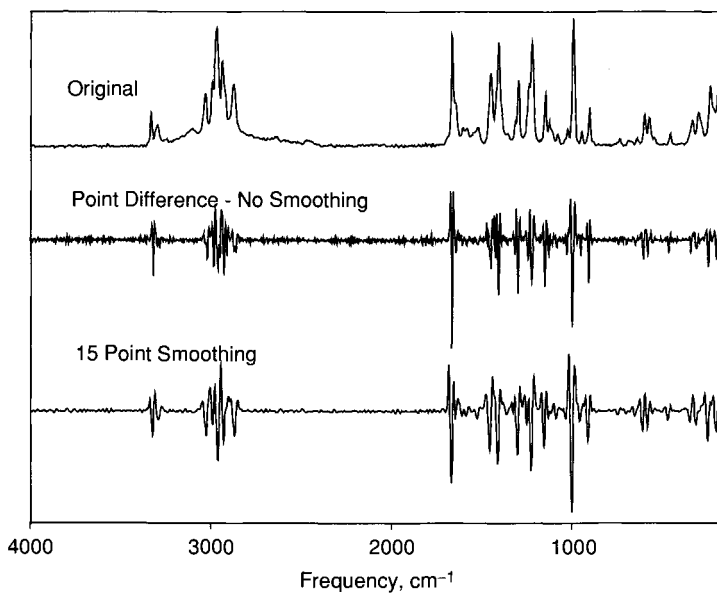


Figure 5-2 Original spectrum, second derivative using point difference and no smoothing and second derivative with a Savitsky–Golay 15-point smooth.

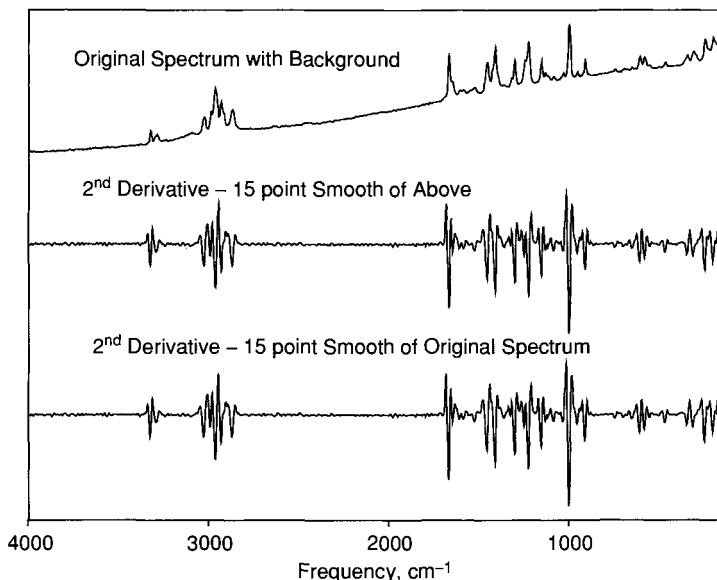


Figure 5-3 Original spectrum with a background added, second derivative with a Savitsky–Golay 15-point smooth and second derivative of the original, flat spectrum with a Savitsky–Golay 15-point smooth.

broad background interferences, whereas the library spectrum of the same compound may have a flat background. As shown in Fig. 5-3, by taking the derivative of both the unknown and the known, a positive identification can be made.

5.1.3 NORMALIZATION

It is important that the intensity range of spectra be on the same or similar scales before combining or comparing spectra. The scales can be made similar by normalizing all the spectra involved in a particular manipulation to the same value. For example, consider several spectra of mixtures each containing the same compound. We might divide each of the spectra by the intensity at the central frequency of a band in the spectrum of the common compound so that the intensity of all the spectra would be 1.0 at that frequency and the remaining spectral intensities relative to the selected frequency. In this case, we say that the spectra are *normalized* to the same frequency.

For cases in which the spectra do not share a common band, it might be better to normalize the spectra so that the total area under the spectrum is 1.0. Prior to normalizing by any method, it is important to zero the baseline of the spectra by subtracting the minimum intensity from the intensities at every frequency. Normalizing the total area under the spectral curve is most useful for searching libraries and for putting the unknown and library spectra on the same scale. In this method, the intensity at each frequency in the spectrum is divided by the square root of the sum of the squares of all the intensities, i.e.,

$$I(v) = \frac{I(v)}{\sqrt{\sum [I(v)^2]}} \quad (5-1)$$

where the sum is over all frequencies. An example of normalizing the total area under the spectrum is shown in Fig. 5-4. The original spectra are shown on the left side of the figure. Each of the spectral plots has identical Raman intensity ranges of 0–80. For display purposes, all four spectra could be expanded to full scale. However, for direct comparison with unknown spectra, it is advantageous to scale the spectra by normalizing the total area under the spectrum, as shown on the right side of Fig. 5-4. This method has the advantage that it is independent of the spectral features; i.e., it is not dependent on any single band. The disadvantage to this method is that the background can make significant contributions to the normalization. In fact, the major contributor may be background intensities, and these can distort the spectrum. For example, you might want to compare an unknown having a strong background with a flat library spectrum. If both the spectra are normalized so that the total areas under the spectra equal 1.0, the library spectrum may consist of a number of sharp bands, whereas the unknown may

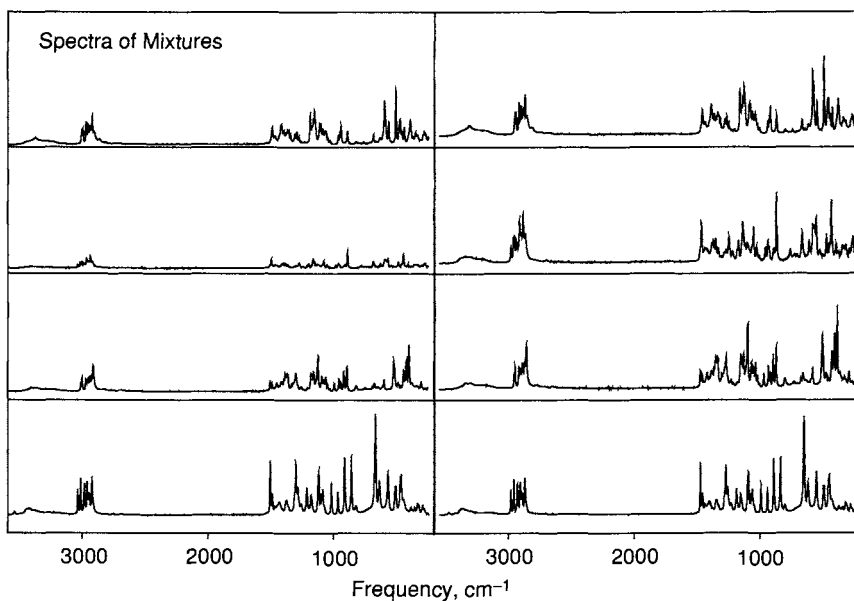


Figure 5-4 Left: Raman spectra of four sugars exhibiting considerable relative intensity differences. Right: Same spectra normalizing the total spectral area for each of the spectra to 1.0.

have major background contributions, and most matching routines would fail to recognize the similarity. This is exactly the benefit of using the derivatives discussed earlier, since derivatives can be used to remove extraneous background information so that the bands will be the major contributors in the spectra.

5.1.4 STANDARD NORMAL VARIANCE (SNV)

In using Raman spectroscopy for monitoring changes in any real chemical system, such as in a process control situation, background slopes can vary from one spectrum to the next. Generally, we are interested in the changing band intensities and not the changing slopes of the baselines. As shown in the preceding section, backgrounds can be eliminated by taking derivatives; however, the original spectral pattern is lost and noise is emphasized unless a smoothing routine is applied. Sloping baseline variations from spectrum to spectrum can be reduced using a technique referred to as *standard normal variate (SNV) transformation* (5). Calculation of the SNV at each wavelength removes slope variation on an individual sample basis by the following equation:

$$\text{SNV}(v) = \frac{[I(v) - \bar{I}(v)]}{\sqrt{\sum [I(v) - \bar{I}(v)]^2 / n - 1}} \quad (5-2)$$

where $\text{SNV}(v)$ is the modified SNV spectrum, $I(v)$ is the Raman scattering intensity at each frequency, $\bar{I}(v)$ is the average Raman scattering intensity at each frequency, and n is the number of frequencies.

An example of applying the SNV method to data with different sloping backgrounds is shown in Fig. 5-5. The spectra on the left were measured for various concentrations of the same component, and the spectra have greatly different backgrounds. The spectra on the right were produced by the SNV method; the backgrounds are now very similar, and the major differences in the spectra are due to the band intensities. The application of Eq. (5-2) is very rapid. The background is not removed, but all the backgrounds are similar, and the spectral band intensities can be compared.

5.1.5 BASELINE FLATTENING

In the preceding sections we have addressed methods that handle variable background problems either by taking derivatives or by making the backgrounds similar using the SNV method. It is also possible to artificially alter the baseline of the spectrum by fitting the baseline (with a function) and subtracting this fit line or curve from the spectrum. This is not an unreasonable approach for small sloping backgrounds; however, for large sloping backgrounds, removal of the background also can affect the band shapes.

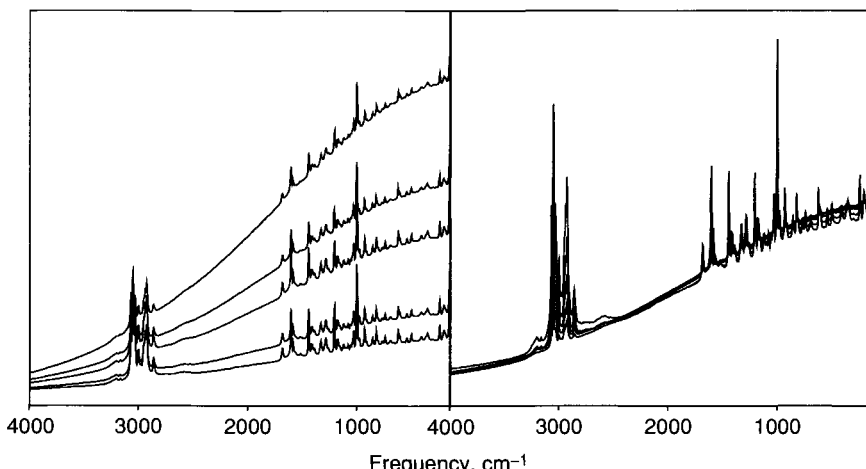


Figure 5-5 Left: Four Raman spectra of the same polypeptide at slightly different concentrations but with large sloping background differences. Right: Same spectra after applying the SNV transform to all the spectra.

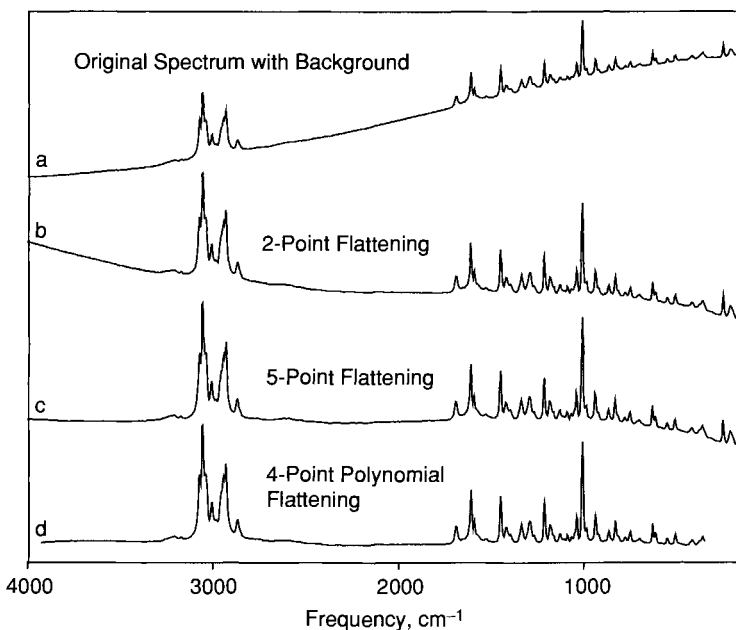


Figure 5-6 Effect of different baseline flattening routines: (a) original spectrum; (b) two-point linear fit of baseline; (c) five-point linear fit of baseline; (d) four-point polynomial fit of baseline.

Thus the distortion really depends on the slope because large slopes can cause severe distortions of the bands. Moreover, great care has to be exercised in selecting the appropriate function for the baseline flattening. Examples of different functions are shown in Fig. 5-6. The original spectrum with a sloping, slightly curved background was treated with both linear and polynomial fits. In the first case, a two-point linear fit was used. The user chooses the two points for fitting a straight line to the baseline, and this straight line is then subtracted from the spectrum. As can be seen, the baseline of the resulting spectrum has an S shape. In the next case, a five-point linear fit was used; five frequencies are selected by the user, and straight lines fitted between each consecutive pair of points are subtracted from the spectrum. The five-point smooth is better than the two-point smooth, but the spectrum still has curved sections. In the last case, a four-point polynomial (quartic equation) fit was applied to the spectrum. Again, the user selects the four points, that are then fitted with a fourth-degree polynomial, which is subtracted from the spectrum. The last method produced the flattest baseline for the spectrum.

It should be emphasized that any baseline alterations to correct sloping backgrounds should be avoided, especially by one new to the field. Important information may be lost in the flattening process, and important spectral bands may be distorted.

5.1.6 SPECTRAL SUBTRACTION

Subtraction is possibly the most used, and often overused, spectral manipulation technique. It is an extremely useful technique because it attempts to obtain spectra of pure components by removing interfering spectral features caused by solvents or other analytes in mixtures. It is also used to remove unwanted background features. Spectral subtraction can be very successful for separating spectra of pure components in the case of mixtures of solid compounds. As long as the various chemical components do not interact and the *S/N* ratio is good, subtractions can be very successful.

One of the most common uses of subtraction techniques is to remove a solvent spectrum from the spectrum of a solution. In most every case there is a solute–solvent interaction, and the spectra of all components in the solution have changed from those of the pure compounds. The changes can occur in band frequencies, intensities, and shapes. The user may gain some insight by performing the subtraction, but the spectra will be distorted. Examples of typical distortions are shown in Fig. 5-7 (6). The top spectrum is a mixture of EDTA and water, and the second spectrum is that of pure water. Two subtractions are shown. The first was based on removal of the water band

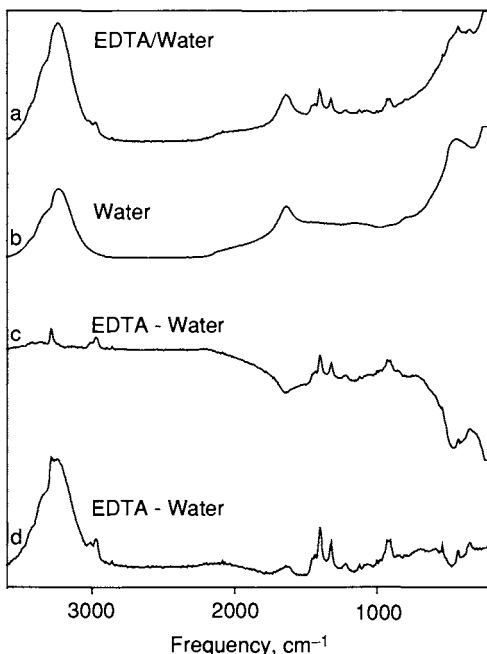


Figure 5-7 Effects of spectral subtraction: (a) Raman spectrum of EDTA–water mixture; (b) Raman spectrum of water; (c) Raman spectrum of EDTA–water minus water; (d) Raman spectrum of EDTA–water minus water.

at $3,245\text{ cm}^{-1}$; the resulting spectrum is reasonably flat above $2,200\text{ cm}^{-1}$, but contains strong negative bands below $2,000\text{ cm}^{-1}$. The second result is reasonably flat below $2,200\text{ cm}^{-1}$ but contains the strong water band at $\sim 3,245\text{ cm}^{-1}$. The difficulty is due to the fact that EDTA is hydrogen-bonded to water, so both the water spectrum and the EDTA spectrum have changed in the mixture. This problem is typical of many subtractions. Spectral subtraction can be a very powerful technique for detecting components at low concentrations or those having weak spectral features, but care must be exercised when performing subtractions because the appearance of new or negative bands may not represent the true spectra of the analyte in question.

5.2 Full-Spectra Processing Methods

Early methods for performing quantitative analyses with spectra involve selecting a few representative frequencies for the components in the samples. Typically, an analytical frequency (or wavelength) would be selected for each of the chemical components in a mixture. The analytical frequencies were selected from spectral regions in which the other components did not interfere or only weakly interfered. For qualitative analyses involving spectral searches, the frequencies and possibly the relative intensities for several important bands from the spectra were cataloged and used to represent the spectrum of that compound. Thus the library spectra were represented by a number of frequencies and relative intensities. An unknown hopefully would be represented by a similar set of frequencies and intensities. In both quantitative and qualitative determinations, selection of appropriate spectral information was subjective, and consequently, the results were just as subjective. Some spectroscopists became very good at recognizing spectral patterns and were able to match patterns of unknown spectra with library spectra or even assign chemical groups to a specific set of bands in the spectrum of the unknown. In the same way, some quantitative determinations were very successful when only a limited number of analytes were involved, and great care was used in selecting the analytical frequencies.

The advent of personal computers greatly facilitated the application of spectroscopic methods for both quantitative and qualitative analysis. It is no longer necessary to be a spectroscopic expert to use the methods for chemical analyses. Presently, the methodologies are easy and fast and take advantage of all or most of the spectral data. In order to understand the basis for most of the current processing methods, we will address two important techniques: *principal component analysis* (PCA) and *partial least squares* (PLS). When used for quantitative analysis, PCA is referred to as *principal component regression* (PCR). We will discuss the two general techniques of PCR and PLS separately, but we also will show the relationship between the two.

5.2.1 PRINCIPAL COMPONENT REGRESSION (PCR)

Principal component regression is simply PCA followed by a regression. We will start with an explanation of PCA. If we have a single chemical component dissolved in a solvent, all the bands in the spectrum of that component would increase with concentration. Within a single band, all the intensities go up and down together. Thus there is a linear relationship between the intensities of all the bands, and we say that the intensities are *colinear*. The intensity at any single frequency would suffice to represent the concentration of a component. All the other information could be discarded. In the case of two components, there is a certain set of spectral features to represent each of the components, but all the intensities for each individual component are again colinear. If each component had a single band or a single frequency without any interference from the other component, that frequency could be used to represent the concentration of that component. However, in most real cases, the possibility of non-interfering spectra is unlikely. Spectra of both components are likely to interfere with each other at most, if not all, frequencies. We have different spectral patterns for the two components but not a single frequency without interference. The intensities within each spectral pattern are colinear; thus the intensities at all the frequencies cannot be used to represent the concentration of that component since this would cause overfitting of the data. We are left with a dilemma in that we need to somehow use all or as much of the spectral pattern without introducing colinear information.

The beauty of PCA is that it takes a set of spectra without knowing anything about the concentrations of the components and finds a set of orthogonal representations for the data set. In the case of a two-component chemical system with all the spectral band intensities linearly related to the concentrations, PCA extracts two orthogonal representations, which are referred to as *loading spectra* or *principal components* (PCs). The idea of orthogonality is that the problem of colinearity has been completely removed. All the original spectra can be expressed as a linear combination of these two orthogonal loading spectra; i.e., the original spectra are simply a sum of these two orthogonal spectra. The coefficients in this summation are referred to as *scores*, and the concentrations of the two components are directly related to the scores.

In a more formal sense, the original Raman spectra of a set of mixtures containing various concentrations of the desired components can be set up in a matrix format, with each row of the matrix containing the intensities of each Raman spectrum. This matrix, which we will call \mathbf{R} , contains m rows of spectra, each with w frequencies. PCA expresses this \mathbf{R} matrix as a product of two matrices

$$\mathbf{R} = \mathbf{SL}^t, \quad (5-3)$$

where \mathbf{L}' contains the loading spectra in rows (with f frequencies) and scores in columns of \mathbf{S} . The rows of \mathbf{L}' are orthonormal, and the columns of \mathbf{S} are orthogonal. The rows of \mathbf{R} are not independent because each row can be expressed as a linear combination of the loading spectra; however, the rows of \mathbf{L}' are independent (orthonormal) of each other. If both sides of Eq. (5-3) are right-multiplied by the \mathbf{L} matrix, i.e.,

$$\mathbf{RL} = \mathbf{SL}'\mathbf{L}, \quad (5-4)$$

this reduces to

$$\mathbf{S} = \mathbf{RL} \quad (5-5)$$

Since the rows of \mathbf{L}' and the columns of \mathbf{L} are orthonormal, the product $(\mathbf{L}'\mathbf{L}) = \mathbf{I}$ (Identity Matrix). Thus the scores in each row of the \mathbf{S} matrix are the dot products of the corresponding original spectrum in the \mathbf{R} matrix with each of the loading spectra in the \mathbf{L} matrix. The dot product is the sum over all frequencies of the products of intensities for two spectra.

The PCA process reduces the dimensionality of the data set. For example, consider the spectra of five mixtures of solutions of the chemical warfare agent ethyl-*N,N*-dimethylphosphoroamidocyanide (GA) in water shown on the left side in Fig. 5-8. The spectra of the pure components are shown

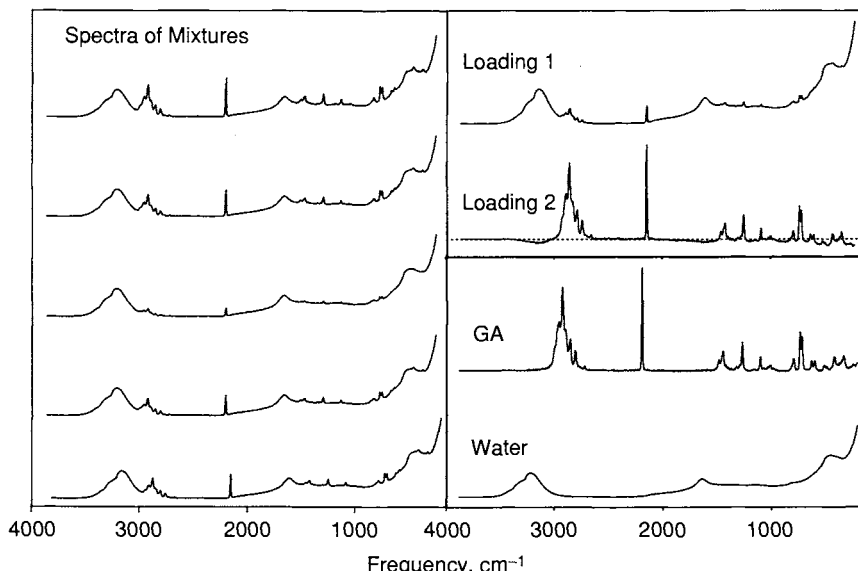


Figure 5-8 Left: Raman spectra of synthetic mixtures of GA in water. Right, top: First two principal component (loading) spectra from PCA. Right, bottom: Raman spectra of pure components.

on the bottom right of the figure, and the two loading spectra (principal components) are shown on the top right of the figure. The first loading spectrum accounts for the most variance in the original data set. Basically, it is the least-squares regression fit of the original mixture spectra, and as such, it is nearly the average of the original mixture spectra (7, 8). The second loading spectrum accounts for the most variance in the data set after all the mixture spectra have been made orthogonal to the first loading spectrum. Thus the original mixture spectra are made orthogonal to the first loading, and the remaining residuals are again fitted in a least-squares sense with the best loading that accounts for the most variance. For a two-component system, the second loading vector expresses the difference between the spectra of the two components as found in the mixture spectra. The horizontal (dashed) line through loading 2 in Fig. 5-8 represents zero intensity. Most of the band contours above the dashed line are due to the GA compound, whereas the contours below the zero line are due to the broad bands of water.

The five mixture spectra in Fig. 5-8 were generated synthetically by adding various combinations of the GA and water spectra. Thus each of the mixture spectra can be expressed as a linear combination of the two pure component spectra for GA and water. In real mixtures, some of the bands of GA would be shifted due to hydrogen bonding, and it would not be possible to express the mixture spectra as a linear combination of the pure components because the spectra of the pure components change in the mixtures. This is one of the main benefits of PCA. In the present example, the mixture spectra can be expressed as a linear combination of the pure component spectra or the loading spectra. In spectra of real mixtures, the mixture spectra can still be expressed as a linear combination of the loading spectra because these spectra are obtained from the actual mixture spectra without any knowledge of the pure spectra or the concentrations of the components. Thus the five mixture spectra on the left can always be expressed as a linear combination of loading spectra because the loading spectra will account for any interactions or other changes in the spectra. In the case of interactions, some of the bands may become nonlinear, and it may be necessary to fit the nonlinearity with additional loading spectra. In the present example, only two loading spectra are needed because it is an ideal situation. The third loading spectrum simply would contain noise. However, in real cases, a third or even fourth loading might be used to account for nonlinearities or other changes in the mixture spectra.

PCA is simply a method for reducing the dimensionality of the data set and for removing dependent data (8). Although each of the five mixture spectra in Fig. 5-8 contain almost 4,000 data points, each can be expressed as a sum of two spectra (loadings or pure) containing $\sim 4,000$ data points each. Thus the dimensionality is reduced from $5 \times 4,000$, or 20,000 data points, to $2 \times 4,000 + 10$, or 8,010 values (the value of 10 is for the two coefficients

for each of the five spectra). For 50 mixture spectra, the dimensionality is reduced from 200,000 (or $50 \times 4,000$) to 8,100 (or $2 \times 4,000 + 100$) values so that the process leads to a significant reduction. At the same time that the dimensionality is reduced, the dependency is removed by fitting the spectra with two spectra (loadings or pure). Instead of picking two or several frequencies, which have some dependency, to represent the concentrations of material, we can use the coefficients or scores in the linear combination. As stated earlier, the columns of the score matrix \mathbf{S} are orthogonal, and as such, they remove the dependency. Thus concentrations can be expressed as a function of the scores

$$\mathbf{C} = \mathbf{PS}, \quad (5-6)$$

where \mathbf{C} is a matrix of the concentrations of the two components in separate rows for each of the mixtures, \mathbf{S} contains rows of scores for each mixture spectrum, and \mathbf{P} is a proportionality matrix. Typically, spectra are measured for a set of standard mixtures with known concentrations. The loading vectors and scores are determined by PCA. The known concentrations are used as input to the \mathbf{C} matrix, and this matrix is regressed onto the score matrix \mathbf{S} to calculate the proportionality matrix \mathbf{P} .

The concentration of an unknown can be predicted by measuring its spectrum, determining its score from the predetermined loadings as

$$\mathbf{S}_{\text{unk}} = r_{\text{ink}} \mathbf{L}, \quad (5-7)$$

and multiplying the scores by \mathbf{P} as in Eq. (5-6). This procedure is known as *principal component regression* (PCR) because the concentrations have been regressed onto the scores from PCA. The regression is performed during the calibration. Thus, during the analysis of an unknown, its spectrum is multiplied by the calibration matrices to predict the concentrations of the analytes.

5.2.2 PARTIAL LEAST SQUARES (PLS)

As discussed earlier, in principal component analysis, the loadings are calculated independent of the concentrations of standard mixtures. In partial least squares (PLS), the spectra and the concentrations are fitted by an alternating procedure that accounts for the maximum variance in both the spectra and concentrations (9–11). There are two versions of partial least squares: PLS1 maximizes the fit to the concentrations of one selected component, whereas PLS2 maximizes the fit to the concentrations of all components. PLS1 is a bit easier to understand and will be discussed here.

The general procedure for performing PLS is similar to that for PCR. Spectra of a number of standard samples with known concentrations are measured. For PLS1, the user is requested to specify the (j^{th}) component to

be fitted by the routine; actually all components are predicted, but the fit of the selected component is optimized. The PLS1 routine multiplies (weights) each of the original spectra by the normalized concentrations of the selected component. These weighted spectra are added together, and the total spectral area is normalized to 1.0 to produce a weight loading vector \mathbf{w}_i where i refers to the first loading vector. The original spectra are multiplied by this weight loading vector to determine the scores for the j^{th} component, i.e.,

$$\mathbf{S}_i = \mathbf{R}\mathbf{w}_i. \quad (5-8)$$

The scores in this column vector \mathbf{S}_i are normalized. The concentrations of the j^{th} component are then regressed onto the normalized scores to obtain a regression coefficient \mathbf{b}_i , and the original spectra are multiplied by the scores to obtain the first loading vector, i.e.,

$$\mathbf{l}_i = \mathbf{R}\mathbf{S}_i. \quad (5-9)$$

Starting with spectra and concentrations, the first pass through the data produces a column weight loading vector \mathbf{w}_i , a column loading vector \mathbf{l}_i , a column vector of scores \mathbf{s}_i , and a regression coefficient \mathbf{b}_i . This is the best fit of the spectra and concentrations with a single pass through the data. From these best fits, residual spectra and residual concentrations are calculated. The second pass through the data finds the best fits for these residual spectra and concentrations; the processing is exactly the same as that described for the first pass. Third, fourth, fifth, and more passes can be applied to the data until most of the variance in the spectra and concentrations have been accounted for by the loading vectors and scores.

The PLS1 algorithm was applied to a synthetic spectra of mixtures of sucrose and fructose. The mixture spectra were generated by adding together spectra of pure compounds multiplied by known coefficients. These coefficients were then used as the concentrations in this hypothetical problem. The original spectra, the spectra of the pure components, and the loading spectra are shown in Fig. 5-9. Fructose was selected arbitrarily as the component for optimizing the processing. The loading spectra for PLS1 are similar to those that would be produced by PCA, although they are weighted by the concentrations of fructose. The first loading spectrum is similar to the average of the two pure components. Sucrose has bands of about the same intensity at 1,040 and $1,125\text{ cm}^{-1}$, whereas sucrose has a band of about the same intensity at $1,085\text{ cm}^{-1}$. In loading 1, these three bands appear with about equal intensity. In loading 2, the two sucrose bands are positive and the fructose band is negative. Several other analogous relations can be found by comparing the loading spectra with the spectra of the pure components. It is evident from the loadings that loading 1 is similar to the average of the spectra of the pure components, whereas loading 2 expresses the differences between the spectra.

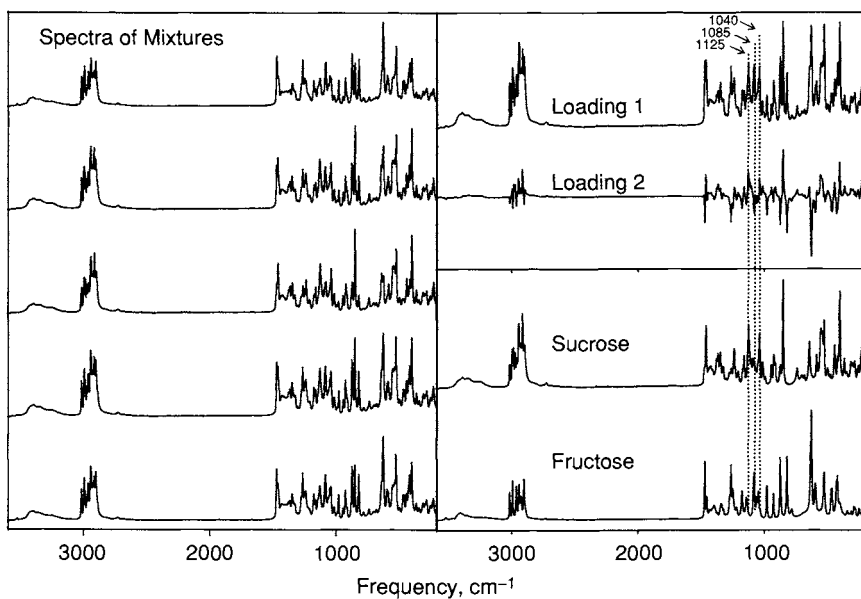


Figure 5-9 Left: Raman spectra of synthetic mixtures of sucrose and fructose. Right, top: First two loading spectra from PLS1. Right, bottom: Raman spectra of pure components.

5.3 Quantitative Analysis

Both PCR and PLS are multivariate methods for performing quantitative analysis on chemical systems containing several components. The methods apply to any type of optical spectroscopic data. In absorption spectroscopy, a background spectrum is measured without a sample (or with the solvent) in the optical beam, then a spectrum of the sample (or solution) is measured, and the ratio of these two is used to calculate the amount of light transmitted through the sample, which is related through a log function to the absorbance and concentration. Raman spectroscopy is a scattering rather than an absorption technique, and a ratio method cannot be used to determine the amount of light scattered unless an internal standard is present in the sample. In absorption spectroscopy, the power of the source, the throughput of the spectrometer, and the sensitivity of the detector can be ascertained without a sample in the instrument. In Raman, we have no signal without a sample; thus there is no background information. There are ways around this dilemma, but they may require some adaptation of the method or sample. In the case of solutions, the solvent can be measured with zero concentration of the solutes. For low concentrations of solution, we can assume that the concentration of the solvent is unchanged, and bands of the solvent can be used to normalize

any changes in the laser, spectrometer throughput, or detector sensitivities. Another useful method is to add an internal standard to a sample. The internal standard should be a stable molecule having a Raman spectrum with a few peaks. In any event, care has to be taken to guarantee that the instrumental parameters have not changed during the measurements and that the observed spectral changes are due only to changes in sample concentrations.

Use of PCR and PLS methodologies has become standard, and the methodologies are available in many software packages; however, some basic limitations and suggested protocols should be considered. The first problem with any modeling method is to determine the number of standard samples required to train, validate, and test the model. Most users prefer to use a minimum number of samples, but this often can lead to disastrous results. One should first consider the range of concentrations in unknown samples and the required accuracy and precision needed. The standards should encompass the entire possible range of concentrations of the analytes in unknown samples. Once the range is determined, the accuracy should be addressed next. For a small range, it is possible to predict accurate concentrations using a few standard samples in the training set. For a large range, accurate predictions require many, many standard samples in the training set. Precision is often related to the stability of the instrumentation and environmental conditions; however, precision is also tied into the range of concentrations, since a large range can lead to lower precision.

The number of samples in the training set must be larger than the number of spectrally different components (principal components). A good rule of thumb is that the number of samples should be 2.5 times the number of principal components. The number of samples in a validation set should be about the same size as the training set. The number of samples in the testing set is usually left up to the operator and strongly depends on the types of samples being investigated.

There are two schools of thought on validating a model developed with a training set of standard samples. Some investigators prefer to use a separate validation set. They measure a large set of standard samples, train with half the samples and validate with the other half. Other investigators prefer to use a cross-validation method, which is now referred to as the *predicted residual error sum of squares* (PRESS). In the PRESS method, each sample is treated as an unknown, and the remaining samples are used to train and predict the concentration of the one sample. All the samples are treated individually as unknowns, and their concentrations are predicted with all the remaining samples. In this way, each sample is considered independently. The sum of the squares of the residual concentrations from all the predicted unknowns is used to calculate a standard error of prediction (SEP), i.e.,

$$\text{SEP}_j = \sqrt{\frac{\sum [c_{ij} - \hat{c}_{ij}]^2}{n - 1}}, \quad (5-10)$$

where c_{ij} and \hat{c}_{ij} are the known and predicted concentrations for the i^{th} sample of the j^{th} component and n is the number of samples. In performing cross-validation, it is important to check for predicted concentrations that lie outside an expected range. Such samples are referred to as *outliers*. These may be detected from differences in predicted and known concentrations of the training set or from the spectral residuals, i.e., the differences between the actual and predicted spectra. An F statistic can be used to determine the probability of a sample being an outlier, and details of this method are given in Ref. 9.

The number of principal components or loading vectors in PCR and PLS is a rather gray area and is rarely easy to determine. Currently, the best method for selecting the optimal number of loading vectors is to use the cross-validation PRESS method and calculate SEPs for a reasonable range of loading vectors. The number is selected as that number producing the lowest SEP value. However, for systems of multiple analytes, it is often found that the optimal number is different for each analyte. The number should be selected for each analyte. Using PLS1, the entire modeling scheme is optimized for each analyte, and the number of loading vectors should optimize the results for the selected analyte.

There are two data pretreatment methods particularly useful for quantitative determinations. The first is *mean centering*, which refers to subtracting the average spectrum from all the spectra in the training set. This has the effect of removing overall bias from the set since it causes all the spectra to add to zero. Improvements are limited to better numerical accuracy, but it also removes bias not correlated with any component concentration. *Variance scaling* can be used to emphasize spectral changes due to components that have weak instrument responses. The spectra are scaled so that the intensity at each frequency has unit variance in the training set. This procedure may be beneficial when naturally occurring variances in the spectra are unrelated to analyte concentrations.

5.4 Spectral Searches

Searching spectral libraries is very important for identifying an unknown compound and for trying to identify chemical groups in new compounds. A spectral library can be generated by the user or can be purchased commercially. The techniques for performing library searches have reached a high level of maturity and are used routinely in most spectroscopy laboratories. A number of matrices are used to match a target spectrum with either the

identical library spectrum or the most similar library spectrum. The metrics used to match spectra attempt to find the most similarity between the target and library spectrum.

Most of the early metrics for matching spectra were based on peak-pick methods. The user and, later, computers pick all the peaks having intensities above a selected threshold level. The frequencies of these peaks and sometimes the relative intensities were used for determining the similarity. In the case of frequencies, a table of the prominent frequencies for the target compound was generated. The library consisted of similar tables for each of its entries. The same threshold for selecting peaks was used for the target and the library. Generally, the library and unknown spectra were normalized to some value. Matching of peaks would be positive if both the target and the library entry had a band within a selectable frequency window. Either a forward or a reverse search could be performed. In the forward search, the criterion for matching is the number of peaks from the target spectrum that match the library entry. In the reverse search, the criterion for matching is the number of peaks from the library entry that match the target spectrum. The latter method has the advantage that the unknown target spectrum might be a mixture of two or more components. In the forward search, the percentage of bands from the target spectrum that matched the library spectrum would be determined, and bands due to other components would not be counted. In the reverse search, the percentage of bands from the library entry that matched the target spectrum would be determined, and all bands from the library entry might appear in the target spectrum of the mixture.

Search algorithms have advanced over the years to the point that most of the spectral data are used in the search. The methods are referred to as *full-spectra searches* because the entire spectral pattern is used in the matching procedure. Again, a number of similarity metrics are used, but most produce similar results. Typically, the spectral range for the search is selectable, and the library and target spectra are all normalized so that the total spectral area is 1.0. Either the Euclidean distance or the dot product between the target and library entries is calculated. The Euclidean distance is defined as

$$\text{Dist}_j = \sqrt{\sum [r_{\text{unk},i} - r_{j,i}]^2}, \quad (5-11)$$

where $r_{\text{unk},i}$ is the intensity of the i^{th} frequency for the unknown, $r_{j,i}$ is the intensity of the i^{th} frequency for the j^{th} library entry, and the sum is over all i frequencies. The smaller this distance, the greater is the similarity. The dot-product metric is given by

$$\text{DP}_j = \sum [r_{\text{unk},i} \cdot r_{j,i}], \quad (5-12)$$

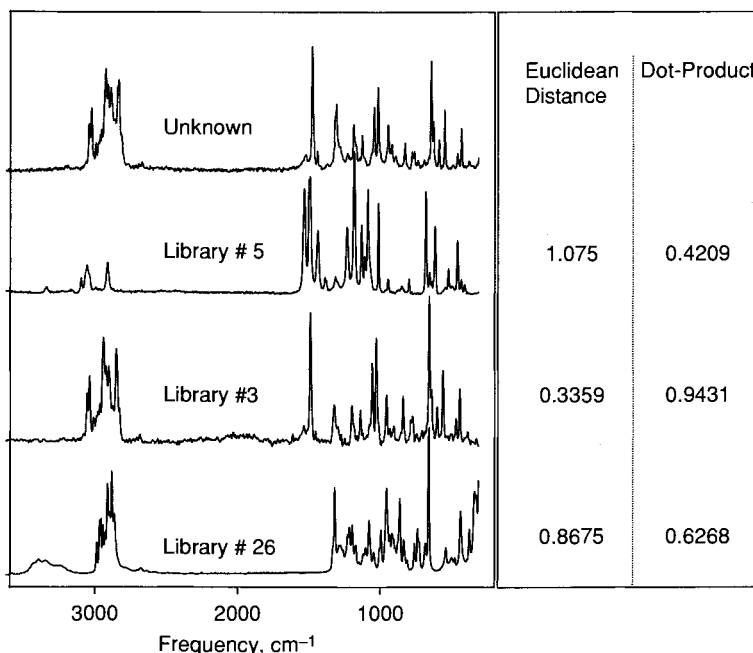


Figure 5-10 Raman spectra of an unknown samples and three library spectra. On the right two columns are the Euclidean distances and dot products of the unknown spectrum with each of the three library spectra.

where the sum is over all frequencies. For a perfect match with normalized spectra, the dot product = 1.0. Both these metrics produce identical results for library searches.

An example of search results is shown in Fig. 5-10. An unknown spectrum (ibuprofen tablet) is compared with three library spectra. The unknown and each of the library spectra were interpolated so that the number of frequencies, the first and last frequencies, and the frequency increment were identical for all the spectra. Next, the baseline minimum was subtracted from each of the spectra, and each of the spectra was normalized so that the total area was 1.0. Finally, the Euclidean distances and dot products were calculated using Eqs. (5-9) and (5-10), respectively. Library spectrum 3 had the smallest Euclidean distance and the largest dot product with the unknown spectrum. Spectrum 3 corresponds to pure ibuprofen powder, so the correct match was obtained.

Many spectroscopic software packages come with search engines, or search engines can be purchased as add-ons to a package. The software will work on commercial libraries or provide mechanisms for generating libraries from your own spectral data.

5.5 Discriminant Analysis

5.5.1 MAHALANOBIS DISTANCE METRIC

Many spectroscopic applications involve finding the similarity or differences between a number of samples. Often it is known that a sample belongs to one of several classes, and it is just a matter of finding which class. These types of analyses have fallen under the chemometric title of *cluster analysis* or *discriminant analysis*. The determinations seem rather simple, but they often involve finding very small differences between similar spectral data. The techniques of discriminant analysis are becoming increasingly important in medical diagnostics and process automation. Here we will briefly discuss the Mahalanobis distance metric because it has been used mostly in recent years. The reader should also be aware of the *K*-nearest neighbor (4) technique and artificial neural networks methodologies (12).

The Mahalanobis distance metric (13) is designed to determine an in-class or out-of-class value from the spectrum of an unknown sample. The metric is trained using spectra of samples known to be in the target class. In its simplest rendition, the Mahalanobis distance is the Euclidean distance of a target spectrum from the average spectrum of the training set, i.e.,

$$D_{\text{Euclid}} = \sqrt{\sum [r_{\text{unk},i} - r_{\text{ave},i}]^2}, \quad (5-13)$$

where $r_{\text{unk},i}$ is the intensity of the i^{th} frequency for the unknown, $r_{\text{ave},i}$ is the intensity of the i^{th} frequency for the average spectrum of the training set, and the sum is over all i frequencies. This gives an absolute distance, but a distance relative to the training set is more appropriate. To obtain a relative distance, the standard deviation for the distances of all samples in the training set is calculated, and the D_{Euclid} is divided by the standard deviation to produce the relative Mahalanobis distance (MD). An unknown with a relative MD > 3 is considered to be outside the group. In three-dimensional space, this MD would enclose the training spectra in a sphere.

In more advanced formulation of the Mahalanobis distance metric (13), the difference spectrum \mathbf{diff} between the target and the average is calculated and stored as a vector with f coordinates corresponding to the f frequencies. The Mahalanobis distance is given by the equation

$$D = [\mathbf{diff}^t \mathbf{M} \mathbf{diff}]^{1/2} \quad (5-14)$$

where \mathbf{diff}^t is a row vector containing the difference values at each of the f frequencies, \mathbf{diff} is a column vector of the same values, and \mathbf{M} is an $f \times f$ matrix containing the inverse of the covariance matrix, whose elements are given by

$$\text{Element}_{jk} = \sum (r_j - \bar{r}_j)(r_k - \bar{r}_k), \quad (5-15)$$

where r is the intensity, j and k are indices representing the spectral frequencies, the average values are average intensities over all the training spectra for the j^{th} and k^{th} frequencies, and the summation is over all the samples in the training group. To understand the influence of weighting the \mathbf{diff} vectors by the \mathbf{M} matrix, consider a three-dimensional case. Equation (5-12) could define an ellipsoidal shape depending on the values of the elements in the \mathbf{M} matrix. Should the \mathbf{M} matrix be the unit matrix, Eq. (5-14) would define a sphere and would revert to Eq. (5-13). In f -dimensional space, which we are dealing with here, we cannot picture the clustering of Mahalanobis points, but the three-dimensional comparison helps to visualize the difference between the results of Eqs. (5-13) and (5-14).

In the preceding description of the Mahalanobis distance, the number of coordinates in the distance metric is equal to the number of spectral frequencies. As discussed earlier in the section on principal component analysis, the intensities at many frequencies are dependent, and by using the full spectrum, we fit the noise in addition to the real information. In recent years, Mahalanobis distance has been defined with PCA or PLS scores instead of the spectral frequencies because these techniques eliminate or at least reduce most of the overfitting problem. The overall application of the Mahalanobis distance metric is the same except that the r_i intensity values are replaced by the scores from PCA or PLS. An example of a Mahalanobis distance calculation on a set of Raman spectra for 25 carbohydrates is shown in Fig. 5-11. The 25 spectra were first subjected to PCA, and it was found that the first three principal components could account for most of the variance in the spectra. It was first assumed that all 25 spectra belonged to the same class because they were all carbohydrates. However, as shown in the three-dimensional plot in Fig. 5-11, the spectra can be clearly divided into three separate classes, with two of the spectra almost equal distance from each of the three classes. Most of the components in the upper left class in the two-dimensional plot were sugars; however, some sugars were found in the other two classes. For unknowns, scores have to be calculated from the principal components and processed in the same way as the spectral intensities.

5.5.2 SCORE PLOTS

A very useful method of discriminating between samples from different classes is to plot PCA or PLS scores in two or three dimensions. This is very similar to the Mahalanobis distance discussed earlier in Fig. 5-11, except that it is limited to two or three dimensions, and the Mahalanobis distance can be constructed for n dimensions. Score plots do provide a good visual understanding of the underlying differences between data from samples belonging to different classes.

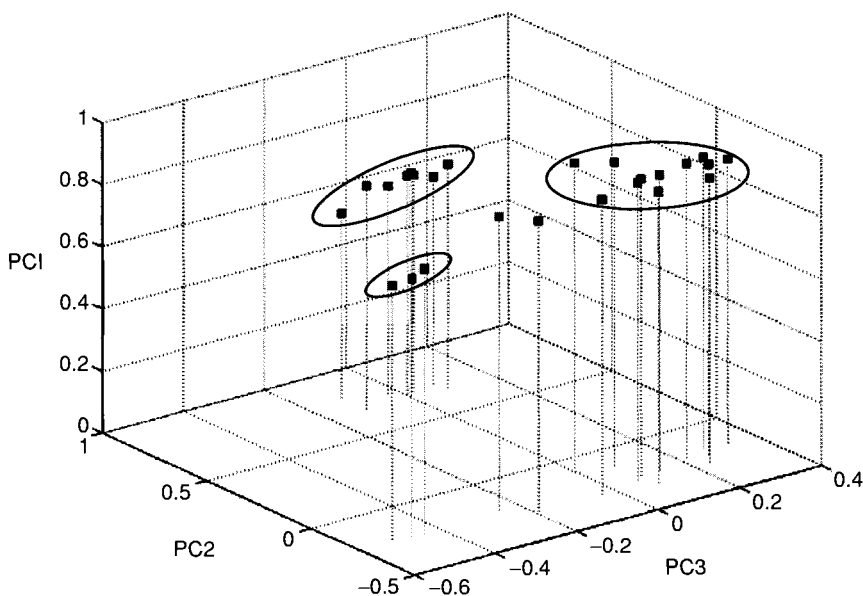


Figure 5-11 Results of a Mahalanobis distance calculation on 25 Raman spectra of carbohydrates (Food Technology, Dairy and Food Science, Royal Veterinary and Agricultural University, Denmark). The spectra were subjected to principal component analysis, and the first three PCs were used to characterize the spectra.

Recently, chemometrics was used to improve the predictive power of Raman spectroscopy to process postconsumer plastics (4). Six commonly used polymers were investigated in this study; their Raman spectra and second-derivative spectra are shown in Fig. 5-12. The second-derivative spectra were used to remove varying background interferences that appeared in some of the samples. PCA was then applied to 188 mean-centered second-derivative spectra from 103 samples of the six materials. The score plot of PC2 versus PC1 is shown in Fig. 5-13a. The scores for five of the six classes of samples clustered without overlap; however, class 2 (HDPE) and class 4 (LDPE) appeared to overlap in the figure. The spectra for the samples in these two classes were processed by PCA without including the other four classes, and the resulting score plot is shown in Fig. 5-13b; the two classes are completely separated, which shows that the method is quite accurate in predicting sample classes and has practical implications for recycling plastic materials.

There are many other practical examples of using chemometric methods to make Raman spectroscopy into a real-time monitoring method (14–18). One such example is the use of Raman for process control in the curing of polymers (18). The Raman spectra of a commercial cyanate ester resin,

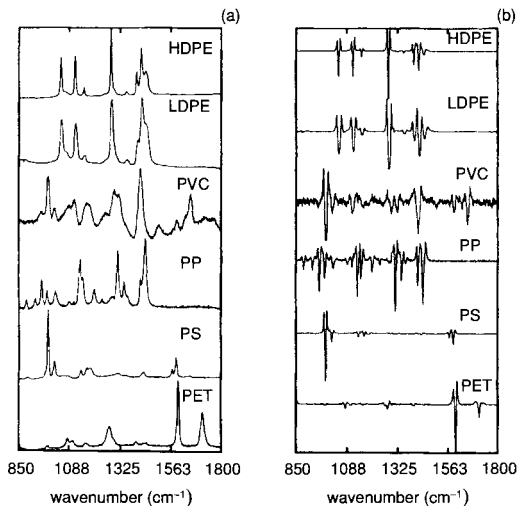


Figure 5-12 (a) Raman spectra. (b) Second-derivative spectra. HDPE, high-density polyethylene; LDPE, low-density polyethylene; PVC, polyvinyl chloride; PP, polypropylene; PS, polystyrene; PET, polyethylene terephthalate. (Reprinted with permission from Ref. 4.)

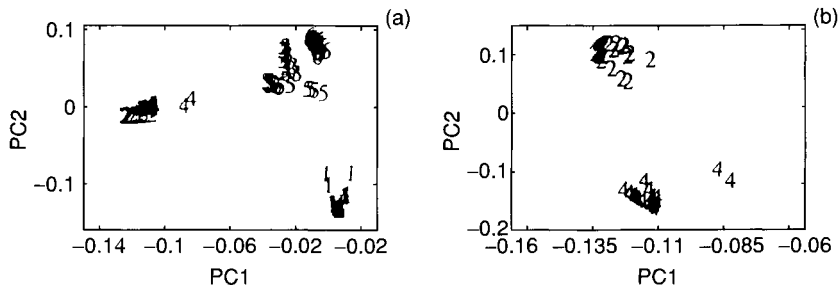


Figure 5-13 Score plots: 1 = PET; 2 = HDPE; 3 = PVC; 4 = LDPE; 5 = PP; 6 = PS. (a) All samples used in PCA. (b) Samples 2 and 4 only in PCA. (Reprinted with permission from Ref. 4.)

AroCy L-10 (Ciba Specialty Chemicals), as a function of curing time are shown in Fig. 5-14. A number of bands are increasing and decreasing as a consequence of the curing, but it is difficult to pick a single band to represent the amount of curing. Instead of using a single band, the spectra were subjected to PCA, and the scores were plotted versus the curing time. It was found that the score for PC2 versus time produced an ideal metric because the (scaled) score values overlaid the percentage cure, as shown in Fig. 5-15. PCA had to be applied to one curing experiment. The principal components obtained from that experiment could be used to predict all future curing of the same material. Thus this was an ideal monitoring method for polymer curing.

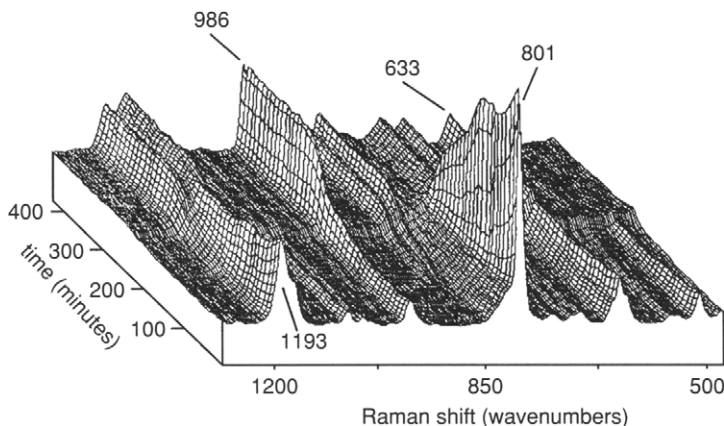


Figure 5-14 Raman spectra of AroCy L-10 resin as a function of curing time. (Reprinted with permission from Ref. 18.)

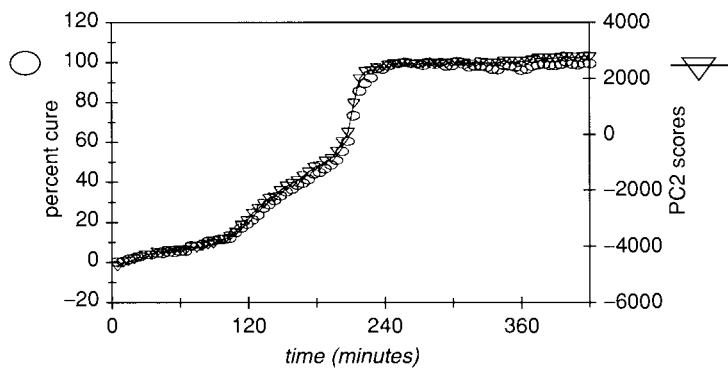


Figure 5-15 Percentage cure and PC2 score as a function of curing time for AroCy L-10 resin. (Reprinted with permission from Ref. 18.)

References

1. C. W. Brown, R. J. Obremski, and P. Anderson, *Appl. Spectrosc.* **40**, 734 (1986).
2. A. Savitsky and M. J. E. Golay, *Anal. Chem.* **36**, 1627 (1964).
3. A. O'Grady, A. C. Dennis, D. Denvir, J. J. McGarvey, and S. E. J. Bell, *Anal. Chem.* **73**, 2058 (2001).
4. R. Allen, J. J. Kalivas, and R. G. Rodriguez, *Appl. Spectrosc.* **53**, 672 (1999).
5. R. J. Barnes, M. S. Dhanoa, and S. J. K. Lister, *Appl. Spectrosc.* **43**, 772 (1989).

6. R. E. Barletta, private communication.
7. H. Wold, "Multivariate Analysis" (P. R. Krishnalal, ed.), p. 391. Academics Press, San Diego, 1966.
8. S. M. Donahue and C. W. Brown, *Anal. Chem.* **63**, 980 (1991).
9. D. M. Haaland and E. V. Thomas, *Anal. Chem.* **60**, 1193 (1988).
10. P. Geladi and B. R. Kowalski, *Anal. Chim. Acta* **185**, 1 (1987).
11. K. R. Beebe and B. R. Kowalski, *Anal. Chem.* **59**, 1007A (1985).
12. S. S. Cross, R. F. Harrison, and R. L. Kennedy, *Lancet* **346**, 1075 (1995).
13. H. L. Mark and D. Tunnell, *Anal. Chem.* **57**, 1449 (1985).
14. S. Kokot, N. A. Tuan, and L. Rintoul, *Appl. Spectrosc.* **51**, 387 (1997).
15. F. Adar, R. Geiger, and J. Noonan, *Appl Spectrosc. Rev.* **32**, 445 (1997) and references therein.
16. S. P. Mulvaney and C. D. Keating, *Anal. Chem.* **72**, 145R (2000) and references therein.
17. M. G. Shim, L. W. K. Song, N. E. Marcon, and B. C. Wilson, *Photochem. Photobiol.* **72**, 146 (2000).
18. J. B. Cooper, *Chem. Intell. Lab Syst.* **46**, 231 (1999).

Chapter 6

Biochemical and Medical Applications

As stated in Section 1.8, Raman spectroscopy is ideal for studies of biochemical and medical systems mainly for two reasons: (1) Since water is a weak Raman scatterer, it does not interfere with Raman spectra of solutes in aqueous solution. (2) By taking advantage of resonance Raman scattering, it is possible to selectively enhance particular chromophoric vibrations using a small quantity of biological samples. As a result, biochemical and medical applications of Raman spectroscopy have increased explosively in recent years, and a number of review articles and monographs have already provided comprehensive coverage of this field. (See General References at the end of Chapter 1.) Here, we demonstrate its utility using selected examples. Only oxygen-binding proteins are covered in the first three subsections.

This chapter is divided into two sections. Section 6.1 is concerned with applications of Raman spectroscopy to biochemistry. Related topics to this section are found in Section 3.3.3 of Chapter 3 (SER spectra of dipeptides) and Section 4.1.2 of Chapter 4 (Raman (RR) spectra of peptides, proteins, porphyrins, enzymes and nucleic acids). Section 6.2 describes medical applications of Raman spectroscopy as analytical and diagnostic tools. In contrast to biochemical samples discussed in the former section, medical samples in the latter section contain a number of components such as proteins, nucleic acids, carbohydrates and lipids, etc. Thus, Raman spectra of medical samples are much more complex and must be interpreted with caution.

6.1 Biochemical Applications

6.1.1 HEMOGLOBIN AND MYOGLOBIN

Heme proteins such as hemoglobin (Hb), myoglobin (Mb) and cytochromes contain the heme group (iron protoporphyrin, Fig. 6-1) as the active site of their biological functions. As discussed in Section 1.15, porphyrin rings are ideal for RR studies because strong resonance enhancement is produced without interference from the rest of the protein when the laser wavelength is chosen to coincide with $\pi-\pi^*$ transitions of the porphyrin ring. Since many review articles (1) are available on RR spectra of heme proteins, only brief discussions on RR spectra of Hb—O₂ and TR³ spectra of the Hb—Co photoproduct are presented in this subsection.

Myoglobin (MW ~ 16,000) is an oxygen storage protein in animal muscles. Figure 6-2 shows the well-known crystal structure of Mb as determined by x-ray analysis. It is a monomer containing 153 amino acids and an iron protoporphyrin that is linked to the proximal histidine (F8) of the peptide chain. Figure 6-3 illustrates the structural changes caused by oxygenation. In the deoxy state, the iron is divalent and high spin, and the iron atom is out of the porphyrin plane (~ 0.6 Å). Upon oxygenation, the O₂ molecule coordinates to the vacant axial position, and the heme plane becomes planar. The iron in the oxy state is low spin and its oxidation state is close to Fe(III). Hemoglobin (MW ~ 64,000) is an oxygen transport protein in animal blood. It consists of four subunits (α_1 , α_2 , β_1 and β_2) each of which takes a structure similar to that of Mb. However, they are not completely independent of each other; the oxygen affinity of each subunit depends upon the number of subunits that are already oxygenated (cooperativity).

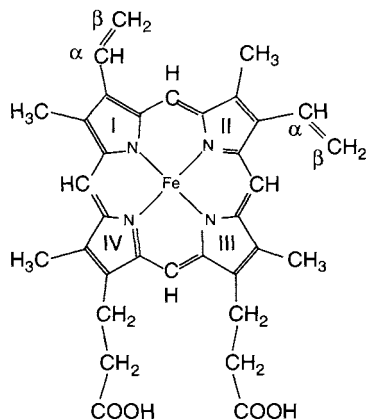


Figure 6-1 Structure of iron protoporphyrin IX.

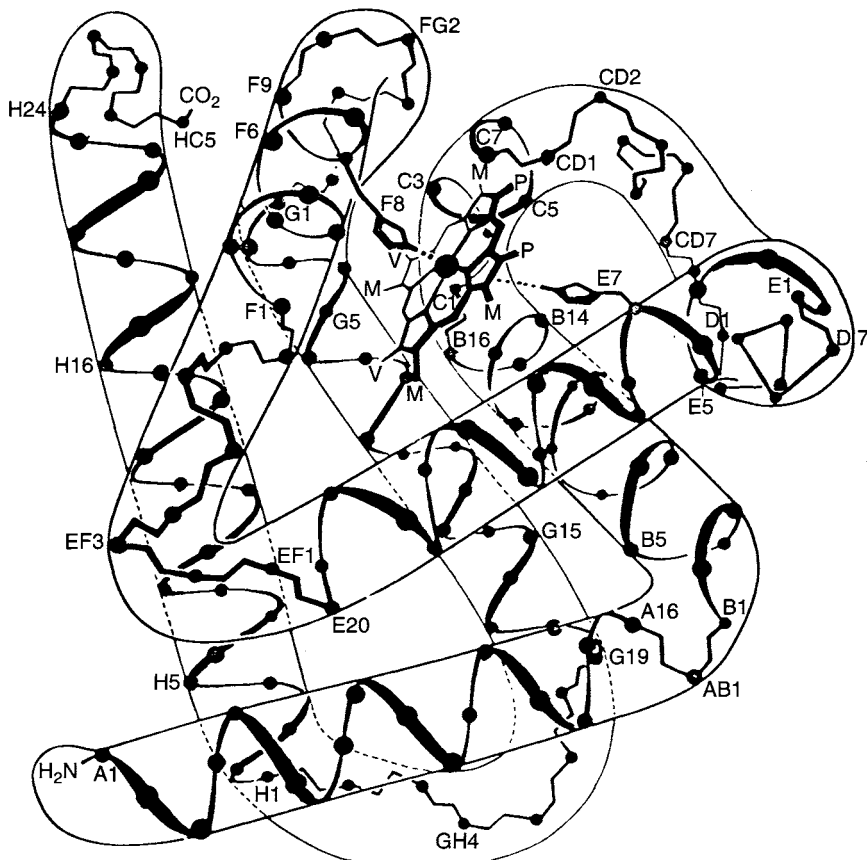


Figure 6-2 Structure of sperm-whale myoglobin. (Reproduced with permission from Dickerson, "The Proteins," Vol. 2, 2nd Ed. Academic Press New York, 1964.)

Figure 6-4 shows the RR spectra of oxy- and deoxy-Hb obtained by Spiro and Strekas (2). It is seen that the bands at 1,358 (Band I), 1,473 (Band II), 1,552 (Band III) and 1,607 (Band IV) cm^{-1} of the deoxy state are shifted to 1,374, 1,506, 1,586 and 1,640 cm^{-1} , respectively, upon oxygenation. These bands correspond to the ν_4 , ν_3 , ν_{19} and ν_{10} of Ni(OEP) discussed in Section 4.1.2. The ν_4 (Band I) is an oxidation state marker, and its upshift from 1,358 to 1,374 cm^{-1} indicates oxidation from Fe(II) to Fe(III). The ν_3 (Band II), ν_{19} (Band III) and ν_{10} (Band IV) are core-size-sensitive, and their upshifts upon oxygenation support high to low spin conversion. Although the $\nu(\text{O}_2)$ of Hb— O_2 has not been observed in RR spectra, IR studies have shown it in the superoxo (O_2^-) region from 1,160 to 1,100 cm^{-1} . (For complexity of IR

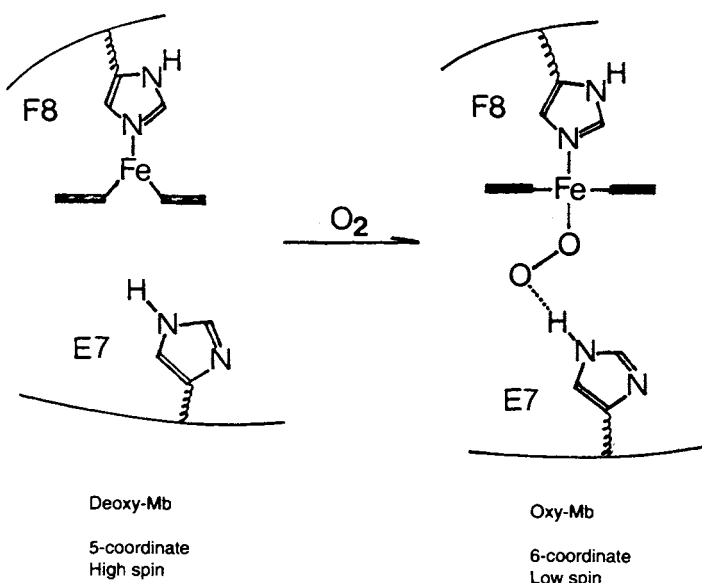


Figure 6-3 Schematic diagram of deoxy- and oxy-myoglobin near the active site.

spectra, see Ref. 3.) Thus, the best formulation of the Fe— O_2 bond is Fe(III)— O_2^- .

As discussed in Section 3.6 the Fe— O_2 moiety can take either end-on or side-on geometry. Duff *et al.* (4) observed two $\nu(Fe—O_2)$ of Hb— O_2 at 567 and 540 cm^{-1} when Hb was oxygenated by $^{16}O^{18}O$. These frequencies are exactly the same as those of Hb— $^{16}O_2$ and Hb— $^{18}O_2$, respectively. Thus, their results provide definitive evidence to support the end-on structure. According to x-ray analysis, the Fe— O_2 bonding is stabilized by a hydrogen bond between the bound O_2 and the N—H group of distal histidine (E7) as shown in Fig. 6-3. The presence of such hydrogen bonding is also supported by RR studies of Kitagawa *et al.* (5), who observed a small upshift (2 cm^{-1}) of the $\nu(O_2)$ of Co-substituted Mb— O_2 at 1,134 cm^{-1} by $H_2O—D_2O$ exchange.

In normal Hb, the $\nu(Fe—N)$ of the proximal histidine (F8) is near 220 cm^{-1} (6). In mutant Hb such as Hb M Iwate and Hb M Boston, F8 histidine and E7 histidine are replaced by tyrosine residues, respectively. In five-coordinate ferric α subunits of these compounds, the $\nu(Fe—O^-$ (phenolate)) bands are observed at 589 and 603 cm^{-1} , respectively (7).

Raman spectra of short-lived species of heme proteins can be obtained by using TR^2/TR^3 techniques (Section 3.5). Terner *et al.* (8) employed this method to monitor structural changes of Hb—CO (low spin) following the photolysis. Figure 6-5 shows the TR^3 spectra obtained by 576 nm pulse

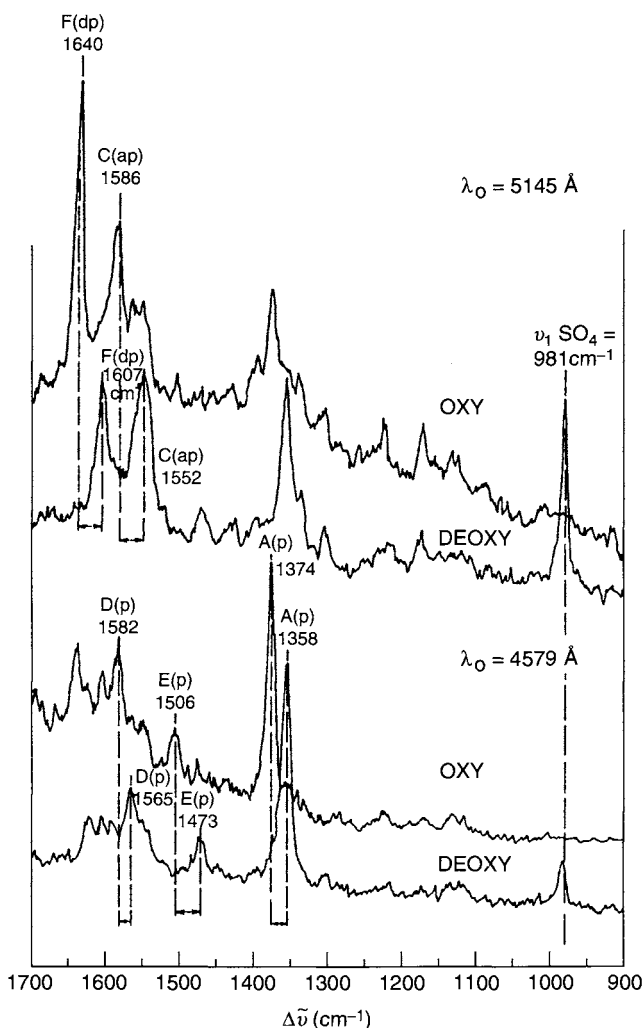


Figure 6-4 RR spectra of oxy- and deoxy-hemoglobin in the $\alpha-\beta$ (5,145 Å) and Soret (4,579 Å) scattering regions. Frequency shifts for corresponding bands are marked by the arrows between vertical broken lines. (Reproduced with permission from Ref. 2. Copyright 1974 American Chemical Society.)

excitation of deoxy Hb (trace c) and the Hb—CO photoproduct with ~ 30 ps (trace a) and ~ 20 ns (trace b) pulses.* It is seen that the spectra of the photoproduct are almost identical to that of deoxy Hb. Since ν_{10} , ν_{19} and ν_{11} are all spin state sensitive, these observations suggest that a

*ns: nano (10^{-9}) sec. ps: pico (10^{-12}) sec.

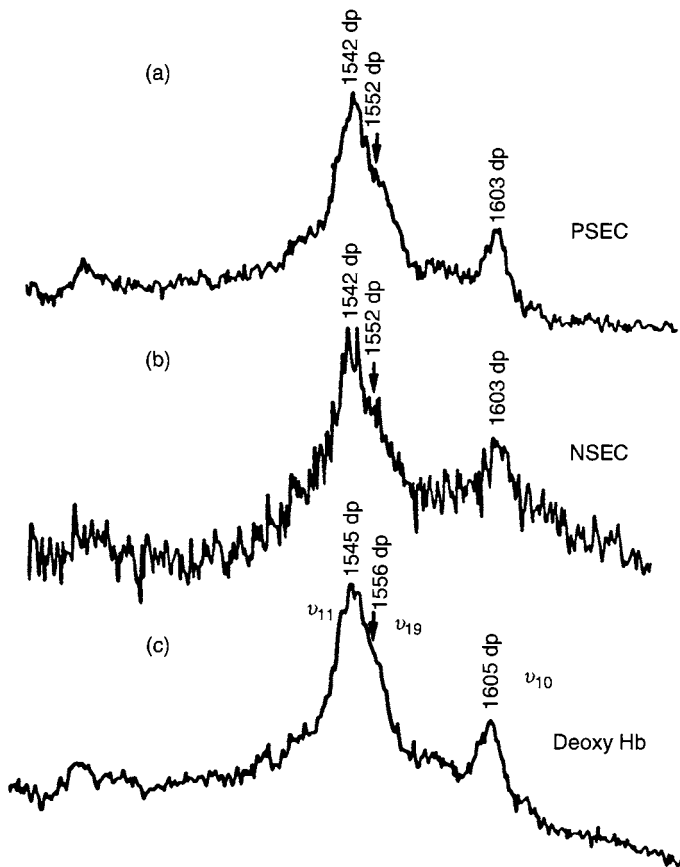


Figure 6-5 RR spectra obtained with 576 nm pulsed laser excitation from a synchronously pumped dye laser. (a) and (b), the Hb—Co photoproduct obtained with ~ 30 ps and ~ 20 ns pulses, respectively. (c) Deoxy-Hb. (Reproduced with permission from Ref. 8.)

high spin Fe(II) species has been produced by the photolysis of Hb—CO within ~ 30 ps. This spin conversion is $\sim 10^3$ times faster than typical spin conversion rates in the ground state of Fe(II) complexes. Terner *et al.* suggest that the photolysis pathway involves intersystem crossing for the initially excited singlet $\pi-\pi^*$ state to a low-lying excited state of Hb—CO. The observed small downshifts in going from deoxy Hb to the photoproduct indicate a slightly larger core-size of the latter relative to the former. (The Fe atom in the photoproduct is closer to the heme plane than in deoxy Hb (~ 0.6 Å).) These downshifts are seen even when the laser pulses are lengthened to ~ 20 ns. This may suggest that the slow relaxation to the structure of deoxy Hb is associated with changes in the globin tertiary structure.

6.1.2 CYTOCHROMES AND PEROXIDASES

Another class of heme proteins containing iron protoporphyrin as the active center includes enzymes such as cytochrome P-450 and horseradish peroxidase (HRP). The former is a monooxygenase enzyme (MW \sim 50,000) that catalyzes hydroxylation reaction of substrates such as drugs, steroids and carcinogens:

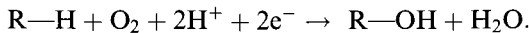


Figure 6-6 shows a proposed reaction cycle of cytochrome P-450 (9). In contrast to Hb and Mb, its Fe center is axially bound to a mercaptide sulfur

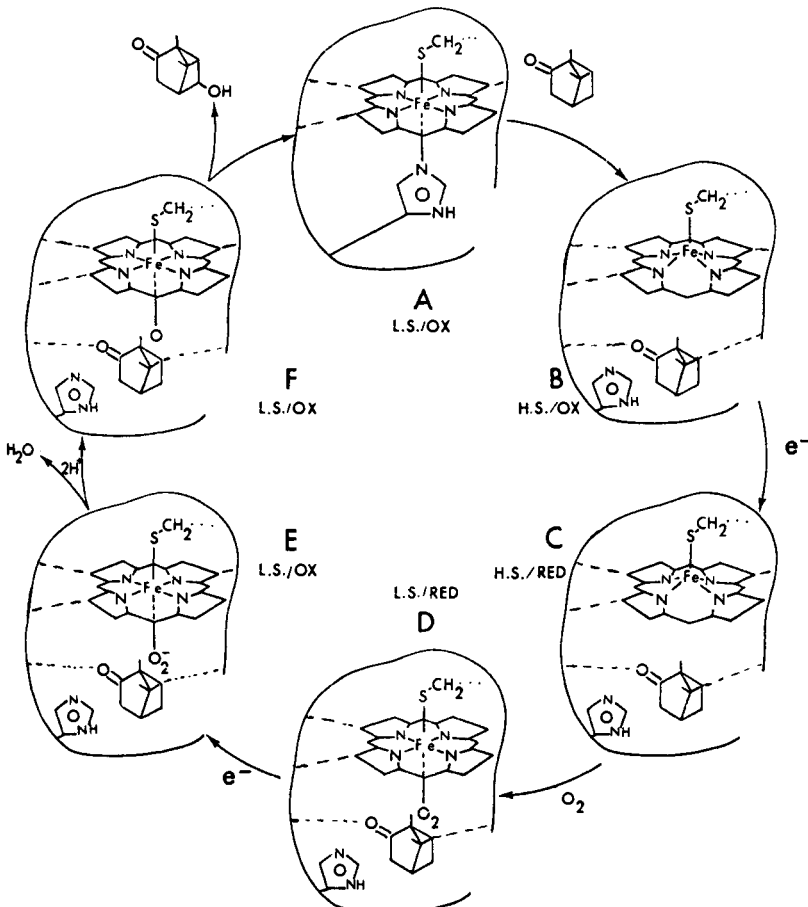
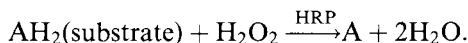


Figure 6-6 Reaction cycle of cytochrome P-450. (Reproduced with permission from Ref. 9.)

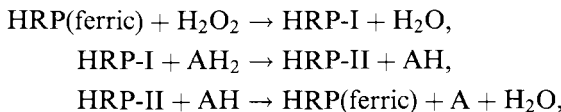
(RS^-) of a cysteinyl residue. In fact, the $\nu(\text{Fe}-\text{S}^-)$ vibration of cytochrome P-450 cam (camphor as the substrate) (B-state) has been observed at 351 cm^{-1} by Champion *et al.* (10). The oxidation state marker band of C-state was observed at $1,346 \text{ cm}^{-1}$ by Ozaki *et al.* (11). It is much lower than the corresponding band of deoxy-Hb at $1,356 \text{ cm}^{-1}$. This marked lowering has been attributed to the strong π -basicity of the thiolate ligand, which donates electrons via the Fe ($d\pi$)-porphyrin ($p\pi^*$) overlap. As stated in the preceding section, the $\nu(\text{O}_2)$ of oxy-Hb has not been observed by Raman spectroscopy. However, Bangcharoenpaurpong *et al.* (12) were able to observe the $\nu(\text{O}_2)$ of cytochrome P-450 cam (D-state) at $1,140 \text{ cm}^{-1}$ in RR spectra (420 nm excitation).

According to the reaction cycle shown in Fig. 6-6, oxoferryl ($\text{O}=\text{Fe(IV)}$) porphyrin is formed in F-state via the O—O bond breaking. This cleavage is partially facilitated by the weakening of the O—O bond due to the thiolate ligand in the trans position. The marked difference in biological function between Hb and Mb (reversible O_2 binding) and cytochrome P-450 (O—O bond cleavage) is largely attributed to the difference in the axial ligand (imidazole nitrogen vs. thiolate sulfur).

Horseradish peroxidase (MW $\sim 40,000$) catalyzes the oxidation of organic and inorganic compounds by H_2O_2 :



The reaction cycle of HRP involves two intermediates, HRP-I and HRP-II:



Thus, HRP-I (green) and HRP-II (red) have oxidation states higher than the native Fe(III) state by two and one, respectively. It has been found that both intermediates are oxoferryl (Fe(IV)) porphyrins and that HRP-II is low spin Fe(IV), whereas HRP-I is its π -cation radical, which is one electron deficient in the porphyrin π -orbital of HRP-II.

As expected from its high oxidation state, HRP-II exhibits the ν_4 at $1,377 \text{ cm}^{-1}$, which is the highest among heme proteins (13). The $\nu(\text{Fe}=\text{O})$ vibrations of HRP-II were first reported by Hashimoto *et al.* (13) and Terner *et al.* (14) almost simultaneously. Figure 6-7 shows the RR spectra of HRP-II obtained by the former workers. Upon reacting HRP with H_2O_2 at alkaline pH, a new band appears at 787 cm^{-1} that is shifted to 790 cm^{-1} by $^{56}\text{Fe}/^{54}\text{Fe}$ substitution, and to 753 cm^{-1} by $\text{H}_2^{16}\text{O}_2/\text{H}_2^{18}\text{O}_2$ substitution. Thus, this band was assigned to the $\nu(\text{Fe}=\text{O})$ of HRP-II. In neutral solution, the corresponding band was observed at 774 cm^{-1} , which was shifted to 740 cm^{-1} by

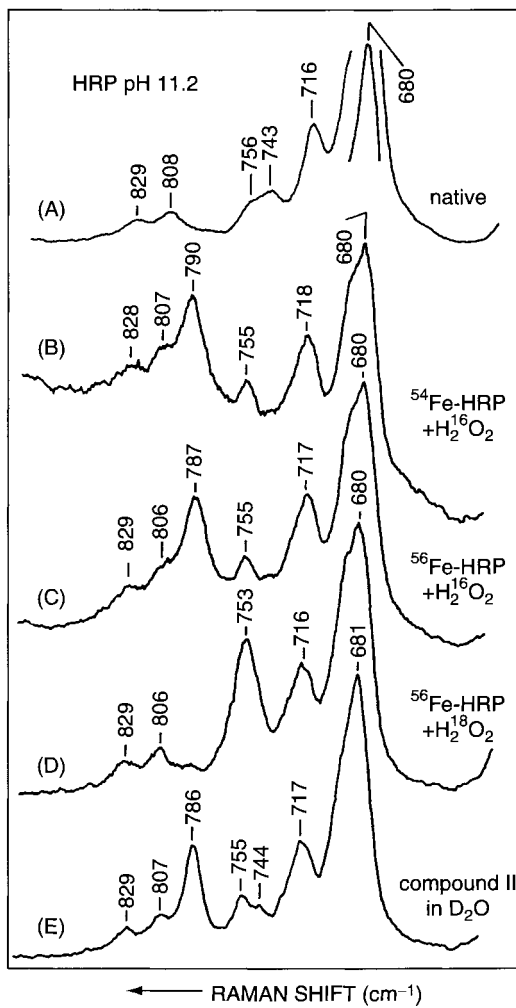


Figure 6-7 RR spectra of HRP-II at $\text{pH} = 11.2$ (406.7 nm excitation). (Reproduced with permission from Ref. 13.)

$\text{H}_2^{16}\text{O}_2/\text{H}_2^{18}\text{O}_2$ substitution. The observed downshift of the $\nu(\text{Fe}=\text{O})$ in going from alkaline to neutral solution has been attributed to the formation of a hydrogen bond in neutral solution as depicted in Fig. 6-8 (13). These $\nu(\text{Fe}=\text{O})$ frequencies are much lower than those of $\text{O}=\text{Fe}(\text{TPP}-d_8)$ (853 cm^{-1} (Section 3.2.3) because HRP-II is six-coordinate. Kitagawa's review (15) provides more information on RR spectra of reaction intermediates of heme proteins.

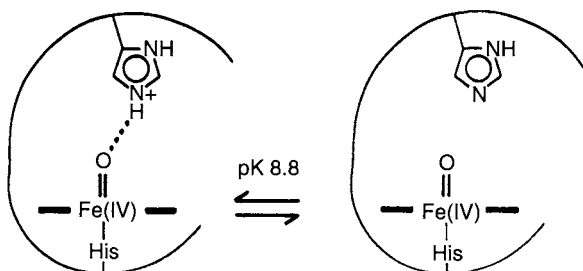


Figure 6-8 Equilibrium between hydrogen-bonded and non-hydrogen-bonded structures of HRP-II. (Reproduced with permission from Ref. 13.)

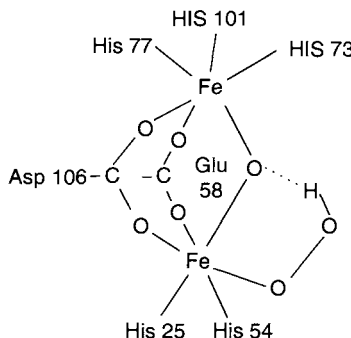


Figure 6-9 Active site structure of oxy-hemerythrin.

6.1.3 NON-HEME RESPIRATORY PROTEINS

Hemerythrin (Hr) is a non-heme oxygen carrier found in invertebrate phyla. Hr isolated from a sipunculan worm (MW \sim 108,000) consists of eight identical subunits, and each contains 113 amino acids and two Fe atoms (16). The deoxyform (colorless) turns to pink upon oxygenation (“pink blood”), and one molecule of O_2 binds to a pair of Fe atoms. Originally, Kurtz *et al.* (17) measured the RR spectra of oxy-Hr with isotopically scrambled dioxygen ($^{16}O_2/^{16}O^{18}O/^{18}O_2 \cong 1:2:1$) and found that $\nu(^{16}O^{18}O)$ near 820 cm^{-1} splits into two peaks, indicating non-equivalence of the two oxygen atoms. This finding was also supported by the RR spectra of the $\nu(\text{Fe}-\text{O}_2)$ region ($510-470\text{ cm}^{-1}$). However, the structure of the active site was not clear. Later, Stenkamp *et al.* (18) proposed the structure shown in Fig. 6-9 based on x-ray studies; the coordinated dioxygen is protonated and forms an intramolecular hydrogen bond with the μ -oxo bridge oxygen. This structure was supported by RR studies by Shiemke *et al.* (19). Figure 6-10 shows the low-frequency RR spectra of oxy-Hr obtained by these workers.

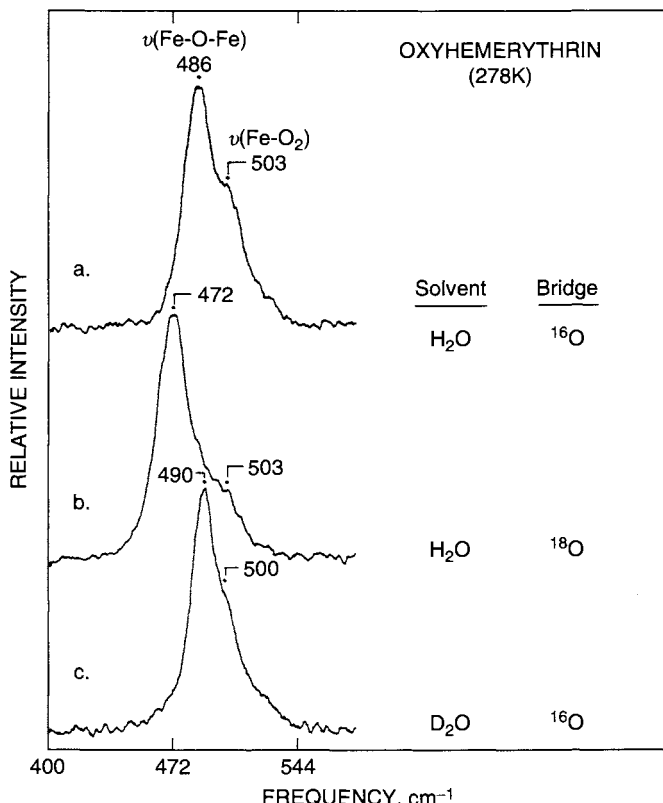


Figure 6-10 RR spectra of oxy-hemerythrin (excitation at 363.8 nm near $O_2^{2-} \rightarrow Fe(III)CT$ transition). (Reproduced with permission from Ref. 19. Copyright 1986 American Chemical Society.)

The bands at 753 (not shown), 503 and 486 cm^{-1} were assigned to the ν_a ($FeOFe$), $\nu(Fe-O_2)$ and ν_s ($FeOFe$), respectively. The fact that the latter two bands are shifted to 500 and 490 cm^{-1} , respectively, in D_2O solution provided definitive evidence for the intramolecularly hydrogen-bonded structure.

Hemocyanins (Hc) are oxygen-transport proteins found in the blood of insects, crustacea and other invertebrates ($MW \sim 10^5 - 10^7$) (20). One of the smallest Hc ($MW \sim 450,000$) extracted from spiny lobster consists of six subunits, each containing two Cu atoms. Upon oxygenation, the deoxy-form (Cu(I), colorless) turns to blue (Cu(II), “blue blood”) by binding one molecule of O_2 per two Cu atoms. Freedman *et al.* (21) measured the RR spectra of oxy-Hc extracted from crustacea and observed the $\nu(O_2)$ near 750 cm^{-1} , which shifts to $\sim 705\text{ cm}^{-1}$ upon $^{16}O_2/^{18}O_2$ substitution. In contrast to oxy-Hr, the two O atoms of the coordinated O_2 were found to be equivalent since

its $^{16}\text{O}^{18}\text{O}$ adduct exhibited a single $\nu(^{16}\text{O}^{18}\text{O})$ band at 728 cm^{-1} (22). Using $^{63}\text{Cu}/^{65}\text{Cu}$ isotopic techniques, Larrabee and Spiro (23) assigned the $\nu(\text{Cu—N(Im)})$ at 267 and 226 cm^{-1} (363.8 nm excitation). Recent studies support the active site structure shown in Fig. 6-11 (24).

6.1.4 DRUG-DNA INTERACTIONS

Basically, three types of interaction are involved in drug-DNA complexes; intercalation, groove binding and covalent bonding, which are often reinforced by hydrogen-bonding and/or coulombic interaction. Raman spectroscopy has become a powerful technique in elucidating the mode of interaction. In particular, RR spectroscopy has the advantages that drug vibrations can be selectively resonance-enhanced if the drug has a strong absorption in the visible region.

Both aclacinomycin (ACM) and adriamycin (ADM) are antitumor and antibiotic drugs that bind to DNA. Figure 6-12 shows their structures, and Fig. 6-13 shows the RR spectra of these drugs mixed with poly(dA-dT) and poly(dG-dC) obtained by Nonaka *et al.* (25). It is seen that the fluorescence background is prominent in ADM-poly(dA-dT) but is quenched in ADM-poly(dG-dC). On the other hand, a strong fluorescence background is observed for ACM-poly(dG-dC) but is quenched for ACM-poly(dA-dT). These results suggest that ADM is intercalated between the G-C/C-G sequence, whereas ACM is intercalated between the A-T/T-A sequence of DNA.

A long, flexible molecule such as distamycin (Fig. 6-14) binds to A,T-rich regions in the minor groove of DNA via hydrogen bonding. Figure 6-15 shows the Raman spectra of distamycin alone and its mixture with DNA obtained by Lu *et al.* (26). It is seen that the amide I band at $1,620\text{ cm}^{-1}$ is upshifted to $1,634\text{ cm}^{-1}$, whereas the pyrrole ring mode at $1,437\text{ cm}^{-1}$ is

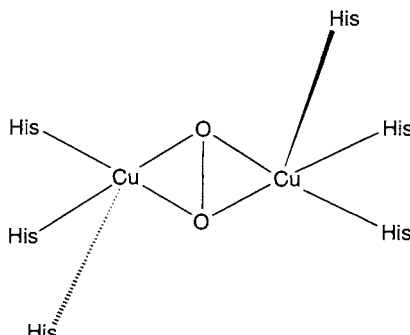


Figure 6-11 Structure of oxy-hemocyanin. (Reproduced with permission from Ref. 24.)

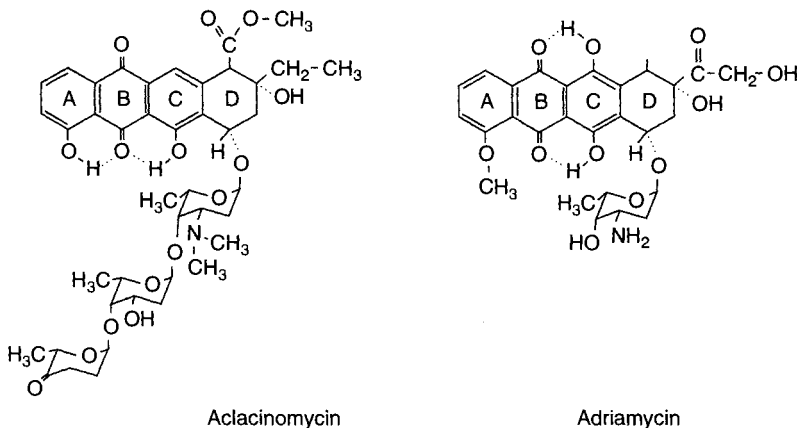


Figure 6-12 Structures of aclacinomycin and adriamycin.

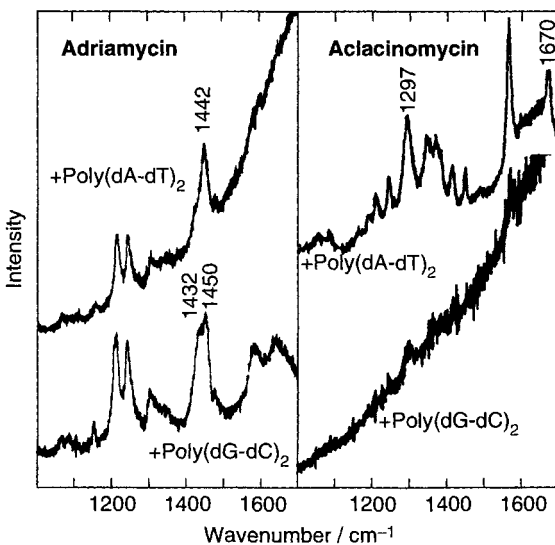


Figure 6-13 Left: RR spectra of adriamycin mixed with poly(dA-dT) and poly(dG-dC) (457.9 nm excitation). Right: RR spectra of aclacinomycin mixed with poly(dA-dT) and poly(dG-dC) (406.7 nm excitation).

downshifted to 1,430 cm⁻¹ when distamycin is mixed with DNA. These changes suggest that the pyrrole ring and the peptide group are nearly coplanar in the free state, and that this coplanarity is destroyed when distamycin is bound inside the minor groove of DNA. When these groups are coplanar, a considerable amount of electron migration is expected to occur from the pyrrole ring to the peptide group via resonance:

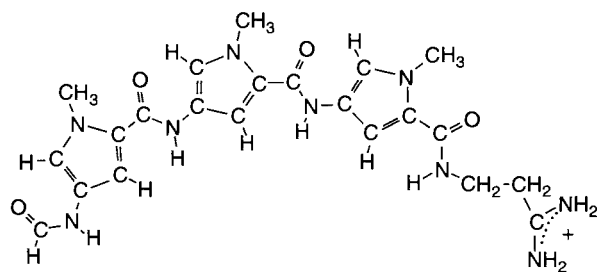


Figure 6-14 Structure of distamycin.

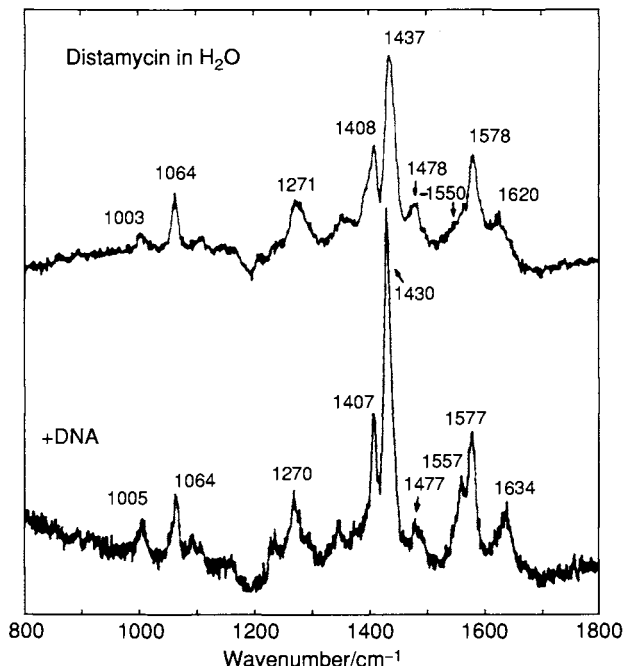
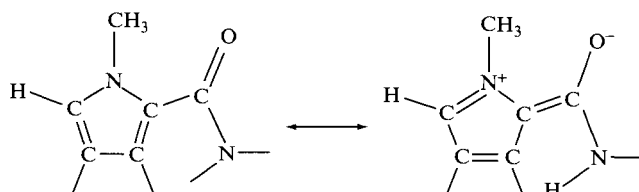


Figure 6-15 Raman spectra of distamycin (upper trace) and distamycin mixed with DNA (lower trace). (488,0 nm excitation).



When this resonance is disrupted on DNA binding, the amide I band would shift to higher and the pyrrole ring band to lower frequency. Such conformational change also accounts for the observed sharpening of Raman bands upon DNA binding. In the free state, all the internal rotational angles around the C—C and C—N bonds connecting the pyrrole ring and the peptide group fluctuate in a narrow range around 0°. However, this fluctuation causes broadening of the vibrational bands. Upon binding to DNA, the conformation of distamycin is fixed by the steric requirements in the minor groove, and the bands become sharper.

Strahan *et al.* (27) discovered a novel phenomenon that water-soluble copper porphyrin, CuP4 ($M = \text{Cu(II)}$) ($X = \text{N}^+ - \text{CH}_3$) and $Y = \text{H}$ in Fig. 4-4, which is intercalated between GC/CG sequence of DNA, is translocated to the ATAT site upon electronic excitation of CuP4 by a pulsed laser. As shown in Fig. 6-16, the RR spectrum of CuP4–DNA obtained by high-power pulsed laser exhibits new bands at 1,550 and 1,346 cm^{-1} (trace B) that are not observed by CW laser excitation (trace A). These new bands do not appear with low-power pulsed laser excitation, and they are observed with poly(dA-dT) (trace C) but not with poly(dG-dC) (trace E). They have been attributed to an electronically excited CuP4 that was stabilized by forming a π -cation radical exciplex, $(\text{CuP4})^+(\text{AT})^-$, at an AT site. If oligonucleotides contain GC/CG as well as ATAT or a longer A/T sequence, the exciplex bands are observed as seen in traces G and H. More elaborate experiments show that, in these cases, some of the intercalated porphyrin at the GC/CG site is translocated to the ATAT site (major groove binding) by electronic excitation within 35 ns (Fig. 6-17). Vibrational studies on drug–nucleic acid interactions have been reviewed by Manfait and Theophanides (28).

6.1.5. PLANTS AND BACTERIA

Carotenoids are widely distributed among plants and animals and are ideal for RR studies because their vibrations can be selectively enhanced by choosing the exciting laser wavelength in the strong $\pi-\pi$ transition of a carotenoid pigment. Figure 6-18 shows the RR spectra (488 nm excitation) of β -carotene in live carrot root, canned carrot juice and of pure all-trans β -carotene in *n*-hexane obtained by Gill *et al.* (29). The intense peaks at 1,527 and near 1,160 cm^{-1} are due to the $\nu(\text{C}=\text{C})$ and $\nu(\text{C}—\text{C})$ of β -carotene, respectively.

Bacteria such as *E. coli* are colorless, and their chromophores such as proteins and nucleic acids absorb below 300 nm. Thus, RR spectra of bacteria can be obtained only by using UV laser excitation. Figure 6-19 shows the UVRR spectra of *E. coli* obtained by Britton *et al.* (30). The observed peaks

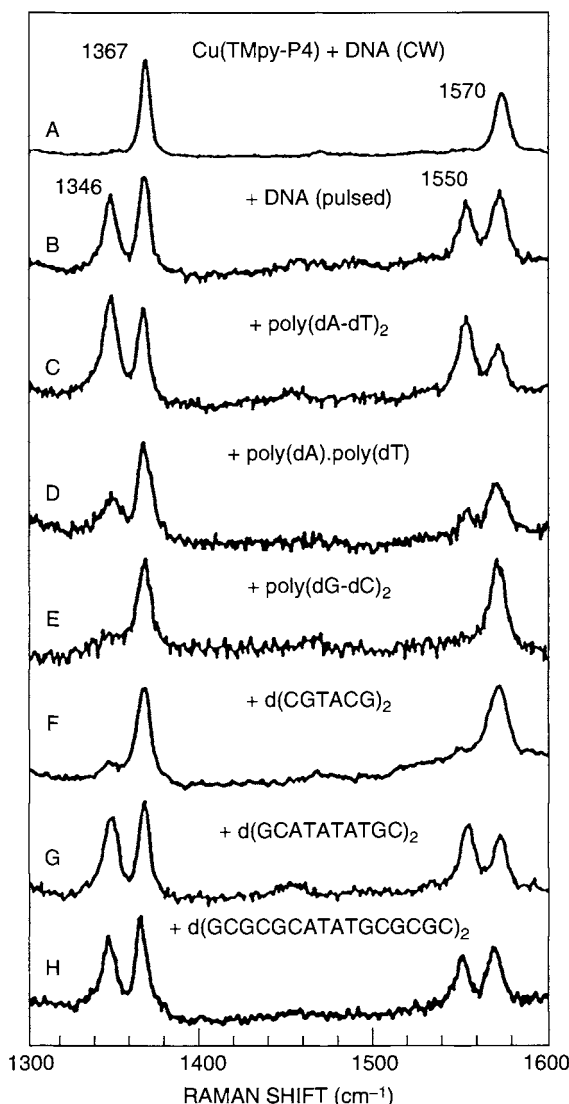


Figure 6-16 RR spectra of Cu(TMpy-P4)-nucleic acid complexes. All the spectra were obtained by using pulsed laser excitation at 416 nm except for the top spectrum (CW, 406.7 nm excitation).

have been assigned based on UV excitation profiles of individual amino acids and nucleotides. It was found that the 222.5 nm excitation spectrum is dominated by vibrations due to aromatic amino acids; 1,614 (Tyr), 1,558 (Trp), 1,178 (Tyr) and 1,008 cm⁻¹ (Tyr), whereas the 250.9 nm excitation spectrum is dominated by vibrations of nucleic acid bases: 1,623 (U, Trp, Tyr), 1,580

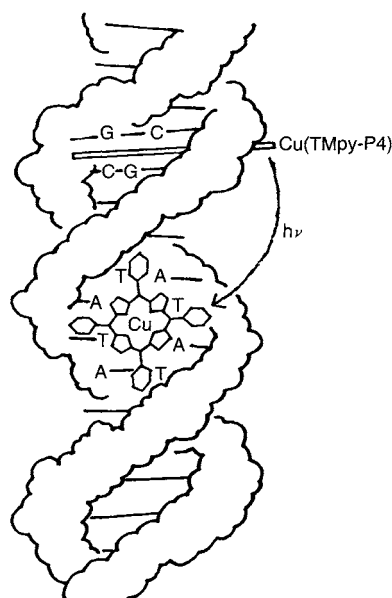


Figure 6-17 Schematic diagram showing translocation of Cu(TMpy-P4) from GC to ATAT site upon electronic excitation.

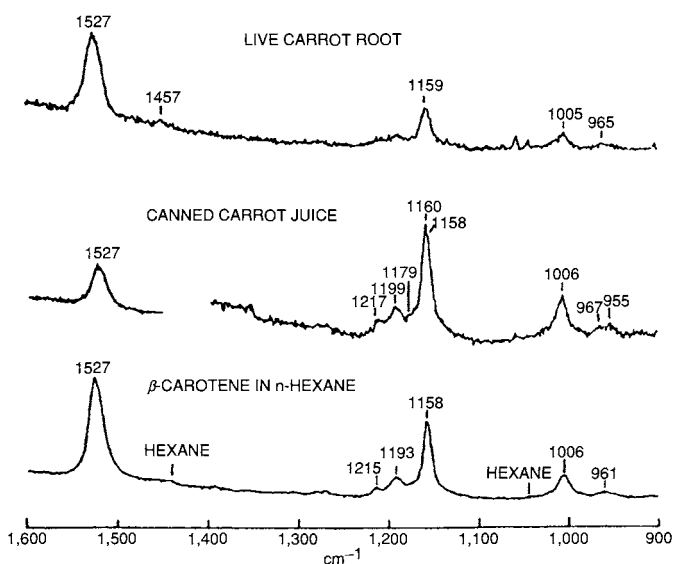


Figure 6-18 RR spectra of β -carotene in live carrot root (top), canned carrot juice (middle), and *n*-hexane (bottom; pure all trans form, 488 nm excitation). (Reproduced with permission from *Nature* from Ref. 29. Copyright 1970 Macmillan Magazines Limited.)

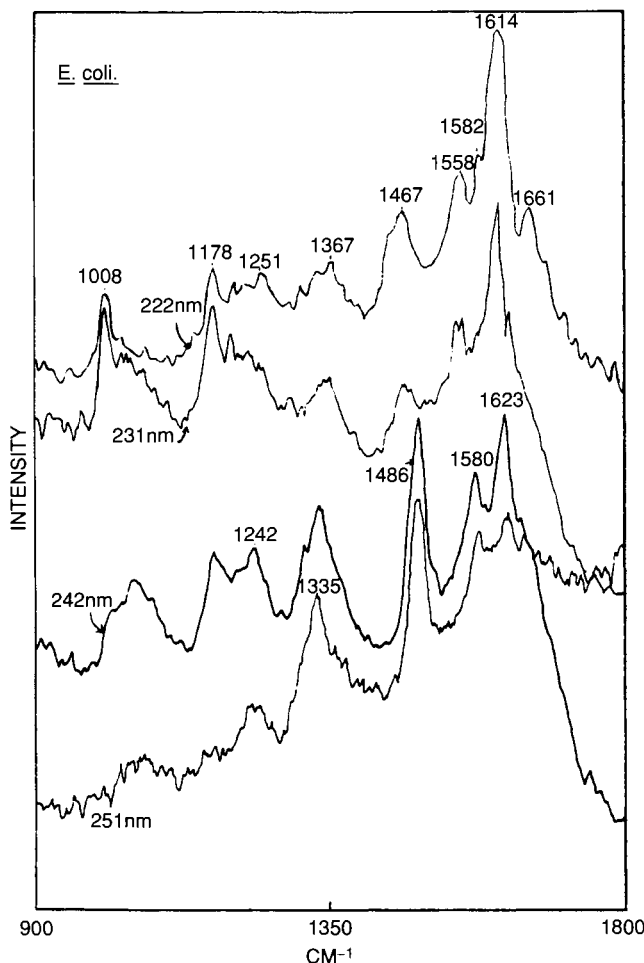


Figure 6-19 UVRR spectra of *E. coli* excited at 222.5, 230.6, 242.4, and 251.0 nm. (Reproduced with permission from Ref. 30)

(A, G), 1,486 (A, G), 1,335 (A, G) and 1,242 cm⁻¹ (U)*. Such selective enhancement is possible because aromatic amino acids absorb in the 230–190 nm region while nucleic acid bases absorb in the 260–240 nm region.

The UVRR spectra shown in Fig. 6-19 were obtained by using the conventional method which gives average spectra of a large number of bacterial cells in different physiological states. Recently, Schuster *et al.* (31) obtained Raman spectra of single bacterial cells using confocal Raman microspectroscopy (Section 3.2.5). Figure 6-20 shows the Raman spectrum (632.8 nm

*For nomenclatures of these amino acids and bases of nucleic acids, see Section 4.1.2.

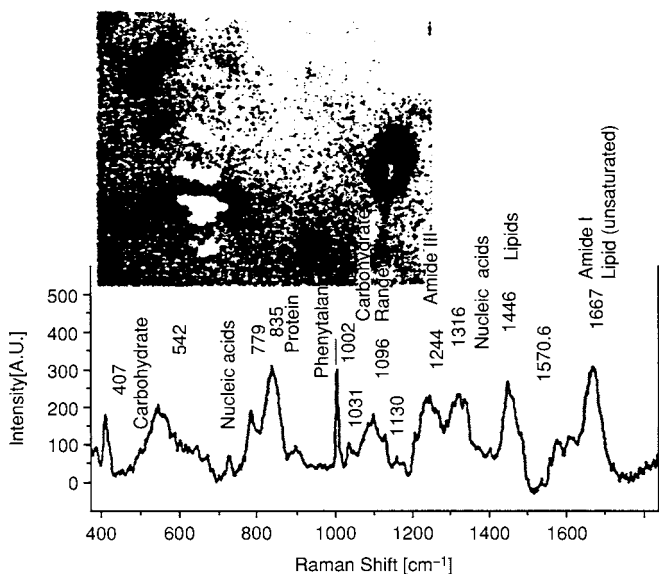


Figure 6-20 Raman spectrum of a single *Clostridium* cell of on a CaF_2 carrier, of a size about $2\ \mu\text{m}$ by $4\ \mu\text{m}$. The wavenumbers of the Raman shift and some tentative attributions of the major bands are given. The inset is a video image showing a single *Clostridium* cell in the focused laser beam of the Raman microscope and the diffraction pattern arising from the small object of a size in the range of the laser light wavelength. It can also be seen that the diameter of the laser focus, which partly determines the sampling volume by the excitation of the Raman effect, is about the same size as the cell. (Reproduced with permission from Ref. 31.)

excitation, 8 mW) of a single cell of bacterium *Clostridium beiferinckii* of a size about $2\ \mu\text{m}$ by $4\ \mu\text{m}$. The observed bands have been assigned to proteins, carbohydrates, lipids and nucleic acids as indicated in the figure. These workers also demonstrated that differences in chemical compositions in a single cell and between cells can be detected by comparing Raman spectra.

6.2 Medical Applications

Due to recent advancements in instrumentation, Raman spectroscopy has become one of the most powerful tools in medical research. Such advancements include development of new lasers, FT-Raman spectroscopy, CCD detectors, confocal Raman microscopy, Raman imaging, fiber optic probes, and computer software. In the following, the utility of Raman spectroscopy in medical science is demonstrated by using selected examples. A more complete coverage of the field is found in review articles by Ozaki (32) and Levin *et al.* (33).

6.2.1 SKIN, NAILS, AND HAIR

de Faria and de Souza (34) measured the Raman spectra (632.8-nm excitation, 7 mW) of human skin and nails by using a Raman microscope. The samples ($\sim 1\text{ mm}^2$ by $20\text{ }\mu\text{m}$) were taken from the outermost layers. Figure 6-21 shows the Raman spectra of human skin (trace a) and nails (trace b). The samples were photobleached to minimize fluorescence, and the residual emission was rejected by spatial filtering. The major peaks in Fig. 6-21 originate in proteins and lipids. The band at 528 cm^{-1} is due to the $\nu(\text{S}-\text{S})$ of keratin.

Wilson *et al.* (35) measured the Raman spectra (1064-nm excitation, 40 mW) of human hair to assess the degradation state of archaeological and forensic hair samples. In this case, single fibers were mounted as for bulk fibers, and their Raman spectra were measured using a Raman microscope. Figure 6-22 compares the Raman spectra of three degraded hair samples (traces 1, 2, and 3) against a modern standard (trace 4). Here, the samples for traces 1, 2, and 3 were taken from an exposed forensic sample (1964), a body in a wood coffin (1753–1845) and a body in a cast (*ca.* 600), respectively. Broadening of the amido bands at 1654 , 1451 , and 1301 cm^{-1} and the $\nu(\text{S}-\text{S})$ band near 530 cm^{-1} clearly indicate degradation and proteinaceous breakdown.

6.2.2 LENS PROTEINS

Lens aging and opacification can be monitored *in situ* via structural changes in lens proteins observed in Raman spectroscopy. Ozaki *et al.* (36) have carried out an extensive study on mouse lens proteins. Figure 6-23 shows the

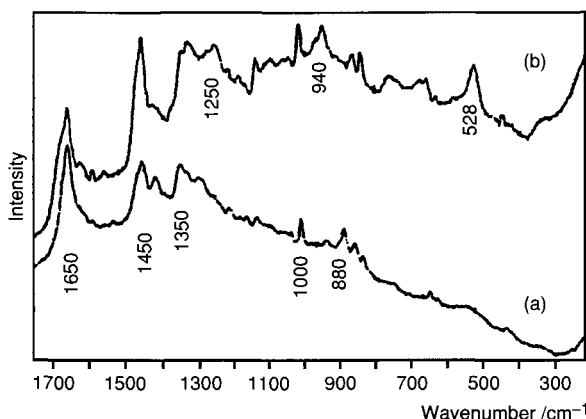


Figure 6-21 Raman spectra of (a) human skin and (b) nail excited at 632.8 nm. Laser power *ca.* 5 mW at the sample; acquisition time, 30 min. (Reproduced with permission from Ref. 34.)

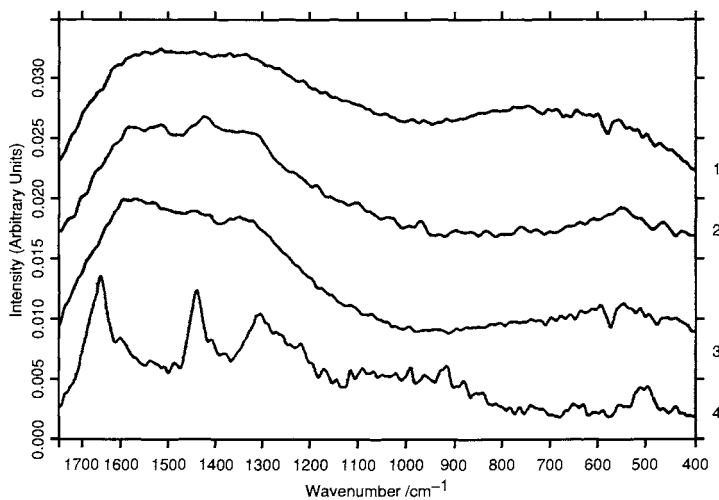


Figure 6-22 Degraded human hair samples (1, 2 and 3) against a modern standard (4). Note the marked loss of the Amide I $\nu(\text{C}=\text{O})$ peak (1653 cm^{-1}) and broadening of the vibrational bands suggesting progressive breakdown of the proteinaceous structure. (Reproduced with permission from Ref. 35.)

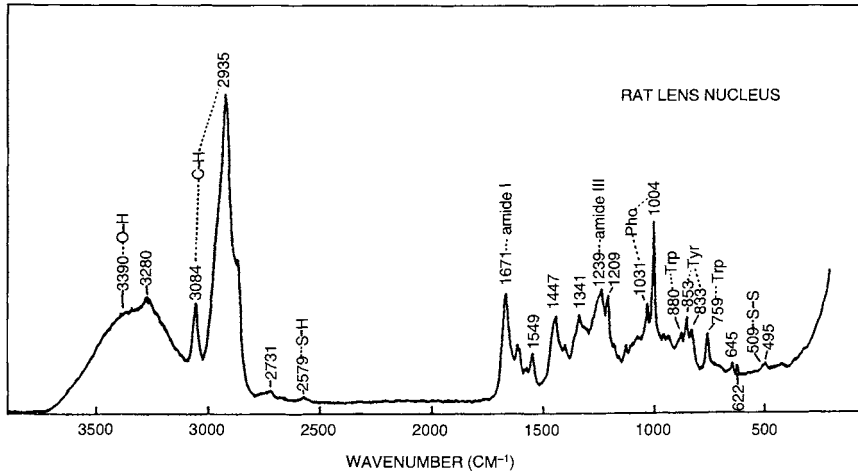


Figure 6-23 Raman spectrum of a SD-strain rat lens nucleus (5 months old). 488 nm excitation, 120 mW. (Reproduced with permission from Ref. 36.)

Raman spectrum and band assignments of a rat lens nucleus. It was found that relative intensities of $\nu(\text{OH})$ (lens water) at $3,390\text{ cm}^{-1}$ and $\nu(\text{SH})$ (lens protein) at $2,579\text{ cm}^{-1}$ decrease markedly during the first four months of aging, and that these changes are parallel to the intensity decrease in the

tryptophan (Trp) band at 880 cm^{-1} and the intensity increase in the $\nu(\text{S}-\text{S})$ band at 510 cm^{-1} . These observations suggest that the aging process involves lens dehydration and the $2\text{SH} \rightarrow \text{S}-\text{S}$ conversion caused by an environmental change of the Trp residue (37).

In contrast to aging, lens opacification (cataract formation) is characterized by (1) the intensity increase of the $\nu(\text{OH})$ at $3,390\text{ cm}^{-1}$, and (2) the change in relative intensity of the tyrosine (Tyr) doublet near 840 cm^{-1} . (1) is a better marker of opacification because the change is larger and observable even in precataractous stage (38).

Figure 6-24 shows the fluorescence and Raman spectra of a human lens of 14 years of age obtained by Yu *et al.* (39, 40). It is seen that fluorescence dominates the spectra when the exciting wavelength is shorter than 514.5 nm , while Raman bands are observed when it is longer than 514.5 nm . Thus, 514.5 nm is regarded as the critical wavelength (λ_c) of this particular lens. The λ_c of a normal lens increases with age; the λ_c is near 680 nm for a normal lens of a 78-year-old human. A plot of λ_c vs. age for normal lens has been obtained using 11 normal lenses. Any deviation of λ_c from such a plot may be regarded as a sign of deterioration of a lens.

To circumvent the preceding fluorescence problem, Nie *et al.* (41) measured the Raman spectra of human lenses by using near-IR ($1,064\text{-nm excitation}$) FT-Raman spectroscopy. Their results show that the tryptophan bands at 880 and 760 cm^{-1} show significant decreases in intensity with aging, whereas the phenylalanine band at $1,004\text{ cm}^{-1}$ and the tyrosine bands at $1,208$, 851 , and 830 cm^{-1} remain unchanged. Since the former bands originate in the five-membered ring of tryptophan, these workers concluded that the opening of its five-membered ring progresses with aging. However, the six-membered ring of tryptophan is unaffected because the band near $1,550\text{ cm}^{-1}$ that is due to the six-membered ring does not show any intensity decrease on aging. These authors also noted that tryptophan concentration remains essentially unchanged during the ages of 20 to 60 years, but its decrease is accelerated during the ages of 60 to 70 years.

6.2.3 GALLSTONES

Gallstones show complicated microstructures that reflect the history of their formation. Ishida *et al.* (42) studied the microstructures of a cholesterol-bilirubin gallstone by using the MOLE and FT-IR spectroscopy. Figure 6-25 is a micrograph showing its layered structure. The compositions at the six points indicated were determined by comparing the spectra obtained from each point with those of pure compounds. For example, Fig. 6-26 shows the Raman spectra of the yellow (point c) and brown (point d) located in the midlayer ($514.5\text{-nm excitation}$, $\sim 50^\circ\text{C}$). These spectra are dominated by

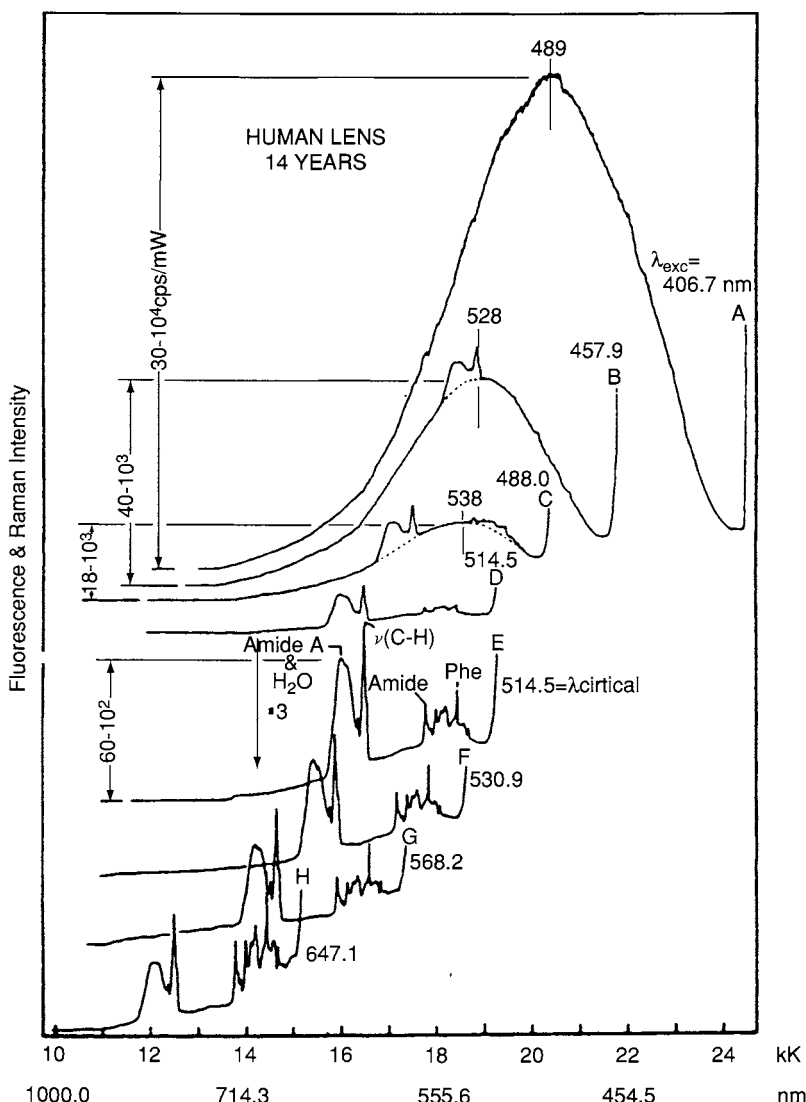


Figure 6-24 Fluorescence and Raman spectra of a 14-year-old human lens (nucleus center) obtained with excitation at various wavelengths indicated. (Reproduced with permission from Refs. 39, 40. Copyright © 1987 John Wiley & Sons, Ltd.)

bilirubin vibrations due to RR effect, although cholesterol bands are seen at $1,680$ and $1,450\text{ cm}^{-1}$ ($\nu(\text{C}=\text{C})$ and $\delta(\text{CH}_2)$, respectively). Table 6-1 summarizes the results of their microanalysis determined by using a combination of MOLE, FT-IR, and EPMA (electron probe x-ray microanalysis).

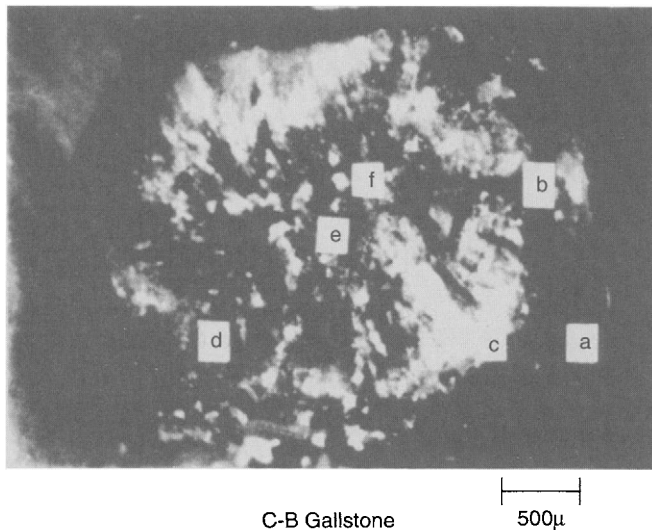


Figure 6-25 Optical micrograph of a cholesterol–bilirubin gallstone. (Reproduced with permission from Ref. 42.)

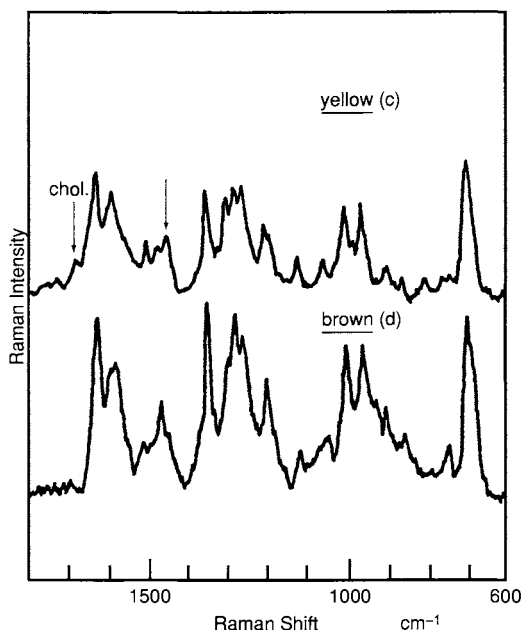


Figure 6-26 Raman spectra of the yellow (c) and brown areas located in the midlayer of a cholesterol–bilirubin gallstone. The Raman bands indicated by arrows correspond to those of cholesterol. (Reproduced with permission from Ref. 42.)

Table 6-1 Microstructure of Cholesterol–Bilirubin Gallstone Characterized by EPMA, MOLE, and FT-IR

Microstructure		Notation ^a	Inorganic elements (EPMA)	Chemical structures (MOLE and FT-IR)
Location	Color			
Outer layer	Light yellow	a	Not detected	Cholesterol
	Light brown	b	Not detected	Cholesterol
	Yellow	c	Ca, P	$\text{Ca}_3(\text{PO}_4)_2$, cholesterol–bilirubin (salt and acid forms)
Midlayer	Brown	d	Ca, P	$\text{Ca}_3(\text{PO}_4)_2$, cholesterol–bilirubin (salt and acid forms)
	Brown	e	Ca	Bilirubin (salt and acid forms)
	White particle	f	Ca	Ca salt of fatty acid (Ca palmitate)

^aThe alphabetical notations correspond to those indicated in the microscopic image in Fig. 6-25.

6.2.4 MEDICAL DIAGNOSIS

Raman spectroscopy can be used to distinguish nonmalignant and malignant tissues taken from breast, colon, liver, and other parts of human body. For example, Nithipatikom *et al.* (43) compared the Raman spectra (632.8-nm excitation) of normal, cirrhotic (benign), and malignant liver tissues using confocal Raman microscopy. The spectra shown in Fig. 6-27 were obtained as the averages of spectra collected from 10–15 different spots, each spot being $\sim 2\mu\text{m}$ in diameter ($\sim 6\text{-}\mu\text{m}$ -thick tissue), normalized to the $1,450\text{-cm}^{-1}$ band. Red blood cells (RBCs) are often a troublesome component in tissue detection because they are one of the major contributors to Raman spectra. In fact, the bands at $1,578$ (not shown) and $1,253\text{ cm}^{-1}$ are largely due to

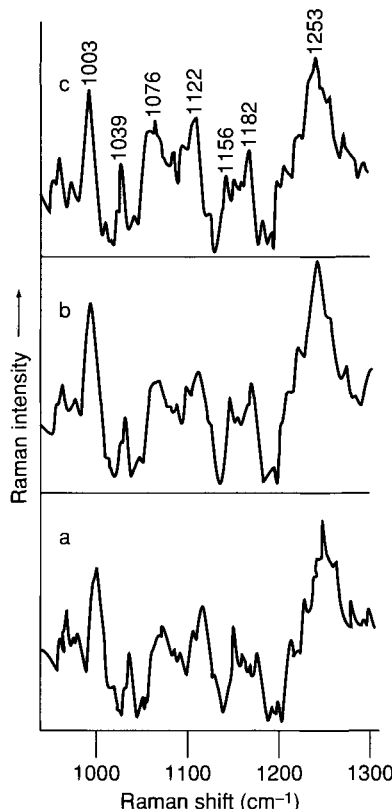


Figure 6-27 Raman spectra of (a) normal, (b) cirrhotic (benign), and (c) malignant liver tissues in the 900 to $1,300\text{-cm}^{-1}$ region. The spectra in the $2,800$ to $3,200\text{-cm}^{-1}$ region were identical in each case. Average of (a) 10, (b) 13, and (c) 10 fifteen-minute acquisitions at different points on the sample tissue. The background was subtracted, and the spectra are normalized to the $1,450\text{-cm}^{-1}$ band. (Reproduced with permission from Ref. 43.)

RBCs. Thus the variation in the $1,253/1,578\text{-cm}^{-1}$ ratio indicates varying contributions of RBCs among the three samples. The band at $1,122\text{ cm}^{-1}$ is also due to RBCs. These RBC vibrations may appear as a result of preresonance enhancement of heme protein vibrations due to proximity of the exciting line to heme absorption bands.

In Table 6-2, peak intensities of the three types of tissues are compared. It is seen that the intensities at $1,039$ and $1,076\text{ cm}^{-1}$ increase in going from normal to cirrhotic to cancerous tissues. The same trend is seen in the intensity ratio of the $1,182/1,156\text{-cm}^{-1}$ bands. Since RBC contributions to these two bands are similar, this ratio can also be used for cancer diagnosis. The increased intensity of the $1,182\text{-cm}^{-1}$ band may indicate an increase in production of α -fetoprotein, which is a specific antigen for hepatoma and embryonal carcinoma. The band at $1,039\text{ cm}^{-1}$ may be due to the phenylalanine residue. Finally, the band at $1,076\text{ cm}^{-1}$ is due to the symmetric PO_2 vibration of the DNA backbone (Section 4.1.2), and its increase in Raman intensity indicates an increase in the DNA concentration in cancer tissues.

As another example, Richards-Kortum *et al.* (44) measured the UVRR spectra (257-nm excitation) of normal and malignant breast and cervical cells. This exciting line was chosen to selectively resonance-enhanced vibrations due to nucleic acids and proteins containing aromatic amino acids such as tyrosine (Tyr) and tryptophan (Trp). Figure 6-28 compares the UVRR spectra of normal and malignant breast cells, which are normalized to the $1,480\text{-cm}^{-1}$ band of the nucleotide. It is seen that the normal cell spectrum is more intense than the malignant cell spectrum in the $1,700$ to $1,500\text{cm}^{-1}$ and $1,440$ to $1,330\text{-cm}^{-1}$ ranges. On the other hand, the opposite trend is seen near the $1,330\text{-cm}^{-1}$ band. More precisely, the intensity ratios of the $1,480$ (nucleotide)/ $1,614$ (protein), $1,480$ (nucleotide)/ $1,540$ (protein), and $1,330$ (uracil in RNA)/ $1,480$ (nucleotide) cm^{-1} always increase on malignancy. These trends hold both for breast and cervical cells. The nucleic acid to

Table 6-2 Raman Intensities and Intensity Ratios in Liver Tissues^a

Frequency (cm^{-1})	Normal	Cirrhosis	Cancer
1,039	1,070	1,130	1,300
1,076	1,480	1,660	1,930
1,578 ^b	2,610	3,200	2,810
$1,253/1,578^c$	1.12	1.05	1.00
$1,182/1,156^d$	0.73	1.16	1.30

^aPeak intensities after subtracting a common baseline and normalizing to the $1,450\text{-cm}^{-1}$ band.

^bPrimary RBC band, useful as intensity reference for RBC contribution to other bands.

^cIntensity ratio accounts for varying RBC contribution between samples.

^dThe $1,156$ and $1,182\text{-cm}^{-1}$ bands are equally affected by RBC contributions and are compared directly for visualization purposes.

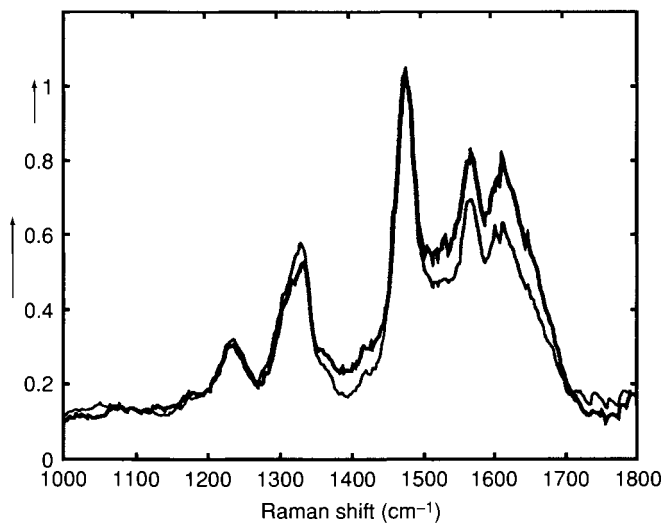


Figure 6-28 UVRR spectra of normal (thick line) and malignant (thin line) breast cells. The spectra are normalized to the nucleotide peak at $1,480\text{ cm}^{-1}$. (Reproduced with permission from Ref. 44.)

protein ratio is known to increase in malignant cells (45). The intensity ratio of $1,330/1,480\text{ cm}^{-1}$ is sensitive to changes in nucleotide base stacking. However, the relationship between the changes in this ratio and changes in nucleotides associated with malignancy is not clear.

In the preceding two examples, Raman spectra were obtained from tissues and cell samples *ex vivo*. Recently, Buschman *et al.* (46) were able to measure Raman spectra of sheep arterial walls *in vivo* using a miniature fiberoptic probe. They have demonstrated that the *in vivo* intravascular Raman signal obtained directly from a blood vessel is a simple summation of signals from the blood vessel wall and blood itself. This technique may be useful in predicting the risk of arterial plaque rapture and determining plaque composition in human arteries.

References

1. For example, see T. G. Spiro, "The resonance Raman spectroscopy of metalloporphyrins and heme proteins," in "Iron Porphyrins" (A. B. P. Lever and H. B. Gray, eds.), Part II. Addison-Wesley, Reading, MA, 1983.
2. T. G. Spiro and T. C. Strekas, *J. Am. Chem. Soc.* **96**, 338 (1974).
3. K. Nakamoto, *Coord. Chem. Rev.* **100**, 363 (1990).
4. L. Duff, E. H. Appleman, D. F. Shriner, and I. M. Klotz, *Biochem. Biophys. Res. Commun.* **90**, 1098 (1979).

5. T. Kitagawa, M. R. Ondrias, D. L. Rousseau, M. Ikeda-Saito, and T. Yonetani, *Nature* **298**, 869 (1982).
6. T. Kitagawa, K. Nagai, and M. Tsubaki, *FEBS Lett.* **104**, 376 (1979).
7. K. Nagai, T. Kagimoto, A. Hayashi, F. Taketa, and T. Kitagawa, *Biochemistry* **22**, 1305 (1983).
8. J. Terner, J. D. Stong, T. G. Spiro, M. Nagumo, M. Nicol, and M. A. El-Sayed, *Proc. Natl. Acad. Sci. USA* **78**, 1313 (1981).
9. L. S. Alexander and H. M. Goff, *J. Chem. Educ.* **59**, 179 (1982).
10. P. M. Champion, B. R. Stallard, G. C. Wagner, and I. C. Gunsalus, *J. Am. Chem. Soc.* **104**, 5469 (1982).
11. Y. Ozaki, T. Kitagawa, Y. Kyogoku, Y. Imai, C. Hashimoto-Yutsudo, and R. Sato, *Biochemistry* **17**, 5826 (1978).
12. O. Bangcharoenpauppong, A. K. Rigos, and P. M. Champion, *J. Biol. Chem.* **261**, 8089 (1986).
13. S. Hashimoto, Y. Tatsuno, and T. Kitagawa, *Proc. Japan Acad.* **60B**, 345 (1984); *Proc. Natl. Acad. Sci. USA* **83**, 2417 (1986).
14. J. Terner, A. J. Sitter, and M. Reczek, *Biochim. Biophys. Acta* **828**, 73 (1985); *J. Biol. Chem.* **260**, 7515 (1985).
15. T. Kitagawa, "Resonance Raman spectra of reaction intermediates of heme enzymes," in "Advances in Spectroscopy" (R. J. H. Clark and R. E. Hester, eds.), Vol. 13. John Wiley, New York, 1986.
16. D. M. Kurtz, Jr., D. F. Shriver, and I. M. Klotz, *Coord. Chem. Rev.* **24**, 145 (1977).
17. D. M. Kurtz, Jr., D. F. Shriver, and I. M. Klotz, *J. Am. Chem. Soc.* **98**, 5033 (1976).
18. R. E. Stenkamp, L. C. Sieker, L. H. Jensen, J. D. McCallum, and J. Sanders-Loehr, *Proc. Natl. Acad. Sci. USA* **82**, 713 (1985).
19. A. K. Shiemke, T. M. Loehr, and J. Sanders-Loehr, *J. Am. Chem. Soc.* **108**, 2437 (1986).
20. W. H. Woodruff, R. B. Dyer, and J. R. Schoonover, "Resonance Raman spectroscopy of blue copper proteins," in "Biological Applications of Raman Spectroscopy" (T. G. Spiro, ed.), Vol. 3. John Wiley, New York, 1988.
21. T. B. Freedman, J. Sanders-Loehr, and T. M. Loehr, *J. Am. Chem. Soc.* **98**, 2809 (1976).
22. T. J. Thamann, J. Sanders-Loehr, and T. M. Loehr, *J. Am. Chem. Soc.* **99**, 4187 (1977).
23. J. A. Larabee and T. G. Spiro, *J. Am. Chem. Soc.* **102**, 4217 (1980).
24. J. Ling, K. D. Sharma, J. Sanders-Loehr, T. M. Loehr, R. S. Czernuszewicz, R. Fraczkiewicz, L. Nestor, and T. G. Spiro, to be published.
25. Y. Nonaka, M. Tsuboi, and K. Nakamoto, *J. Raman Spectrosc.* **21**, 133 (1990).
26. D. S. Lu, Y. Nonaka, M. Tsuboi, and K. Nakamoto, *J. Raman Spectrosc.* **21**, 321 (1990).
27. G. D. Strahan, D. S. Lu, M. Tsuboi, and K. Nakamoto, *J. Phys. Chem.* **96**, 6450 (1992).
28. M. Mansait and T. Theophanides, "Drug-nucleic acid interactions," in "Advances in Infrared and Raman Spectroscopy" (R. J. H. Clark and R. E. Hester, eds.), Vol. 13. John Wiley, 1986.
29. D. Gill, R. G. Kilponen, and L. Rimai, *Nature* **227**, 743 (1970).
30. K. A. Britton, R. A. Dalterio, W. H. Nelson, D. Britt, and J. F. Sperry, *Appl. Spectrosc.* **42**, 782 (1988).
31. K. C. Schuster, I. Reese, E. Urlaub, J. R. Gapes, and B. Lendl, *Anal. Chem.* **72**, 5529 (2000).
32. Y. Ozaki, *Appl. Spectrosc. Rev.* **24**, 259 (1988).
33. Y. Guan, E. N. Lewis, and I. W. Levin, "Biomedical applications of Raman spectroscopy: Tissue differentiation and potential clinical usage," in "Analytical Applications of Raman Spectroscopy" (M. J. Pelletier, ed.), Chap. 7. Blackwell Science, Oxford, England, 1999.
34. D. L. A. de Faria and M. A. de Souza, *J. Raman Spectrosc.* **30**, 169 (1999).
35. A. S. Wilson, H. G. M. Edwards, D. W. Farwell, and R. C. Janaway, *J. Raman Spectrosc.* **30**, 367 (1999).

36. Y. Ozaki and K. Iriyama, "Potential of Raman Spectroscopy in medical science," in "Laser Light Scattering Spectroscopy of Biological Objects" (J. Stepanek, P. Anzenbacher, and B. Sedlacek, eds.). Elsevier, Amsterdam, 1987.
37. Y. Ozaki, A. Mizuno, K. Itoh, M. Yoshiura, T. Iwamoto, and K. Iriyama, *Biochemistry* **22**, 6254 (1983).
38. Y. Ozaki, A. Mizuno, K. Itoh, and K. Iriyama, *Tech. Biol. Med.* **5**, 269 (1984).
39. N.-T. Yu, M. Bando, and J. F. R. Kuck, Jr., *Invest. Ophthalmol. Vis. Sci.* **26**, 97 (1985).
40. N.-T. Yu, D. C. DeNagel, D. J.-Y. Ho, and J. F. R. Kuck, "Ocular lenses," in "Biological Applications of Raman Spectroscopy" (T. G. Spiro, ed.), Vol. 1, p. 47. John Wiley, New York, 1987.
41. S. Nie, K. L. Bergbauer, J. F. R. Kuck, Jr., and N.-T. Yu, *Exp. Eye Res.* **51**, 619 (1990).
42. H. Ishida, R. Kamoto, S. Uchida, A. Ishitani, Y. Ozaki, K. Iriyama, E. Tsukie, K. Shibata, F. Ishihara, and H. Kameda, *Appl. Spectrosc.* **41**, 407 (1987).
43. S. R. Hawi, W. B. Campbell, A. Kajdacsy-Balla, R. Murphy, F. Adar, and K. Nithipatikom, *Cancer Lett.* **110**, 35 (1996).
44. Y. Yazdi, N. Ramanujam, R. Lotan, M. F. Mitchell, W. Hittelman, and R. Richards-Kortum, *Appl. Spectrosc.* **53**, 82 (1999).
45. J. K. Frost, "Pathologic processes affecting cells from inflammation to cancer" in "Comprehensive Cytopathology" (M. Bibbo, ed.). W. B. Saunders, Philadelphia, 1991.
46. H. P. Buschman, E. T. Marple, M. L. Wach, B. Bennett, T. C. Bakker Schut, H. A. Bruining, A. V. Bruschke, A. van der Laarse, and G. J. Puppels, *Anal. Chem.* **72**, 3771 (2000).

Chapter 7

Industrial, Environmental and Other Applications

7.1 Industrial Applications

Industrial applications of the Raman effect have garnered intense interest since the introduction of FT-Raman instrumentation. Concurrent with FT-Raman instrumentation developments have been the fiber optics improvements and the advent of new detectors. These three factors have synergized and have led to the present interest in Raman spectroscopy. This has brought the Raman effect from the laboratory and into the plant, where *in-situ* measurements are now possible in a number of industrial environments.

7.1.1 SURFACES (COATINGS)

(a) *An Application in the Paint Industry*

It has been advantageous to use the FT-Raman method to study various dynamic processes of interest in the paint industry. One such study was the study of an emulsion polymerization reaction whereby a FT-Raman system actually monitored the process (1).

Polymer latices* are of extreme technological importance in the development of water-borne paint systems. One method for the production of these latices involves emulsion polymerization, which allows careful control of

*The plural of latex, taken from *Webster's Collegiate Dictionary*.

particle size and morphology. Despite the fact that such polymerizations have been conducted for many years, they still are not too well understood. Spectroscopic techniques that can be used to study these reactions are hindered by the presence of water (e.g., infrared). In the case of Raman spectroscopy, the presence of water does not affect the quality of the spectrum.

This study illustrates a particular use of FT-Raman spectroscopy (Section 2.4.2) to monitor an emulsion polymerization of an acrylic/methacrylic copolymer. There are four reaction components to an emulsion polymerization: water-immiscible monomer, water, initiator, and emulsifier. During the reaction process, the monomers become solubilized by the emulsifier. Polymerization reactions were carried using three monomers: BA (butyl acrylate), MMA (methyl methacrylate), and AMA (allyl methacrylate). Figure 7-1 shows the FT-Raman spectra of the pure monomers, with the strong $\nu C=C$ bands highlighted at 1,650 and 1,630 cm^{-1} . The reaction was made at 74°C. As the polymerization proceeded, the disappearance of the $C=C$ vibration could be followed, as illustrated in Fig. 7-2, which shows a plot of the concentration of the $\nu C=C$ bonds in the emulsion with reaction time. After two hours of the monomer feed, 5% of the unreacted double bonds remained. As the

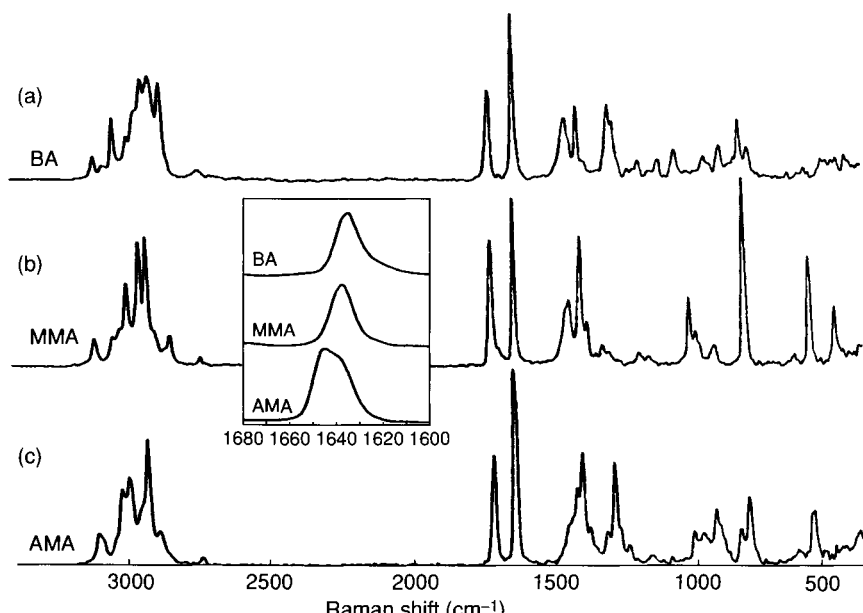


Figure 7-1 FT-Raman spectra of monomers: (a) BA, (b) MMA, (c) AMA (inset shows $C=C$ stretching region). (Reproduced from G. Ellis, M. Claybourne, and S. E. Richards, *Spec. Acta.* 46A, 227, Copyright 1990, with permission from Pergamon Press Ltd., Headington Hill Hall, Oxford OX3 0BW, UK.)

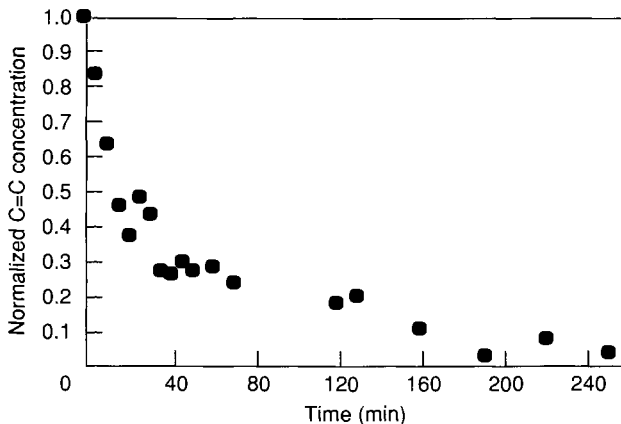


Figure 7-2 Concentration of C=C double bonds in the emulsion with reaction time. (Reproduced from G. Ellis, M. Claybourne, and S. E. Richards, *Spec. Acta.* 46A, 227, Copyright 1990, with permission from Pergamon Press Ltd., Headington Hill Hall, Oxford OX3 OBW, UK.)

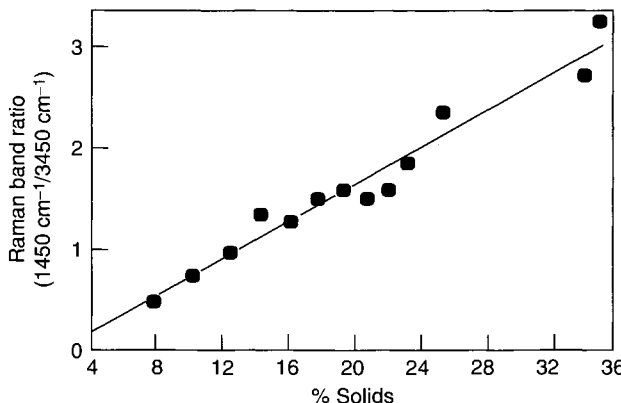


Figure 7-3 Relative Raman intensity of ratios of $1,450/3,450\text{ cm}^{-1}$ bands vs. solids content in the emulsion. (Reproduced from G. Ellis, M. Claybourne, and S. E. Richards, *Spec. Acta.* 46A, 227, Copyright 1990, with permission from Pergamon Press Ltd., Headington Hill Hall, Oxford OX3 OBW, UK.)

polymerization proceeded and the solids content increased, the S/N ratio (measured between the CH_2 deformation band at $1,450\text{ cm}^{-1}$ and the background at $2,500\text{ cm}^{-1}$) of the spectrum improved from 10:1 at 7% solids to 70:1 at 35% solids. Figure 7-3 shows a plot of the ratio of the Raman bands at $1,450$ and $3,450\text{ cm}^{-1}$ vs. the percent solids formed. This application illustrates the feasibility of monitoring a dynamic process by FT-Raman spectroscopy in the paint industry.

7.1.2 FOOD INDUSTRY

Fluorescence problems occurring with conventional Raman spectroscopy precluded the use of this technique in studying food and agricultural substances. However, with the advent of FT-Raman, renewed interest has arisen in these studies.

The study was conducted on a series of lipids such as oils, tallow and butter. Figures 7-4 and 7-5 illustrate Raman spectra of sunflower, corn, sesame, rapeseed and olive oils and peanut, beef tallow and butter, respectively. The study determined that the iodine number of the lipid containing foodstuffs could be estimated by measuring the FT-Raman spectra. The presence of double bonds in the unsaturated fatty acids in lipids provides a method of

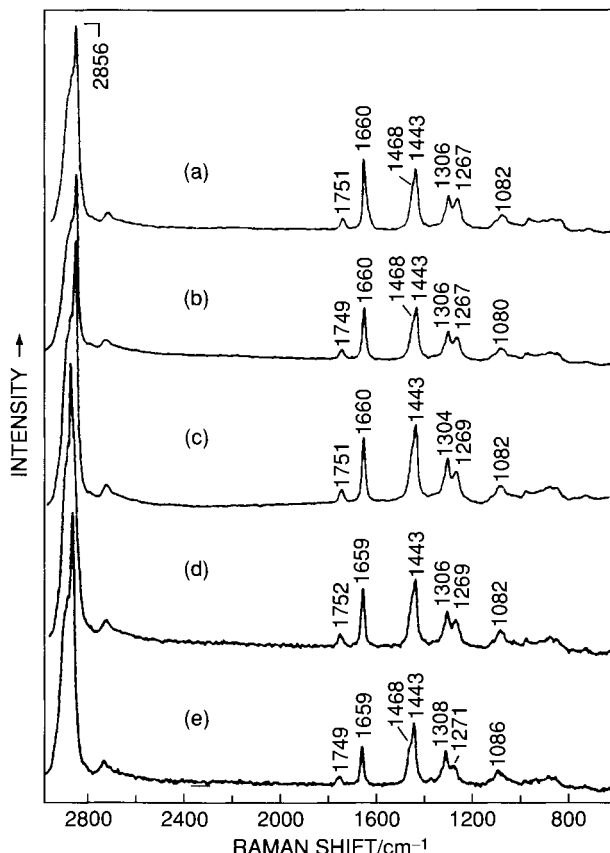


Figure 7-4 MIR FT Raman spectra of (a) sunflower, (b) corn, (c) sesame, (d) rapeseed, and (e) olive oils. (Reproduced from Y. Ozaki, R. Cho, K. Ikegaya, S. Muraishi and K. Kawauchi, *Applied Spectroscopy*, **46**, 1503 (1992), used with permission.)

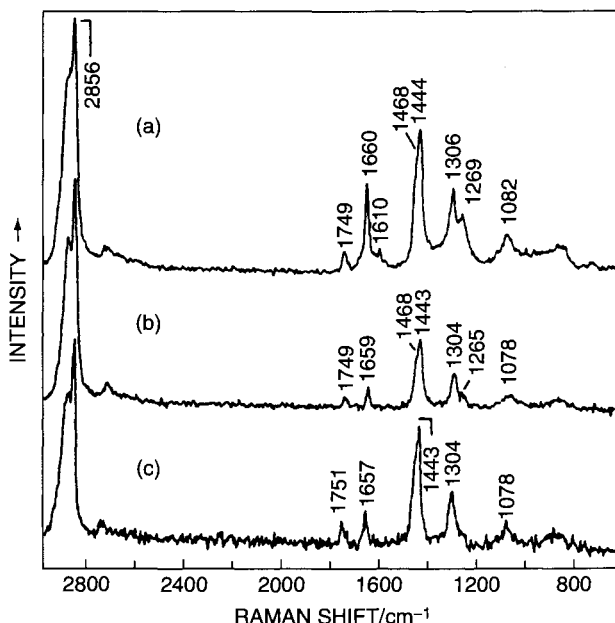
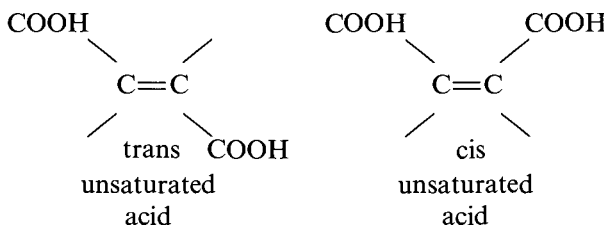


Figure 7-5 MIR FT Raman spectra of (a) peanut, (b) beef tallow, and (c) butter. (Reproduced with permission from Ref. 2.)

determining unsaturation (3). In treatment with iodine, two atoms of iodine are added per double bond of the unsaturated fatty acid. The related molar ratio that is measured with respect to these bonds is known as the iodine number. It indicates the unsaturation level of the fat-containing food products. The higher the iodine value, the greater the unsaturation. In Fig. 7-4, the bands near $1,660$ and $1,443\text{ cm}^{-1}$ are due to the $\nu(\text{C}=\text{C})$ stretching mode of the cis unsaturated fatty acid part, and the CH_2 scissoring mode of the saturated fatty acid part, respectively. The $\nu(\text{C}=\text{C})$ stretching mode of the unsaturated fatty acids is very sensitive to the configuration around the $\text{C}=\text{C}$ bond. For example, the trans unsaturated fatty acid shows the $\nu(\text{C}=\text{C})$ stretching modes in the $1,670$ – $1,680\text{ cm}^{-1}$ range, while the cis configuration shows the mode at $1,650$ – $1,660\text{ cm}^{-1}$.



In Fig. 7-4 the $\nu(\text{C}=\text{C})$ stretch is located at $1,660\text{ cm}^{-1}$, indicating that most of the fatty acids studied are in the cis configuration around the $\nu(\text{C}=\text{C})$ bond. Figure 7-6 plots the iodine number vs. the ratio of the intensities of I_{1658}/I_{1443} . As the iodine number increases the intensity ratio also increases, indicative of increasing cis-type unsaturated fatty acids in the lipids studied. Table 7-1 shows the iodine number and the percentage of fatty acids present in the fats described earlier.

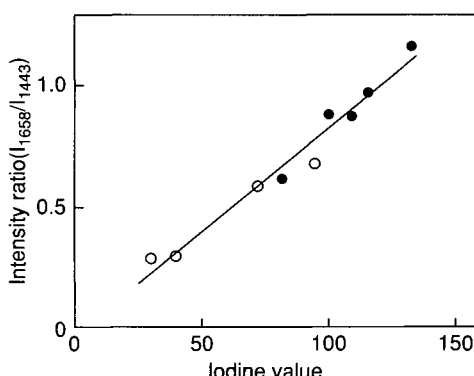


Figure 7-6 Iodine value vs. the intensity ratios of two bands at $1,658$ and $1,443\text{ cm}^{-1}$ (I_{1658}/I_{1443}) for fat-containing foodstuffs investigated. (Reproduced with permission from Ref. 2.)

Table 7-1 Iodine Value (Number) and Percentages of Fatty Acids Constituting Lipids of Foods Investigated

	Iodine Value	Palmitic Acid	Stearic Acid	Oleic Acid	Linoleic ^b Acid	Linolenic ^b Acid
Sunflower oil	136	8%	3%	25%	59%	3%
Corn oil	118	10	6	34	48	1
Sesame oil	111	8	4	40	42	—
Rapeseed oil ^a	102	2	2	15	14	8
Olive oil	83	11	2	74	9	—
Peanut	96	9	5	52	23	—
Yolk	73	11	15	38	33	—
Beef tallow	40	28	24	44	3	—
Butter	31	25	9	33	5	2

^aRapeseed oil contains large amounts of erucine oil ($\text{C}_{21}\text{H}_{41}\text{COOH}$).

^bLinolenic acid has one more $\text{C}=\text{C}$ in its chain than linoleic acid.

7.1.3 DYE INDUSTRY

It has been common knowledge that conventional Raman spectroscopy has failed in attempting to analyze dyes or dyestuffs. Most of the common dyes fluoresce intensely when excited in the visible. However, with the introduction of FT-Raman, the characterization of dyes has improved dramatically. Raman spectra are obtained, which are free of fluorescence and/or resonance effects. One such study involving the investigation of low levels of dyestuffs in acrylic fibers is presented (4).

The acrylic fibers studied are based on an acrylonitrile (94%), methacrylate (6%) copolymer with a diameter of 12-20 microns. The cell used for the measurement is illustrated in Fig. 7-7. Resolution was 3 cm^{-1} , and 50–150 scans were taken. Figure 7-8 shows the Raman spectra of a blue dye fiber, red dye fiber and an undyed methacrylic fiber. The dye vibrations can be readily observed. Figure 7-9 shows the subtraction spectrum (blue dyed fiber minus the undyed fiber). The subtracted spectrum (a) is compared to a blue cobalt dye (b), and the agreement is excellent.

The technique is more diagnostic in terms of detail, because the IR spectra are dominated by intense polymer absorptions, which cannot be eliminated completely by computer subtraction.

The results presented here illustrate that dye spectra may be obtained quickly and yield useful information. Small percentages of dye (1–2%) provide discernible bands. Computer subtraction can be used to remove the excess acrylic polymer bands. Here, also, the use of a micro FT-Raman instrument would be advantageous in lowering the sample size to be investigated.

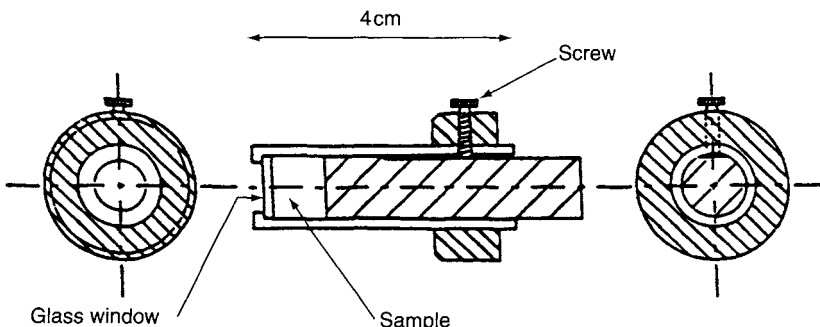


Figure 7-7 Fiber cell used for recording FT Raman spectra of fibers of dyes. (Reproduced from D. Bourgeois and S. P. Church, *Spec. Acta* **46A**, 295, Copyright 1990, with permission from Pergamon Press Ltd., Headington Hill Hall, Oxford OX3 0BW, UK.)

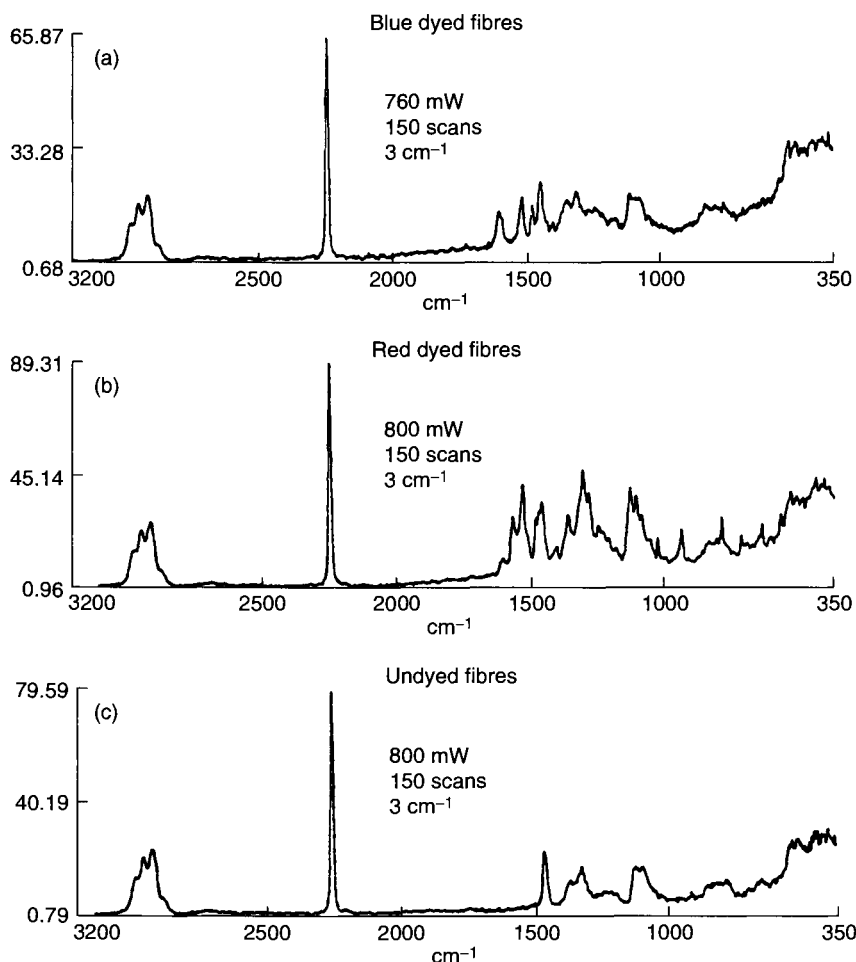


Figure 7-8 FT Raman spectra of acrylic fibers: (a) blue-dyed, (b) red-dyed, (c) undyed. (Reproduced from D. Bourgeois and S. P. Church, *Spec. Acta* **46A**, 295, Copyright 1990, with permission from Pergamon Press Ltd., Headington Hill Hall, Oxford OX3 0BW, UK.)

7.1.4 METAL CORROSION STUDIES

Laser Raman spectroscopy has played a major role in the study of electrochemical systems (see Section 3.4). The technique provides molecular-specific information on the structure of the solid-solution interfaces *in situ* and is particularly suited for spectroelectrochemical studies of corrosion and surface film formation. Metals such as Pb, Ag, Fe, Ni, Co, Cu, Cr, Ti, Au and Sn, stainless steel and other alloys in various solutions have been studied by the technique.

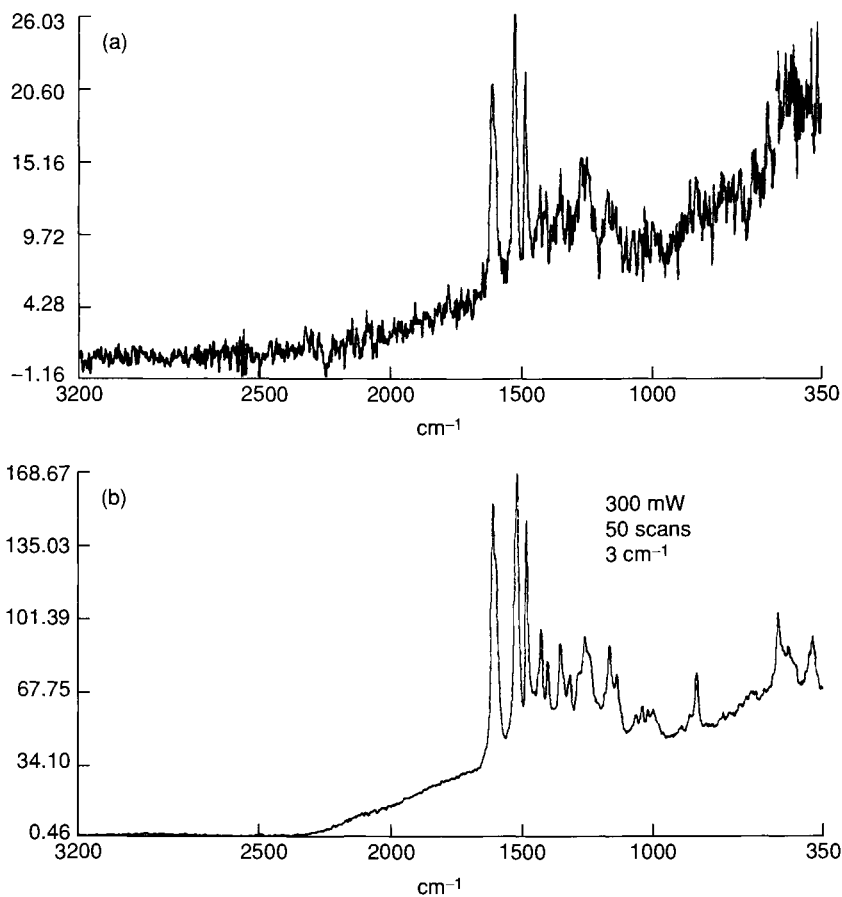


Figure 7-9 (a) FT Raman subtraction spectrum (blue-dyed fibers minus undyed fibers) showing the spectrum of the blue due after removal of acrylic polymer bands. (b) FT Raman spectrum of pure "Blue Cobalt" dye. (Reproduced from D. Bourgeois and S. P. Church, *Spec. Acta* **46A**, 295, Copyright 1990, with permission from Pergamon Press Ltd., Headington Hill Hall, Oxford OX3 OBW, UK.)

A typical experimental layout for this technique is demonstrated in Fig. 7-10 (5). Generally Ar^+ , Kr^+ , and tunable dye lasers (see Section 2.2) are used, although NIR lasers can also be used. Various detectors have been used, such as photomultiplier tubes, diode arrays, silicon photon imaging detectors, and silicon intensified target. We shall describe the study of the corrosion of lead in dilute Na_2SO_4 solutions (6). The interest in lead corrosion is based on a better understanding of the deactivation mechanism in lead-acid batteries as well as simulating metallic corrosion in light water reactors.

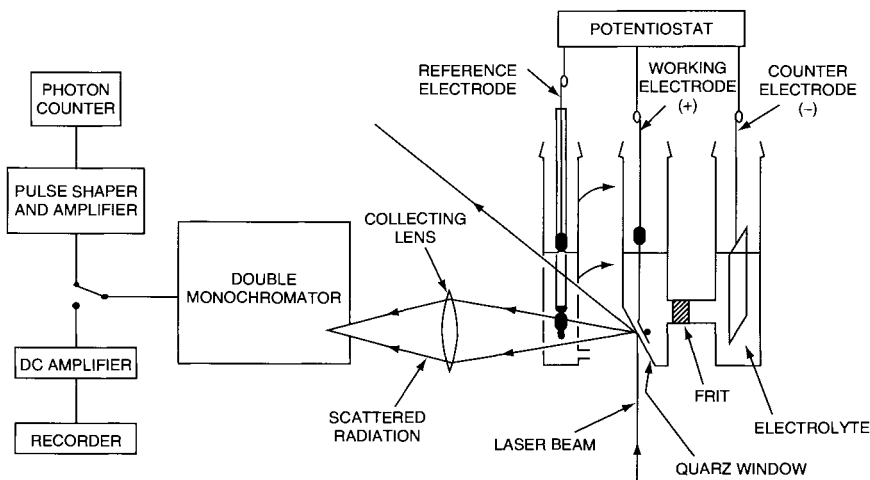


Figure 7-10 Experimental setup for laser Raman spectroelectrochemical studies. (Reprinted from Ref. 5 by permission of Kluwer Academic Publishers.)

In dilute solutions of Na_2SO_4 with an applied anodic potential of -0.85 V , the Raman spectrum was measured. The lead working electrode was made by melting lead shot onto a nickel support under a helium atmosphere, followed by filing to the desired shape and size. The external $\text{Ag}/\text{Ag}_2\text{SO}_4$ reference electrode was connected to the electrolytic cell via a long Teflon tube filled with zirconium oxide sand and saturated $\text{Na}_2\text{SO}_4/\text{Ag}_2\text{SO}_4$ solution. Figure 7-11 shows the temperature dependence of the Raman spectra observed. Bands are observed at 149 and 976 cm^{-1} , consistent with PbO and SO_4^{2-} vibrations, respectively, and the relative intensities were in accordance with an assignment of vibrations of PbO and SO_4^{2-} entities. The two phases were considered to be PbOPbSO_4 and $3\text{PbOPbSO}_4 \cdot \text{H}_2\text{O}$. The spectra persist with an increase in temperature to 553 K . This result agrees with x-ray diffraction data of the surface of the electrode, as well as the interpretation of cyclic voltammograms. At a higher voltage ($-0.1 \text{ vs. Ag/Ag}_2\text{SO}_4$), the spectra observed as a function of temperature gave evidence for PbSO_4 , which was confirmed by x-ray diffraction data. The results for both electrolytic oxidations of lead indicated three phases formed at the surface (PbSO_4 , PbOPbSO_4 , and $3\text{PbOPbSO}_4 \cdot \text{H}_2\text{O}$). Figure 7-12 shows the temperature dependency of the Raman spectra observed for lead in dilute Na_2SO_4 at -0.1 V .

7.1.5 PETROLEUM INDUSTRY

After Sir Raman's discovery of the Raman effect, petroleum scientists attempted to use the technique in order to study components of petroleum

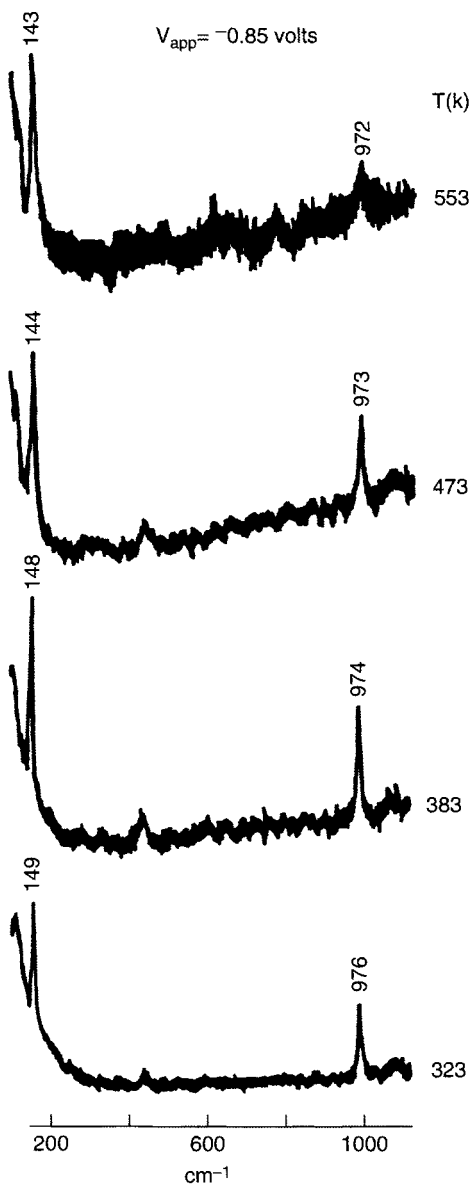


Figure 7-11 Temperature dependence of Raman spectra of lead in dilute solutions of Na_2SO_4 with applied voltage (anodic potential) of -0.85 V . (Reproduced with permission from Ref. 6.)

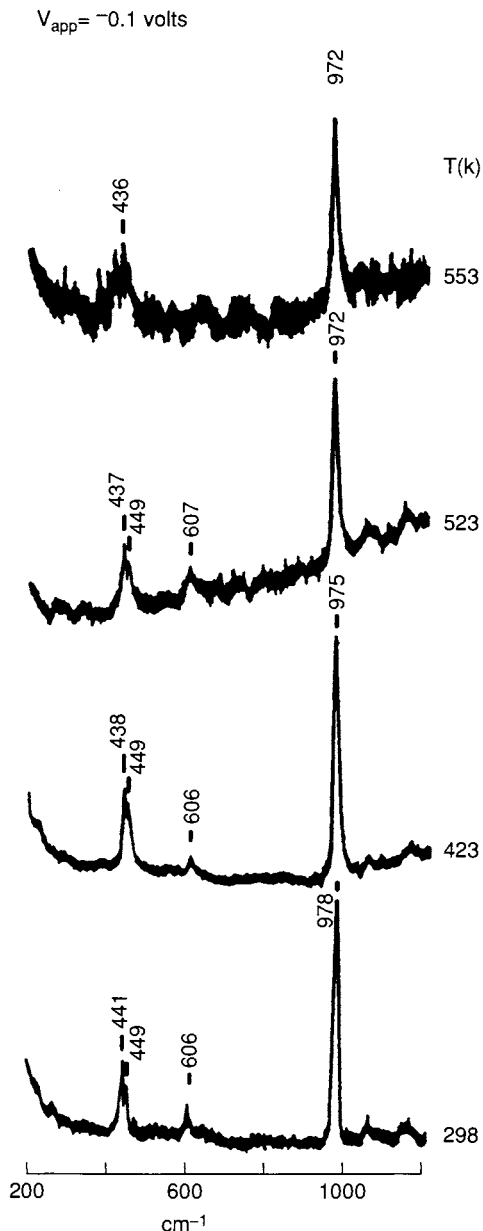


Figure 7-12 Temperature dependence of Raman spectra of lead in dilute solutions of Na_2SO_4 with applied anodic potential of -0.1 V. (Reproduced with permission from Ref. 6.)

products. However, because of fluorescence problems, the interest waned. Today, in view of FT-Raman spectroscopy's (Section 2.4.2) capability to ameliorate fluorescence, renewed interest in the method has been generated. An application for the study of blended gasolines, using FT-Raman spectroscopy, is described below (7).

After the addition of tetraethyllead to gasoline was prohibited, the oil companies were forced to make unleaded gasolines. In order to prevent engine knocking, the car manufacturers lowered the compression ratio of the engine, and oil companies changed the hydrocarbon composition of gasolines to incorporate more branched alkanes and aromatics to increase the octane number. Benzene and toluene were some additives, as well as ethanol in some cases.

It was now necessary to be able to probe the composition of these blended gasolines for the additives present. The vibrational spectroscopies are excellent probes, and both IR and Raman spectroscopies can provide vital information concerning methyl/methylene ratios and identify the additives present in blended gasoline. This application pertains to the use of Raman spectroscopy to probe blended gasolines for additives.

Some of the frequencies that are useful as diagnostics for blended gasolines are listed as follows: For aliphatic groups:

- (1) $2,960\text{--}2,870\text{ cm}^{-1}$, CH stretch in methyl groups;
- (2) $2,925\text{--}2,850\text{ cm}^{-1}$, CH stretch in CH_2 groups;
- (3) $2,890\text{ cm}^{-1}$, CH stretch in CH group.

For aromatic groups:

- (1) $3,080\text{--}3,010\text{ cm}^{-1}$, CH stretch in benzene and derivatives and olefins;
- (2) $1,000\text{ cm}^{-1}$, ring stretching in substituted phenyl rings;
- (3) $825\text{--}680\text{ cm}^{-1}$, bending modes in substituted phenyl rings.

For ethanol:

- (1) 880 cm^{-1} diagnostic for ethanol.

Figure 7-13 shows the FT-Raman spectra of blended gasolines of various octane numbers. It may be observed that as the octane number increases there are increases in the methyl/methylene ratio ($3,053/2,870\text{ cm}^{-1}$) and $1,000/2,870\text{ cm}^{-1}$ ratio, the latter indicative of aromatic additives. Table 7-2 shows the relative intensities of the aromatic bands with the grade of gasoline. The intensities at $3,053$ and $1,000\text{ cm}^{-1}$ increase with octane number. The 780 cm^{-1} band intensity increases, and this is indicative of the substituted phenyl ring (e.g., toluene). The 743 cm^{-1} band increases as well, indicating a *t*-butyl group (iso-octane).

Figure 7-14 illustrates the intensities of the spectra of ethanol and three gasolines with varying octane numbers, all advertised as gasohol containing

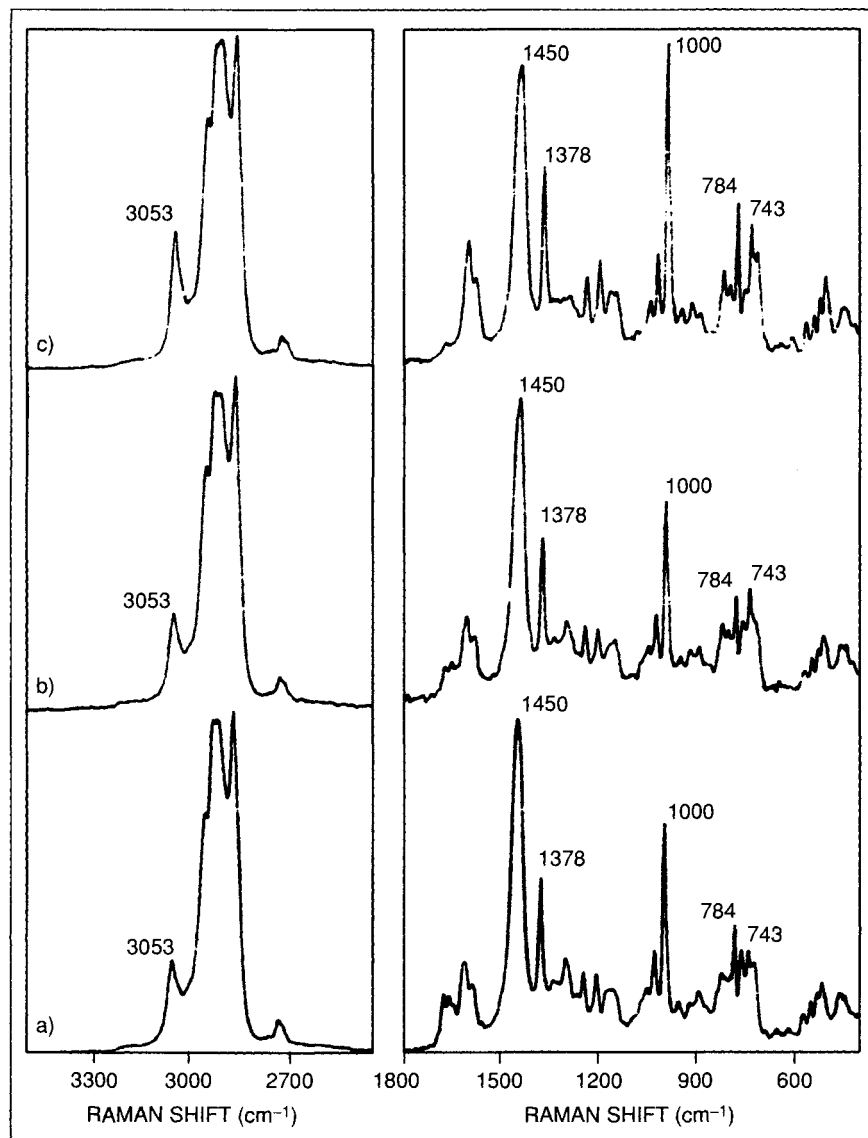


Figure 7-13 FT Raman spectra of blended gasolines: (a) 87 octane, (b) 89 octane, and (c) 93 octane (reproduced with permission, Ref. 7).

Table 7-2 Relative Intensity of Aromatic Bands in FT-Raman Spectra of Gasolines

Gasoline Grade	Octane Number	3,053/ 2,870 cm ⁻¹	1,000/ 2,870 cm ⁻¹
Regular unleaded	Octane 87	0.264	0.158
Intermediate unleaded	Octane 89	0.284	0.161
Premium unleaded	Octane 93	0.387	0.236

10% ethanol. In these spectra a band at 880 cm⁻¹ is diagnostic for alcohol. For the 90% octane gasoline, the 880 cm⁻¹ band is not readily apparent, and it can be presumed that this gasoline is lacking ethanol. Additionally, the concentration of aromatic and branched hydrocarbons is significantly greater in the 90% octane gasoline, as compared to the lower octane gasolines.

It should be noted that IR could provide similar results. However, Raman spectroscopy is more sensitive to the concentration of unsaturated hydrocarbons in the fuels.

For a review on the process control applications of Raman spectroscopy in the petroleum industry, see Ref. 8. For a remote fiber optics study of Raman analysis of xylene, see Ref. 9. It appears that Raman spectroscopy can play an increased role in the petroleum field now that fluorescence is minimized.

7.1.6 METAL REFINING OF ORES

In the metal refining of ores, the metal is solubilized in an aqueous solution. The optical control of metal refining requires quick, accurate analysis of the major chemical species present in solution. Raman spectroscopy and resonance Raman are used to identify the amine complexes of Co, Ni, and Cu species, as well as ammonia sulfate and sulfamate, present in these industrial solutions. The Raman spectra of an industrial plant solution from mine tailings are shown in Fig. 7-15. Each solution contains one or more metal species, sulfate, sulfamate, ammonia, ammonium sulfate, and water. From a comparison with model ammine complexes, the vibrations in the spectra are identifiable. Bands were observed at 615, 980 and 1,110 cm⁻¹ and were assigned to the sulfate ion. No bands were observed for free ammonia. A band at 376 cm⁻¹ was assigned to the $\text{Ni}(\text{NH}_3)_6^{2+}$ specie. A band at 490 cm⁻¹ was assigned to the $\text{Co}(\text{NH}_3)_6^{3+}$ specie.

The results indicate that Raman spectroscopy can be useful in the mining industry. All the major species in metal refining solutions can be identified at concentrations below typical values. A distinct advantage is apparent in studying aqueous solutions of this type using Raman spectroscopy because

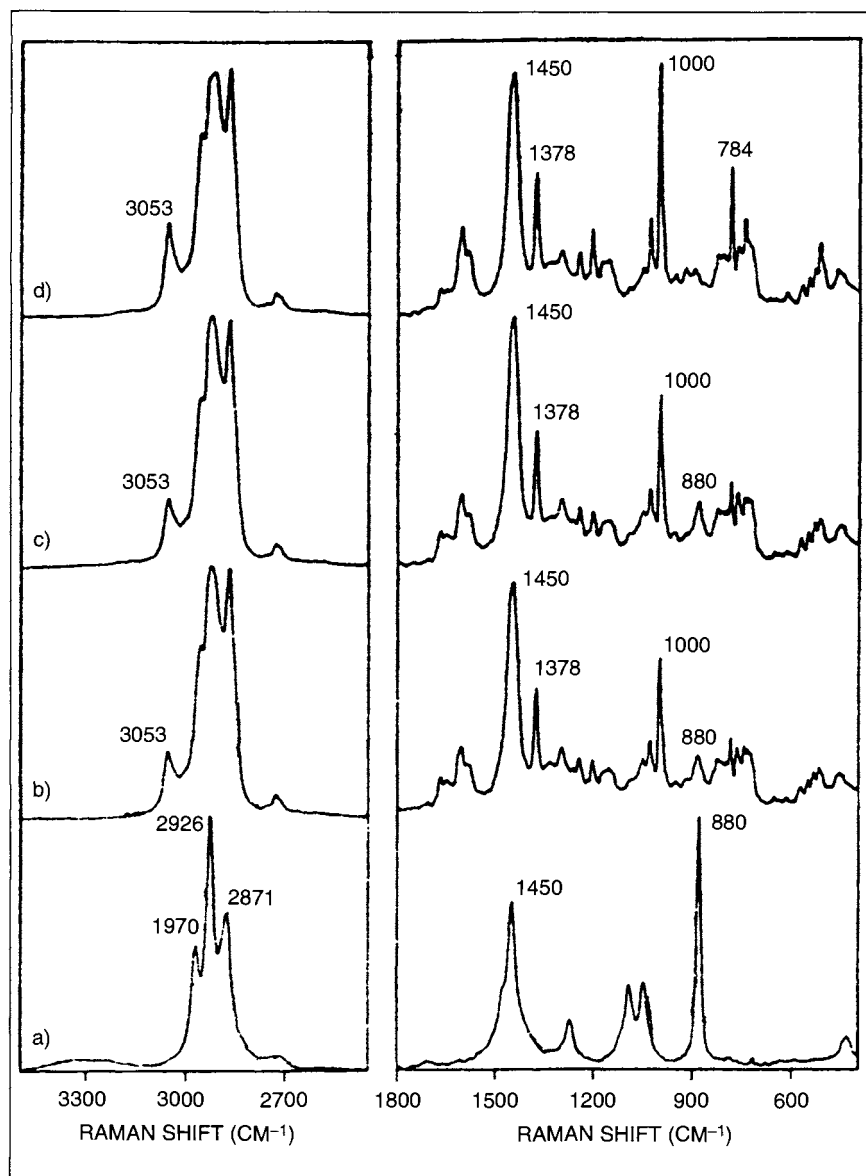


Figure 7-14 FT Raman spectra of (a) ethanol, (b) 87 octane gasohol, (c) 89 octane gasohol, and (d) 90 octane gasohol (reproduced with permission, Ref. 7).

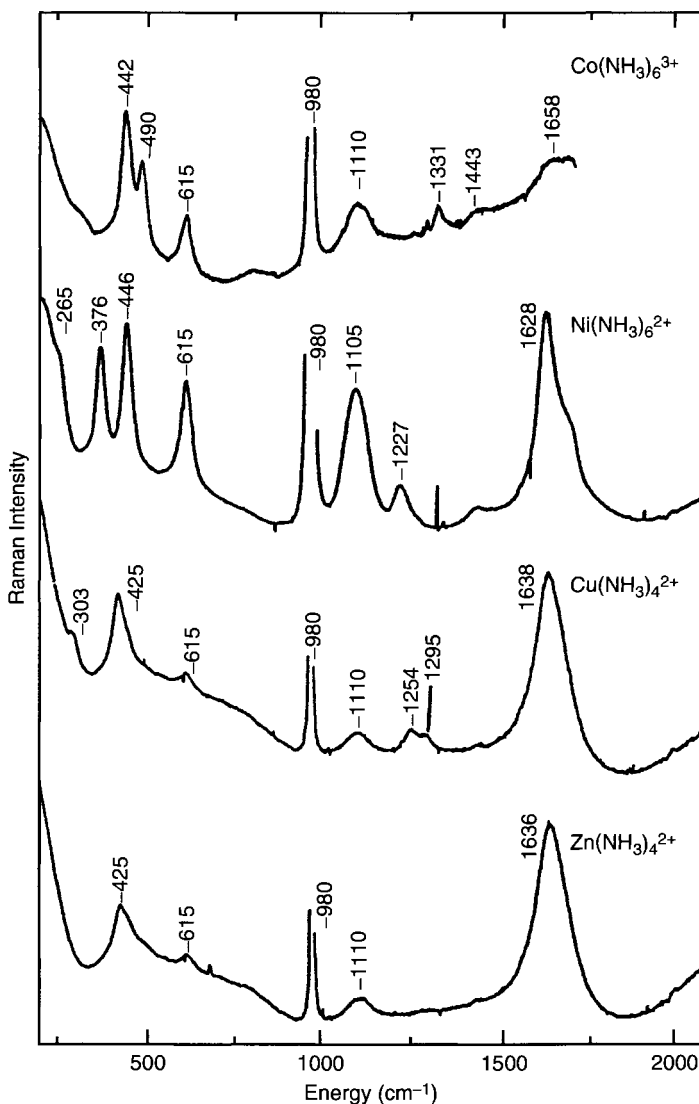


Figure 7-15 Raman spectra of $\text{Co}(\text{NH}_3)_6^{3+}$, $\text{Ni}(\text{NH}_3)_6^{2-}$, $\text{Cu}(\text{NH}_3)_4^{2+}$, and $\text{Zn}(\text{NH}_3)_4^{2+}$ model compounds. Concentrations were 3.5 g Co/liter, 50 g Ni/liter, 5 g Cu/liter, and 5 g Zn/liter, respectively. The Raman spectra were excited with 400 mW of 457.9-nm light for a total accumulation time of 10 min. (Reproduced with permission from Ref. 10.)

water is a weak scatterer compared with infrared where it is a strong absorber and would make identification of the constituents of the solutions difficult.

7.1.7 LUMBER/PAPER INDUSTRY

The use of Raman spectroscopy in the lumber/paper industry has been found to be feasible using the FT-Raman technique. Earlier results using a visible laser were limited due to the laser-induced fluorescence created with most wood samples. Measures to circumvent fluorescence were time-consuming, and the signal-to-noise (S/N) ratio was poor. With most wood samples, using a near-IR laser excitation, fluorescence essentially was eliminated.

A recent study of black spruce using FT-Raman with Nd:YAG laser excitation (1,064 nm) proved successful (11). The goal in these studies was to be able to assign Raman features to the constituents of black spruce, cellulose, lignin, and hemicellulose. Black spruce is a soft wood. Any results obtainable could be applicable to all soft woods, and since soft woods are similar to hardwoods, the Raman bands observed could be assigned to cellulose and lignin. Hemicellulose contributions were not assignable because they were hidden under the cellulose bands.

7.2 Environmental Applications

Several examples where Raman spectroscopy has played an important role in environmental analyses will be presented.

7.2.1 GROUND WATER ANALYSIS

Hazardous materials in trace amounts, such as metallic ions, find their way into the water system. It is necessary to be able to detect these materials *in situ* and in real time. Recently (12), such a method was found involving the SERS technique using optical fibers. The technique monitors the ions in aqueous solutions, measuring the changes in the Raman spectra of indicators, which form complexes with the metallic ions. The indicators used were Eriochrome Black T (EBT), 4-(2-pyridylazo)resorcinol (PAR), cresol red, methyl red and 4-pyridinethiol.

Figure 7-16 illustrates the spectra of EBT- Cu^{2+} , of blank EBT, and the difference spectrum (traces a, b, c, respectively). The intensity of the band at $1,403\text{ cm}^{-1}$ in the difference spectrum corresponds to the Cu^{2+} concentration in solution. The $1,274\text{ cm}^{-1}$ band present in the uncomplexed EBT (trace b) disappears upon complexation. A calibration curve for detection of Cu^{2+}

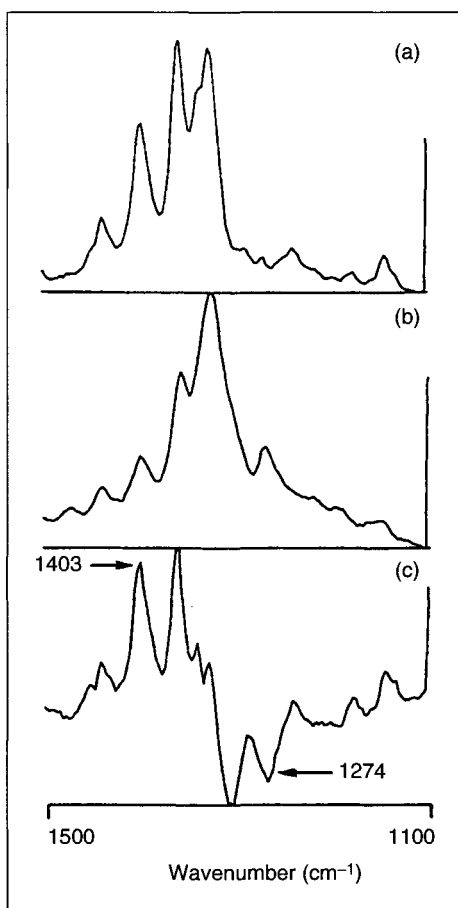


Figure 7-16 SERS spectra of (a) 1.8×10^{-4} M EBT and 1.8×10^{-4} M Cu^{2+} ; (b) 1.8×10^{-4} M EBT only; and (c) the difference spectrum of (a) – (b). (a) and (b) were obtained with 3-s integration times and 20 mW of 531 nm light for resonance excitation of EBT. (Reproduced with permission from Ref. 12.)

with EBT was made by plotting I_{1403}/I_{1274} vs. $\text{pCu}^{2+}(-\log \text{Cu}^{2+})$ concentration. This is illustrated in Fig. 7-17.

Figure 7-18a shows the spectrum of blank PAR. Figure 7-18b shows its spectrum in the presence of Pb^{2+} , and Fig. 7-18c the spectrum in the presence of Fe^{3+} . Similar calibration curves could be formulated. For the Pb^{2+} concentration, plotting of I_{1323}/I_{1005} vs. $\text{pPb}^{2+}(-\log \text{Pb}^{2+})$ can be used for the detection of Pb^{2+} . Likewise, a plot of I_{1329}/I_{1362} vs. pFe^{3+} can be used for

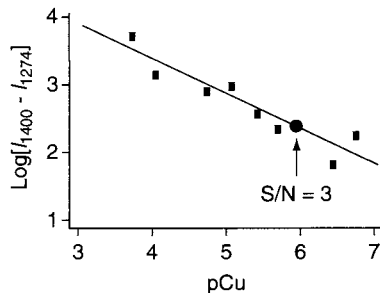


Figure 7-17 Calibration curve for detection of Cu^{2+} with EBT. The detection limit of 85 ppb is illustrated where $S/N = 3$. (Reproduced with permission from Ref. 12.)

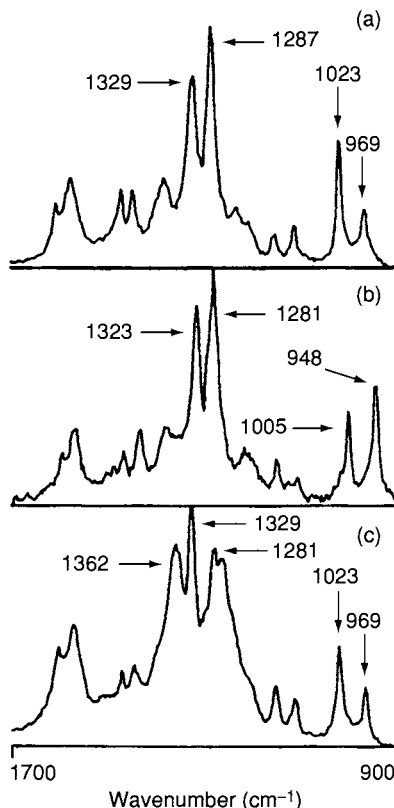


Figure 7-18 SERS spectra of etched silver foil that is coated with anchored thiolate of the indicator PAR disulfide (PARDS) immersed in (a) a blank solution showing PARDS only, (b) in the presence of Pb^{2+} , and (c) in the presence of Fe^{3+} . Spectra were obtained with 5-s integration times and 5 mW of 514.5 nm light for resonance excitation of PARDS. (Reproduced with permission from Ref. 12.)

detection of the Fe^{3+} concentration in ground water by the SERS technique. The technique is particularly effective when used with optical fibers. Silver substrates provide the largest enhancements of the Raman signal, but rapidly degrade in air or water. A method of forming a durable, strongly enhancing SERS surface on silver is to roughen the fiber end followed by depositing a layer of silver, whereby some of degradation of the silver surface is avoided.

7.2.2 FRESH WATER AND SEAWATER ANALYSIS

Trace amounts of the nitrite ion (NO_2^-) are indicative of the extent of pollution and eutrophication. The multitude of methods that can measure nitrite ion concentrations, such as colorimetry, chemiluminescence or fluorimetry, are not capable of detecting subnanomole amounts of nitrite. These also suffer from interference problems. A highly sensitive and selective method for the determination of low concentrations of nitrite in aqueous solutions using surface-enhanced resonance Raman (SERRS) has been developed (13) (see Section 3.3).

The method uses a silver hydrosol active substrate. A charge-coupled device was used as the detector. All measurements were made with a 180° scattering geometry. The 507.1 nm line of an Ar-ion in laser (Spectra-Physics Model 2020) was used for excitation with a laser power of 6–8 mW at a resolution of 2 cm^{-1} . Prior to inducing the SERRS effect, the nitrite was transformed into a colored azo dye.

The dye has an azo form (Fig. 7-19 (1) and (2a)) and a hydrazone form (2b). The hydrazone form is the predominant form. The difference between the azo and hydrazone forms is that the $\text{N}=\text{N}$ bond is associated with the azo forms (1) and (2), and the quinoid ring is associated with the hydrazone form (2b). The SERRS spectra of the azo dye at high, neutral and low pH solutions are shown in Fig. 7-20. Figure 7-21 shows the SERRS spectra compared to the resonance spectra (RR) at pH 2 and 12. The observed Raman bands and the tentative assignments are listed in Table 7-3. In basic solutions the SERRS spectrum of the azo dye looks the same as the RR spectrum (Fig. 7-21). In acidic solutions (Fig. 7-21), they differ, with two new bands at 1,328 and $1,283\text{ cm}^{-1}$ appearing in the SERRS spectrum. For the purpose of quantitative analyses the Raman measurements were made at high pH. The SERRS spectrum (Fig. 7-20) in basic solution has the bands at $1,422\text{ cm}^{-1}$ ($\text{N}=\text{N}$ band) and at 1,328 and $1,383\text{ cm}^{-1}$, which show high selectivity and can be used for analytical purposes. Figure 7-22 shows analytical curves for the azo dye. It may be observed that linear relationships exist between the SERRS intensity and the dye concentration. For purposes of accuracy, an internal standard such as pyridine (10^{-3} M) was added to compensate for changes in excitation energy and for variations in sample positioning and optical

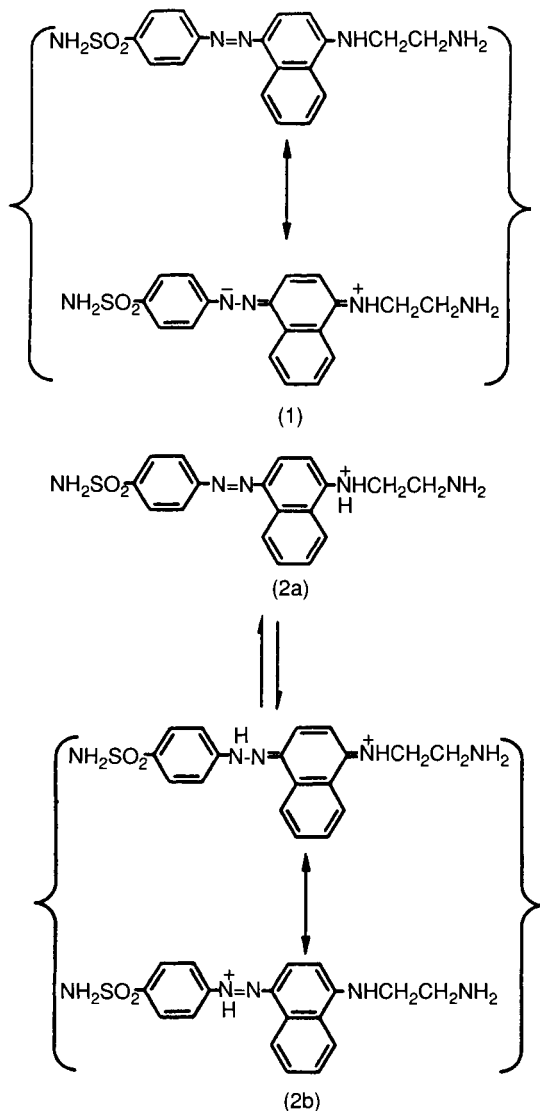


Figure 7-19 Structures of (1) basic and (2) acidic forms of the azo dye.

alignment. Figure 7-23 shows the SERRS spectra of the azo dye in seawater, a was 35 m deep, and b, 500 m deep.

Limits of detection for the nitrite ion are 0.02 nM. Reproducibility of the method is satisfactory. The method is simple, is rapid, and demonstrates advantages over the high-sensitivity laser-induced fluorescent techniques,

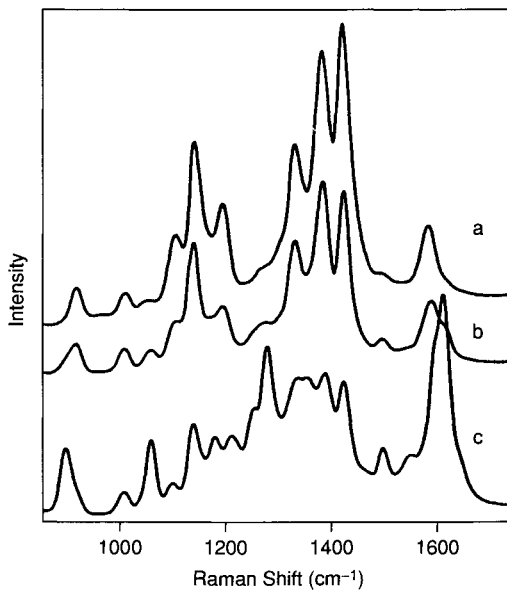


Figure 7-20 SERRS spectra of $1 \mu\text{M}$ azo dye in different pH solutions: (a) pH = 12; (b) pH = 7; (c) pH = 1. (Reproduced with permission from Ref. 13.)

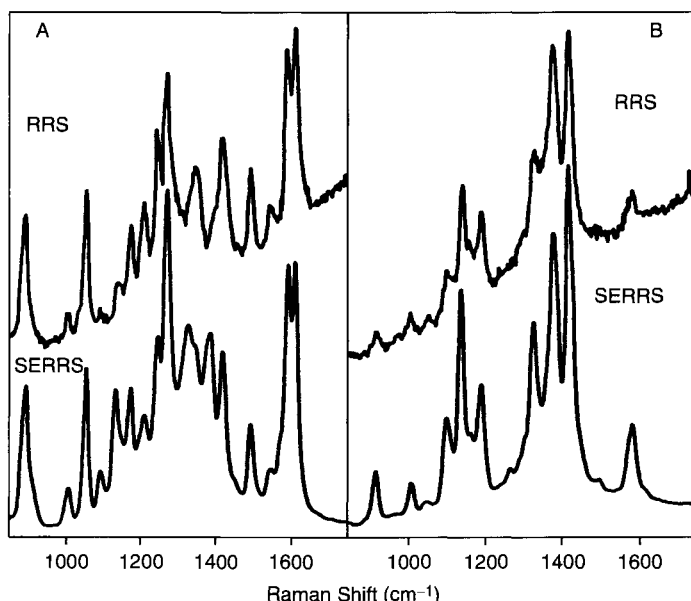


Figure 7-21 Comparison of SERRS spectra and RR spectra of $10 \mu\text{M}$ azo dye in different pH solutions: (a) pH = 2; (b) pH = 12. (Reproduced with permission from Ref. 13.)

Table 7-3 Tentative Assignment of Observed Raman Bands^{a,b}

pH = 2		pH = 12	
1,620 vs	N'-ring C=C stretch		
1,597 vs	S-ring stretch	1,582 m	8a or 8b
1,546 vs	?		
1,496 m	S-ring 19a	1,499 vs 1,450 vvw 1,422 vs	S-ring 19a N'-ring 19b N=N stretch
1,425 sh	C—N' stretch	1,383 vs	S-ring 19b
1,351 sh	N'-ring C—C stretch	1,328 s	Ph—NMe ₂
1,278 s	C—N stretch	1,266 vw	S-ring 14
1,253 s	S-ring Ph—NH—N		
1,214 m	?	1,193 m	9a
1,177 m	S-ring 9a	1,163 vw	9a coupled
1,145 w	C—N stretch	1,142 s 1,101 m 1,006 w	C—N stretch 18b ?
1,062 s	18a or b	915 m	5
897 m	3		

which require low temperatures and more complex sample preparation. The technique demonstrates the usefulness of the SERRS method for trace analysis in fresh water and seawater.

7.2.3 CHARACTERIZATION OF ORGANOPHOSPHORUS PESTICIDES

Pesticide contamination of our fruits and vegetables is a primary concern of many nations of the world. These substances are toxic to human beings, and therefore, some quick and reliable method of analyzing them is necessary. In addition, the method should be noninvasive and not dangerous to the experimentalist. Attention has turned to study of these materials by the Raman technique. Although at first thought one might consider IR spectroscopy to be a reliable technique, the sampling techniques, such as mulling with KBr or CsI, involve grinding of the pesticide, and this could be harmful. Although precautions could be taken by sampling in a glovebox, this would require time.

One such study using Raman spectroscopy to characterize organophosphorus pesticides has been reported (14) and appears to demonstrate

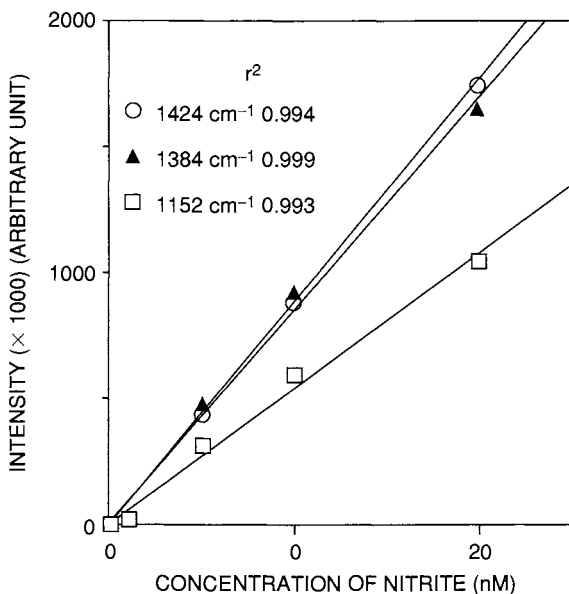


Figure 7-22 Analytical curves of azo dyes. (Reproduced with permission from Ref. 13.)

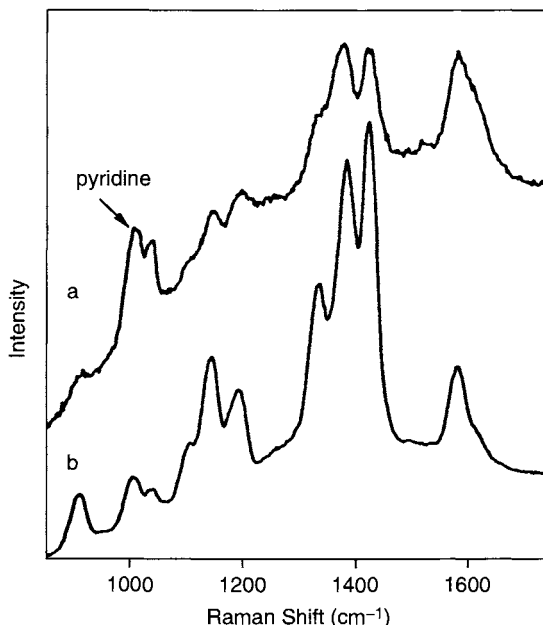


Figure 7-23 SERRS spectra of azo dye in seawater with internal standard (1 mM pyridine) at different depths: (a) 35 m; (b) 500 m. (Reproduced with permission from Ref. 13.)

characteristic functional bands that enable one to distinguish between different pesticides. Table 7-4 lists the six most intense Raman frequencies. Characteristic functional frequencies were identified for the P=S, P=O, P—S, P—(OCH₃)₂, and P(OC₂H₅)₂ groups. No photodecomposition of the pesticides was observed.

7.2.4 FORENSIC ANALYSIS AND ILLICIT DRUGS

Heretofore, Raman spectroscopy has not played a role in forensic science because of the fluorescent problems and the sample alignment, which is time-consuming. As a consequence, the technique was never seriously considered as a routine tool to study forensic materials. However, with the development of FT-Raman spectroscopy, the technique is now being reexamined. One such application in forensic science follows (15).

A FT-Raman spectrometer with excitation from a Nd:YAG laser at 1.064 μm and an GaInAs detector was used to collect the Raman data. The range for the Raman spectra was 400–3,200 cm^{-1} at a resolution of 6 cm^{-1} and 200 mW power.

Figure 7-24 records the Raman spectra of three pure alkaloids (heroin, morphine and codeine) in the 400–1,800 cm^{-1} range. Figure 7-25 shows the spectra of a cut sample of amphetamine sulfate, the cutting agent, sorbitol, the subtraction spectrum, and pure amphetamine sulfate. Subtraction of the cutting agent from the cut sample gives the spectrum of amphetamine sulfate, which agrees with the spectrum of pure amphetamine sulfate. It appears that the technique is well suited for identification of illicit drugs. The technique utilizes small samples with no sample preparation and is non-destructive. The only possible problems that might be encountered are those where the material is contaminated with a highly fluorescent compound (e.g., a fluorescent cutting agent), or a very dark material and a thermally sensitive substance. The effect of a fluorescent cutting agent is illustrated in Fig. 7-26, where fluorescence of the sample makes the identification of the drug virtually impossible. The capability of attaching a microscope to an FT-Raman, which is now commercially available, should make this technique even more attractive (see Section 3.2).

7.3 Other Applications

7.3.1 NATURAL GAS

Natural gas is considered to be one of the cleanest fuels for power plants and potentially for automobiles. The composition of natural gas varies widely depending strongly on its source. A gas sample may contain anywhere from

Table 7-4 Organophosphorus Pesticides and Frequencies of Their Major Raman Bands

OPP ^{**}	Raman spectrum*		IUPAC name
	Wavenumber (cm ⁻¹) of band,		
DDVP	2,859 s, 1,645 s, 1,462 m, 761 s, 661 m, 341 m		2,2-Dichlorovinyl dimethyl phosphate
Phosdrin	2,960 s, 2,928 s, 2858 m, 1,722 m, 1,661 s, 739 m		Methyl 3-(dimethoxy- phosphinyloxy) but-2-enoate
Naled	2,962 s, 2,859 s, 1,455 mw, 764 ms, 351 s, 237 s		1,2-Dibromo-2,2-dichloroethyl dimethyl phosphate
Metasystox-R	2,936 s, 2881 m, 2852 m, 1,253 m, 651 ms, 394 m		S-2-Ethylsulfinyl ethyl O, O- dimethyl phosphorothioate
Methamidophos	3,010 ms, 2,936 s, 2,849 s, 777 ms, 701 s, 564 ms		O,S-Dimethyl phosphoramidothioate
Co-Ral	1,731 ms, 1,616 ms, 1,558 s, 1,347 m, 1,204 s, 646 m		O,O-Diethyl phosphorothioate
Diazinon	3,076 mw, 2,971 ms, 2,927 s, 1,101 m, 991 ms, 554 m		O,O-Diethyl O-2-isopropyl-6- methylpyrimidin-4-yl phosphorothioate
Parathion-methyl	3,080 s, 2958 s, 2,849 m, 1,590 s, 1,350 s, 658 m		O,O-Dimethyl O-4-nitrophenyl phosphorothioate
Guthion	1,674 m, 1,580 m, 1,333 m, 1,309 m, 1,271 ms, 654 s		S-(3,4-Dihydro-4-oxobenzo[d]- [1,2,3]-triazin-3-ylmethyl) O,O-Dimethyl phosphorodithioate
Cygon	2,993 m, 2,948 s, 2,936 s, 1,166 m, 649 s, 497 s		O,O-Dimethyl-S- methylcarbamoylmethyl phosphorodi-thioate
Disyston	2,927 s, 1,282 m, 1,099 m, 752 m, 657 s, 534 bm		O,O-Diethyl S-2-ethylthioethyl phosphorodithioate
Ethion	2,928 s, 1,100 m, 786 m, 662 s, 519 bm, 331 m		O,O,O',O'-Tetraethyl S,S'-methylene bis(phosphorodithioate)
Malathion	2,937 s, 1,736 m, 1,454 ms, 861 m, 655 s, 501 bm		Diethyl (dimethoxyphosphino- thiylthio)succinate
Zolone	3,077 s, 2,972 s, 2,945 s, 1,619 s, 693 ms, 650 s		S-6-Chloro-2, 3-dihydro-2- oxobenzoxazol-3-ylmethyl O,O-diethyl phosphorodithioate

*Note: ms = medium strong; s = strong; m = medium; mw = medium weak; bs = broad shoulder; bm = broad medium.

** OPP = organophosphorus pesticide.

75 to 97% methane, 0.5 to 15% ethane, and 0.2 to 7% propane plus varying fractions of the larger hydrocarbons. At present, the compositions and heat content (expressed as British thermal units, or BTUs) of gas traveling through transmission lines are measured periodically at state boundaries by gas

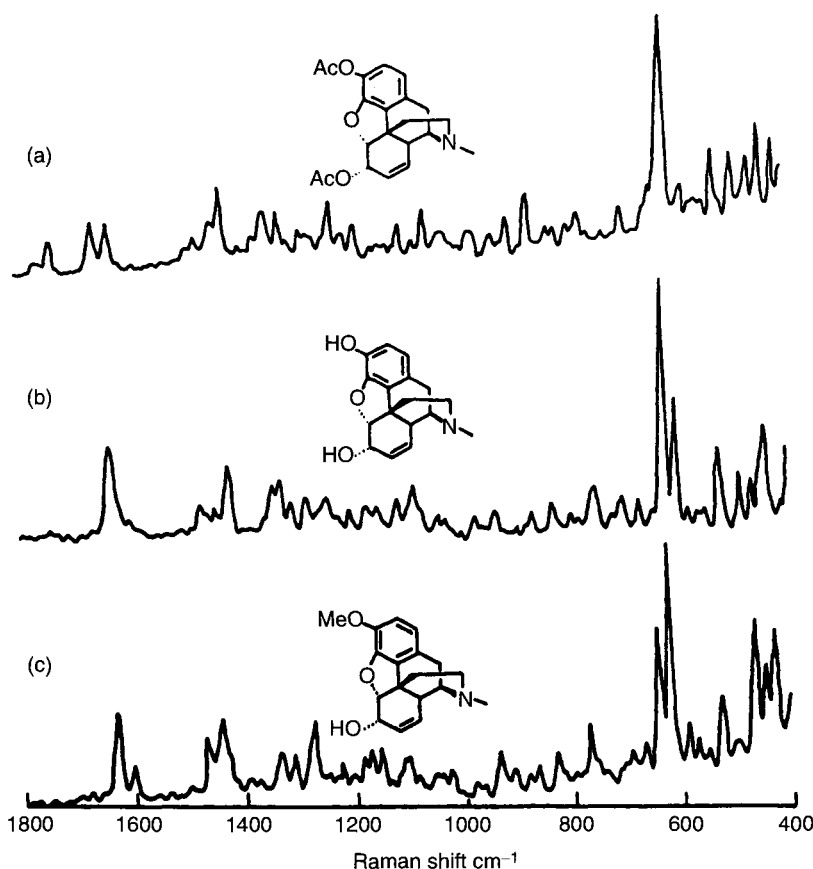


Figure 7-24 FT Raman spectra of pure alkaloids: (a) heroin, (b) morphine, and (c) codeine. 50 scans, 6 cm^{-1} resolution, incident laser power 200 mW. Scanning time 3 minutes. (Reproduced with permission from Ref. 15. Copyright © 1989 John Wiley & Sons, Ltd.)

chromatography. Natural gas for industry and homes is sold by BTU content, but the amount consumed at most locations is measured by a volume-flowmeter. It certainly would be more accurate to measure the BTUs consumed by each user. Moreover, the potential use of natural gas for powering automobiles might well require engines to be adjusted for the BTU content of the gas; thus it will be imperative to measure BTUs of the gas going into the fuel tank.

Spectroscopic methods offer the potential of providing real-time BTU values. BTUs are directly related to the size of the hydrocarbon. Actually, BTU is directly related to the number of CH , CH_2 , and CH_3 groups and CH_4 (methane) in a sample of gas; i.e., it is independent of the structure of the molecule as a whole. In vibrational spectra, the relative intensities of the bands

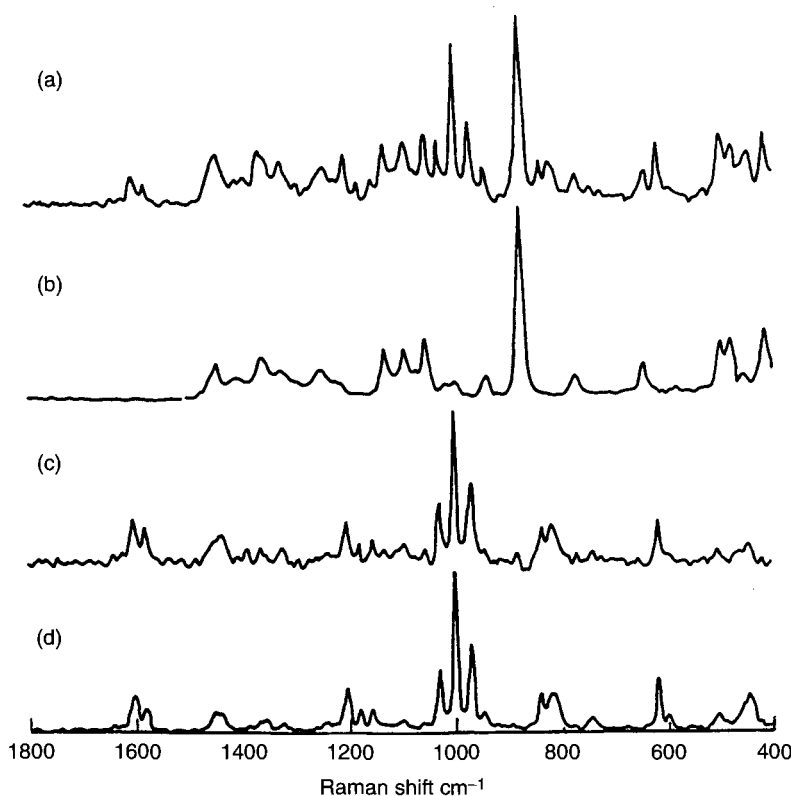


Figure 7-25 FT Raman spectra of (a) 23% amphetamine sulfate in sorbitol, and (b) pure sorbitol. Computer subtraction gives (c) the predicted spectrum of amphetamine sulfate while (d) shows the actual spectrum recorded for a sample of pure amphetamine sulfate. All spectra had 50 scans, 6 cm^{-1} resolution, and 200 mW of incident laser power. Scanning time was 3 minutes. (Reproduced with permission from Ref. 15. Copyright © 1989 John Wiley & Sons, Ltd.)

are proportional to the relative number of chemical groups. In the near-IR spectrum (16), absorbances can be used to predict concentrations and BTUs, and Raman band intensities can be used for the same predictions. In addition to hydrocarbons, natural gas also contains varying amounts of nitrogen. Nitrogen cannot be measured by IR, but it does have a strong Raman band at $\sim 2,330\text{ cm}^{-1}$. Thus it appears that the Raman effect might be ideal for building a BTU monitor.

The possibility of using Raman spectroscopy to monitor BTUs was suggested in 1980 (17). A set of 10 samples containing methane and isobutane in nitrogen were prepared and used to determine the feasibility of using Raman spectra to predict concentrations of the three analytes. The differences between spectrometrically and gravimetrically determined concentrations did

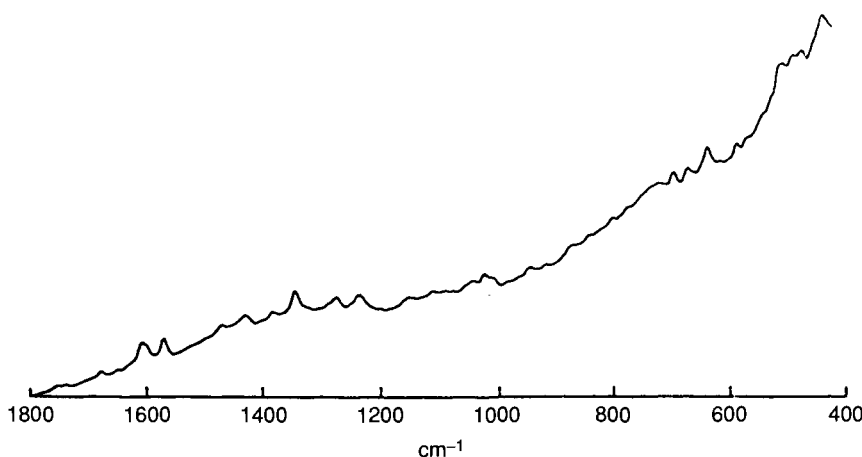


Figure 7-26 Spectrum of cut heroin. (Reproduced with permission from Ref. 15. Copyright © 1989 John Wiley & Sons, Ltd.)

not exceed 0.002 mole fraction using a single frequency for each component. A synthetic natural gas sample was prepared gravimetrically containing nitrogen, methane, ethane, propane, butanes, and pentanes at typical concentrations found in real samples. The Raman spectrum of this sample is shown in Fig. 7-27. Individual bands were observed for all the components except the pentanes, which were present at concentrations of < 0.0025 mole fraction. It could well be that pentanes scatter at wavelengths very similar to those of the butanes, since this is the case for these species in near-IR absorption spectra (16). It still needs to be shown that Raman spectra can be used to predict concentrations and BTUs with the precision and accuracy required by the industry, but this limited study strongly supports this possibility.

7.3.2 PHARMACEUTICALS

One of the main advantages of Raman spectroscopy over IR is that water is a weak Raman scatterer. The spectrum of water causes little interference so that spectra of solutes can be measured in aqueous solutions. A good example of the reduced interference from water is shown for two pharmaceuticals in Fig. 7-28. The Raman spectra of damp and dry samples of acetaminophen and ibuprofen are shown in the figure. Bands due to water are not observed in the spectra. Near and mid-IR of these same samples exhibited relatively strong absorbances due to water. These Raman spectra were measured on a dispersive instrument and were excited with an Ar-ion laser emitting at 488 nm. The background for the acetaminophen sample is flat, whereas ibuprofen exhibits a background characteristic of fluorescence.

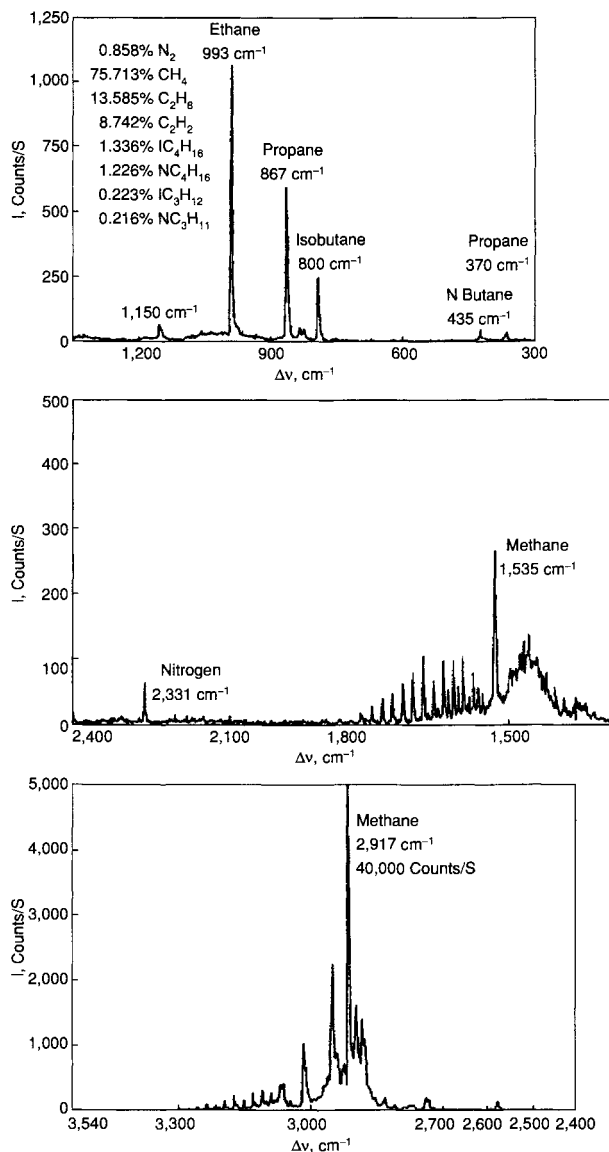


Figure 7-27 Raman spectra of an eight-component synthetic natural gas mixture. (Reproduced with permission from Ref. 17.)

One of the goals of the Food and Drug Administration (FDA) and the pharmaceutical industry is to be able to identify the active ingredients in tablets. It has been shown that the Raman spectra of excipients, gel capsules,

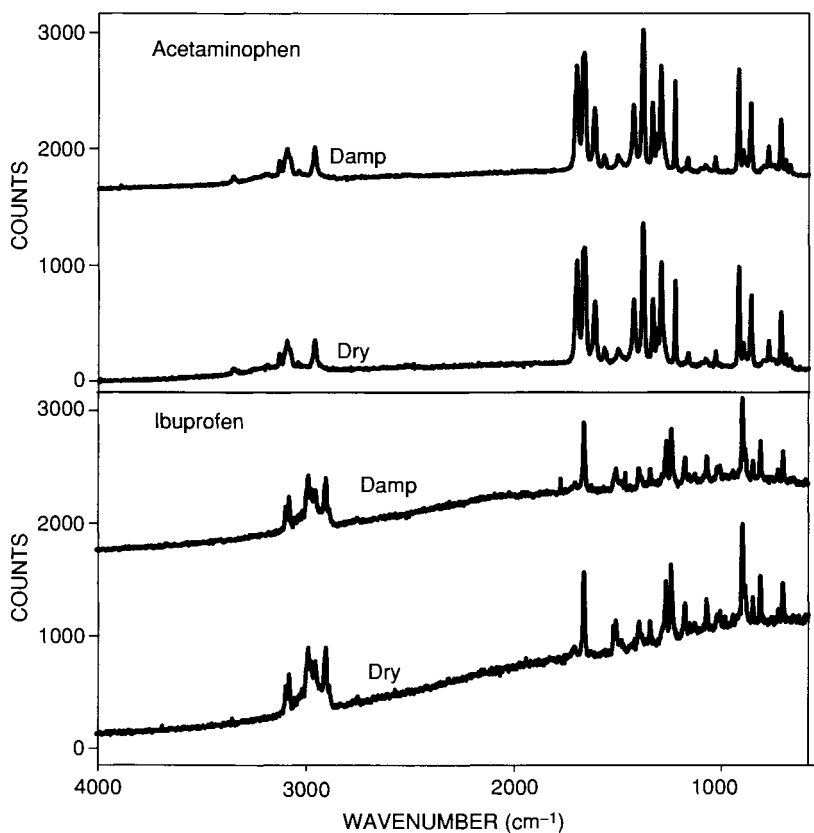


Figure 7-28 Raman spectra of damp and dry acetaminophen and ibuprofen measured with an argon-ion laser exciting at 488 nm.

and blister packs are often weaker than those of the active ingredients (17). The spectra of acetaminophen as a pure powder and in tablet form are shown in Fig. 7-29. The powder spectrum is the same as in Fig. 7-28, which was measured on a dispersive instrument in the visible region. The tablet spectrum was measured on a FT-Raman instrument and was excited with an Nd:YAG laser at 1,064 nm. The spectra compare very well considering that one was measured with a dispersive system on the pure compound and the other was measured with an FT system on a tablet.

Another example comparing spectra for a pure medicinal measured with a dispersive system and spectra of tablets measured on an FT system is shown in Fig. 7-30. As mentioned earlier, the Raman spectrum of ibuprofen measured in the visible region exhibits a fluorescence background. This interference is eliminated by going to the near-IR region for the measurements. In the

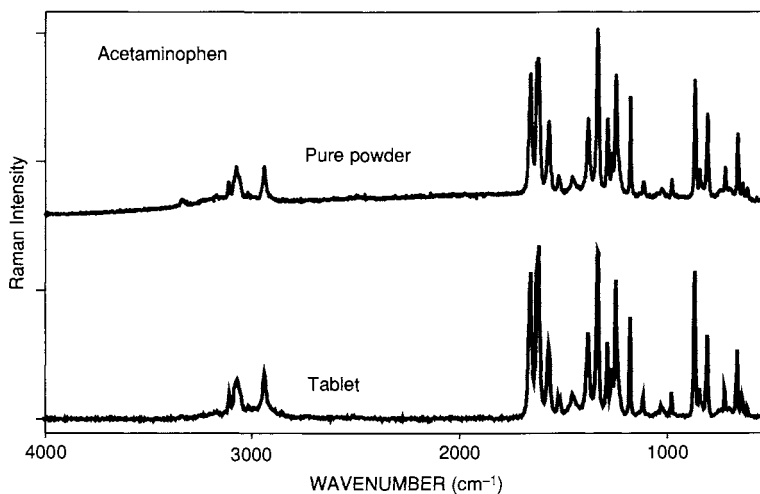


Figure 7-29 Raman spectra of acetaminophen as a pure powder and a tablet. The pure powder spectrum is the same as in Fig. 7-28, whereas the tablet spectrum was measured with an FT-Raman in the near-IR.

In the present case, the spectrum of dry ibuprofen (from Fig. 7-28) was flattened to remove the effects of fluorescence by using a multipoint fit (see Sect. 5.1.5). The spectrum of the white tablet measured on the FT-Raman instrument matches very well with that of the pure compound. The spectrum of the brown tablet has considerable background interference, but the bands still match well. Both the tablets have a medium-sized band at $\sim 1,450\text{ cm}^{-1}$ that is stronger than the band in the pure powder. All the other major bands are very similar, so the tablets can be identified clearly as ibuprofen.

There are numerous other potential uses of Raman spectroscopy in pharmaceutical analyses. One of the more promising areas is in the detection and identification of polymorphic materials (18, 19). Many medicinals exist in several polymorphic forms. The bioavailability of the medicinal may depend on the crystalline form that is present in a tablet. Moreover, a particular medicinal may be patent protected by claiming a certain polymorphic form. Thus, determining the solid-state form of the medicinal can be crucial from the viewpoints of both biological activity and legal requirements. Raman spectra provide excellent characterizations of different polymorphs, as is illustrated for the six polymorphic forms of the drug Cimetidine shown in Fig. 4-24 (19). These Raman spectra clearly exhibit major differences that can be used for identifying the polymorphic form. Raman can be used to determine the polymorphic form of a pure compound and of the active ingredient in tablets.

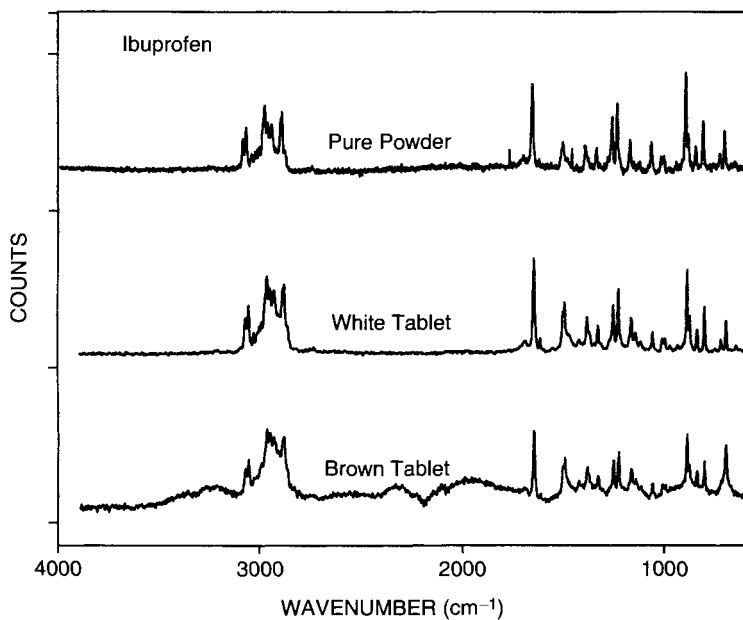


Figure 7-30 Raman spectra of ibuprofen as a pure powder, a white tablet, and a brown tablet. The pure powder spectrum is the same as in Fig. 7-28; however, the baseline was flattened with a five-point function. Both the tablet spectra were measured with an FT-Raman in the near-IR.

7.3.3 POLYMERS

Raman spectroscopy can play several unique roles in monitoring polymers. Raman spectra can be used to identify the morphology of polymers (18) and to monitor the curing of polymeric materials. A good example of the latter is the setup to monitor the curing of epoxy (20) that is shown in Fig. 7-31. As can be seen from the figure, a fiberoptic probe was inserted into the bulk epoxy material. The spectra of the uncured and cured polymers shown in Fig. 7-32 are significantly different, so the curing process can be monitored easily. In this way, optimal curing conditions such as temperature, time, pressure, and humidity can be determined from within the bulk material without damage to the material.

Another good example of using Raman spectroscopy in the polymer industry is to investigate polymer blends. Raman microimages have been used to investigate the spatial distributions of the components in a blend of brominated poly(isobutylene-co-*para*-methylstyrene (BIMS) and *cis*-1,4-polybutadiene (BR) containing silica, zinc stearate, thiate, and other additives (21). A Raman spectrum of a blend is shown in Fig. 7-33. Specific bands can be assigned to BIMS, BR, silica, and zinc stearate. A $10 \times 10 \mu\text{m}$ contour

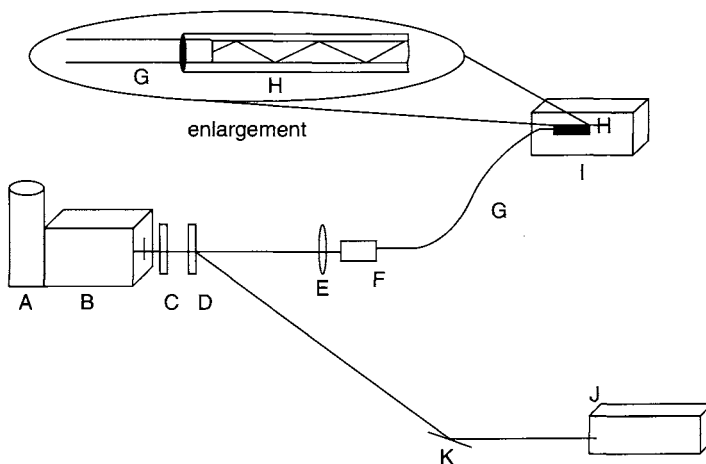


Figure 7-31 Diagram of instrumental setup for monitoring polymer curing: (a) CCD detector; (b) spectrograph; (c) holographic filter; (d) beam splitter; (e) lens; (f) ST-connector (*fiberoptic connector); (g) fiberoptic; (h) Teflon tube filled with polymer; (i) bulk polymer; (j) laser with bandpass filter; (k) mirror. (Reproduced with permission from Ref. 20.)

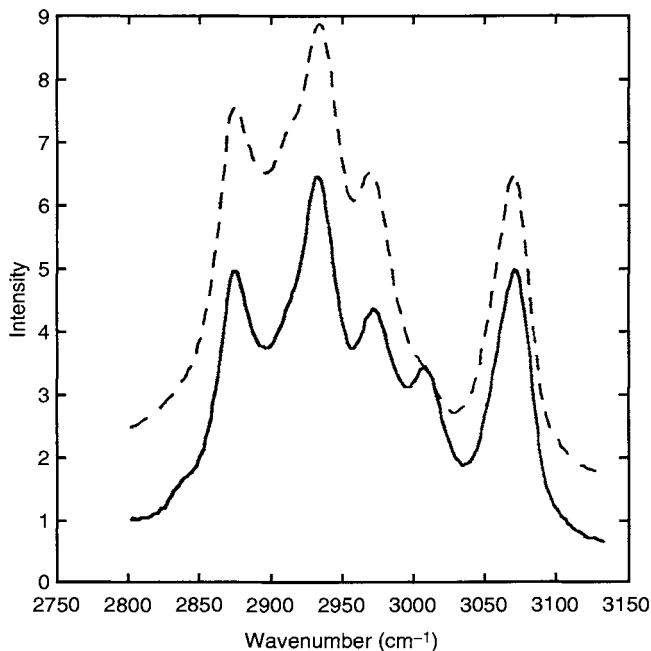


Figure 7-32 Fiber optic Raman spectra of uncured (solid line) and cured (dashed line) epoxy. (Reproduced with permission from Ref. 20.)

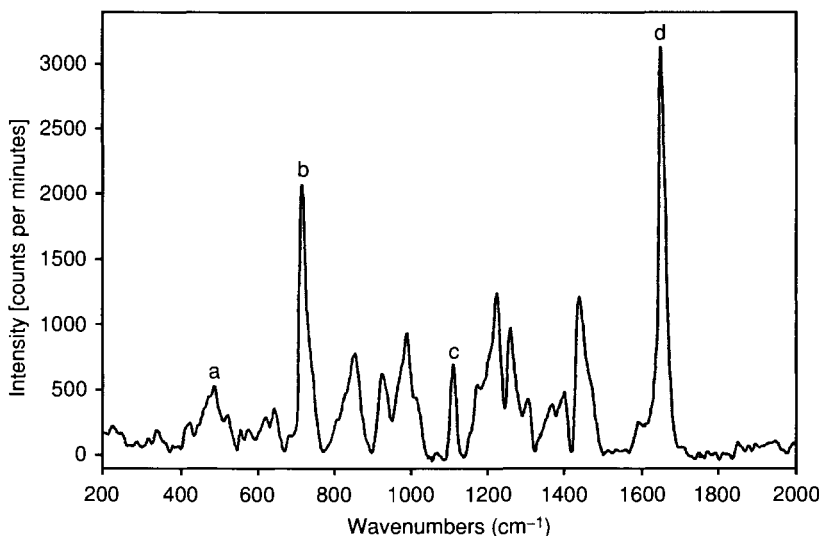


Figure 7-33 Typical Raman spectrum for a BIMS–BR blend with silica, zinc stearate, thiate U, and other additives. (a) A band at about 490 cm^{-1} assigned to silica; (b) a band at 714 cm^{-1} assigned to the CH_2 rocking mode of the BIMS backbone; (c) a band at $1,118\text{ cm}^{-1}$ assigned to hydrocarbon chain vibrations of zinc stearate; (d) a band at $1,648\text{ cm}^{-1}$ assigned to the $\text{C}=\text{C}$ stretching vibrations of the cis-polybutadiene backbone. (Reproduced with permission from Ref. 21.)

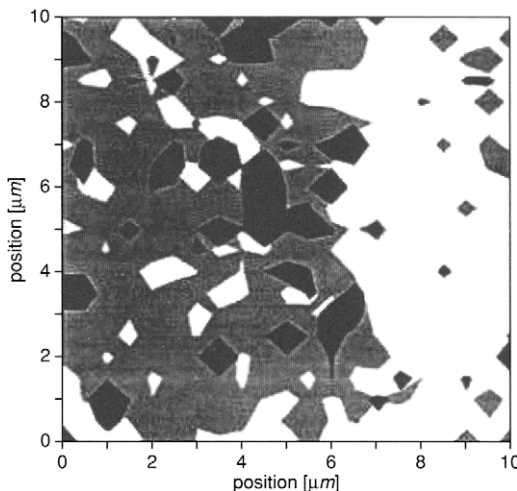


Figure 7-34 Contour map for a cured blend with a 50:50 BIMS–BR ratio. The regions in gray correspond to about 41% surface area and represent BIMS domains. Silica domains are shown in black and cover about 15%. The remaining surface is covered by the BR component. (Reproduced with permission from Ref. 21.)

map obtained from a Raman microimage is shown in Fig. 7-34 (refer to Section 3.2.5 for information of microimages). It is known that BIMS and BR do not mix well and form separate domains in blends. This image shows that the silica stays primarily in the BIMS regions. This same investigation also used the Raman microimages to monitor curing of the these blends.

There are numerous other example of using Raman both for investigating polymers and for process control (18). The advent of smaller, less expensive instruments undoubtedly will lead to greater use of Raman in the polymer industry.

References

1. G. Ellis, M. Claybourne, and S. E. Richards, *Spec. Acta* **46A**, 227 (1990).
2. Y. Ozaki, R. Cho, K. Ikegawa, S. Muraishi, and K. Kawauchi, *Appl. Spectrosc.* **46**, 1503 (1992).
3. J. Goral and V. Zichy, *Spec. Acta* **46A**, 253 (1990).
4. D. Bourgeois and S. P. Church, *Spec. Acta* **46A**, 295 (1990).
5. C. A. Melendres, "Laser Raman spectroscopy: Principles and applications to corrosion studies," in "Electrochemical and Optical Techniques for the Study and Monitoring of Metallic Corrosion" (M. G. S. Ferreira and C. A. Melendres, eds.), pp. 355–388, and references therein. Kluwer Academic Publishers, The Netherlands, 1991.
6. J. J. McMahon, W. Ruther, and C. A. Melendres, *J. Electrochem. Soc.* **135**, 557 (1988).
7. M. J. Smith, G. Kemeny, and F. Walder, *Nicolet FT-Raman Application Notes, AN-9142* (1992).
8. J. B. Cooper, "Process Control Applications for Raman Spectroscopy in the Petroleum Industry" In Analytical applications of Raman Spectroscopy, M. J. Pelletier, ed., P. 193, Blackwell Science, Ltd., London, 1999.
9. J. B. Cooper, P. E. Cletcher, T. M. Vess, and W. T. Welch. *Appl. Spectrosc.* **49**, 586, (1995).
10. K. J. Schmidt, K. H. Michaelian and G. R. Loppnow, *Appl. Spectrosc.* **53**, 139, (1999).
11. U. P. Agarwal and S. A. Ralph, *Appl. Spectrosc.* **51**, 1648, (1997).
12. K. I. Mullen, D. X. Wang, L. G. Crane and K. T. Carreon, *Spectrosc.*, **7(5)**, 24 (1992).
13. K. Xi, S. K. Sharma, G. T. Taylor and D. W. Muenow, *Appl. Spectrosc.*, **46**, 819 (1992)
14. P. A. Tanner and K-H Leung, *Appl. Spectrosc.*, **50**, 565 (1996).
15. C. M. Hodges and J. Akhavan, *Spec. Acta.*, **46A**, 303 (1990), C. M. Hodges, P. J. Hendra, H. A. Willis and T. Farley, *J. Raman Spectroscopy* **20**, 745 (1989).
16. S. M. Donahue, C. W. Brown, B Caputo and M. D. Modell, *Anal. Chem.*, **60**, 1873 (1988).
17. D. E. Diller and R. F. Chang, *Appl. Spectrosc.*, **34**, 411 (1980).
18. F. Adar, R. Geiger, J. Noonan, *Applied Spectrosc. Rev.*, **32(1&2)**, 45 (1997).
19. G. Jalsovszky, O Egyed, S. Holly and B. Hegedus, *Appl. Spectrosc.*, **49**, 1142 (1995).
20. J. F. Aust, K. S. Booksh and M. L. Myrick, *Appl. Spectrosc.*, **50**, 382 (1996).
21. R. Appel, T. W. Zerda and W. H. Waddell, *Appl. Spectrosc.*, **54**, 1559 (2000).

Appendix 1

Point Groups and Their Character Tables

Taken from K. Nakamoto, "Infrared and Raman Spectra of Inorganic and Coordination Compounds," Wiley and Sons, New York, 1978. Reprinted with permission of John Wiley and Sons, Inc.

C_s	E	$\sigma(xy)$		
A'	+1	+1	T_x, T_y, R_z	$\alpha_{xx}, \alpha_{yy}, \alpha_{zz}, \alpha_{xy}$
A''	+1	-1	T_z, R_x, R_y	α_{yz}, α_{xz}

C_2	E	$C_2(z)$		
A	+1	+1	T_z, R_z	$\alpha_{xx}, \alpha_{yy}, \alpha_{zz}, \alpha_{xy}$
B	+1	-1	T_x, T_y, R_x, R_y	α_{yz}, α_{xz}

C_i	E	i		
A_g	+1	+1	R_x, R_y, R_z	all components of α
A_u	+1	-1	T_x, T_y, T_z	

C_{2v}	E	$C_2(z)$	$\sigma_v(xz)$	$\sigma_v(yz)$		
A_1	+1	+1	+1	+1	T_z	$\alpha_{xx}, \alpha_{yy}, \alpha_{zz}$
A_2	+1	+1	-1	-1	R_z	α_{xy}
B_1	+1	-1	+1	-1	T_x, R_y	α_{xz}
B_2	+1	-1	-1	+1	T_y, R_x	α_{yz}

C_{3v}	E	$2C_3(z)$	$3\sigma_v$		
A_1	+1	+1	+1	T_z	$\alpha_{xx} + \alpha_{yy}, \alpha_{zz}$
A_2	+1	+1	-1	R_z	
E	+2	-1	0	$(T_x, T_y), (R_x, R_y)$	$(\alpha_{xx} - \alpha_{yy}, \alpha_{xy}), (\alpha_{yz}, \alpha_{xz})$

C_{4v}	E	$2C_4(z)$	$C_4^2 \equiv C_2''$	$2\sigma_v$	$2\sigma_d$		
A_1	+1	+1	+1	+1	+1	T_z	$\alpha_{xx} + \alpha_{yy}, \alpha_{zz}$
A_2	+1	+1	+1	-1	-1	R_z	
B_1	+1	-1	+1	+1	-1		$\alpha_{xx} - \alpha_{yy}$
B_2	+1	-1	+1	-1	+1		α_{xy}
E	+2	0	-2	0	0	$(T_x, T_y), (R_x, R_y)$	$(\alpha_{yz}, \alpha_{xz})$

C_p^n (or S_p^n) denotes that the C_p (or S_p) operation is carried out successively n times.

$C_{\infty v}$	E	$2C_\infty^\phi$	$2C_\infty^{2\phi}$	$2C_\infty^{3\phi}$	\dots	$\infty\sigma_v$		
Σ^+	+1	+1	+1	+1	\dots	+1	T_z	$\alpha_{xx} + \alpha_{yy}, \alpha_{zz}$
Σ^-	+1	+1	+1	+1	\dots	-1	R_z	
Π	+2	$2 \cos \phi$	$2 \cos 2\phi$	$2 \cos 3\phi$	\dots	0	$(T_x, T_y), (R_x, R_y)$	$(\alpha_{yz}, \alpha_{xz})$
Δ	+2	$2 \cos 2\phi$	$2 \cos 2.2\phi$	$2 \cos 3.2\phi$	\dots	0		$(\alpha_{xx} - \alpha_{yy}, \alpha_{xy})$
Φ	+2	$2 \cos 3\phi$	$2 \cos 2.3\phi$	$2 \cos 3.3\phi$	\dots	0		
\dots	\dots	\dots	\dots	\dots	\dots	\dots		

C_{2h}	E	$C_2(z)$	$\sigma_h(xy)$	i		
A_g	+1	+1	+1	+1	R_z	$\alpha_{xx}, \alpha_{yy}, \alpha_{zz}, \alpha_{xy}$
A_u	+1	+1	-1	-1	T_z	
B_g	+1	-1	-1	+1	R_x, R_y	α_{yz}, α_{xz}
B_u	+1	-1	+1	-1	T_x, T_y	

D_3	E	$2C_3(z)$	$3C_2$		
A_1	+1	+1	+1		$\alpha_{xx} + \alpha_{yy}, \alpha_{zz}$
A_2	+1	+1	-1	T_z, R_z	
E	+2	-1	0	$(T_x, T_y), (R_x, R_y)$	$(\alpha_{xx} - \alpha_{yy}, \alpha_{xy}), (\alpha_{yz}, \alpha_{xz})$

$D_{2d} \equiv V_d$	E	$2S_4(z)$	$S_4^2 \equiv C_2''$	$2C_2$	$2\sigma_d$		
A_1	+1	+1	+1	+1	+1		
A_2	+1	+1	+1	-1	-1		
B_1	+1	-1	+1	+1	-1		
B_2	+1	-1	+1	-1	+1		
E	+2	0	-2	0	0	$(T_x, T_y), (R_x, R_y)$	$(\alpha_{yz}, \alpha_{xz})$

D_{3d}	E	$2S_6(z)$	$2S_6^2 \equiv 2C_3$	$S_6^3 \equiv S_2 \equiv i$	$3C_2$	$3\sigma_d$		
A_{1g}	+1	+1	+1	+1	+1	+1		
A_{1u}	+1	-1	+1	-1	+1	-1		
A_{2g}	+1	+1	+1	+1	-1	-1		
A_{2u}	+1	-1	+1	-1	-1	+1		
E_g	+2	-1	-1	+2	0	0	(R_x, R_y)	$(\alpha_{xx} - \alpha_{yy}, \alpha_{xy}), (\alpha_{yz}, \alpha_{xz})$
E_u	+2	+1	-1	-2	0	0	(T_x, T_y)	

D_{4d}	E	$2S_8(z)$	$2S_8^2 \equiv 2C_4$	$2S_8^3$	$S_8^4 \equiv C_2''$	$4C_2$	$4\sigma_d$		
A_1	+1	+1	+1	+1	+1	+1	+1		
A_2	+1	+1	+1	+1	+1	-1	-1		
B_1	+1	-1	+1	-1	+1	+1	-1		
B_2	+1	-1	+1	-1	+1	-1	+1		
E_1	+2	$+\sqrt{2}$	0	$-\sqrt{2}$	-2	0	0	(T_x, T_y)	
E_2	+2	0	-2	0	+2	0	0		$(\alpha_{xx} - \alpha_{yy}, \alpha_{xy})$
E_3	+2	$-\sqrt{2}$	0	$+\sqrt{2}$	-2	0	0	(R_x, R_y)	$(\alpha_{yz}, \alpha_{xz})$

$D_{2h} \equiv V_h$	E	$\sigma(xy)$	$\sigma(xz)$	$\sigma(yz)$	i	$C_2(z)$	$C_2(y)$	$C_2(x)$	
A_g	+1	+1	+1	+1	+1	+1	+1	+1	
A_u	+1	-1	-1	-1	-1	+1	+1	+1	
B_{1g}	+1	+1	-1	-1	+1	+1	-1	-1	
B_{1u}	+1	-1	+1	+1	-1	+1	-1	-1	
B_{2g}	+1	-1	+1	-1	+1	-1	+1	-1	
B_{2u}	+1	+1	-1	+1	-1	-1	+1	-1	
B_{3g}	+1	-1	-1	+1	+1	-1	-1	+1	
B_{3u}	+1	+1	+1	-1	-1	-1	-1	+1	

D_{3h}	E	$2C_3(z)$	$3C_2$	σ_h	$2S_3$	$3\sigma_v$		
A'_1	+1	+1	+1	+1	+1	+1		
A''_1	+1	+1	+1	-1	-1	-1		
A'_2	+1	+1	-1	+1	+1	-1		
A''_2	+1	+1	-1	-1	-1	+1		
E'	+2	-1	0	+2	-1	0	(T_x, T_y)	$(\alpha_{xx} - \alpha_{yy}, \alpha_{xy})$
E''	+2	-1	0	-2	+1	0	(R_x, R_y)	$(\alpha_{yz}, \alpha_{xz})$

D_{4h}	E	$2C_4(z)$	$C_4^2 \equiv C_2''$	$2C_2$	$2C_2'$	σ_h	$2\sigma_v$	$2\sigma_d$	$2S_4$	$S_2 \equiv i$	
A_{1g}	+1	+1	+1	+1	+1	+1	+1	+1	+1	+1	$\alpha_{xx} + \alpha_{yy}, \alpha_{zz}$
A_{1u}	+1	+1	+1	+1	-1	-1	-1	-1	-1	-1	
A_{2g}	+1	+1	+1	-1	-1	-1	-1	-1	+1	+1	
A_{2u}	+1	+1	+1	-1	-1	-1	+1	+1	-1	-1	R_z
B_{1g}	+1	-1	+1	+1	-1	+1	+1	-1	-1	+1	T_z
B_{1u}	+1	-1	+1	+1	-1	-1	-1	+1	+1	-1	$\alpha_{xx} - \alpha_{yy}$
B_{2g}	+1	-1	+1	-1	+1	+1	-1	+1	+1	+1	α_{xy}
B_{2u}	+1	-1	+1	-1	+1	-1	+1	-1	+1	-1	
E_g	+2	0	-2	0	0	-2	0	0	0	+2	(R_x, R_y)
E_u	+2	0	-2	0	0	+2	0	0	0	-2	(T_x, T_y)

D_{5h}	E	$2C_5(z)$	$2C_5^2$	σ_h	$5C_2$	$5\sigma_v$	$2S_5$	$2S_3^3$		
A'_1	+1	+1	+1	+1	+1	+1	+1	+1	+1	$\alpha_{xx} + \alpha_{yy}, \alpha_{zz}$
A''_1	+1	+1	+1	-1	+1	-1	-1	-1	-1	
A'_2	+1	+1	+1	-1	-1	-1	+1	+1	+1	
A''_2	+1	+1	+1	-1	-1	+1	-1	-1	-1	R_z
E'_1	+2	$2\cos 72^\circ$	$2\cos 144^\circ$	+2	0	0	$+2\cos 72^\circ$	$+2\cos 144^\circ$	T_z	
E''_1	+2	$2\cos 72^\circ$	$2\cos 144^\circ$	-2	0	0	$-2\cos 72^\circ$	$-2\cos 144^\circ$	(T_x, T_y)	$(\alpha_{yz}, \alpha_{xz})$
E'_2	+2	$2\cos 144^\circ$	$2\cos 72^\circ$	+2	0	0	$+2\cos 144^\circ$	$+2\cos 72^\circ$	(R_x, R_y)	$(\alpha_{xy} - \alpha_{yz}, \alpha_{xy})$
E''_2	+2	$2\cos 144^\circ$	$2\cos 72^\circ$	-2	0	0	$-2\cos 144^\circ$	$-2\cos 72^\circ$		

T_d	E	$8C_3$	$6\sigma_d$	$6S_4$	$3S_4^2 \equiv 3C_2$		
A_1	+1	+1	+1	+1	+1		$\alpha_{xx} + \alpha_{yy} + \alpha_{zz}$
A_2	+1	+1	-1	-1	+1		
E	+2	-1	0	0	+2		
F_1	+3	0	-1	+1	-1	(R_x, R_y, R_z)	$(\alpha_{xx} + \alpha_{yy} - 2\alpha_{zz}, \alpha_{xx} - \alpha_{yy})$
F_2	+3	0	+1	-1	-1	(T_x, T_y, T_z)	$(\alpha_{xy}, \alpha_{yz}, \alpha_{xz})$

O_h	E	$8C_3$	$6C_2$	$6C_4$	$3C_4^2 \equiv 3C_2''$	$S_2 \equiv i$	$6S_4$	$8S_6$	$3\sigma_h$	$6\sigma_d$		
A_{1g}	+1	+1	+1	+1	+1	+1	+1	+1	+1	+1		$\alpha_{xx} + \alpha_{yy} + \alpha_{zz}$
A_{1u}	+1	+1	+1	+1	+1	-1	-1	-1	-1	-1		
A_{2g}	+1	+1	-1	-1	+1	+1	-1	+1	+1	-1		
A_{2u}	+1	+1	-1	-1	+1	-1	+1	-1	-1	+1		
E_g	+2	-1	0	0	+2	+2	0	-1	+2	0		
E_u	+2	-1	0	0	+2	-2	0	+1	-2	0		
F_{1g}	+3	0	-1	+1	-1	+3	+1	0	-1	-1	(R_x, R_y, R_z)	
F_{1u}	+3	0	-1	+1	-1	-3	-1	0	+1	+1	(T_x, T_y, T_z)	
F_{2g}	+3	0	+1	-1	-1	+3	-1	0	-1	+1		
F_{2u}	+3	0	+1	-1	-1	-3	+1	0	+1	-1		

\mathbf{I}_h	E	$12C_3$	$12C_3^2$	$20C_3$	$15C_2$	i	$12S_{10}$	$12S_{10}^3$	$20S_6$	15σ	
A_g	1	1	$\frac{1}{2}(1 + \sqrt{5})$	$\frac{1}{2}(1 - \sqrt{5})$	1	1	$\frac{1}{2}(1 - \sqrt{5})$	$\frac{1}{2}(1 + \sqrt{5})$	1	1	$\alpha_{xx} + \alpha_{yy} + \alpha_{zz}$
F_{1g}	3	$\frac{1}{2}(1 + \sqrt{5})$	$\frac{1}{2}(1 - \sqrt{5})$	0	-1	3	$\frac{1}{2}(1 - \sqrt{5})$	$\frac{1}{2}(1 + \sqrt{5})$	0	-1	(R_x, R_y, R_z)
F_{2g}	3	$\frac{1}{2}(1 - \sqrt{5})$	$\frac{1}{2}(1 + \sqrt{5})$	0	-1	3	$\frac{1}{2}(1 + \sqrt{5})$	$\frac{1}{2}(1 - \sqrt{5})$	0	-1	
G_g	4	-1	-1	1	0	4	-1	-1	1	0	
H_g	5	0	0	-1	1	5	0	0	-1	1	
A_u	1	1	1	1	1	-1	-1	-1	-1	-1	$(2\alpha_{zz} - \alpha_{xx} - \alpha_{yy},$
F_{1u}	3	$\frac{1}{2}(1 + \sqrt{5})$	$\frac{1}{2}(1 - \sqrt{5})$	0	-1	-3	$-\frac{1}{2}(1 - \sqrt{5})$	$-\frac{1}{2}(1 + \sqrt{5})$	0	1	$\alpha_{xx} - \alpha_{yy},$
F_{2u}	3	$\frac{1}{2}(1 - \sqrt{5})$	$\frac{1}{2}(1 + \sqrt{5})$	0	-1	-3	$-\frac{1}{2}(1 + \sqrt{5})$	$-\frac{1}{2}(1 - \sqrt{5})$	0	1	$\alpha_{xy}, \alpha_{yz}, \alpha_{xz}$
G_u	4	-1	-1	1	0	-4	1	1	-1	0	
H_u	5	0	0	-1	1	-5	0	0	1	-1	

Appendix 2

General Formulas for Calculating the Number of Normal Vibrations in Each Symmetry Species

Most of these tables were quoted from G. Hertzberg, "Molecular Spectra and Molecular Structure," Vol. II: "Infrared and Raman Spectra of Polyatomic Molecules." Van Nostrand, Princeton, New Jersey, 1945.

For a simple method to derive these tables, see K. Nakamoto and M. A. McKinney, J. Chem. Educ., 77, 775 (2000).

A. Point Groups Including Only Nondegenerate Vibrations

Point Group	Total Number of Atoms	Species	Number of Vibrations ^a
C ₂	$2m + m_0$	<i>A</i>	$3m + m_0 - 2$
		<i>B</i>	$3m + 2m_0 - 4$
C _s	$2m + m_0$	<i>A'</i>	$3m + 2m_0 - 3$
		<i>A''</i>	$3m + m_0 - 3$
C _i ≡ S ₂	$2m + m_0$	<i>A_g</i>	$3m - 3$
		<i>A_u</i>	$3m + 3m_0 - 3$
C _{2v}	$4m + 2m_{xz} + 2m_{yz} + m_0$	<i>A₁</i>	$3m + 2m_{xz} + 2m_{yz} + m_0 - 1$
		<i>A₂</i>	$3m + m_{xz} + m_{yz} - 1$
		<i>B₁</i>	$3m + 2m_{xz} + m_{yz} + m_0 - 2$
		<i>B₂</i>	$3m + m_{xz} + 2m_{yz} + m_0 - 2$
C _{2h}	$4m + 2m_h + 2m_2 + m_0$	<i>A_g</i>	$3m + 2m_h + m_2 - 1$
		<i>A_u</i>	$3m + m_h + m_2 + m_0 - 1$
		<i>B_g</i>	$3m + m_h + 2m_2 - 2$
		<i>B_u</i>	$3m + 2m_h + 2m_2 + 2m_0 - 2$

Continued

A. *Continued*

Point Group	Total Number of Atoms	Species	Number of Vibrations ^a
$D_{2h} \equiv V_h$	$8m + 4m_{xy} + 4m_{xz}$ $+ 4m_{yz} + 2m_{2x}$ $+ 2m_{2y} + 2m_{2z} + m_0$	A_g	$3m + 2m_{xy} + 2m_{xz} + 2m_{yz} + m_{2x} + m_{2y} + m_{2z}$
		A_u	$3m + m_{xy} + m_{xz} + m_{yz}$
		B_{1g}	$3m + 2m_{xy} + m_{xz} + m_{yz} + m_{2x} + m_{2y} - 1$
		B_{1u}	$3m + m_{xy} + 2m_{xz} + 2m_{yz} + m_{2x} + m_{2y} + m_{2z} + m_0 - 1$
		B_{2g}	$3m + m_{xy} + 2m_{xz} + m_{yz} + m_{2x} + m_{2z} - 1$
		B_{2u}	$3m + 2m_{xy} + m_{xz} + 2m_{yz} + m_{2x} + m_{2y} + m_{2z} + m_0 - 1$
		B_{3g}	$3m + m_{xy} + m_{xz} + 2m_{yz} + m_{2y} + m_{2x} - 1$
		B_{3u}	$3m + 2m_{xy} + 2m_{xz} + m_{yz} + m_{2x} + m_{2y} + m_{2z} + m_0 - 1$

^aNote that m is always the number of sets of equivalent nuclei not on any element of symmetry; m_0 is the number of nuclei lying on all symmetry elements present; m_{xy} , m_{xz} , m_{yz} are the numbers of sets of nuclei lying on the xy , xz , yz plane, respectively, but not on any axes going through these planes; m_2 is the number of sets of nuclei on a twofold axis but not at the point of intersection with another element of symmetry; m_{2x} , m_{2y} , m_{2z} are the numbers of sets of nuclei lying on the x , y , z axis if they are twofold axes, but not on all of them; m_h is the number of sets of nuclei on a plane σ_h but not on the axis perpendicular to this plane.

B. Point Groups Including Degenerate Vibrations

Point Group	Total Number of Atoms	Species	Number of Vibrations ^a
D_3	$6m + 3m_2 + 2m_3 + m_0$	A_1	$3m + m_2 + m_3$
		A_2	$3m + 2m_2 + m_3 + m_0 - 2$
		E	$6m + 3m_2 + 2m_3 + m_0 - 2$
C_{3v}	$6m + 3m_v + m_0$	A_1	$3m + 2m_v + m_0 - 1$
		A_2	$3m + m_v - 1$
		E	$6m + 3m_v + m_0 - 2$
C_{4v}	$8m + 4m_v + 4m_d + m_0$	A_1	$3m + 2m_v + 2m_d + m_0 - 1$
		A_2	$3m + m_v + m_d - 1$
		B_1	$3m + 2m_v + m_d$
		B_2	$3m + m_v + 2m_d$
		E	$6m + 3m_v + 3m_d + m_0 - 2$
$C_{\infty v}$	m_0	\sum^+	$m_0 - 1$
		\sum^-	0
		\prod	$m_0 - 2$
		Δ, Φ, \dots	0
$D_{2d} \equiv V_d$	$8m + 4m_d + 4m_2 + 2m_4 + m_0$	A_1	$3m + 2m_d + m_2 + m_4$
		A_2	$3m + m_d + 2m_2 - 1$
		B_1	$3m + m_d + m_2$
		B_2	$3m + 2m_d + 2m_2 + m_4 + m_0 - 1$
		E	$6m + 3m_d + 3m_2 + 2m_4 + m_0 - 2$

Continued

B. *Continued*

Point Group	Total Number of Atoms	Species	Number of Vibrations ^a
D_{3d}	$12m + 6m_d + 6m_2 + 2m_6 + m_0$	A_{1g}	$3m + 2m_d + m_2 + m_6$
		A_{1u}	$3m + m_d + m_2$
		A_{2g}	$3m + m_d + 2m_2 - 1$
		A_{2u}	$3m + 2m_d + 2m_2 + m_6 + m_0 - 1$
		E_g	$6m + 3m_d + 3m_2 + m_6 - 1$
		E_u	$6m + 3m_d + 3m_2 + m_6 + m_0 - 1$
D_{4d}	$16m + 8m_d + 8m_2 + 2m_8 + m_0$	A_1	$3m + 2m_d + m_2 + m_8$
		A_2	$3m + m_d + 2m_2 - 1$
		B_1	$3m + m_d + m_2$
		B_2	$3m + 2m_d + 2m_2 + m_8 + m_0 - 1$
		E_1	$6m + 3m_d + 3m_2 + m_8 + m_0 - 1$
		E_2	$6m + 3m_d + 3m_2$
D_{3h}	$12m + 6m_v + 6m_h + 3m_2 + 2m_3 + m_0$	E_3	$6m + 3m_d + 3m_2 + m_8 - 1$
		A'_1	$3m + 2m_v + 2m_h + m_2 + m_3$
		A''_1	$3m + m_v + m_h$
		A'_2	$3m + m_v + 2m_h + m_2 - 1$
		A''_2	$3m + 2m_v + m_h + m_2 + m_3 + m_0 - 1$
		E'	$6m + 3m_v + 4m_h + 2m_2 + m_3 + m_0 - 1$
D_{4h}	$16m + 8m_v + 8m_d + 8m_h + 4m_2 + 4m'_2 + 2m_4 + m_0$	E''	$6m + 3m_v + 2m_h + m_2 + m_3 - 1$
		A_{1g}	$3m + 2m_v + 2m_d + 2m_h + m_2 + m'_2 + m_4$
		A_{1u}	$3m + m_v + m_d + m_h$
		A_{2g}	$3m + m_v + m_d + 2m_h + m_2 + m'_2 - 1$
		A_{2u}	$3m + 2m_v + 2m_d + m_h + m_2 + m'_2 + m_4 + m_0 - 1$
		B_{1g}	$3m + 2m_v + m_d + 2m_h + m_2 + m'_2$
		B_{1u}	$3m + m_v + 2m_d + m_h + m'_2$
		B_{2g}	$3m + m_v + 2m_d + 2m_h + m_2 + m'_2$
		B_{2u}	$3m + 2m_v + m_d + m_h + m_2$
		E_g	$6m + 3m_v + 3m_d + 2m_h + m_2 + m'_2 + m_4 - 1$
		E_u	$6m + 3m_v + 3m_d + 4m_h + 2m_2 + 2m'_2 + m_4 + m_0 - 1$
D_{5h}	$20m + 10m_v + 10m_h + 5m_2 + 2m_5 + m_0$	A'_1	$3m + 2m_v + 2m_h + m_2 + m_5$
		A''_1	$3m + m_v + m_h$
		A'_2	$3m + m_v + 2m_h + m_2 - 1$
		A''_2	$3m + 2m_v + m_h + m_2 + m_5 + m_0 - 1$
		E'_1	$6m + 3m_v + 4m_h + 2m_2 + m_5 + m_0 - 1$
		E''_1	$6m + 3m_v + 2m_h + m_2 + m_5 - 1$
		E'_2	$6m + 3m_v + 4m_h + 2m_2$
		E''_2	$6m + 3m_v + 2m_h + m_2$

Continued

B. *Continued*

Point Group	Total Number of Atoms	Species	Number of Vibrations ^a
D_{6h} $24m + 12m_v + 12m_d$ $+ 12m_h + 6m_2$ $+ 6m'_2 + 2m_6 + m_o$	$24m + 12m_v + 12m_d$ $+ 12m_h + 6m_2$ $+ 6m'_2 + 2m_6 + m_o$	A_{1g}	$3m + 2m_v + 2m_d + 2m_h + m_2 + m'_2 + m_6$
		A_{1u}	$3m + m_v + m_d + m_h$
		A_{2g}	$3m + m_v + m_d + 2m_h + m_2 + m'_2 - 1$
		A_{2u}	$3m + 2m_v + 2m_d + m_h + m_2 + m'_2 + m_6 + m_0 - 1$
		B_{1g}	$3m + m_v + 2m_d + m_h + m'_2$
		B_{1u}	$3m + 2m_v + m_d + 2m_h + m_2 + m'_2$
		B_{2g}	$3m + 2m_v + m_d + m_h + m_2$
		B_{2u}	$3m + m_v + 2m_d + 2m_h + m_2 + m'_2$
		E_{1g}	$6m + 3m_v + 3m_d + 2m_h + m_2 + m'_2 + m_6 - 1$
		E_{1u}	$6m + 3m_v + 3m_d + 4m_h + 2m_2 + 2m'_2 + m_6 + m_0 - 1$
		E_{2g}	$6m + 3m_v + 3m_d + 4m_h + 2m_2 + 2m'_2$
		E_{2u}	$6m + 3m_v + 3m_d + 2m_h + m_2 + m'_2$
		\sum_g^+	m_∞
		\sum_u^+	$m_\infty + m_0 - 1$
D_{∞h} $2m_\infty + m_0$	$2m_\infty + m_0$	\sum_g^-, \sum_u^-	0
		Π_g	$m_\infty - 1$
		Π_u	$m_\infty + m_0 - 1$
		Δ_g, Δ_u	0
		Φ_g, Φ_u, \dots	0
T_d $24m + 12m_d$ $+ 6m_2 + 4m_3 + m_0$	$24m + 12m_d$ $+ 6m_2 + 4m_3 + m_0$	A_1	$3m + 2m_d + m_2 + m_3$
		A_2	$3m + m_d$
		E	$6m + 3m_d + m_2 + m_3$
		F_1	$9m + 4m_d + 2m_2 + m_3 - 1$
		F_2	$9m + 5m_d + 3m_2 + 2m_3 + m_0 - 1$
O_h $48m + 24m_h + 24m_d$ $+ 12m_2 + 8m_3$ $+ 6m_4 + m_0$	$48m + 24m_h + 24m_d$ $+ 12m_2 + 8m_3$ $+ 6m_4 + m_0$	A_{1g}	$3m + 2m_h + 2m_d + m_2 + m_3 + m_4$
		A_{1u}	$3m + m_h + m_d$
		A_{2g}	$3m + 2m_h + m_d + m_2$
		A_{2u}	$3m + m_h + 2m_d + m_2 + m_3$
		E_g	$6m + 4m_h + 3m_d + 2m_2 + m_3 + m_4$
		E_u	$6m + 2m_h + 3m_d + m_2 + m_3$
		F_{1g}	$9m + 4m_h + 4m_d + 2m_2 + m_3 + m_4 - 1$
		F_{1u}	$9m + 5m_h + 5m_d + 3m_2 + 2m_3 + 2m_4 + m_0 - 1$
		F_{2g}	$9m + 4m_h + 5m_d + 2m_2 + 2m_3 + m_4$
		F_{2u}	$9m + 5m_h + 4m_d + 2m_2 + m_3 + m_4$

Continued

B. *Continued*

Point Group	Total Number of Atoms	Species	Number of Vibrations ^a
I_h	$m_0 + 12m_5 + 20m_3 + 30m_2 + 60m_v + 120m$	A_g	$m_5 + m_3 + m_2 + 2m_v + 3m$
		A_u	$m_v + 3m$
		F_{1g}	$m_5 + m_3 + 2m_2 + 4m_v + 9m - 1$
		F_{1u}	$m_0 + 2m_5 + 2m_3 + 3m_2 + 5m_v + 9m - 1$
		F_{2g}	$m_3 + 2m_2 + 4m_v + 9m$
		F_{2u}	$m_5 + 2m_3 + 3m_2 + 5m_v + 9m$
		G_g	$m_5 + 2m_3 + 3m_2 + 6m_v + 12m$
		G_u	$m_5 + 2m_3 + 3m_2 + 6m_v + 12m$
		H_g	$2m_5 + 3m_3 + 4m_2 + 8m_v + 15m$
		H_u	$m_5 + 2m_3 + 3m_2 + 7m_v + 15m$

^aNote that m is the number of sets of nuclei not on any element of symmetry; m_0 is the number of nuclei on all elements of symmetry; m_2, m_3, m_4, \dots are the numbers of sets of nuclei on a twofold, threefold, fourfold, ... axis but not on any other element of symmetry that does not wholly coincide with that axis; m'_2 is the number of sets of nuclei on the twofold axis called C'_2 in the preceding character tables; m_v, m_d, m_h are the numbers of sets of nuclei on planes $\sigma_v, \sigma_d, \sigma_h$, respectively, but not on any other element of symmetry.

Appendix 3

Direct Products of Irreducible Representations

This material was reproduced with permission from E. B. Wilson, J. C. Decius and P. C. Cross, "Molecular Vibrations," McGraw-Hill, New York, 1955.

$$\begin{aligned}
 A \times A &= A, & B \times B &= A, & A \times B &= B, & A \times E &= E, & B \times E &= E, \\
 A \times F &= F, & B \times F &= F, & g \times g &= g, & u \times u &= g, & u \times g &= u \\
 ' \times ' &= ', & '' \times '' &= ', & ' \times '' &= '', & A \times E_1 &= E_1, & A \times E_2 &= E_2, \\
 B \times E_1 &= E_2, & B \times E_2 &= E_1.
 \end{aligned}$$

Subscripts on A or B :

$$\begin{aligned}
 1 \times 1 &= 1, & 2 \times 2 &= 1, & 1 \times 2 &= 2, \text{ except for } D_2 \equiv V \text{ and } D_{2h} \equiv V_h, \text{ where} \\
 1 \times 2 &= 3, & 2 \times 3 &= 1, & 1 \times 3 &= 2.
 \end{aligned}$$

Doubly degenerate representations:

For $C_3, C_{3h}, C_{3v}, D_3, D_{3h}, D_{3d}, C_6, C_{6h}, C_{6v}, D_6, D_{6h}, S_6, O, O_h, T, T_d, T_h$:

$$\begin{aligned}
 E_1 \times E_1 &= E_2 \times E_2 = A_1 + A_2 + E_2, \\
 E_1 \times E_2 &= B_1 + B_2 + E_1,
 \end{aligned}$$

For $C_4, C_{4v}, C_{4h}, D_{2d}, D_4, D_{4h}, S_4$: $E \times E = A_1 + A_2 + B_1 + B_2$

For groups in above lists which have symbols A, B , or E without subscripts, read $A_1 = A_2 = A$, etc.

Triply degenerate representations:

For T_d, O, O_h : $E \times F_1 = E \times F_2 = F_1 + F_2$

$$\begin{aligned}
 F_1 \times F_1 &= F_2 \times F_2 = A_1 + E + F_1 + F_2 \\
 F_1 \times F_2 &= A_2 + E + F_1 + F_2
 \end{aligned}$$

For T, T_h : Drop subscripts 1 and 2 from A and F

Linear molecules ($C_{\infty v}$ and $D_{\infty h}$):

$$\Sigma^+ \times \Sigma^+ = \Sigma^- \times \Sigma^- = \Sigma^+; \quad \Sigma^+ \times \Sigma^- = \Sigma^-$$

$$\Sigma^+ \times \Pi = \Sigma^- \times \Pi = \Pi; \quad \Sigma^+ \times \Delta = \Sigma^- \times \Delta = \Delta; \quad \text{etc.}$$

$$\Pi \times \Pi = \Sigma^+ + \Sigma^- + \Delta$$

$$\Delta \times \Delta = \Sigma^+ + \Sigma^- + \Gamma$$

$$\Pi \times \Delta = \Pi + \Phi$$

Appendix 4

Site Symmetries for the 230 Space Groups

Taken with permission from J. R. Ferraro and J. S. Ziomek, "Introductory Group Theory and Its Application to Molecular Structure." Plenum Press, New York, 1975.

Space Group ^a		Site Symmetries ^b
1 <i>P1</i>	C_1^1	$C_1(1)$
2 <i>P1̄</i>	C_i^1	$8C_i(1); C_1(2)$
3 <i>P2</i>	C_2^1	$4C_2(1); C_1(2)$
4 <i>P2₁</i>	C_2^2	$C_1(2)$
5 <i>B₂</i> or <i>C₂</i>	C_2^3	$2C_2(1); C_1(2)$
6 <i>Pm</i>	C_s^1	$2C_s(1); C_1(2)$
7 <i>Pb</i> or <i>Pc</i>	C_s^2	$C_1(2)$
8 <i>Bm</i> or <i>Cm</i>	C_s^3	$C_s(1); C_1(2)$
9 <i>Bb</i> or <i>Cc</i>	C_s^4	$C_1(2)$
10 <i>P2/m</i>	C_{2h}^1	$8C_{2h}(1); 4C_2(2); 2C_s(2); C_1(4)$
11 <i>P2₁/m</i>	C_{2h}^2	$4C_i(2); C_s(2); C_1(4)$
12 <i>B2/m</i> or <i>C2/m</i>	C_{2h}^3	$4C_{2h}(1); 2C_i(2); 2C_s(2); C_s(2); C_1(4)$
13 <i>P2/b</i> or <i>P2/c</i>	C_{2h}^4	$4C_i(2); 2C_2(2); C_1(4)$
14 <i>P2₁/b</i> or <i>P2₁/c</i>	C_{2h}^5	$4C_i(2); C_1(4)$
15 <i>B2/b</i> or <i>C2/c</i>	C_{2h}^6	$4C_i(2); C_2(2); C_1(4)$
16 <i>P222</i>	D_2^1	$8D_2(1); 12C_2(2); C_1(4)$
17 <i>P222₁</i>	D_2^2	$4C_2(2); C_1(4)$
18 <i>P2₁2₁2</i>	D_2^3	$2C_2(2); C_1(4)$
19 <i>P2₁2₁2₁</i>	D_2^4	$C_1(4)$
20 <i>C222₁</i>	D_2^5	$2C_2(2); C_1(4)$
21 <i>C222</i>	D_2^6	$4D_2(1); 7C_2(2); C_1(4)$
22 <i>F222</i>	D_2^7	$4D_2(1); 6C_2(2); C_1(4)$
23 <i>I222</i>	D_2^8	$4D_2(1); 6C_2(2); C_1(4)$
24 <i>I2₁2₁2₁</i>	D_2^9	$3C_2(2); C_1(4)$
25 <i>Pmm2</i>	C_{2v}^1	$4C_{2v}(1); 4C_s(2); C_1(4)$
26 <i>Pmc2₁</i>	C_{2v}^2	$2C_s(2); C_1(4)$
27 <i>Pcc2</i>	C_{2v}^3	$4C_2(2); C_1(4)$
28 <i>Pma2</i>	C_{2v}^4	$2C_2(2); C_s(2); C_1(4)$
29 <i>Pca2₁</i>	C_{2v}^5	$C_1(4)$
30 <i>Pnc2</i>	C_{2v}^6	$2C_2(2); C_1(4)$
31 <i>Pmn2₁</i>	C_{2v}^7	$C_s(2); C_1(4)$

Continued

Appendix 4 *Continued*

Space Group ^a		Site Symmetries ^b
32 <i>Pba2</i>	C_{2v}^8	$2C_2(2); C_1(4)$
33 <i>Pna2</i> ₁	C_{2v}^9	$C_1(4)$
34 <i>Pnn2</i>	C_{2v}^{10}	$2C_2(2); C_1(4)$
35 <i>Cmm2</i>	C_{2v}^{11}	$2C_{2v}(1); C_2(2); 2C_s(2); C_1(4)$
36 <i>Cmc2</i> ₁	C_{2v}^{12}	$C_s(2); C_1(4)$
37 <i>Ccc2</i>	C_{2v}^{13}	$3C_2(2); C_1(4)$
38 <i>Amm2</i>	C_{2v}^{14}	$2C_{2v}(1); 3C_s(2); C_1(4)$
39 <i>Abm2</i>	C_{2v}^{15}	$2C_{2v}(2); C_s(2); C_1(4)$
40 <i>Ama2</i>	C_{2v}^{16}	$C_2(2); C_s(2); C_1(4)$
41 <i>Aba2</i>	C_{2v}^{17}	$C_2(2); C_1(4)$
42 <i>Fmm2</i>	C_{2v}^{18}	$C_{2v}(1); C_2(2); 2C_s(2); C_1(4)$
43 <i>Fdd2</i>	C_{2v}^{19}	$C_2(2); C_1(4)$
44 <i>Imm2</i>	C_{2v}^{20}	$2C_{2v}(1); 2C_s(2); C_1(4)$
45 <i>Iba2</i>	C_{2v}^{21}	$2C_2(2); C_1(4)$
46 <i>Ima2</i>	C_{2v}^{22}	$C_2(2); C_s(2); C_1(4)$
47 <i>Pmmm</i>	D_{2h}^1	$8D_{2h}(1); 12C_{2v}(2); 6C_s(4); C_1(8)$
48 <i>Pnnn</i>	D_{2h}^2	$4D_2(2); 2C_i(4); 6C_2(4); C_1(8)$
49 <i>Pccm</i>	D_{2h}^3	$4C_{2h}(2); 4D_2(2); 8C_2(4); C_s(4); C_1(8)$
50 <i>Pban</i>	D_{2h}^4	$4D_2(2); 2C_i(4); 6C_2(4); C_1(8)$
51 <i>Pmma</i>	D_{2h}^5	$4C_{2h}(2); 2C_{2v}(2); 2C_2(4); 3C_s(4); C_1(8)$
52 <i>Pnna</i>	D_{2h}^6	$2C_i(4); 2C_2(4); C_1(8)$
53 <i>Pmna</i>	D_{2h}^7	$4C_{2h}(2); 3C_2(4); C_s(4); C_1(8)$
54 <i>Pcca</i>	D_{2h}^8	$2C_i(4); 3C_2(4); C_1(8)$
55 <i>Pbam</i>	D_{2h}^9	$4C_{2h}(2); 2C_2(4); 2C_s(4); C_1(8)$
56 <i>Pccn</i>	D_{2h}^{10}	$2C_i(4); 2C_2(4); C_1(8)$
57 <i>Pbcm</i>	D_{2h}^{11}	$2C_i(4); C_2(4); C_s(4); C_1(8)$
58 <i>Pnnm</i>	D_{2h}^{12}	$4C_{2h}(2); 2C_2(4); C_s(4); C_1(8)$
59 <i>Pmmm</i>	D_{2h}^{13}	$2C_{2v}(2); 2C_i(4); 2C_s(4); C_1(8)$
60 <i>Pbcn</i>	D_{2h}^{14}	$2C_i(4); C_2(4); C_1(8)$
61 <i>Pbca</i>	D_{2h}^{15}	$2C_i(4); C_1(8)$
62 <i>Pnma</i>	D_{2h}^{16}	$2C_i(4); C_s(4); C_1(8)$
63 <i>Cmcm</i>	D_{2h}^{17}	$2C_{2h}(2); C_{2v}(2); C_i(4); C_2(4); 2C_s(4); C_1(8)$
64 <i>Cmca</i>	D_{2h}^{18}	$2C_{2h}(2); C_i(4); 2C_2(4); C_s(4); C_i(8)$
65 <i>Cmmm</i>	D_{2h}^{19}	$4D_{2h}(1); 2C_{2h}(2); 6C_{2v}(2); C_2(4); 4C_s(4); C_1(8)$
66 <i>Cccm</i>	D_{2h}^{20}	$2D_2(2); 4C_{2h}(2); 5C_2(4); C_s(4); C_1(8)$
67 <i>Cmma</i>	D_{2h}^{21}	$2D_2(2); 4C_{2h}(2); C_{2v}(2); 5C_2(4); 2C_s(4); C_1(8)$
68 <i>Ccca</i>	D_{2h}^{22}	$2D_2(2); 2C_i(4); 4C_2(2); C_1(8)$
69 <i>Fmmm</i>	D_{2h}^{23}	$2D_{2h}(1); 3C_{2h}(2); D_2(2); 3C_{2v}(2); 3C_2(4); 3C_s(4); C_1(8)$
70 <i>Fddd</i>	D_{2h}^{24}	$2D_2(2); 2C_i(4); 3C_2(4); C_1(8)$
71 <i>Immm</i>	D_{2h}^{25}	$4D_{2h}(1); 6C_{2v}(2); C_i(4); 3C_s(4); C_1(8)$
72 <i>Ibam</i>	D_{2h}^{26}	$2D_2(2); 2C_{2h}(2); C_i(4); 4C_2(4); C_s(4); C_1(8)$
73 <i>Ibca</i>	D_{2h}^{27}	$2C_i(4); 3C_2(4); C_1(8)$
74 <i>Imma</i>	D_{2h}^{28}	$4C_{2h}(2); C_{2v}(2); 2C_2(4); 2C_s(4); C_1(8)$
75 <i>P4</i>	C_4^1	$2C_4(1); C_2(2); C_1(4)$
76 <i>P4</i> ₁	C_4^2	$C_1(4)$
77 <i>P4</i> ₂	C_4^3	$3C_2(2); C_1(4)$

Continued

Appendix 4 *Continued*

Space Group ^a		Site Symmetries ^b
78 <i>P</i> 4 ₃	C_4^4	$C_1(4)$
79 <i>I</i> 4	C_4^5	$C_4(1); C_2(2); C_1(4)$
80 <i>I</i> 4 ₁	C_4^6	$C_2(2); C_1(4)$
81 <i>P</i> 4̄	S_4^1	$4S_4(1); 3C_2(2); C_1(4)$
82 <i>I</i> 4̄	S_4^2	$4S_4(1); 2C_2(2); C_1(4)$
83 <i>P</i> 4/m	C_{4h}^1	$4C_{4h}(1); 2C_{2h}(2); 2C_4(2); C_2(4); 2C_s(4); C_1(8)$
84 <i>P</i> 4 ₂ /m	C_{4h}^2	$4C_{2h}(2); 2S_4(2); 3C_2(4); C_s(4); C_1(8)$
85 <i>P</i> 4/n	C_{4h}^3	$2S_4(2); C_4(2); 2C_i(4); C_2(4); C_1(8)$
86 <i>P</i> 4 ₂ /n	C_{4h}^4	$2S_4(2); 2C_i(4); 2C_2(4); C_1(8)$
87 <i>I</i> 4/m	C_{4h}^5	$2C_{4h}(1); C_{2h}(2); S_4(2); C_4(2); C_i(4); C_2(4); C_s(4); C_1(8)$
88 <i>I</i> 4 ₁ /a	C_{4h}^6	$2S_4(2); 2C_i(4); C_2(4); C_1(8)$
89 <i>P</i> 422	D_4^1	$4D_4(1); 2D_2(2); 2C_4(2); 7C_2(4); C_1(8)$
90 <i>P</i> 4 ₂ 12	D_4^2	$2D_2(2); C_4(2); 3C_2(4); C_1(8)$
91 <i>P</i> 4 ₁ 22	D_4^3	$3C_2(4); C_1(8)$
92 <i>P</i> 4 ₁ 212	D_4^4	$C_2(4); C_1(8)$
93 <i>P</i> 4 ₂ 22	D_4^5	$6D_2(2); 9C_2(4); C_1(8)$
94 <i>P</i> 4 ₁ 212	D_4^6	$2D_2(2); 4C_2(4); C_1(8)$
95 <i>P</i> 4 ₃ 22	D_4^7	$3C_2(4); C_1(8)$
96 <i>P</i> 4 ₃ 212	D_4^8	$C_2(4); C_1(8)$
97 <i>I</i> 422	D_4^9	$2D_4(1); 2D_2(2); C_4(2); 5C_2(4); C_1(8)$
98 <i>I</i> 4 ₁ 22	D_4^{10}	$2D_2(2); 4C_2(4); C_1(8)$
99 <i>P</i> 4mm	C_{4v}^1	$2C_{4v}(1); C_{2v}(2); 3C_s(4); C_1(8)$
100 <i>P</i> 4bm	C_{4v}^2	$C_4(2); C_{2v}(2); C_s(4); C_1(8)$
101 <i>P</i> 4 ₂ cm	C_{4v}^3	$2C_{2v}(2); C_2(4); C_s(4); C_1(8)$
102 <i>P</i> 4 ₂ nm	C_{2v}^4	$C_{2v}(2); C_2(4); C_s(4); C_1(8)$
103 <i>P</i> 4cc	C_{4v}^5	$2C_4(2); C_2(4); C_1(8)$
104 <i>P</i> 4nc	C_{4v}^6	$C_4(2); C_2(4); C_1(8)$
105 <i>P</i> 4 ₂ mc	C_{4v}^7	$3C_{2v}(2); 2C_s(4); C_1(8)$
106 <i>P</i> 4 ₂ bc	C_{4v}^8	$2C_2(4); C_1(8)$
107 <i>I</i> 4mm	C_{4v}^9	$C_{4v}(1); C_{2v}(2); 2C_s(4); C_1(8)$
108 <i>I</i> 4cm	C_{4v}^{10}	$C_4(2); C_{2v}(2); C_s(4); C_1(8)$
109 <i>I</i> 4 ₁ md	C_{4v}^{11}	$C_{2v}(2); C_s(4); C_1(8)$
110 <i>I</i> 4 ₁ cd	C_{4v}^{12}	$C_2(4); C_1(8)$
111 <i>P</i> 42m	D_{2d}^1	$4D_{2d}(1); 2D_2(2); 2C_{2v}(2); 5C_2(4); C_s(4); C_1(8)$
112 <i>P</i> 42c	D_{2d}^2	$4D_2(2); 2S_4(2); 7C_2(4); C_1(8)$
113 <i>P</i> 4 ₂ 1m	D_{2d}^3	$2S_4(2); C_{2v}(2); C_2(4); C_s(4); C_1(8)$
114 <i>P</i> 4 ₂ 1c	D_{2d}^4	$2S_4(2); 2C_2(4); C_1(8)$
115 <i>P</i> 4m ₂	D_{2d}^5	$4D_{2d}(1); 3C_{2v}(2); 2C_2(4); 2C_s(4); C_1(8)$
116 <i>P</i> 4c2	D_{2d}^6	$2D_2(2); 2S_4(2); 5C_2(4); C_1(8)$
117 <i>P</i> 4̄b ₂	D_{2d}^7	$2S_4(2); 2D_2(2); 4C_2(4); C_1(8)$
118 <i>P</i> 4n2	D_{2d}^8	$2S_4(2); 2D_2(2); 4C_2(4); C_1(8)$
119 <i>I</i> 4m2	D_{2d}^9	$4D_{2d}(1); 2C_{2v}(2); 2C_2(4); C_s(4); C_1(8)$
120 <i>I</i> 4c2	D_{2d}^{10}	$D_2(2); 2S_4(2); D_2(2); 4C_2(4); C_1(8)$
121 <i>I</i> 42m	D_{2d}^{11}	$2D_{2d}(1); D_2(2); S_4(2); C_{2v}(2); 3C_2(4); C_s(4); C_1(8)$
122 <i>I</i> 42d	D_{2d}^{12}	$2S_4(2); 2C_2(4); C_1(8)$
123 <i>P</i> 4/mmm	D_{4h}^1	$4D_{4h}(1); 2D_{2h}(2); 2C_{4v}(2); 7C_{2v}(4); 5C_s(8); C_1(16)$

Continued

Appendix 4 *Continued*

Space Group ^a		Site Symmetries ^b
124 <i>P4/mcc</i>	D_{4h}^2	$D_4(2); C_{4h}(2); D_4(2); C_{4h}(2); C_{2h}(4); D_2(4); 2C_4(4); 4C_2(8); C_s(8); C_1(16)$
125 <i>P4/nbm</i>	D_{4h}^3	$2D_4(2); 2D_{2d}(2); 2C_{2h}(4); C_4(4); C_{2v}(4); 4C_2(8); C_s(8); C_1(16)$
126 <i>P4/nnc</i>	D_{2h}^4	$2D_4(2); D_2(4); S_4(4); C_4(4); C_i(8); 4C_2(8); C_1(8)$
127 <i>P4/nbm</i>	D_{2h}^5	$2C_{4h}(2); 2D_{2h}(2); C_4(4); 3C_{2v}(4); 3C_s(8); C_1(16)$
128 <i>P4/nnc</i>	D_{2h}^6	$2C_{4h}(2); C_{2h}(4); D_2(4); C_4(4); 2C_2(8); C_s(8); C_1(16)$
129 <i>P4/nmm</i>	D_{4h}^7	$2D_{2d}(2); C_{4v}(2); 2C_{2h}(4); C_{2v}(4); 2C_2(8); 2C_s(8); C_1(16)$
130 <i>P4/ncc</i>	D_{4h}^8	$D_2(4); S_4(4); C_4(4); C_i(8); 2C_2(8); C_1(16)$
131 <i>P4₂/mmc</i>	D_{4h}^9	$4D_{2h}(2); 2D_{2d}(2); 7C_{2v}(4); C_2(8); 3C_s(8); C_1(16)$
132 <i>P4₂/mcm</i>	D_{4h}^{10}	$D_{2h}(2); D_{2d}(2); D_{2h}(2); D_{2d}(2); D_2(4); C_{2h}(4); 4C_{2v}(4); 3C_2(8); 2C_s(8); C_1(16)$
133 <i>P4₂/nbc</i>	D_{4h}^{11}	$3D_2(4); S_4(4); C_i(8); 5C_2(8); C_1(16)$
134 <i>P4₂/nnm</i>	D_{4h}^{12}	$2D_{2d}(2); 2D_2(4); 2C_{2h}(4); C_{2v}(4); 5C_2(8); C_s(8); C_1(16)$
135 <i>P4₂/mbc</i>	D_{4h}^{13}	$C_{2h}(4); S_4(4); C_{2h}(4); D_2(4); 3C_2(8); C_s(8); C_1(16)$
136 <i>P4₂/mmn</i>	D_{4h}^{14}	$2D_{2h}(2); C_{2h}(4); S_4(4); 3C_{2v}(4); C_2(8); 2C_s(8); C_1(16)$
137 <i>P4₂/nmc</i>	D_{4h}^{15}	$2D_{2d}(2); 2C_{2v}(4); C_i(8); C_2(8); C_s(8); C_1(16)$
138 <i>P4₂/ncm</i>	D_{4h}^{16}	$D_2(4); S_4(4); 2C_{2h}(4); C_{2v}(4); 3C_2(8); C_s(8); C_1(16)$
139 <i>I4/mmm</i>	D_{4h}^{17}	$2D_{4h}(1); D_{2h}(2); D_{2d}(2); C_{4v}(2); C_{2h}(4); 4C_{2v}(4); C_2(8); 3C_s(8); C_1(16)$
140 <i>I4/mcm</i>	D_{2h}^{18}	$D_4(2); D_{2d}(2); C_{4h}(2); D_{2h}(2); C_{2h}(4); C_4(4); 2C_{2v}(4); 2C_2(8); 2C_s(8); C_1(16)$
141 <i>I4₁/amd</i>	D_{4h}^{19}	$2D_{2d}(2); 2C_{2h}(4); C_{2v}(4); 2C_2(8); C_s(8); C_1(16)$
142 <i>I4₁/acd</i>	D_{4h}^{20}	$S_4(4); D_2(4); C_i(8); 3C_2(8); C_1(16)$
143 <i>P3</i>	C_3^1	$3C_3(1); C_1(3)$
144 <i>P3₁</i>	C_3^2	$C_1(3)$
145 <i>P3₂</i>	C_3^3	$C_1(3)$
146 <i>R3</i>	C_3^4	$C_3(1); C_1(3)$
147 <i>P3̄</i>	C_{3i}^1	$2C_{3i}(1); 2C_3(2); 2C_i(3); C_1(16)$
148 <i>R3̄</i>	C_{3i}^2	$2C_{3i}(1); C_3(2); 2C_i(3); C_1(6)$
149 <i>P312</i>	$D_{\bar{3}}^1$	$6D_3(1); 3C_3(2); 2C_2(3); C_1(6)$
150 <i>P321</i>	$D_{\bar{3}}^2$	$2D_3(1); 2C_3(2); 2C_2(3); C_1(6)$
151 <i>P3₁12</i>	$D_{\bar{3}}^3$	$2C_2(3); C_1(6)$
152 <i>P3₁21</i>	$D_{\bar{3}}^4$	$2C_2(3); C_1(6)$
153 <i>P3₂12</i>	$D_{\bar{3}}^5$	$2C_2(2); C_1(6)$
154 <i>P3₂21</i>	$D_{\bar{3}}^6$	$2C_2(3); C_1(6)$
155 <i>R32</i>	$D_{\bar{3}}^7$	$2D_3(1); C_3(2); 2C_2(3); C_1(6)$
156 <i>P3m1</i>	C_{3v}^1	$3C_{3v}(1); C_s(3); C_1(6)$
157 <i>P31m</i>	C_{3v}^2	$C_{3v}(1); C_3(2); C_s(3); C_1(6)$
158 <i>P3c1</i>	C_{3v}^3	$3C_3(2); C_1(6)$
159 <i>P31c</i>	C_{3v}^4	$2C_3(2); C_1(6)$
160 <i>R3m</i>	C_{3v}^5	$C_{3v}(1); C_s(3); C_1(6)$
161 <i>R3c</i>	C_{3v}^6	$C_3(2); C_1(6)$
162 <i>P3̄1m</i>	$D_{\bar{3}d}^1$	$2D_{3d}(1); 2D_3(2); C_{3v}(2); 2C_{2h}(3); C_3(4); 2C_2(6); C_s(6); C_1(12)$
163 <i>P3̄1c</i>	$D_{\bar{3}d}^2$	$D_3(2); C_3(2); 2D_3(2); 2C_3(4); C_i(6); C_2(6); C_1(12)$
164 <i>P3̄m1</i>	$D_{\bar{3}d}^3$	$2D_{3d}(1); 2C_{3v}(2); 2C_{2h}(3); 2C_2(6); C_s(6); C_1(12)$
165 <i>P3̄c1</i>	$D_{\bar{3}d}^4$	$D_3(2); C_3(2); 2C_3(4); C_i(6); C_1(6); C_2(12)$
166 <i>R3̄m</i>	$D_{\bar{3}d}^5$	$2D_{3d}(1); C_{3v}(2); 2C_{2h}(3); 2C_2(6); C_s(6); C_1(12)$

Continued

Appendix 4 *Continued*

Space Group ^a		Site Symmetries ^b
167 $R\bar{3}c$	D_{3d}^6	$D_3(2); C_{3i}(2); C_3(4); C_i(6); C_2(6); C_1(12)$
168 $P6$	C_6^1	$C_6(1); C_3(2); C_2(3); C_1(6)$
169 $P6_1$	C_6^2	$C_1(6)$
170 $P6_5$	C_6^3	$C_1(6)$
171 $P6_2$	C_6^4	$2C_2(3); C_1(6)$
172 $P6_4$	C_6^5	$2C_2(3); C_1(6)$
173 $P6_3$	C_6^6	$2C_3(2); C_1(6)$
174 $P\bar{6}$	C_{3h}^1	$6C_{3h}(1); 3C_3(2); 2C_s(3); C_1(6)$
175 $P6/m$	C_{6h}^1	$2C_{6h}(1); 2C_{3h}(2); C_6(2); 2C_{2h}(3); C_3(4); C_2(6); 2C_s(6); C_1(12)$
176 $P6_3/m$	C_{6h}^2	$C_{3h}(2); C_{3i}(2); 2C_{3h}(2); 2C_3(4); C_i(6); C_s(6); C_1(12)$
177 $P622$	D_6^1	$2D_6(1); 2D_3(2); C_6(2); 2D_2(3); C_4(4); 5C_2(6); C_1(12)$
178 $P6_{12}2$	D_6^2	$2C_2(6); C_1(12)$
179 $P6_{52}22$	D_6^3	$2C_2(6); C_1(12)$
180 $P6_{22}22$	D_6^4	$4D_2(3); 6C_2(6); C_1(12)$
181 $P6_{42}22$	D_6^5	$4D_2(3); 6C_2(6); C_1(12)$
182 $P6_{33}$	D_6^6	$4D_3(2); 2C_3(4); 2C_2(6); C_1(12)$
183 $P6mm$	C_{6v}^1	$C_{6v}(1); C_{3v}(2); C_{2v}(3); 2C_s(6); C_1(12)$
184 $P6cc$	C_{6v}^2	$C_6(2); C_3(4); C_2(6); C_1(12)$
185 $P6_3cm$	C_{6v}^3	$C_{3v}(2); C_3(4); C_s(6); C_1(12)$
186 $P6_3mc$	C_{6v}^4	$2C_{3v}(2); C_s(6); C_1(12)$
187 $P6m2$	D_{3h}^1	$6D_{3h}(1); 3C_{3v}(2); 2C_{2v}(3); 3C_s(6); C_1(12)$
188 $P\bar{6}c2$	D_{3h}^2	$D_3(2); C_{3h}(2); D_3(2); C_{3h}(2); 3C_3(4); C_2(6); C_s(6); C_1(12)$
189 $P\bar{6}2m$	D_{3h}^3	$2D_{3h}(1); 2C_{3h}(2); C_{3v}(2); 2C_{2v}(3); C_3(4); 3C_s(6); C_1(12)$
190 $P\bar{6}2c$	D_{3h}^4	$D_3(2); 3C_{3h}(2); 2C_3(4); C_2(6); C_s(6); C_1(12)$
191 $P6/mmm$	D_{6h}^1	$2D_{6h}(1); 2D_{3h}(2); C_{6v}(2); 2D_{2h}(3); C_{3v}(4); 5C_{2v}(6); 4C_s(12); C_1(12)$
192 $P6/mcc$	D_{6h}^2	$D_6(2); C_{6h}(2); D_3(4); C_{3h}(4); C_6(4); D_2(6); C_{2h}(6); C_3(8); 3C_2(12); C_s(12); C_1(24)$
193 $P6_3/mcm$	D_{6h}^3	$D_{3h}(2); D_{3d}(2); C_{3h}(4); D_3(4); C_6(4); C_{2h}(6); C_{2v}(6); C_3(8); C_2(12); 2C_2(12); C_1(24)$
194 $P6_3/mmc$	D_{6h}^4	$D_{3d}(2); 3D_{3h}(2); 2C_{3v}(4); C_{2h}(6); C_{2v}(6); C_2(12); 2C_s(12); C_1(24)$
195 $P23$	T^1	$2T(1); 2D_2(3); C_3(4); 4C_2(6); C_1(12)$
196 $F23$	T^2	$4T(1); C_3(4); 2C_2(6); C_1(12)$
197 $I23$	T^3	$T(1); D_2(2); C_3(4); 2C_2(6); C_1(12)$
198 $P2_13$	T^4	$C_3(4); C_1(12)$
199 $I2_13$	T^5	$C_3(4); C_2(6); C_1(12)$
200 $Pm3$	T_h^1	$2T_h(1); 2D_{2h}(3); 4C_{2v}(6); C_3(8); 2C_s(12); C_1(24)$
201 $Pn3$	T_h^2	$T(2); 2C_3(4); D_2(6); C_3(8); 2C_2(12); C_1(24)$
202 $Fm3$	T_h^3	$2T_h(1); T(2); C_{2h}(6); C_{2v}(6); C_3(8); C_2(12); C_s(12); C_1(24)$
203 $Fd3$	T_h^4	$2T(2); 2C_3(4); C_3(8); C_2(12); C_1(24)$
204 $Im3$	T_h^5	$T_h(1); D_{2h}(3); C_{3i}(4); 2C_{2v}(6); C_3(8); C_s(12); C_1(24)$
205 $Pa3$	T_h^6	$2C_{3i}(4); C_3(8); C_1(24)$
206 $Ia3$	T_h^7	$2C_{3i}(4); C_3(8); C_2(12); C_1(24)$
207 $P432$	O^1	$2O(1); 2D_4(3); 2C_4(6); C_3(8); 3C_2(12); C_1(24)$
208 $P4_232$	O^2	$T(2); 2D_3(4); 3D_2(6); C_3(8); 5C_2(12); C_1(24)$
209 $F432$	O^3	$2O(1); T(2); D_2(6); C_4(6); C_3(8); 3C_2(12); C_1(24)$
210 $F4_132$	O^4	$2T(2); 2D_3(4); C_3(8); 2C_2(12); C_1(24)$

Continued

Appendix 4 *Continued*

Space Group ^a		Site Symmetries ^b
211 <i>I</i> 432	<i>O</i> ⁵	<i>O</i> (1); <i>D</i> ₄ (3); <i>D</i> ₃ (4); <i>D</i> ₂ (6); <i>C</i> ₄ (6); <i>C</i> ₃ (8); 3 <i>C</i> ₂ (12); <i>C</i> ₁ (24)
212 <i>P</i> 4 ₃ 32	<i>O</i> ⁶	2 <i>D</i> ₃ (4); <i>C</i> ₃ (8); <i>C</i> ₂ (12); <i>C</i> ₁ (24)
213 <i>P</i> 4 ₁ 32	<i>O</i> ⁷	2 <i>D</i> ₃ (4); <i>C</i> ₃ (8); <i>C</i> ₂ (12); <i>C</i> ₁ (24)
214 <i>I</i> 4 ₁ 32	<i>O</i> ⁸	2 <i>D</i> ₃ (4); 2 <i>D</i> ₂ (6); <i>C</i> ₃ (8); 3 <i>C</i> ₂ (12); <i>C</i> ₁ (24)
215 <i>P</i> 43 <i>m</i>	<i>T</i> _d ¹	2 <i>T</i> _d (1); 2 <i>D</i> _{2d} (3); <i>C</i> _{3v} (4); 2 <i>C</i> _{2v} (6); <i>C</i> ₂ (12); <i>C</i> _s (12); <i>C</i> ₁ (24)
216 <i>F</i> 43 <i>m</i>	<i>T</i> _d ²	4 <i>T</i> _d (1); <i>C</i> _{3v} (4); 2 <i>C</i> _{2v} (6); <i>C</i> _s (12); <i>C</i> ₁ (24)
217 <i>I</i> 43 <i>m</i>	<i>T</i> _d ³	<i>T</i> _d (1); <i>D</i> _{2d} (3); <i>C</i> _{3v} (4); <i>S</i> ₄ (6); <i>C</i> _{2v} (6); <i>C</i> ₂ (12); <i>C</i> _s (12); <i>C</i> ₁ (24)
218 <i>P</i> 43 <i>n</i>	<i>T</i> _d ⁴	<i>T</i> (2); <i>D</i> ₂ (6); 2 <i>S</i> ₄ (6); <i>C</i> ₃ (8); 3 <i>C</i> ₂ (12); <i>C</i> ₁ (24)
219 <i>F</i> 43 <i>c</i>	<i>T</i> _d ⁵	2 <i>T</i> (2); 2 <i>S</i> ₄ (6); <i>C</i> ₃ (8); 2 <i>C</i> ₂ (12); <i>C</i> ₁ (24)
220 <i>I</i> 43 <i>d</i>	<i>T</i> _d ⁶	2 <i>S</i> ₄ (6); <i>C</i> ₃ (8); <i>C</i> ₂ (12); <i>C</i> ₁ (24)
221 <i>Pm</i> 3 <i>m</i>	<i>O</i> _h ¹	2 <i>O</i> _h (1); 2 <i>D</i> _{4h} (3); 2 <i>C</i> _{4v} (6); <i>C</i> _{3v} (8); 3 <i>C</i> _{2v} (12); 3 <i>C</i> _s (24); <i>C</i> ₁ (48)
222 <i>Pn</i> 3 <i>n</i>	<i>O</i> _h ²	<i>O</i> (2); <i>D</i> ₄ (6); <i>C</i> ₃ (8); <i>S</i> ₄ (12); <i>C</i> ₄ (12); <i>C</i> ₃ (16); 2 <i>C</i> ₂ (24); <i>C</i> ₁ (48)
223 <i>Pm</i> 3 <i>n</i>	<i>O</i> _h ³	<i>T</i> _h (2); <i>D</i> _{2h} (6); 2 <i>D</i> _{2d} (6); <i>D</i> ₃ (8); 3 <i>C</i> _{2v} (12); <i>C</i> ₃ (16); <i>C</i> ₂ (24); <i>C</i> _s (24); <i>C</i> ₁ (48)
224 <i>Pn</i> 3 <i>m</i>	<i>O</i> _h ⁴	<i>T</i> _d (2); 2 <i>D</i> _{3d} (4); <i>D</i> _{2d} (6); <i>C</i> _{3v} (8); <i>D</i> ₂ (12); <i>C</i> _{2v} (12); 3 <i>C</i> ₂ (24); <i>C</i> ₁ (48)
225 <i>Fm</i> 3 <i>m</i>	<i>O</i> _h ⁵	2 <i>O</i> _h (1); <i>T</i> _d (2); <i>D</i> _{2h} (6); <i>C</i> _{4v} (6); <i>C</i> _{3v} (8); 3 <i>C</i> _{2v} (12); 2 <i>C</i> _s (24); <i>C</i> ₁ (48)
226 <i>Fd</i> 3 <i>c</i>	<i>O</i> _h ⁶	<i>O</i> (2); <i>T</i> _h (2); <i>D</i> _{2d} (6); <i>C</i> _{4h} (6); <i>C</i> _{2v} (12); <i>C</i> ₄ (12); <i>C</i> ₃ (16); <i>C</i> ₂ (24); <i>C</i> _s (24); <i>C</i> ₁ (48)
227 <i>Fd</i> 3 <i>m</i>	<i>O</i> _h ⁷	2 <i>T</i> _d (2); 2 <i>D</i> _{3d} (4); <i>C</i> _{3v} (8); <i>C</i> _{2v} (12); <i>C</i> _s (24); <i>C</i> ₂ (24); <i>C</i> ₁ (48)
228 <i>Fd</i> 3 <i>c</i>	<i>O</i> _h ⁸	<i>T</i> (4); <i>D</i> ₃ (8); <i>C</i> ₃ (8); <i>S</i> ₄ (12); <i>C</i> ₃ (16); 2 <i>C</i> ₂ (24); <i>C</i> ₁ (48)
229 <i>Im</i> 3 <i>m</i>	<i>O</i> _h ⁹	<i>O</i> _h (1); <i>D</i> _{4h} (3); <i>D</i> _{3d} (4); <i>D</i> _{2d} (6); <i>C</i> _{4v} (6); <i>C</i> _{3v} (8); 2 <i>C</i> _{2v} (12); <i>C</i> ₂ (24); 2 <i>C</i> _s (24); <i>C</i> ₁ (48)
230 <i>Ia</i> 3 <i>d</i>	<i>O</i> _h ¹⁰	<i>C</i> _{3i} (8); <i>D</i> ₃ (8); <i>D</i> ₂ (12); <i>S</i> ₄ (12); <i>C</i> ₃ (16); 2 <i>C</i> ₂ (24); <i>C</i> ₁ (48)

Note the following equivalent nomenclatures: $C_i \equiv S_2$, $C_s \equiv C_{1h}$, $D_2 \equiv V$, $D_{2h} \equiv V_h$, $D_{2d} \equiv V_d$, and $C_{3i} \equiv S_6$.

^aN. F. M. Henry and K. Lonsdale (Eds.), "International Tables for X-Ray Crystallography," Vol. 1, Kynoch Press, Birmingham, U.K., 1965.

^bR. S. Halford, J. Chem. Phys. 14, 8 (1946).

Appendix 5

Determination of the Proper Correlation Using Wyckoff's Tables

Taken from W. G. Fateley, F. R. Dollish, N. T. McDevitt and F. F. Bentley, "Infrared and Raman Selection Rules for Molecular and Lattice Vibrations: The Correlation Method," Wiley-Interscience, New York, 1972, courtesy of Wiley-Interscience.

Space Group Number		Site Correlation					
		$C_2(z)$	$C_2(y)$	$C_2(x)$	$\sigma(xy)$	$\sigma(zx)$	$\sigma(yz)$
D_2^l	16	D_2^1	q, r, s, t	m, n, o, p	i, j, k, l		
	17	D_2^2		c, d	a, b		
	18	D_2^3	a, b				
	20	D_2^5		b	a		
	21	D_2^6	i, j, k	g, h	e, f		
	22	D_2^7	g, h	f, i	e, j		
	23	D_2^8	i, j	g, h	e, f		
	24	D_2^9	c	b	a		
C_{2v}^i	25	C_{2v}^1			e, f	g, h	
	26	C_{2v}^2				a, b	
	28	C_{2v}^4				c	
	31	C_{2v}^7				a	
	35	C_{2v}^{11}			d	e	
	36	C_{2v}^{12}				a	
	38	C_{2v}^{14}			c	d, e	
	39	C_{2v}^{15}			c		
	40	C_{2v}^{16}				b	
	42	C_{2v}^{18}			d	c	
	44	C_{2v}^{20}			c	d	
	46	C_{2v}^{22}				b	

Continued

Continued

Space Group Number	Site Correlation					
	$C_2(z)$	$C_2(y)$	$C_2(x)$	$\sigma(xy)$	σzx	$\sigma(yz)$
D_{2h}^i						
47	D_{2h}^1	q, r, s, t	m, n, o, p	i, j, k, l	y, z	w, x
48	D_{2h}^2	k, l	i, j	g, h		u, v
49	D_{2h}^3	a, b, c, d, m, n, o, p	k, l	i, j	q	
50	D_{2h}^4	k, l	i, j	g, h		
51	D_{2h}^5	e, f	a, b, c, d, g, h		i, j	k
52	D_{2h}^6	c		d		
53	D_{2h}^7		g	a, b, c, d, e, f		h
54	D_{2h}^8	d, e	c			
55	D_{2h}^9	a, b, c, d, e, f			g, h	
56	D_{2h}^{10}	c, d				
57	D_{2h}^{11}			c	d	
58	D_{2h}^{12}	a, b, c, d, e, f			g	
59	D_{2h}^{13}	a, b			f	e
60	D_{2h}^{14}		c			
62	D_{2h}^{16}				c	
63	D_{2h}^{17}		c	a, b, e	g	f
64	D_{2h}^{18}		e	a, b, d		f
65	D_{2h}^{19}	e, f, k, l, m	i, j	g, h	p, q	o
66	D_{2h}^{20}	c, d, e, f, i, j, k	h	g	l	n
67	D_{2h}^{21}	g, l	e, f, j, k	c, d, h, i		m
68	D_{2h}^{22}	g, h	f	e		
69	D_{2h}^{23}	e, i, j	d, h, k	c, g, l	o	n
70	D_{2h}^{24}	g	f	e		
71	D_{2h}^{25}	i, j	g, h	e, f	n	m
72	D_{2h}^{26}	c, d, h, i	g	f	j	
73	D_{2h}^{27}	e	d	c		
74	D_{2h}^{28}	e	c, d, g	a, b, f	i	h

Space Group Number	C_2			C_2'			C_2''			C_2		
	σ_h	σ_d	σ_v	σ_h	σ_d	σ_v	σ_h	σ_d	σ_v	σ_h	σ_d	σ_v
D_4^i	89 D_4^1	i		e, f, l, m, n, o			j, k					
	90 D_4^2	d					e, f, a, b					
	91 D_4^3			a, b			c					
	92 D_4^4						a					
	93 D_4^5	g, h, i		a, b, c, d, j, k, l, m			e, f, n, o					
	94 D_4^6	c, d					a, b, e, f					
	95 D_4^7			a, b			c					
	96 D_4^8						a					
	97 D_4^9	f		c, h, i			d, g, j					
	98 D_4^{10}	c		f			a, b, d, e					
C_{4v}	99 C_1						c, e, f			d		
	100 C_2^{4v}									b, c		
	101 C_3^{4v}									a, b, d		
	102 C_4^{4v}									a, c		
	105 C_7^{4v}									a, b, c, d, e		
	107 C_9^{4v}									b, d		
	108 C_{10}^{4v}									c		
	109 C_{11}^{4v}									b, d		
										a, c		
D_{2d}^i	111 D_{2d}^1			m			i, j, k, l					
	112 D_{2d}^2			k, l, m			g, h, i, j					
	113 D_{2d}^3			d								
	114 D_{2d}^4			c, d								
	115 D_{2d}^5						h, i					
	116 D_{2d}^6	g, h, i					e, f					
	117 D_{2d}^7	e, f					g, h					
	118 D_{2d}^8	e, h					f, g					

Continued

Continued

			C_2	C'_2	C'''_2	C_2 σ_v	C_2 σ_d	σ_h	σ_v	σ_d
		Space Group Number								
		119	D_{2d}^9	g, h						
		120	D_{2d}^{10}	e, h						
		121	D_{2d}^{11}	f, g						
		122	D_{2d}^{12}	f, g						
				d						
	D_{4h}^i	123	D_{4h}^1	e, f, l, m, n, o	j, k					
		124	D_{4h}^2	f, k, l	j					
		125	D_{4h}^3	c, d, k, l	e, f, i, j					
		126	D_{4h}^4	c, i, j	h					
		127	D_{4h}^5	c, d, g, h	f					
		128	D_{4h}^6	d, g	i, j					
		129	D_{4h}^7	a, b, d, e, g, h	h					
		130	D_{4h}^8	a, f	i					
		131	D_{4h}^9	a, b, c, d, j, k, l, m	g, h, i					
		132	D_{4h}^{10}	b, d, e, l, m	e, f, n					
		133	D_{4h}^{11}	a, c, i, j	a, c, i, j					
		134	D_{4h}^{12}	a, b, h, i	c, j					
		135	D_{4h}^{13}	a, b, c, i, j	d, e, f, k, l					
		136	D_{4h}^{14}	a, c, e, f	d, g					
		137	D_{4h}^{15}	c, h	a, b, f, g					
		138	D_{4h}^{16}	D, g	a, b, f					
		139	D_{4h}^{17}	f	a, c, d, g, h					
				c, i, j	d, f, h, k					
	D_{4h}^i	140	D_{4h}^{18}	b, j	g					
		141	D_{4h}^{19}	c, d, f	k					
		142	D_{4h}^{20}	e	h					

Space Group Number	C_2	C_2'	C_2''	Space Group Number			σ_v	σ_d	Space Group Number	σ_h	σ_v
				C_{6v}^l	C_{6v}^l	C_{6v}^l					
D_6^l	177 D_6^l	i	j, k	c, d, l, m				d	D_{3h}^l	l, m	n
178	D_6^2	a	b		183 C_{4v}^3				187 D_{3h}^2	188 D_{3h}^2	k
179	D_6^3	a	b		185 C_{4v}^4				189 D_{3h}^5	j, k	i
180	D_6^4	e, f	g, h	i, j	186 C_{6v}^4	a, b, c			190 D_{3h}^4	h	
181	D_6^5	e, f	g, h	i, j							
182	D_6^6	a, g	b, c, d, h								

Space Group Number	C_2	C_2'	$C_2^{..}$	Space Group Number			σ_h	σ_d	σ_v
				C_{2v}	$C_{2v}^{..}$	$C_{2v}^{..}$			
D_{4h}^l	191 D_{6h}^1	i	j, k	l, m, c, d	p, q		h, o	n	
192	D_{6h}^2	g, i	j	c, k	l				
193	D_{6h}^3	a, g	b, d, f, i	j					
194	D_{6h}^4	a, g, i	b, c, d, h	j	k, e, f				

	Space Group Number		C_2	C'_2	$3C_2$	$C_2, 2C'_2$
O^i	207	O^1	h	i, j		
	208	O^2	h, i, j	k, l	d	e, f
	209	O^3	i	g, h		d
	210	O^4	f	g		
	211	O^5	g	h, i		d
	212	O^6		d		
	213	O^7		d		
	214	O^8	f	g, h		c, d

	Space Group Number		C_2	$3C_2$	$C_2, 2C'_2$	C'_2, σ_h	C_2, σ_h	C_2, σ_d	σ_h	σ_d
O_h^i	221	O_h^1				i, j	h		k, l	m
	222	O_h^2		g		h				
	223	O_h^3		b		c, d, j	f, g, h		k	
	224	O_h^4	d, h		f	i, j		g	k	
	225	O_h^5			d	h, i		g	j	k
	226	O_h^6				c, h	e		i	
	227	O_h^7				h		f		g
	228	O_h^8		f		g				
	229	O_h^9				i, d, h	g		j	k
	230	O_h^{10}	f		c	g				

Appendix 6

Correlation Tables

We wish to express our gratitude for permission to reproduce these tables from the book of W. G. Fateley *et al.* for the use of their comprehensive tables (1). Reprinted with permission of John Wiley and Sons, Inc., New York.

C_4	C_2	C_6	C_3	C_2	C_1	D_2	C_2^z	C_2^y	C_2^x	D_3	C_3	C_2
A	A	A	A_1	A	A							
B	A	B	A	B	A	B_1	A	B	B	A_2	A	B
E	$2B$	E_1	E	$2B$	$2A$	B_2	B	A	B	E	E	$A + B$
		E_2	E	$2A$	$2A$	B_3	B	B	A			

D_4	C'_2 D_2	C''_2 D_2	C_4	C_2	C'_2 C_2	C''_2 C_2	D_5	C_5	C_2
A_1	A	A	A	A	A	A	A_1	A	A
A_2	B_1	B_1	A	A	B	B	A_2	A	B
B_1	A	B_1	B	A	A	B	E_1	E_1	$A + B$
B_2	B_1	A	B	A	B	A	E_2	E_2	$A + B$
E	$B_2 + B_3$	$B_2 + B_3$	E	$2B$	$A + B$	$A + B$			

D_6	C_6	C'_2 D_3	C''_2 D_3	D_2	C_3	C_2	C'_2 C_2	C''_2 C_2
A_1	A	A_1	A_1	A	A	A	A	A
A_2	A	A_2	A_2	B_1	A	A	B	B
B_1	B	A_1	A_2	B_2	A	B	A	B
B_2	B	A_2	A_1	B_3	A	B	B	A
E_1	E_1	E	E	$B_2 + B_3$	E	$2B$	$A + B$	$A + B$
E_2	E_2	E	E	$A + B_1$	E	$2A$	$A + B$	$A + B$

C_{2v}	$\sigma(zx)$			$\sigma(yz)$		
	C_2	C_s	C_s	C_{3v}	C_3	C_s
A_1	A	A'	A'	A_1	A	A'
A_2	A	A''	A''	A_2	A	A''
B_1	B	A'	A''	E	E	$A' + A''$
B_2	B	A''	A'			

C_{4v}	C_4	σ_v	σ_d	C_s	σ_v	σ_d
		C_{2v}	C_{2v}		C_s	C_s
A_1	A	A_1	A_1	A	A'	A'
A_2	A	A_2	A_2	A	A''	A''
B_1	B	A_1	A_2	A	A'	A''
B_2	B	A_2	A_1	A	A''	A'
E	E	$B_1 + B_2$	$B_1 + B_2$	$2B$	$A' + A''$	$A' + A''$

C_{5v}	C_5		C_s
	C_5	C_s	C_s
A_1	A	A'	
A_2	A	A''	
E_1	E_1	$A' + A''$	
E_2	E_2	$A' + A''$	

C_{6v}	C_6	σ_v	σ_d	$\sigma_v \rightarrow \sigma(zx)$	C_3	C_2	σ_v	σ_d
		C_{3v}	C_{3v}	C_{2v}			C_s	C_s
A_1	A	A_1	A_1	A_1	A	A	A'	A'
A_2	A	A_2	A_2	A_2	A	A	A''	A''
B_1	B	A_1	A_2	B_1	A	B	A'	A''
B_2	B	A_2	A_1	B_2	A	B	A''	A'
E_1	E_1	E	E	$B_1 + B_2$	E	$2B$	$A' + A''$	$A' + A''$
E_2	E_2	E	E	$A_1 + A_2$	E	$2A$	$A' + A''$	$A' + A''$

C_{2h}	C_2	C_s	C_i	C_{3h}	C_3	C_s	C_1	$C_{3i} \equiv S_6$	C_3	C_i	C_1
A_g	A	A'	A_g	A'	A	A'	A	A_g	A	A_g	A
B_g	B	A''	A_g	E'	E	$2A'$	$2A$	E_g	E	$2A_g$	$2A$
A_u	A	A''	A_u	A''	A	A''	A	A_u	A	A_u	A
B_u	B	A'	A_u	E''	E	$2A''$	$2A$	E_u	E	$2A_u$	$2A$

$C_{\infty v}$	C_{6v}	C_{4v}	C_{3v}	C_{2v}
$A_1 \equiv \Sigma^+$	A_1	A_1	A_1	A_1
$A_2 \equiv \Sigma^-$	A_2	A_2	A_2	A_2
$E_1 \equiv \Pi$	E_1	E	E	$B_1 + B_2$
$E_2 \equiv \Delta$	E_2	$B_1 + B_2$	E	$A_1 + A_2$
$E_3 \equiv \Phi$	$B_2 + B_1$	E	$A_1 + A_2$	$B_1 + B_2$
$E_4 \equiv \Gamma$	E_2	$A_1 + A_2$	E	$A_1 + A_2$
...				

$D_{\infty h}$	D_{6h}	C_{6v}	C_{3v}	D_{4h}	C_{4v}	C_{2v}	$C_{\infty v}$
Σ_g^+	A_{1g}	A_1	A_1	A_{1g}	A_1	A_1	$\Sigma^+ \equiv A_1$
Σ_g^-	A_{2g}	A_2	A_2	A_{2g}	A_2	A_2	$\Sigma^- \equiv A_2$
Π_g	E_{1g}	E_1	E	E_g	E	$B_1 + B_2$	$\Pi \equiv E_1$
Δ_g	E_{2g}	E_2	E	$B_{1g} + B_{2g}$	$B_1 + B_2$	$A_1 + A_2$	$\Delta \equiv E_2$
...							
Σ_u^+	A_{2u}	A_1	A_1	A_{2u}	A_1	A_1	$\Sigma^+ \equiv A_1$
Σ_u^-	A_{1u}	A_2	A_2	A_{1u}	A_2	A_2	$\Sigma^- \equiv A_2$
Π_u	E_{1u}	E_1	E	E_u	E	$B_1 + B_2$	$\Pi \equiv E_1$
Δ_u	E_{2u}	E_2	E	$B_{1u} + B_{2u}$	$B_1 + B_2$	$A_1 + A_2$	$\Delta \equiv E_2$
...							

C_{4h}	C_4	S_4	C_{2h}	C_2	C_s	C_i	C_1	C_{5h}	C_5	C_s	C_1
A_g	A	A	A_g	A	A'	A_g	A	A'	A	A'	A
B_g	B	B	A_g	A	A'	A_g	A	E'_1	E_1	$2A'$	$2A$
E_g	E	E	$2B_g$	$2B$	$2A''$	$2A_g$	$2A$	E'_2	E_2	$2A'$	$2A$
A_u	A	B	A_u	A	A''	A_u	A	A''	A	A''	A
B_u	B	A	A_u	A	A''	A_u	A	E''_1	E_1	$2A''$	$2A$
E_u	E	E	$2B_u$	$2B$	$2A'$	$2A_u$	$2A$	E''_2	E_2	$2A''$	$2A$

C_{6h}	C_6	C_{3h}	S_6	C_{2h}	C_3	C_2	C_s	C_i	C_1
A_g	A	A'	A_g	A_g	A	A	A'	A_g	A
B_g	B	A''	A_g	B_g	A	B	A''	A_g	A
E_{1g}	E_1	E''	E_g	$2B_g$	E	$2B$	$2A''$	$2A_g$	$2A$
E_{2g}	E_2	E'	E_g	$2A_g$	E	$2A$	$2A'$	$2A_g$	$2A$
A_u	A	A''	A_u	A_u	A	A	A''	A_u	A
B_u	B	A'	A_u	B_u	A	B	A'	A_u	A
E_{1u}	E_1	E'	E_u	$2B_u$	E	$2B$	$2A'$	$2A_u$	$2A$
E_{2u}	E_2	E''	E_u	$2A_u$	E	$2A$	$2A''$	$2A_u$	$2A$

D_{2h}	D_2	$C_2(z)$ C_{2v}	$C_2(y)$ C_{2v}	$C_2(x)$ C_{2v}	$C_2(z)$ C_{2h}	$C_2(y)$ C_{2h}	$C_2(x)$ C_{2h}
A_g	A	A_1	A_1	A_1	A_g	A_g	A_g
B_{1g}	B_1	A_2	B_2	B_1	A_g	B_g	B_g
B_{2g}	B_2	B_1	A_2	B_2	B_g	A_g	B_g
B_{3g}	B_3	B_2	B_1	A_2	B_g	B_g	A_g
A_u	A	A_2	A_2	A_2	A_u	A_u	A_u
B_{1u}	B_1	A_1	B_1	B_2	A_u	B_u	B_u
B_{2u}	B_2	B_2	A_1	B_1	B_u	A_u	B_u
B_{3u}	B_3	B_1	B_2	A_1	B_u	B_u	A_u

$D_{2h}(\text{cont.})$	$C_2(z)$ C_2	$C_2(y)$ C_2	$C_2(x)$ C_2	$\sigma(xy)$ C_s	$\sigma(zx)$ C_s	$\sigma(yz)$ C_s	C_i
A_g	A	A	A	A'	A'	A'	A_g
B_{1g}	A	B	B	A'	A''	A''	A_g
B_{2g}	B	A	B	A''	A'	A''	A_g
B_{3g}	B	B	A	A''	A''	A'	A_g
A_u	A	A	A	A''	A''	A''	A_u
B_{1u}	A	B	B	A''	A'	A'	A_u
B_{2u}	B	A	B	A'	A''	A'	A_u
B_{3u}	B	B	A	A'	A'	A''	A_u

D_{3h}	C_{3h}	D_3	C_{3v}	$\sigma_h \rightarrow \sigma_v(zy)$		C_3	C_2	σ_h	σ_v
				C_{2v}				C_s	C_s
A'_1	A'	A_1	A_1	A_1		A	A	A'	A'
A'_2	A'	A_2	B_2		A	B	A'	A''	
E'	E'	E	E	$A_1 + B_2$		E	$A + B$	$2A'$	$A' + A''$
A''_1	A''	A_1	A_2	A_2		A	A	A''	A''
A''_2	A''	A_2	A_1	B_1		A	B	A''	A'
E''	E''	E	E	$A_2 + B_1$		E	$A + B$	$2A''$	$A' + A''$

D_{4h}	D_4	C'_2 D_{2d}	C''_2 D_{2d}	C_{4v}	C_{4h}	C'_2 D_{2h}	C''_2 D_{2h}	C_4	S_4
A_{1g}	A_1	A_1	A_1	A_1	A_g	A_g	A_g	A	A
A_{2g}	A_2	A_2	A_2	A_2	A_g	B_{1g}	B_{1g}	A	A
B_{1g}	B_1	B_1	B_2	B_1	B_g	A_g	B_{1g}	B	B
B_{2g}	B_2	B_2	B_1	B_2	B_g	B_{1g}	A_g	B	B
E_g	E	E	E	E	E_g	$B_{2g} + B_{3g}$	$B_{2g} + B_{3g}$	E	E
A_{1u}	A_1	B_1	B_1	A_2	A_u	A_u	A_u	A	B
A_{2u}	A_2	B_2	B_2	A_1	A_u	B_{1u}	B_{1u}	A	B
B_{1u}	B_1	A_1	A_2	B_2	B_u	A_u	B_{1u}	B	A
B_{2u}	B_2	A_2	A_1	B_1	B_u	B_{1u}	A_u	B	A
E_u	E	E	E	E	E_u	$B_{2u} + B_{3u}$	$B_{2u} + B_{3u}$	E	E

D_{4h} (cont.)	C'_2 D_2	C''_2 D_2	C_{2v}, σ_v C_{2v}	C_{2v}, σ_d C_{2v}	C'_2 C_{2v}	C''_2 C_{2v}
A_{1g}	A	A	A_1	A_1	A_1	A_1
A_{2g}	B_1	B_1	A_2	A_2	B_1	B_1
B_{1g}	A	B_1	A_1	A_2	A_1	B_1
B_{2g}	B_1	A	A_2	A_1	B_1	A_1
E_g	$B_2 + B_3$	$B_2 + B_3$	$B_1 + B_2$	$B_1 + B_2$	$A_2 + B_2$	$A_2 + B_2$
A_{1u}	A	A	A_2	A_2	A_2	A_2
A_{2u}	B_1	B_1	A_1	A_1	B_2	B_2
B_{1u}	A	B_1	A_2	A_1	A_2	B_2
B_{2u}	B_1	A	A_1	A_2	B_2	A_2
E_u	$B_2 + B_3$	$B_2 + B_3$	$B_1 + B_2$	$B_1 + B_2$	$A_1 + B_1$	$A_1 + B_1$

D_{4h} (cont.)	C_2	C'_2	C''_2	C_2	C'_2	C''_2	σ_h	σ_v	σ_d	C_i
	C_{2h}	C_{2h}	C_{2h}	C_2	C_2	C_2	C_s	C_s	C_s	
A_{1g}	A_g	A_g	A_g	A	A	A	A'	A'	A'	A_g
A_{2g}	A_g	B_g	B_g	A	B	B	A'	A''	A''	A_g
B_{1g}	A_g	A_g	B_g	A	A	B	A'	A''	A''	A_g
B_{2g}	A_g	B_g	A_g	A	B	A	A'	A''	A'	A_g
E_g	$2B_g$	$A_g + B_g$	$A_g + B_g$	$2B$	$A + B$	$A + B$	$2A''$	$A' + A''$	$A' + A''$	$2A_g$
A_{1u}	A_u	A_u	A_u	A	A	A	A''	A''	A''	A_u
A_{2u}	A_u	B_u	B_u	A	B	B	A''	A'	A'	A_u
B_{1u}	A_u	A_u	B_u	A	A	B	A''	A''	A'	A_u
B_{2u}	A_u	B_u	A_u	A	B	A	A''	A'	A''	A_u
E_u	$2B_u$	$A_u + B_u$	$A_u + B_u$	$2B$	$A + B$	$A + B$	$2A'$	$A' + A''$	$A' + A''$	$2A_u$

D_{5h}	D_5	C_{5v}	C_{5h}	C_5	$\sigma_h \rightarrow \sigma(zx)$		σ_h	σ_v
					C_{2v}	C_2		
A'_1	A_1	A_1	A'	A	A_1	A	A'	A'
A'_2	A_2	A_2	A'	A	B_1	B	A'	A''
E'_1	E_1	E'_1	E'_1	$E_1 + B_2$	$A_1 + B_2$	$A + B$	$2A'$	$A' + A''$
E'_2	E_2	E'_2	E'_2	E_2	$A_1 + B_2$	$A + B$	$2A'$	$A' + A''$
A''_1	A_1	A_2	A''	A	A_2	A	A''	A''
A''_2	A_2	A_1	A''	A	B_2	B	A''	A'
E''_1	E_1	E_1	E''_1	E_1	$A_2 + B_2$	$A + B$	$2A''$	$A' + A''$
E''_2	E_2	E_2	E''_2	E_2	$A_2 + B_2$	$A + B$	$2A''$	$A' + A''$

D_{6h}	D_6	C'_2	C''_2	C_{6v}	C_{6h}	C''_2	C'_2	$\sigma_h \rightarrow \sigma(xy)$
		D_{3h}	D_{3h}			D_{3d}	D_{3d}	$\sigma_v \rightarrow \sigma(yz)$
A_{1g}	A_1	A'_1	A'_1	A_1	A_g	A_{1g}	A_{1g}	A_g
A_{2g}	A_2	A'_2	A'_2	A_2	A_g	A_{2g}	A_{2g}	B_{1g}
B_{1g}	B_1	A''_1	A''_2	B_2	B_g	A_{2g}	A_{1g}	B_{2g}
B_{2g}	B_2	A''_2	A''_1	B_1	B_g	A_{1g}	A_{2g}	B_{3g}
E_{1g}	E_1	E''	E''	E_1	E_{1g}	E_g	E_g	$B_{2g} + B_{3g}$
E_{2g}	E_2	E'	E'	E_2	E_{2g}	E_g	E_g	$A_g + B_{1g}$
A_{1u}	A_1	A''_1	A''_1	A_2	A_u	A_{1u}	A_{1u}	A_u
A_{2u}	A_2	A''_2	A''_2	A_1	A_u	A_{2u}	A_{2u}	B_{1u}
B_{1u}	B_1	A'_1	A'_2	B_1	B_u	A_{2u}	A_{1u}	B_{2u}
B_{2u}	B_2	A'_2	A'_1	B_2	B_u	A_{1u}	A_{2u}	B_{3u}
E_{1u}	E_1	E'	E'	E_1	E_{1u}	E_u	E_u	$B_{2u} + B_{3u}$
E_{2u}	E_2	E''	E''	E_2	E_{2u}	E_u	E_u	$A_u + B_{1u}$

D_{6h} (cont.)	C_6	C_{3h}	C'_2 D_3	C''_2 D_3	σ_v	σ_d	S_6	D_2
A_{1g}	A	A'	A_1	A_1	A_1	A_1	A_g	A
A_{2g}	A	A'	A_2	A_2	A_2	A_2	A_g	B_1
B_{1g}	B	A''	A_1	A_2	A_2	A_1	A_g	B_2
B_{2g}	B	A''	A_2	A_1	A_1	A_2	A_g	B_3
E_{1g}	E_1	E''	E	E	E	E	E_g	$B_2 + B_3$
E_{2g}	E_2	E'	E	E	E	E	E_g	$A + B_1$
A_{1u}	A	A''	A_1	A_1	A_2	A_2	A_u	A
A_{2u}	A	A''	A_2	A_2	A_1	A_1	A_u	B_1
B_{1u}	B	A'	A_1	A_2	A_1	A_2	A_u	B_2
B_{2u}	B	A'	A_2	A_1	A_2	A_1	A_u	B_3
E_{1u}	E_1	E'	E	E	E	E	E_u	$B_2 + B_3$
E_{2u}	E_2	E''	E	E	E	E	E_u	$A + B_1$

D_{6h} (cont.)	C_2 C_{2v}	C'_2 C_{2v}	C''_2 C_{2v}	C_2 C_{2h}	C'_2 C_{2h}	C''_2 C_{2h}	C_3	C_2 C_2
A_{1g}	A_1	A_1	A_1	A_g	A_g	A_u	A	A
A_{2g}	A_2	B_2	B_1	A_g	B_g	B_g	A	A
B_{1g}	B_1	A_2	B_2	B_g	A_g	B_g	A	B
B_{2g}	B_2	B_1	A_2	B_g	B_g	A_g	A	B
E_{1g}	$B_1 + B_2$	$A_2 + B_1$	$A_2 + B_2$	$2B_g$	$A_g + B_g$	$A_g + B_g$	E	$2B$
E_{2g}	$A_1 + A_2$	$A_1 + B_2$	$A_1 + B_1$	$2A_g$	$A_g + B_g$	$A_g + B_g$	E	$2A$
A_{1u}	A_2	A_2	A_2	A_u	A_u	A_u	A	A
A_{2u}	A_1	B_1	B_2	A_u	B_u	B_u	A	A
B_{1u}	B_2	A_1	B_1	B_u	A_u	B_u	A	B
B_{2u}	B_1	B_2	A_1	B_u	B_u	A_u	A	B
E_{1u}	$B_2 + B_1$	$A_1 + B_2$	$A_1 + B_1$	$2B_u$	$A_u + B_u$	$A_u + B_u$	E	$2B$
E_{2u}	$A_2 + A_1$	$A_2 + B_1$	$A_2 + B_2$	$2A_u$	$A_u + B_u$	$A_u + B_u$	E	$2A$

D_{6h} (cont.)	C'_2 C_2	C''_2 C_2	σ_h C_s	σ_d C_s	σ_v C_s	C_i
A_{1g}	A	A	A'	A'	A'	A_g
A_{2g}	B	B	A'	A''	A''	A_g
B_{1g}	A	B	A''	A'	A''	A_g
B_{2g}	B	A	A''	A''	A'	A_g
E_{1g}	$A + B$	$A + B$	$2A''$	$A' + A''$	$A' + A''$	$2A_g$
E_{2g}	$A + B$	$A + B$	$2A'$	$A' + A''$	$A' + A''$	$2A_g$
A_{1u}	A	A	A''	A''	A''	A_u
A_{2u}	B	B	A''	A'	A'	A_u
B_{1u}	A	B	A'	A''	A'	A_u
B_{2u}	B	A	A'	A'	A''	A_u
E_{1u}	$A + B$	$A + B$	$2A'$	$A' + A''$	$A' + A''$	$2A_u$
E_{2u}	$A + B$	$A + B$	$2A''$	$A' + A''$	$A' + A''$	$2A_u$

D_{2d}	$C_2 \rightarrow C_2(z)$			C_2	C'_2	C_s
	S_4	D_2	C_{2v}	C_2	C_2	
A_1	A	A	A_1	A	A	A'
A_2	A	B_1	A_2	A	B	A''
B_1	B	A	A_2	A	A	A''
B_2	B	B_1	A_1	A	B	A'
E	E	$B_2 + B_3$	$B_1 + B_2$	$2B$	$A + B$	$A' + A''$

D_{3d}	D_3	C_{3v}	S_6	C_3	C_{2h}	C_2	C_s	C_i
A_{1g}	A_1	A_1	A_g	A	A_g	A	A'	A_g
A_{2g}	A_2	A_2	A_g	A	B_g	B	A''	A_g
E_g	E	E	E_g	E	$A_g + B_g$	$A + B$	$A' + A''$	$2A_g$
A_{1u}	A_1	A_2	A_u	A	A_u	A	A''	A_u
A_{2u}	A_2	A_1	A_u	A	B_u	B	A'	A_u
E_u	E	E	E_u	E	$A_u + B_u$	$A + B$	$A' + A''$	$2A_u$

D_{4d}	D_4	C_{4v}	S_8	C_4	C_{2v}	C_2	C'_2	C_s
						C_2	C'_2	
A_1	A_1	A_1	A	A	A_1	A	A	A'
A_2	A_2	A_2	A	A	A_2	A	B	A''
B_1	A_1	A_2	B	A	A_2	A	A	A''
B_2	A_2	A_1	B	A	A_1	A	B	A'
E_1	E	E	E_1	E	$B_1 + B_2$	$2B$	$A + B$	$A' + A''$
E_2	$B_1 + B_2$	$B_1 + B_2$	E_2	$2B$	$A_1 + A_2$	$2A$	$A + B$	$A' + A''$
E_3	E	E	E_3	E	$B_1 + B_2$	$2B$	$A + B$	$A' + A''$

D_{5d}	D_5	C_{5v}	C_5	C_2	C_s	C_i
A_{1g}	A_1	A_1	A	A	A'	A_g
A_{2g}	A_2	A_2	A	B	A''	A_g
E_{1g}	E_1	E_1	E_1	$A + B$	$A' + A''$	$2A_g$
E_{2g}	E_2	E_2	E_2	$A + B$	$A' + A''$	$2A_g$
A_{1u}	A_1	A_2	A	A	A''	A_u
A_{2u}	A_2	A_1	A	B	A'	A_u
E_{1u}	E_1	E_1	E_1	$A + B$	$A' + A''$	$2A_u$
E_{2u}	E_2	E_2	E_2	$A + B$	$A' + A''$	$2A_u$

D_{6d}	D_6	C_{6v}	C_6	D_{2d}	D_3	C_{3v}
A_1	A_1	A_1	A	A_1	A_1	A_1
A_2	A_2	A_2	A	A_2	A_2	A_2
B_1	A_1	A_2	A	B_1	A_1	A_2
B_2	A_2	A_1	A	B_2	A_2	A_1
E_1	E_1	E_1	E_1	E	E	E
E_2	E_2	E_2	E_2	$B_1 + B_2$	E	E
E_3	$B_1 + B_2$	$B_1 + B_2$	$2B$	E	$A_1 + A_2$	$A_1 + A_2$
E_4	E_2	E_2	E_2	$A_1 + A_2$	E	E
E_5	E_1	E_1	E_1	E	E	E

D_{6d} (cont.)		D_2	C_{2v}	S_4	C_3	C_2	C'_2	C_2	C_s
A_1		A	A_1	A	A	A	A	A	A'
A_2		B_1	A_2	A	A	A	B	A''	
B_1		A	A_2	B	A	A	A	A''	
B_2		B_1	A_1	B	A	A	B	A'	
E_1		$B_2 + B_3$	$B_1 + B_2$	E	E	$2B$	$A + B$	$A' + A''$	
E_2		$A + B_1$	$A_1 + A_2$	$2B$	E	$2A$	$A + B$	$A' + A''$	
E_3		$B_2 + B_3$	$B_1 + B_2$	E	$2A$	$2B$	$A + B$	$A' + A''$	
E_4		$A + B_1$	$A_1 + A_2$	$2A$	E	$2A$	$A + B$	$A' + A''$	
E_5		$B_2 + B_3$	$B_1 + B_2$	E	E	$2B$	$A + B$	$A' + A''$	

S_4	C_2	C_1	S_8	C_4	C_2	C_1
A						
B	A	A	B	A	A	A
E	$2B$	$2A$	E_1	E	$2B$	$2A$

T	D_2	C_3	C_2	C_1
A	A	A	A	A
E	$2A$	E	$2A$	$2A$
F	$B_1 + B_2 + B_3$	$A + E$	$A + 2B$	$3A$

T_h	T	D_{2h}	S_6	D_2
A_g	A	A_g	A_g	A
E_g	E	$2A_g$	E_g	$2A$
F_g	F	$B_{1g} + B_{2g} + B_{3g}$	$A_g + E_g$	$B_1 + B_2 + B_3$
A_u	A	A_u	A_u	A
E_u	E	$2A_u$	E_u	$2A$
F_u	F	$B_{1u} + B_{2u} + B_{3u}$	$A_u + E_u$	$B_1 + B_2 + B_3$

T_h (cont.)	C_{2v}	C_{2h}	C_3	C_2	C_s	C_i	C_1
A_g	A_1	A_g	A	A	A'	A_g	A
E_g	$2A_1$	$2A_g$	E	$2A$	$2A'$	$2A_g$	$2A$
F_g	$A_2 + B_1 + B_2$	$A_g + 2B_g$	$A + E$	$A + 2B$	$A' + 2A''$	$3A_g$	$3A$
A_u	A_2	A_u	A	A	A''	A_u	A
E_u	$2A_2$	$2A_u$	E	$2A$	$2A''$	$2A_u$	$2A$
F_u	$A_1 + B_1 + B_2$	$A_u + 2B_u$	$A + E$	$A + 2B$	$2A' + A''$	$3A_u$	$3A$

T_d	T	D_{2d}	C_{3v}	S_4	D_2	C_{2v}
A_1	A	A_1	A_1	A	A	A_1
A_2	A	B_1	A_2	B	A	A_2
E	E	$A_1 + B_1$	E	$A + B$	$2A$	$A_1 + A_2$
F_1	F	$A_2 + E$	$A_2 + E$	$A + E$	$B_1 + B_2 + B_3$	$A_2 + B_1 + B_2$
F_2	F	$B_2 + E$	$A_1 + E$	$B + E$	$B_1 + B_2 + B_3$	$A_1 + B_1 + B_2$

T_d (cont.)	C_3	C_2	C_s
A_1	A	A	A'
A_2	A	A	A''
E	E	$2A$	$A' + A''$
F_1	$A + E$	$A + 2B$	$A' + 2A''$
F_2	$A + E$	$A + 2B$	$2A' + A''$

O	T	D_4	D_3	C_4	$3C_2$	$C_2, 2C'_2$	D_2
A_1	A	A_1	A_1	A	A	A	
A_2	A	B_1	A_2	B	A	B_1	
E	E	$A_1 + B_1$	E	$A + B$	$2A$	$A + B_1$	
F_1	F	$A_2 + E$	$A_2 + E$	$A + E$	$B_1 + B_2 + B_3$	$B_1 + B_2 + B_3$	
F_2	F	$B_2 + E$	$A_1 + E$	$B + E$	$B_1 + B_2 + B_3$	$A + B_2 + B_3$	

O (cont.)	C_3	C_2	C'_2
A_1	A	A	A
A_2	A	A	B
E	E	$2A$	$A + B$
F_1	$A + E$	$A + 2B$	$A + 2B$
F_2	$A + E$	$A + 2B$	$2A + B$

O_h	O	T_d	T_h	T	D_{4h}	D_{3d}	C_{3v}	D_3	$C_{3i} \equiv S_6$
A_{1g}	A_1	A_1	A_g	A	A_{1g}	A_{1g}	A_1	A_1	A_g
A_{2g}	A_2	A_2	A_g	A	B_{1g}	A_{2g}	A_2	A_2	A_g
E_g	E	E	E_g	E	$A_{1g} + B_{1g}$	E_g	E	E	E_g
F_{1g}	F_1	F_1	F_g	F	$A_{2g} + E_g$	$A_{2g} + E_g$	$A_2 + E$	$A_2 + E$	$A_g + E_g$
F_{2g}	F_2	F_2	F_g	F	$B_{2g} + E_g$	$A_{1g} + E_g$	$A_1 + E$	$A_1 + E$	$A_g + E_g$
A_{1u}	A_1	A_2	A_u	A	A_{1u}	A_{1u}	A_2	A_1	A_u
A_{2u}	A_2	A_1	A_u	A	B_{1u}	A_{2u}	A_1	A_2	A_u
E_u	E	E	E_u	E	$A_{1u} + B_{1u}$	E_u	E	E	E_u
F_{1u}	F_1	F_2	F_u	F	$A_{2u} + E_u$	$A_{2u} + E_u$	$A_1 + E$	$A_2 + E$	$A_u + E_u$
F_{2u}	F_2	F_1	F_u	F	$B_{2u} + E_u$	$A_{1u} + E_u$	$A_2 + E$	$A_1 + E$	$A_u + E_u$

O_h (cont.)	C_3	C_2, σ_d D_{2d}	C'_2, σ_h D_{2d}	C_{4v}	D_4	C_{4h}	S_4	C_4
A_{1g}	A	A_1	A_1	A_1	A_1	A_g	A	A
A_{2g}	A	B_1	B_2	B_1	B_1	B_g	B	B
E_g	E	$A_1 + B_1$	$A_1 + B_2$	$A_1 + B_1$	$A_1 + B_1$	$A_g + B_g$	$A + B$	$A + B$
F_{1g}	$A + E$	$A_2 + E$	$A_2 + E$	$A_2 + E$	$A_2 + E$	$A_g + E_g$	$A + E$	$A + E$
F_{2g}	$A + E$	$B_2 + E$	$B_1 + E$	$B_2 + E$	$B_2 + E$	$B_g + E_g$	$B + E$	$B + E$
A_{1u}	A	B_1	B_1	A_2	A_1	A_u	B	A
A_{2u}	A	A_1	A_2	B_2	B_1	B_u	A	B
E_u	E	$A_1 + B_1$	$A_2 + B_1$	$A_2 + B_2$	$A_1 + B_1$	$A_u + B_u$	$A + B$	$A + B$
F_{1u}	$A + E$	$B_2 + E$	$B_2 + E$	$A_1 + E$	$A_2 + E$	$A_u + E_u$	$B + E$	$B + E$
F_{2u}	$A + E$	$A_2 + E$	$A_1 + E$	$B_1 + E$	$B_2 + E$	$B_u + E_u$	$A + E$	$B + E$

^aTo find correlations with smaller subgroups, carry out the correlation in two steps: for example, if the correlation of O_h with C_{2v} is desired, use the table to pass from O_h to T_d and then employ the table for T_d to go on to C_{2v} .

O_h (cont.)	$3C_2$ D_{2h}	$C_2, 2C'_2$ D_{2h}	C_2, σ_h C_{2v}	C_2, σ_d C_{2v}
A_{1g}	A_g	A_g	A_1	A_1
A_{2g}	A_g	B_{1g}	A_1	A_2
E_g	$2A_g$	$A_g + B_{1g}$	$2A_1$	$A_1 + A_2$
F_{1g}	$B_{1g} + B_{2g} + B_{3g}$	$B_{1g} + B_{2g} + B_{3g}$	$A_2 + B_1 + B_2$	$A_2 + B_1 + B_2$
F_{2g}	$B_{1g} + B_{2g} + B_{3g}$	$A_{1g} + B_{2g} + B_{3g}$	$A_2 + B_1 + B_2$	$A_1 + B_1 + B_2$
A_{1u}	A_u	A_u	A_2	A_2
A_{2u}	A_u	B_{2u}	A_2	A_1
E_u	$2A_u$	$A_u + B_{1u}$	$2A_2$	$A_1 + A_2$
F_{1u}	$B_{1u} + B_{2u} + B_{3u}$	$B_{1u} + B_{2u} + B_{3u}$	$A_1 + B_1 + B_2$	$A_1 + B_1 + B_2$
F_{2u}	$B_{1u} + B_{2u} + B_{3u}$	$A_u + B_{2u} + B_{3u}$	$A_1 + B_1 + B_2$	$A_2 + B_1 + B_2$

O_h (cont.)	C'_2, σ_h C_{2v}	$3C_2$ D_2	$C_2, 2C'_2$ D_2	C_2, σ_h C_{2h}	C'_2, σ_h C_{2h}
A_{1g}	A_1	A	A	A_g	A_g
A_{2g}	B_1	A	B_1	A_g	B_g
E_g	$A_1 + B_1$	$2A$	$A + B_1$	$2A_g$	$A_g + B_g$
F_{1g}	$A_2 + B_1 + B_2$	$B_1 + B_2 + B_3$	$B_1 + B_2 + B_3$	$A_g + 2B_g$	$A_g + 2B_g$
F_{2g}	$A_1 + A_2 + B_2$	$B_1 + B_2 + B_3$	$A + B_2 + B_3$	$A_g + 2B_g$	$2A_g + B_g$
A_{1u}	A_2	A	A	A_u	A_u
A_{2u}	B_2	A	B_1	A_u	B_u
E_u	$A_2 + B_2$	$2A$	$A + B_1$	$2A_u$	$A_u + B_u$
F_{1u}	$A_1 + B_1 + B_2$	$B_1 + B_2 + B_3$	$B_1 + B_2 + B_3$	$A_u + 2B_u$	$A_u + 2B_u$
F_{2u}	$A_1 + A_2 + B_1$	$B_1 + B_2 + B_3$	$A + B_2 + B_3$	$A_u + 2B_u$	$2A_u + B_u$

O_h (cont.)	σ_h C_s	σ_d C_s	C_2 C_2	C'_2 C_2	C_i	C_1
A_{1g}	A'	A'	A	A	A_g	A
A_{2g}	A'	A''	A	B	A_g	A
E_g	$2A'$	$A' + A''$	$2A$	$A + B$	$2A_g$	$2A$
F_{1g}	$A' + A''$	$A' + 2A''$	$A + 2B$	$A + 2B$	$3A_g$	$3A$
F_{2g}	$A' + 2A''$	$2A' + A''$	$A + 2B$	$2A + B$	$3A_g$	$3A$
A_{1u}	A''	A''	A	A	A_u	A
A_{2u}	A''	A'	A	B	A_u	A
E_u	$2A''$	$A' + A''$	$2A$	$A + B$	$2A_u$	$2A$
F_{1u}	$2A' + A''$	$2A' + A''$	$A + 2B$	$A + 2B$	$3A_u$	$3A$
F_{2u}	$2A' + A''$	$A' + 2A''$	$A + 2B$	$2A + B$	$3A_u$	$3A$

I_h	I	C_5	C_3	C_2	C_1
A_g	A	A	A	A	A
A_u	A	A	A	A	A
F_{1g}	F_1	$A + E_1$	$A + E$	$A + 2B$	$3A$
F_{1u}	F_1	$A + E_1$	$A + E$	$A + 2B$	$3A$
F_{2g}	F_2	$A + E_2$	$A + E$	$A + 2B$	$3A$
F_{2u}	F_2	$A + E_2$	$A + E$	$A + 2B$	$3A$
G_{1g}	G_1	$E_1 + E_2$	$2A + E$	$2A + 2B$	$4A$
G_{1u}	G_1	$E_1 + E_2$	$2A + E$	$2A + 2B$	$4A$
H_g	H	$A + E_1 + E_2$	$A + 2E$	$3A + 2B$	$5A$
H_u	H	$A + E_1 + E_2$	$A + 2E$	$3A + 2B$	$5A$

References

- W. G. Fateley, F. R. Dollish, N. T. McDevitt, and F. F. Bentley, "Infrared and Raman Selection Rules for Molecular and Lattice Vibrations: The Correlation Method." Wiley-Interscience, New York, 1972.

Appendix 7

Principle of Laser Action

The principle of laser action is based on “population inversion.” At thermal equilibrium, the ratio of populations at the ground and excited states is determined by the Maxwell–Boltzmann distribution law (Section 1.3). Namely, the population at the excited state decreases exponentially as the transition energy ($h\nu$) increases. To maintain such equilibrium, molecules at the excited state revert to the ground state by emitting photons of $h\nu$ (spontaneous emission). Thus, the population at the ground state is always larger than that in the excited state. Under such a circumstance, a photon of $h\nu$ is more likely to be absorbed by the ground state species than to stimulate emission from the excited state. “Stimulated emission” occurs when the population at the excited state becomes larger than that in the ground state (population inversion). Then, the first few spontaneously emitted photons “stimulate” emissions of others, leading to a cascade of emissions that have the same energy ($h\nu$) and phase as the original photon. The population inversion can be created by combining a laser medium (gas/liquid/solid) with a power supply (flash lamp, electrical discharge, etc.), and the laser beam thus obtained is amplified by trapping it in an optical cavity (resonator).

The structure of a CW gas laser has been shown in Section 2.2. In the He–Ne laser, He (1 mm Hg) and Ne (0.1 mm Hg) gases are mixed in the plasma tube. As shown in Fig. 1, the He atoms are excited to the 1S and 3S states by electrical discharge to create population inversion. Collisions of these excited state He atoms with Ne atoms produce excited-state Ne atoms, which produce stimulated emission at 632.8 and 1,152.3 nm. The latter is eliminated by using a prism. In an Ar-ion laser, the population inversion is created by collision with energetic electrons, and the excited-state Ar ion emits a series of lines, including those of 488.0 and 514.5 nm.

In the case of a Nd:YAG (*neodymium-doped yttrium aluminum garnet*), the Nd^{3+} ion doped in a YAG crystal is excited to the $^4F_{3/2}$ state by flash lamp. Then, the transition from this state to the $^4I_{11/2}$ state produces a laser beam at 1,064 nm. This beam is converted into giant pulses with huge power and narrow width by using the Q-switching, cavity-dumping and mode locking techniques (1). For example, a Quanta-Ray DCR-3 Nd:YAG

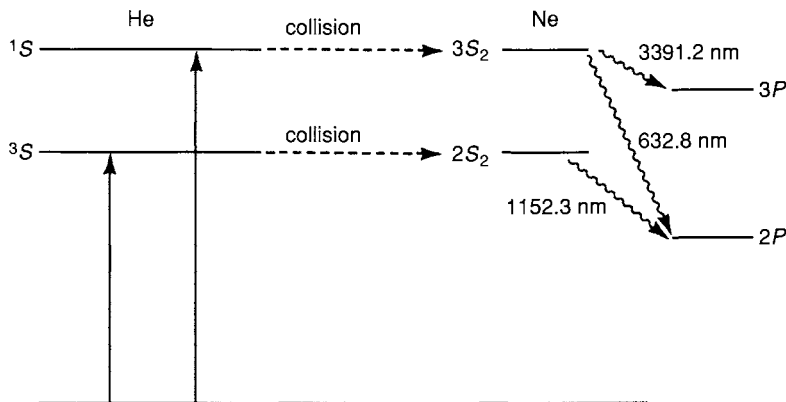


Figure 1

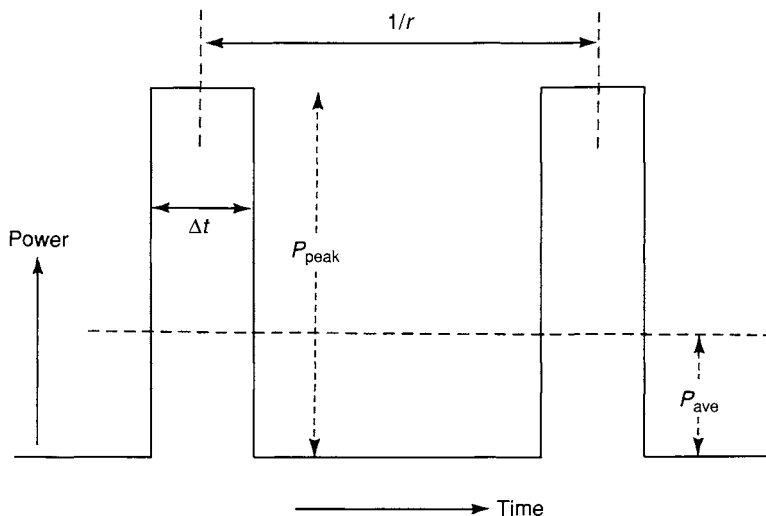


Figure 2

(Q-switching) laser provides pulses that have 7–9 ns width, ~ 100 MW peak power and an optimum repetition rate of 20 Hz.

Figure 2 shows the relationship between the peak power and the average power. It is seen that

$$P_{\text{ave}} = P_{\text{peak}} \times r \times \Delta t,$$

where r is the repetition rate and Δt is the pulse width. In the case of a CW laser, $r = 1$ and $\Delta t = 1$. Thus,

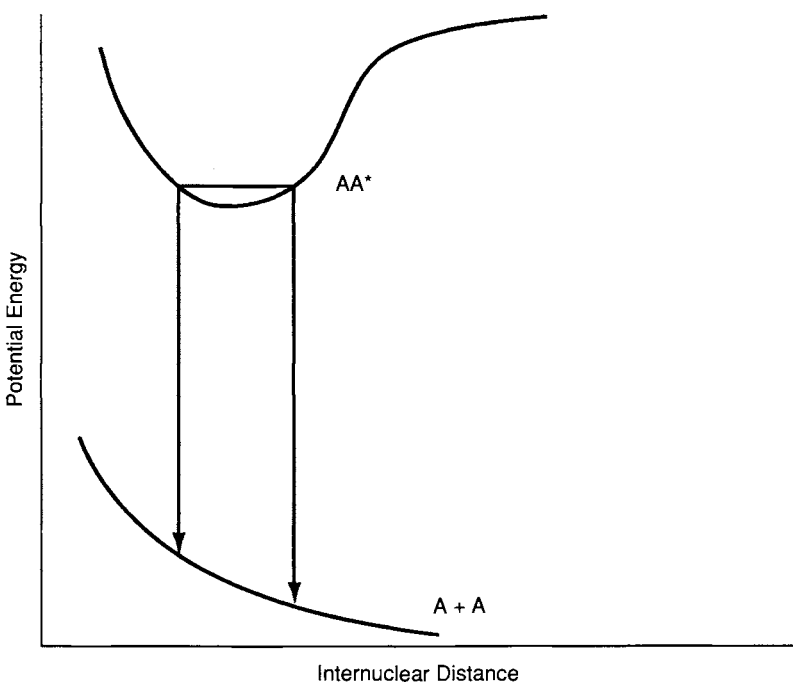


Figure 3

$$P_{\text{ave}} = P_{\text{peak}}$$

The structure of a dye laser is basically the same as that of a gas laser except that a circulating dye solution is used instead of a gas. Large organic dye molecules such as rhodamine 6G exhibit strong absorption bands ($\pi-\pi^*$ transitions) in the visible region. An energy level diagram of such a dye may be represented by Fig. 3-23 in Chapter 3. The absorption band due to $S_0(v=0) \rightarrow S_1(v'=0, 1, 2, \dots)$ transitions is broad and continuous because each electronic level is accompanied by a series of vibrational levels that are blurred by rotational and collisional broadening. Molecules excited to various sublevels of S_1 fall to the $v'=0$ state via radiationless transitions, and then revert to $S_0(v=0, 1, 2, \dots)$ to give fluorescence. Some S_1 state molecules fall to T_1 (triplet) state via intersystem crossing and cause phosphorescence ($T_1 \rightarrow S_0$ transitions), which limits dye performance. If a dye solution is irradiated by a strong laser beam or flash lamp, "population inversion" is created, and stimulated emission occurs from all occupied levels of S_1 , resulting in a strong but broad fluorescence band. This emission can be confined into a narrow, selective wavelength region by adding wavelength selective devices to the dye cavity.

The principle of excimer lasers is based on the fact that rare gas atoms such as Kr and Xe can form molecules, “excimers,” at their electronic excited states (Fig. 3). If rare gases at high pressures are irradiated by rapid electrical discharge, the resulting “population inversion” produces tunable, high-power pulsed laser beams in the vacuum UV region (Kr_2^* , 146 nm; Xe_2^* , 172 nm). Rare-gas halide excimers provide laser lines in the UV region (KrCl^* , 222 nm; KrF^* , 249 nm; XeCl^* , 308 nm; and XeF^* , 351 nm).

For more information, the reader should consult reference books and review articles concerning lasers.

References

1. C. Breck Hitz, “Understanding LASER Technology.” PennWell Publishing Co., Tulsa, Oklahoma, 1985.
2. For example, J. Hecht, “The Laser Guidebook.” McGraw-Hill, New York, 1986.
3. For example, J. C. Wright and M. J. Wirth, *Anal. Chem.* **52**, 1087A (1980).

Appendix 8

Raman Spectra of Typical Solvents

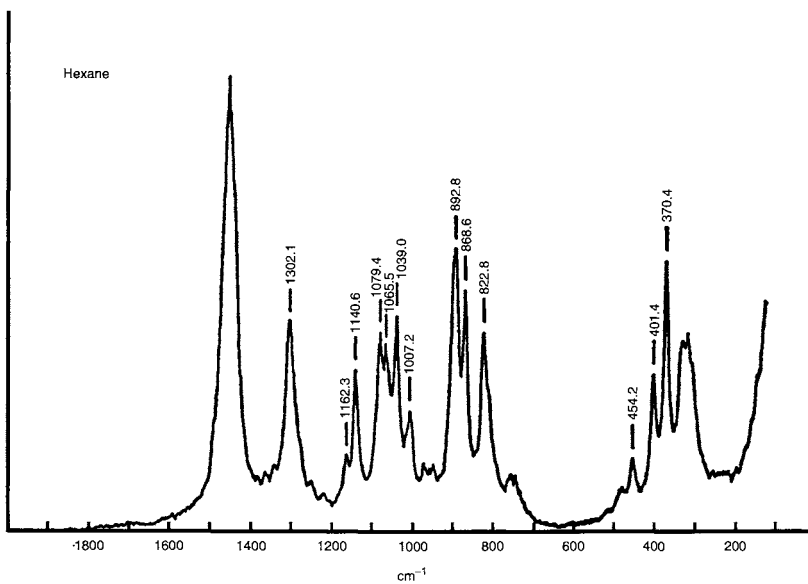
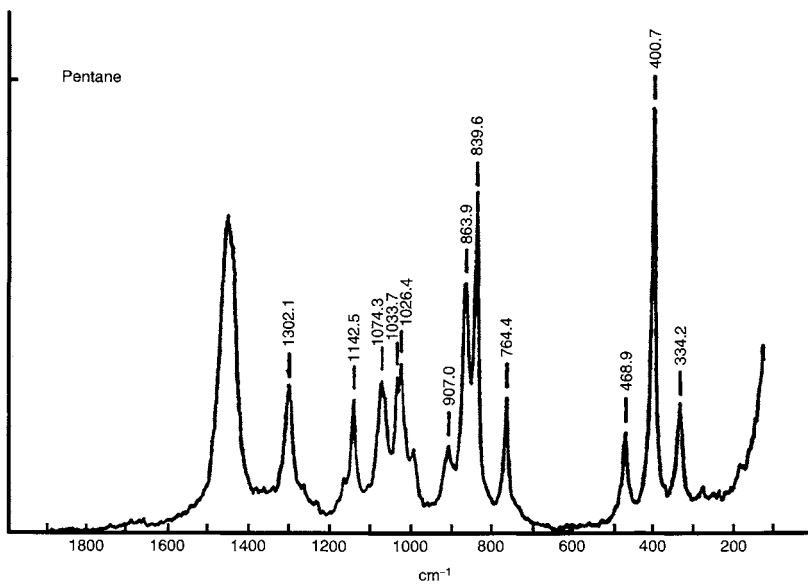
The Raman spectra shown here were reproduced with permission from H. Hamaguchi and A. Hirakawa, "Raman Spectroscopic Methods," Gakukai Shupan Center and Japan Spectroscopy Society, Tokyo, 1988. The following experimental conditions were employed:

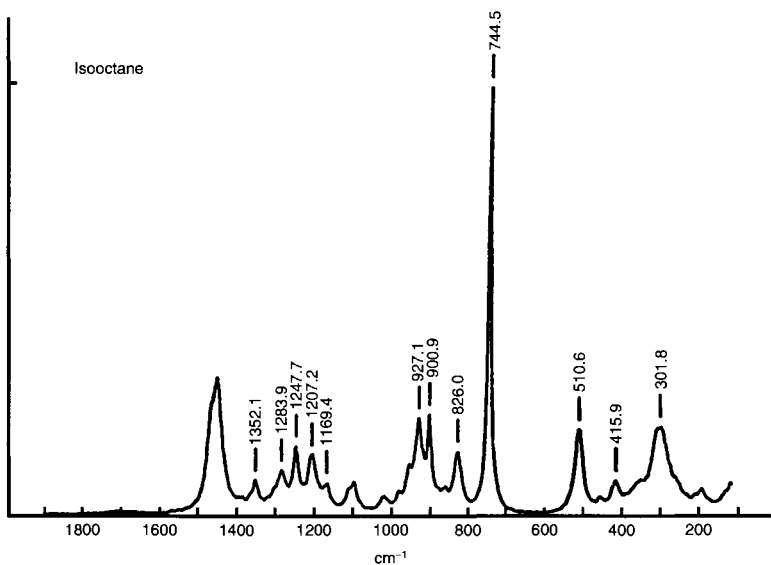
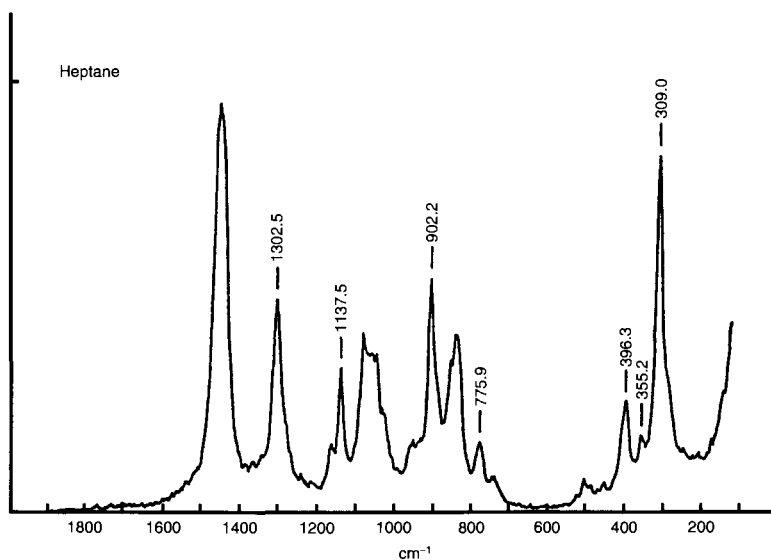
Source: Coherent CR-2 Ar-ion laser, 488.0 nm, \sim 100 mW.

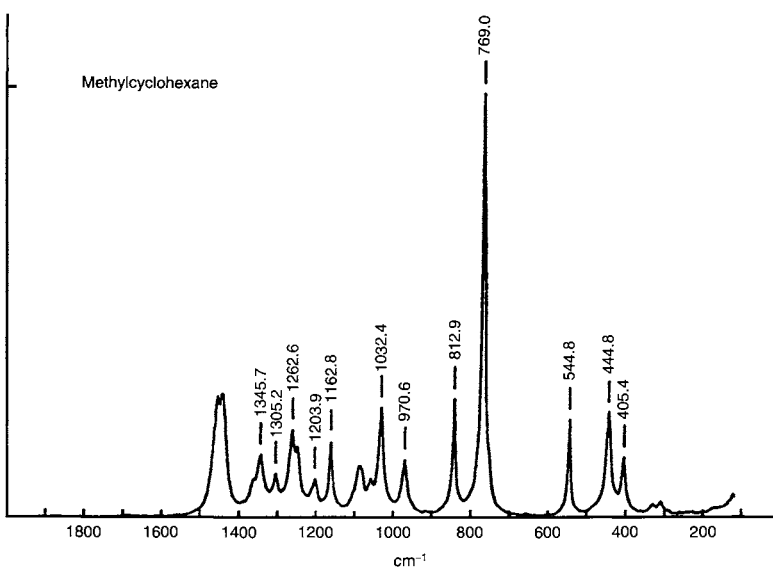
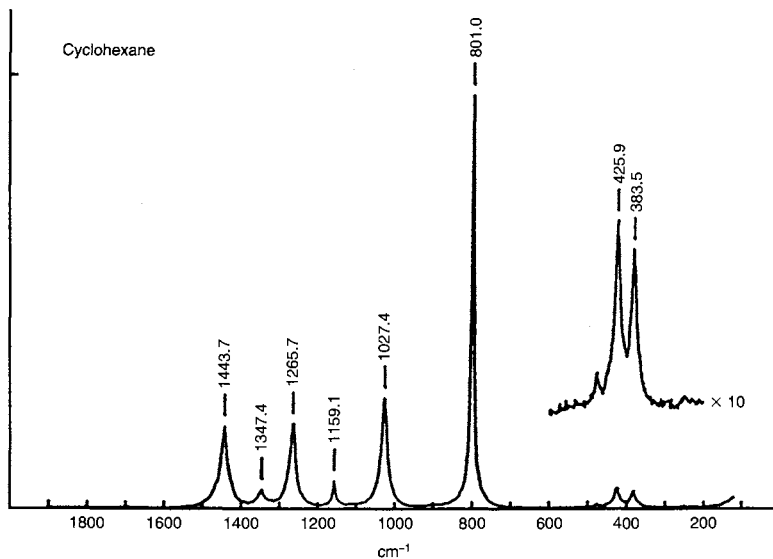
Spectrometer: Spex Model 1877 triple polychromator with $100 \mu\text{m}$ slit width (resolution, $\sim 5 \text{ cm}^{-1}$)

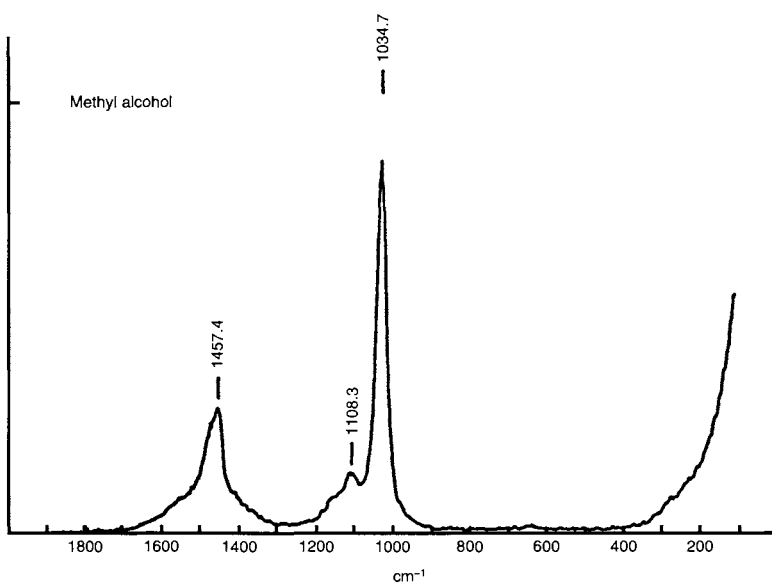
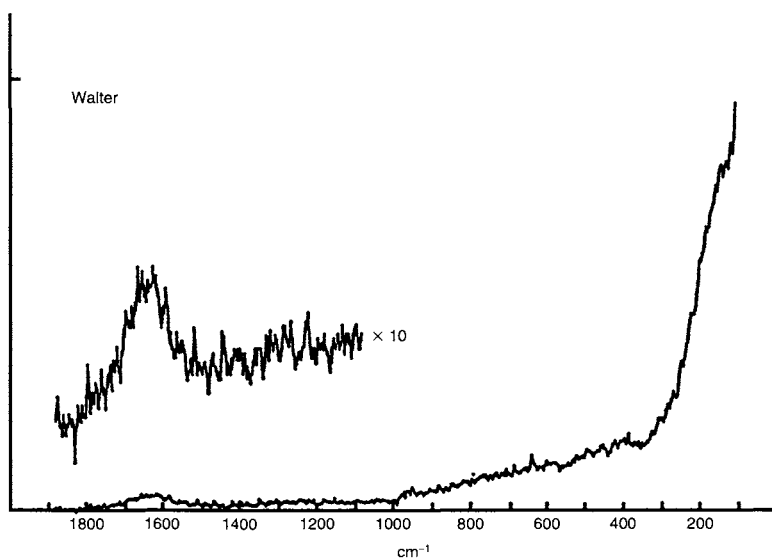
Detector: PAR OMA-III System with Model 1420 intensified diode array detector

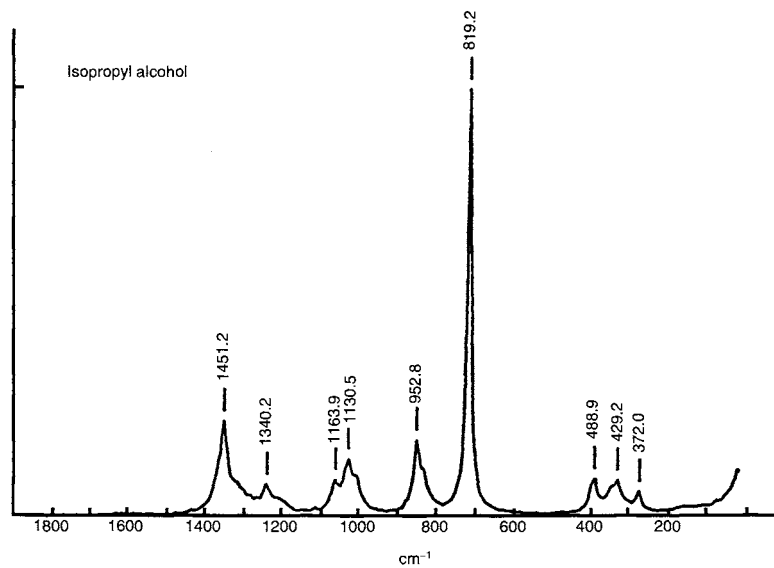
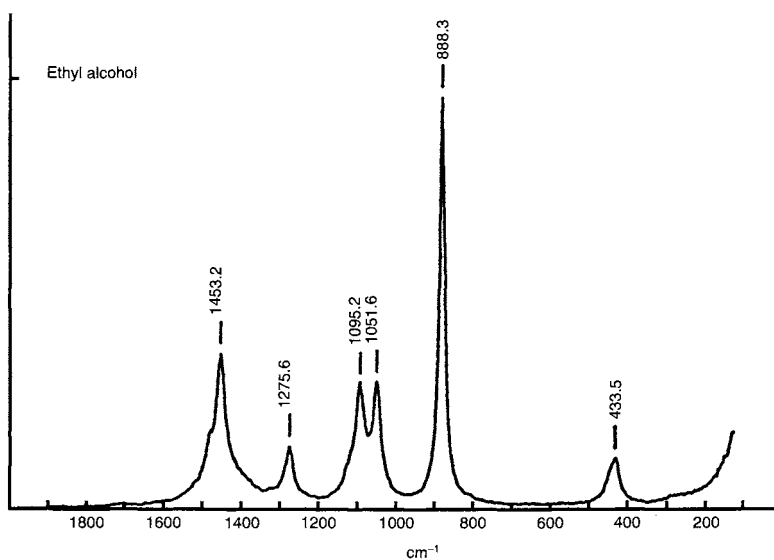
Frequency calibrations were made by using Ne emission lines. Accuracy of wavenumbers given in the Figures is $\pm 1 \text{ cm}^{-1}$.

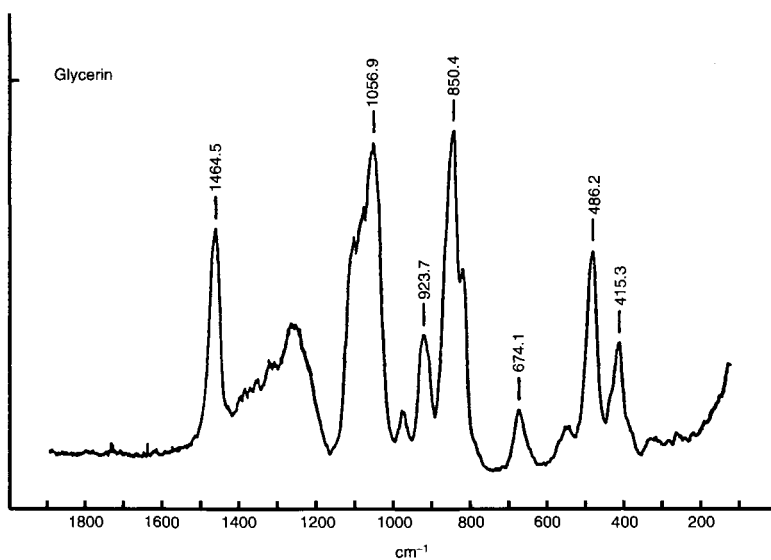
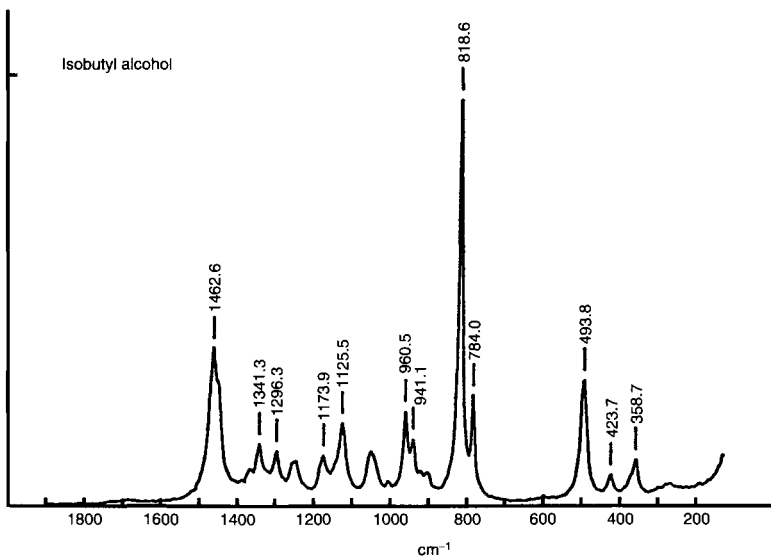


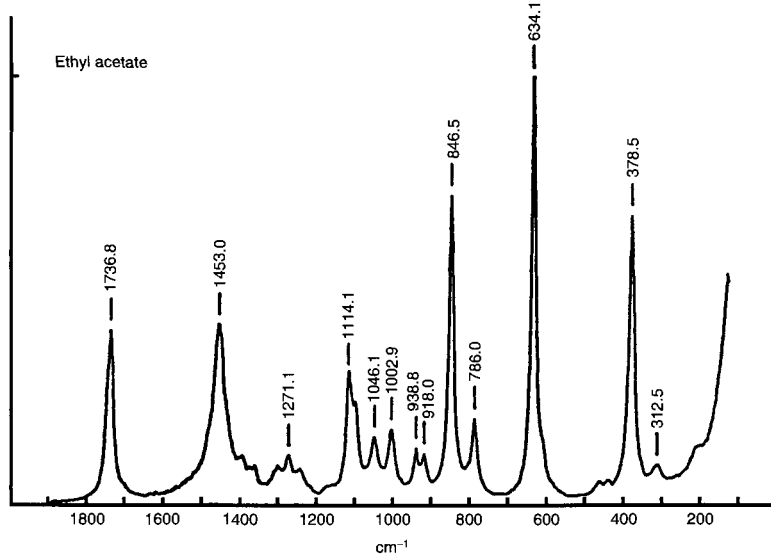
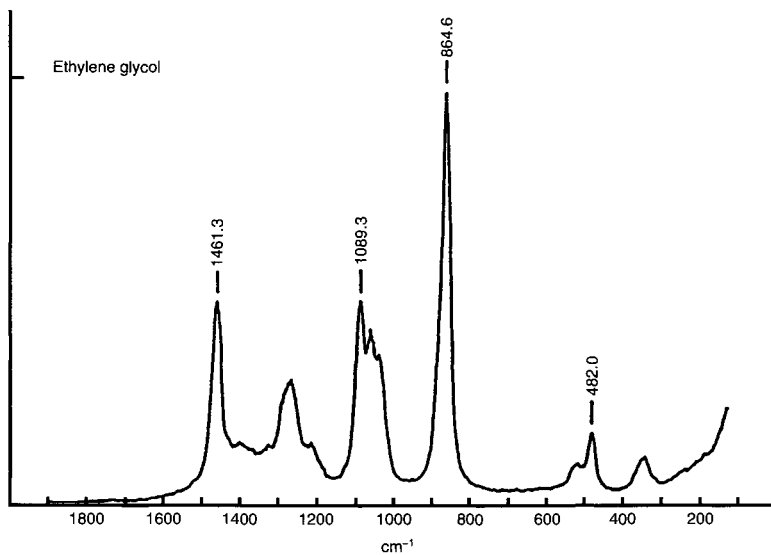


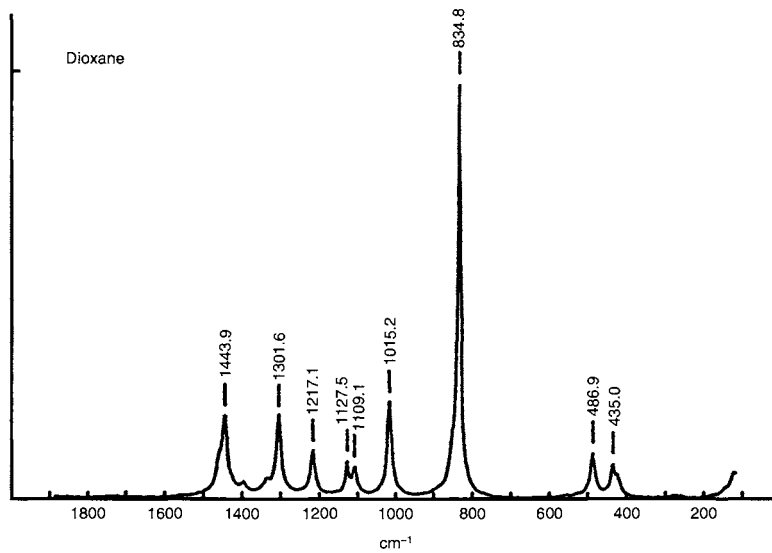
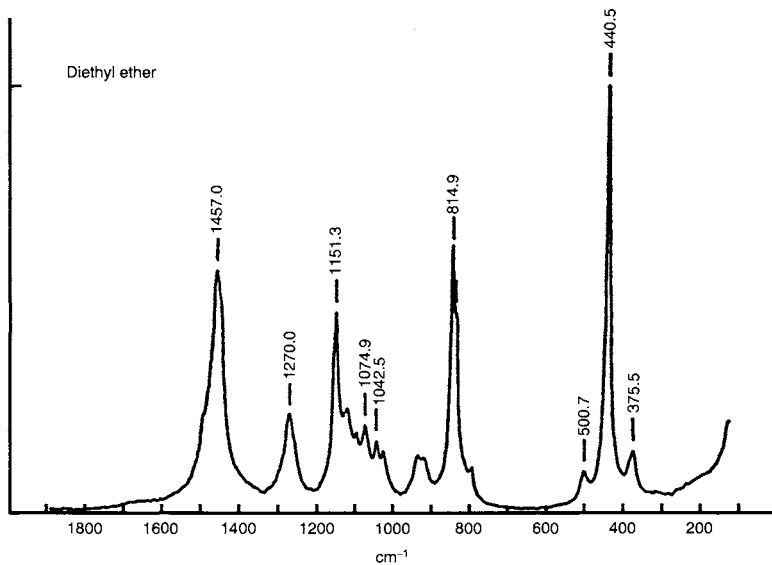


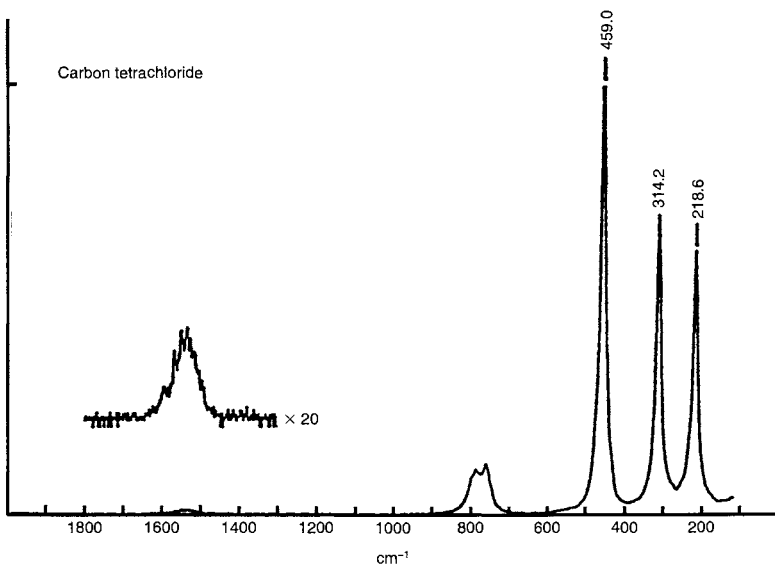
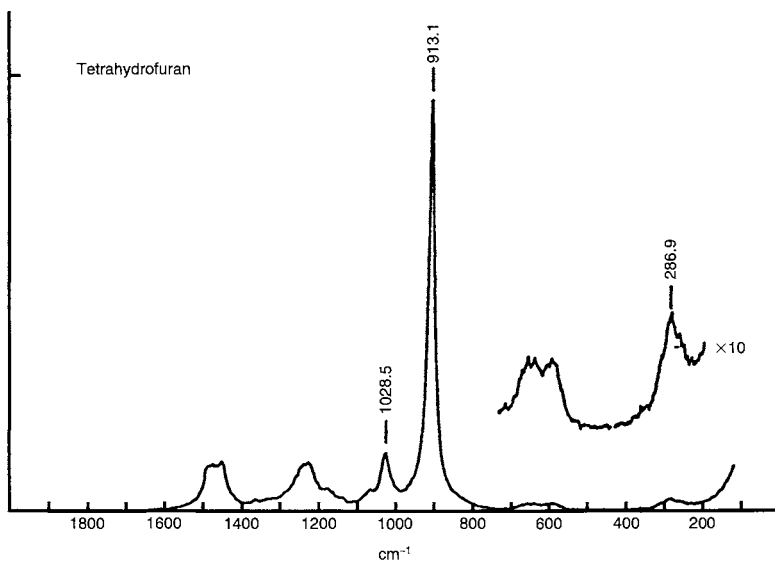


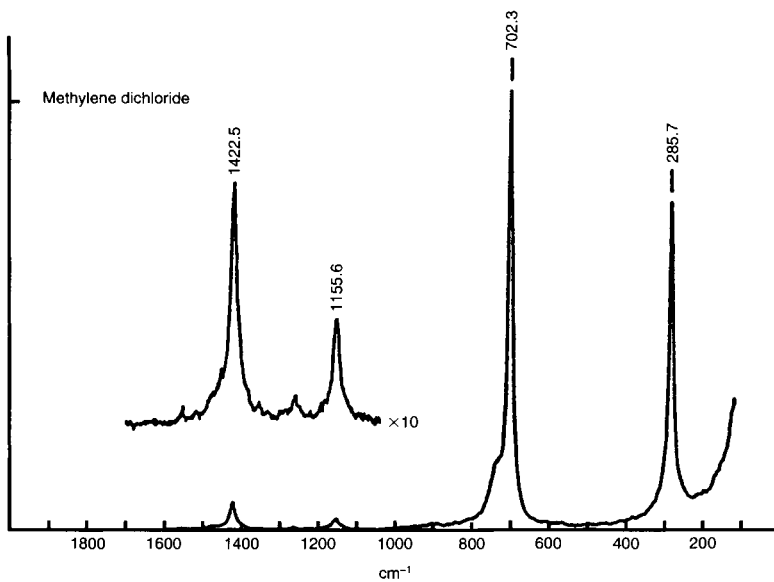
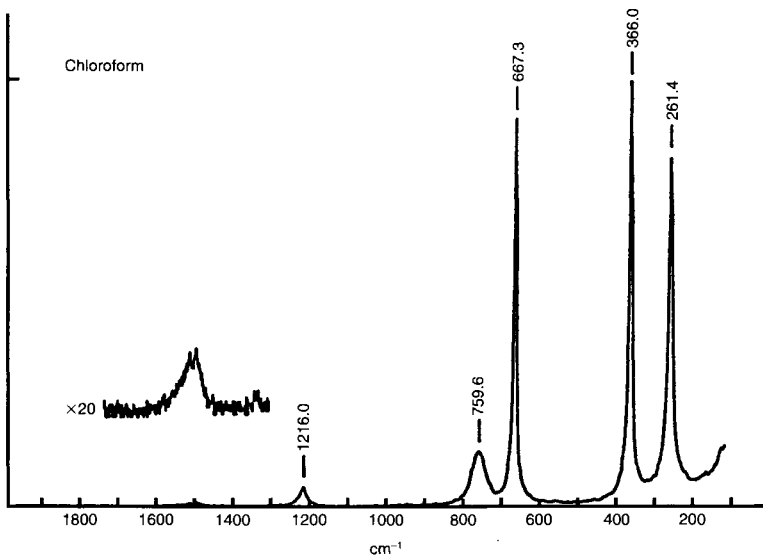


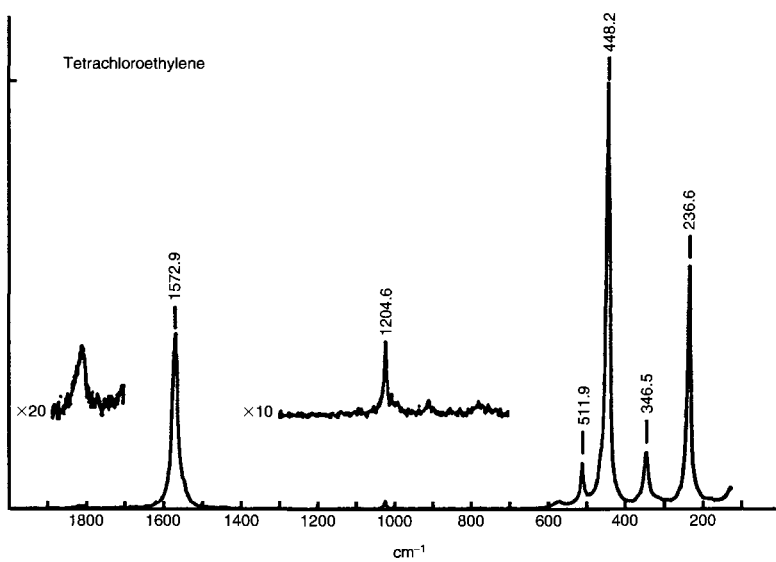
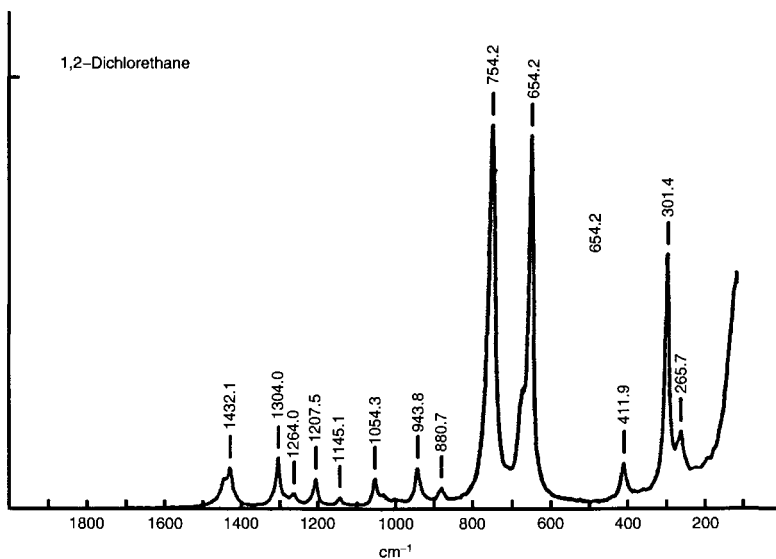


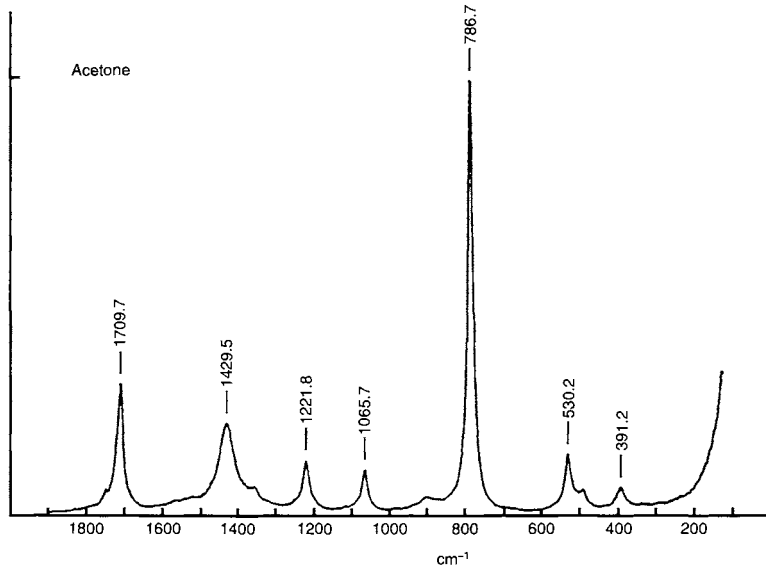
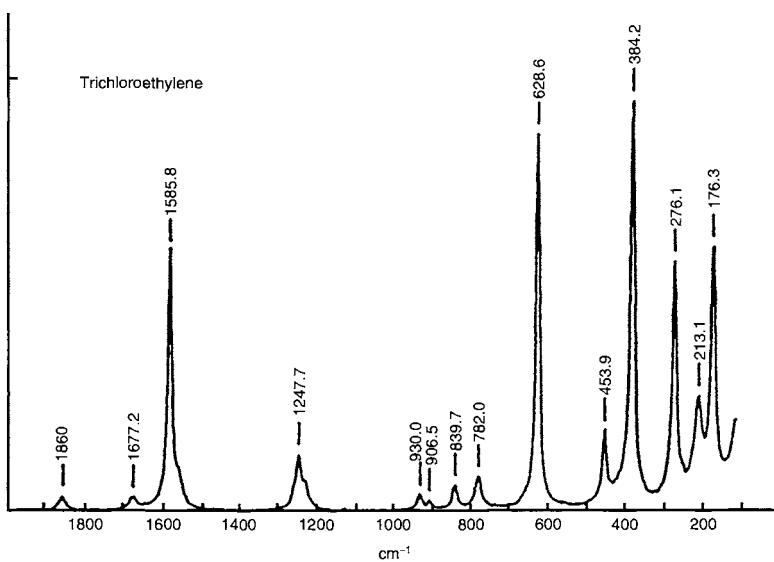


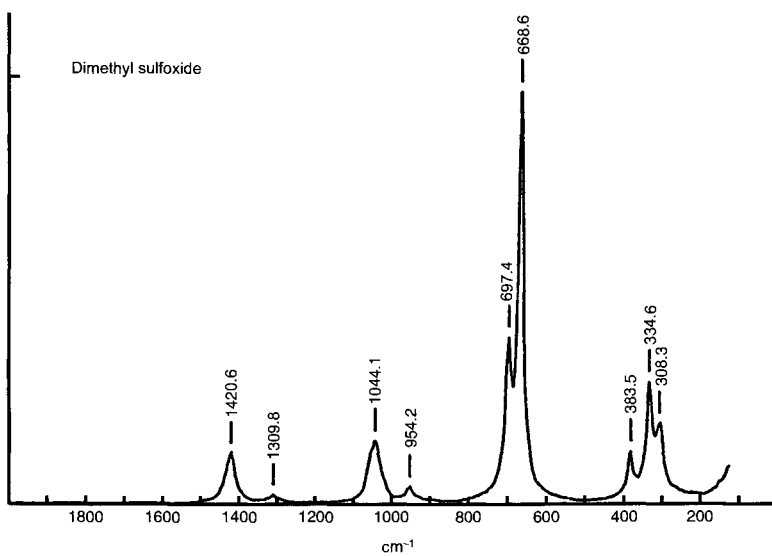
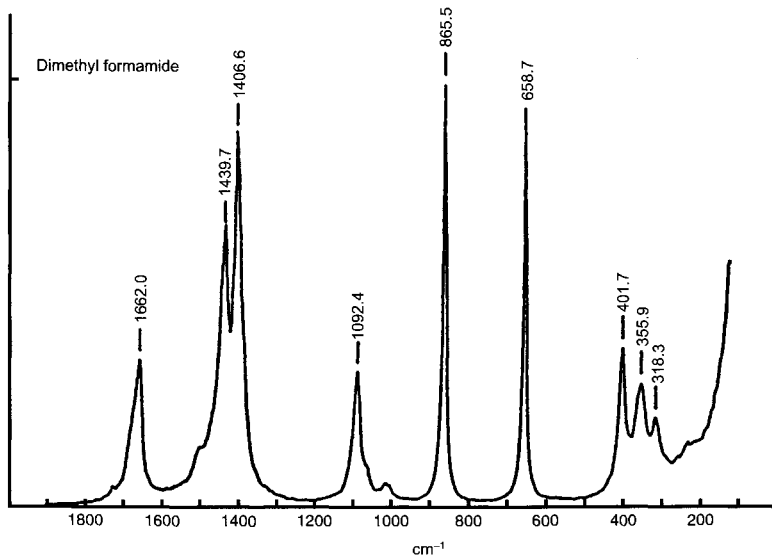


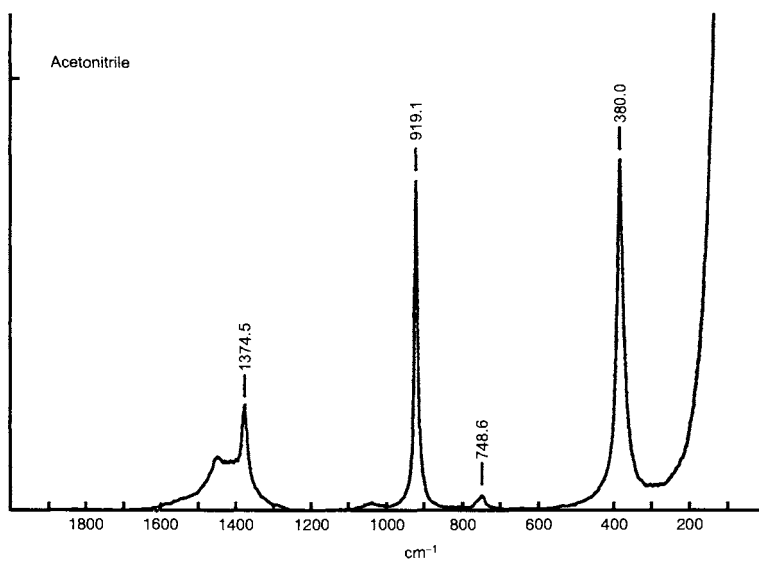
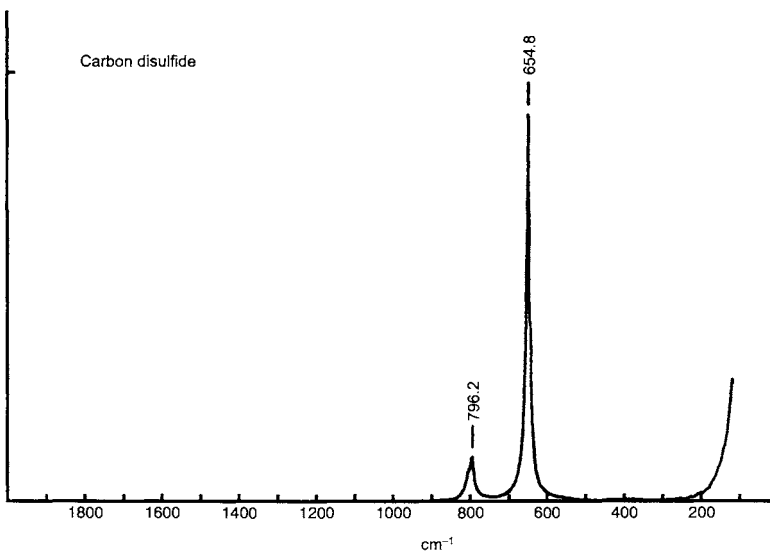


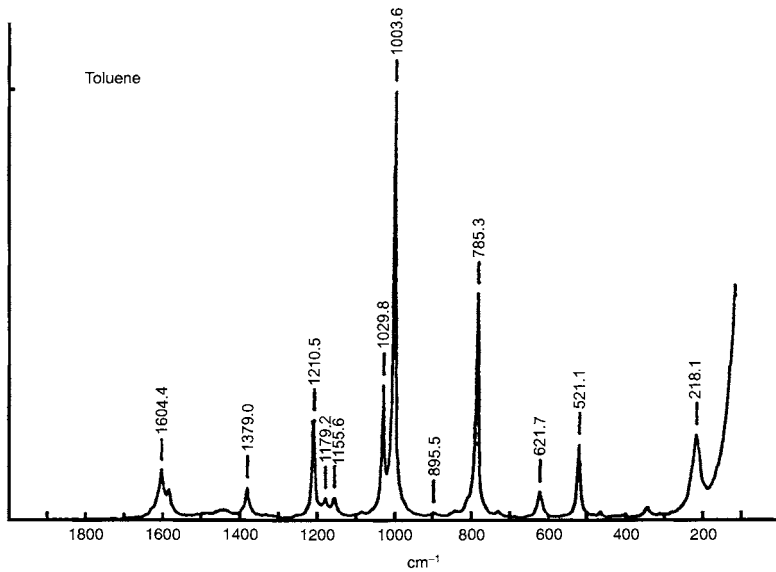
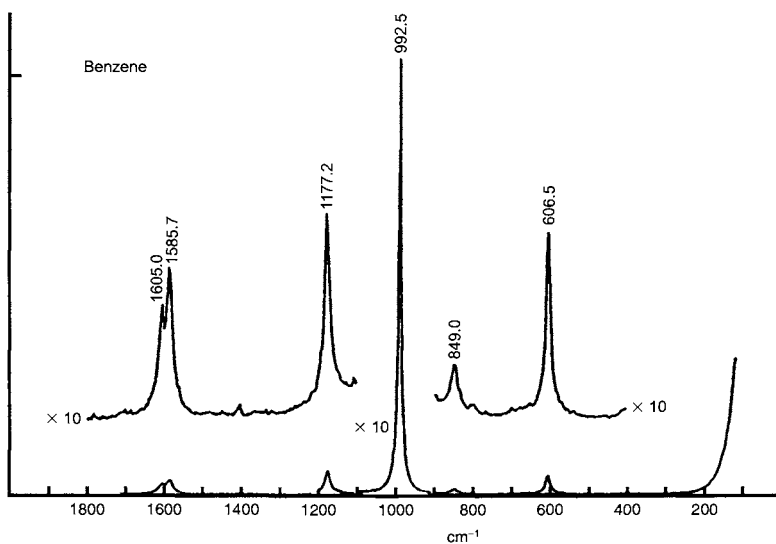












Index

- Acoustic branch, 68
- Acoustic optical tunable filters (AOTF), 189–191
- Analytical applications, 267
 - discriminant analysis, 288–292
 - preprocessing for, 267–277
 - processing methods for, 277–282
 - quantitative analysis, 283–285
 - spectral searches, 285–287
- Anharmonic oscillator, 11
- Anomalous polarization, 29
- Anti-Stokes lines, 15
- Backscattering geometry, 135–136
- Band assignments, 86–88
- Baseline flattening, 274–275
- Biochemical applications, 157, 166, 296–313
 - bacteria, 309–313
 - cytochrome and peroxidases, 301–304
 - drug-DNA interactions, 306–309
 - drugs, 350, 354–358
 - hemoglobin and myoglobin, 296–300
 - nonheme proteins, 304–306
 - plants, 309–311
- Black spruce, 342
- Bravais lattice, 63, 66
- Brillouin zone, 68, 70
- Buckminster fullerenes, 255–258
 - salts of, 257, 258

- Calibration (instrument), 117–123
 - frequency, 117–120
 - intensity, 120–123
- Cancer, diagnosis of, 320–321
- Carbon nanotubes, 258
- Center of symmetry, 34
- Ceramic superconductors, 260–263
- Character tables, 43–46, 364–370
- Charge-coupled device (CCD), 115–116
- Chemometrics, 267
- Cluster analysis, 288
- Coherent anti-Stokes Raman spectroscopy (CARS), 199–200
- Colinearity, 278
- Colored compounds, sampling techniques for, 130–133
- Colorless compounds, sampling techniques for, 127–130
- Comparison, IR vs. Raman, 26–27
- Confocal microscope, 160–161
- Correlation method, 72–78
- Correlation tables, 74–78, 390–401
- Crystal systems, 63
- CW gas lasers, 97–99
- Dark current, 114
- Data processing methodologies, 267
 - baseline flattening, 274–275
 - derivatives, 270–272
 - normalization, 272–274
 - partial least squares (PLS), 281–283
 - principal component regression (PCR), 278–281
 - smoothing spectra, 268–270
 - spectral subtraction, 276–277
 - standard normal variance, 273–274
- Davydov splitting, 77
- Depolarization ratio, 27–30
- Depolarized band, 29
- Detectors, 112–117
- Diatom molecules
 - energy levels of, 7
 - vibration of, 7–13
- Difference spectroscopy, 138–139, 233–234
- Diode lasers, 100–102
- Discriminant analysis, 288–292
- Dispersive Raman spectroscopy, 106–107
- Dissociation energy, 11, 19
- DNA, 219–221
 - interactions with drugs, 306–309

- Drug-DNA interactions, 306–309
Dye lasers, 102–103
- Electromagnetic spectrum, 6
Energy units, 2–6
Environmental applications, 345
 aqueous pollutants, 345–348
 fresh water and seawater analysis, 345–358
 ground water analysis, 342–345
 pesticides, 164, 348–350, 351
 water contaminants, 164, 345–348
- Excimer lasers, 102, 176
- Excitation profiles, 122–123, 172
- Excitation sources, 96–97
- F-matrix, 83–84
- Factor group, 66, 70–72
- Factor-group symmetry, 239
- Fiber optic interfaces, 123–124
- Fiber optics, 123–127
- Filters, 111
 AOTF, 189–191
 LCTF, 189–190
- Fluorescence, 16, 27
 issues of, 107–108, 137
- Force constant, 18, 79, 85–86
- Forensic analysis, 350
- Franck-Condon overlap, 56–57
- Frequency, 3–4
- Fresh water analysis, 345–350
- FT-Raman, 107–112
 microscopy, 158–160
 spectroscopy, 107–112
- Full spectrum processing methods, 277–282
- G-matrix, 84, 85
- Gallstones, 316–319
- Gases, sampling techniques for, 128, 132
- Generalized valence force field (GVFF), 83
- Glass inclusions, 157–158
- Glide plane, 61–62
- Gradient refractive index (GRIN), 124
- Ground water analysis, 342–345
- Halford-Honig method, 70, 72–78
- Hard wood, 342
- Harmonic oscillator, 9–12

- Heisenberg uncertainty principle, 11
- Hemoglobin, 296–300
- Hermann-Mauguin nomenclature, 34, 64
- Herzberg formulas, 50–51, 371–375
- High-pressure Raman spectroscopy, 147–154
 - applications of, 151–153
 - instrumentation for, 148–150
 - principles of, 148
- High-temperature cells, 134
- Historical background, 1–2
 - detectors, 2
 - instrumentation, 1–2
 - optical systems, 2
- Holograph notch filters, 111
- Human lenses, 314–316
- Hydrogen, metallization of, 153–154
- Hydrogen Raman shifter, 103
- Hyper Raman effect, 195–197
- Identity, 31–32
- Illegal drugs, 350
- Illumination, sample, 103–105
- Image slice, 188
- Industrial applications, 325
 - chemical processes, 124–125
 - dyes, 331–332
 - food, 328–330
 - lumber/paper, 342
 - metal corrosion, 332–334
 - ores, 339–342
 - paints, 325–327
 - petroleum, 334–339
 - silicon contaminants, 156
- Instrumentation, 95
 - backscattering, 135–136
 - CCD, 115–116
 - detection, 112–117
 - difference spectroscopy, 138–139
 - fiber optic, 123–127
 - Ge, 117
 - high pressure studies, 147–153
 - InGaAs, 117
 - InSb, 117
 - monochromator, 106–107
 - Nd:YAG, 99, 117
 - photodiode array, 115
 - photon counting, 113–115

- platinum silicide, 117
- sampling techniques, 123–135
- silicon-InGaAs, 117
- special cells, 133–135
- Instrument calibration, 117–123
 - for frequency, 117–120
 - for intensity, 120–123
- indene, 118
- internal standard, 118
- laser plasma lines, 118–119
- Ne emission lines, 119–120, 120–121
- Intermolecular interactions, 233–236
- Internal coordinates, 79, 81
- Internal vibrations, 70
- Inverse polarization, 29, 61
- Inverse Raman effect, 199
- Irreducible representations, 43–46
 - direct products, 376–377
 - linear molecules, 47
 - molecules of high symmetry, 48
 - nonlinear molecules, 46–47
- Isotope shifts, band assignments, 86–89
- Kinetic energy, representation of, 84
- Laser photolysis, 221–225
- Lasers
 - characteristics of, 176
 - CW gas, 97–99
 - diode, 100–102
 - dye, 102–103
 - excimer, 102, 176
 - Nd:YAG, 99, 117, 176
 - nitrogen, 103
 - tunable, 102
- Lattice, external, 70
- Lattice vibrations, 68–70
 - acoustic, 68, 70
 - internal, 70
 - librations, 70
 - optical, 68, 70
 - phonons, 70
 - rotations, 70
 - translations, 70
- Liquid crystal tunable filters (LCTF), 189–190
- Liquids, sampling techniques for, 128, 130–131

- Loading spectra, 278
- Low-temperature cells, 134–135
- Lumber/paper industry, 342
- Mahalanobis distance (MD), 288–289
- Mass effects, 18
- Matrix-isolation Raman spectroscopy, 179
 - applications of, 182–184
 - instrumentation for, 181–182
 - principles of, 179–181
- Maxwell-Boltzmann distribution law, 12, 16
- Mean centering, 285
- Mechanism of spectral activity, 13–17
 - IR, 14, 15
 - Raman, 14, 15
- Medical applications, 126–127, 157, 313
 - diagnostic, 320–322
 - gallstones, 316–319
 - ophthalmic, 314–316
 - skin, hair, and nails, 314
- Metal refining industry, 339–342
- Miniature Raman spectrometers, 140–143
- Miscellaneous applications
 - glass inclusions, 157–158
 - natural gas, 350–354
 - polymers, 358–361
- Molecular structure, 208
 - iron-porphyrin, 214–217
 - M–M bonds, 225–228
 - nucleic acid, 219–221
 - peptides and proteins, 217–219
 - structure determination, 208–214
 - structure-sensitive vibrations, 214–221
 - unstable species, 221–225
 - vibrations of large amplitudes, 228–232
- Monochromators, 106–107
- Morse potential, 11
- Mutual exclusion principle, 25
- Myoglobin, 296–300
- Natural gas industry, 350–354
- Nd:YAG lasers, 99, 117, 176
- Nitrogen lasers, 103
- Nonlinear Raman spectroscopy, 194–202
- Normal coordinate analysis, 79
 - internal coordinates, 79

- F-matrix, 83
- G-matrix, 84
 - symmetry coordinates, 81
- Normal modes, 19, 21
- Normal vibrations, 19
 - classification by symmetry, 48, 371–375
 - in crystals, 67–70
- Normalization, 272–274
- Ophthalmic applications, 314–316
- Optical branch, 68
- Ores, 339–342
- Organic superconductors, 258–260
- Organophosphorus pesticides, 164, 348–350
- Outliers, 285
- Partial least squares (PLS), 281–283
- Peroxidase, 301–304
- Pesticides, 164, 348–350, 351
- Pharmaceutical industry, 354–358
- Phase transitions, 151, 244–248
- Phonon modes, 70
- Photoacoustic Raman spectroscopy (PARS), 200–202
- Photodiode array detection, 115
- Photon counting, 113–115
- Planes of symmetry, 32–34
- PLS method, 284
- Point groups, 35, 36–37
 - classification rules, 35–42
- Point symmetry, 31
- Polarizability, 15, 23
 - single crystal, 78, 79
- Polarizability ellipsoid, 23–24
- Polarization, 23
- Polarized band, 28
- Pollutants
 - dissolved, 345–348
 - pesticides, 164, 348–350, 351
- Polymer manufacture, 358–361
- Polymorphs, 239–244
- Potential energy, representation of, 83
- Preresonance, 17
- Pressure calibration, 148
- Pressure studies, 147–154
 - instrumentation for, 148–150
 - phase transitions, 151–153

- Pressure studies (*continued*)
metallization of hydrogen, 153–154
solid coordination compounds, 152–153
- Primitive unit cell, 64
- Principal component analysis (PCA), 278–280
- Principal component regression (PCR), 278–281
- Quantitative analysis, 283–285
- Raman difference spectroscopy, 138–139, 233–234
- Raman effects
normal, 16
preresonance, 17
resonance, 16, 54–61
stimulated, 197–199
- Raman imaging spectrometry, 188
applications of, 192–193
instrumentation for, 188–192
principles of, 188
- Raman mapping, 160–161
- Raman microscopy, 154, 316, 320
- Raman scattering, 15–16
resonance, 17, 56
- Raman spectra, 406–421
derivative, 270–282
excited states, 225–227
normalization of, 272–277
origin of, 13–17
S/N ratio in, 268
typical solvents, 406–421
- Raman spectroelectrochemistry, 168
applications of, 170–174
instrumentation for, 168–170
- Rayleigh scattering, 14
- Readout noise, 116
- Representations, 43
irreducible, 43–48
reducible, 43–45
- Resonance Raman scattering, 17, 54
- Respiratory proteins, 304–306
- Rotation axes, 32
- Rotation reflection axes, 34–35
- Ruby calibration method, 148, 149
- Sample illumination, 103–105
- Sampling techniques, 123–137

- Savitsky-Golay method, 268–269
Schoenflies nomenclature, 34
Schrödinger equation, 10
Score plots, 288–292
Screw axis, 30, 61
Seawater analysis, 345–348
Selection rules
 IR, 22–25, 52–54
 Raman, 22–25, 52–54
SERS, 161–163, 236–238
 applications of, 164–168
 biological molecules, 166
 catalysis, 166
 electrochemical processes, 166–168
 instrumentation for, 163–164
 principles of, 163
Silicon, contaminants in, 156
Site correlation, 390–401
Site group, 66
Site symmetry, 378–383
 choice of, 70–72
Smoothing spectra, 268–270
Solid state applications, 237–238
 ceramic superconductors, 260–263
 compressibilities, 253–254
 coordination compounds, pressure studies of, 152–153
 C-T organic superconductors, 258–260
 electric conductors, 254
 fullerenes, 255–258
 nonstoichiometry, 248–250
 phase transitions, 244–248
 polymorphs, 239–244
 sampling techniques for, 129–130, 131–132
 solid solutions, 250–253
 solid(s), 70–78
 solutions, 250–253
Soret bands, 58
Space group symmetry, 70–72
 distribution, 63
 factor group, 66, 70–72
 glide plane, 61–62
 screw axis, 61
 site group, 66
 symbolism, 64
Space-filling requirement, 35
Special cells, 133–135

- Special techniques, 147
 - CARS, 199–200
 - FT-Raman microscopy, 158–160
 - high pressure, 147–153
 - matrix isolation, 179–184
 - nonlinear Raman spectroscopy, 194–200
 - PARS, 200–202
 - Raman imaging spectrometry, 188–194
 - Raman mapping, 160–161
 - Raman microscopy, 154–158
 - SERRS, 164, 236
 - SERS, 161–168, 236–238
 - time-resolved spectroscopy, 174, 300
 - 2D correlation Raman spectroscopy, 184–188
- Spectral region, 6
- Spectral searches, 285–287
- Spectral subtraction, 276–277
- Standard normal variance (SNV), 273–274
- Stimulated Raman effect, 197–199
- Stokes lines, 15
- Structural chemistry applications, 207
 - donor-acceptor, 233–234
 - intermolecular interactions, 233
 - iron-porphyrin, 214–217
 - M-M bonds, 225–228
 - molecular orientation, 236–237
 - molecular structure, 208–214
 - nucleic acid, 219–221
 - peptides and proteins, 217–219
 - solute-solvent, 234–236
 - structure determination, 208–214
 - structure-sensitive vibrations, 214–221
 - unstable species, 221–225
 - vibrations of large amplitudes, 228–232
- Superconductors, 257
 - ceramic, 260–263
 - organic, 258–260
- Surface mapping, 160–161
- Surface scanning, 132–133
- Symmetry, 30–31
 - center, 34
 - identity, 31–32
 - planes of, 32–34
 - rotation, 32
 - rotation-reflection, 34

- Symmetry coordinates, 81–82
- Symmetry selection rule, 52–54, 208–214
- Temperature measurements, 136–137
- Thermostated cells, 133
- Time-domain spectroscopy, 109
- Time-resolved Raman spectroscopy, 174, 300
 - applications of, 177–179
 - instrumentation for, 176–177
 - principles of, 174–175
- Tunable lasers, 102
- 2D correlation Raman spectroscopy, 184–188
 - applications of, 186–188
 - principles of, 184–185
- Unit cell, 61, 65, 70, 72
 - body-centered, 65
 - choice of site symmetry, 70, 72
 - face-centered, 65
 - primitive, 64, 65
 - rhombohedral, 65
 - side-centered, 65
- UV resonance cells, 135
- UV resonance Raman (UVRR), 219, 221, 309–310, 312
- Variance scaling, 285
- Vibrational quantum number, 10
- Vibrations
 - acoustic, 68, 70
 - classification by symmetry, 48–51
 - coupled, 88
 - in crystals, 67–70
 - in diatomic molecules, 7–13
 - in polyatomic molecules, 19–21
 - internal, 48–51, 70
 - lattice, 67–70
 - librations, 70
 - of large amplitude, 228–232
 - optical, 68, 70
 - rotations, 70
 - translations, 70
- Vibronic coupling operator, 58
- Wave motion, 69–70
- Wavelength, 3

- Wavelength selectors, 105–112
Wavenumber, 3–4
 corrected for anharmonicity, 11
Wave vector, 67
Wyckoff tables, use of, 70–72, 384–389
- Zirconia calibration method, 149



9 780122541056

ISBN 0-12-254105-7